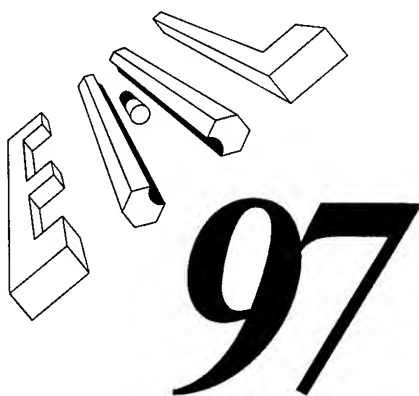


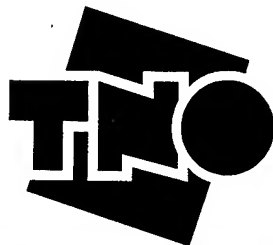
6TH EUROPEAN SYMPOSIUM ON ELECTROMAGNETIC LAUNCH TECHNOLOGY

THE HAGUE, 25 - 28 MAY, 1997



# PROCEEDINGS

ORGANISED BY  
TNO PML-PULSE PHYSICS LABORATORY  
DELFT, THE NETHERLANDS



**DISTRIBUTION STATEMENT A**

Approved for public release  
Distribution Unlimited

# REPORT DOCUMENTATION PAGE

Form Approved OMB No. 0704-0188

Public reporting burden for this collection of information is estimated to average 1 hour per response, including the time for reviewing instructions, searching existing data sources, gathering and maintaining the data needed, and completing and reviewing the collection of information. Send comments regarding this burden estimate or any other aspect of this collection of information, including suggestions for reducing this burden to Washington Headquarters Services, Directorate for Information Operations and Reports, 1215 Jefferson Davis Highway, Suite 1204, Arlington, VA 22202-4302, and to the Office of Management and Budget, Paperwork Reduction Project (0704-0188), Washington, DC 20503.

|  |   |  |  |  |
|--|---|--|--|--|
| 1. AGENCY USE ONLY (Leave blank)   |   | 2. REPORT DATE<br><br>3 June 1997                              | 3. REPORT TYPE AND DATES COVERED<br><br>Conference Proceedings       |  |
| 4. TITLE AND SUBTITLE<br><br>6th European Symposium on Electromagnetic Launch Technology   |   |  | 5. FUNDING NUMBERS<br><br>F6170897W0050                              |  |
| 6. AUTHOR(S)<br><br>Conference Committee   |   |  |  |  |
| 7. PERFORMING ORGANIZATION NAME(S) AND ADDRESS(ES)<br><br>TNO Prins Maurits Laboratory, Pulsed Physics Laboratory<br>Schoemakerstraat 97<br>Delft 2628 VK<br>Netherlands   |   |  | 8. PERFORMING ORGANIZATION<br>REPORT NUMBER<br><br>N/A               |  |
| 9. SPONSORING/MONITORING AGENCY NAME(S) AND ADDRESS(ES)<br><br>EOARD<br>PSC 802 BOX 14<br>FPO 09499-0200   |   |  | 10. SPONSORING/MONITORING<br>AGENCY REPORT NUMBER<br><br>CSP 97-1019 |  |
| 11. SUPPLEMENTARY NOTES  |   |  |  |  |
| 12a. DISTRIBUTION/AVAILABILITY STATEMENT<br><br>Approved for public release; distribution is unlimited.  |   |  | 12b. DISTRIBUTION CODE<br><br>A                                      |  |
| 13. ABSTRACT (Maximum 200 words)<br><br>The Final Proceedings for 6th European Symposium on Electromagnetic Launch Technology, 25 May 1997 - 28 May 1997<br><br>The Topics covered include: Pulsed power supplies, accelerators and projectiles and systems. |   |  |  |  |
| 14. SUBJECT TERMS<br><br>Electromagnetics, Pulsed Power  |   |  | 15. NUMBER OF PAGES<br><br>487                                       |  |
|  |   |  | 16. PRICE CODE<br>N/A  |  |
| 17. SECURITY CLASSIFICATION<br>OF REPORT<br><br>UNCLASSIFIED   | 18. SECURITY CLASSIFICATION<br>OF THIS PAGE<br><br>UNCLASSIFIED | 19. SECURITY CLASSIFICATION<br>OF ABSTRACT<br><br>UNCLASSIFIED | 20. LIMITATION OF ABSTRACT<br><br>UL                                 |  |

**DTIC QUALITY INSPECTED 4**

NSN 7540-01-280-5500

Standard Form 298 (Rev. 2-89)  
Prescribed by ANSI Std. Z39-18  
298-102



**6th European Symposium on Electromagnetic Launch Technology**

**The Hague, 25 - 28 May, 1997**



**P R O C E E D I N G S**

---

ORGANISED BY  
TNO PML-PULSE PHYSICS LABORATORY  
DELFT, THE NETHERLANDS

19970715 197

## 6th European Symposium on Electromagnetic Launch Technology

---

| CONTENT  | Section | Page      |
|--|---------|-----------|
| Technical Programme                                | 1       | 1 - 5     |
| Authors Index                                      | 2       | 6 - 7     |
| General: Welcome Address                           | 3       | 8 - 12    |
| Pulsed Power Supplies: oral presentations          | 4       | 13 - 56   |
| Pulsed Power Supplies: poster presentations        | 5       | 57 - 101  |
| Accelerators and Projectiles: oral presentations   | 6       | 102 - 245 |
| Accelerators and Projectiles: poster presentations | 7       | 246 - 452 |
| Systems: oral presentations                        | 8       | 453 - 482 |
| Systems: poster presentations                      | 9       | -----     |
| List of participants                               | 10      | 483 - 487 |

---

*Notepaper: at the end of the book*

---

### Acknowledgement

*We wish to thank the following for their contribution to the success of this conference:*

United States Air Force European Office of Aerospace Research and Development - EOARD.

## Technical Programme

**Monday, 26 May, 1997**

# = PAGE NUMBER PROCEEDINGS

□ = POSTER NUMBER

### **Theme: General**

- 09.00 - 09.20 Welcome and Opening Address  
# 8 Dr. Willem J. Kolkert, TNO PML - Pulse Physics Laboratory, Delft, The Netherlands  
**Progress in Electromagnetic Launch Technology**
- 09.20 - 09.50 Keynote Address  
Mr. E.A. van Hoek, MSc, Ministry of Defence, Director Scientific Research and Development, The Netherlands  
**The Electron, a Force to be Reckoned with**

### **Theme: Pulsed Power Supplies**

- Chairman Prof. J. Schot
- 10.00 - 10.20 **Pulsed Power Supply Technologies for All Electric Vehicle Integration**  
# 13 *H.G. Wisken, Th.H.G.G. Weise*
- 10.20 - 10.40 **Magnetohydrodynamic (MHD) Generators**  
# 19 *I.R. McNab*
- 10.40 - 11.20 COFFEE BREAK & POSTER PRESENTATIONS
- # 57 **300 kA Test Results of the 1 MA Resonant Series Counterpulse Opening Switch System**  
□ 1 *E. Van Dijk, P. Van Gelder*
- # 65 **Estimation of Compression Pulsed Generator Range of Application Limits for Current Supply with Inductive Load**  
□ 2 *V.T. Chemerys*
- # 77 **Capacitor Free Self-Excitation of Brushless Compulsator**  
□ 3 *V.T. Chemerys, I.S. Petuhov*
- # 86 **The Analysis of Linear Magnetic Flux Compressor Pulse Power Supplies**  
□ 4 *A.P. Glinov, A.E. Poltanov, A.K. Kondratenko, V.N. Ryndin, G.I. Simonova*
- # 94 **Superconducting Inductive Pulsed Power Supply for Electromagnetic Launchers: Experimental Investigation of Laboratory Set-up and Design Aspects for Further Development**  
□ 5 *W. Weck, P. Ehrhart, M. Heeg, A. Müller, E. Sturm, H. Schölderle, G. Reiner*
- 11.20 - 11.40 **High Action Switching for Next Generation Multi-megajoule Power Conditioning System**  
# 28 *H. Singh, D. Eccleshall, J. Creedon, T. Burke, T. Podlesak, I. McNab, J. Pappas, J. Sarjeant*
- 11.40 - 12.00 **All Film Energy Storage Capacitors**  
# 36 *M. Bramoullé*
- 12.00 - 12.20 **Low Weight and Size Pulse Forming Unit, Switched by a Novel High Current Rate SCR**  
# 42 *E. Spahn, G. Buderer, E. Ramezani*
- 12.20 - 12.40 **Recent Developments in Bipolar Lead-Acid Battery Technology at TNO**  
# 50 *P. Van Gelder, M. Wollersheim, B. Mosterdijk, W. De Jong*

Monday, 26 May, 1997

---

**Theme: Accelerators and Projectiles**

Chairman Mr. D. C. Haugh

14.00 - 14.20 **Rail Launcher with Contact-Studs to Accelerate Long-Rod Projectiles**  
# 102 *P. Lehmann, F. Jamet, V. Wegner, A.-G. Schmitt*

14.20 - 14.40 **On Electromagnetic 3-Dimensional Effects in Square-bore and Round-bore Rail Accelerators**  
# 109 *A.J. Schoolderman*

14.40 - 15.00 **High-current Arc Erosion of Explosively Compacted Mo/Cu and W/Cu Electrodes**  
# 117 *G.A. Shvetsov, V.I. Maly, A.G. Anisimov, S.V. Stankevich, A.V. Solovov, T.S. Teslenko*

15.00 - 16.00 COFFEE BREAK & POSTER PRESENTATIONS

# 246 **Advanced Low Cost Rails and Armatures for Rail Launchers**  
☐ 6 *R.A. Marshall*

# 253 **Effects of the Initial Conditions on the Results of Launch Experiments with Fibre Armatures**  
☐ 7 *W. Karthaus, M. Koops, T. Huijser*

# 261 **Electrothermal Acceleration of Microparticles**  
☐ 8 *E.Ya. Shcolnikov, I.L. Kolensky, S.P. Maslennikov, A.V. Melnik, N.N. Nechaev, A.V. Chebotarev, S.M. Bakhrakh, S.P. Egorshin, A.N. Tarasova, S.A. Shaverdov*

# 269 **The Angle Point and Velocity Skin-Effect Roles at Different Stages of Electromagnetic Launch**  
☐ 9 *V.V. Savitchev, M.P. Galanin*

# 277 **The Analysis of Contact Surfaces Melting Process at Solid Armature Launching**  
☐ 10 *M.P. Galanin, A.D. Lebedev, V.V. Savitchev, B.A. Uryukov*

# 285 **Numerical Simulation of Mechanical Effects in Composite Sabots for Railguns by the Finite Element Method**  
☐ 11 *C. Müller*

# 293 **Experimental Study of the Current Distribution in a Multi-Armature Projectile**  
☐ 12 *A.-G. Schmitt, R. Charon, F. Hatterer, J. Wey, D. Eckenfels*

# 301 **Metallurgical Examination of 90mm Armatures Recovered after Firing**  
☐ 13 *D.G. Jones, G.M.G. Hainsworth*

# 306 **Systematic Analysis of Various Electrodes in a Railgun Accelerator with a Linear Current Density of  $j \sim 500$  kA/cm**  
☐ 14 *A.P. Lototsky, A.D. Lebedev, Yu.A. Halimullin*

16.00 - 16.30 Panel Discussion  
**Near term development issues of Pulsed Power Supplies and their impact on systems.**  
Moderator: Dr. Willem J. Kolkert  
Panel Members: Mr. Frantz Caillaud, Dr. I.R. McNab, Dr. V. Wegner, Dr. H. Wisken

**Tuesday, 27 May, 1997**

---

**Theme: Accelerators and Projectiles**

Chairman Dr. Th. Weise

09.00 - 09.20 **On Scaling Relations for Hypervelocity Electromagnetic Launch Processes**  
# 124 *M. Koops, A.J. Schoolderman*

09.20 - 09.40 **Apparent Enhanced Burn Rates of Solid Propellants due to Plasmas**  
# 134 *C.R. Woodley, S. Fuller*

09.40 - 10.00 **A Civilian Application of Coil Launchers Technology-Elevators for High-Rise Buildings**  
# 142 *Z. Zabar, E. Levi, L. Birenbaum*

10.00 - 10.20 **Physics of Plasma-Fluid Interaction - Key to a Complete Numerical Model of the ET-Gun**  
# 150 *K. Darée, D. Hensel, K. Zimmermann*

10.20 - 11.20 COFFEE BREAK & POSTER PRESENTATIONS

# 314 **Metal Projectile Acceleration in Muzzle-Fed Railgun**  
☐ 15 *Yu.A. Halimullin, Yu.A. Kareev, A.P. Lototsky*

# 322 **Re-establishing of a Compact Structure of a Plasma Armature in a Barrel of a Railgun**  
☐ 16 *A.P. Lototsky, L.G. Kotova, Yu.A. Halimullin*

# 330 **Pellet Injector with the Liner Compression of the Propellant Gas**  
☐ 17 *Yu.A. Kareev, V.P. Bazilevski, A.I. Kolchenko, V.P. Novikov*

# 335 **Mathematical Simulation of Projectile Free Motion in Coil Gun without Mechanical Leading Elements**  
☐ 18 *V.T. Chemerys, Y.N. Vaskovsky, L.N. Dynnik*

# 343 **Current Distribution in the Contact Zone of Railgun**  
☐ 19 *V.T. Chemerys, Y.N. Vaskovsky*

# 353 **Influence of the Temperature Dependence of the Yield Point of Rail Materials on the Kinematic Characteristic of Railguns**  
☐ 20 *V.P. Chistyakov*

# 358 **ETC Launcher Experiments at Seoul National University**  
☐ 21 *K.H. Paek, S.T. Kim, H.J. Kwon, K.H. Chung, K.W. Whang, K.J. Chung*

# 363 **Low Power Electrothermal Enhancements to the Modular Propelling Charge System**  
☐ 22 *S.R. Fuller, G.F. Savell*

# 371 **Experimental Observation of the Rail Resistance Contribution to Muzzle Voltage**  
☐ 23 *J.V. Parker*

# 379 **Calculation of Plasma Radiation for the Simulation of Plasma Ignition and Combustion in ETC-Guns**  
☐ 24 *K. Kappen, U.H. Bauder*

Chairman Prof. Dr. W. Rutgers

11.20 - 11.40 **40mm Armature Development at the Defence Research Agency**  
# 157 *D.C. Haugh*

11.40 - 12.00 **3D Softly Coupled Electromagnetic/Thermal/Structural Analysis Using MEGA-DYNA3D**  
# 165 *C. Leyden, R. Critchley, J.A. Downey*

12.00 - 12.20 **Factors Influencing Choice of Bore Geometry for Rail Launchers**  
# 170 *R.A. Marshall*

**Tuesday, 27 May, 1997**

---

- 12.20 - 12.40    **Three Simplified Approaches to Investigation of High-Current Sliding Contact in the Rail Launcher**  
# 178                    *V.T. Chemerys*
- 12.40 - 14.00    LUNCH
- Chairman        Dr. W.J. Kolkert
- 14.00 - 14.30    **Invited Speaker**  
# 188                    ICA C. Cannavó, DGA , France  
**Last Results of Trilateral Cooperation France-Germany-Netherlands**
- 14.40 - 15.00    **Experiments with Brush Armatures**  
# 194                    *H. Peter, R. Charon*
- 15.00 - 15.20    **Experiments to Measure Gouging Threshold Velocity for Various Metals Against Copper**  
# 202                    *F. Stefani, J.V. Parker*
- 15.20 - 15.40    **About Localization of Electrical Current in Sliding Metal Contact**  
# 209                    *A.P. Glinov, V.A. Frolov, M.A. Bykov, B.S. Schastnykh, A.K. Kondratenko, A.E. Poltanov*
- 15.40 -16.20    COFFEE BREAK & POSTER PRESENTATIONS
- # 385                    **Rail Accelerator Control Using Spline-Algorithms for Launch Velocity Stabilization**  
☐ 25                    *V.A. Alexandrov, I.B. Azanov, M.M. Khrustalev, S.S. Obyedennikov, N.I. Pipin, V.K. Tyutin, V.I. Yudas*
- # 392                    **Preliminary Results of Experimentally Validated Applied Electromagnetic Issues of Railguns**  
☐ 26                    *W.J. Sarjeant, I. Kohlberg, C. Le, R. Zowarka*
- # 400                    **Model and Numerical Simulation of Lightweight Projectiles Acceleration Process in Electrothermal Launchers with Ablative and Non-Ablative Barrels**  
☐ 27                    *D. Zoler*
- # 408                    **Method of Analysis of Propelling Gas in Electrothermal Launcher**  
☐ 28                    *A.M. Voronov, Th.H.G.G. Weise*
- # 414                    **ETC-Technologies - Categories, Physical Principles and Interior Ballistic Performances**  
☐ 29                    *Th.H.G.G. Weise, H.-K. Haak*
- # 422                    **Electromagnetic Limits to the Performance and Efficiency of Rail Launchers**  
☐ 30                    *T.E. James*
- # 430                    **Numerical Simulation of Electrothermal Accelerators**  
☐ 31                    *K. Gruber, U.H. Bauder*
- 16.20 - 16.40    **Investigation of Transverse Striations on Aluminum Rails**  
# 217                    *L.C. Woods, A. Yeoh*
- 16.40 - 17.00    **Investigation of the Metal Contact Crisis in a Railgun with Sectioned Rails**  
# 224                    *Yu.A. Kareev, L.G. Kotova, A.T. Kuharenko, Yu.A. Halimullin*
- 17.00 - 17.30    **Panel Discussion**  
**Near term development issues of Accelerators and Projectiles and their impact on systems**  
Moderator: Dr. F. Jamet  
Panel Members: Mr. D. Ch. Haugh, Mr. W. Karthaus, Dr. J. Kruse, Mrs Dr. P. Lehmann

**Wednesday, 28 May, 1997**

---

**Theme: Accelerators and Projectiles**

Chairman Mr W. Karthaus

09.00 - 09.20 **Numerical Modelling of the Internal Ballistics of an Electrothermal Launcher**  
# 230 *Y. Jordan, J-M. Lombard, Fr. Caillau, O. Vallée*

09.20 - 09.40 **Defence Research Agency 90mm Projectile Launches at the Green Farm Electric**  
withdrawn **Armament R&D Facility**  
*T. Wolfe, P. Riedy, F. LeVine, D. Lewis, D. Haugh*

09.40 - 10.00 **Investigation of the Performance of Rail Conductor Materials**  
# 237 *Ch. Persad, Sh. Phillips, J. Stolk, A. Yeoh, Z. Eliezer*

10.00 - 10.50 COFFEE BREAK & POSTER PRESENTATIONS

# 435 **A Generalized Goodness Factor Criterion Applied to Advanced Rotating Electrical**  
☐ 32 **Machines for Hypervelocity Accelerators?**  
*M.D. Driga*

# 445 **Preliminary Findings on Magnetic Shielding Effectiveness for Electromagnetic (EM)**  
☐ 33 **Railgun Applications**  
*C. Le, A. Zielinski*

**Theme: Systems**

Chairman Dr. F. Jamet

10.50 - 11.20 **Invited Speaker**  
Dr. H.D. Fair, Director of the Institute for Advanced Technology, The University of Texas at  
Austin , USA  
# 453 **Electromagnetic Launch Technology: A Review of the U.S. National Program**

11.20 - 12.00 **Potentiality of Electric Guns in the Field of Land Armaments**  
# 461 *Fr. Caillau, Th. Vaillant*

12.00 - 12.20 **Weapon Charging Effects on Land Vehicle Mobility with Shared Prime Power**  
# 469 *S. Fish, B. Barth, T. Savoie*

12.20 - 12.40 **Magnetodynamic Storage as a Main Storage in a Diesel-electric Main Battle Tank**  
# 475 *G. Reiner, P. Ehrhart, M. Heeg, A.M. Jean-Jacques, W. Weck*

12.40 - 13.00 AWARDS AND CLOSING REMARKS

## AUTHORS INDEX

---

- ALEXANDROV, V.A., 385  
ANISIMOV, A.G., 117  
AZANOV, I.B., 385  
BAKHRAKH, S.M., 261  
BARTH, B., 469  
BAUDER, U.H., 379, 430  
BAZILEVSKI, V.P., 330  
BIRENBAUM, L., 142  
BRAMOULLÉ, M., 36  
BUDERER, G., 42  
BURKE, T., 28  
BYKOV, M.A., 209  
CAILLAU, Fr., 230, 461  
CANNAVÓ, C., 188  
CHARON, R., 194, 293  
CHEBOTAREV, A.V., 261  
CHEMERYS, V.T., 65, 77, 178, 335, 343  
CHISTYAKOV, V.P., 353  
CHUNG, K.H., 358  
CHUNG, K.J., 358  
CREEDON, J., 28  
CRITCHLEY, R., 165  
DARÉE, K., 150  
DE JONG, W., 50  
DOWNEY, J.A., 165  
DRIGA, M.D., 435  
DYNNIK, L.N., 335  
ECCLESHALL, D., 28  
ECKENFELS, D., 293  
EGORSHIN, S.P., 261  
EHRHART, P., 94, 475  
ELIEZER, Z., 237  
FAIR, H.D., 453  
FISH, S., 469  
FROL'TSOV, V.A., 209  
FULLER, S.R., 134, 363  
GALANIN, M.P., 269, 277  
GLINOV, A.P., 86, 209  
GRUBER, K., 430  
HAAK, H.-K., 414  
HAINSWORTH, G.M.G., 301  
HALIMULLIN, Yu.A., 224, 306, 314, 322  
HATTERER, F., 293  
HAUGH, D.C., 157  
HEEG, M., 94, 475  
HENSEL, D., 150  
HUIJSER, T., 253  
JAMES, T.E., 422  
JAMET, F., 102  
JEAN-JACQUES, A.M., 475  
JONES, D.G., 301  
JORDAN, Y., 230  
KAPPEN, K., 379  
KAREEV, Yu.A., 224, 314, 330  
KARTHAUS, W., 253  
KHRUSTALEV, M.M., 385  
KIM, S.T., 358  
KOHLEBERG, I., 392  
KOLCHENKO, A.I., 330  
KOLENSKY, I.L., 261  
KOLKERT, W.J., 8  
KONDRATENKO, A.K., 86, 209  
KOOPS, M., 124, 253  
KOTOVA, L.G., 224, 322  
KUHAARENKO, A.T., 224  
KWON, H.J., 358  
LE, C., 392, 445  
LEBEDEV, A.D., 277, 306  
LEHMANN, P., 102  
LEVI, E., 142  
LEYDEN, C., 165  
LOMBARD, J.-M., 230  
LOTOTSKY, A.P., 306, 314, 322  
MALY, V.I., 117  
MARSHALL, R.A., 170, 246  
MASLENNIKOV, S.P., 261  
MCNAB, I.R., 19, 28  
MELNIK, A.V., 261  
MOSTERDIJK, B., 50  
MÜLLER, A., 94  
MÜLLER, C., 285  
NECHAEV, N.N., 261  
NOVIKOV, V.P., 330  
OBYDENNIKOV, S.S., 385  
PAEK, K.H., 358  
PAPPAS, J., 28  
PARKER, J.V., 202, 371  
PERSAD, Ch., 237  
PETER, H., 194  
PETUHOV, I.S., 77  
PHILLIPS, Sh., 237  
PIPIN, N.I., 385  
PODLESK, T., 28  
POLTANOV, A.E., 86, 209  
RAMEZANI, E., 42  
REINER, G., 94, 475  
RYNDIN, V.N., 86  
SARJEANT, W.J., 28, 392  
SAVELL, G.F., 363  
SAVITCHEV, V.V., 269, 277  
SAVOIE, T., 469  
SCHASTNYKH, B.S., 209  
SCHMITT, A.-G., 102, 293  
SCHÖLDERLE, H., 94  
SCHOOLDERMAN, A.J., 109, 124  
SHAVERDOV, S.A., 261



## AUTHORS INDEX

---

SHCOLNIKOV, E.Ya., 261  
SHVETSOV, G.A., 117  
SIMONOVA, G.I., 86  
SINGH, H., 28  
SOLOVOV, A.V., 117  
SPAHN, E., 42  
STANKEVICH, S.V., 117  
STEFANI, F., 202  
STOLK, J., 237  
STURM, E., 94  
TARASOVA, A.N., 261  
TESLENKO, T.S., 117  
TYUTIN, V.K., 385  
URYUKOV, B.A., 277  
VAILLANT, Th., 461  
VALLÉE, O., 230  
VAN DIJK, E., 57  
VAN GELDER, P., 50, 57  
VASKOVSKY, Y.N., 335, 343  
VORONOV, A.M., 408  
WECK, W., 94, 475  
WEGNER, V., 102  
WEISE, Th.H.G.G., 13, 408, 414  
WEY, J., 293  
WHANG, K.W., 358  
WISKEN, H.G., 13  
WOLLERSHEIM, M., 50  
WOODLEY, C.R., 134  
WOODS, L.C., 217  
YEOH, A., 217, 237  
YUDAS, V.I., 385  
ZABAR, Z., 142  
ZIELINSKI, A., 445  
ZIMMERMANN, K., 150  
ZOLER, D., 400  
ZWORKA, R., 392

## **WELCOME AND OPENING ADDRESS**

Dr. Willem J. Kolkert  
Manager, TNO PML-Pulse Physics Laboratory

### **Progress in Electromagnetic Launch Technology**

Studies of electromagnetic and related launch concepts and their weapon carriers were initiated in Europe in the early eighties.

Since then both the scientific and technical progress achieved in this new defence research area and the dramatic change in political and strategic military circumstances have created new ways of thinking with respect to fighting land, air and sea battles.

Increased requirements placed on amongst others system effectiveness, maintainability, operability, on multi-role usability and survivability have led to weapon system concepts where only one type of energy carrier is being used for performing the different functions, i.e. propulsion/traction, protection and fire power. This creates a distinct advantage for operations in vastly different and remote areas. What is meant here is the concept of an "All electric combat vehicle", an "All electric ship" and a "More electric fighter plane".

This sketches the background of the prosperous growth of the European EML Society (EEMLS) which was founded at Delft in 1988 and which has been organising annual Topical Meetings and bi-annual European Symposia since then.

On behalf of the Organising Committee of European Symposia on EML Technology, it is my pleasure, ladies and gentlemen, to welcome you here in the Hague, as attendees of the 6th European Symposium on EML Technology, which is hosted by TNO and organised under the auspices of the EEMLS.

This symposium is the principal forum in 1997 for the exchange of information on electric energy launch technology amongst scientist, engineers, industrialists and users. Topics which are discussed include electrically driven launchers and weapons, hypervelocity projectiles, energy generation, storage, conditioning and pulse forming, numerical simulation, materials, diagnostics and weapon system studies. Representatives of more than eleven nations will present some 65 papers in oral and poster sessions. For the first time the Organising Committee installed a Paper Selection and Review Committee who did an excellent job in reviewing the selected technical papers which you may find in your personal proceedings. Their efforts are highly appreciated.

Next to the general introductory theme, the symposium programme covers three themes, i.e. pulsed power supplies, accelerators and projectiles and systems, which are covered in sessions. They are organised to maximise the exchange of information and give attendees the opportunity to focus on the theme of their interest. Both the first and second symposium day are finalised with a panel discussion on the potential of the technologies presented under a theme.

We are honoured to have Mr E.A. van Hoek, Director Scientific Research and Development of the Netherlands MoD, as our distinguished keynote speaker. Both Dr. Harry Fair, director of the IAT, Texas, USA and ICA C. Cannavó, DGA, French MoD are our invited speakers and will brief us respectively on the status of the US programme on electric energy weapon technology and the trilateral French, German, Netherlands programme on electric energy gun technology.

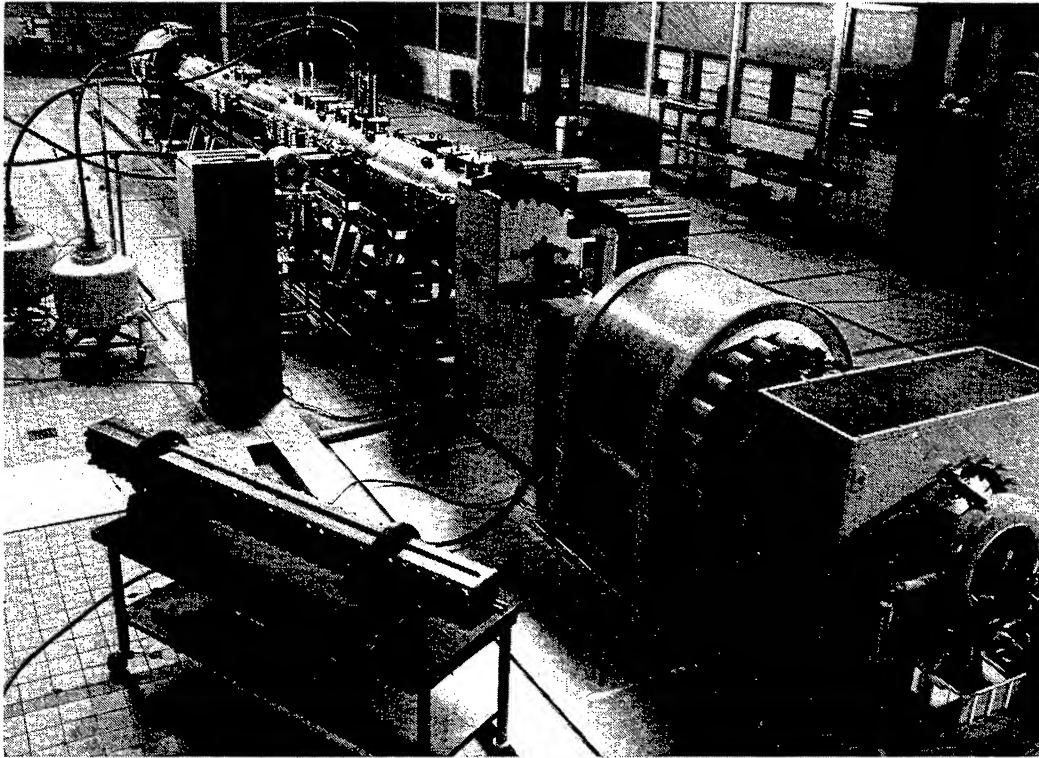
This year also highlights a decade of intensive and prosperous cooperation between the Netherlands and the USA concerning Electromagnetic Launch Technology. After establishing the Pulse Physics Laboratory at Delft in 1986, TNO in joint projects with BMDO and US Army ARDEC, has developed many new concepts and solved scientific and technical aspects of rail accelerators, armatures, fast discharge batteries and very high current semiconductor opening switches, successfully.

This collaboration resulted in many articles and reports and in PhD and master degrees of students from technical universities and colleges, Royal Naval Academy and Royal Military Academy.

Next to the United States, Europe has developed a substantial infrastructure and international network to elaborate EML technology. New initiatives concern the EUCLID-CEPA 16 programme on 'Electrical Energy Technology', the NATO long term scientific studies on "Pulsed Power Systems", "Mobile Electric Weapon Platform" and the still to start "All Electric Ship" study. In the Netherlands a 50M\$ programme on "an all electric demo ship" has been formulated. Together with the US several international conferences on the subjects mentioned have been organised.

Besides military applications (i.e. real time adaptable, higher muzzle velocity (2 to 4 km/s) and/or longer range (5-80 km) weapons) the spectrum of potential applications of electric energy launch systems include aircraft and satellite launch, the acceleration of materials to very high velocities for equation of state or impact physics studies and cancer treatment. As the technology continues to mature, the envisioned applications are beginning to be actively pursued, and although much technical progress has been achieved, thresholds remain to be taken, particularly for the successful applications to light-weight weapon system.

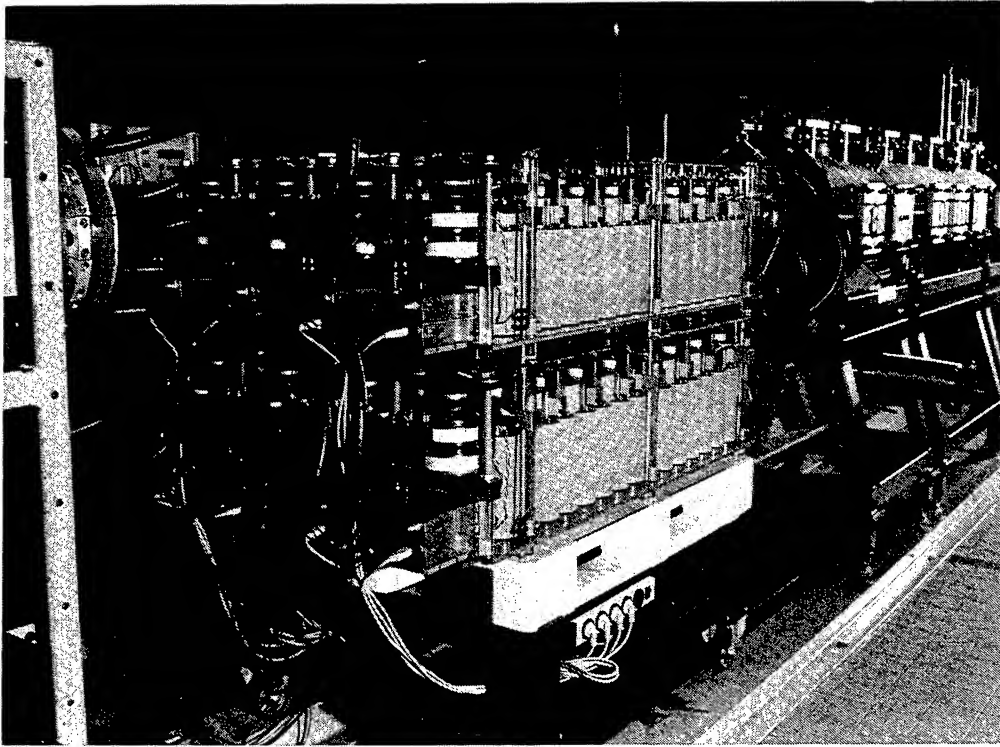
The understanding of the physics and chemistry of electrically driven plasma accelerators is growing while a valuable data set of parameters determining the complex interior ballistic cycle of electrothermal (chemical) gun concepts has been established. Present interest concerns large calibre applications for which new energetic working fluids are under investigation. They concern more phases, multi-component solids, slurries/gels and liquids. Physical modelling and numerical simulations focus these days on the phenomena occurring in the SPETC (Solid Propellant Electro Thermal Chemical) and in the ET gun concept. Next to an increase in muzzle velocity major advances have been achieved in modelling leading to a significantly improved control of the launch cycle and reduction of instabilities.



*Advanced repetitive 6.7 MJ electromagnetic launch system at TNO PML-Pulse Physics Laboratory*

As reflected in the papers presented at this symposium electromagnetic rail launchers continue to dominate as the type of launcher most frequently investigated. We have seen a dramatic change in the way armature performance has been perceived. The scene has changed from solely research on plasma armatures to research on promising fibre (brush) armatures these days. The potential of saboted, multi-segmented armatures of different materials and assembled in different geometry's is being explored at different institutes. The pioneering work and the excellent results obtained at the Pulse Physics Laboratory are well-known in this respect. In several research projects, large calibre armatures are being developed and evaluated at Mega-Ampere, Mega Joule scale.

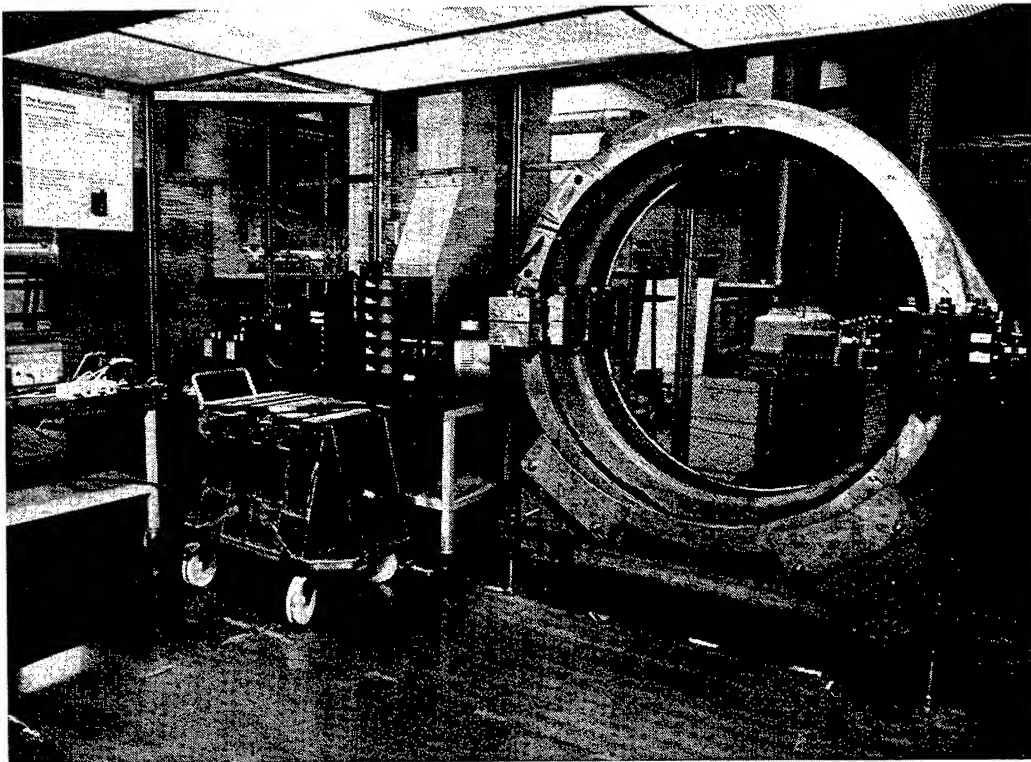
Rail accelerators constructed from composite and ceramic materials with weights and stiffness comparable to conventional gun barrels are now being used. Designs with an improved specific inductance have been manufactured. Physical models developed make it possible to analyse in 3D the mechanical, thermal and electromagnetic aspects of the acceleration process in a rail gun. Unfortunately, the full spectrum of physical processes in armatures which are in motion and at their interface with stationary rails cannot be modelled, yet. This delays progress in optimising arc-erosion-free rail guns for e.g. air defence gun weapon systems.



*400 kA, series resonant counter pulse semiconductor opening switch*

Despite their intrinsic high efficiency electromagnetic coil guns continue to be pursued on a modest scale, as technological and engineering difficulties still have to be solved. The most significant challenge for the development and application of electric energy launch technology still is the availability of compact pulsed power supplies. Most promising these days are the compulsator and the fast discharge bipolar battery combined with an inductor/pulse transformer.

Although progress has been achieved in increasing energy and power density of capacitors, flywheels and superconducting inductors, their weight and volume still exceed the requirements. The technical challenge is there and routes are being found to overcome difficulties as highlighted in papers concerning semiconductor switch technology, all-film storage capacitors, high pulsed current bipolar batteries, SMES and rotating machines.



*100kJ, 250 kA bipolar battery based pulsed power supply*

Electric energy launch technology continues to proceed gradually and the many issues to be discussed and shared justify to have symposia like this.

It is therefore highly appreciated that both TNO and the United States Air Force European Office of Research and Development support this event.

I wish you some stimulating days where collaboration and mutual support can be established and were the social events strengthen our interactions.

---



## The Electron, .. a Power to be reckoned with

97

Keynote address for the 6 th symposium on  
EML Technology

by Ernst A. van Hoek, Director Research and Development  
MoD, the Netherlands



## The Physics

97

- The Title ? Non-sense ?
- The clean concept of EM
- from Newton to Maxwell
- to Lorentz and Einstein
- the attractiveness



## The History

- Early attempts
- Star Wars
- Technology explosion



## Promises and Problems

- Controllable / high muzzle velocity :  
 $E = 1/2 m.v^2$
- Practical difficulties
  - power generation
  - power switching
  - transfer





## Recent EML work

97

- SDIO and BMDI
- European
  - ISL + NL
  - UK
- Rest of the World



## Current Perspectives

97

- US
  - Defense Science & Technology Strategy
  - Basic Research Plan
  - Defense Technology Objectives
  - ETC more than EML
- Europe ?



## Wider perspectives

97

- The planning horizon
- The relative ETC success
- other competitors: RAMjets
- Wider EM applications



## Future EM world

97

- Direct Energy
- High Power Microwave
- EM armour
- EM and micron technology, or  
EM versus micron technology ?



## The All Electric World

97

- Electric Ships
- Electric (land) vehicles
- The information age
- EM and EO



## Future Road

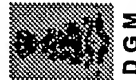
97

- A knowledge based world
  - Maintain know how
  - Follow Techno Development, Relevancy
  - Threat evolution
- Combined, Multidisciplinary approaches
- Cooperation and broad horizon



## Future Road (2)

- US
  - continue knowledge build up
  - Modest experimentation
- Europe
  - EUCLID -- new CEPA ?
  - ISL +
  - maintain basic know how
- A Trans-Atlantic challenge ?
  - NATO RTO / RTA opportunities ?
  - Opportunities with Partners ? !



## Conclusions

- Progress is not easy
  - does not come automatically
- All electric approaches are IN
- Consider EM in wider perspective
- Cooperate

# Pulsed Power Supply Technologies for All electric vehicle Integration

H.G. Wisken, TH.G.G. Weise

TZN Forschungs- und Entwicklungszentrum Unterlüß GmbH  
Neuensothriether Str. 20, 29345 Unterlüß  
Federal Republic of Germany

**Abstract—** Pure electric gun technologies, i.e. railguns and electrothermal guns are investigated up to a progressed technical status. These types of guns require several ten megajoules of electrical energy for each shot in an anti-armour vehicle application.

The existing gap of about one order of magnitude between existing and required status of the energy density of pulsed power supply systems for these electric gun applications is an ongoing technical challenge. A solution of this problem in the near term future cannot be identified.

Nevertheless, the existing gap between the performance of conventional gun technologies and modern armour plating technologies require urgent measures to realize a significant performance increase of anti-armour barrel weapons. Due to their reduced electrical energy requirement Electrothermal Chemical Gun Technologies are of increasing interest for the realization of a near term performance upgrade of anti-armour as well as anti-air weapon systems.

The paper gives an overview on various levels of ETC-Technologies. The electric energy requirements for these ETC levels are introduced and different pulsed power supply system concepts are presented and analysed. Some selected solutions are evaluated in detail and the design concepts based on existing component technologies are presented.

## I Introduction

Until 1989 many investigations have been performed in Germany in order to identify the advantages of electrothermal guns [1,2]. In comparison to conventional guns it has been demonstrated successfully that with pure electrothermal guns (calibre 45 mm / calibre 105 mm) muzzle velocity can be increased up to 2300-2400 m/s. The conducted pulse power systems for these experiments mostly needed a huge volume and have a "laboratory status" [1,3].

The next step for the long term future is the integration of electric gun systems into vehicles. Therefore, it is necessary to develop a combined system of a compact power supply in combination with an improved electric gun. It seems that new technologies of ETC-gun systems can meet these basic requirements. First demonstrations are performed with a compact 1/4 MJ Pulse Forming Network (PFN) for ETC guns [4]. These investigations demonstrate that today energy densities of 1.2 MJ/m<sup>3</sup> for repetitive fired PFNs can be realized.

## II Classification of ETC-Technology

ETC-Technology can be separated in different ETC-mechanisms. Figure 1 gives a schematic overview about a possible classification of ETC - Technologies in four categories due to their electric energy requirements. Depending on the used ETC mechanism the energy varies from 75 kJ to 5 MJ (Type A-D). In order to complete the classification the category of an electrothermal gun (Type E) is also shown.

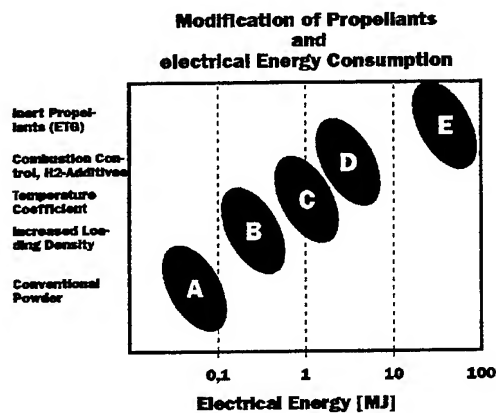


Figure 1: Classification of ETC-Technologies

The method, function and advantage of each ETC-Gun Type (A to D) is presented and described in detail in [5].

Table 1 shows the expected major interior ballistic influence of different categories of ETC systems.

The necessary stored electrical energy of ETC-Technology is directly related to the expected increase of muzzle energy  $W_o$  and muzzle velocity  $v_o$ . Every ETC-category needs an adjusted pulse power supply system that additionally has to fulfill the requirements of system integration and operative boundary conditions. These boundary conditions influences directly the layout of the pulsed power supply.

| Type | Measure                                       | $W_o$ | $v_o$ |
|------|---|-------|-------|
| A    | electrical Ignition                           |       |       |
| B    | electrical controlled Ignition                | ++    | +     |
| C    | electrical Control of Temperature Coefficient | ++    | +     |
| D    | electrical Combustion Control, H2 Generation  | ++    | ++    |
| E    | electrical Conversion of inert Propellant     | ++    | +++   |

Table 1:Interior Ballistic Influence

## III Boundary conditions for an ETC-gun in an all electric vehicle

The following boundary conditions were assumed for an 120 mm ETC-gun application in an all electric vehicle (AEV):

|   |        |
|---|--------|
| Calibre of the ETC gun  | 120 mm |
| Repetition Rate   | 5 s    |
| Number of shots in sequence                                       | 10     |
| Time between a sequence   | 1 min  |
| Charging Time for the PPS   | 3 s    |
| Maximum continuous power of the generator for ETC-gun application | 500 kW |
| (not for electrical wheel drive)                                  |        |

Furthermore it is assumed that there are restrictions in volume and mass for the Pulsed Power Supplies (PPS). Integration conditions in an all electric vehicle allows only a few cubic metres of volume and a few tons of weight.

These assumed boundary conditions can be modified in a wide range. The following layouts of the PPS are not totally completed in detail for system integration but the results are a good valuation.

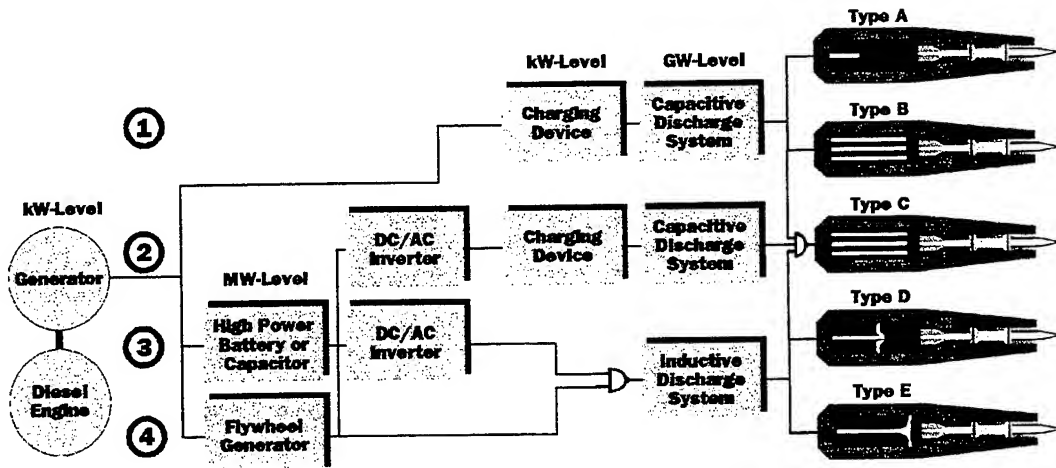


Figure 2: Pulsed power supply technologies and requirements for ETC-Guns in all electric vehicles

#### IV Pulse Power Supply Technologies for ETC-Technology

Figure 2 shows the structure of different PPS technologies for ETC applications taking the boundary conditions under account. Every ETC-type (A to E) needs a specially adjusted power supply. It is assumed that new technologies can be used for pulse power systems. As reported in [6, 7] these new technologies are investigated, i.e. high power batteries or capacitors, flywheel generators, capacitive and inductive storages.

The electrical energy is generated via a generator that is connected with the primary energy source, for example a

diesel engine. The maximum power feeding continuously the PPS via generator was assumed to be 500 kW.

Figure 2 shows 4 different structures of power supply systems. Structure 1 is directly connected with the generator via a charging device and a capacitive discharging system. The electric power of the generator is high enough to charge the capacitive discharge system between two shots in sequence. The structures 2, 3 and 4 need an additional intermediate storage between generator and the capacitive or inductive discharge system. Such an additional storage provides the average electric power for the number of shots for one sequence. Depending on the

| Parameter           | Type A       | Type B       | Type C       | Type D               | Type E               |
|---------------------|--------------|--------------|--------------|----------------------|----------------------|
| Stored Energy       | 75 kJ        | 300 kJ       | 900 kJ       | 2,5 MJ               | 70 MJ                |
| Charging Power      | 25 KW        | 100 KW       | 300 kW       | 830 kW               | 23 MW                |
| Charging Technology | Gen./Charger | Gen./Charger | Gen./Charger | Gen./FWG<br>Gen./HPB | Gen./FWG<br>Gen./HPB |
| PPS-Technology      | Capacitor    | Capacitor    | Capacitor    | Inductor             | Inductor             |
| Load Voltage        | 11 kV        |              |              |                      | 22 kV                |
| Pulsewidth          | 500 $\mu$ s  | 2 ms         | 4 ms         | 5,5 ms               | 5 ms                 |
| Pulseshape (Power)  |              |              |              |                      |                      |
| PPS-Modules         | 1            | 2+4 PFN      | 6            | 8                    | 1                    |

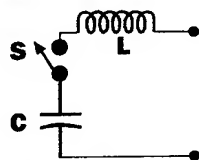
Table 2: Basic requirements for different ETC-Categories (120 mm gun)

integration conditions (Mass and Volume) the intermediate storage can be realised with a flywheel generator or high power batteries. If the pulsed power supply of an ETC-type, for example type D or E, needs a very high energy (near 5 MJ or more) superconducting energy supply can meet the requirements of system integration in future.

The basic requirements of pulsed power supply systems and their pulse shapes for different 120 mm ETC-guns are shown in table 2. Basic studies lead to this data which are today under investigation. It is assumed that the load voltage is constant during the discharge time and has the half value of the charging voltage.

ETC- type A needs a power supply with a stored energy of 75 kJ to generate a simple pulse shape with a duration of 500  $\mu$ s in order to ignite the gun powder in an effective way to reduce the jitter of primary ignition. Therefore the power supply can be connected directly to the generator.

#### ETC Type A pulse power supply circuit



**C:** Capacitor 75 kJ, 22kV  
**S:** High power switch  
**L:** Inductance

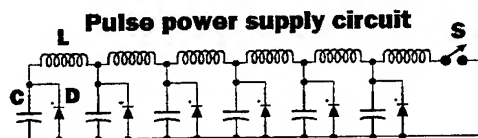
Figure 3: PPS for ETC Type A

Figure 3 shows a simple capacitive discharge system that can generate pulse shapes for ETC- type A. It consists of a simple LC-circuit and a high power switch.

ETC-type B needs a more complex

pulseshape with a duration of 2 ms (table 2). During the first 500  $\mu$ s the created pulse shape has the same form as ETC type A. After this time the electrical energy improves the burning rate and the generation of propellant gas. Therefore, an increased loading density can be used. The expected electrical stored energy for this application is 300 kJ for one shot. The average charging power is 100 kW. Therefore this discharge system can also be directly connected to the generator. The pulseshape of the electric discharge is more complex. It can be realized with a capacitive discharge system which is shown in figure 4.

#### ETC Type B



**S:** High power switch

**Six modules :**

**C:** Capacitor 50kJ, 22kV  
**D:** Crowbar Diode 22kV, 90 kA  
**L:** Inductance

Figure 4: PPS for ETC Type B

The circuit consists of a pulse forming network, based on six capacitors and inductances. Such a network can be built up in a modular form. The power supply for ETC-type C needs a pulseshape that is controlled during the discharging process to control the temperature coefficient of the powder charge. The expected stored electric energy is 900 kJ for this application. This results in an average charging power of 300 kW that can be fed by the generator. The electrical circuit is shown in Figure 5.



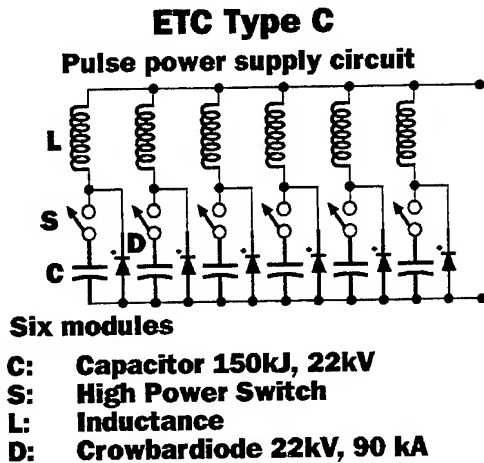


Figure 5: PPS for ETC Type C

It consists of a capacitive discharging system consisting of six equal modules. The modules can be discharged in a sequence. The goal is to generate an optimal electrical pulseshape for the production of propellant gases and to convert electrical energy for the ignition of chemical reactions.

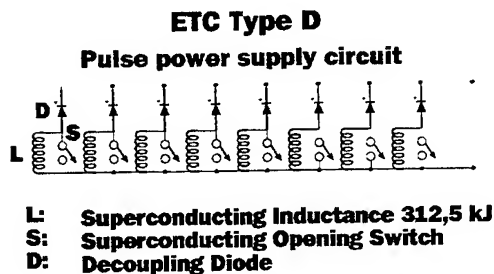


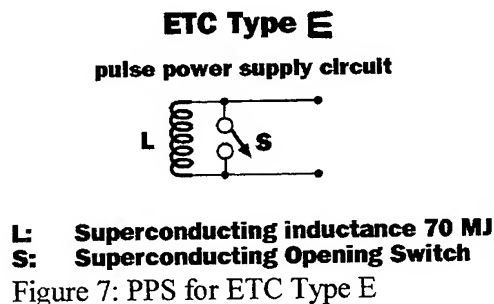
Figure 6: PPS for ETC Type D

The power supply for ETC-type D works in the same way as ETC type C. In comparison to type C it is expected that type D needs a longer pulse duration of 5,5 ms. Additional the stored energy is about 2,5 MJ that results in an average charging power of 830 kW. To meet the boundary requirements it is necessary to integrate an intermediate storage flywheel generator or a high power battery as shown in figure 2.

Figure 6 shows the electrical circuit. The circuit consists of 8 equal superconducting inductive discharge

circuits. Today this seems to be the solution for a power supply to meet in future the requirements of mass and volume. The pulseshape is generated by a controlled opening of each module with a superconducting opening switch. Superconducting technology for pulse power applications are investigated in a study by Magnet Motor [6].

ETC-type E is an electrothermal 120 mm gun that needs a power supply with a stored energy of 70 MJ. This results in an average charging power of 23 MW. That means an intermediate storage is necessary. The pulse shape requires a simple superconducting circuit which is shown in figure 7.



These basic considerations for an ETC-pulse power technologie in combination with pulse power supply systems demonstrate that in future it is possible to integrate ETC-Technology in all electric vehicles. The success of the ongoing studies will decide which ETC-application has the best chance to be realized.

## V Conclusion

This paper presents different combinations of ETC-gun types and their required pulse power supply systems. In comparison to pure ET-gun ETC-technologie needs a much smaller average electric power and electric energy. This reduces the mass and volume of the

pulsed power system.

Different ETC-technologies with their power supply systems are discussed under assumed boundary conditions. These basic considerations show that the necessary energy for ETC-pulse power systems is distributed and depends on the used ETC-category.

### References

- [1] Th. H.G.G. Weise, Recent Experimental Results obtained from 45mm ET-Gun investigations Proceedings 4th European Symposium on Electromagnetic Launch Technology, 1993, Celle
- [2] Th. H.G.G. Weise et al., Setup and Performance of a 105mm Electrothermal Gun, 8th Symposium on Electromagnetic Launch Conference, 1996, Baltimore
- [3] Th. H.G.G. Weise et al., Feuerstellung 2000: A 30MJ Electric Gun Facility, Proceedings of the 5th European Symposium on Electromagnetic Launch Technology, Toulouse, 1995
- [4] D. Bhasavamich et al., Demonstration of a Modular, Repetitive-Fired 1/4-MJ PFN for ETC Guns, 8th Symposium on Electromagnetic Launch Conference, 1996, Baltimore
- [5] Th. H.G.G. Weise, H.-K. Haak, ETC-Technologies categories, Physical Principles and Interior Ballistic Performances, Presented at the 6th EEML Symposium, 1997, Delft
- [6] M. Heeg et al., Set-Up of Magnetodynamic and superconducting Power Supplies for Electric Gun Applications, Proceedings 4th European Symposium on Electromagnetic Launch Technology, 1993, Celle
- [7] P. Kurzweil, O. Schmid, High performance metaloxide supercapacitors 6th International Seminar on doublelayer capacitors and similar energy storage devices, 9-11 Dec. 96, Deerfield Beach, Florida

# Magnetohydrodynamic (MHD) Generators

Ian R. McNab

Institute for Advanced Technology, The University of Texas at Austin  
4030-2 W. Braker Lane, Suite 200, Austin, Texas 78759-5329

**Abstract**—A brief overview of magnetohydrodynamic (MHD) generator technology is given. The fundamental physical principles are reviewed and the various generator geometries based on these principles are described. Reasons for interest in the technology are provided and the present status of development is discussed. An outline of recent Russian experiments in which an MHD generator has been used to power high velocity small bore electric railgun is given.

## I. INTRODUCTION

The objectives for this paper are to describe the fundamentals of MHD power generation, to overview the present state of the art, and to discuss possible application to electric guns.

## II. FUNDAMENTAL PHYSICS

A fundamental experimental observation shows that a material of length ( $L$ ) passing through a magnetic field ( $B$ ) at a velocity ( $u$ ) generates a voltage ( $V_{gen}$ ) given by:

$$V_{gen} = BLu. \quad (1)$$

The generated *voltage* is independent of the conductivity of the material; i.e., this expression is equally true for a poor conductor as well as for a good conductor. However, the *current* ( $I$ ) that flows into a circuit depends on the internal and external resistances ( $R_{int}$  and  $R_{ext}$ ) according to Ohm's law:

$$I = \frac{V_{gen}}{R_{int} + R_{ext}}. \quad (2)$$

Defining a load factor,  $K$ , as:

$$K = \frac{R_{ext}}{R_{int} + R_{ext}}, \quad (3)$$

the voltage across the load resistance can be expressed as:

$$V_L = KuBL. \quad (4)$$

As  $R_{int}$  becomes high,  $K$  and  $I \rightarrow 0$  even though  $R_{ext}$  is finite. Also,  $V_L \rightarrow 0$ , unless  $R_{ext}$  is correspondingly high. This applies to the voltage measuring device, which should therefore have a very high impedance to measure the generated voltage if the material conductivity is low.

For a useful generator, the voltage-generating material should be an electric conductor, such as a solid metal, liquid metal or ionized gas. If a liquid metal or ionized gas is used, it usually has to be constrained to flow through a duct or channel as it passes through a magnetic field. (Of course, this is not true in most natural and astrophysical interactions.)

For a conductivity,  $\sigma_e$ , the current density in the channel between the electrodes is:

$$J = \sigma_e uB(1 - K), \quad (5)$$

and the electric field in the channel is:

$$E = KuB. \quad (6)$$

Combining these gives the power density per unit volume for the MHD generator:

$$P = \sigma_e u^2 B^2 K(1 - K). \quad (7)$$

The power density is maximized when  $K = 0.5$  (for  $\sigma_e = 10$  siemens/m,  $u = 1000$  m/s, and  $B = 5$  T) and is  $62.5 \text{ MW/m}^3$ . Thus, for a 1 second pulse, the energy delivered from the MHD generator to the load would be  $62.5 \text{ MJ}$  per cubic meter of channel volume.

A significant potential advantage of the MHD generator is that no moving parts are intrinsically required to produce electricity — except the fluid itself — which replaces the metallic conductors in a high speed conventional generator. Of course, in practice, some auxiliaries may be necessary.

The basic MHD generator geometry is shown in Fig. 1 for a continuous electrode configuration. A single electrode at each of the top and bottom of the duct walls (an anode and a cathode) is used to extract the electrical energy from the gas and transfer it, via electrical leads, to the load.

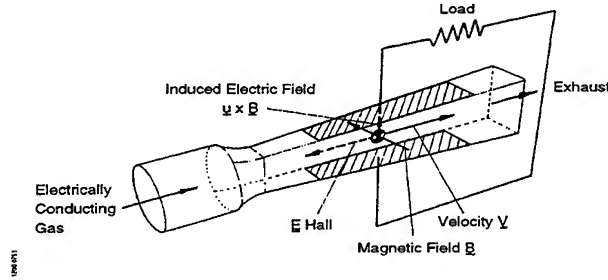


Fig. 1. Basic MHD generator geometry [1].

Unfortunately, in most cases the presence of the Hall effect complicates this simple picture. The Hall effect arises when a magnetic field is present. The magnetic field modifies electron motion in the conducting gas or plasma as it flows through the duct. Instead of traveling in a straight line determined by the electric field gradient, the path of an electron becomes an interrupted arc motion ("cycloidal") at an angle to the applied magnetic field. The resulting effect is that the plasma conductivity can be described as a tensor quantity. That is, application of an electric field in one direction causes a current to flow in a different direction. For a coordinate system aligned with the magnetic field, the angle between the electric field and current vectors is the Hall angle.

In a simple static medium, Ohm's law describes the relationship between the scalar current density,  $j$ , and scalar electric field,  $E$ , as:

$$j = \sigma_e E. \quad (8)$$

In a moving medium, Ohm's law becomes a vector relationship:

$$\mathbf{j} = \sigma_e \mathbf{E}^* = \sigma_e \left( \mathbf{E} + \mathbf{u} \times \mathbf{B} + \frac{\nabla p_e}{n_e e} \right), \quad (9)$$

where the  $\mathbf{u} \times \mathbf{B}$  term reflects the transformation from the stationary to the moving frame and the last term includes an effect due to the electron pressure gradient. In a magnetic field Ohm's law is further modified as:

$$\mathbf{j} = \sigma_e \mathbf{E}^* = \sigma_e \left( \mathbf{E} + \mathbf{u} \times \mathbf{B} + \frac{\nabla p_e}{n_e e} \right) - \mathbf{j} \times \beta_e, \quad (10)$$

where the Hall parameter for electrons is:

$$\beta_e = \sigma_e \mathbf{B} / n_e e. \quad (11)$$

This generalized Ohm's law reflects the fact that, in the plane perpendicular to  $\mathbf{B}$ , the current density ( $\mathbf{j}$ ) flows at the Hall angle  $\theta = \tan^{-1} \beta_e$  to  $\mathbf{E}^*$ . This gives rise to several generator geometries, as shown in Fig. 2.

A significant Hall effect causes the continuous electrode generator to be inefficient because the current is forced to flow at an angle relative to the electric field, which increases the internal resistance by a factor  $(1 + \beta_e^2)$ .

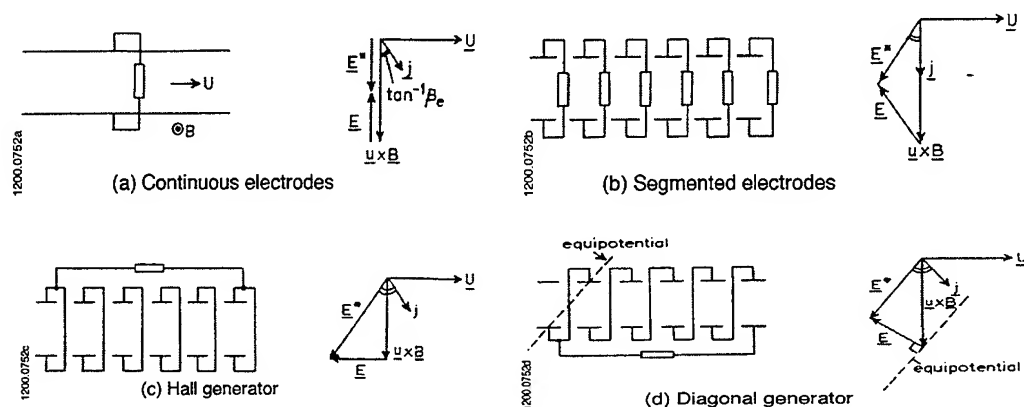


Fig. 2. Current distributions between segmented electrodes. (a) In absence of Hall effect; (b) Hall effect present but no shorting; (c) with shorting between adjacent segments; and (d) with extreme shorting [1].

To overcome this, the electrode can be divided into many short segments, separated by insulators, each of which has its own load. This enables the Hall electric field to be established axially. This opposes the ion motion in the gas and, through collisional coupling, slows down the neutral gas. (Slowing down the gas enables its kinetic energy to be extracted so that electrical power can be generated.) Since the electrode is (usually) an equipotential surface, the current actually enters and leaves it at the Hall angle. For uniform conductivity and Hall effect, the current distribution for finite segmentation has been solved analytically, as shown in Fig. 3. Current concentrations occur on edges of the electrodes. In extreme cases, the electric potential between adjacent pairs of electrodes can cause shorting to occur.

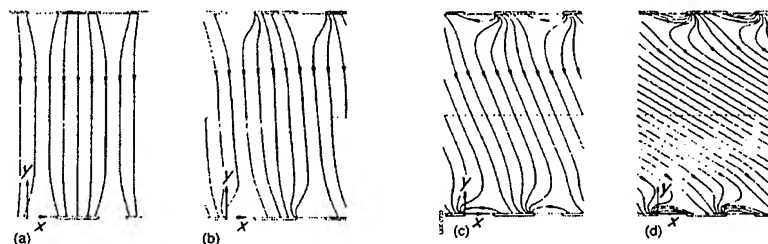


Fig. 3. Current distribution between segmented electrodes. (a) In absence of Hall effect; (b) Hall effect present but no shorting; (c) with shorting between adjacent segments; and (d) with extreme shorting [2].

In most situations, the segmented electrode generator is considered inconvenient because of the multiple loads, so that the diagonal or Hall generator geometry is chosen. For Hall parameters of one to five, the diagonal generator is preferred, although it has the disadvantage that the electrode "stagger" must be chosen to match one operating condition. Departure from this condition for any reason will cause the operating efficiency to decrease significantly. As the Hall parameter gets higher, the axially connected Hall generator becomes increasingly efficient.

Most gases are not good electrical conductors, except at very high temperatures. It is therefore generally necessary to add an easily ionizable material to the gas to improve its conductivity. The materials usually chosen are alkali metals (Na, K, Cs) or their compounds, such as sulfates or carbonates.

The conductivity produced by these materials can be found from:

$$\sigma = \sigma_e + \sigma_i = \frac{n_e e^2}{m_e \nu_{e-\text{tot}}} + \frac{n_i e^2}{m_i \nu_{i-\text{tot}}}, \quad (12)$$

where the two terms on the right-hand side of the equation represent the electronic and ionic contributions to the conductivity. In general, because of the much higher mass of ions, the second term can be neglected in most cases. In this equation,  $n$  is the number density of the species,  $e$  is the charge on the electron,  $m$  is the species mass and  $\nu$  is the collision frequency of the species with other particles present in the gas.

The electron number density,  $n_e$ , is obtained from Saha's equation, which assumes thermal equilibrium in the ionization process; for single ionization (only one electron removed from the outer shell of electrons) this is:

$$\frac{n_e^2}{n_a - n_e} = \left( \frac{2\pi m_e k T_e}{h^2} \right)^{3/2} \exp\left(\frac{e V_I}{k T_e}\right), \quad (13)$$

where  $T_e$  is temperature,  $V_I$  is the ionization potential of the gas additive,  $h$  is Planck's constant and  $k$  is Boltzmann's constant. The collision frequency ( $\nu_{e-\text{tot}}$ ) is obtained from the collision cross-sections ( $Q$ ) of the species present (some of which are not well-known):

$$\nu_{e-\text{tot}} = \nu_{e-e} + \nu_{e-i} + \nu_{e-n} = \sum_{e-j} \left( \frac{8kT_e}{\pi m_e} \right)^{1/2} n_j Q_{e-j}. \quad (14)$$

The net result is that, in the mid-temperature range, the electrical conductivity of the working fluid is strongly dependent on temperature and somewhat dependent on pressure and the amount of the seeding fraction.

Pure gas systems, based on noble gases with pure alkali metal seeding, have several potential advantages (including minimal erosion of the duct materials by chemical action compared with fossil-fuel burning systems) especially including an electron temperature that may be elevated compared with the gas (heavy particle) temperature. Since the degree of ionization in Saha's equation is determined by the *electron* temperature, there is the possibility that the bulk gas temperature can be kept to an acceptable level (1500 to 2000 K) while the ionization level corresponds to a significantly higher temperature — perhaps > 3000 K. (Note that the concept of "temperature" implies a Maxwellian energy distribution while the electron density has to be sufficiently high for electron collisional processes to be the dominant loss mechanism.)

The most practical and efficient method of producing non-equilibrium ionization is by Ohmic dissipation ( $I^2R$  heating) within the plasma by the magnetically-induced internal current. The elevation of the electron temperature is determined from the balance of Ohmic dissipation with electron-neutral collisional energy dissipation:

$$\frac{j^2}{\sigma} = \left( \frac{3m_e}{m_n} \right) \nu_{en} n_e k (T_e - T_n). \quad (15)$$

With some assumptions, this becomes:

$$T_e - T_n \sim \frac{m_n u^2 \beta_e^2}{3k} \sim 40 \beta_e^2, \quad (16)$$

for a flow velocity of 1000 m/s. A significant electron temperature elevation therefore requires  $\beta_e > 1$ .

Unfortunately, it is found that these same conditions also give rise to fast-growing electrothermal instabilities, which cause current striations in the plasma structure in the channel and can substantially disrupt the energy extraction process. Hence, generators of this type seek to find an operating regime in which some benefit can be obtained from the electron temperature elevation and consequent enhanced ionization, without creating major instabilities.

The primary measure of the efficiency of extracting a significant amount of energy from the gas into an external electrical load is that the ratio of the Lorentz force exerted electrically on the gas should be comparable to the convective rate of change of momentum as the gas passes through the magnetic field. This is measured by the interaction parameter,  $S$ , which is the ratio of these quantities:

$$S \sim \frac{\mathbf{j} \times \mathbf{B}}{\rho \mathbf{u} \cdot \nabla \mathbf{u}} \sim \frac{\sigma_e B^2 L}{\rho u} \quad (17)$$

A significant interaction requires  $S \geq 1$ . As an example, for a kerosene-oxygen mixture with 0.75% potassium seeding at 3000 K and 3 atmospheres ( $\rho = 0.33 \text{ kg/m}^3$ ),  $\sigma_e = 30 \text{ S/m}$ , so for a velocity of 1000 m/s,  $S = 0.1 B^2 L$  and a good interaction would be achieved with  $L = 4 \text{ m}$  and  $B = 4 \text{ T}$ .

Another useful parameter is the magnetic Reynolds number ( $R_m$ ), which provides a measure of the magnetic field produced by the current developed in the generator compared with the externally applied magnetic field:

$$R_m = \mu_0 \sigma_e u L \quad (18)$$

For the above values,  $R_m = 0.15$ . Since  $R_m < 1$ , the self-induced magnetic field in this case is small and the external magnetic field completely diffuses through the MHD channel and is not convected along by the plasma. When  $R_m \gg 1$ , the applied magnetic field may be significantly distorted and it is necessary to modify the channel and electrode design to take this into account.

### III. MHD GENERATOR TYPES AND APPLICATIONS

In most highly industrialized countries, large amounts of electricity (tens to hundreds of GW) are generated and distributed. Even small increases in the efficiency of this process can have substantial economic returns and will reduce the quantity of raw fuel needed. Obtaining such efficiency increases has been an ongoing process for many years and was particularly emphasized during the "energy crisis" in the 1970's and 1980's. In most countries, baseload power generation is provided by coal-fired stations and achieving improvements in this area was one of the primary objectives for research on MHD in the US, UK, Russia, and France at that time.

The concept was that a coal-fired combustor would be used to achieve high operating temperatures, with the aid of either oxygen-enriched or pre-heated air. Potassium salts would typically be added to provide the desired electrical conductivity; recovery and recycling of this seeding material would be economically and technically necessary. After passing through the MHD generator section and extracting electrical energy, the outgoing gas would still be hot enough to be used to raise steam in conventional boilers, which would then feed conventional steam turbines. Thus, the MHD section could be thought of as a "topping cycle" that could add perhaps 15% increase in efficiency to a steam cycle with perhaps 35% thermal efficiency. If achievable, this would be a substantial benefit. Issues to be resolved are the increased cost of the extra MHD-related equipment, its lifetime and operational effectiveness. To a large extent, the justification for investing in this technology rests on the cost of raw fuel. Technical problems that were addressed focused on the generator channel and how to make electrode materials that would conduct electricity for thousands of hours without maintenance under conditions where deposition of alkali-metal loaded coal slag occurred. With the passing of the energy "crisis" all of these efforts have now ended.

At the same time as the above efforts were taking place, a smaller but comparable effort was being made on techniques for improving the efficiency of baseload nuclear power generation. Most nuclear reactors are designed only to operate at temperatures that are matched to the steam generating equipment, however, a few high temperature reactors have been built and operated. Examples are the Dragon reactor (UK), TFTR (Germany), and the General Atomics Peach Bottom reactor (US). In these systems, the inert gas helium is used as the reactor coolant and pyrolytic carbon or silicon nitride coated fissile particles are

the reactor fuel. Without an MHD generator, the advantage of a high operating temperature is that gas turbines could be used in place of steam turbines, thereby increasing the Carnot efficiency of the entire process. With MHD, as for the fossil fuel system, the MHD generator would operate as a topping cycle to the gas turbine plant to yield an even more efficient system. Because of the potential for fission by-product diffusion through the fuel coating (which would be undesirable in that it would contaminate the entire cooling circuit), the upper temperature for such reactors is much lower than for an air-preheated coal plant — perhaps 1800 K versus 3000 K. Cesium or potassium would therefore be used (and recovered and recycled) as the seed material. More importantly, the possibility for non-equilibrium conductivity would enhance the performance at moderate Hall parameters.

Considerable research was devoted to this approach in the US, UK, Europe, Russia, and Japan in experiments with shock tubes, blowdown tunnels and closed loops using seeded helium and argon. However, all effort is now stopped, except for a small amount of research in Japan. So far as is known, there is no significant effort to develop a high temperature gas reactor at present.

The inherent simplicity of the MHD generator concept (no moving parts) led to a number of efforts to build short pulse power generators (1 to 10 secs) for specialized applications, usually for the military. Avco-Everett built the large experimental Mark 5 system in 1965, as shown in Fig. 4. Using liquid fuels it was able to generate 30 MWe for a few seconds. The channel walls were originally made of wood and were self-protected by carbonization. The magnet was conventional air-cored copper design and was initially fed from an external supply until sufficient power was developed by the generator, whereupon it was “boot-strapped” by feeding part of the output power back to the magnet.

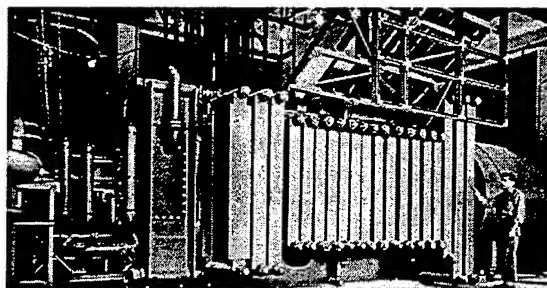


Fig. 4. Avco Mark 5 generator.

In Russia, a series of transportable “Pamir” generators were built and used for geophysical prospecting, while in the US, STD Inc. built a hybrid (solid fuel-liquid oxidant) system that was mounted on the back of a trailer. This generated 5 to 10 MWe and was designed to be used by the USAF as a power source for lasers or microwave experiments [4]. This effort was terminated two years ago when the USAF made a decision to purchase a Pamir 3U generator for the USAF Phillips Laboratory in 1994. This generator, shown in Fig. 5, delivers 30 kA at 500 V (15 MWe) to a load for 10 sec. The total mass is about 18 tons and the total volume about 60 m<sup>3</sup>. Eight commissioning shots were undertaken with this generator in February/March 1995 during initial tests at Edwards Air Force Base [5].

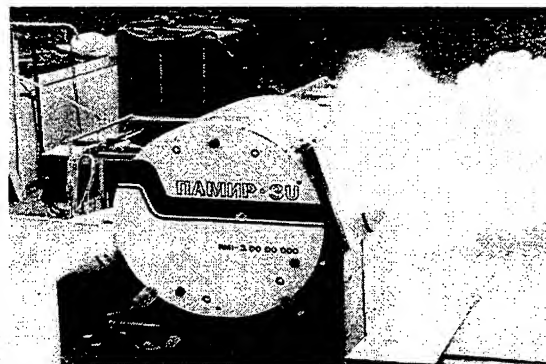


Fig. 5. Pamir-3U generator under test [5].



A second class of short pulse generators has been studied for applications that require sub-second power pulses. The Hercules Corp. undertook work in the US with cesium picrate seeded explosives in the 1960's and 1970's [6]. Typical pulse lengths were 100  $\mu$ s and conductivities up to  $10^4$  S/m were obtained, leading to  $R_m \sim 1$ . LLNL and Artec Inc. developed explosively driven argon systems in the early 1980's. The conceptual configuration is shown in Fig. 6 [7]. These achieved gas temperatures, pressures and flow velocities so high (30,000 K, 10 kilobars and 27 km/s) that no seeding was necessary. GW and MJ pulses of 10 to 100  $\mu$ s duration were achieved. Experiments using shaped charges and 155-mm howitzer barrels were also conducted in the UK [8]. An evaluation of these systems for ground-mobile weapon systems was undertaken for the Ballistic Missile Defense Office, Huntsville in 1984 [9]. The objective was to obtain 20 pulses per second of 10 to 12  $\mu$ s duration at 20 kV and 50 kJ for a directed energy device. It was found that the high  $R_m$  distorts the applied magnetic field and reduced the potential output.

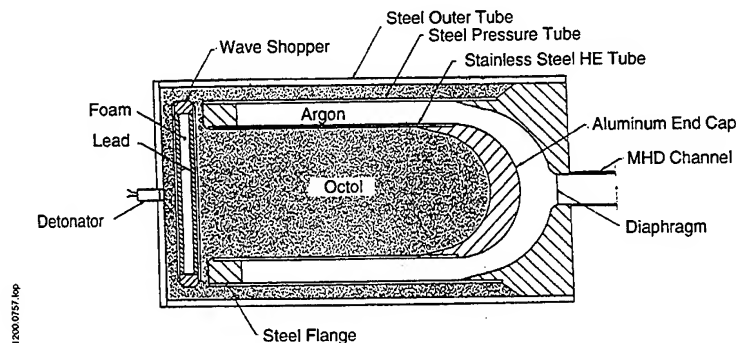


Fig. 6. Artec plasma source [7].

Transformation of the output current and pulse stretching is necessary to match the output of fast devices like this to an electric gun, although the amount of stretching required may be less for an ETC igniter than for the railgun and other guns.

In response to the concern about the relatively low conductivity of gases (compared with metallic conductors), some research was undertaken on MHD generators that used liquid metals as the conductor in closed-loop systems. The liquid metal choices are limited and NaK was often used. This has the advantages of a high electrical conductivity compared to plasma and an electrical conductivity that is independent of temperature. In principle, AC generators could be developed at near-room temperatures, which would be advantageous for utility power generation, since it would eliminate the inverters and rectifiers necessary for a conventional DC MHD system. With a liquid metal, it is necessary to provide some method of thermodynamically coupling to a heat source. A two-phase approach was used at JPL in which mixer and separator sections were used to combine and separate the liquid metal electrodynamic working fluid and the compressible thermodynamic gas or vapor working fluid. An alternative approach using two-phase NaK-N<sub>2</sub> emulsions operating at high void fractions was studied by ANL. So far as is known, there is no ongoing work at present in this field.

#### IV. APPLICATION TO ELECTRIC GUNS

A US study concluded that a pulsed MHD generator was not well suited to a small EM gun [10] and, so far as is known, the only experiments undertaken recently in which an MHD generator has actually been used to power an electric gun have been at the "Soyuz" organization in Moscow, Russia [11]. The "Mustang" facility uses a solid propellant MHD generator and pulse transformer. The maximum MHD generator current that was fed into the primary transformer winding was 25 kA and the maximum current output from the transformer secondary into the gun was 1 MA. A small bore railgun was the load and projectile muzzle velocities > 4 km/s were achieved with 9.5 MJ input.

The Mustang arrangement is shown in Fig. 7 and its operation is as follows. Closing the oil hydraulic switch discharges the pre-charged capacitor bank and initiates a current of  $\sim 10$  kA in the magnet and transformer primary. The primary acts as the inductive storage coil and is charged up by the MHD generator. When the inductor is fully charged, the explosive switch 3M2 is closed to short the MHD generator out of the circuit. Explosive switches 3M3 and 3M4 then close the (previously open-circuited) pulsed

transformer secondary at the same time as the projectile is inserted into the launcher. The energy stored in the transformer primary is coupled into the secondary (at about 62% efficiency) to energize the railgun and launch the projectile. After the projectile leaves the railgun, explosive switches 3M5 and 3M6 short the launcher out of the circuit to prevent continued current flow into the launcher. Switch 3M7 shorts out the muzzle to prevent rail erosion after the projectile has been launched.

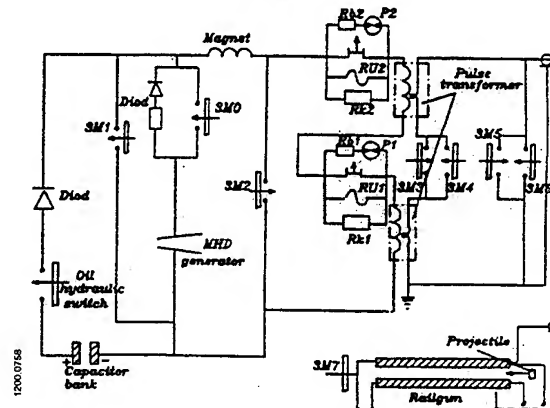


Fig. 7. Mustang set-up and operation [11].

## V. SUMMARY

At present, there is little interest in MHD technology for continuous utility power generation, whether coal-fired, nuclear or using liquid metal working fluids coupled to any heat source. Explosively driven generators have demonstrated very high power but operate at pulse lengths shorter than needed for most electric guns. In contrast, hybrid solid fuel-liquid oxidant powered systems can provide pulsed operation over a few seconds, but the low plasma electrical conductivities result in a high generator internal impedance and modest currents (tens of kA), so that high efficiency pulsed transformers are needed to couple effectively to large railguns.

Light weight systems *may* be possible for ETC guns, where the energy demand is less than for the railgun and where the pulse length is shorter. For transportable systems, magnet technology will be an important weight driver and high temperature superconductors may help in the future, if high current conductors can be developed.

## VI. ACKNOWLEDGMENT

This work was supported by the U.S. Army Research Laboratory (ARL) under contract DAAA21-93-C-0101.

## VII. REFERENCES

- [1] I. R. McNab, "Magnetoplasmodynamic electrical power generation," *IEE (UK) Student's Quarterly Journal*, Sept. 1969, pp. 13-17.
- [2] M. G. Haines and I. R. McNab, "Magnetohydrodynamic power dynamics," *Physics in Technology (UK)*, vol. 5, 1975, pp. 278-300.
- [3] M. G. von Bonsdorff, I. R. McNab, and B. C. Lindley, "Nuclear MPD gas turbine power plant," *Electricity from MHD*, vol. II, pp. 663-682. Published by the International Atomic Energy Agency, Vienna, Austria, 1966.
- [4] S. T. Demetriades and C. D. Maxwell, "Pulsed operation of a combustion MHD generator," *IEEE Pulsed Power Conference*, 1991, pp. 457-460.
- [5] D. W. Price, et al., "Pamir-3U MHD generator results," *IEEE Pulsed Power Conference*, 1995.
- [6] M. S. Jones, Jr., Proc. 13th Symposium on Engineering Aspects of MHD, Stanford, CA. Late paper No. 3.
- [7] "Pulse electrical power generation studied," *Aviation Week*, April 27, 1981.
- [8] A. B. Crowley, D. W. Leeming, and R. D. Green, "Explosive MHD pulsed power generators," 4th European Symposium on EML Technology, Celle, Germany, May 1993.
- [9] D. W. Cott, "Feasibility of explosively pulsed MHD power for ground mobile weapons systems," *ASME paper 84-AES-5*, February 1984.
- [10] D. J. Butz and V. Levin, "Preliminary study of a propellant-driven pulsed MHD generator-powered small caliber EML," *IEEE Trans. Magn.*, vol. 22, pp. 1416-1422, November 1986.
- [11] Y. P. Babakov, A. V. Plekhanov, and V. B. Zheleznyi, "Range and railgun development results at LS&PA 'Soyuz'," *IEEE Trans. Magn.*, vol. 31, pp. 259-262, January 1995.

## List of Symbols

$L$  = length

$B$  = magnetic field

$u$  = velocity

$V_{gen}$  = voltage

$I$  = current

$R_{int}$  = internal resistance

$R_{ext}$  = external resistance

$K$  = load factor

$\sigma_e$  = conductivity

$J$  = current density

$E$  = electric field

$P$  = power density per unit volume

$\beta_e$  = Hall parameter

$T_e$  = temperature

$V_I$  = ionization potential of gas additive

$h$  = Planck's constant

$k$  = Boltzmann's constant

$Q$  = collision cross-sections

$V_{e-tot}$  = collision frequency

$S$  = interaction parameter

$R_m$  = magnetic Reynolds number

# **High Action Switching for Next Generation Multi-megajoule Power Conditioning System**

*by*

*H. Singh, D. Eccleshall, J. Creedon, T. Burke, T. Podlesak  
U.S. Army Research Laboratory, SEDD, AMSRL-SE-DP  
Pulse Power Center, Fort Monmouth, NJ 07703-5601*

*I. McNab, IAT and J. Pappas, CEM  
University of Texas at Austin*

*J. Sarjeant  
State University of New York at Buffalo*

## **SUMMARY**

Pulse discharge technology is being studied to achieve increased muzzle velocities in electric guns. Systems using rotating machines such as compulsators have been examined for generating, storing and shaping pulse energy. Discharge parameters exceed the capabilities of existing state of the art switches and, as a result switch modules constructed of series-parallel devices are necessary. In all systems being investigated large values of coulomb transfer are typical. High pressure spark gaps, silicon controlled rectifiers and triggered vacuum switches are capable of switching relatively large values of coulombs are considered to be the most promising candidates. For the silicon controlled rectifier the action rating (current squared times pulse width) is the most significant parameter and it can be used to derive peak current, pulse width and coulomb limits for a given device diameter. For spark gap and triggered vacuum switches, life and it's dependence on the accumulated total coulomb transfer is believed to be the dominant rating factors. Ratings and limitations of silicon controlled rectifiers, triggered vacuum switches and high pressure spark gaps are discussed.

## INTRODUCTION

Pulse discharge technology is being studied as a way of achieving increased projectile muzzle velocity and energy for electric gun applications. Emphasis has been placed on using electromagnetic railgun launchers (EML) [1], [2]. Systems showing the most promise have been rotating machines such as the compulsator. However, for these generators the pulse power requirements generally exceed obtainable ratings of a single state of the art (SOTA) switch making it necessary to use multiple switch modules [3]. The consequence of this is that the number of active components is large and switch volumes may be unsatisfactory for some mobile applications.

### 1. Switches for Electric Guns

In electric gun pulser circuits the switch must meet peak voltage, peak current, action, charge, rate of rise of current, reverse blocking and recovery requirements that exceed some or all of the electrical ratings for a single device. For these applications silicon controlled rectifier (SCR) modules, high pressure spark gaps (SG) and triggered vacuum switches (TVS) are most often proposed as switches. Mercury ignitrons [4] were used in early feasibility studies but they are not considered suitable for use in mobile platforms of interest to the Army. Other well known switches such as thyratrons, back-lighted thyratrons and pseudo-spark gaps have limited coulomb capability and they have not been considered. The orientation-independent ignitron [5] is somewhat comparable to the SG and TVS in electrical capabilities but it is in an emerging technology phase and is not considered a candidate for the near term.

Because of the incompatibility of gun power requirements and individual switch performance use must be made of switch modules. Each module is composed of multiple series-parallel arrangements of components consisting of silicon controlled rectifiers, diodes, capacitors and resistors. Auxiliary circuits including voltage dividers, snubber circuits and gate drivers need to be developed. The number of components making up each module imposes demanding reliability limits as well as the potential need for redundancy and fusing. As a result the overall switch volume can be substantial and a major portion of the limited space available for a system has to be allocated to the switch.

### 2. Pulse Power using Rotating Machines for Energy Storage

EML system analysis indicates that the square wave load current pulse can be achieved by coupling the outputs of a multiphase generator. Both full wave and half wave rectification of 2 to 6 phase systems can produce nearly square wave current pulses. Constant current in the load results in less jerk and higher efficiencies and is thought to represent the optimum load pulse shape. Figure 1 shows typical line currents and their envelope for a 4 phase half wave generator. The sum of the line current gives the load current which has an approximate constant value. There are two drawbacks to this approach from the viewpoint of the switches. One is that, depending on the launch time and the repetition rate of the generator, several conduction periods for each line current can take place in each system firing. This determines the coulomb requirement per line. For an SCR switch it also establishes the resulting junction temperature due to dissipation. The rise in junction temperature has been shown to be a good indication of life in number of pulses [6], [7]. A second drawback to the multiphase system is that reverse voltage must be blocked to prevent reverse conduction. For launch times of interest rotating machines have a high rotational frequency resulting in  $dI/dt$  and  $dV/dt$  that are significantly higher than for 60 hertz applications. Meeting the reverse blocking requirement will be a major challenge for the TVS with its limited range of  $dI/dt$  and  $dV/dt$  for blocking. The high pressure spark gap has very limited reverse blocking capability, and this is true of most gas switches. The symmetric SCR has the best promise of meeting these requirements but volume consuming snubber circuits will be required.

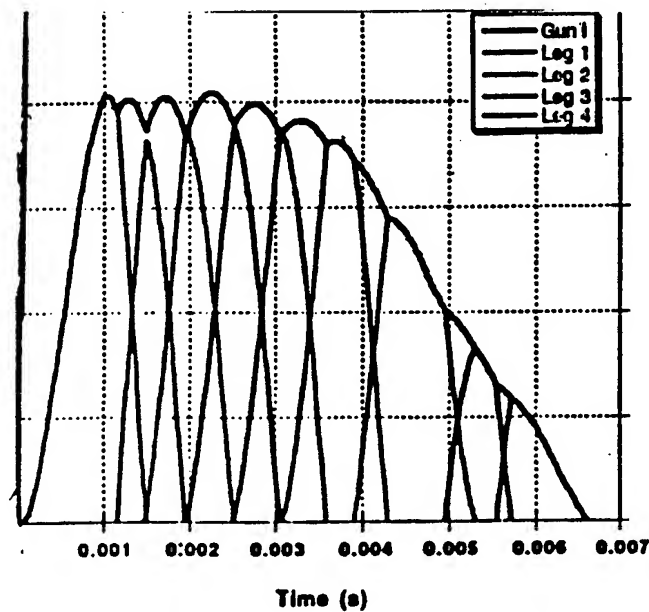


Figure 1: Line currents and load current for a 4-phase half-wave source.

TABLE 1

SWITCH PARAMETER FOR HIGH ENERGY EML APPLICATIONS

| Parameter                         | Range of Values |
|-----------------------------------|-----------------|
| Peak Current (megamperes)         | 1 to 4          |
| Peak Voltage (kilovolts)          | 5 to 20         |
| Pulse Width (milliseconds)        | 1 to 4          |
| Action (gigajoule/ohm)            | 5 to 10         |
| $dI/dt$ (kiloamperes/microsecond) | 8 to 12         |
| Charge (kilocoulombs)             | 2 to 3          |

### 3. Pulse Power for EML Using Capacitive Circuits

Capacitive energy storage was used in some of the early EML feasibility studies because of its convenience and availability. However, with 1.5 joules per gram energy density as the SOTA for film capacitors, the volume required to provide the megajoule energy is too large to be practical for some applications. Laboratory and fixed station installations such as the 52 megajoule ARDEC facility [8] use multiple pulse forming modules made up of energy storage capacitors, pulse shaping inductors and switches. The modules can be discharged in series or in parallel to obtain a desired load pulse.

#### 4. Comparison of Switch Parameters

Typical parameters that impact the design of a switch for high energy EML applications are listed in Table 1. A single high pressure spark gap (SG) or a triggered vacuum switch (TVS) can meet the forward voltage hold-off requirements. However, silicon controlled rectifiers (SCR) must be connected in series. To meet peak current, charge, and  $dI/dt$  requirements parallel connection of all switch types is needed. Action limits are discussed in section 6 but again parallel devices will be needed. For reliability all device parameters must be well below failure limits. With the auxiliary circuits called for by the use of parallel and series connected devices, the design of a switch module will require significant effort for the high action high repetition multi-megajoule application foreseen for the future.

#### 5. Estimates for Limits

The pacing parameter which must not be exceeded for the solid state device is the action rating. This rating represents a level at which the device has a high probability of permanent failure caused by fusing. Action in a switch is also a measure of the impact that occurs in a short interval of time due to a force associated with the high energy pulse. The force introduces stresses and strains in the switch and these stresses can induce micro cracks and fractures which can ultimately lead to device failure. Materials subject to self-induced (JxB) forces can become deformed and in practice rigid and massive mounting structures are employed to restrict the deformation. This is successful to some extent but it does not eliminate the possibility of exceeding the tensile strength of the internal structure and materials. If the value of the action exceeds the fusing limit of a solid state device then failure is catastrophic. As a result, it is usual to operate solid state switches at action levels well below their fusing limit.

Action is given by the product of the square of the root mean current times the full width of the pulse for sinusoidal current wave shapes. Figure 2 shows action limits for a number of commercial phase controlled SCR's as a function of total cathode area. The action values were obtained from SPCO data sheets [9]. The data shown is for 4500 volt and 2200-2500 volt devices. The solid curve is a regression fit of data from several manufacturers. The data points plotted by the symbol + represent failure limits obtained at ARL's Pulse Power Center (PPC) using capacitor pulse forming networks with a pulse width (T) of 450 microseconds at the half maximum points [10], [11], [12]. For the PPC tests the root mean square current was equal to the peak current. The agreement between the regression curve and the experimental values obtained at PPC supports the hypothesis that an empirical relationship for action as a function of area can be given by:

$$\text{Action} = 6.2 \times 10^3 \times A^{1.75} \text{ amperes}^2 \cdot \text{sec.} \quad (1)$$

where A is the total cathode area in  $\text{cm}^2$ . The fusing limit for commercial SCR's for sinusoidal pulses is given by:

$$\text{Action} = 0.5 I_{\text{max}}^2 \times T \quad (2)$$

Relationships (1) and (2) can be used to predict peak current, charge transfer and action limits for solid state switches.

For the high pressure air spark gap and the triggered vacuum switch life, expressed as a number of pulses and the ability to accomplish reverse voltage blocking are the pacing factors [13], [14]. For these devices the amount of electrode material sputtered during high current pulses is proportional to the accumulated charge transferred and is approximately equal to  $10^{-5}$  milligram per coulomb [14], [15]. Widening of the gap spacing results in unreliable triggering action and failure to fire with the SG.

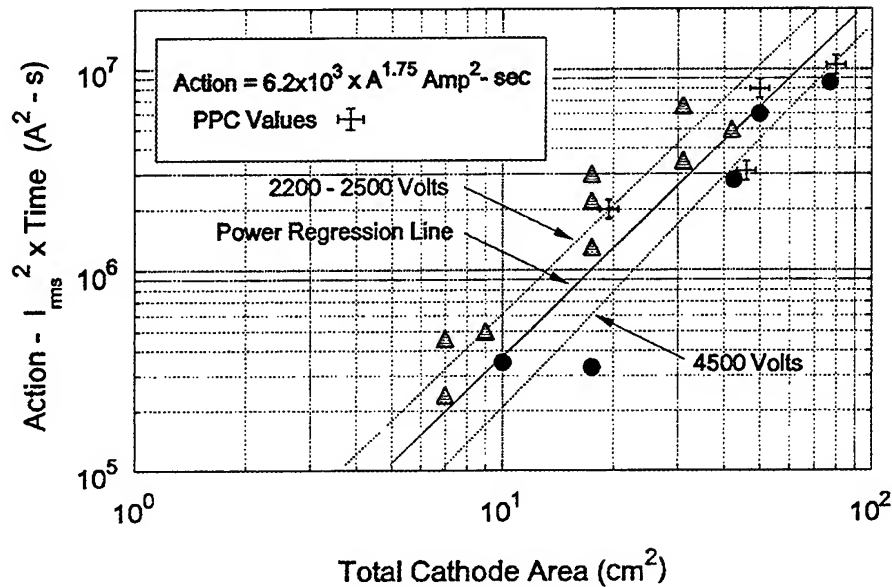


Figure 2: Action limits versus total cathode area.

A similar life relationship occurs for the triggered vacuum switch [13] except the widening of the gap increases the probability of a pre-fire event. Since charge is given by the integral of the current pulse as a function of time the peak current limit for a given pulse width can be determined for both devices if the dependence of life on charge is known. Although action and life (number of pulses) can be used to establish current, charge and pulse width limits, other rating factors such as  $dI/dt$  and  $dV/dt$  and reverse blocking must also be considered.

Reverse blocking is the peak voltage that can be applied across the device in reverse direction immediately after it has conducted high current in the forward direction without breakdown occurring. Reverse voltage blocking is a critical parameter when using rotating machines having multiphases.

An SCR can be made symmetrical and block voltage in both directions by using a thicker silicon wafer which results in higher on state voltage drop and higher thermal resistance. The SCR reverse blocking capability is dependent on the  $dI/dt$  and  $dV/dt$  of the inverse waveform. The maximum reverse  $dV/dt$  for SCR is approximately 50 volts/ $\mu\text{sec}$ . For values exceeding this snubbers must be used to reduce the  $dV/dt$  of each switch to a safe level. The need for snubber and balancing techniques impacts the individual switch volume and in some instances may result in excessive overall switch volume for some system applications.



The TVS is capable of reverse blocking under some  $di/dt$  and  $dV/dt$  conditions [13]. The ability to withstand application of reverse voltage immediately after forward conduction is not usually obtainable with high current gas closing switches and high pressure spark gaps have a limited capability in this regard.

A comparison of SCR, SG and TVS capabilities are summarized in Table 2. Comparison of the limits shown in Table 2 with the switch parameters required for EML applications (Table 1) illustrates the magnitude of multiple devices required to meet objectives.

**TABLE 2**  
**COMPARISON OF SWITCH CAPABILITIES**

|                            | SCR  |       | SG     |        | TVS     |         |
|----------------------------|------|-------|--------|--------|---------|---------|
|                            | SOTA | LIMIT | SOTA   | LIMIT  | SOTA    | LIMIT   |
| Action MA <sup>2</sup> sec | 15   | 40    | 50     | 500    | 10      | 150     |
| Peak Voltage (kV)          | 4    | 10    | >100   | >100   | 100     | None    |
| Peak Current (kA)          | 150  | 250   | 300    | 1000   | 125     | 500     |
| Charge Coulombs (C)        | 125  | 210   | 200    | 700    | 100     | 425     |
| Voltage Drop (V)           | 10   | 10    | 50-200 | 50-200 | 100-200 | 100-200 |

## 6. Emerging Technology

Meeting future switching requirements for multi-megajoule repetitive operation will depend strongly on emerging technology and thermal management. The SCR is a mature technology; however, a number of recent developments would result in a significant reduction in the size and weight of the switching package for electric gun application. Increasing the diameter from 100mm to 125mm will result in a 50% increase of peak current and charge. Currently 125mm devices are being evaluated at PPC [12].

The SOTA SCR design is based on pressure contact between the silicon semiconductor and the metal contacts. The Electric Power Research Institute (EPRI) has developed an all-silicon bonded package that results in a 60 percent reduction in the size and weight of the SCR. The thermal resistance of the silicon package was measured to be 50 percent less than the conventional SCR package. This would result in reduced thermal management system weight, volume; and it would improve life and reliability. The Mitsubishi Company of Japan recently announced the availability of ultra high power Light Triggered Thyristors. These devices utilize 150mm diameter wafers and are rated for a maximum voltage of 8 kV. They should be capable of greater than 400 kA of peak current. The light trigger feature will make it much easier to fabricate series and parallel switch packages.

Some improvement in spark gap switches might be possible if development studies were conducted. Employment of graphite electrodes offers some advantages for reduced evaporation. Re-entrant electrode designs and metal wall envelopes are currently used in several of the SOTA devices resulting in improved life. These designs could be further optimized. SG's exhibit a loss of reliability at high coulomb transfers due to surface eruptions and distortions causing field enhancement sites. Achievement of multiple cathode arc spots could improve life. Some potential exists for developing improved triggering systems. The need for purging and gas replenishment ultimately will limit repetition rate capabilities.

The use of silicon carbide as the semiconductor material for high power switches has great promise. The high breakdown voltage and operating temperature in comparison with silicon can result in an order of magnitude improvement in current density and peak operating voltage. The high thermal conductivity reduces the thermal management system. The silicon carbide power switch is in a very early stage of development [16]. The major challenge is the production of large area material that is defect-free. Present prototype devices area are limited to areas less than 1 square millimeter. The material problem must be solved before fabrication problems such as ohmic contacts and damage free etching can be completely solved.

TVS technology is based on work done in the USA. Recently the device has been further developed with emphasis on high peak current-high coulomb applications. In its present stage of development the TVS is competitive with solid state switches with respect to peak current capability and it is superior to solid state devices in coulomb transfer capability. A single device can meet the high voltage requirement for electric gun modulators. Switch closure is usually initiated by applying a pulse voltage between a trigger electrode and the negative electrode. The trigger pin or electrode is prone to being shorted by sputtered debris. No other auxiliary or housekeeping facilities are required. For limited peak currents the TVS exhibits reverse voltage blocking capability. The limiting parameters on reverse blocking are both  $dV/dt$  and  $dI/dt$  and there are acceptable and unacceptable ranges of both. To obtain the reverse blocking capability it is necessary to avoid anode spots. By operating in the diffuse mode anode temperatures can be maintained below the onset temperature for the formation of an anode spot to some degree. The range can be extended somewhat by the use of a saturable reactor.

### CONCLUSION

The development of large diameter SCR's will reduce the switch volume requirements. However, the need for series connected devices to meet the voltage levels still results in large numbers of devices and auxiliaries. The SCR most nearly meets the reverse blocking requirement. High pressure spark gaps are not considered viable for future repetitive applications because of the need for volume purging and gas replenishment between pulses. The TVS holds the most promise of meeting the volume constraint and current development may improve its peak current and blocking capabilities.

### REFERENCES

- [1] J. R. Kitzmiller, S. B. Pratap et al, "Optimization and Critical Design Issues of the Air Core Compulsator for the Cannon Caliber Electromagnetic Launcher System (CCEML)," IEEE Transactions on Magnetics, Vol. 31, No. 1, JAN 95.
- [2] R. L. Fuller, J. R. Kitzmiller and R. F. Thelen, "Testing of an Air Core Compulsator Driven 0.60 Caliber Railgun System," IEEE Transactions on Magnetics, Vol. 31, No. 1, JAN 95.
- [3] H. Singh, et al, "Comparison of Switching Technologies for a Tactical EML Application," IEEE Transactions on Magnetics, JAN 97.
- [4] R. Kihara, D. B. Cummings, et al, "Commercial High Current Ignitron Development," Proceedings of the 7th IEEE Pulsed Power Conference, Monterey, CA, 1989
- [5] W. O. Eckhardt, H. Gallagher, et al, "Orientation Independent Ignitron High Power Closing Switch," Technical Report to Defense Nuclear Agency for Contract No. DNA001-87-C-0089, FEB 90.
- [6] J. Somos, D. Piccone, et al, "Power Semiconductors Empirical Diagrams Expressing Life as a Function of Temperature Excursion," Proceedings of 1992 EML Technology Symposium, Austin, TX.
- [7] M. Adler, "Accurate Calculations of the Forward Drop and Power Dissipation in Thyristors," IEEE Transactions on Electron Devices, JAN 78.

- [8] T. Coradeschi, et al, "52 Megajoule Electric Gun Test Facility," IEEE Transactions on Magnetics, JAN 93.
- [9] Commercial literature published by SPCO, Malvern, PA.
- [10] R. Pastore, H. Singh, S. Schneider, "Solid State Switch Array as a Replacement for Spark Gaps," Proceedings of the 6th BMDO/ONR Pulse Power meeting, 1993, pp. 39-43.
- [11] T. Podlesak, et al, "Solid State Switches for Electric Gun Applications," IEEE Transactions on Magnetics, JAN 97.
- [12] T. Podlesak, et al, "A Compact Lightweight 125mm Thyristor for Pulsed Power Applications," 1996 Power Modulator Symposium.
- [13] Y. Chen, R. Dethlefsen, et al, "High Coulomb Triggered Vacuum Switch," Proceedings of IEEE 9th Pulsed Power Conference, 1993, pp. 938-991.
- [14] A. L. Donaldson, "Gas Discharge Closing Switch," Section 5b, Plenum Press, NY, 1990.
- [15] D. Bhasavanich, S. Hitchcock, et al, "Development of a Compact, High Energy Spark Gap Switch and Trigger Generation System," Proceedings of the 8th IEEE Pulsed Power Conference, pp. 343-345, 1991.
- [16] K. Xie, J. H. Zhao, T. Burke et al, "Fabrication and Characterization of 6H-SiC, Switching Devices," Proceedings of 9th Pulse Power Conference, JUN 93, pp. 821-824.

# **ALL FILM ENERGY STORAGE CAPACITORS.**

Michel BRAMOULLÉ

21850 Saint-Apollinaire - FRANCE.

## **SUMMARY.**

This paper describes the evolution of the large energy storage capacitors, from all paper to all film design. Starting by a description of the technologies used in the 80's, it exposes the new objectives required by the new projects. The design of the all film technology is analysed, based on the d.c filter experience. The transfer of this knowledge to the energy storage application explains the capacity of improvement still remaining for this technology. Finally, examples and tests results show that these products are perfectly safe, with a high level of performance in term of energy density and unit energy.

## **1 - INTRODUCTION.**

The evolution of the large energy storage capacitors has been very slow all over the thirty last years. The market was reduced, compared to thus of the power factor correction ; therefore, the manufacturers of dielectrics were not very disposed to develop new materials to improve their performances

As a matter of fact, the technology of these capacitors has been based on known technologies for d.c. filtering adapted to the specifications of the energy storage requirements.

Even now, this rule is followed : the new design is a knock-on effect of all the improvements performed, for 6 years, on the d.c. filter capacitors used in the converter applications.

In the meantime, new requirements have appeared, mainly in term of safety and specific energy, becoming necessary due to the increase of the capacitors bank energy, and the energy per unit.

The all film capacitors are now able to work at a high level of specific energy under totally safe conditions.

## 2 - SITUATION IN THE 80's.

The design of the energy storage capacitors was based on 2 main factors :

### - Dielectrics

Usually the dielectrics were paper layers wound with the electrodes : the number of the layers were typically 4 to 5 according to the optimal values of breakdown of the whole insulation (see fig 1).

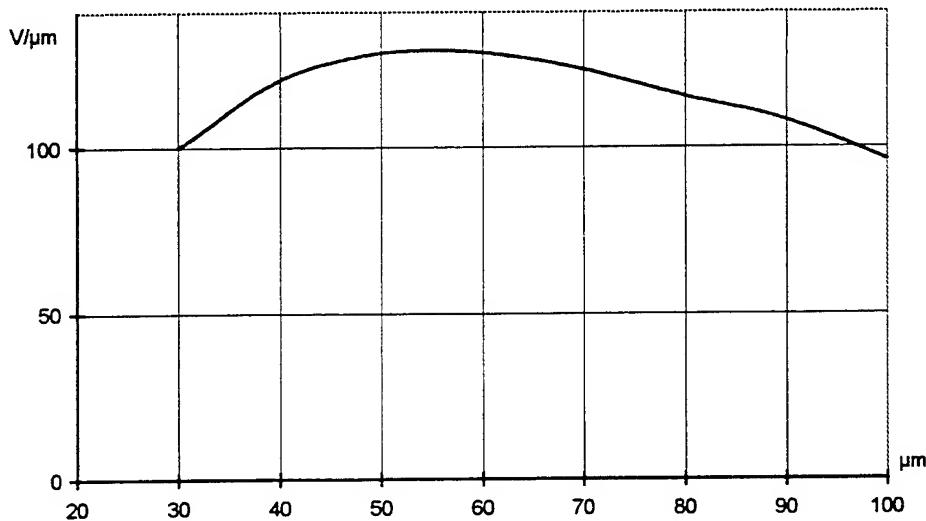


Fig 1. Breakdown vs. dry paper thickness

Due to this optimum, the voltage of the capacitor was a multiple of about 10kV.

The quality of the paper has been improved in two directions : increase of the density from 1.1 to 1.35, and also reduction of the weak points inside each layer.

The castor oil gave excellent results as an impregnate, because of the particular chemical links between it and the cellulose.

In parallel with this all paper dielectric, some other types of insulation were used, based on a mix between film (polyester or polypropylen) and paper, acting as a impregnating layer, in addition to its insulating properties.

### - Electrodes

Plain aluminium were wound, either with tabs, or extended foils to collect the current.

Thickness of aluminium was depending on the current crossing and typically comprised between 5 and 20 microns

The final result was characterised as following :

- Good homogeneity of the dielectric.

- Limitation of the stress due to the electrode edges.
- Optimisation of the voltage near 10kV (in the all paper design).
- Breakdown leading to explosion when the dielectric failed.
- Specific density limited to 550 J/l.

This situation was blocked, even if some investigations were carried out to find new films (ex : PVdF).

A major improvement was introduced when using a metallization on a layer of paper or of film. In both cases, the self healing process led to a significant gas emission, during the local breakdown ; the capacitor can was bulging significantly.

### 3 - NEW OBJECTIVES.

At the end of the 80's a new situation appears characterized by :

#### 3.1. New projects.

- \* The electrical launchers (rail, plasma and induction systems) need large energy bank (10 to 50 Megajoules)
- \* Simulation equipment based on huge lasers using some hundreds of megajoules.

#### 3.2. New requirements.

In the large projects mentioned above, unit energy per can becomes larger and larger, reaching today 100kJ.

In case of uncontrolled short circuit, inside the can, the explosion is practically guaranteed. Such a situation is not admissible at all.

For this reason, the safety is considered as a major criterium in the design of the capacitor.

Consequently, it is asked the capacitor to have a "smooth" evolution all along its lifetime which is ended, not by an explosion, but by a moderate change in the capacitance value.

In addition, size and prices of the whole energy banks must be reduced through an increase of the specific energy.

This new approach is expressed through following general specifications concerning this product :

|                                  |   |
|----------------------------------|---|
| Energy :                         | 50 to 100kJ   |
| Voltage :                        | 20 to 30kV  |
| Reversal :                       | 10% normal working.<br>65% to 90% (faulty conditions) |
| Lifetime* :                      | 10 000 shots  |
| Specific energy :                | 600 to 1000 J/liter                                   |
| No explosion at the end of life. |   |

\* Lifetime obtained when the drop of the capacitance reaches 5%.

#### 4 - FUNDATION OF A NEW D.C. CAPACITOR.

In 1989, started in TPC, a study on the d.c. filter capacitors which were previously based on a metallized paper design. For the reasons described above, the capacity of improvement of this technology was considered as very low.

For the new projects concerning the rolling stock, this situation was far to be satisfactory ; lighter and more safe products were required.

In 1990 the first capacitor with a new concept appeared, based on a combination of

- polypropylen film.
- segmented metallization.
- liquid impregnant.

Over the 6 following years, the size and the weight of these capacitors have been strongly reduced, with a factor 4.

This was made possible by the wide capacity of evolution of the combination.

The main properties of this capacitor are :

- the safety : no remaining short circuit ; only a drop of capacitance due to a fuse effect of the gates located on the metallization. At the end of life, the capacitance has lost 2% (typical value), without any swelling of the can.

Even, in case of working conditions exceeding in a large scale those of the specifications, the breakdown of film is always controlled by the fuses. Fig 2 shows a test result obtained when energizing a 20 liters capacitor at 1.8 times its nominal voltage ; at the end of the test, capacitance has disappeared and the swelling of the can is limited to an acceptable width.

- the weight : the density of the dielectric drops from 1.3 (paper) to 0.9 (polypropylene) and consequently, the density of the capacitor, from 1.65 to 1.25.

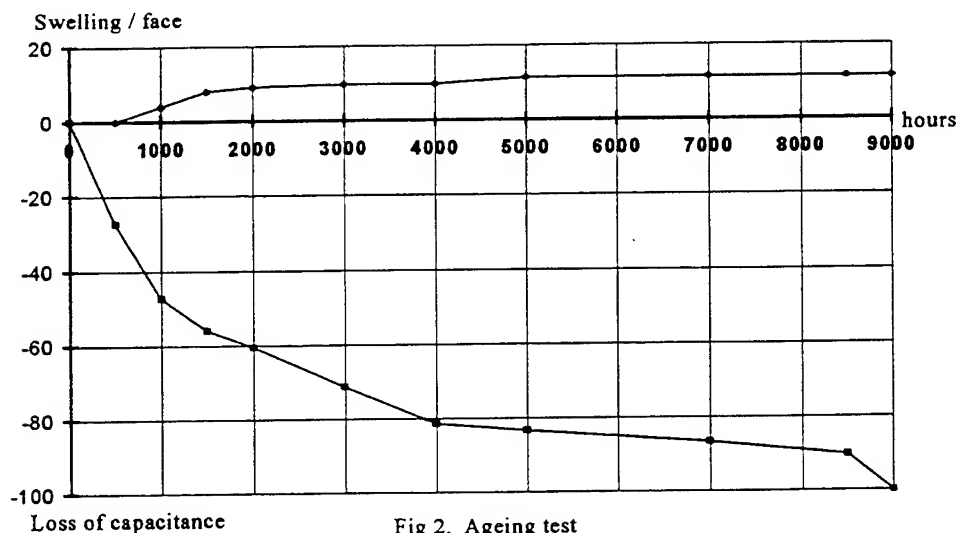


Fig 2. Ageing test

## 5 - TRANSFER TO ENERGY STORAGE.

This study is carried out with the support of the French Commissariat à l'Energie Atomique, for the Megajoule Project.

### 5.1. Dielectric stress.

The first objective is to reinforce the safety properties of the d.c. filter capacitors. This is made possible by increasing the speed of interruption of the faulty current in the dielectric breakdown, during the self healing process. In addition, in order to reduce the inrush current itself in the failed point, the segmentation system is maintained, using different calibration of the fuse, and a modified resistivity of the metallization.

In these conditions, when only a weak point occurs, the self healing process is sufficient to restore the dielectric properties of the film ; if more than one puncture occurs in the same area, increasing the interruption time, and consequently, the level of the inrush current, the fuse works.

In the first situation, only a few  $\text{cm}^2$  are cancelled, in the second one, some  $10\text{s cm}^2$ . Compared to the metallized surface of a capacitor, these surfaces can be considered as negligible.

The two combined protection processes allow to increase the stress applied on the polypropylen film.

This stress is limited by the reversal of the voltage. Fig. 3 shows the derating obtained when testing the capacitors between 10 and 90% reversal, using steps of growing stress, on the base of 1000 shots per step.

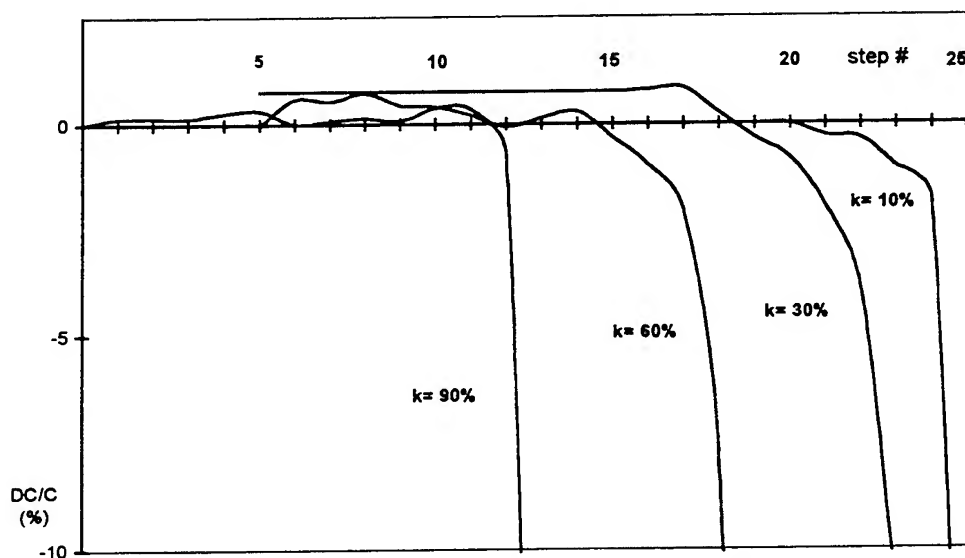


Fig 3. Capacitance drop vs 1000 shots/step



## 5.2. Current.

With these large capacitors, using metallized film, the discharge current could lead to a limitation of the performances ; compared to the d.c. filter, the  $I^2t$  ( $I$  : peak current -  $t$  : first pulse width) becomes important. In this situation, we also follow the knowledge on the filtering capacitors ; resistivity of the metallization reenforced edges, and dimensions of the fuses are calculated to withstand the full short circuit for a reduced number of shots.

## 5.3 - Résultats.

The all film technology is applied to an industrial size capacitor with

|                   |                                     |
|-------------------|-------------------------------------|
| Energy :          | 100kJ                               |
| Voltage :         | 24kV                                |
| Lifetime* :       | 10 000 shots.                       |
| Reversal :        | 10 %                                |
|                   | with 25 shots at 70%                |
| Peak current :    | 42kA (72kA under faulty conditions) |
| Dimensions        | Length : 510mm                      |
|                   | Width : 332mm                       |
|                   | Height : 853mm                      |
| Terminals :       | 2 outputs - flat design.            |
| Volume :          | 144 liter                           |
| Specific energy : | ~ 700 joules / liters.              |
| Weight :          | ~ 130kg (Density : 1.11kg/l)        |

\* Lifetime reached when capacitance looses 5%.

After 10 000 shots, the capacitance looses 1.8% and after 20 000 shots, 2.5%.

## CONCLUSION.

The all film design for energy storage capacitors has to be placed in the normal evolution of the dielectrics ; the paper layers have completely disappeared in the power factor correction and the d.c. filter capacitors ; it was still remaining in the discharge capacitors.

Now, this last use disappears.

According to the weight and volume reductions obtained, for 5 years, on the d.c. filter capacitors, with the same basic design, it is expected, also on the energy storage capacitors, a similar evolution and the last results obtained on the 100kJ units show that the 1000 joules/liter level, already reached on small units, will be obtained on the large capacitors in 1997.

# Low Weight and Size Pulse Forming Unit, Switched by a Novel High Current Rate SCR

E. Spahn, G. Buderer

French-German Research Institute of Saint-Louis (ISL)  
5, rue du Général Cassagnou, F-68301 SAINT-LOUIS CEDEX, France

E. Ramezani

ABB Semiconductors AG  
Fabrikstr. 3, CH-5600 Lenzburg/Switzerland

*Abstract-* The 50 kJ pulse forming units (PFU) for the 10 MJ ISL-facility PEGASUS, switched by SCR's, are equipped with 30  $\mu$ H inductors in order to decouple the units inductively for security reasons and to limit the maximum current to 60 kA. This limitation is obliged by the application of thyristors with an admissible maximum current of 90 kA.

Due to novel SCR's [1], developed by ABB Semiconductors and ISL, with a maximum current of more than 120 kA and a current rate  $dI/dt$  higher than 5 kA/ $\mu$ s it is feasible to design and build a 50 kJ-PFU without the above mentioned inductor. So weight, size and costs of the 50 kJ-module will decrease drastically. Furthermore the output current pulse is shorter. So more flexibility is possible for total current pulses, shaped by several units triggered with different time delays. Besides this the railgun current after shoot-out is considerably reduced. The novel PFU with its electrical properties due to a railgun application will be presented in the paper.

## 1. Introduction

At the ISL pulse forming units (PFU) have been developed as power supplies for electromagnetic guns [1]. One PFU consists of a capacitor with an energy of 50 kJ, a thyristor (CSF 672-11000) as main switch, a semiconducting diode (DSA 1508-12000) as crowbar switch, a pulse shaping inductor ( $L = 28 \mu$ H) and a coaxial cable, which connects the PFU to the load (see Fig. 1). The applied semiconducting devices have a blocking voltage of 11 kV (thyristor) and 12 kV (semiconducting diode) respectively [2, 3]. These devices were developed at ISL and subsequently industrialized by ABB Semiconductors AG/Switzerland.

The primary circuit of the PFU, being composed of capacitor, SCR and crowbar diode, is set up with a very low stray inductance ( $L < 100$  nH) in order to minimise the losses and the parasitic voltage occurring, when the SCR is switched off by the crowbar diode [2]. This immense low stray inductance could be realized by arranging the reverse conductor cylindrically around the semiconducting switches (see Fig. 2).

For the 10 MJ-facility PEGASUS a pulse forming network (PFN) of 200 50 kJ-modules will be built up and operated at a voltage of 10.75 kV. First tests showed that the PFN works with a high reliability.

One of the main works to be done on electric guns concerns the reduction of size and weight of the PFN's in order to install electric guns on vehicles (e. g. tanks). Therefore considerations were made to decrease size and weight of the above described 50 kJ-PFU's.

One step is to downsize volume and mass of the capacitors by enhancing the energy density. This will be done by the appropriate manufacturers and developments are going on. Size and mass of the semiconducting Si-based switches are already optimised [3]. So we focus on the pulse shaping inductor.

The inductance requires about 20 % of size and weight of the whole PFU. The inductor ( $L = 30 \mu$ H) fulfils two tasks within the PFU.

1. Entire electrical decoupling of the modules within a larger PFN.
  2. Limitation of the maximum current to 50 kA and of the maximum current rate ( $dI/dt$ ) to 350 A/ $\mu$ s.
- These limitations are essential in order to not exceed the current and current rate capabilities of the applied SCR's [3].

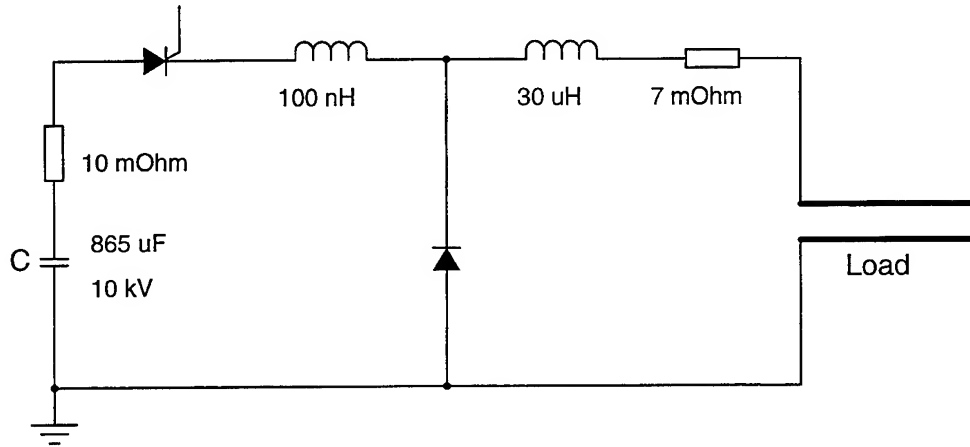


Fig. 1: Electrical circuit of a 50 kJ-PFU.

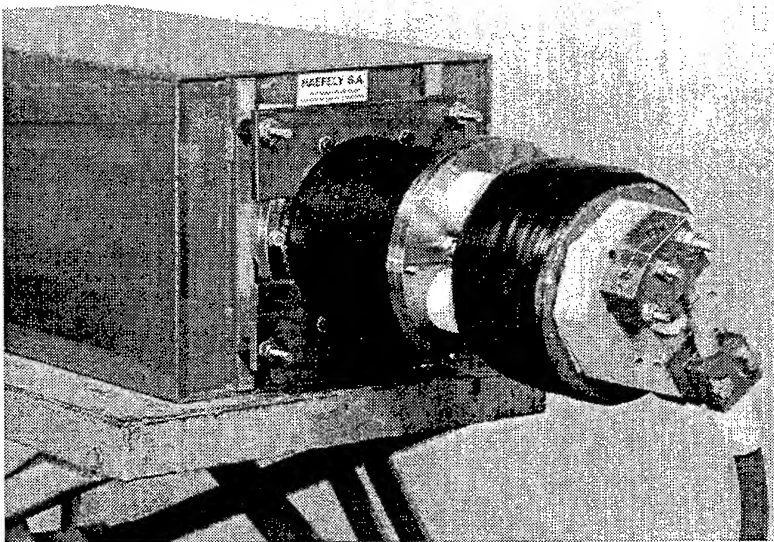


Fig. 2: Set-up of a 50 kJ-PFU.

If there were a SCR available with a current capability of more than 100 kA and an admissible current rate of several kA/ $\mu$ s, it would be possible to decrease the inductance of the 50 kJ-PFU. That means the inductor could be reduced or totally renounced. So volume, mass and costs of the PFU could be diminished drastically.

In co-operation, ABB Semiconductors and the ISL developed a novel high current rate SCR [4], which can meet the requirements of a main switch of a 50 kJ-PFU with a strongly decreased inductance.

In the first part of the paper this special device and its electric properties will be sketched out.

In the second part a 50 kJ-module applied with such a device will be presented and the occurring difficulties concerning above all the operation of such PFU's within a larger PFN will be discussed.

## 2. Novel high current rate SCR

An ideal semiconductor device qualified for handling high voltages and currents as a closing switch is the asymmetric thyristor (ASCR). In order to enable a fast turn-on capability (in the nanosecond range) the cathode and gate regions are highly interdigitated as known from a GTO-device. This leads to a quasi-axial turn-on process, similar to that of a diode turn-on. A further turn-on optimisation at a given blocking voltage is obtained

by the application of a buffer-layer structure with an appropriately optimised doping profile. Then the silicon wafer can be designed with a substantially smaller thickness resulting in better turn-on capabilities. This is of particular significance at blocking voltages above about 4 kV and helps to reduce the number of series-connected devices in high voltage (several ten kV) switching applications.

Since the interdigitated silicon wafer has an extremely large gate periphery a gate current with a high current rate and a high peak value is required in order to minimise the turn-on time and the turn-on switching losses. In order to operate the trigger circuit at a voltage in the order of a few ten volts the device has a specially designed gate configuration with a very low gate inductance (few nH). This was realized by placing a ring-shaped gate contact around the circular ceramic insulator near the cathode plane (see Fig. 3). In this way, and by utilizing a large-area parallel current path to gate and cathode, both the stray inductance and the gate cathode resistance could be decreased in a manner that gate current rates of one kA/ $\mu$ s and current peak values of more than one kA could be achieved with a power supply voltage of the trigger circuit in the range of 20 to 30 V.

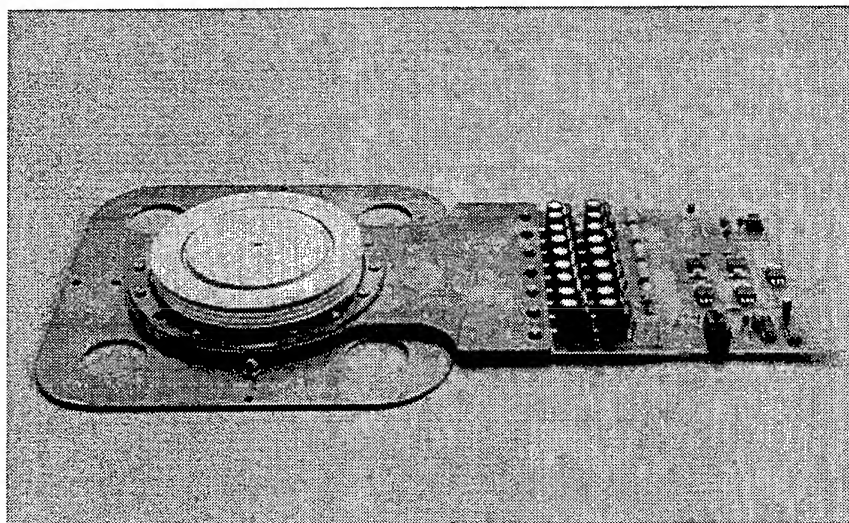


Fig. 3: Novel high-current SCR with gate unit.

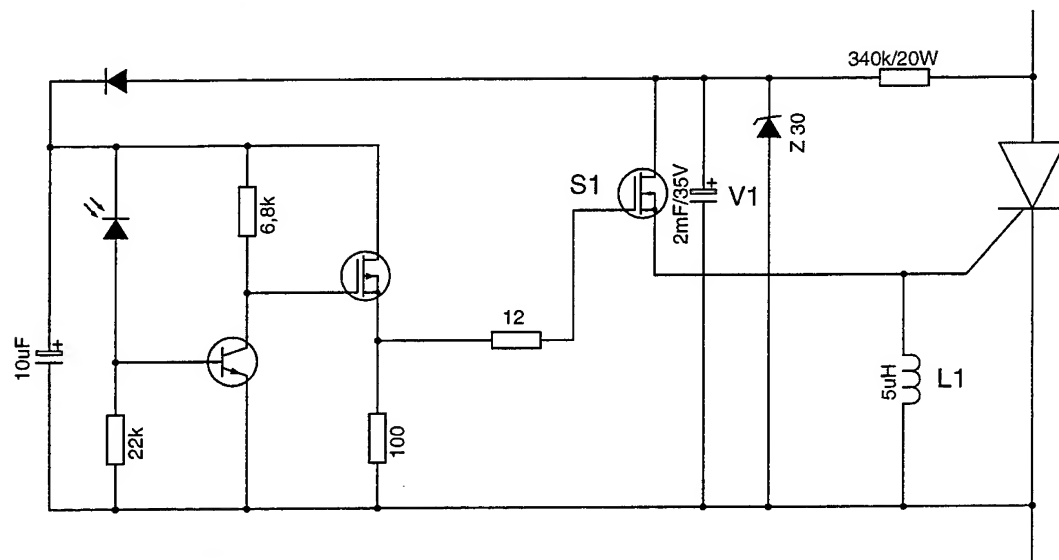


Fig. 4: Diagram of the gate circuit.

In Fig. 4 the trigger circuit is represented schematically. As mentioned above the voltage V1 for operating the gate unit is about 30 V. S1 represents a parallel connection of 10 n-channel MOSFET's in order to achieve an on-resistance below 5 m $\Omega$ . Between gate and cathode a small inductance L1 of about 5  $\mu$ H is positioned. So gate and cathode are short circuited before the device is ignited. This is required to guarantee a safe blocking behaviour. Because the inductance of L1 is much higher than the gate-cathode inductance the gate current is nearly not influenced.

A typical gate pulse is shown in Fig. 5. Due to the very low stray inductance between gate and cathode the gate current rises up to a peak value of more than 1 kA. The initial current rise rate is in the order of a few hundred A/ $\mu$ s. The current pulse was measured with a thyristor current between anode and cathode of 30 kA with the help of a small Rogowski coil, which was positioned around the gate lead (see Fig. 3). When there is a thyristor (load) current the gate current is even higher.

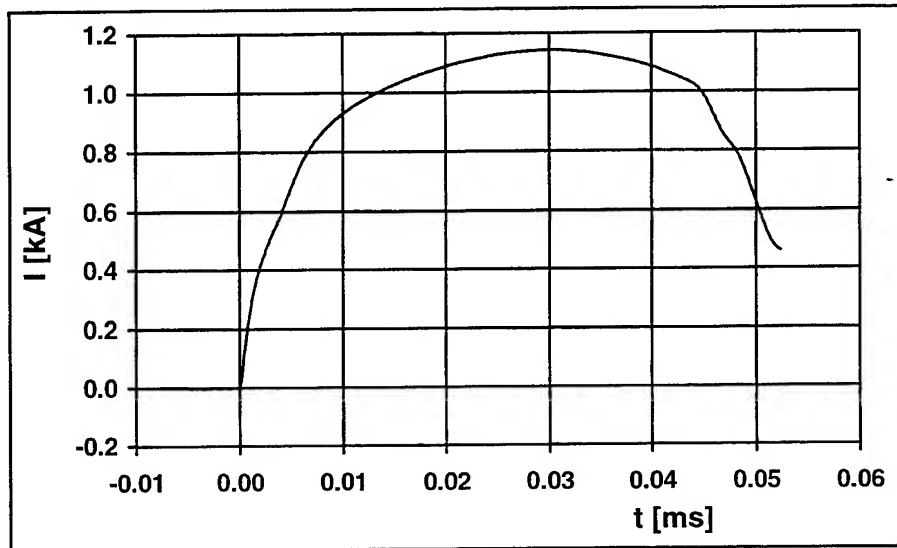


Fig. 5: Typical gate current pulse as a function of time.

The laboratory circuit, which was applied to investigate the switching behaviour of the novel SCR is shown in Fig. 6. It consists of a capacitor bank with a variable capacitance, a free-wheeling or crowbar diode for protecting the SCR against reversal voltages, the SCR with its associated gate circuit and an inductor, whose inductance is also variable.

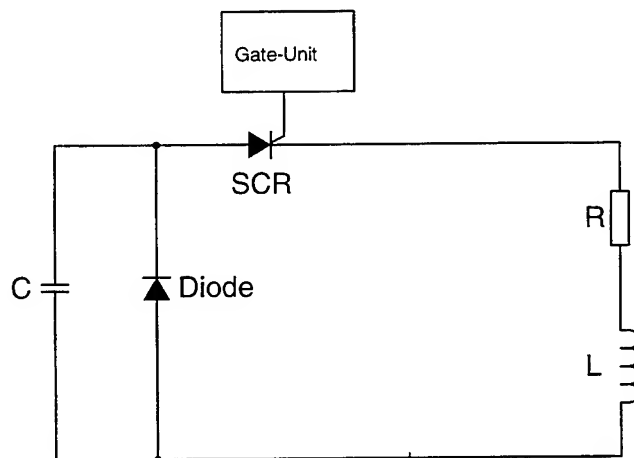


Fig. 6: Test circuit for the investigation of the switching behaviour of the novel SCR.

By selecting appropriate values for the inductance and the capacitance the thyristor was investigated concerning its turn-on behaviour. The destination was to determine the limit for the current peak value and the current rate  $dI/dt$ .

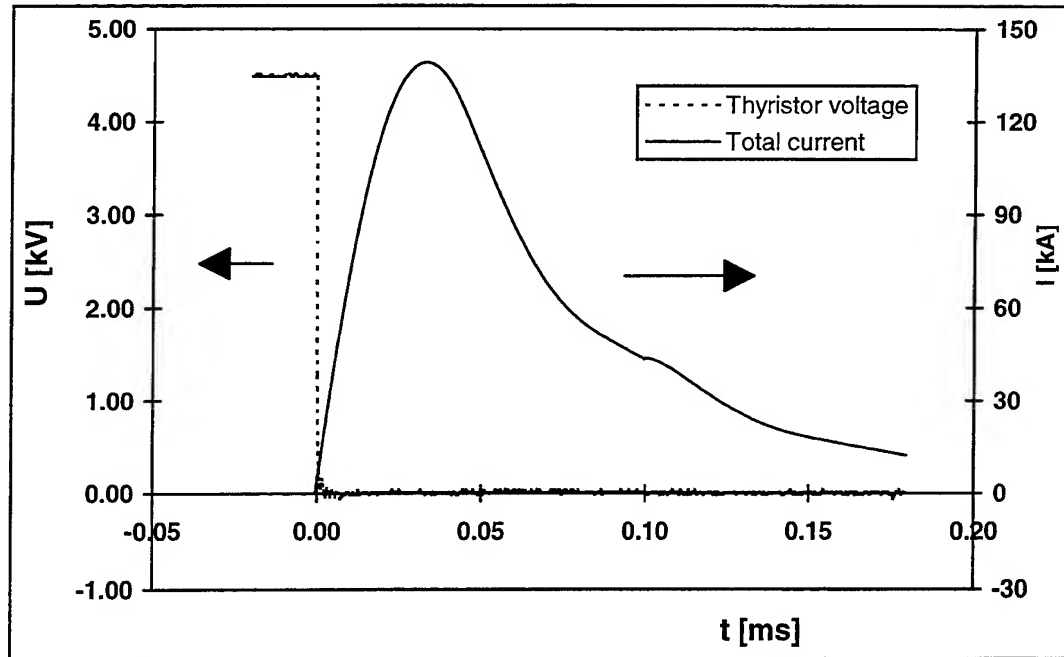


Fig. 7: Turn-on behaviour of the thyristor.

In Fig. 7 the turn-on behaviour of the device is shown by representing the thyristor current and voltage.

The current rises up to a value of 140 kA within a time of about 30  $\mu$ s. It has to be pointed out that this value does not represent the limit for the peak current, but with our test circuit no higher current values could be achieved, because, since we did not use a serial configuration of several devices during the test period, the operating voltage was limited to the maximum blocking voltage of one device (4.5 kV). The initial current rate was about 7.5 kA/ $\mu$ s and the maximal admissible action integral ( $\int I^2 dt$ ) was determined to be not higher than  $1.2 \cdot 10^6$  A<sup>2</sup>s for single pulse applications.

The turn-on voltage, dropping down to a few volts within about 100 ns after the device has been triggered, shows that the turn-on losses are negligibly small and the turn-on resistance of the device is less than 1 m $\Omega$ .

So, concerning the turn-on behaviour the novel SCR seems to be qualified as main switch for a 50 kJ-PFU with a reduced inductance. Nevertheless it has to be investigated how a serial configuration of several SCR's allowing an operating voltage of 10 kV works and how the devices behave, when they are switched off by a crowbar diode. Therefore a 50 kJ-module with reduced inductance was built up.

### 3. 50 kJ-PFU, equipped with the novel SCR

A 50-kJ module comparable to the one represented in Fig. 2 was set up by applying the novel SCR as main switch. In order to reduce size, weight and costs of the PFU the inductance of the module was diminished by leaving out the 28  $\mu$ H inductor. A pulse shaping inductance of about 4  $\mu$ H was adjusted by the arrangement of the capacitor and the semiconducting switches ( $L \approx 0.8$   $\mu$ H) and a coaxial cable with a length of 12 m ( $L = 3.2$   $\mu$ H). For test purposes this cable also represents the load and therefore it is short-circuited at the end ( $R \approx 8.5$  m $\Omega$ ). So the new PFU consists of the following elements:

- 50 kJ-capacitor
- novel SCR (see above) as main switch
- semiconducting diode (DSA 1508-12000) as crowbar switch
- coaxial cable as connector to the load

In order to operate the PFU at a voltage of 10 kV it is necessary to configure three thyristors ( $V_{\text{DRM}} = 4.5 \text{ kV}$ ) in series.

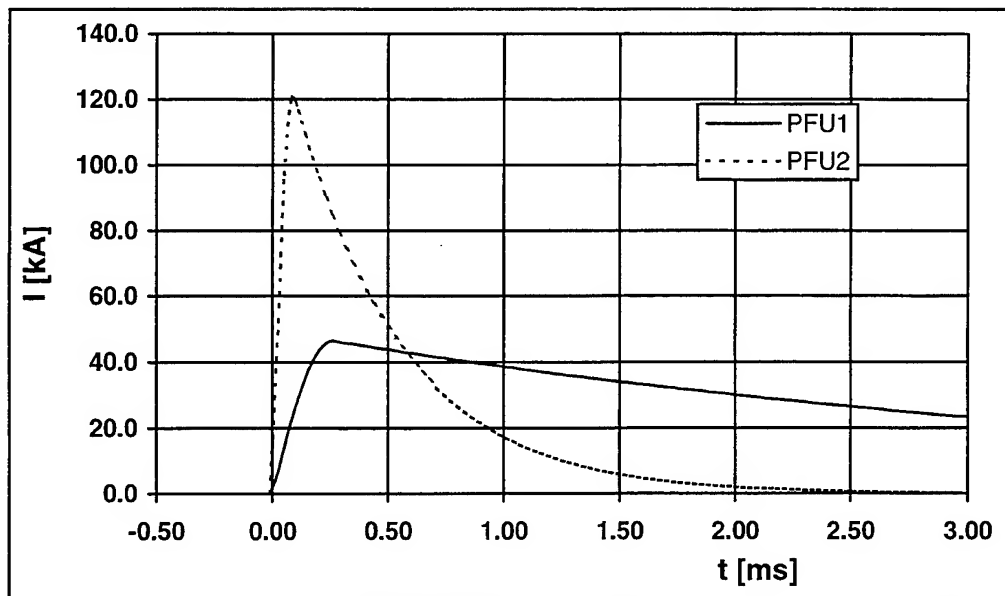


Fig. 8: Total current of the high and low inductance PFU's as a function of time.

In Fig. 8 the calculated total currents of the old (PFU1;  $L = 30 \mu\text{H}$ ) and the new (PFU2;  $L = 4 \mu\text{H}$ ) 50 kJ pulse forming units are represented as a function of time. The current pulse yielded by PFU2 is much shorter. The current rise time is about  $90 \mu\text{s}$  in comparison to  $250 \mu\text{s}$  of PFU1. The current maximum is with a value of about 120 kA nearly three times higher than that of PFU1. The initial current rate  $dI/dt$  is  $2.5 \text{ kA}/\mu\text{s}$  and the action integral ( $\int I^2 dt$ ) determined from the thyristor current is in the order of  $1 \cdot 10^6 \text{ A}^2\text{s}$ . So the maximum current, the current rise rate and the action integral are below the admissible values of the novel SCR (see section 2).

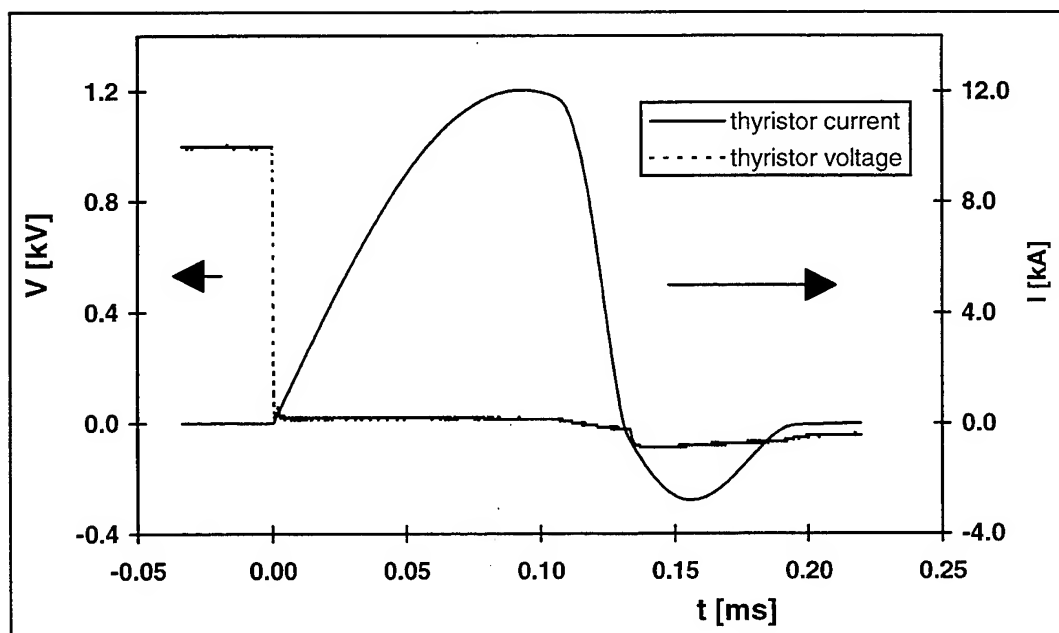


Fig. 9: Temporal behaviour of thyristor current and voltage.

The current behaviour of the novel SCR, when operated as main switch in PFU2, is shown in Fig. 9. In order to avoid the risk of damaging the device the investigations were made at an operating voltage of 1 kV. When the crowbar diode takes the thyristor current shortly after the current maximum is achieved, the thyristor current drops down rapidly and becomes negative. The fact that the current also flows in blocking direction of the SCR means that the charge carrier density is not going to zero, when the forward current passes zero. The reason is that the charge carrier lifetime is high in order to enhance the device conductivity. Nevertheless the charge carrier density decreases. This results in a thyristor voltage, which also becomes negative and is in the order of -100 V. That means that the energy dissipated into the thyristor during turn-off achieves a critical value even with a maximum forward current of only 12 kA. So the conclusion can be drawn that the thyristor will be damaged, when the forward current and in consequence also the negative current during thyristor turn-off are further enhanced. In order to protect the SCR measurements have to be taken.

There exist several kinds of snubber circuits for protecting the thyristor in the turn-off phase (e. g. RC-circuit, antiparallel diode, serial diode) [5]. In order to enable a compact set-up and because the negative voltage occurring during thyristor turn-off is relatively low [2] ( $V < 500$  V) due to the very small stray inductance in the thyristor circuit we decided to install the snubber circuit with the serial diode.

A P-Spice simulation of the thyristor current when using a serial diode is represented in Fig. 10 (operating voltage: 10 kV). During turn-off the negative current is limited to less than 10 kA and is dropping back to zero within a time period in the order of one microsecond. So the energy dissipated at the SCR during turn-off is low and the device will not be damaged even with a forward current maximum of more than 120 kA (see Fig. 10).

That means a snubber circuit consisting of a serial diode is sufficient to protect the SCR during turn-off. The set-up with the serial diode is feasible in a very compact manner, because only one diode with a blocking voltage of less than 1 kV is required and this diode may be integrated in the SCR device.

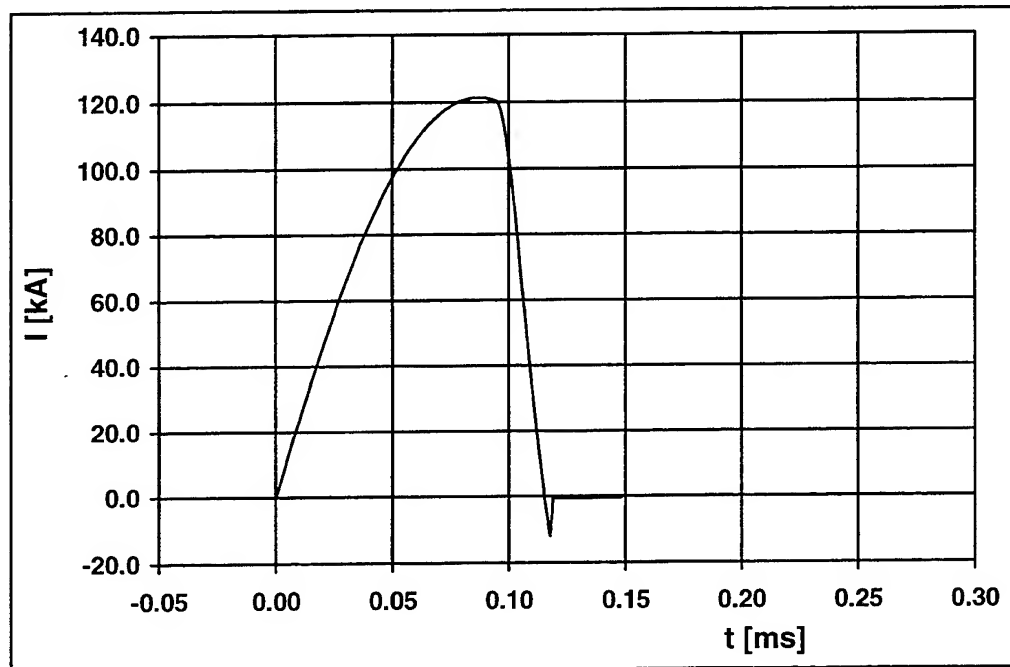


Fig. 10: Thyristor current as a function of time, when using a serial diode as snubber device.

It could thus be demonstrated that the novel ABB-ISL SCR enables to set up a 50 kJ-SCR without the necessity of a pulse shaping inductor.



#### 4. Summary and conclusions

A novel SCR with extremely high peak current values ( $I_{\max} > 140$  kA) and current rates ( $dI/dt > 15$  kA/ $\mu$ s) was developed by ISL and ABB Semiconductors AG/Switzerland. By applying this device as a main switch in a capacitor driven 50 kJ-pulse forming unit for electric guns, size, mass and costs of 50 kJ-module can be reduced by about 20 %. This is done by leaving out the inductor, which is required in the conventional 50 kJ-PFU to limit the current maximum to about 50 kA.

Due to shorter current pulses generated by the novel PFU the flexibility in respect of shaping total current pulses by switching on several PFU's with temporal delays enhances. Besides this the current pulse decreases faster because the inductance is diminished drastically. So the part of the current in a railgun at shoot-out can be highly reduced and thus the efficiency of the whole railgun facility can be enhanced and there will be less muzzle flash. In the future a small PFN out of the novel PFU's will be built up and operated with a railgun. Besides this considerations for the PEGASUS facility are made to replace the conventional PFU's by the novel ones in the latest stages in order to reduce the shoot-out current in the rails.

#### References

- [1] E. SPAHN, F. HATTERER, G. BUDERER  
Compact 40 kH-pulse forming unit, switched by semiconductors  
IEEE Trans. on Magnetics, vol. 31, pp. 78-83, January 1995
- [2] E. SPAHN, G. BUDERER, W. WENNING, V. WEGNER, F. JAMET  
The Application of Semiconductor Switches in Railguns  
4th European Symposium on EML-Technology, Celle (Germany), May 1993
- [3] E. SPAHN, E. RAMEZANI  
High Voltage Thyristor Switch for Pulse Power Applications  
5th European Symposium on EML-Technology, Toulouse (France), April 1995
- [4] E. SPAHN, G. BUDERER, E. RAMEZANI  
A Novel High Current Rate SCR for Pulse Power Applications  
22nd International Power Modulator Symposium, Boca Raton, Florida, June 1996
- [5] K. HEUMANN, R. STUMPE  
Thyristors-Properties and Applications  
Teubner Verlag 1974, pp. 123-138

## **Recent developments in bipolar lead-acid battery technology at TNO**

Maurice Wollersheim, Peter van Gelder, Wilco de Jong, Boy Mosterdijk

TNO Prins Maurits Laboratory - Pulse Physics Laboratory  
visiting address: Schoemakerstraat 97, 2628 VK Delft, the Netherlands  
mailing address: PO Box 45, 2280 AA Rijswijk, the Netherlands  
phone: +31-(0)15-2697011, fax: +31-(0)15-2621268

and

Michel Saakes

TNO Environment, Energy Research and Process Innovation  
PO box 6011, 2600 JA Delft, the Netherlands  
phone : +31-(0)15-2697638, fax: +31-(0)15-2569670

### **Abstract**

The bipolar lead-acid battery currently tested at the Pulse Physics Laboratory and under development at TNO Environment, Energy Research and Process Innovation, is an excellent candidate for pulsed power applications that require multiple high power and high current pulses. At the Pulse Physics Laboratory, the combination of such a battery (as a primary energy source) and an inductor (pulse transformer) is investigated as an intermediate energy storage and pulse forming component. For this application, a battery is required that can deliver currents up to tens of kA's (peak power of tens of MW's) and energy extraction times of tens of milliseconds.

A research programme is being performed in order to better understand and improve the functioning of the fast-discharge bipolar lead-acid battery. Recent efforts directed towards the improvement of the electrode substrate materials for the bipolar plate has resulted in a patent been taken out on a corrosion free non-metallic substrate. Improvement of the specific power and energy and optimisation of the construction of the bipolar lead-acid battery has led so far to working 12V bipolar battery prototypes using paste technology and with a specific power of 750 W/kg, at a discharge rate of 230 W/Wh using a pulsed discharge current. In order to operate this type of fast-discharge lead-acid battery reliably and repetitively, a battery management system that controls all cells individually was developed at the Pulse Physics Lab. Furthermore, to test the performance of the battery, a programmable electronic load was built that can sink currents up to 10 kA. The amplitude of the discharge current is controlled by a computer and follows a programmed current-time profile.

### **1 . Introduction**

Many electrical defence applications (e.g. pulsed lasers, high power microwaves, railgun) require a special kind of power supply that can deliver high power energy pulses repetitively. Generally, these kind of power supplies are built up with two main components. Firstly, a primary energy source (e.g. combustion engine plus electric generator, battery, fuel cell etc.) that is capable of delivering the desired energy for one or more pulses but usually not at the required power level. For this we use a pulse forming network (PFN) which converts low power energy pulses into high power energy pulses (energy is conserved but the pulse width is decreased considerably). Components of PFN's are: capacitors, inductors, special rotating machines (e.g. compulsator) and switch systems.

In this paper we will discuss the combination of a bipolar lead-acid battery (as a primary energy source) and an inductor (pulse transformer) as an intermediate energy storage and pulse forming component. For our application we need a battery with peak power of MW's and energy extraction times of tens of milliseconds. For the development of this battery, it is essential to know the required  $P_s/E_s$ -ratio, i.e. specific power  $P_s$  (in W/kg) and specific energy  $E_s$  (in Wh/kg). In our case and for pulsed power applications in general, the required  $P_s/E_s$ -ratio is much higher than for e.g. electric vehicle applications ( $P_s/E_s=5-10$  [h<sup>-1</sup>]), as will be shown in the model calculation of a pulsed power supply as described in the next section.

## 2. Model calculation of a pulsed power supply based on a battery and pulse transformer

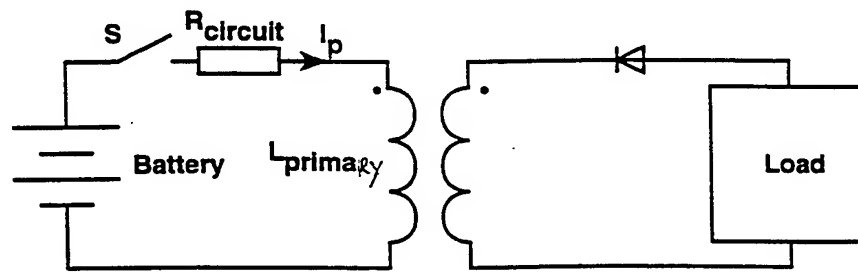


Figure 1 Electric circuit of a battery-pulse transformer based pulsed power supply

As soon as switch S is closed a current will start to flow in the primary circuit (battery,  $R_{circuit}$  and  $L_{primary}$ ). This current can be described as a function of time  $t$ :

$$I_p(t) = I_{p(max)}(1 - e^{-\frac{t}{\tau}}) \quad (1)$$

Here  $I_{p(max)}$  is the maximum attainable current ( $I_{p(max)} = V_{battery}/R_{circuit}$ ) in the primary circuit and  $\tau$  is the characteristic time constant of the primary circuit ( $\tau = L_{primary}/R_{circuit}$ ),  $R_{circuit}$  is the total resistance in the primary circuit. As the rate of current rise is positive, the diode in the secondary is reversedly biased; therefore no secondary current flows. As soon as the primary current reaches the desired level the switch is opened quickly and all magnetic energy coupled with the primary windings of the transformer is transferred to the secondary windings, resulting in a transformation of the primary current multiplied by the turns ratio into the secondary circuit.

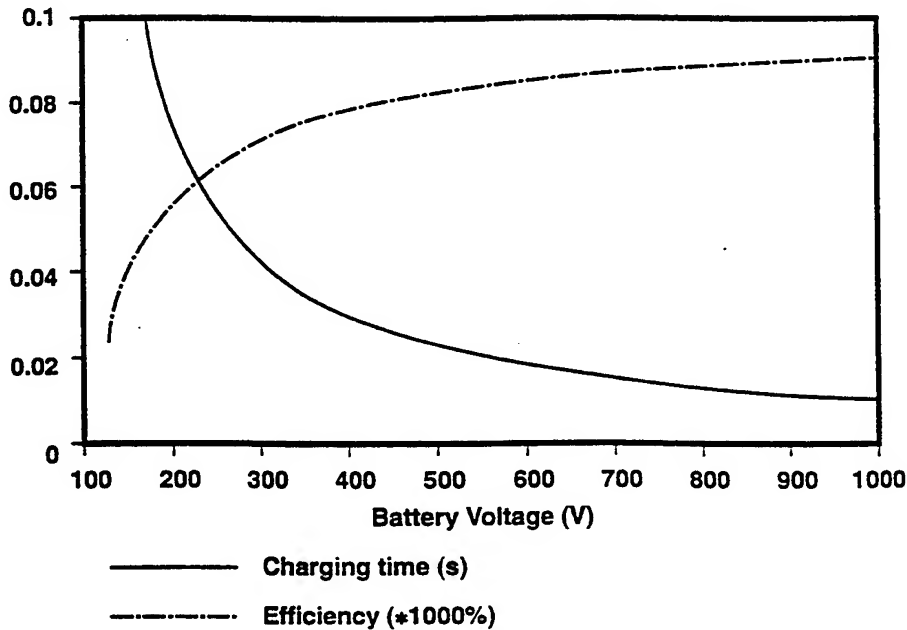
At the start of the charging process, all energy will initially be stored in the inductor. As the charging process progresses, more energy will increasingly be dissipated in the resistor. Therefore the charging efficiency ( $\eta$ ) is only 100% at the start and decreases hereafter. The longer the charging process continues, the more energy is stored in the inductor but also the more energy is dissipated in the circuit resistance; i.e. the efficiency of charging decreases with charging time. The charging efficiency  $\eta$  is given by the ratio of the stored magnetic energy  $E_L(t)$  and the delivered battery energy  $E_{batt}(t)$ :

$$\eta = \frac{E_L(t)}{E_{batt}(t)} = \frac{\frac{1}{2} L_{primary} I_p^2(t)}{\int_0^t V_b I_p(t) dt} = \frac{1 + e^{-\frac{t}{\tau}} - 2e^{-\frac{t}{\tau}}}{2(\frac{t}{\tau} - 1 + e^{-\frac{t}{\tau}})} \quad (2)$$

For the battery/inductor combination we are interested in an optimum where (i) the inductor is charged with the rated energy at a high efficiency ( $\eta$ ) and (ii) the mass of the system is as low as possible. For instance, decreasing the internal resistance of the inductor decreases the dissipative losses and increases the efficiency but at the same time increases the mass of the inductor. In the following discussion the optimization process is demonstrated by an example. Here however, we will only consider the battery and try to optimise it for the given task/requirements (as summarised in Table 1), i.e. finding the optimum battery voltage and size (Ah).

*Table 1 Electric circuit parameters and battery requirements*

|  |   |
|--|---|
| Inductance                                     | $L_{primary} = 1\text{mH}$                |
| Circuit resistance without battery             | $R_{circuit} = 10\text{m}\Omega$          |
| Max. current                                   | $I = 10\text{kA}$ (stored energy is 50kJ) |
| Maximum charging time inductor                 | 70ms                                      |
| Number of discharges (at 10Hz repetition rate) | $\eta_p = 400$                            |



*Figure 2 Charging efficiency and time required to charge the inductor ( $I_p = 10\text{kA}$ ) as a function of the battery terminal voltage*

Figure 2 shows that as the battery voltage increases, the charging time decreases and the charge efficiency increases. In order to charge the inductor up to 10kA in 70ms we need a battery terminal voltage of 215V.

The maximum battery power  $P_m = 215\text{V} \times 10\text{kA} = 2.15\text{MW}$ . The energy  $E$  delivered  $\eta_p \times 50\text{kJ} / \eta = 34.48\text{ MJ} = 9878\text{ Wh}$ . This results in a P/E ratio = 230W/Wh.

Comparing this figure of source requirement with a P/E ratio of 10W/Wh for traction batteries, indicates that we are developing a special high-power battery. If we knew the Ragone diagram for this battery, we could calculate the required mass of the battery and choose the appropriate battery voltage and energy content to optimise the battery/inductor combination. Figure 3 shows an example of a Ragone diagram of a bipolar lead-acid battery cell. Take notice that the Ragone diagram of a battery system that consists of many identical cells which are connected in series and in parallel is the same as the Ragone diagram of one individual cell.

In this diagram the P/E-ratio line of 230W/Wh is drawn too. The point of intersection (point C) of this line with the Ragone diagram gives us point B on the specific energy axis; this point is called  $E_s(B)$ . The mass of battery can now be calculated by the formula:

$$M_{bat} = \frac{E_{batt}(V_b, \eta)}{E_s(B)} \quad (3)$$

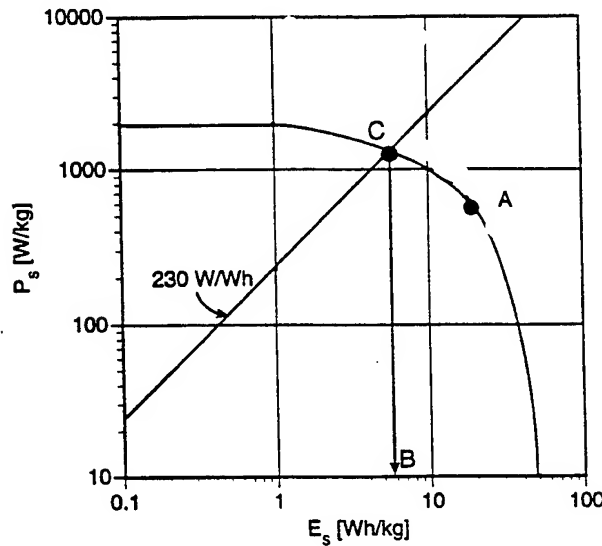


Figure 3 Typical Ragone diagram of a lead-acid battery

$E_{batt}$  is the energy delivered by the battery and is a function of the battery terminal voltage and charging efficiency. Increasing the battery voltage, decreases the charging time and increases the charging efficiency (see also figure 2), but does this also decrease the mass of the battery?

Before trying to answer this question we have to look at point A on the Ragone diagram. At this point the product  $P_s \cdot E_s$  has its maximum. If the intersection of the P/E-line and the Ragone diagram lies considerably to the right of point A (where the specific power rises relatively quicker than the specific energy decreases), one should increase the battery voltage and the mass of the battery will decrease (the Ragone diagram doesn't change, but the P/E-ratio does).

Unfortunately, in practice the point of intersection of the P/E-line lies far left of point A, and therefore increasing the voltage will not decrease the mass of the battery. A more precise optimisation can only be made when the Ragone diagram of the actual battery is measured under the actual pulsed, high current (10kA) discharge conditions.

### 3. Development of the bipolar lead-acid battery

During the last decades the development of lead-acid batteries has shown large progress. Examples of this development are the valve-regulated recombinant lead-acid batteries (maintenance free) [1], a thin-film battery developed by Bolder Technologies [2] and a bipolar lead-acid battery developed by e.g. Johnson Controls [3], Arias Research Associates [4-6] and Bipolar Technology [7-8]. They represent a major step forward both in the use and possible new areas for application of lead-acid batteries. One application for lead-acid batteries is for pulsed power devices. However, because of the very large current pulses at a relative high voltage, the use of conventional batteries (e.g. starter batteries) would lead to an unacceptably high weight for the battery package because of the relatively low specific power of current batteries (limited at approximately 200W/kg). Only a significant increase of the specific power would bring a pulsed power application within reach. One way to achieve this is to use a bipolar battery configuration as was shown at the Pulse Physics Laboratory [9-11]. It has been shown that in principle a specific power of 1kW/kg or more with lead plates is feasible using a fast discharge bipolar lead-acid battery [3,11]. However, the discharge time was limited to about 50ms because of the used electrochemical formation technique resulting in a low capacity per unit of area.

The development of such a bipolar battery however has been severely delayed since a good candidate for the bipolar plate was missing. The material for the bipolar plate must fulfil the following requirements: low density, chemically stable in sulfuric acid, electrochemically stable towards lead dioxide (no corrosion), good conductivity, no catalytic effects on the evolution of hydrogen and oxygen gas, mechanical and dimensional stability, flexibel, low cost, non-toxic.

Pure lead plates are subject to corrosion when used as a substrate for the bipolar plate. Especially the presence of lead dioxide and sulfuric acid puts extreme demands to the electrochemical and chemical stability of the substrate material which is covered on one side with lead dioxide and on the other side with lead. Many materials have been proposed in literature and patents to serve as a substrate e.g. coated titanium, iron, thermoplastics (PE, PP) filled with carbon black, glasfibers coated with  $\text{SnO}_2$  etc..

At TNO Environment, Energy Research and Process Innovation, a new type of composite substrate has been developed (patent pending) for the construction of bipolar lead-acid batteries. The main reason for developing this new substrate for the bipolar plate, was the lack of a proper bipolar plate material. Using this substrate, a series of bipolar lead-acid batteries has been built using different technologies for applying the active mass, e.g. thermal formation, Planté formation (corrosion process) and paste formation. It was shown that the Planté formation process for constructing a bipolar lead-acid battery, using the developed substrate for the bipolar plate, gave highly reproducible results [12]. However, at high discharge current densities, it was found that pasted bipolar lead-acid batteries gave a much higher utilisation grade of the active mass at high discharge current densities. Using an improved design, pasted 12V bipolar lead-acid batteries, discharged at a C-rate of 230 W/Wh (discharge time 15.7 s), have given a specific power of 750 W/kg. Further improvement is going on and it is estimated that, at the given C-rate of 230 W/Wh for the pulsed power discharge, a specific power of more than 1000 W/kg will be obtained.

#### 4. Programmable Electronic Load

In order to test the performance of the newly developed bipolar batteries (discharge behaviour for determining the Ragone diagram), a universal programmable electronic load (PEL) has been designed and built. The PEL is an electronic system that can be applied as an electrical load for any type of voltage source (e.g. batteries, fuel cells etc.). The amplitude of the current (discharge current in case a battery is the source) that the electronic load can sink, is adjustable between 0 en 10kA. Moreover, the amplitude of the current can be easily programmed as a function of time. The electronic load is configured for testing batteries with an open circuit voltage of max. 40 Volts, but the PEL could easily be adapted for higher voltages without excessive costs and effort.

The condition that the current sinked by the PEL has to be programmable (load impedance should be variable) precludes the use of inductive and capacitive load elements. The load impedance is made up of a large number of paralleled resistors, each of which can be switched in or out by an in series placed semiconductor switch. Different types of semiconductor switches have been examined for this application: power transistors, GTO's and IGBT's. The IGBT has been chosen as it can switch high currents (10-500A) at high voltages (1200V). This high hold-off voltage is necessary because during the switching off of the current through a load resistor and its parasitic inductance, a high transient switch voltage is generated. A protective snubber circuit (RC-network) is placed across the IGBT in order to limit this switching voltage. Figure 4 shows schematically the different parts of which the PEL is made up.

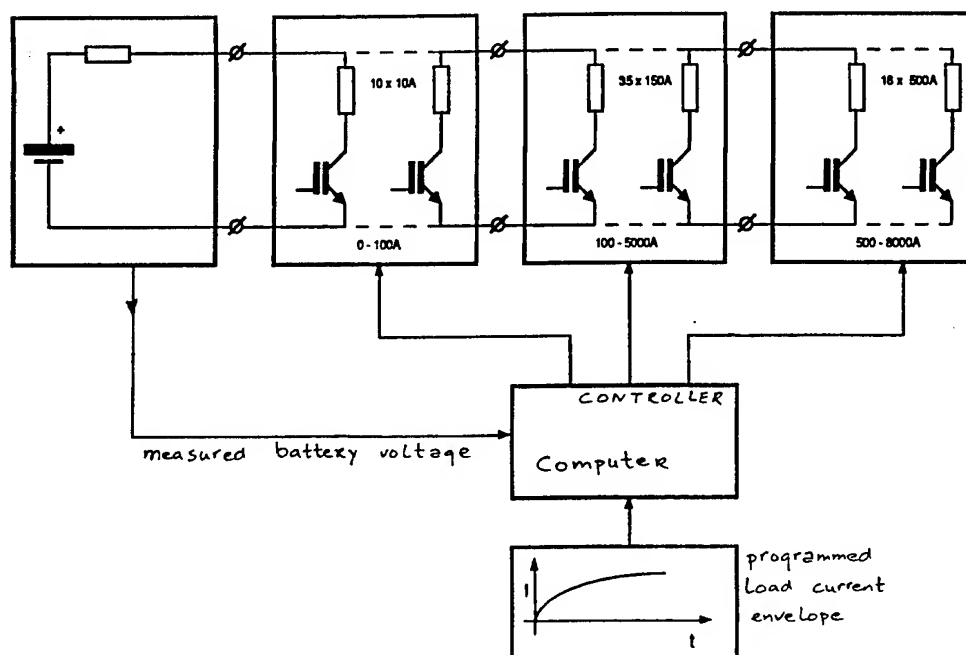


Figure 4 Simplified diagram of the programmable electronic load

The electronic load comprises of the switched load resistors and a computerized controller. As we want to achieve a large as possible dynamic range of the load current (0-10kA, smallest step 20A) with the smallest number of load resistors, the load impedance is divided in 3 different groups; 10 branches of 20A, 35 branches of 150A and 16 branches of 500A (note that these are current levels at the nominal voltage of the battery). The number of 150 and 500A IGBT's was also defined to some extent by the availability of the 500A-1200V IGBT's. Nevertheless, this choice of load resistors fulfils the requirements of adjustability of the load current: 0-10kA +/- 20 A.

The computerized controller is implemented on a Personal Computer (DOS) and its task is to switch the appropriate IGBT's on or off. In order for the computer to compute the correct switch actions it needs input information. Firstly, the number of load resistors and their resistivity. Secondly, the desired load current profile as a function of time. And finally, the terminal voltage of the battery during the discharge. This voltage is measured real-time with a sampling frequency of 5kHz. At the same frequency the 20 and 150A branches are switched on or off. The 500A branches are switched at a lower frequency (1kHz).

So far the PEL has been tested up to current of 2kA, only using the 20 and 150A branches. The test results showed good controllability of the current indicating that there is a low mutual inductance between the load branches.

## 5. Conclusions

The fast discharge bipolar battery currently under development has an excellent current sourcing capability. The patented composite substrate for the bipolar electrode overcomes several major problems which weren't properly solved in other designs. The combination of this battery and a pulse transformer (or inductor) gives a pulsed power source with good power and energy ratings. In order to find the optimum battery voltage and size (Ah) the model calculations (leading to a source/task requirement of 230W/Wh) have to be combined with the measured Ragone diagram of the bipolar battery.

## 7. References

- [1] D. Brendt and U. Teutsch, J. Electrochem. Soc., **143** (1996)790
- [2] Tristan Juergens, Robert F. Nelson, J. of Power Sources, **53** (1995) 201
- [3] Douglas C. Pierce, Proceedings of the 36th Power Sources Symposium, 6-9 June 1994, Cherry Hill, New Jersey, p. 221
- [4] J.L. Arias, J.J. Rowlette and E.D. Drake, J. of Power Sources, **40** (1992) 63
- [5] D.L. Harbaugh, 27th ISATA, Aachen, Germany, 1994, p. 129
- [6] John J. Rowlette, Proceedings of the 8th annual battery Conference on applications and advances, California State University, Long Beach, January 12-14, 1993
- [7] Rodney M. LaFollette, Fall Meeting of the Electrochemical Society, Miami Beach, Florida, October 9-14, 1994, p. 260
- [8] Rodney M. LaFollette, Final Report for Ballistic Missile Defense Organization, 14 March 1994
- [9] W. Karthaus, W.J. Kolkert, J. Nowee, IEEE Transactions on Magnetics, **25** (1989) 284
- [10] M. Kaanders, W. Mosterdijk, P. van Gelder, 9th IEEE Pulsed Power Conference, Albuquerque (NM), 1993, p. 99-102
- [11] M. Wollersheim, W. Mosterdijk, TNO-report "first generation bipolar battery" (in Dutch), PML A-83 (1993), The Netherlands
- [12] M. Saakes, D. Schellevis, D. van Trier, M. Wollersheim, "Performance and use of composite substrate-based lead-acid batteries for pulsed power applications", 5th ELBC, 1-4 October, 1996, Barcelona, Spain.



## 300 kA TEST RESULTS OF THE 1 MA RESONANT SERIES COUNTERPULSE OPENING SWITCH SYSTEM

Edwin van Dijk  
Laboratory for Power Electronics and Electrical Machines  
Delft University of Technology  
Mekelweg 4, NL-2628 CD Delft, the Netherlands

Peter van Gelder  
TNO PML - Pulse Physics Laboratory  
Schoemakerstraat 97, NL-2628 VK Delft, the Netherlands

### Summary

At the Pulse Physics Laboratory, research is being performed to develop a counterpulse technique for the controlled interruption of very high currents in inductive storage pulsed power systems. Presently, a repetitive mechanical high current opening switch is applied to commutate current to an inductive load (for example a rail accelerator) from a storage inductor charged by a homopolar generator. To increase the current level the mechanical switch is able to interrupt, the application of a counterpulse technique and a separate closing switch looks promising. Otherwise, the arc that would occur between the contacts of the switch during opening and closing at high currents (mega-ampere level), would severely damage the contacts.

To prevent the damage caused by arcing, the current must be reduced to zero or a low level before opening the switch. To be able to achieve this, the resonant series counterpulse circuit is proposed. The circuit incorporates units consisting of a capacitor bank of electrolytic capacitors with parallel connected diodes and a thyristor connected in series. Upon command, these units will create a resonant counterpulse current through the opening switch. The net current through the switch reduces to zero and the switch is opened without damaging the contacts.

Other counterpulse circuits utilise capacitors such that they experience a voltage reversal and high initial voltages are required. The resonant series counterpulse circuit uses capacitors in such a way that they do not experience a voltage reversal and they only need an initial voltage of a few hundred volts. This means that electrolytic capacitors can be used with the advantages of a higher lifetime and a relatively higher energy density at lower voltage and smaller weight.

Another advantage of the circuit is that there is no pre-current flowing through the load before the resonant current is activated. Normally, this is the case because of the resistive division of the current between the opening switch and the load, causing heating of the load. In the resonant series counterpulse circuit, the thyristors prevent this.

The units have been designed to generate currents up to 50 kA. By placing several units in parallel, higher counterpulse currents can be generated. This paper will shortly discuss the operation of the resonant series counterpulse circuit and the control electronics and present experimental results of the parallel operation of eight units at a current of 300 kA.

### Introduction

The resonant series counterpulse circuit has been described and analysed in [1] and is meant to assist a repetitive mechanical opening switch for pulsed power applications in the controlled interruption of currents up to the mega-ampere level. It consists of a capacitor bank with parallel diodes and a series counterpulse switch, consisting of thyristors. Figure 1 shows the circuit. This circuit is connected in series with the inductive load. A separate closing switch, which also consists of thyristors, is connected parallel to the opening switch.

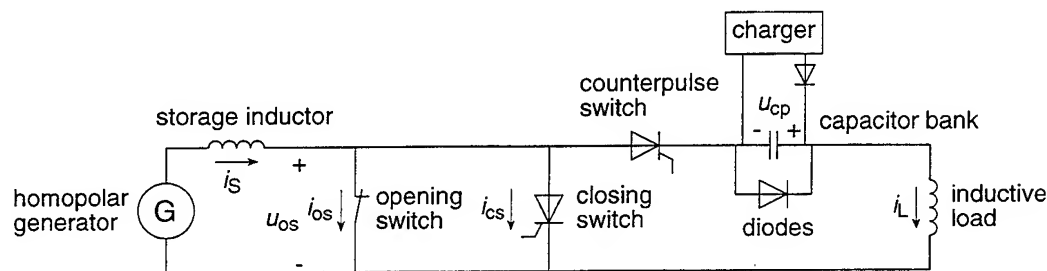


Figure 1 The resonant series counterpulse circuit in an inductive storage pulsed power system

The operation of the circuit is based on a resonance between the capacitor bank of the resonant series counterpulse circuit and the inductance of the load and parasitic inductance of the opening switch and the connections. When the counterpulse switch is closed, the capacitor bank will discharge through the load and the opening switch, creating a resonant counterpulse current through the opening switch. The net current through the latter reduces to zero and then the switch is opened. At this moment, energy from the storage inductor is transferred to the load. When the capacitor bank has been fully discharged, the diodes start to conduct and take over the current. The voltage across the capacitors remains near zero.

The resonant series counterpulse circuit utilises the capacitor bank in such a way that there is no voltage reversal across the bank. This way, electrolytic capacitors can be used with the advantage of a relatively high energy density of 500 J/kg at a voltage of about 450 V, resulting in a relatively small mass and volume. The required initial voltage of the capacitor is only a few hundred volts. This makes the resonant series counterpulse circuit for very high currents feasible to build.

In other counterpulse circuits [2], the capacitor bank experiences a voltage reversal during the counterpulse process. The capacitor bank has a high capacitance (up to several Farads) and is initially charged to a voltage of a few hundred volts up to a kilovolt. In circuits where the capacitor bank is in parallel with the opening switch and the load, the voltage may even become higher because of a high load voltage. All this means that the counterpulse capacitor bank of these other counterpulse circuits is very big in mass and volume.

The resonant series counterpulse circuit has several advantages. The main advantage is that the opening switch opens at zero or low current and closes at low voltage. This means that no arc or only a minor one occurs at the contacts of the switch and that the contacts are not damaged. Another advantage of the circuit is that there is no pre-current flowing through the load before the resonant current is activated. Normally, this is the case because of the resistive division of the source current between the opening switch and the load, causing unwanted pre-heating of the load. In the resonant series counterpulse circuit, the counterpulse switch consisting of thyristors, prevents this.

At the Pulse Physics Laboratory, a repetitive mechanical high current opening switch [3] is applied to commutate current to a rail accelerator. The energy source consists of a compact pulsed homopolar generator with a storage inductor in series [4]. The kinetic energy of rotation of the homopolar generator is stored as magnetic energy in the inductor. The requirements for the high current opening switch are very severe. It must be able to conduct currents up to the mega-ampere level for several tenths of a second, open within a millisecond, remain open for a few milliseconds and withstand a voltage of a few kilovolts, and close again. This cycle has to be performed at a repetition rate up to 10 Hz for the application with a rail accelerator load.

At the moment, work is being performed at the Pulse Physics Laboratory to develop the resonant series counterpulse circuit for currents up to the mega-ampere level. The circuit consists of units capable to handle currents up to 50 kA. Eight 50 kA-units have been built. Connected in parallel, they provide a circuit for operation with

currents up to 400 kA. Two more units will be built this year for operation with currents up to 500 kA.

### Operation of the resonant series counterpulse circuit

The whole process of counterpulsing the current through the opening switch and commutation of the source current into the load and back to the opening switch can be divided into six stages [1]. These stages are indicated in the current and voltage waveforms depicted in Figure 2. The currents and voltages are also indicated in the circuit of Figure 1. The different stages are indicated by their Roman numerals in Figure 2. Here, the source current  $i_s$  is considered to be constant ( $I_s$ ). Switching actions are assumed to take place instantaneously. The figure is not on scale. A more detailed description and analyses of the different stages are given in [1].

**Stage I:** The source current  $I_s$ , generated by the homopolar generator and storage inductor, is flowing through the closed opening switch. The closing switch is open. The counterpulse capacitor bank has been charged to a specified initial voltage  $U_{ini}$  by means of a separate charger. The counterpulse switch is blocking the capacitor bank voltage. The current  $i_L$  through the load equals zero.

**Stage II:** At time  $t_{trig}$ , the counterpulse switch is closed, leading to a resonance between the capacitor bank and the inductance of both the load and the opening switch. The resonant current flows through the load and the opening switch, opposing the current from the source. The load current  $i_L$ , which is the resonant counterpulse current, increases and the current  $i_{os}$  through the opening switch decreases. With appropriate values of the capacitance and the initial voltage of the capacitor bank, the opening switch current  $i_{os}$  is reduced to zero.

**Stage III:** At time  $t_{o,os}$ , the opening switch current  $i_{os}$  is zero and the switch is opened. The load current  $i_L$  now equals the source current  $I_s$  and the capacitor bank is further discharged. Energy is transferred from the storage inductor and the capacitor bank to the load.

**Stage IV:** At time  $t_D$ , the capacitor bank has been discharged and the diodes start conducting the load current  $i_L$ . The capacitor bank voltage  $u_{cp}$  remains near zero. A small oscillation in the voltages may occur due to the parasitic inductances in series with the diodes and the capacitors of the capacitor bank.

**Stage V:** At time  $t_{s,cs}$ , the closing switch is closed and the current  $i_{cs}$  starts to flow through it. The load current  $i_L$  decreases. The voltage  $u_{os}$  across the opening switch

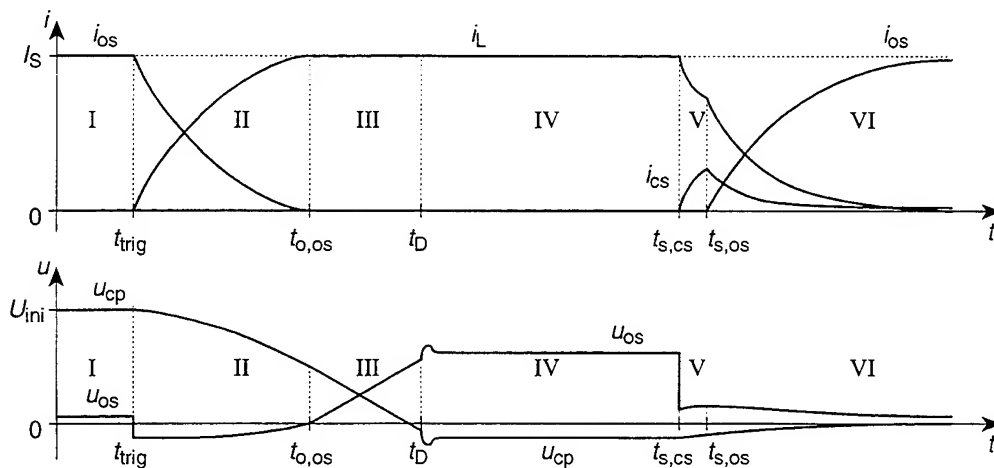


Figure 2 Current and voltage waveforms of the resonant series counterpulse circuit (not on scale); upper graph: currents through the opening switch ( $i_{os}$ ), the closing switch ( $i_{cs}$ ) and the load ( $i_L$ ), lower graph: voltages across the opening switch ( $u_{os}$ ) and the capacitor bank ( $u_{cp}$ )

reduces to a low value. This guarantees that the opening switch doesn't have to close at a high voltage imposed by the load, which would cause arc erosion at the contacts of the opening switch.

*Stage VI:* At time  $t_{s,os}$ , the opening switch is closed at low voltage and current starts to flow through it. Both the load current  $i_L$  and the closing switch current  $i_{cs}$  decrease to zero. The impedance of the closing switch should be higher than the impedance of the opening switch, so that the current commutates from the closing switch to the opening switch. When the closing switch current  $i_{cs}$  is low or zero, the closing switch can be opened for the next cycle.

After stage VI, the circuit can be returned to stage I by charging the capacitor bank to the specified initial voltage  $U_{ini}$ . This way, it is possible to achieve repetitive operation with the resonant series counterpulse circuit. The charger, however, must be able to charge the capacitor bank fast enough to allow for the required switching frequency.

### Experimental set-up

The resonant series counterpulse circuit consists of a number of parallel 50 kA-units. This gives the flexibility to use the circuit for different current ratings and with a different total capacitance of the capacitor bank. Each unit consists of a capacitor bank of electrolytic capacitors with parallel connected diodes and a thyristor connected in series. A second thyristor is used for the closing switch function. The construction of the units is described in detail in [5]. The units are designed for currents up to 50 kA and the electrolytic capacitors of the unit can be charged to a voltage up to 400 V. The capacitance of the capacitor bank of a single unit is 180 mF. A picture of the resonant series counterpulse circuit with eight 50 kA-units is shown in Figure 3. A schematic diagram of the experimental set-up is depicted in Figure 4. The source current is delivered by a homopolar generator of 6.7 MJ and a storage inductor of 6.7  $\mu$ H [4].

The 50 kA-units are connected in parallel with each other by means of coaxial cables with a length of 1.5 m. Both the core and the shield of the cables are made of fine stranded tinned copper conductors with a diameter of 0.4 mm, providing flexibility to the cables. The total area of both the core and the shield of the cables is 50 mm<sup>2</sup>. The cables have a resistance of 0.70 m $\Omega$ /m and an inductance of 0.26  $\mu$ H/m. The cables are

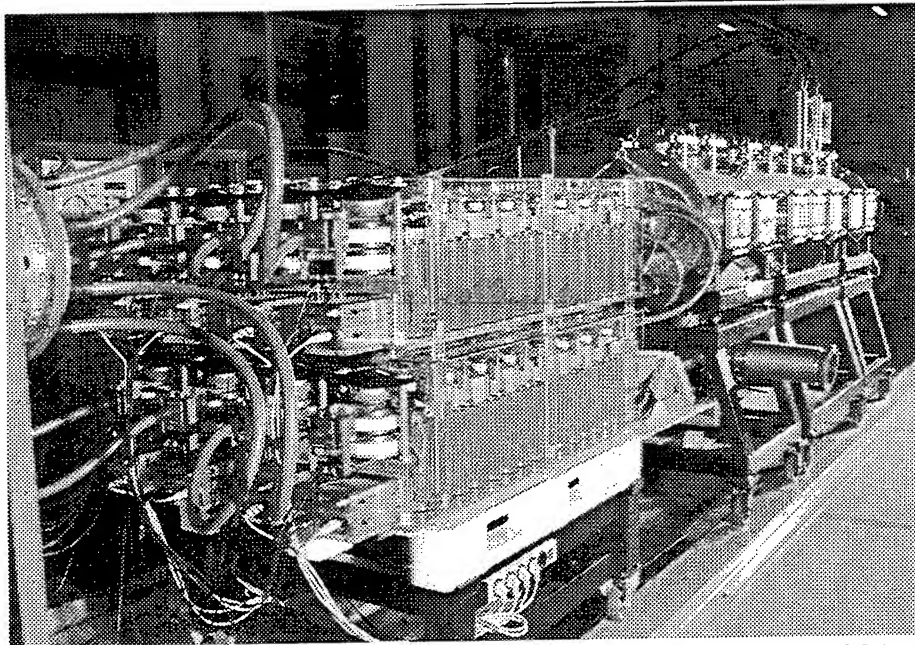


Figure 3 Picture of the resonant series counterpulse circuit with eight 50 kA-units

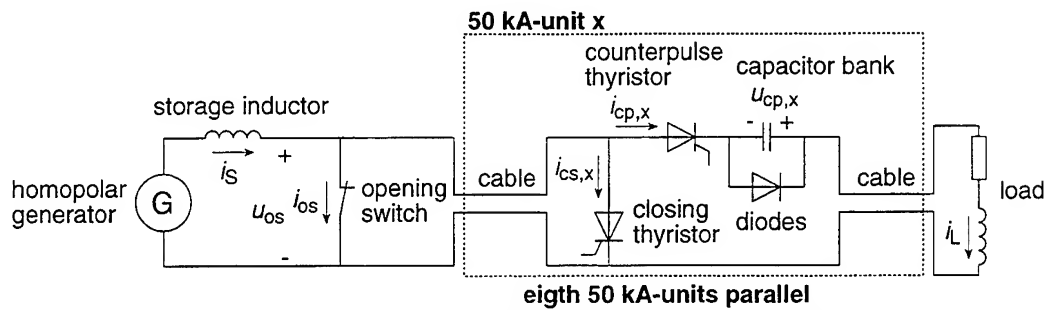


Figure 4 Schematic diagram of the experimental set-up

connected to aluminium discs in a circular way, to provide for symmetrical connections.

The load consists of two aluminium discs. The cables are connected to these discs in a circular way as well. The two disc are connected to each other with four massive aluminium cylinders with a diameter of 27 mm and a length of 50 mm.

### Control electronics

The control electronics determine the moments at which the counterpulse switch and the closing switch have to be triggered and monitors the occurrences of fault conditions in the resonant series counterpulse circuit. When a fault occurs in the circuit, the closing switch must be closed immediately to protect the opening switch. Figure 5 shows a simple block diagram of the control electronics. The *counterpulse trigger* and *close trigger* signals are sent via optical fibres to the trigger units of the counterpulse thyristors and closing thyristors of each 50 kA-unit.

An optical angle encoder is used to determine the trigger moments for the counterpulse switch and the closing switch in normal operation. The opening switch is a mechanical switch, consisting of two sets of copper brushes (positive and negative polarity) and a rotating copper drum [3]. The rotating drum has a insulating strip, so that during rotation of the drum, the switch opens and closes. The duration of the open state of the switch depends on the speed of rotation of the drum. The optical angle encoder is connected to the drum to record the angle of the rotor. This is then used to determine the trigger signals *counterpulse 1* at time  $t_{\text{trig}}$  and *close* at time  $t_{s,cs}$  for the counterpulse switch and the closing switch respectively. The angle at which the switch opens at time  $t_{o,os}$  is known in advance and the time difference of time  $t_{o,os}$  and time  $t_{\text{trig}}$  can be adjusted. The angle at which the trigger signal *close* is generated can also be adjusted.

The timing and opening switch voltage control unit detects whether the *counterpulse trigger* signal was generated in time. It compares the opening switch voltage  $u_{os}$  with the reference voltage  $U_{\text{ref1}}$ . During opening of the opening switch, the insulating strip of the drum slides underneath the brushes. The contact area between the brushes and the drum decreases. Hence, the opening switch resistance and voltage increase. When the counterpulse switch is triggered, the opening switch current and voltage decrease. If the *counterpulse trigger* signal is not generated by the *counterpulse 1* signal, the opening switch voltage will reach the reference voltage  $U_{\text{ref1}}$  and the timing and opening switch voltage control unit will generate the *counterpulse 2* signal.

The fault detection unit detects a number of fault conditions and generates the *fault* signal. The *fault* signal immediately generates a *close trigger* signal to trigger the closing switch. The fault conditions are monitored by the timing and opening switch voltage control unit, the counterpulse unit control unit and the trigger units of each counterpulse thyristor of the 50 kA-units.

The timing and opening switch voltage control unit monitors four fault conditions. If the opening switch voltage reaches the reference voltage  $U_{\text{ref2}}$ , the counterpulse switch has not been triggered and the *no trigger* signal is generated. When the opening switch opens at time  $t_{o,os}$ , the opening switch voltage increases. If this voltage increase does not occur within a certain (adjustable) time from time  $t_{\text{trig}}$ , the *early trigger* signal

is generated. If the opening switch voltage reaches the reference voltage  $U_{ref3}$  during the opening time period of the opening switch, the *high voltage* signal is generated. In case a fault condition has occurred, the timing and opening switch voltage control unit generates the *safety* signal, and thus the *close trigger* signal, every time the opening switch voltage reaches the reference voltage  $U_{ref1}$ .

The capacitor bank voltage control unit monitors two fault conditions. It compares the capacitor bank voltages of each of the 50 kA-units with the reference voltage  $U_{ref,cp}$ . When the capacitor bank voltage of a unit drops below this reference voltage, the unit is considered to be discharged. If a discharge occurs while there was no *counterpulse trigger* signal, the *spontaneous discharge* signal is generated. If one or more units do not discharge after a *counterpulse trigger* signal is generated, the *partial discharge* signal is generated.

The trigger unit of each counterpulse thyristor of the 50 kA-units can generate the *trigger unit x fault* signal, where x stands for the number of the unit. This may happen when a counterpulse thyristor is not triggered after the *counterpulse trigger* signal is received by the trigger unit, or when the current through the thyristor becomes higher (65 kA) than the nominal value of 50 kA.

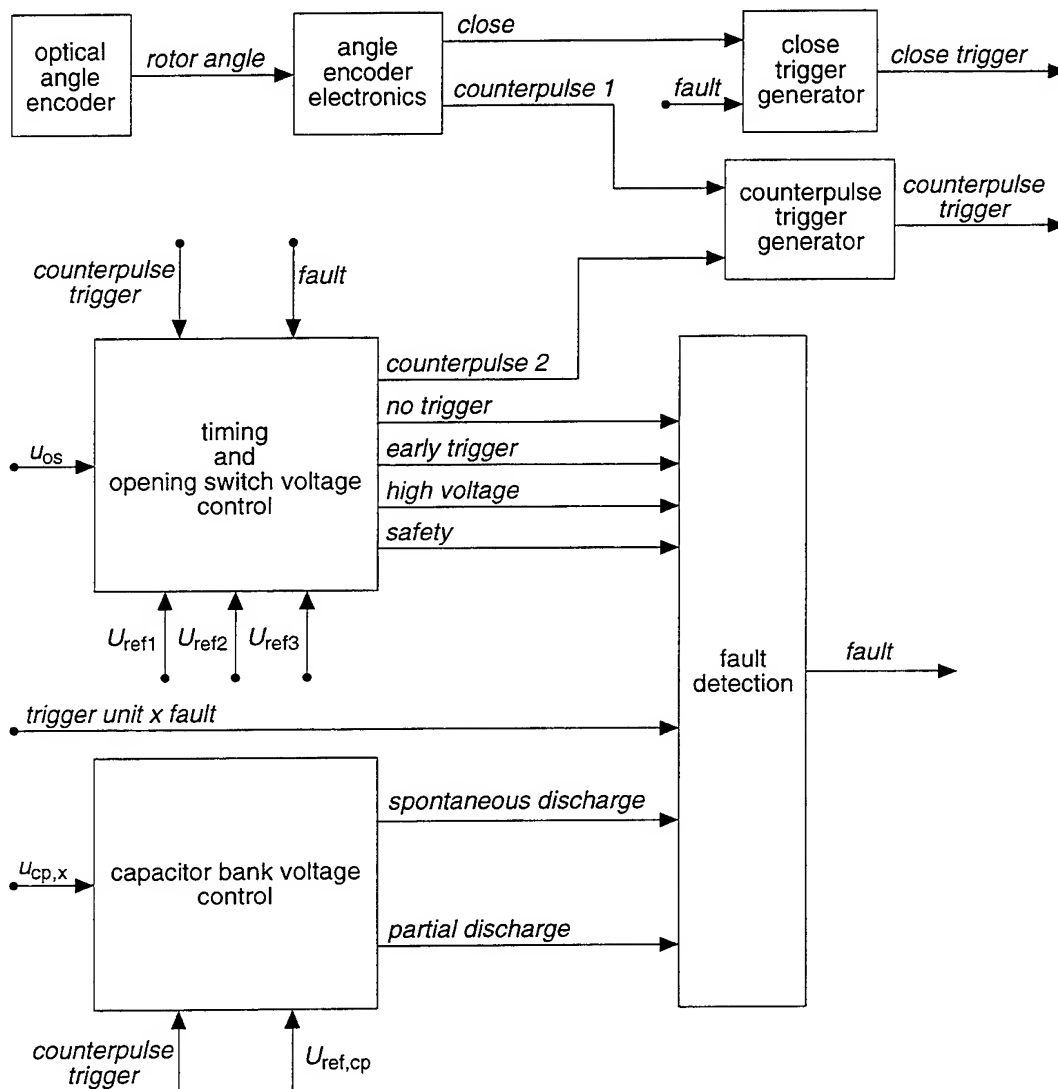


Figure 5 Simple block diagram of the control electronics

## Experimental results

The results of measurements of a 300 kA experiment with eight parallel units are shown in Figure 6. Figure 6(a) shows the current  $i_L$  through the load. Figure 6(b) shows the current  $i_{os}$  through the opening switch and the voltage  $u_{os}$  across the opening switch. Figure 6(c) shows the source current  $i_s$  and the total current  $i_{cs}$  through the closing switch. The closing switch current  $i_{cs}$  is the sum of all the measured currents through the closing thyristors of the units. Figure 6(d) shows the currents  $i_{cp,1}$  and  $i_{cs,1}$  through the counterpulse thyristor and the closing thyristor respectively and the voltage across the capacitor bank of unit 1 (lower left unit in Figure 3).

The measurements shown in Figure 6 demonstrate the operation of the resonant series counterpulse circuit. The initial voltage of the capacitor banks of the units was 204 V. The counterpulse thyristors were triggered at time  $t_{trig} = 5.24$  ms. The load current then increased and the opening switch current and voltage decreased. The behaviour of the opening switch voltage just before time  $t_{trig}$  resulted from the reducing of the contact area of the brushes of the opening switch. The opening switch opened at time  $t_{o,os} = 5.77$  ms. At this moment, the load current had reached its maximum value. The opening switch current was not exactly zero but slightly negative (about 2 kA) resulting in a small negative peak in the opening switch voltage. At time  $t_D = 6.44$  ms, the capacitor banks of the units had been discharged. The closing thyristors were triggered at time  $t_{s,cs} = 8.09$  ms. The opening switch voltage then reduced to about 45 V. The opening switch closed at time  $t_{s,os} = 8.55$  ms. During the energy transfer from the storage inductor to the load, the source current decreased from about 300 kA to about 265 kA.

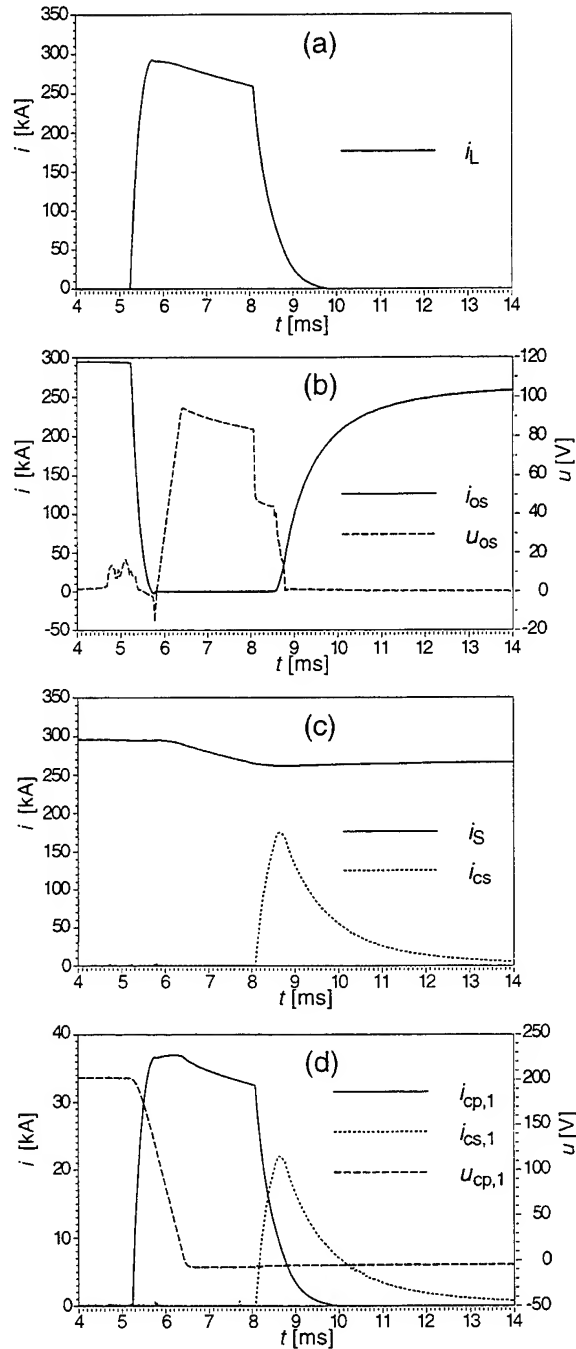


Figure 6 Current and voltage waveforms of a 300 kA experiment: (a) load current  $i_L$ , (b) opening switch current  $i_{os}$  and opening switch voltage  $u_{os}$ , (c) source current  $i_s$  and closing switch current  $i_{cs}$ , (d) counterpulse thyristor current  $i_{cp,1}$ , closing thyristor current  $i_{cs,1}$  and capacitor bank voltage  $u_{cp,1}$  of unit 1

The current sharing of the load current and the closing switch current among the eight units was almost equal. The measurements showed that the counterpulse thyristor currents, the closing thyristor currents and the voltages across the capacitor banks of the units were similar to those of unit 1, shown in Figure 6(d).

### Conclusions

The resonant series counterpulse technique has been described and analysed in [1]. It is meant to assist a repetitive mechanical opening switch [3] for pulsed power applications in the controlled interruption of currents at the mega-ampere level. The circuit uses a pre-charged capacitor bank and a thyristor switch in series with the inductive load to create a resonant counterpulse current in the mechanical opening switch. In this way, the opening switch can be opened at a low or zero current. A separate closing switch prevents closing of the opening switch at high voltage. The advantage for operation of the mechanical opening switch at low current and low voltage is that no arc erosion occurs at the contacts of the switch.

Compared with other counterpulse circuits [2], the advantage of the resonant series counterpulse circuit is that the counterpulse capacitor bank does not experience a voltage reversal. Therefore, electrolytic capacitors, which have a high energy density at a relatively low voltage, can be applied. The remaining energy of the capacitor bank after the opening switch has been opened, is transferred to the load. The required initial voltage of the capacitor bank is only a few hundred volts, whereas it may be above a kilovolt in other circuits. Another advantage is that the load does not experience a pre-current, which causes unwanted pre-heating of the load.

Experimental results have demonstrated the operation of eight parallel 50 kA-units with currents up to 300 kA. Current sharing between the units is almost equal. Future work will comprise the construction of two more 50 kA-units and testing the circuit with currents up to 500 kA. At the Pulse Physics Laboratory, the resonant series counterpulse circuit will be used for rail accelerator applications.

### Acknowledgement

The authors thank Prof. J.A. Schot, S.W.H. de Haan of the Delft University of Technology and Dr. W.J. Kolkert of TNO PML-Pulse Physics Laboratory for their encouragement and support.

The authors also greatly acknowledge the work of Thijs van Leeuwen in building the units, André Kops in designing the electronic circuitry and Boy Mosterdijk and Erik Olthof in assisting with the experiments at the TNO PML-Pulse Physics Laboratory.

This work is funded by TNO Defence Research, the Netherlands.

### References

- [1] E. van Dijk and P. van Gelder, "A Resonant Series Counterpulse Technique for High Current Opening Switches", *IEEE Trans. Magn.*, vol. 31, pp. 84-89, January 1995.
- [2] E.M. Honig, *Repetitive Energy Transfers from an Inductive Energy Store*. Los Alamos National Laboratory, Report no. LA-10238-T, Los Alamos, 1984.
- [3] T. McCormick and J. Barber, "A 500 kA repetitive opening switch", *IEEE Trans. Magn.*, vol. 22, pp. 1613-1618, November 1986.
- [4] E. Tuinman, "The compact pulsed homopolar generator facility at PML-Pulse Physics", *Proc. 1st European Symposium on EML Technology*, Delft, September 1988.
- [5] E. van Dijk and P. van Gelder, "100 kA Test Results of the 1 MA Resonant Series Counterpulse Opening Switch System", *10th IEEE International Pulsed Power Conference*, Albuquerque, pp. 1303-1308, July 1995.



# ESTIMATION OF COMPRESSION PULSED GENERATOR RANGE OF APPLICATION LIMITS FOR CURRENT SUPPLY WITH INDUCTIVE LOAD

Volodymyr T. Chemerys

Institute of Electrodynamics, National Academy of Sciences of Ukraine  
56 Peremoga Avenue, Kiev-57, 252680 Ukraine

**Summary** - A subject of paper is the special rotating electric machine for pulsed current generation on the principle of magnetic flux compression under interaction of two identical windings situated one of them on the stator and other on the rotor. The special procedure was developed for pre-designing calculation of internal parameters and energy generated. This procedure is based on the combination of transient analysis solution for the circuit (generator and inductive load) together with elements of standard theory of electric machine including some corrections to account the pulsed character of currents in the windings. The computing program for personal computer is created to realize this procedure. The search of optimal parameters of load is foreseen in this program at the initial stages of calculation. For the search of the best combination of technical parameters as the solution of multi-parametric problem of optimization with energy (or specific energy) generated as object function, the special subroutine of solution obtaining by LP-search method is involved in the program software. Subroutine is created using the results of work *I.M. Sobol, R.B. Statnikov* (Russia). The procedure mentioned was used for production of series calculation as the pulsed current parameters as pulsed energy in load close to optimal value. The field of solutions was restricted by the frequency of rotation 1500... 16000 rpm and by the allowable tangential velocity on the surface of rotor equal to 150 or 300 m/s. Diameter of rotor was a variable parameter in the limits of 0.16...1.0 m. The factor of inductance varying (the measure of efficiency of energy amplification in machine for one pulse) was provided the high enough (near 400) by the proper choice of designing parameters. Magnetic induction in the gap under calculations was maintained not far away from linear part of magnetizing curve. The family of curves for pulsed energy in load and for pulsed current duration as the functions of rotation frequency were obtained inside this field of solution. More pulsed energy is generating at low frequency of rotation and can reach 100...200 kJ if the rotor diameter is near 0.75...1.0 m, more pulsed power is generating at more high frequency with limitation of energy by the mechanical solidity of rotor with respect to centrifugal forces. The allowable time of work before heating of windings conductors for a given temperature is varying for different diameters of rotor. The optimal geometry of slots depends on the time of work of generator. Generator for a single pulse must have a rotor with concentrated poles, the wide and undep slots are more profitable here. Generators for the pulses generation with frequency of rotor rotation can have more deep and not wide slots. This peculiarity corresponds to known classic results obtained by Prof. *Ivan Postnikov* in 1937.

## 1. Introduction

Besides of the contributions made by the European and American scientists, many achievements in the field of pulsed power generation are connected with names of FSU scientists, partially Russia and Ukraine. The problem of short-time significant value of electromagnetic power was initiated by famous physicist P. L. Kapitsa in his investigations of the ultrahigh magnetic field [1]. The electromechanical pulsed generator known as "P. Kapitsa - M. Kostenko machine" was developed in his works as well as the

electrochemical sources of current. The next great contribution in the pulsed power generation was made by the group of academician A. D. Saharov [2], [3] using the explosively driven electric generator. The mentioned works had a principal significance for the technique of the strong pulsed current generation. Theoretical and practical aspects of this field were developed by many followed scientists and engineers. Participation of the known scientist Prof. I. M. Postnikov, leader of Ukrainian scientific school in the area of electromechanics during 50th-80th years, in the investigation and designing of big rotating pulsed generators together with academician M. P. Kostenko is less known, but in his first dissertation the important results were obtained which save their fundamental meaning to-day [4]. I. M. Postnikov classified the main and most effective schemes of electromechanical pulsed current generation, first of them in view of the pair series identical windings situated one of them on the rotor and second on the stator of electrical machine. He divided the possible designing features of such machine in according with two main application: generation of single extra pulse or generation of many consecutive pulses. Very different demands to machine follow from this two situations, and it is naturally to differ machines dependently on its purpose: 1) to convert into single pulse of electrical power much as possible of kinetic energy stored by rotor; 2) to convert the flow of mechanical energy from drive in the series of electrical pulses at relatively small change of kinetic energy of rotor during each pulse. Concerning the second situation the useful contribution was made by the research works of academician

L.I. Mandelshtam who developed the theory and experiment of parametric process at rotating induction generator self-excitation at capacitance load [5] first applied in practice by Winter-Günter in 1931. The next step in a rotating pulsed generator progress was made in the result of Efremov Electrophysical Institute activity in Russia during 80th [6], where the methods of control by the operation of rotating generator were developed significantly concerning the classic scheme of machine described by Prof. Ivan Postnikov. This wave of investigation was supported by the efforts of researchers in Kyiv (Institute of Electrodynamics). Simultaneously in Russia (Tomsk Polytechnic) the strong group led by Prof. G. A. Sypailov, Chair of Electric Machines, until occupied by the research of classic shock generators, now joined to this investigations, have performed the series of useful inventions in the field of creation and industrial application of pulsed power rotating generators. The pulsed generators were fastened for a long time to design and technology of traditional three-phase alternators, and only special applications needs have yielded to creation of machines made on the own new technological base subjugated to features of application. And now this row of results may be completed by the great compulsators created in USA by the Center of Electromechanics and Institute of Advanced Technology in University of Texas at Austin.

As it may be seen from several publications, the problem of limitations inherent of electromechanical rotating generators was in the center of attention for a long time. This problem solution is connected closely with modern state of electrotechnic industry, with materials available and modern technology, but the principal questions must be clear at any case, independently on the designing possibilities. To obtain the answer on the question interested it was necessary to develop the proper theoretical and numerical model suitable for prognosis of generator parameters attainable. The work presented belongs to the scale of investigations in which the such attempts were undertaken.

## 2. Scheme of Calculation for Finding of Generated Pulse Parameters

Rotating pulsed generator under consideration was chosen in according with classic scheme of machine with two identical windings connected in series through sliding contact (Fig.1). It was assumed that generator had the usual ferromagnetic core as in stator as in rotor manufactured from the thin sheets of steel. To optimize the such compression generator for the operation in the wide range of time intervals (from short-time up to long) the many-criteria approach was fulfilled on the base of results given in the work [7]. This

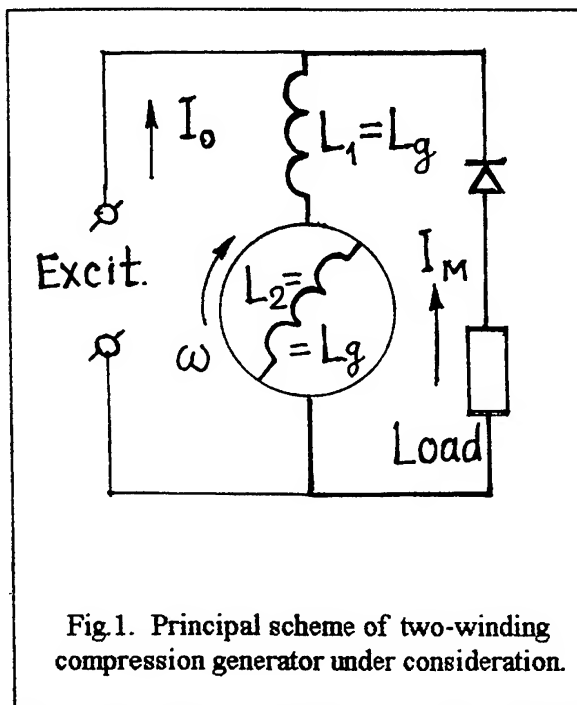


Fig.1. Principal scheme of two-winding compression generator under consideration.

approach does not need the analytical representation of the objection function and allows dialogue between designer and computer during optimization. The calculation scheme was built in combination of analytical and numerical results partially using correlations presented in the published materials [8]-[10]. The method of calculation used in this work allows to define the optimal parameters of load, efficiency of generator, the pulsed current parameters and windings temperature at the adiabatic heating conditions after preliminary choice of the main dimensions of rotor and stator as well as the tooth zone dimensions. The number of turns in the windings and level of magnetic induction in the air gap and in the steel of rotor and stator

yoke were chosen previously also. The main parameter of compression generator is a coefficient of inductance variation  $k_L = L_{\max} / L_{\min}$ , where  $L_{\max}$  is the resulting inductance of machine at the coinciding of magnetic axis of stator and rotor windings, and  $L_{\min}$  is the inductance of machine at the magnetic axis's of rotor and stator windings are opposite. These magnitudes were defined by the next correlations:  $L_{\max} = 4L_g + L_{\sigma 1} + L_{\sigma 2}$ ;  $L_{\min} = L_{\sigma 1} + L_{\sigma 2}$ , here  $L_g$  is the main inductance of the one windings of stator or rotor,  $L_{\sigma 1}$  and  $L_{\sigma 2}$  are the leakage inductances of stator and rotor windings respectively. The usual expressions from the theory of electrical machines were used to define these inductances. The value of  $k_L$  depends on the coefficient of magnetic coupling of rotor and stator windings  $k_{12} = M / L_g$ :  $k_L = (1 + k_{12}) / (1 - k_{12})$ , here  $M$  is mutual inductance of stator and rotor windings. To reach a well indexes of generator operation it is necessary to have exact equality of main inductances of stator and

rotor windings, and we consider them equal absolutely. Optimal values of different types of loads are given by the next expressions:

$$\text{ohmic load} - R^* = (1/\pi)\omega L_g(1-k_{12})^{1/2};$$

$$\text{inductive load} - L^* = 2L_g(1-k_{12});$$

$$\text{capacitive load} - C^* = 8/\omega^2 L_g.$$

Pulse current duration  $\tau_{0.5}$ , measured on the level of 0.5 amplitude value, is the same for all kinds of loads:  $\tau_{0.5} = 0.5T(1-k_{12})^{1/2}$ , here  $T$  is period of inductance varying;  $\omega = 2\pi/T$ . General expression for a rated value of peak magnetic energy in the windings at short-connected generator has the view  $W_{sc} = k_L L_{max} I_0^2$ , where  $I_0$  is a current of initial excitation. Coefficient  $k_L$  is able to be a value for estimation of rated energy amplification in the machine. Very important parameter of generator circuit is damping factor  $\delta_R = R/\omega L_{max}$ , the total resistance of circuit  $R$  must be used here. This value has the essential influence on the real process by reducing all the energy indexes and increasing the pulse duration. In fact under affect of damping factor energy amplification is less then current amplification, and current amplification is less then  $k_L$ . Energy in optimal loads of different kinds at  $k_L > 25$  and may be written through energy of short-connected generator:

$$\text{inductive load} - 0.25 W_{sc};$$

$$\text{ohmic load} - \text{near } 0.4 W_{sc};$$

$$\text{capacitive load} - \text{near } 0.5 W_{sc}.$$

As the differential equation for current time dependence has the approximate analytical solution [9], [10], it is possible to built a calculation model for search of designing parameters of generator only in algebraic expressions.

If generator is made for the single pulse generation, the rated current density in his windings may be taken from condition of allowable temperature of conductor at adiabatic heating and may be greatly more in comparison with generator for periodic pulse produced with frequency of rotor rotation or close to it. Shock alternators of traditional designing can sustain the single current density up to  $250 \text{ A/mm}^2$  while at continuous periodic pulse generation it cannot be more then  $10 \text{ A/mm}^2$  without additional cooling.

A detail investigation of the constructive parameters totality influence on the specific energy index of a generator was made for ohmic and inductive loads using the mathematic model of machine together with optimization program which was developed on the base of the LP-search method [7]. This procedure was applied for its testing to generator with low value of tangential velocity (50 m/s) to exclude out of consideration the problem of mechanical solidity of windings and its attachment in the slots.

### 3. Procedure of Optimization and Its Testing with Ohmic Load

The problem of optimization was set as multi-criterion problem about search of the vector of varying parameters, which must satisfy to given parametric and functional

limitations and deliver the extremum of objection function totality (or quality criteria) implying the best correlation between this criteria and fulfillment of some restrictions introduced by the designer in the process of optimization.

Decision of this problem is performing in three stages: 1) making of test tables; 2) choice of criterial restrictions; 3) control of feasibility by the computing, and, if necessary, return to the first or second stage with changing of initial data. Making of the test tables is performing on the computer with using of program, which finds the probe points as the points of the LP consecutivity [7] uniformly situated in the area of parameters, restricted by the parametric limitations. For each point of such consecutivity the all local criteria are calculated and for each criterion the obtained magnitudes are situated in a table increasingly with showing of the probe point number. On the second stage a designer analyses the tables obtained and introduces the limitations on the criterion under searching. When the optimal decision of multi-criteria problem is searching, the procedure of comparison for two vector criteria of quality must be developed. In [7] it was proposed to use the totality by Pareto to build the compromise dependence between two main criteria of quality.

For the numeric example was taken a generator with diameter of rotor 0.32 m, frequency of rotation 3000 rpm. Magnetic system of machine contained 4 poles with distributed windings. The main results of a described procedure realizations were the next. Optimization of generator with ohmic load have shown the specific indexes of machine in the limits from 100 J/kg up to 5 J/kg inside of the range of continuous periodic pulse operation time 1 -- 2000 s respectively with frequency of pulse repetition 100 Hz (corresponds to 3000 rpm). During the optimization the main dimensions of the generator, dimensions of the tooth zone, magnetic induction in the core and in the air gap were chosen as the varying parameters inside of two-sided limitations. The parameters of external Ohmic load were constantly accepted from the condition of the best accordance with generator. As the functional limitation the peak value of radial magnetic pressure on the surface of generator windings conductors was accepted ( $15 \text{ MN/m}^2$ ). The next values were chosen as the criteria of quality: the specific energy dissipated in a load; duration of the current pulse in the load; time of continuous generator operation before heating of the windings on  $100^\circ \text{C}$ ; coefficient  $k_L$  of the total inductance of generator changing at the rotor turn on the one pole division. With initial number of tests 128, the number of points in which this limitations were fulfilled, was significantly decreased after introduction of criterial limitations. For example, if the generator supposed operated in the short-time regime only one point could be obtained at calculation, when the limitations on the quality criteria were chosen the next: specific pulsed energy more then 86 J/kg, absolute value of energy in the load more then 60 kJ, time of operation more then 5 s, pulse duration not more then 0.6 ms,  $k_L \geq 100$ . By reducing of limitation on the specific energy it was possible to have the new points for compromise curve by Pareto. In results the full compromise line was built with calculation of totality of constructive parameters of generator for each of its point. This curve is shown in Fig.2 only for two criteria of quality used: 1) specific energy given to load (on unity of generator mass); 2) duration of pulse. The compromise line is conducted through Pareto points, others probe points lie below the curve.

This data analysis shows the next features: the pulse duration in the range considered didn't change strongly and was near 0.55 ms, as the frequency of the rotation was constant; generator for a short time operation (5 s) must have relatively small depth of slots (0.07 of pole division) and magnetic induction of excitation near 1.5 T, while the generator for a more long time of operation (2,000 s)

must have a more low induction 0.91 T and more great depth of slots (0.4 of pole division). This difference obtained by the formal way as result of optimization is corresponding fully to theoretical ideas about peculiarities of generator designing at different conditions of operation. These peculiarities of design for both case correspond to known classic conception described by Prof. Ivan Postnikov in 1937 [4]. Comparison of internal parameters of generator for two points near the edges of compromise curve is given in Table 1.

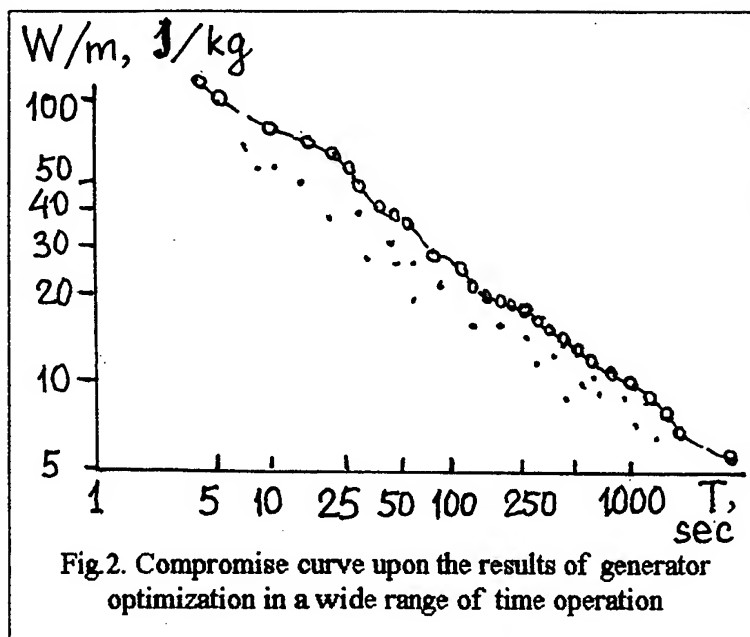


Fig 2. Compromise curve upon the results of generator optimization in a wide range of time operation

Table 1. Constructive parameters of compression generator at different time of operation ( $k_L = 300$ ).

| Time of operation, [sec] | Length to diameter of rotor, $l_s / D_A$ | Gap induction (eff), [T] | Yoke induction (eff), [T] | Slot width to teeth division, $b_s / t_z$ | Slot depth to pole division, $h_s / \tau$ |
|--------------------------|--|--------------------------|---------------------------|---|---|
| 5                        | 2.5                                      | 1.5                      | 1.96                      | 0.59                                      | 0.064                                     |
| 1000                     | 3.4                                      | 0.91                     | 1.9                       | 0.53                                      | 0.42                                      |

To reach a specific indexes meanings which can enable generator to be a competitive source of the pulsed current in comparison with capacitive store sources, the optimization procedure similar spent here must be perform with using of a high value of limiting tangential rotor velocity allowable for a modern material of high solidity.

The main tendency which is needed to be overcome during the optimization of compression generator is contradiction between necessity to increase the volume of conductors in the slot to reduce the inner damping of energy, from one side, and to decrease the height of the slots (and thickness of the layer of conductors) to improve the magnetic coupling between stator and rotor and coefficient of total inductance variation in account of the more small value of a magnetic flux leakage in the slots, from the other side.

#### 4. Results of Calculations with Inductive Load

Principal difference of inductive load and pure ohmic load is in location of additional resistance and inductance in circuit. The real inductive load always contains internal resistance, and these two case don't need a strict separation if we don't want to simplify the analysis. External inductance always can be added to inductance of leakage of generator as value reducing coefficient  $k_L$ . External resistance influences on the resulting damping of circuit occurs by the same way as the internal resistance of generator windings. If all the resistances are considered as linear elements of circuit, it is enough correctly count the energy location in all elements of circuit.

The software developed was applied to analysis of compression generator at operation with inductive load. It was a technological inductor in the form of cylindrical solenoid for magneto-pulsed forming without ware under processing inside. This inductor dimensions

Table 2. Constant parameters of generator for line of energy at constant diameter in Fig.3.

| Line number                                 | 1    | 2    | 3    | 4    | 5    |
|---|------|------|------|------|------|
| Relative diameter of rotor                  | 1    | 0.64 | 0.41 | 0.32 | 0.25 |
| Current density (eff), [A/mm <sup>2</sup> ] | 60   | 95   | 150  | 180  | 230  |
| Continious operation time,[sec]             | 1084 | 443  | 181  | 116  | 74   |

were chosen in according with condition of optimal load after choice of the main dimensions of generator. Magnetic induction peak inside of inductor on the surface of its turns was calculated. Resistance of inductor was found upon its turn data and was included in the calculating scheme. In the result of series calculations the field of the possible regimes of generator operation was covered in the range of rotor frequency of rotation 1,500 - 16,000 rpm and energy in the load 1 - 100 kJ. Basic value of rotor

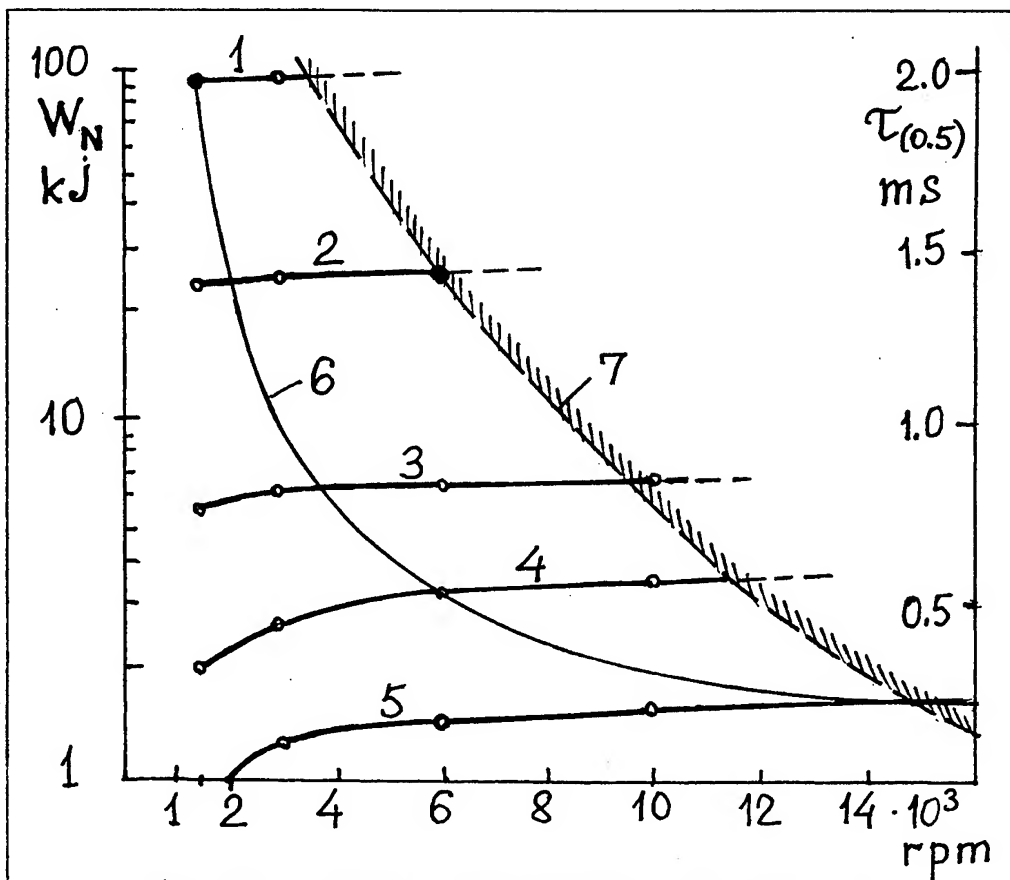


Fig.3. The results of generator calculation in the wide range of rotation frequency (1...5 - the pulsed energy in the load; 6 - the pulse duration; 7 - limitation on the allowable tangential velocity 150 m/s).

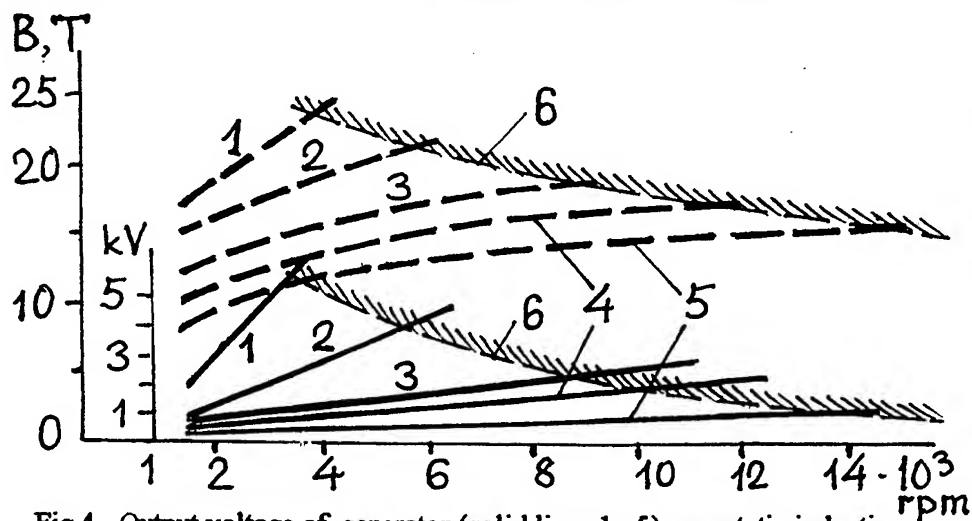


Fig.4. Output voltage of generator (solid lines 1...5), magnetic induction inside of load inductor (broken lines 1...5), limitation curve (6).



diameter was taken 0.735 m (150 m/s tangential velocity of surface occurs near 4000 rpm). Diameter of rotor for every other case was defined through this basic value. Allowable tangential velocity on the surface of rotor (50 - 300 m/s) presents the main constructive limitation for generator application as the pulsed power source. Other dimensions of machine were chosen to obtain the high enough (on the level 300) coefficient of inductance change  $k_L$ . A length of active zone was chosen at reasonable limits and was believed constant for each value of rotor diameter. Energy given to load  $W_N$ , pulsed current duration  $\tau_{(0.5)}$ , possible time of operation  $T$  and peak value of induction inside of load solenoid  $B_{Nm}$  were found in the result of calculation. This data are presented in the Fig.3, Fig.4; limitation curve in the both figures corresponds to meaning of tangential velocity on the surface of rotor 150 m/s. It may be seen as this velocity in fact plays the role of main limiting factor on the power generated. Displacement of limiting curve in the area more high velocity would allow to obtain a more short pulse with corresponding increasing of power, but energy in the pulse depends mainly on the diameter of rotor and other dimension related. The rows of parameters, which are constant for each line of constant diameter in Fig.3, Fig.4, are given in Table 2. The constant relation between generator minimal inductance and load inductance  $L_{ind}$  close to optimal value is used in Fig.3, Fig.4, namely  $K_N = L_{ind}/L_{min} = 3$ .

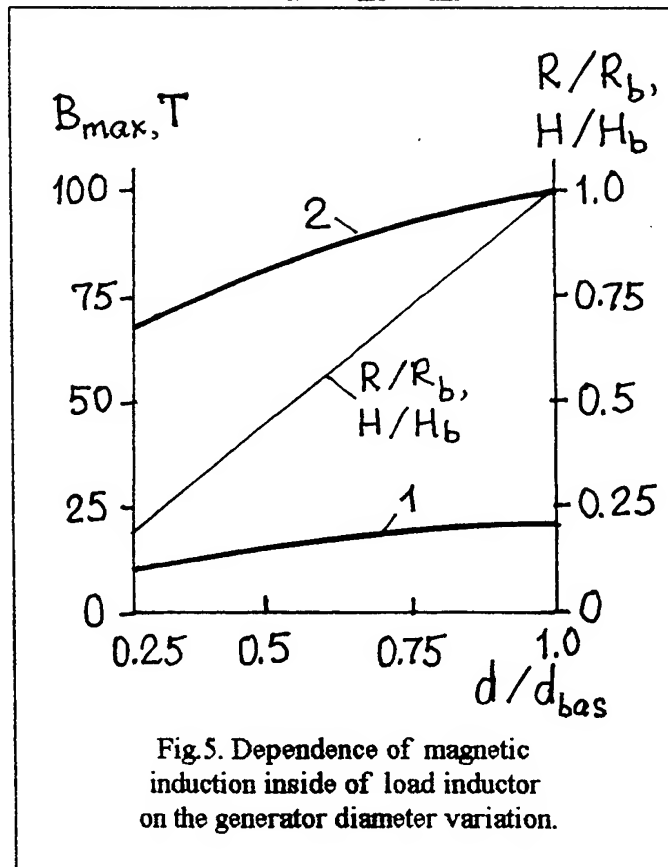


Fig.5. Dependence of magnetic induction inside of load inductor on the generator diameter variation.

Data shown in Fig.3 enable to see a certain contradiction between pulse duration shortening on the frequency of rotation increasing along with limiting curve, from one side, and enhancement of current density in windings, from another side, through lack of space for windings conductors placing, if diameter of rotor is small.

In the Fig.4 the magnetic induction on the surface of turns in load and voltage applied to the load inductor are shown.

To illustrate the influence of the rotor diameter variation on the generator parameters and magnetic induction in the load inductor the results of calculation for 3000 rpm,  $\tau_{(0.5)} = 1$  ms are shown in Fig.5, Fig.6. To reach a more high

amplitude of magnetic induction (curve 2 in Fig.5) it was necessary to decrease the solenoid dimensions with corresponding reduction of its inductance with respect to optimal

value needed for generator. Curve 1 in Fig.5 shows the peak induction in the load of optimal value.

Load solenoid basic dimensions for a curves shown in Fig.5 were the next: 1 - radius  $R_{b(1)} = 8.1$  cm, length  $H_{b(1)} = 8.64$  cm; 2 - radius  $R_{b(2)} = 1.5$  cm, length  $H_{b(2)} = 6.35$  cm. The current values of radius  $R$  and length  $H$  are varying similarly for both curves 1,2 in according with curve 3, Fig.5.

As it is seen in Fig.6, the energy in the load  $W_N$  depends on the diameter of rotor strongly. The internal parameters of generator are given in Fig.6 also. There are the  $k_L = L_{\max} / L_{\min}$  (at constant air gap), current peak value  $I_M$  in the load, current amplification coefficient  $K_i$ , real energy amplification coefficient  $k_W = W_N / W_0$ , where

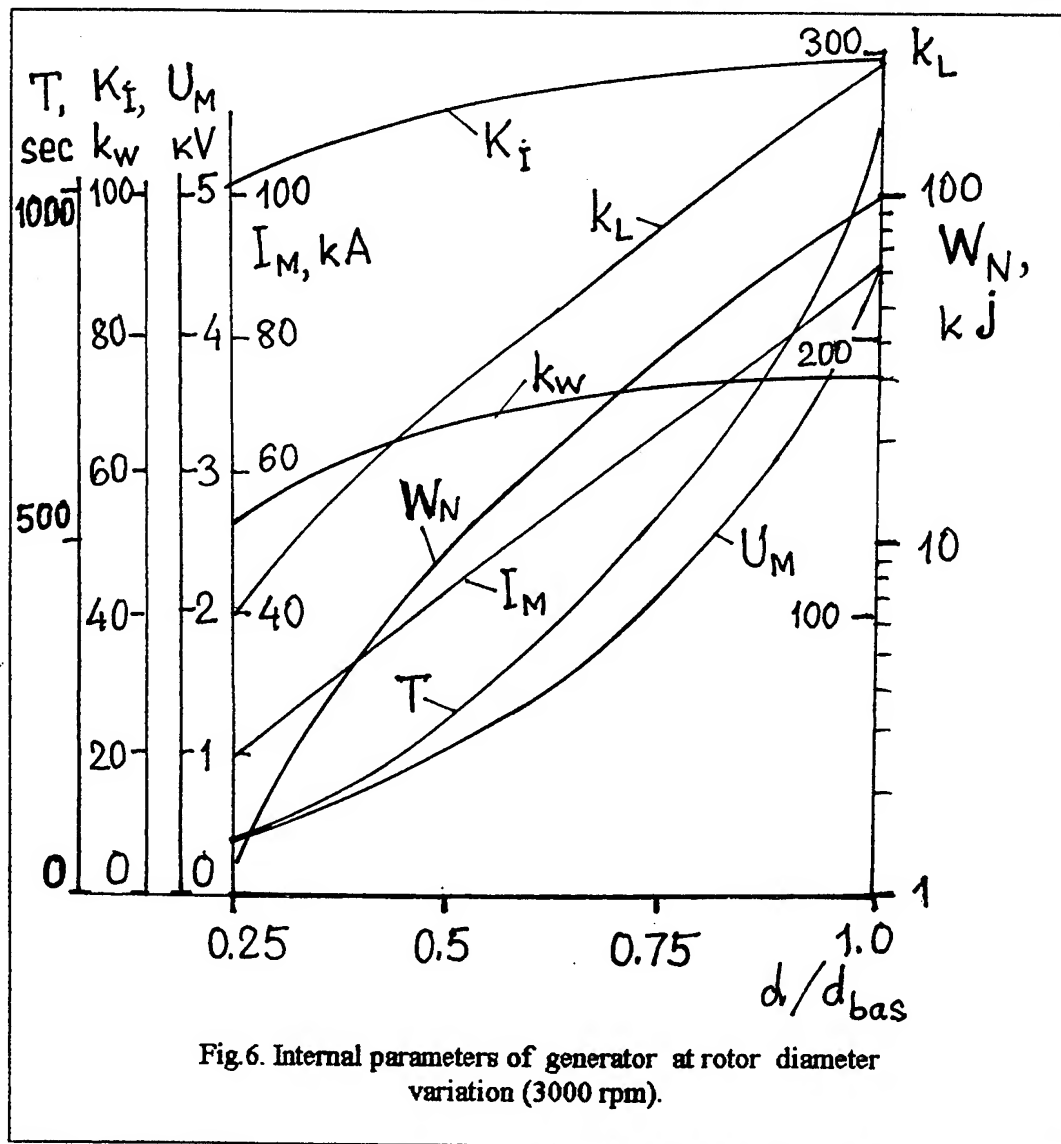


Fig.6. Internal parameters of generator at rotor diameter variation (3000 rpm).

the  $W_0$  is the initial magnetic energy spent on the field excitation, time of continuous operation  $T$  upon condition of winding super-heating on 100 deg.C, output peak voltage

$U_M$ . Basic value of mechanical power of machine was 60 kW in this example. To support the coefficient  $k_L$  on the constant level it would be necessary to reduce the air gap accordingly with diameter. Specific energy per mass unit was approximately constant through the whole range, it was estimated as 100 g/J with assumption that conductors mass is 0.07 of iron mass in generator. The most interesting result of example shown in Fig. 5, Fig. 6 is the feasibility to create the millisecond pulses of magnetic field up to 100 T with generator supply, what may be important for technological applications.

## 5. Conclusions and Recommendations

Calculations described here serve the illustration of possible computational approach at previous analysis of compression generator in the process of anticipated parameters study and have no objection to define real limitations for its operation. The rotating generator of pulsed power with ferrous core may be considered to-day as electromechanical device which characteristics may be predicted safe enough, including influence of non-linearity of core and rotor velocity change during the pulse. But through possible new special applications the problem of its operation at limiting conditions went at the first plane. In this connection the next conclusion may be done. If the electrical processes in the circuit supplied by rotating generator have the tools effective enough for analysis, many calculation procedures are need additionally for analysis of force interaction processes inside generator in detail, beginning from the strict definition of the magnetic field distribution in the tooth zone, strict definition of components of resulting inductance up to analysis of mechanical stresses and shock loading in the windings and keepers stipulated both the electromagnetic forces and the centrifugal forces and inertia. As the experience shows detail analysis of magnetic field in the stage of compression is able to open a large opportunity to improve the coefficient of energy amplification. Small unsymmetry of magnetic flux distribution at this stage is able significantly increase the value  $L_{min}$  with corresponding reduction of  $k_L$ . These problems are actual for the generators having a non-magnetic rotor or completely air core also.

## Acknowledgment

Author thanks his colleague A. Podoltsev for assistance in the calculating algorithm preparing and useful co-operation in investigations during many previous years.

## References

1. P.L. Kapitsa. *Scientific works. Strong magnetic fields.* - Moscow, Science Publ., 1988, 462pp. (in Russian).
2. A.D. Sáharov. *Explosive-magnetic generators.* - Uspehy Fiz. Nauk (Successes of Soviet Physics Journal), 1966, Vol.88, No.4, pp.725-734 (in Russian).

3. A.D. Sáharov, R.Z. Lyudaev. *Magnetic cumulation*. - Doklady AN SSSR (Reports of Academy of Sciences of USSR), 1965, Vol.165, p.65 (in Russian).
4. I.M. Postnikov. *A problem of significant value of electromagnetic power short-time obtaining*. - Trans. of the Leningrad Polytechnic Inst., 1937, Vol.2, No.1, pp.135-156 (in Russian).
5. L.I. Mandelshtam, N.D. Papalexi. *About parametric excitation of electric oscillations*. - JTF (Soviet Journal of Technical Physics), 1934, Vol.3, pp.5-29 (also published in the book: L.I. Mandelshtam. Complete collection of scientific works, Moscow, USSR Academy of Sciences Publ., 1947, Vol.2, pp.85-116 (in Russian).
6. A.S. Druzhynin, V.G. Kuchinsky, B.A. Larionov. *Compression generators*. - In the book: Physics and Techniques of the Pulsed Power Systems, Moscow, Energoatomizdat, 1987, pp.280-295 (in Russian).
7. I.M. Sobol, R.B. Statnikov. *Choice of optimal parameters in the problems with many criteria*. - Moscow, Science Publishers, 1981 (in Russian).
8. A.S. Druzhinin, V.G. Kuchinsky. *Calculation of loading characteristics of compression generator*. - Pre-print No.II-B-0581, Efremov Institute, Leningrad, 1982, 34pp. (in Russian).
9. A.D. Podoltsev. *Analysis of energy parameters for pulsed electromechanical generator of compression type under operation with ohmic, capacitive and inductive loads*. - Pre-print No.432, Institute of Electrodynamics, Kyiv, 1985, 33pp. (In Russian).
10. A.D. Podoltsev, I.S. Petuhov. *Characteristics of energy and parameters of compression generator pulse at operation with ohmic load*. - *Tekhnicheskaya elektrodinamika* (Technical Electrodynamics), 1985, No.3, pp.10-15 (in Russian).

# CAPACITOR-FREE SELF-EXCITATION OF BRUSHLESS COMPULSATOR

Volodymyr T. Chemerys, Igor S. Petuhov

Institute of Electrodynamics, National Academy of Sciences of Ukraine  
56 Peremoga Avenue, Kyiv-57, 252680, Ukraine

**Summary** — Rotational pulse generator with magnetic flux compression usually needs the source for primary excitation. Sometimes, compression ratio or energy amplification factor may be low while output energy is high enough. In this case the cost of primary excitation source may be too high. Hence a development of self-excitation process of pulse generator is important to reduce the cost of a whole pulse unit. The paper presents the results of digital simulation of self-excitation process in two general schemes of brushless compulsator.

It was found that it is necessary to have as minimum three windings, two of them situated on the stator and loaded by two diodes, to provide the self-excitation process. Two cases of rotor circuits compulsator are considered. The first one has the short-circuit rotor winding, the second one has the rotor winding loaded by a diode. All windings have the equal parameters. The mathematic model for transient analysis in generator consists of system of three differential equations with piecewise linear approximation of diodes characteristics. Magnetic core of machine is assumed having a linear properties. The parameters of the mathematical model are: two energy amplification factors (corresponding to coupling of rotor windings with each of stator windings), the relative resistance of the windings, the ratio between the self-inductances of stator windings and the angle between the axes of stator windings.

In the space of the model parameters the regions of self-excitation was found and the coefficient of self-excitation intensity as a function of the parameters was built.

In comparison with early considered results known for a generator having two stator windings with coinciding axes the generalized model allows the arbitrary angle between stator winding what enables to find more effective conditins of self-excitation due to variation of this angle. As was investigated this angle must be close to 90 deg. The maximal speed of magnetic flux increasing in machine may be given numerically as the function of energy amplification factor

$k_w$  by the correlation  $(0.5...1.5) k_w^{0.5}$  for typical cases constructive performance of machine. The numerical solution of system enable also to obtain the shape of current pulses in the windings and conditions of the best concordance with inductive load.

The computational results permit to find the optimal model parameters providing the quick self-excitation process. They may be spreaded also on the case of compression generator with galvanic connection of rotor and stator winding through contact rings and brushes.

## 1. Introduction

There are three main modes of current supply for the exsitation forsing in the rotating pulsed generators: 1) to rectify alternating output voltage; 2) to use the energy storing in the result of magnetic flux amplification if the windings system is non-symmetrical; 3) to discharge the capacitor through exciting winging. In the last case the qudrature component of the main magnetic flux will be caught by the disconnected windings, flux will be amplified after shor connection of this winding, and it will be the needed initial condition for the pulse generation. The conception of the pulsed power obtaining in the machine with two identical one-phase windings on the stator and rotor was expounded with classic clarity by Prof. Ivan M. Postnikov [1], but later he had accepted a point of view about profits of the pulsed power generation using the conventional three-phase alternator [2] due to possible application of the existing

technology of machine production for the purpose of pulsed current technique. The following period of shock generator development was fastened to design of conventional alternator, what led to some delay of progress in this field. The new life of three-phase machine as pulsed current sources in FSU was began after publishing of results concerning of the magnetic flux strengthening in the pulse generator done by Prof. G.A. Sipaylov (Tomsk Polytechnic) [3]. Development of this idea have enabled to create the many types of specialized pulsed sources including the return to classic scheme of compression generator described by Prof. LM. Postnikov.

The most effective application of the third method at self-excitation may be reached in the special pulsed generator likely compulsator [4] or compression generator [5]. The magnetic energy necessary for magnetic field creation and amplification can be stored in the main field of machine.

## 2. Description of the Problem

The purpose of this work is to present the analysis of generator self-excitation under condition of minimal usage of additional elements in its electrical scheme. Among the possible scheme of self-excitation the scheme shown in Fig.1 is chosen for the further analysis. In this scheme the generator contains three windings and two diodes. Two windings are placed on the stator and the third on the rotor. In general case each of stator windings can have the separate contour (it is shown by the broken line "bc" in Fig.1), - it is a "separate scheme" - or can be united in the common circuit (as shown by solid line "ac" in Fig.1) - it is a "united scheme". The rotor winding can be short-circuited or shorting against diode. It was underline in the published

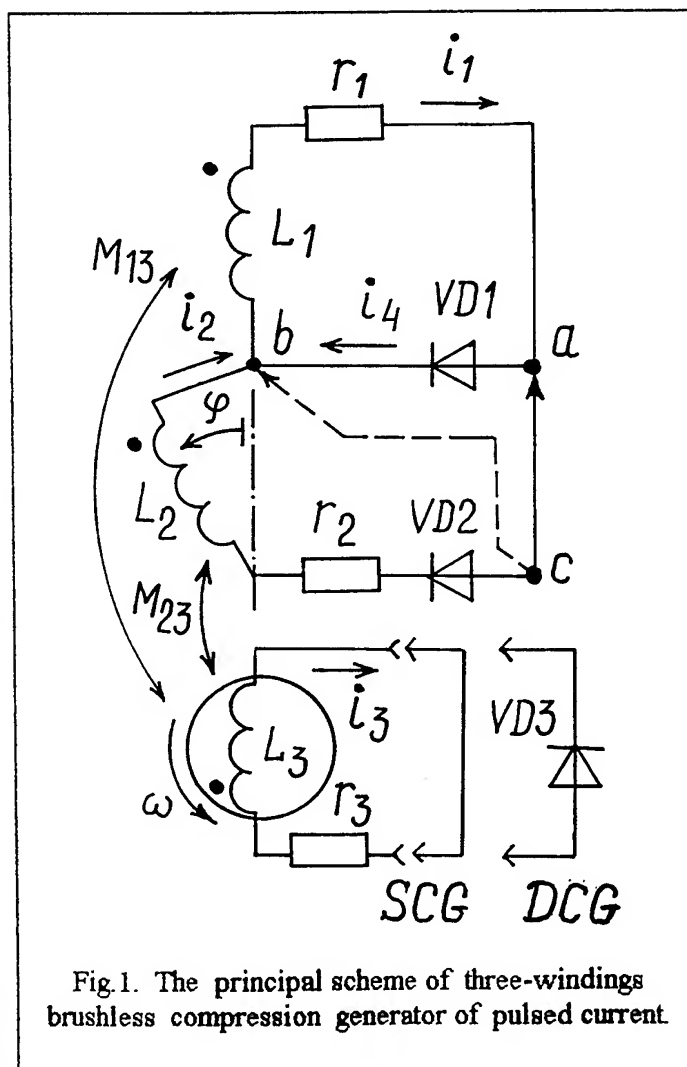


Fig.1. The principal scheme of three-windings brushless compression generator of pulsed current.

works [6]-[8] that brushless generator with diode in rotor winding or at short circuited this winding is close to classic scheme of compression generator [4]. But the addition of winding 2 situated on the stator at arbitrary angle of axis with respect to axis of the main winding 1 transfers the generator shown in Fig.1 rather in the category of cascade compression generators then in the category of generators only having separate winding of excitation. As we hope it will be seen upon the results of this paper.

In the further consideration the next types of brushless generators will be distinguished: 1) generator with short-circuit rotor winding (SCG type); 2) generator with rotor winding shorting against diode (DCG type). The simple linear mathematic model of electric machine was used at analysis, under assumptions of constant frequency of rotation, uniform air gap and sine distribution of the windings along with surfaces of ferromagnetic stator and rotor. At the numerical solution of the model it was taken into account the presence of diodes considered as non-linear elements. Diodes simulation was done by using of series  $r_{vd}$ ,  $L_{vd}$  circuit with changeable parameters. For a right direction of current passing through diode the parameters  $r_{vd}$ ,  $L_{vd}$  in such the circuit to be zero, and for opposite direction of current they were accepted as equal to  $r_{vd} = 500 \omega L_1$ ,  $L_{vd} = 10 L_1$ , where  $\omega$  is the angular frequency of rotation,  $L_1$  is the main inductance of stator winding.

The energy exchange between the windings of a generator may be described by using of energy amplification factor:  $k_{w1,3}$  for the windings 1, 3;  $k_{w2,3}$  for the windings 2, 3 interaction. The expressions for these coefficients were derived in the following form for different variants of generator scheme [7]:

$$\text{for SCG as } k_{w(i,j)} = \frac{1}{1 - k_{M(i,j)}^2}, \text{ and for DCG as } k_{w(i,j)} = \frac{1 + 3k_{M(i,j)}^2}{1 - k_{M(i,j)}^2}.$$

Here  $k_{M(i,j)}$  is the coefficient of magnetic coupling of corresponding windings 1, 3 or 2, 3. It is defined by the next expression:  $k_{M(i,j)} = M_{(i,j)} / ((L_i L_j)^{1/2})$ , where  $L_i$ ,  $L_j$  are the own inductances of windings,  $M_{(i,j)}$  is the mutual inductance between them. Notice that the rated energy amplification factor in the compulsator with a slip rings [5] is equal to compression ratio:  $k_{wc} = k_L = (1 + k_{12}) / (1 - k_{12})$ , if damping is absent [7].

The mathematical model of self-excitation process includes as leading parameters the normalized electromagnetic time constant of the windings  $T_i = \omega L_i / r_i$ , where  $r_i$  is a winding resistance,  $i = \overline{1,3}$ , angle  $\varphi$  between the axes of the windings 1, 2, and ratio  $\lambda = L_1 / L_2$  of the stator windings inductances.

The ratio  $k_f$  of the following pulse amplitude during this process development to the amplitude of the previous pulse serves as the criterion of the intensity of the self-excitation. This ratio may be named as the amplitude rise coefficient during self-excitation. As the mathematic model of machine was adopted, it was possible to be sure that the ratio  $k_f$  is not varying after the several periods, it was the indication of stationary state achievement. The simulating computer program which was solving the

initial value problem, had enables to select the pulses for records before the coefficient  $k_f$  had to reached the stable magnitude near 1. If on the first period of rotation the initial current was close to zero in all the windings, in the beginning of the every next period a small addition of initial current have arised, and this increase led in result to reachment of nominal current in the stator winding 1 which was supposed as output. It is useful to mark that the ortogonal initial mutual position of wingings 1, 3 axes is typical for generator of SCG type (the rotor winding must be designed as free penetrated for magnetic flux across its axis), while the collinear mutual position of windigs 1, 3 axes is typical for generator of DCG type at the begining of the pulse generation.

### 3. The Results Obtained

It is evident, that it is difficult to reach a self-excitation at presence of external load in the circuit through a great dissipation of energy. That is why the self-excitation development was studied with short-connected output of generator. At the initial analysis performance it was convenient to restrict ourselves by the consideration of process at the equality of electromagnetic time constants of all windings included as well as equality of amplification coefficients  $k_{w(1,3)} = k_{w(2,3)} = k_w$ , what does not violate of general character of analysis. The consideration of the self-excitation process in dynamics by numerical solution of the mathematic model have enabled to study the influence of such the parameters as the angle  $\varphi$  between stator windings axes, the resistances of windings, the rated energy amplification factor  $k_w$ , as well as difference between the factors  $k_{w(1,3)}$  and  $k_{w(2,3)}$  on the process development. Most of results are presented for SCG scheme, and certain of them are related to DCG scheme. The main distinctions between SCG and DCG characteristics are pointed out.

The very strong factor of influence is the angle between stator windings axes  $\varphi$ . In Fig.2 the coefficient  $k_f$  dependence on the angle  $\varphi$  is presented for SCG scheme with series connection of 1, 2 windings of stator at  $k_w = 25$ ,  $\lambda = 1$ . The one curve in this figure is shown for DCG type machine at  $T_i = 100$ . It is a typical that all curves for DCG type machine are going below of corresponding curves for SCG type machine. of corresponding curves for SCG type machine. Data about maximal significances of the coefficient  $k_f$  are given also in the Tabl.1 for the several values of  $k_w$ . It is seen in the Fig.2 that the most effective self-excitation is possible if the value of angle  $\varphi$  is near  $\pm 90$  deg.

The curves of the normalized currents in time obtained by simulation are shown in Fig.3 for SCG scheme with  $\varphi = 90$  deg.,  $\lambda = 1$ ,  $T_i = 100$  at  $i = \overline{1,3}$ , and in Fig.4 for DCG scheme with  $\varphi = -90$  deg., remains are the same. The process is going similarly in both schemes, but in SCG type machine (Fig.3) the pulsed current  $i_3$  changes its sign each period in contrary with DCG type where it doesn't change its direction. As the results of modeling show, parameter  $\lambda$  has the strong influence on



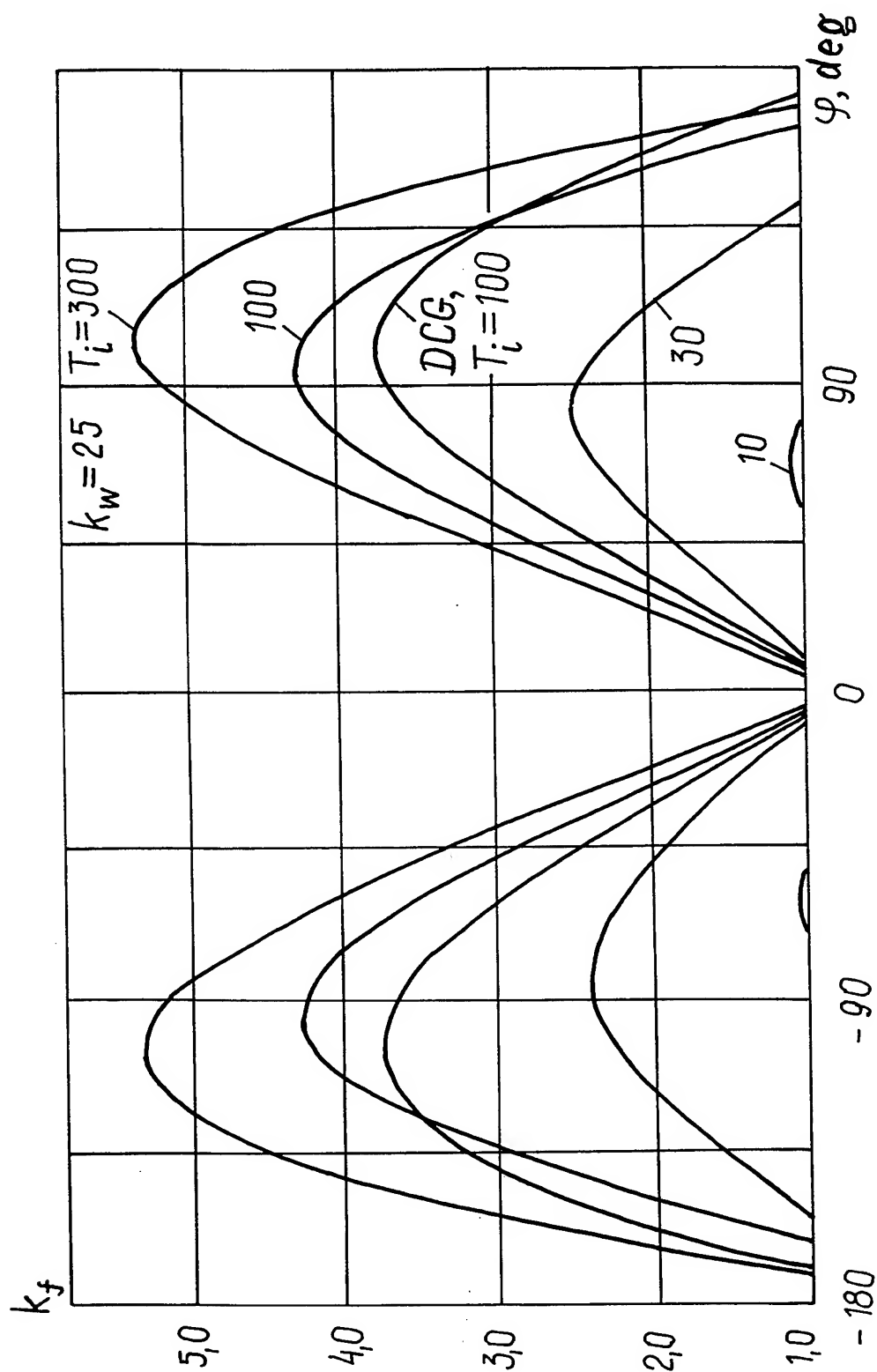


Fig.2. Graphic view of amplitude rise coefficient  $k_f$  dependence on the angle between axes of stator windings at different values of electromagnetic time constant.

Table 1. Maximal values of amplitude rise coefficient  $k_f$   
in the scheme SCG and corresponding angle ( $\varphi$ ).

| $T_i$ | $k_{w(1,2)} = k_{w(2,3)}$ |                |                 |                |
|-------|---------------------------|----------------|-----------------|----------------|
|       | 6.75                      | 12.5           | 25              | 50             |
| 10    | -                         | -              | 1.04 (-63deg.)  | 1.06 (-72deg.) |
| 30    | 1.57 (78deg.)             | 2.0 (61 deg.)  | 2.45 (81 deg.)  | 2.7 (80 deg.)  |
| 100   | 1.98 (87 deg.)            | 2.87 (90 deg.) | 4.23 (94 deg.)  | 5.8 (94 deg.)  |
| 300   | 2.12 (93 deg.)            | 3.26 (99 deg.) | 5.34 (103 deg.) | 8.4 (103 deg.) |

the self-excitation process in the united scheme of windings, when the winding 1 may be considered as the load for winding 2. In the Tabl.2 the values of coefficient  $k_f$  in dependence on  $\lambda$  are presented for several magnitudes of  $k_w$  at  $T_i = 100$  for  $i = \overline{1,3}$ . It may be seen that the small values of  $\lambda$  are preferable in united scheme of windings. It is expedient from a design point of view to perform the windings with angle between axes  $\varphi = 90$  deg. The current  $i_1$  of stator winding 1 is much more then  $i_2$  in winging 2, that agrees very well with a condition of  $L_1 \ll L_2$  as enables to reach of acceptable volume of conductor in the each of windings. It is known that in the pulsed generators the optimal load inductance is reducing along with increasing of energy amplification coefficient [9]. The similar tendency is seen in data of Tabl.2.

Table 2. Maximal values of amplitude rise coefficient  $k_f$   
in the united scheme DCG and corresponding values of angle ( $\varphi$ ).

| $\lambda = L_1 / L_2$ | $k_{w(1,3)} = k_{w(2,3)}$ |                 |                 |
|-----------------------|---------------------------|-----------------|-----------------|
|                       | 25                        | 50              | 100             |
| 0.125                 | 3.81 (85 deg.)            | 5.96 (83 deg.)  | 8.78 (83 deg.)  |
| 0.25                  | 3.87 (90deg.)             | 6.0 (90 deg.)   | 8.74 (90 deg.)  |
| 0.5                   | 3.86 (93 deg.)            | 5.87 (95 deg.)  | 8.48 (92 deg.)  |
| 1.0                   | 3.71 (99 deg.)            | 5.5 (103 deg.)  | 7.82 (100 deg.) |
| 2.0                   | 3.33 (105 deg.)           | 4.76 (105 deg.) | 6.62 (105 deg.) |
| 4.0                   | 2.8 (104 deg.)            | 3.83 (103 deg.) | 5.18 (104 deg.) |
| 8.0                   | 2.30 (99 deg.)            | 2.99 (99 deg.)  | 3.9 (101 deg.)  |

Parameter  $\lambda$  has no essential influence in the separate scheme of windings. Calculations have shown that in such a scheme the less value of  $k_f$  are achievable and extremum of this coefficient lies far away from angle of 90 deg., what is not

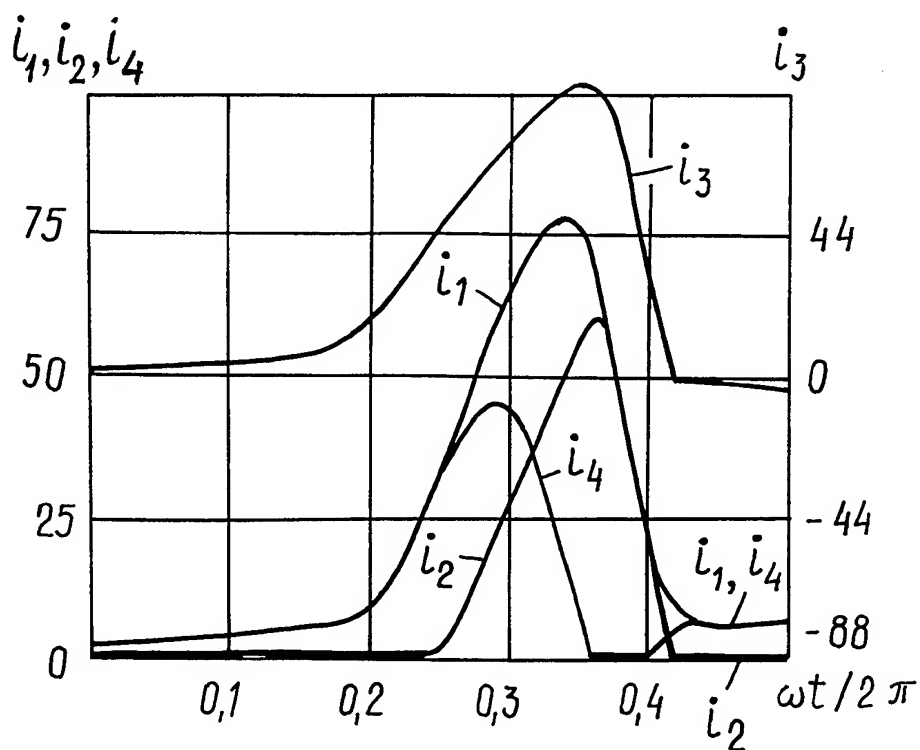


Fig.3. Normalized curves of currents in the windings of SCG type machine by simulation.

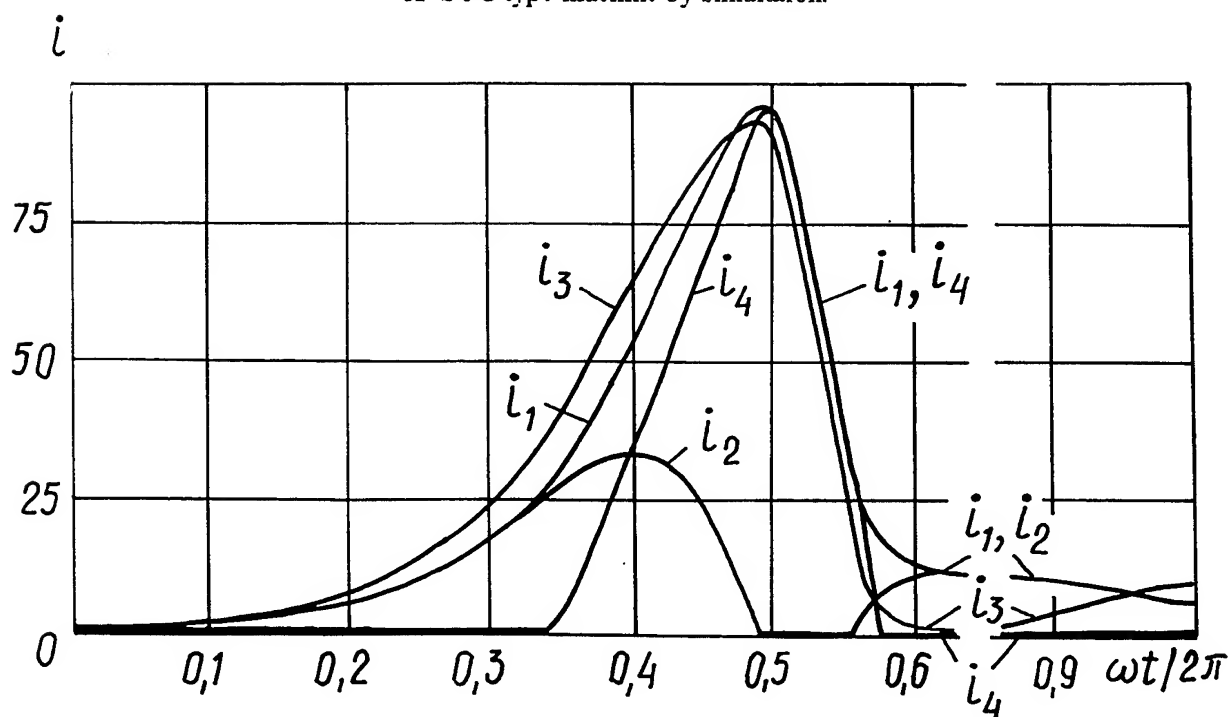


Fig.4. Normalized curves of currents in the windings of DCG type machine by simulation.

suitable for designing. The positive property of separate scheme of windings is concluded in the possibility to obtain the high enough value  $k_f$  at every meanings of  $\lambda$  ratio.

To check the influence of possible difference between  $k_{w(1,2)}$  and  $k_{w(2,2)}$  which can arise, for example, if the inductive load is present in the circuit of winding 1 or 2, the simulation of self-excitation process was spent in two additional variants for DCG type machine for each kind of winding connection (united and separate). The inductive load of optimal value was switched in the stator winding as the first variant, and inductance with value equal to own inductance of stator winding was in the second variant. Initial value of  $k_w$  was taken 12.5, and additional inductance was able to reduce it up to 2.0 with a drop of  $k_f$  almost twice up to value 1.2 - 1.3 when the self-excitation is possible yet, but it is going very slow in comparison with short-connected output case of generator. The efficiency of self-excitation depends strongly on the summary resistance of all the windings. Switching of ohmic load is able to slow down significantly the process self-excitation up to its breaking.

Numerical estimations obtained in the result of analysis spent show that the upper limit of maximal amplitude rise coefficient  $k_f$  can be close to the value  $(0.5...1.5)(k_w)^{1/2}$ .

#### 4. Conclusions and Recommendations

All the variants of internal connections and mutual space position of the stator coils in the scheme of three-windings brushless generator were covered during this work fulfillment. The scheme with connection of stator windings in series contour under their mutually orthogonal space disposition with a presence of two diodes switched in the correspondence with Fig.1 (one of them is in the branch of additional windings, the second is a shunt for the main windings as usual fixator of level) has the most interesting possibilities in the self-excitation performance. Efficiency of self-excitation in such a scheme is the most high if the inductance of additional windings of stator is more then inductance of main windings in 2...8 times, what may be define more correctly at known coefficients of electromagnetic coupling of stator windings with a rotor winding. Connection of rotor winding against with diode doesn't change principally the pulsed energy conversion in the generator but provides the pulses repetition frequency equal to rotation frequency, while at the short connected rotor winding the pulses repetition frequency is twice more in comparison with frequency of rotation. The self-excitation of generator is possible also with separate (insulated) short connection of both stator windings against diodes, efficiency of this scheme is not high as in the united scheme. But separate scheme allows to reach the self-excitation without special making of correspondence between inductive parameters of stator windings, what is a positive property of this scheme.

Analysys developed for two orthogonal windings on the stator of the compression generator turned out to be useful at consideration of two-stage cascade compression generators in the followed investigations: in the brushless performance [10] and using the slip contacts between rotor and stator windings [11].

## References

1. I.M. Postnikov. *A problem of significant value of electromagnetic power short-time obtaining.* - Transactions of the Leningrad Polytechnic Institute, 1937, Vol.2, No.1, pp.135-156 (in Russian).
2. I.M. Postnikov. *About designing of shock generator.* - Transactions of the Leningrad Polytechnic Institute, 1960, No.209, pp.89-98 (in Russian).
3. G.A. Sipaylov, A.V. Loos. *The using of magnetizing affect of amature reaction in the pulsed generators.* - Elektrichestvo (Electricity), 1975, No.12, pp.41-45 (in Russian).
4. W.F. Weldon, M.D. Driga, H.H. Woodson. *Compensated pulsed alternator.* - U.S. Patent No. 4,200,831. Int Cl. H02K 39/00, Apr.29, 1980.
5. V.G. Kuchinski, B.A. Larionov. *Electromechanical pulsed generator.* - Author's certificate of USSR No.934888. Int Cl. H02K 25/00, 1980 (published in 1983, in Russian).
6. I.S. Petuhov, A.D. Podoltsev, V.T. Chemerys. *Brushless compression generator operation in the regime of self-excitation* (Editorial of journal "Technical Electrodynamics", Kyiv). - On Deposite in VINITI, Moscow, Nov.23, 1987, No.8249-B87, 16pp. (in Russian).
7. I.S. Petuhov, A.D. Podoltsev, V.T. Chemerys. *Electromechanical energy conversion in magnetically coupled contours and main indexes of compression generator* (Editorial of journal "Technical Electrodynamics", Kyiv).- On Deposite in VINITI, Moscow, Nov.23, 1987, No.8248-B87, 48pp. (in Russian).
8. P.V. Vassyukevitch. *One-phase generator of unidirectional pulsed current.*- Izv. AN SSSR "Energetika i transport" (News of the USSR Academy of Sciences on Energetics and Transport), 1986, No.3, pp.110-115.
9. A.I. Chuchalin. *Pulsed generators on the base of electromechanical converters.* - Izv. VUZov "Elektromehnika" (News of the High School of USSR on Electromechanics), 1989, No.12, pp.23-33.
10. V.T. Chemerys, A.D. Podoltsev, I.S. Petuhov. *Electromechanical generator of periodic pulsed current.* - Author's certificate of USSR No.1,453,539, Int.Cl. H02K 25/00, Sept.22, 1988.
11. V.T. Chemerys, A.D. Podoltsev, I.S. Petuhov. . *Electromechanical generator of pulsed current.*- Author's certificate of USSR No.1,575,273, Int. Cl. H02K 25/00, March 01, 1990.

# The Analysis of Linear Magnetic Flux Compressor Pulse Power Supplies

A.P. Glinov, A.E. Poltanov, A.K. Kondratenko, V.N. Ryndin and G.I. Simonova

Troitsk Institute for Innovation & Fusion Research

TRINITI, Moscow Reg., 142092 Russia

Phone: (095)334-06-81, Fax: (095)334-51-58

Email: glinov.fly.triniti.troitsk.ru, kondrat.fly.triniti.troitsk.ru

**Abstract.** The theoretical study of the current generation due to the braking of the previously accelerated armature by the magnetic field compression in the multi-rails channel of the railgun is carried out. The resistive-inductive load is considered. The set of the acceptable physical parameters of such compressor is defined. The numerical code, which simulates the work of the generator, is developed. This software takes into account the skin effect and the heating in the rails and in the armature. In a result, the dependence of efficiency of the studied facilities vs. the used materials was found. The practical recommendations for possible ways of optimization of the similar generators are put forward.

## 1. Introduction

The work is devoted to a formulation and analysis of the elementary physical model of the linear ballistic generator used for production and using of the electrical power in the given resistive-inductive load. Such generators, unlike the explosive magnetic flux compressor generators (MFCG) [1,2], we name for a short as the linear generators of the current (LGC) [3]. The main attention was given to the analysis of a variety of the LGC, which are based on the compression of the magnetic stream in the railgun channel by means of a beforehand accelerated modular solid-state armature.

The linear ballistic generators, as well as MFCG, have a rather simple construction, but unlike last they are capable to generate the electric pulses of the current by duration up to a few milliseconds. Almost all elements of their construction, excepting the armature, are reusable. And the basis of researched constructions of the LGC is formed by the electrodynamic launchers with inverse rails. The latters are often multirails and have a sufficiently great value of a linear inductance  $L' > 3-4 \mu\text{H/m}$ .

The LGC can find the application as the alternate radiants of the power supply for impulse electro-physical facilities of various assigning, particularly at a realization of the geophysical electromagnetic explorings.

Unlike the generator [4,5], recommended for a creation of combined electrochemical launcher of macrobodies, in the LGC the compression of the magnetic flux may be carried out solely at the expense of a kinetic energy of an armature. In our work the simplified physical model of the LGC work is investigated analytically and numerically. In a result the explicit solutions of some tasks in view of decrease of a velocity unlike [6] are obtained. Moreover it became possible to define the conditions of the generation of the current and to analyze the influence of the various materials used in the construction of the generator upon the effectiveness of the energy transformation. Also a way of a control of the form of the current impulse by the modification of the linear inductance of the LGC construction is found theoretically.

## 2. Formulation of the Problem

The electrical circuit of the LGC for the direction of the current into the external resistive-inductive load, characterized by inductance  $L_L$  and resistance  $R_L$ , is represented in fig.1.

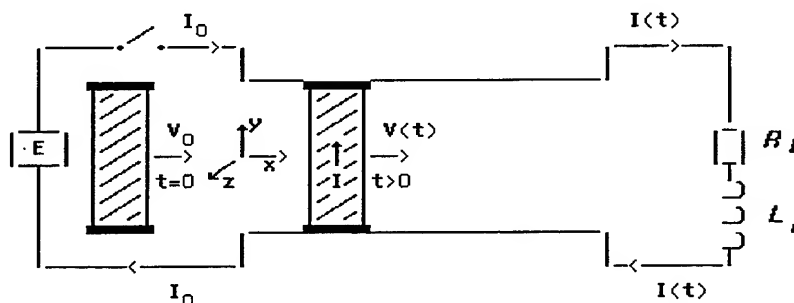


Fig. 1 The scheme of the LGC cut by plane  $z = \text{const}$  and the circuit of the load.

The generator contains the  $n$  conductive parts which are parallel to the plane  $z = \text{const}$  and are divided by isolation strata both electrically and thermally and are joined sequentially through a collector on an output extremity of the LGC. Such construction can ensure great linear inductance of rails. The armature of the LGC consists of  $n$  slices isolated from each other too. The armature velocity and length are  $v$  and  $l_a$ . The length of the generator is  $l$ . The height of electrodes in direction of the axis  $y$  is  $h_r$ .

In the moment  $t = 0$  the external electromotive force  $E$  creates in the electrodes and exterior circuit the initial current  $i_0$ . When  $t \geq 0$  an electrical closure of interrails space by the armature takes place. And cut-off electromotive force of the energization for the initial current occurs.

When  $t = 0$  the armature has the initial velocity  $v = v_0$ . During the time the armature begins to be braked by a magnetic field, originating due to the current through the rails, armature and external circuit. And the kinetic energy of the armature together with the magnetic energy between the rails will be transformed to electrical energy, which will be led into the given load.

The LGC description in view of the thermal heating is defined by the equations

$$m \frac{dv}{dt} = -\frac{L'i^2}{2}(1+k_f), \quad \frac{dx}{dt} = v, \quad \frac{dLi}{dt} + iR = 0 \quad (1)$$

$$L = L_L + L'(l-x), \quad R = R_L + R_a + 2R_r,$$

$$R_r = R'(l-x), \quad R' = \frac{\rho_r n}{w_r \delta_r}, \quad R_a = \frac{\rho_a h_a}{w_a \delta_a} n,$$

$$\rho_{r,a} = \rho_{r,a}^0 [1 + \alpha_{r,a}(T_{r,a} - T_0)], \quad \lambda_{r,a} = (\rho_{r,a} t / \mu_0)^{1/2}$$

$$\delta_r = \min[\lambda_r, h_r], \quad \delta_a = \min[\lambda_a, l_a], \quad \mu_0 = 4\pi \cdot 10^{-7} \text{ H/m}$$

$$C_a \Omega_a \frac{dT_a}{dt} = i^2 R_a, \quad C_r \Omega_r \frac{dT_r}{dt} = i^2 R_r, \quad (2)$$

$$\Omega_a = h_a \delta_a w_a n, \quad \Omega_r = (l-x) \delta_r w_r n$$

We account in (1) the influence of a friction force of the piston along the rails  $F_f = k_f L'i^2/2$  on armature braking. And it is necessary, because it may be essential for the ensuring of the solid metal contact. But we neglect a heat by friction. It can be designated as  $q$ . Accordingly in the 1st and 2nd equation the components  $q_a = q/2$  and  $q_r = q/4$ , where  $q = F_f v$ , are omitted. They are small in our simulations with respect to Joule heat. Because the electrical resistances of the armature and rails are high. It is caused by skin effect.

Here  $m$  - the mass of the armature (of the piston),  $v$  - its velocity,  $t$  - the time,  $L'$  - the linear inductance of the rails per unit of length,  $i$  - the electric current,  $L$  - the full inductance,  $R$  - the full electrical resistance,  $x$  - the piston coordinate,  $C_{r,a}$  - specific thermal capacity of the rails and the armature,  $\Omega_{r,a}$  - a volume of region occupied by current in one rail or armature,  $T_{r,a}$  - a temperature of the rails or armature. Through  $h$  and  $w$  with appropriate indexes are marked a height and breadth of the electrodes and the piston. Magnitudes  $l$  and  $l_a$  - the length of the generator and the armature in direction of axes  $x$ . Through  $R_L$ ,  $R_r$ ,  $R_a$  are designated accordingly the electrical resistance of the load, rail and armature. Similarly the numerals  $\rho$ ,  $\alpha$  with appropriate indexes represent specific electrical resistances and their temperatures coefficients. And the magnitude  $\lambda$  characterizes depth of a skin-stratum. The parameter  $k_f \approx 0.5$  takes into account braking of the piston at the expense of friction about the rails.

In the moment  $t = 0$  the initial conditions are:

$$i = i_0, \quad v = v_0, \quad x = x_0, \quad T_a = T_{a0}, \quad T_r = T_{r0} \quad (3)$$

It is necessary to analyze (1) - (3) up to a moment of the armature embarkation ( $x = l$ ) or up to its stopping ( $v = 0$ ).

### 3. Analytical Study

We shall find an analytical solution of the task when the full electrical resistance of the generator and the load is constant.

Some important results about the LGC work can be received even not deciding the Cauchy problem (1-3).

From (1), requiring  $di/dt > 0$ , it is simple to show, that the monotone amplification of the current  $i(t)$  happens only at realization of a condition  $L'v > R$ . It means that the inductive resistance of the rails of the generator exceeds a summarized ohmic resistance of the generator, the armature and the load.

When  $R \ll L'v$  the magnetic flux  $Li$  will be constant and we shall receive

$$i = i_*(x) = i_0 [l + L_L / L' - x_0] / [l + L_L / L' - x] \quad (4)$$

Whence the maximum amplification factor of current  $K = i / i_0$  is reached at  $x=l$  and for  $x_0=0$  is equal  $(lL' + L_L) / L_L$ . I.e. the generator inductance  $L_G = L'l$  should considerably exceed inductance of a load  $L_L$  for a sufficient amplification of current.

At presence of ohmic losses, the amplification of current will be less.

From (1-3), neglecting the Joule heating and by accepting  $L' = const$ , we shall receive

$$\begin{aligned} v^2 = v_*^2 = v_0^2 + \frac{L'i_0^2}{m} (1 + k_f) [l + L_L / L' - x] \times \\ \times \{1 - [l + L_L / L' - x_0] / [l + L_L / L' - x]\} \\ \omega = l + L_L / L', \quad t = t_*(x) = \end{aligned} \quad (5)$$

$$\begin{aligned} \left\{ \frac{-C_0}{D_0^{3/2}} \ln [D_0 \sqrt{p} + \sqrt{D_0 (D_0 p - C_0)}] - \frac{\sqrt{p(D_0 p - C_0)}}{D_0} \right\} \Big|_{p=\omega-x_0}^{p=\omega-x} \\ C_0 = \frac{L'i_0^2}{m} (1 + k_f) [\omega - x_0]^2, D_0 = V_0^2 + C_0 / (\omega - x_0) \end{aligned} \quad (6)$$

Here and below  $F_{p=a}^{p=b} = F(b) - F(a)$ .

With the help of [7] it is possible to find the first corrections to obtained solutions and for nonzero  $R$ :  $R / (L'v) < 1$

$$\begin{aligned} v^2(x) = D(x) - C(x) / (\omega - x), \\ C(x) = C_0 [1 - (2R / L')] J_1(x), D(x) = D_0 - (2R / L') C_0 J_2(x), \\ J_1(x) = -2D_0^{-1/2} \{ \ln [D_0 p^{1/2} + (D_0 (D_0 p - C_0))^{1/2}] \} \Big|_{p=\omega-x_0}^{p=\omega-x}, \\ J_2(x) = - (2/C_0) [(D_0 p - C_0) / p]^{1/2} \Big|_{p=\omega-x_0}^{p=\omega-x} \end{aligned} \quad (7)$$

The pointed solutions are obtained in appendix. They can be used for assessments of the LGC work.

We shall define conditions of an amplification of the current in the load ( $dv/dt < 0$ ). Let's assume  $R = 0$  since the power losses on the Joule dissipation will slow braking of the armature and it can pass up to a stopping the greater distance.

From (2) we shall discover a coordinate of braking of the armature  $x_s$  ( $v(x_s) = 0$ )

$$\frac{x_s}{l} = \left(1 + \frac{L_L}{L_G}\right) \frac{Q_{k0}}{Q_{m0} + Q_{k0} + Q_{f0}} \quad (8)$$

$Q_{k0}$ ,  $Q_{m0}$ ,  $Q_{f0}$  - accordingly the initial kinetic and magnetic energy and the work of friction ( $x_0 = 0$ ):  $Q_{k0} = mv_0^2 / 2$ ,  $Q_{m0} = (L_L + L_G) i_0^2 / 2$ ,  $Q_{f0} = k_f Q_{m0}$ .

For steady work of the LGC it is necessary that  $x_s > l$ . Or from (8) it is equivalent to a condition  $L_G / L_L < Q_{k0} / (Q_{m0} + Q_{f0})$ . Whence for reaching required magnitude of a working current  $i$  a realization of the following conditions is necessary

$$\frac{i}{i_0} < \frac{L_G + L_L}{L_L} \leq \frac{Q_{k0} + Q_{m0} + Q_{f0}}{Q_{m0} + Q_{f0}} \quad (9)$$

$$l < l_{max} = -\frac{L_L}{2L'} + \sqrt{2 \frac{L_L}{L'_e} \frac{Q_{k0}}{L'i_0^2} + \left(\frac{L_L}{2L'}\right)^2}, \quad L'_e = L' (1 + k_f) \quad (10)$$

We shall below carry out optimization of the law of the modification of the inductance of the generator  $L_G = L_G(x)$  for deriving on the given external load of the required form of the current.



By the auxiliary functions  $\xi = x/l$ ,  $K = i/i_0$ ,  $\varphi = L'/L_L$  the conservation law of the magnetic flux will be noted as

$$I + \int_0^l \varphi(\xi) d\xi = K(\xi) \left\{ I + \int_\xi^l \varphi(\xi) d\xi \right\} \quad (11)$$

When  $L' = dL_G/dx = \text{const}$ ,  $\varphi = \varphi_0 = \text{const}$  follows. And we find from (11)

$$K(\xi) = (I + \varphi_0) / [I + \varphi_0(1 - \xi)] \quad (12)$$

The maximum amplification of a current  $K = I + \varphi_0$  is reached at  $\xi = 1$ .

We shall generalize (12) by entering the parameter  $\alpha$

$$K_\alpha(\xi) = (I + \varphi_0) / [I + \varphi_0(1 - \xi)^\alpha] \quad (13)$$

When  $\alpha = 1$  we obtain a standard solution (12), which corresponds to the constant linear inductance  $L'$  of the rails. The forms of the current in load for any  $\alpha$  and  $K = 10$  are represented in fig. 2. The value  $\alpha = 0$  corresponds to a condition of maintaining of a direct current. And the infinite value of an indicated parameter corresponds to the impulse of the alternating current ( $i \approx Ki_0$ ), which has the step-form. That is of interest for geophysical and electrophysical applications. With growth  $\alpha$  a monotonic filling of the form of the impulse of the alternate current is observed.

By conducting differentiation (13), we shall find the required law of a modification  $L'$ , necessary for a support of the specific form of the current.

$$\varphi_\alpha(\xi) = \varphi_0 \alpha (1 - \xi)^{\alpha-1} \quad (14)$$

According (14) the standard case,  $L' = \text{const}$ , corresponds to  $\alpha = 1$ . For general value of  $\alpha$  the dependence of the dimensionless linear inductance of the rails versus the longitudinal coordinate is shown in fig. 3

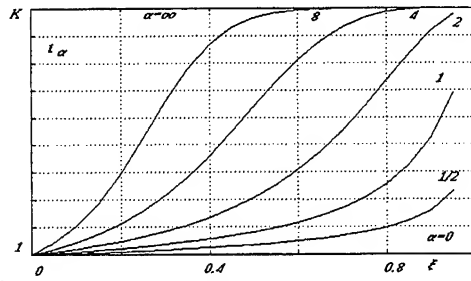


Fig. 2

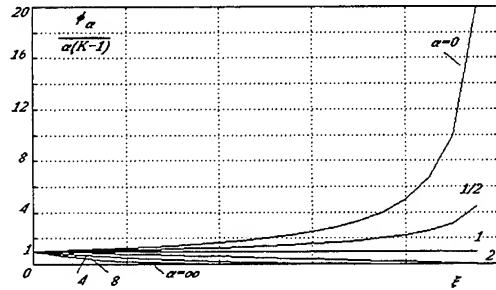


Fig. 3

For  $0 \leq \alpha < 1$  the dimensionless magnitude  $L'$  increases in direction of a throwing of the piston. The decrease of  $L'$  is typical for  $\alpha > 1$ . Thus, for deriving a step-form of an impulse of the electrical current a strong decrease of linear inductance along the channel of the generator is required. The practical realization of the given idea requires of the special reviewing and in the given work is not considered.

#### 4. Numerical Simulation

The calculations were carried out for the aluminium conductive elements of an armature and three types of electrodes with different conductive parts: 1- copper, 2- bronze, 3 - steel. And two basic sets of the numerical simulations, marked hereinafter [a] and [b], accordingly for initial currents  $i_0$  in 10 and 100 kA, have been made. The physical properties of materials are taken from manuals [8-11].

In calculations if another variants are not pointed we accept:  $T_{a,r0} = T_0 = 293K$ ,  $V_0 = 700m/s$ ,  $x_0 = 0$ ,  $l = 2m$ ,  $L_L = 0.5\mu H$ ,  $R_L = 0.35 m\Omega$ ,  $m = 58 g$ ,  $w_{a,r} = 24mm$ ,  $h_{a,r} = 25mm$ ,  $l_a = 10mm$ ,  $L' = 5.2\mu H/m$ ,  $\mu_0 = 4\pi \cdot 10^{-7} H/m$ ,  $n=3$ .

For indicated data the results of numerical experiments are represented in fig. 4 - 7 with indexes "a" and "b" accordingly for variants [a] and [b]. The curves, adequate to the copper rails, were marked on the graphs by asterisks - "\*". The markers, daggers - "×" and circles - "o", correspond to the bronze and steel rails.

The trajectories of a ballistic piston  $x(t)$  are represented in fig. 4 a, b.

The variant [a] ensures stable LGC work irrespective of a type of considered materials for rails. Stoppings of an armature inside the channel of a generator does not happen. In this case the parameters of an operating duty of the LGC are selected according to conclusions of the qualitative analysis. Only a realization of the right inequality (10) were not guaranteed a little. In variant [b] the pointed condition has been not satisfied essentially. However, as have shown calculations, the resistive rails can stabilize a transformation of the kinetic energy of the piston into the electrical power.

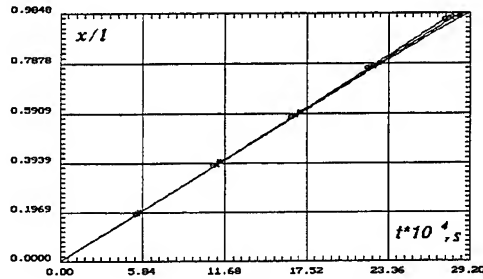


Fig. 4a

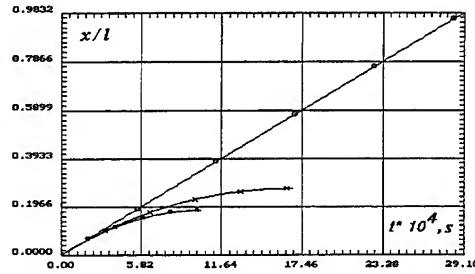


Fig. 4b

The process of braking of the piston at a compression of a magnetic field is represented in fig. 5a,b.

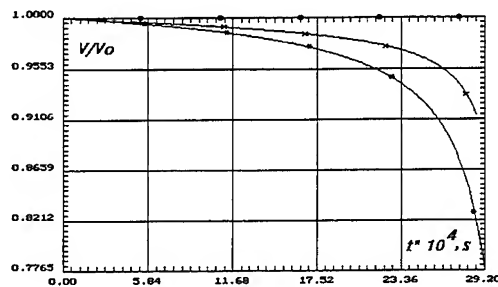


Fig. 5a

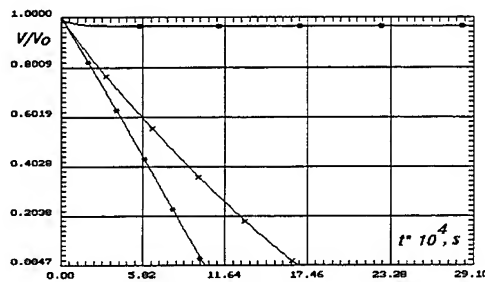


Fig. 5b

Braking of the armature is the most effective at copper rails: 22 % and 100 % for variants [a] and [b]. The kinetic energy of the piston does not decrease practically for [a] at the steel electrodes. A decrease of the velocity for [b] is about 4 %. The bronze buses of the generator give on indicated variants a drop of a velocity  $\approx 8$  % and 100 %.

The amplification factor of the electrical alternate current  $K = i/i_0$  characterizes one of the goal functions of the development of the LGC (fig. 6 a,b).

The amplification of the alternate current ( $K > 1$ ) or support of the direct current  $K \approx 1$  should be supplied for majority of practical applications .

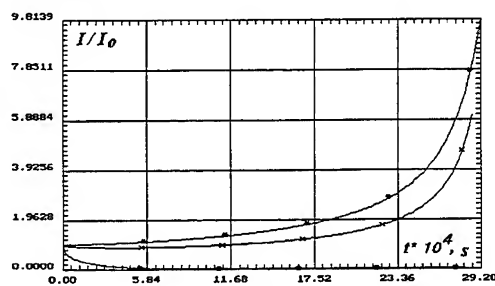


Fig. 6a

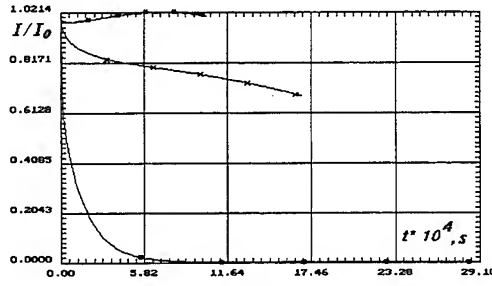


Fig. 6b

According to the results of the section 3:  $K \leq L/L_L$  . And the equality can occur for rather large value of the linear inductance of the rails  $L'$  and the velocity  $v$  of the armature. It is ensuring on the average a dominance of an inductive resistance in buses  $L'v$  over the full ohmic resistance  $R$ .

For infinite electrical conductivity of the rails, armature and external load, the amplification factor of the current according to the left inequality (10) can reach 21.8 . The numerical experiments show that the variant [a] can ensure generation of the current ( $K > 1$ ). However due to the Joule heat

losses in considered actual constructions of generators the amplification factor of the current can be much less of the theoretical prediction. So for copper buses the amplification of the current reaches only the magnitude of 9.8. Due to the bronze rails the current of the load strengthens in 5.9 ones. And the steels electrodes do not generally ensure the amplification of the current, which practically damps.

The resistance  $R$  varies nonmonotonically. Due to the skin effect the magnitude of  $R$  is great at the beginning of the generation cycle. It can cause a decrease of the current in corresponding times (fig. 6 a,b.).

In preferable variant [a] the heating of the piston does not exceed 0.2 , 0.4 and 0.6 % accordingly for rails, made of steel, bronze and copper. It is called by the currents diminution through the armature in case of more resistive rails.

The variant [b] has appeared unfavorable from a point of view of generation of currents also because the heating of the armature is essential, up to tens of per cents. This can cause its plastic deformation.

The heating of the buses in the preferable variant [a] depends on their material but does not exceed 0.13 %. In the alternate variant, [b], it reaches 14 %.

The effectiveness of the LGC work is traced in fig. 7a,b , where efficiency  $\eta$  equals the ratio of the energy in the load to the full initial energy, is represented.

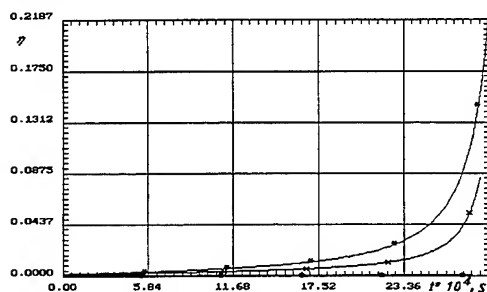


Fig. 7a

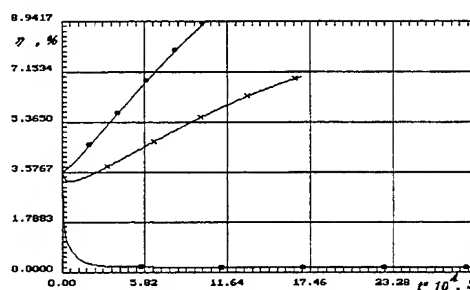


Fig. 7b

In preferable variant [a] the efficiency can reach 22 % for copper buses. The rails from bronze or steel can decrease the effectiveness of transformation the energy by means of the LGC. One of methods of a raise the efficiency is a lowering of the resistance of the rails by their chilldown up to nitrogen temperatures. The variant [b] allows to supply on copper buses only the efficiency up to 9 % without an amplification of the initial current.

With the purpose of the analysis of optimal possibilities of researched constructions LGC the calculations of values of the amplification factor of a current  $K$  (fig. 8) and of the efficiency  $\eta$  (fig. 9) have been made in a range of initial currents from 10 up to 100 kA. This parameters correspond to the moment of an end of the moving of the armature in the channel of the generator.

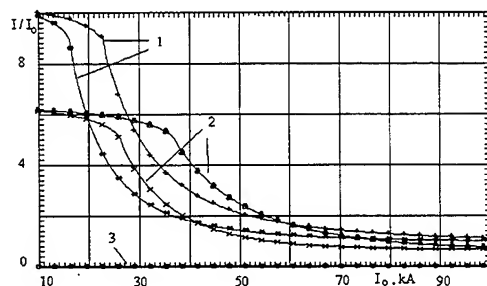


Fig. 8

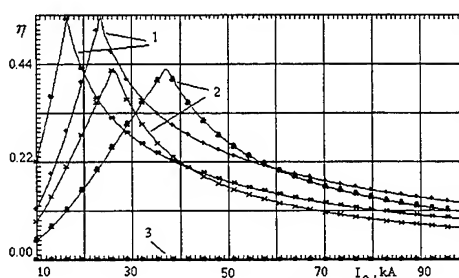


Fig. 9

The cyphers mark a type of materials, used at manufacture of rails: 1 - copper, 2 - bronze, 3 - steel. And upper curves marked on the pictures in identical symbols correspond to a double mass of the piston  $m = 116g$ .

The decreasing of intensity of the amplification of the current (fig. 8) with growth of the initial current is caused by a diminution of a part of the initial kinetic energy of the piston in relation to a full energy of initiation of work LGC. Since the generation of the current is caused largely by transformation

of the kinetic energy of the armature into the electrical energy. So it explains the amplification of the generation of the current with growth of the mass of the piston.

There is the optimum initial current, which ensures maximum efficiency (fig. 9). This current corresponds according to fig. 8 the beginning of a sharp decrease of intensity of the amplification of the current and the used energy in the external load.

## 5. Conclusion

Zero-dimensional non-stationary description of a linear generator of a current (LGC) is developed. This physical model takes into account skin-effect and thermal effects in buses and armature. The appropriate software for the realization of the numerical experiments for an analysis of pointed generators is created. When the summarized electrical resistance of the generator and the external electrical load is constant the analytical solutions which describe the work of the generator are obtained and are investigated. In a result the magnitudes of physical parameters of the LGC which ensure its stable work were found. The variant calculations of concrete constructions LGC as railgun are made and are analysed for various materials of buses and initial conditions. The calculations showed that the developed qualitative analytical theory is useful for the preliminary prognosis of the generation of the current. The analysis of numerical experiments gave possibility to select from a considered class of the constructions the most preferable ones and to define the quantitative parameters of an operation LGC such as efficiency and temperature in buses and armature, etc. The efficiency of similar generators can be optimized. And it can reach according to examining physical and numerical model up to 55 %. A possibility of a control of the form of the impulse of the current by a modification of the linear inductance of the rails is investigated. However for a practical realization of similar idea additional scientific investigations are necessary.

## Appendix: Proof of (7)

We'll find below the solution of problem (1) for nonzero electrical resistance  $R = \text{const.}$

Then, substituting in (1)  $dt$  on  $v dx$ , we shall receive

$$i^2 = -\frac{m}{L'(1+k_f)} \frac{dv^2}{dx}, \quad i(x_0) = i_0 \quad (15)$$

$$\frac{d^2 v}{dx^2} = \frac{2(1-r)}{\omega-x} \frac{dv^2}{dx}, \quad r = \frac{R}{L'v}, \quad v(x_0) = v_0, \quad \frac{dv^2(x_0)}{dx} = -\frac{L'(1+k_f)}{m} i_0^2 \quad (16)$$

When  $R=0$ , the solution of the problem has been found in the part 2 and we designate it as  $v = v_*$ ,  $r = r_*$ .

For small  $R$  the executing of a linearization of equation (16) with respect to the solution with  $R=0$  gives

$$\frac{d^2 v}{dx^2} = \frac{2}{\omega-x} \frac{dv^2}{dx} + F(x), \quad F(x) = -\frac{2r_*(x)}{\omega-x} \frac{dv_*^2}{dx} \quad (17)$$

The initial conditions are as in (16).

The general solution of (17) has for  $F=0$  the expression  $v_*^2(x) = D_0 - C_0/(\omega-x)$ . For  $F \neq 0$  we'll change the constants  $C_0$ ,  $D_0$  on a functions  $C(x)$ ,  $D(x)$ . Then  $v^2(x) = D(x) - C(x)/(\omega-x)$ . In a result

$$\begin{aligned} \frac{dD}{dx} &= -(\omega-x)F(x), \quad D(x_0) = D_0 \\ \frac{dC}{dx} &= -(\omega-x)^2 F(x), \quad C(x_0) = C_0 \\ F(x) &= 2 \frac{R}{L'} \frac{C_0}{(\omega-x)^2 \sqrt{D_0(\omega-x)^2 - C_0(\omega-x)}} \end{aligned} \quad (18)$$

Whence the dependences (7) for  $C(x)$  and  $D(x)$  may be found.

## Nomenclature

Subscripts "a" and "r" refer accordingly to the armature and the rails

|                                |   |
|--------------------------------|---|
| LGC -                          | Linear Generator of Current   |
| n -                            | Number of the LGC facility sections   |
| $x, y, z$ -                    | Cartesian coordinates   |
| $l$ -                          | Length of the generator   |
| $v, m, l_a$ -                  | Velocity, mass and length of the armature along the direction of the piston motion                                  |
| $i(t)$ -                       | Dependence of the current vs. time $t$  |
| $v_0, i_0, x_0$ -              | Velocity, current and x-coordinate of the piston at $t = 0$   |
| $h_{r,a}$ -                    | Size of rails and armature along y-direction  |
| $w_{r,a}$ -                    | Size of rails and armature along z-direction  |
| $k_f$ -                        | Coefficient of the piston motion resistance by friction along the rails   |
| $R, R_a, R_L$ -                | Full electrical resistance, the resistances of the armature, rail and load  |
| $\mu_0$ -                      | Permeability of vacuum  |
| $\lambda_{r,a}$ -              | Size of the current skin zones  |
| $\delta_{r,a}, \Omega_{r,a}$ - | Size and volume of the region occupied by current   |
| $T_{r,a}, C_{r,a}$ -           | Temperature and specific heat capacity  |
| $\rho_{r,a}, \alpha_{r,a}$ -   | Specific electrical resistances and their temperature coefficients  |
| $T_{r0}, T_{a0}$ -             | Initial temperatures of the rails and armature  |
| $L$ -                          | Linear inductance of the rails  |
| $L, L_G, L_L$ -                | Full inductance, inductances of the generator and the load  |
| $K = i / i_0$ -                | Gain of a current   |
| $\xi = x / l$ -                | Dimensionless coordinate of the piston  |
| $\alpha$ -                     | Auxiliary variable characterizing a change of the inductance gradient $L'$ along the direction of the piston motion |
| $\eta$ -                       | Efficiency  |

## References

1. A.D. Sakharov "Magnetoelectric Generators", Sov. Phys. Uspekhi, Vol. 9, 1966, pp. 294-299.
2. G.A. Shvetsov "Explosive Magnetic Hydrodynamics", Novosibirsk, 1992, 88p. (in Russian).
3. P. Mongeau "Combustion Driven Pulsed Linear Generators for Electric Gun Applications" / presented at the 8th EML Symposium.
4. Yu. A. Dreizin "The Electromagnetic Chemical Propulsion Concept" / IEEE Trans. Magn., Vol. 31, No. 1, January 1995, pp. 279-284.
5. Yu. A. Dreizin "A Busgun Design Example", presented at the 7-th EML Symposium.
6. Y.G. Tynnikov, N.A. Tolstokoulakov and A.V. Kryjin "A Ballistic Generator as the Power Supply of Impulse Discharges" / Materials of 1-th All-Union Seminar on Dynamics of Strong-Current Arc Discharge in a Magnetic Field, Novosibirsk, 1990, pp. 263-267 (in Russian).
7. G.B. Dwight "Tables of Integrals and Other Mathematical Formulas", Moscow, Nauka, 1977, 228p. (in Russian).
8. G. Knopfel "Super-Strong Impulse Magnetic Fields", Moscow, Mir 1972, 392 p. (in Russian).
9. Kh. Kikhling "A Manual on Physics", Moscow, Mir 1982, 520p. (in Russian).
10. V.A. Burtsev et al. "Electrical Explosion of Conductors", Moscow, Energoatomizdat 1990, 288p. (in Russian).
11. A.P. Babichev et al. "Physical Magnitudes: A Manual", Moscow, Energoatomizdat 1991, 1232p. (in Russian).

# **Superconducting Inductive Pulsed Power Supply for Electromagnetic Launchers:**

## **Experimental Investigation of Laboratory Set-up and Design Aspects for Further Development**

W. Weck\*, P. Ehrhart, M. Heeg, A. Müller, G. Reiner, H. Schölderle, E. Sturm  
Magnet-Motor GmbH, Petersbrunner Str. 2, D-82319 Starnberg, Germany

**Abstract**— A 0.5 MJ laboratory set-up of a modular superconducting pulsed power supply is described. This combination of a superconducting inductive energy storage with a superconducting pulse switch is performed in standard NbTi technology. Experimental results of laboratory tests are presented. The possibility of pulse shaping by time-controlled triggering of modules is introduced. The technological aspects of increasing the energy density and power density by applying high-grade superconducting materials ( $\text{Nb}_3\text{Sn}$ , HTSC) are discussed.

### **I. INTRODUCTION**

A superconducting inductive energy storage in combination with a superconducting switch is one of the principles that is regarded to be capable of supplying tactical and mobile electromagnetic and hybrid launchers with the required high power pulses.

An inductive device stores the energy in the magnetic field, with the energy density being proportional to the square of the induction  $B$ .

High values of the induction  $B$  and thus sufficient high energy densities cannot be achieved in normal conducting inductive devices but it needs a superconducting material in which the stored current flows free of losses.

The state of superconductivity is valid for the respective materials as long as they are operated below the critical temperature  $T_c$ , the critical induction  $B_c$  and the critical current density  $j_c$ . The three critical conditions influence each other. In order to achieve optimal operating margins for  $B$  and  $j$  it is necessary to use temperatures well below  $T_c$ . For the classical "Low Temperature Superconductors (LTSC)", like NbTi, usually cooling with liquid helium ( $T = 4.2 \text{ K}$ ) is applied. For the "High Temperature Superconductors (HTSC)", which are known now for almost 10 years, the material data show much higher values for  $T_c$ ,  $B_c$  and  $j_c$ . It is expected, that future applications of this type of material will operate well with cooling by liquid nitrogen ( $T = 77 \text{ K}$ ).

The fact that a superconducting material goes instantaneously from the superconducting state to the normal conducting state, when the operating conditions either override one of the critical values  $T_c$ ,  $B_c$  or  $j_c$ , can be applied for interrupting very high currents.

Those devices, which use the transition from the state of resistivity zero to the normal resistivity are referred to as superconducting switches.

This paper will describe a laboratory set-up of NbTi superconducting storage and switch components with an energy capacity of 0.5 MJ and it will present experimental results of this unit.

There will be discussed the further steps of development for increasing the energy density and power density by applying novel superconducting materials ( $\text{Nb}_3\text{Sn}$ , HTSC).

## II. LABORATORY SUPERCONDUCTING INDUCTIVE PULSE POWER SUPPLY

### Operation principle

The charging of the storage is performed by the principle of dividing the inductive storage into several coil segments, which are connected in series during charging and which operate parallel for discharging. The block diagram of this method is shown in Fig.1 at six elements.

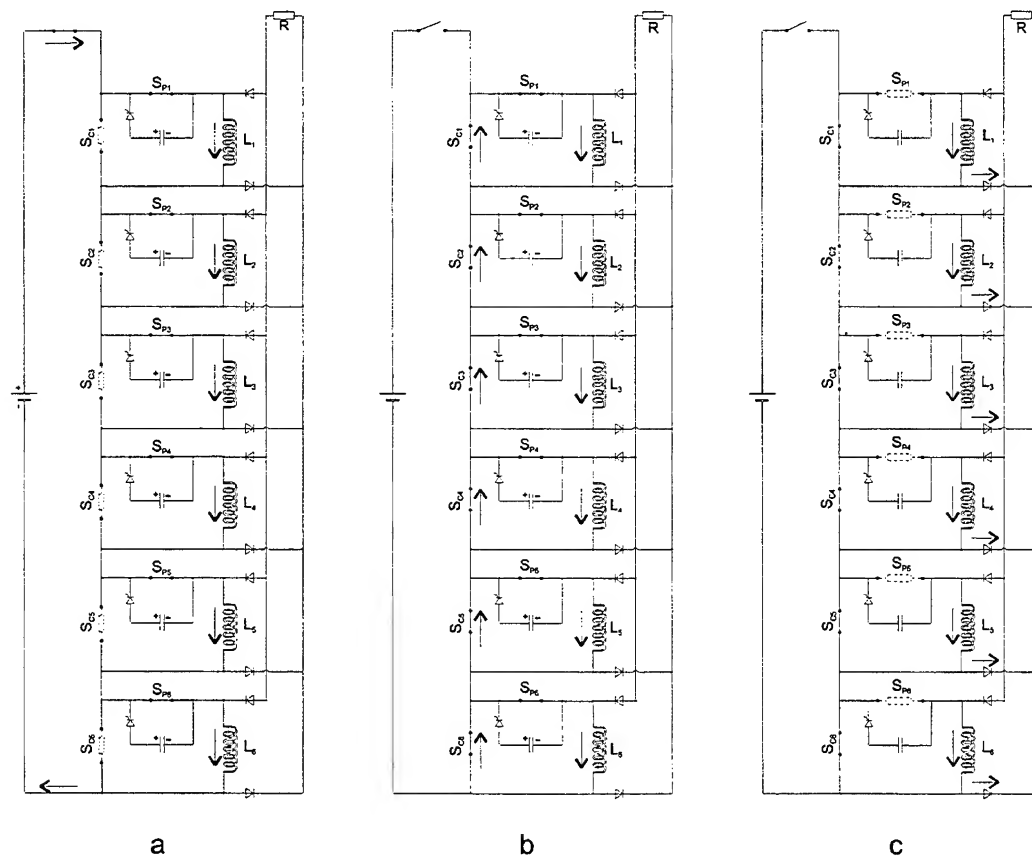


Fig. 1. Block diagram of modular superconducting pulse power supply

- a) charging state
- b) storing state
- c) discharging state

The symbols  $S_p$  and  $S_c$  represent the superconducting power switches and charging switches respectively. The symbols  $L_1$  to  $L_6$  represent the storage coils and  $R$  stands for the external load.

During charging (Fig. 1 a), the charging switches  $S_c$  are heated and thus set to normal conducting state, while the power switches  $S_p$  are still in superconducting state. Generated at the external current source, the charging current is forced into the storage coils.

For storing the energy all switches, which were heated during charging, are set to superconducting state and the prime power supply is shut down (Fig. 1 b). In this state the conservation of energy is possible for several hours.

The output pulse is generated by bringing all power switches  $S_p$  instantaneously to the normal conducting state (Fig. 1 c). This is realized by an additional high current pulse through each power switch element  $S_p$  by discharging a capacitor over a thyristor. The currents of all storage elements are then summed up to the final pulse in the load. The decoupling diodes avoid bypassing currents.

### Design of superconducting storage

For practical reasons it is necessary that a superconducting magnetic storage has as low magnetic stray field to the outside as possible.

On the other hand the device should be as compact as possible and the structure must be able to withstand the mechanical forces that arise from the high magnetic fields.

We have therefore regarded and experimentally investigated an inductive storage, which is composed as a hexagon arrangement of solenoids (Fig. 2).

Although this structure cannot compensate stray fields perfectly to zero it was chosen, because in the solenoidal elements there are almost only mechanical forces of cylindrical symmetry to be dealt with. This means that the support structure for this coil arrangement can be quite simple. A special support structure is only necessary for the attractive forces among the solenoids.

The system consists of identically manufactured storage solenoids. These elements can be manufactured and tested separately. In the complete arrangement the elements are usually connected in series for charging. For discharging they can be switched in series or parallel, in order to adapt voltage and current to the demands of the load.

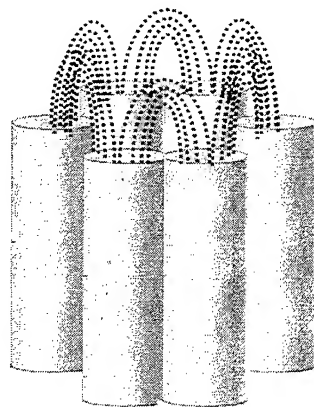


Fig. 2. Principle of compensation of magnetic field in a hexagon of solenoids



TAB.1 : DESIGN DATA OF SUPERCONDUCTING STORAGE

|               | Solenoid element         | Hexagon of 6 solenoid elements<br>( parallel discharge condition ) |
|---------------|--------------------------|--|
| Conductor     | NbTi-s.c. in a Cu matrix | NbTi-s.c. in a Cu matrix   |
| Diameter      | 175 mm                   | 590 mm   |
| Height        | 520 mm                   | 540 mm   |
| Weight        | 23 kg                    | 150 kg   |
| Inductance    | 65 mH                    | 11 mH  |
| Rated current | 1600 A                   | 9600 A   |
| Max. B        | 5.5 T                    | 5.6 T  |

The design data of the current laboratory set-up consisting of 6 solenoids are summarized in Tab. 1.

#### Superconducting opening switch

The superconducting opening switch makes use of the transition from the state of resistivity zero to the normal resistivity. As for this type of opening switch the "off" resistance is not infinite, as would be desired for an ideal switch, the achievable switching power is related to the amount and to the characteristic data of the superconductor material applied.

In order to keep the quantity of material in the switch low it is necessary that the conductor has high current density in the superconducting state and high resistivity in normal conducting state. These conditions in combination with the required dynamic performance are met well within the available LTSC conductors by cabled wires of NbTi filaments in CuNi matrix.

In the practical design the superconducting switch is composed of a long conductor arranged in a very-low-inductance configuration. The minimization of the inductance is essential for achieving fast switching performance and low switching losses.

Another requirement for the superconducting opening switch is a high dielectric strength, which can be optimized by geometrical design and the insulation materials applied.

The design data and characteristics of the of the switching components are presented in Tab. 2.

TAB.2 : DESIGN DATA OF SUPERCONDUCTING SWITCH COMPONENTS

TAB.2 : DESIGN DATA OF SUPERCONDUCTING SWITCH COMPONENTS

|                           | Power switch element       | Charging switch element    |
|---------------------------|----------------------------|----------------------------|
| Conductor                 | NbTi-s.c. in a CuNi matrix | NbTi-s.c. in a CuNi matrix |
| Coil diameter             | 86 mm                      | 74 mm                      |
| Height                    | 450 mm                     | 125 mm                     |
| Weight                    | 8 kg                       | 1.8 kg                     |
| Inductance                | 9.5 $\mu$ H                | 4.3 $\mu$ H                |
| Rated current             | 2000 A                     | 2000 A                     |
| $R_{\text{normal}}$ at 5K | 60 $\Omega$                | 10.5 $\Omega$              |
| Triggering                | current peak               | thermal                    |

### III. EXPERIMENTS

A laboratory set-up of a pulse power supply has been designed and built. The storage elements are 6 solenoids, which are arranged in a hexagon structure. In this first stage of experiments the superconductor material for the storage coils is a cable of NbTi-filament wires with Cu-matrix. To avoid an axial contraction of the windings there are additional supporting rings. In this version the rated energy capacity is 0.5 MJ.

The main part of the residual stray field of the hexagon is located at the end of the solenoids. The center of the hexagon is a region of very low field. It is the preferred location for placing the superconducting power switches. Also the region outside of the solenoids, in the middle between top and bottom has very low stray field, so the charging switches are placed there ( see Fig. 3).

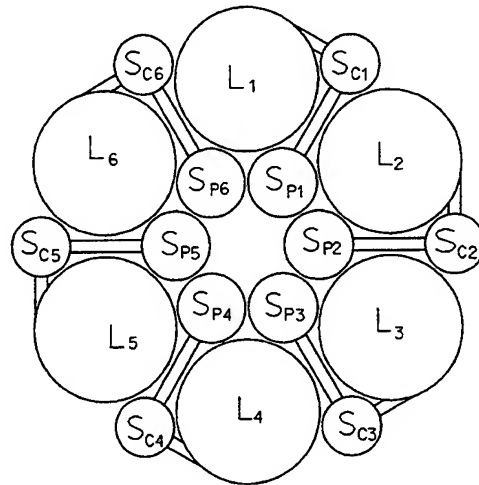


Fig. 3. Principle of hexagonal arrangement of superconducting storage coils and switch elements.

The performance data of each solenoid and switch were evaluated separately. For these tests segments consisting of one charging switch, one power switch and one storage coil, thus representing one sixth of the hexagon, were put together and operated.

In these tests all superconducting switching elements ( power and charging switches ) reached their rated current of 2000 A after a few training steps. This training means that the rated current is usually not reached at first attempt of energizing the device, due to quenching. The current carrying capacity is increased with the number of energizing attempts and quenches. This characteristic is well known for superconducting appliances.

The superconducting storage coils also needed some training steps before they reached their rated energy capacity of 80 kJ. In order to prevent damage to the coils caused by these quenches, the pulse triggering circuitry with capacitor and thyristor (see Fig. 1) is applied as a quench protection unit in this phase of experiments. When spontaneous quenching is detected in one component, a full pulse discharge is triggered at a very short time delay.

The complete system of 6 segments was put together and tested successfully (Fig. 4).

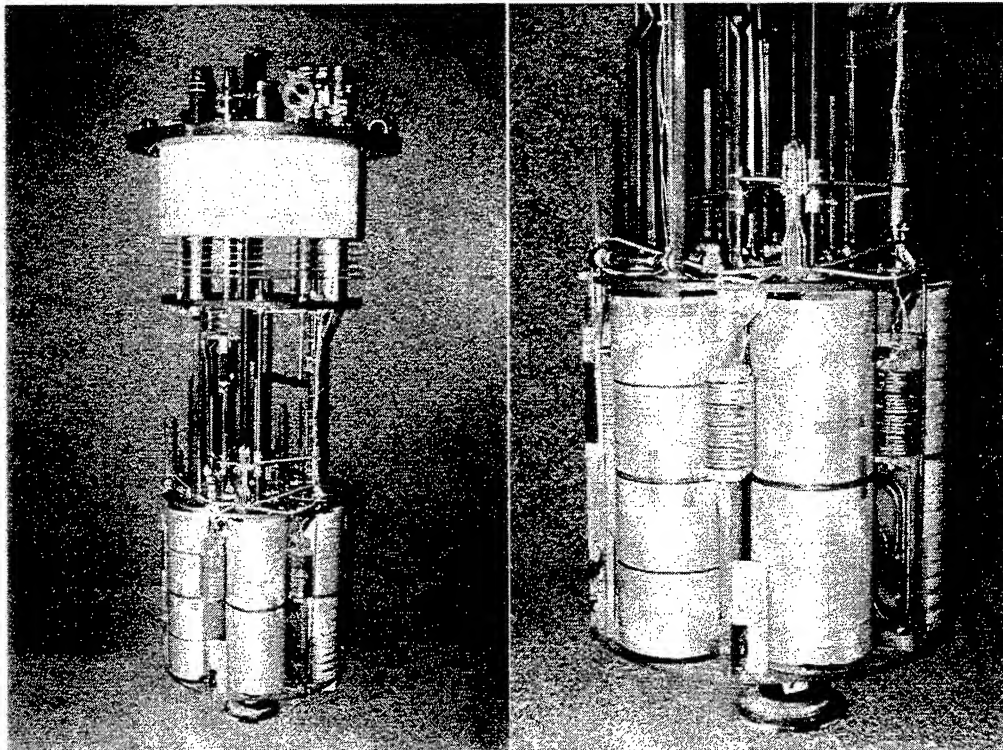


Fig. 4. Laboratory set-up 0.5 MJ of superconducting pulse power supply.

The training of all components has not increased in a combined operation. The arrangement was charged with an average charging power of 8 kW in 60 s. After a definite time of storage the arrangement was discharged and an energy pulse of 480 kJ was achieved at an external load. Fig. 5 shows the discharge pulse with a peak power of 5 MW.

Due to laboratory conditions the peak power ( i.e. the voltage ) at the load was limited for these experiments. High voltage pulses, which had already been demonstrated in preceding laboratory tests with former set-ups, will be carried out in the next tests to come.

#### IV. FURTHER STEPS

For several applications it is interesting, not to have just one single discharge pulse, but to be able to shape the pulse by triggering the opening switches in a sequence with definite short time delays. This operation mode is feasible, as the magnetic coupling of the solenoids and thus the mutual influence during discharge is rather weak, which could be shown by computer simulations of the system (Fig. 6).

The corresponding experiments will be carried out soon.

According to the original concept the laboratory set-up as described in this paper is just a pre-stage of a larger unit. It is planned to raise the energy capacity roughly by a factor of 4 by increasing the central induction  $B$ . For this, additional coils made of  $\text{Nb}_3\text{Sn}$  material shall be inserted into the  $\text{NbTi}$  solenoids.  $\text{Nb}_3\text{Sn}$  allows higher values of  $j$  and  $B$  than  $\text{NbTi}$ , however the preparation of the coils is much more complicated. With these hybrid solenoids an arrangement of two hexagon assemblies stacked onto each other will finally make up a 4 MJ unit.

The design aspects of this unit is described elsewhere /1/.

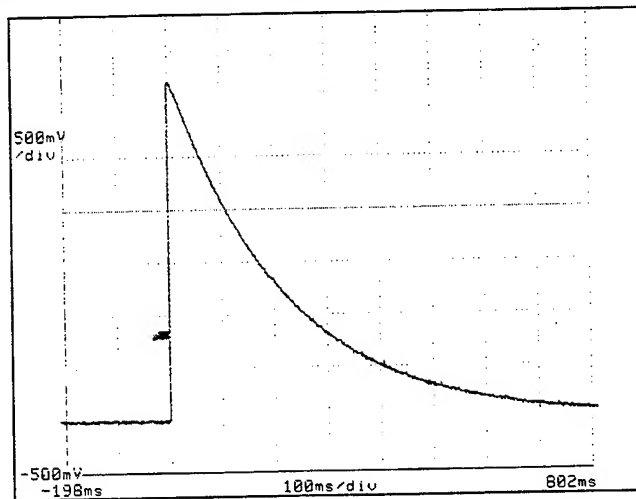


Fig. 5. Discharge pulse at resistive load  
Pulse energy  $E=0.5$  MJ.  
Peak power  $P=5$  MW

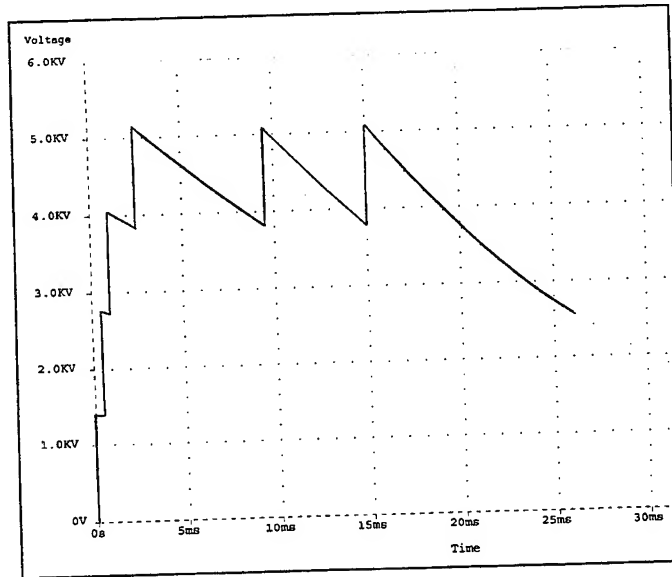


Fig. 6. Example of time-controlled discharge pulses at resistive load (result of computer simulation).

#### IV. CONCLUSION

The experiments presented in this paper show that a superconducting pulse power supply of this type is operable with its basic functions charging, storing and discharging. The demonstrated set-up, with its six fold symmetry has not only original conditions with respect to current and magnetic field but also with mechanical forces. The doubling of the energy contents by stacking two hexagons onto each other is expected to be practicable without additional difficulties.

The further increasing of energy density and power density will be carried out by applying higher-grade superconducting materials like  $\text{Nb}_3\text{Sn}$  and HTSC. The possibility of time-delayed triggering of the elements of this system gives the opportunity of a load-adapted pulse shaping.

#### REFERENCES

- [1] W. Weck, P. Ehrhart, A. Müller, G. Reiner, Proceedings of 8<sup>th</sup> EML Symposium Apr. 21-24, 1996 in Baltimore, to be published in IEEE Trans. on Magnetics

# Rail launcher with contact-studs to accelerate long-rod projectiles

Pascale LEHMANN\*, Francis JAMET, Volker WEGNER and A.-G. SCHMITT

French-Germann Research Institute of Saint-Louis  
5 rue du Général Cassagnou - F 68301 SAINT-LOUIS Cedex - France

**Abstract**—To accelerate in railguns long-rod projectiles with diameters varying between a few mm and 25 mm up to velocities greater than 2000 m/s currents of several MA are necessary. Due to the thermal effects, the current in the rails is limited to a value growing with the rail launcher caliber. To reach higher muzzle velocities the caliber and consequently the mass of the projectile must be increased.

To maintain low projectile diameter and mass while increasing the current, we suggest to use a railgun supplied with contact-studs. The interesting aspects such a railgun compared to classical ones and the range of applications are discussed.

Based on that study, we compare different railguns able to accelerate a penetrator with a fineness ratio  $L/D = 35$  up to velocities of about 2500 m/s. We show that a 80 mm caliber gun will have a length greater than 10 m to reach that performance, whereas a 120 mm railgun supplied with contact-studs, so that the projectile caliber remains 80 mm, gives the same results for an accelerating length of 4.5 m.

A 3D electromagnetic numerical simulation was used to determine the current distribution in the contact-studs and in the armature. We show that a good choice of the armature materials allows to distribute the current along the contact-studs.

## I. INTRODUCTION

The railguns used for military application must be able to accelerate long rod penetrators with fineness ratios varying between 10 and 35 [1]. The diameters of those penetrators range from 5 to 10 mm for the anti-aircraft application and are about 22.5 mm for the anti-tank application.

To lower the launched projectile mass (i.e. the electrical energy) it is interesting to have a gun caliber as small as possible. Unfortunately that cannot be achieved in most cases: firstly the railgun efficiency decreases with the caliber  $D$  (for  $D < 140$  mm [2],[3]) and secondly the currents

necessary to obtain the high required velocities (2000 m/s to 3000 m/s) are very large (a few MA). Due to the rails heating the maximal current is caliber dependent. The maximum current density per unit rail width is commonly admitted to be about 50 to 60 kA/mm.

From the increase of the caliber, in order to reach the desired muzzle velocity, results a correlated increase of both the projectile (sabot + penetrator) mass and the stored electrical energy.

In this paper we study the possibility to use a railgun with contact-studs which allows us to have a caliber large enough to inject the current and simultaneously to keep the projectile diameter small (i.e. a small accelerated mass) [4]. The small full caliber railgun, the large full caliber railgun and the contact-studs railgun are compared.

## II. ACCELERATION OF A PENETRATOR WITH SABOT

In this paper we take for all the studied railguns the same rail geometry: round or square bore. In any case the sabot will have the same length and mass density. The sabot is assimilated to a full cylinder (or a parallelepiped) with a hole for the penetrator.

### A. General case

We first consider a railgun with caliber  $D$  (Fig. 1). The Lorentz force is given by the well known formula:

$$F = BID = \frac{1}{2} L' I^2 = (m_s + m_p) \gamma \quad (1)$$

where  $I$  is the current,  $B$  the magnetic field created by  $I$ ,  $D$  the caliber,  $L'$  the inductance per unit length of the rails,  $m_s$  the sabot mass for the caliber  $D$ ,  $m_p$  the penetrator mass and  $\gamma$  the acceleration in the railgun of caliber  $D$ .

We assume that the current  $I$  injected in the rail

is the maximum possible current ( $I_{\text{rail width}} = I_{d \text{ max}} = 60 \text{ kA/mm}$ ).

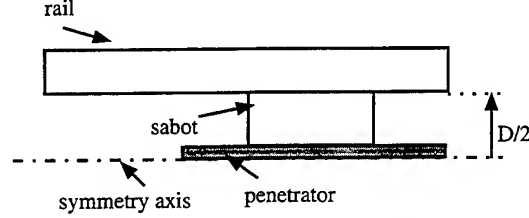


Fig. 1 Scheme of the railgun of caliber D

### B. Influence of the caliber reduction with current density limitation

Now we look at a railgun with a caliber  $d < D$  (Fig. 2). In that case the Lorentz force on the projectile is given by

$$F_2 = d I_2 B_2 = (m_{s2} + m_p) \gamma_2 = \frac{1}{2} L'_2 I_2^2 \quad (2)$$

where  $I_2$  is the current for caliber  $d$ ,  $B_2$  the magnetic field created by  $I_2$ ,  $m_{s2}$  the sabot mass for caliber  $d$ ,  $m_p$  the penetrator mass,  $\gamma_2$  the acceleration in the railgun of caliber  $d$  and  $L'_2$  the inductance per unit length of the rails (caliber  $d$ ).

The current  $I_2$  is chosen to keep the maximum current density:  $I_2/d = I/D = I_{d \text{ max}}$ . From (1) and (2) the ratio of the accelerations of the projectile becomes:

$$\frac{\gamma_2}{\gamma} = \frac{L'_2}{L} \frac{1+a}{1+ak^2} \quad (3)$$

where  $k = D/d$ ,  $L'$  is the inductance per unit length of the rails (caliber  $D$ ),  $L'_2$  the inductance per unit length of the rails (caliber  $d$ ) with  $L'_2 < L'$  (same rail geometry) and  $a = m/M$  with  $m = m_p - A$ ,  $m_s = M - A$  and  $m_{s2} = M/k^2 - A$ .

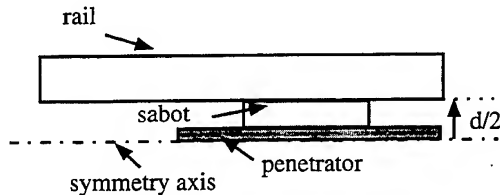


Fig. 2 Scheme of the railgun of caliber d

The parameter "a" represents approximately the ratio of the penetrator mass to the sabot mass. By assuming cylindrical sabots "a" is given by:

$$a = \frac{m}{M} \approx \frac{\Phi L}{DL} \frac{L \rho_p}{l \rho_s} \quad (4)$$

where  $\Phi$  is the penetrator diameter,  $L$  the penetrator length,  $l$  the sabots length,  $\rho_p$  the penetrator specific mass and  $\rho_s$  the sabots specific mass.

Fig. 3 shows the variation of  $L'_2 \gamma_2 / L'_2 \gamma$  as a function of the parameter "a" for different caliber ratios  $k = D/d$ . It can be seen that for each ratio  $k$  the reduction of the sabot mass (the penetrator mass is constant) does not allow the increase of the acceleration because the decrease of the caliber also lowers the current.

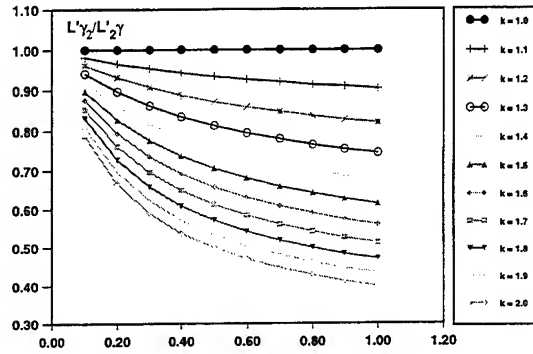


Fig. 3 Variation of the ratio  $L'_2 \gamma_2 / L'_2 \gamma$  as a function of the parameter "a" for different caliber ratios  $k = D/d$

### C. Influence of caliber reduction without current density limitation

If the injected current is less than the maximum current density of about 60 kA/mm then it can be kept when the caliber decreases at least for a limited variation range of  $k$ .

It is interesting to study the case where  $I_2$  is equal to the current  $I$  injected in the railgun of caliber  $D$ . The accelerations ratio is then given by:

$$\frac{\gamma_2}{\gamma} = \frac{L'_2}{L} \frac{k^2(1+a)}{1+ak^2} \quad (5)$$

If we assume in a first rough approximation that the inductance per unit length of the rails  $L'_2$  is equal to  $L'/k$  the acceleration ratio obtained is drawn in Fig. 4 for different values of  $k$  as a function of the parameter "a".

Sometimes it is interesting to reduce the caliber even if the efficiency of the railgun decreases: the mass gain is more important and the stored electric energy will be smaller. This is particularly true for the small values of the parameter "a", i.e. in the

case of a low penetrator mass compared to the sabot mass.

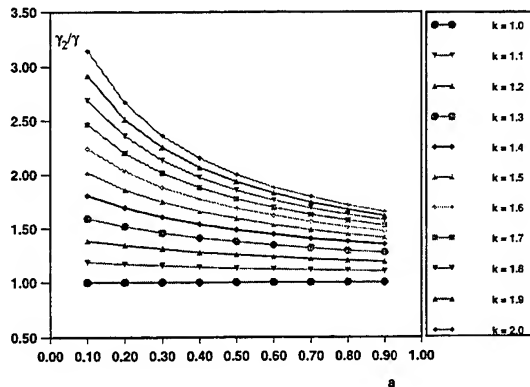


Fig. 4 Variation of the ratio  $\gamma_2/\gamma$  as a function of the parameter  $a$  for different caliber ratios  $k = D/d$  when  $I_2 = I$

#### D. Use of rails with contact-studs: influence on the acceleration

The scheme of the launcher is shown in Fig. 5. The conducting rails have excessive thicknesses (contact-studs) of small width  $l$ , spaced by a distance  $e$  and having a thickness  $f$ . The projectile (penetrator and sabot) of diameter  $d$  moves in the way to be in contact with at least one of those contact-studs. Its length is at least equal to the distance  $l+e$  to make contact with the next contact-stud before leaving the preceding one.

For the current we can assume a railgun with a caliber  $D > d$  and inject a current as high as  $I/D = I_{d \max}$ . The sabot mass will only depend on the distance  $d$  between the contact studs. So we can use a large current while keeping a small total mass.

The force on the projectile is given by:

$$F_3 = dIB_3 = (m_{s2} + m_p)\gamma_3 \quad (6)$$

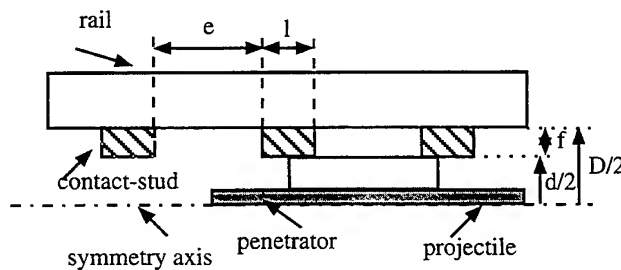


Fig. 5 Scheme of the railgun with contact-studs

where  $I$  is the current for caliber  $D$ ,  $B_3$  the magnetic field created by  $I$ ,  $m_{s2}$  the sabot mass for caliber  $d$ ,  $m_p$  the penetrator mass and  $\gamma_3$  the acceleration.

From (1) and (3) the acceleration ratio can be written:

$$\frac{\gamma_3}{\gamma} = \frac{L'_3}{L'} \frac{k(1+a)}{1+ak^2} \quad (7)$$

where  $k = D/d$ ,  $L'$  is the inductance per unit length of the rails (caliber  $D$ ),  $L'_3$  the inductance per unit length of the rails (caliber  $D$  with contact-studs) with  $L'_3 < L'$  (same rail geometry) and  $a = m/M$  with  $m = m_p - A$ ,  $m_s = M - A$  and  $m_{s2} = M/k^2 - A$ .

If we assume very thin contact-studs ( $l \ll e$  on Fig. 5), the inductance per unit length of the rails  $L'_3$  is about the same as  $L'$  (for caliber  $D$ ) and it results:

$$\frac{\gamma_3}{\gamma} \approx \frac{k(1+a)}{1+ak^2} \quad (8)$$

Fig. 6 shows the variation of the accelerations ratio with and without contact-studs as a function of the parameter "a" for different  $k$  values. The use of contact-studs appears interesting for values of "a" lower than about 0.5. This means that the penetrator mass is less than 50% of the sabot mass in the full caliber ( $D$ ) railgun.

If the small caliber  $d$  is sufficient to inject the total current  $I$ , we remind that it is often more interesting to reduce the caliber like the way described in C.

#### III. EXAMPLE: FROM CALIBER 120 MM TO CALIBER 80 MM

We want to accelerate a penetrator with a fineness ratio  $L/D = 35$  and a mass  $m_p = 5.5$  kg to a velocity of about 2500 m/s in a tube of about 5 m length.



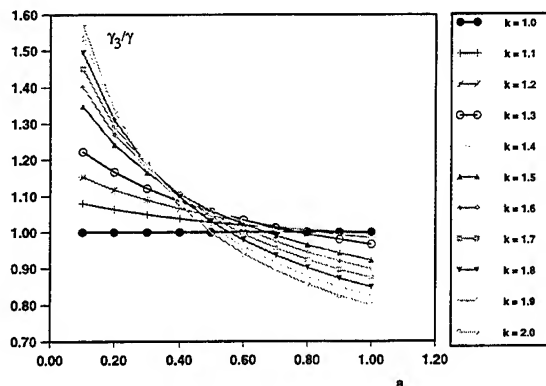


Fig. 6 Variation of the ratio  $\gamma_3/\gamma$  as a function of the parameter "a" for different caliber ratios  $k = D/d$

We assume 3 different launchers with calibers of respectively 120 mm, 80 mm and 120 mm with contact-studs so that the projectile diameter is 80 mm for the latter.

The 3 launchers fed by an electrical energy of 69.2 MJ have been simulated with the code ISLAM [6]. We assume that the current density per unit rail width is 60 kA/mm.

The numerical simulation results obtained with the ISLAM code [6] are given in Table I. For the 120 mm railgun the total projectile mass is about 15 kg. With the maximal current injected in the rails (5.7 MA), the muzzle velocity obtained with a 4.5 m tube is 2000 m/s.

For the 80 mm railgun the projectile mass is about 10 kg and the maximum current is reduced to 3.75 MA. The muzzle velocity of 2400 m/s can be

obtained with a 12 m long tube.

For the railgun with contact-studs the projectile mass is 10 kg ( $d = 80$  mm) and the maximal current reaches 5.7 MA ( $D = 120$  mm). In this case a muzzle velocity of 2500 m/s can be achieved with a 4.5 m long tube. In all three cases the acceleration remains less than  $0.85 \cdot 10^6 \text{ m/s}^2$ .

#### IV. NUMERICAL SIMULATION

A 3D electromagnetic numerical simulation was used to determine the current distribution in the contact-studs and in the projectile. We will show that with a good choice of the armature materials one can distribute the current along the contact-studs.

##### A. Numerical codes

The electromagnetic modeling of the railgun with contact-studs was done with the 3D finite element code EMAS (MacNeal-Schwendler Corporation). EMAS is capable of analyzing all aspects of the magnetic field behavior described by Maxwell's differential equations [7]. We have done the calculations at room temperature without taking into account the velocity skin effect.

For symmetry reasons only a quarter of the railgun cross-section was simulated. We assumed that the whole interface contact-studs-projectile is conducting. The current used as input data in the 3D electromagnetic code EMAS is shown in Fig. 7.

TABLE I  
CHARACTERISTICS OF THE LAUNCHERS OF CALIBERS 120 MM, 80 MM AND 120 MM WITH CONTACT-STUDS FED WITH AN ELECTRICAL ENERGY OF 69.2 MJ.

| caliber                                    | 120 mm<br>full caliber<br>[ $\gamma$ ] | 80 mm<br>full caliber<br>[ $\gamma_2$ ] | 120 mm<br>with contact-studs<br>$\Phi_{int} = 80$ mm [ $\gamma_3$ ] |
|--|--|---|---|
| current<br>density/rail width              | 60 kA/mm                               | 60 kA/mm                                | 60 kA/mm  |
| $M_p$ [kg]                                 | 5,5                                    | 5,5                                     | 5,5   |
| $M_s$ [kg]                                 | 9,7                                    | 4,1                                     | 4,1   |
| $L'$ [ $\mu\text{H/m}$ ]                   | 0,52                                   | 0,48                                    | $\approx 0,52$  |
| $v_0$ [m/s]                                | 2000                                   | 2400                                    | 2500  |
| $\gamma_{max}$<br>[ $10^6 \text{ m/s}^2$ ] | 0,53                                   | 0,34                                    | 0,83  |
| $l_{tube}$ [m]                             | 4,5                                    | 12,0                                    | 4,5   |
| $I_{max}$ [MA]                             | 5,7                                    | 3,75                                    | 5,65  |
| $\gamma_n/\gamma$ ( $n = 2, 3$ )           | 1                                      | 0,64                                    | 1,57  |

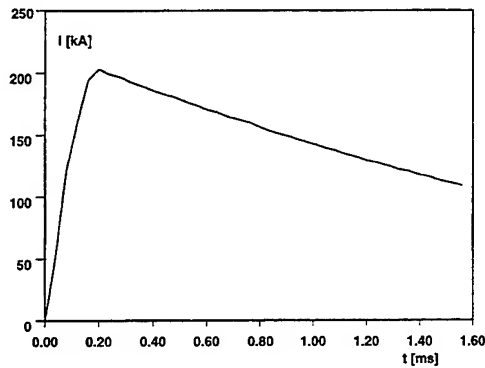


Fig. 7 Current variation versus time used as input data for the code EMAS

### B. Railgun and projectile

The characteristics of the square bore railgun and of the projectiles are given in table II. The notations are those of Fig. 5.

Fig. 8 shows a cut view of the rail with contact-studs and the projectile 2.

A length of 180 mm of the rail launcher around the projectile was modeled and a quarter of the railgun cross-section was simulated.

### C. Current distribution

Fig. 9 shows the current density  $j$  for the projectile 1 as a contour plot. Most of the current is injected in the rear part of the projectile 1 (contact-stud 1 in Fig. 9).

The total current for each contact-stud in contact with the projectile 1 (noted 1 to 4 in Fig. 9) as a function of time is shown in Fig. 10. The contact-stud 1 carries almost 75% of the total current during the whole duration of the shot.

TABLE II

CHARACTERISTICS OF THE MODELIZED RAILGUN AND PROJECTILES

|                | railgun   |
|----------------|---|
| D (mm)         | 27  |
| d (mm)         | 15  |
| f (mm)         | 6   |
| l (mm)         | 8   |
| e (mm)         | 11  |
|                |   |
|                | projectile 1  |
| L (mm)         | 60  |
| material       | Al  |
| $\sigma$ (S/m) | $3.54 \cdot 10^7$   |
|                |   |
|                | projectile 2  |
| L (mm)         | 60  |
| materials      | Ti, Al alloy, Cu: 20 mm each  |
| $\sigma$ (S/m) | $1.25 \cdot 10^6$ (Ti), $1.82 \cdot 10^7$ (Al alloy), $5.8 \cdot 10^7$ (Cu) |

To improve the current distribution in the contact-studs we simulated the same railgun with a projectile made of three different materials. The rear end of the projectile is made of Ti, the middle part of an Al alloy and the front part of Cu (Fig. 8 and Table II).

The current density  $j$  for the projectile 2 (see Table II), the rail and the contact-studs are shown as a contour plot in Fig. 11 at  $t = 200 \mu\text{s}$ . Even at that early time the current is well distributed in the first two contact-studs. The total current for each contact-stud in contact with the projectile (noted 1 to 4 in Fig. 11) as a function of time is shown in Fig. 12. In the contact-studs 1 and 2 (Fig. 11) the current maximum has the same value but there is a time difference between the two maxima like in the case where the rails are in one part and the projectile has two armatures [8].

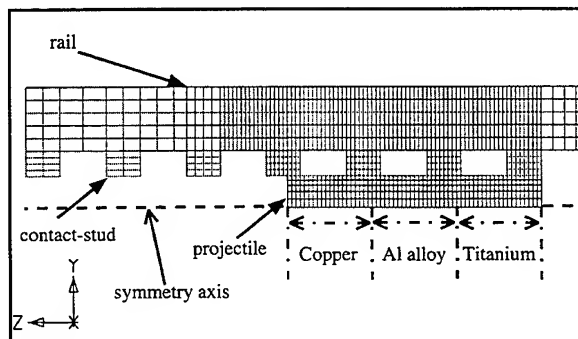


Fig. 8 Cut view of the modeled railgun and projectile 2

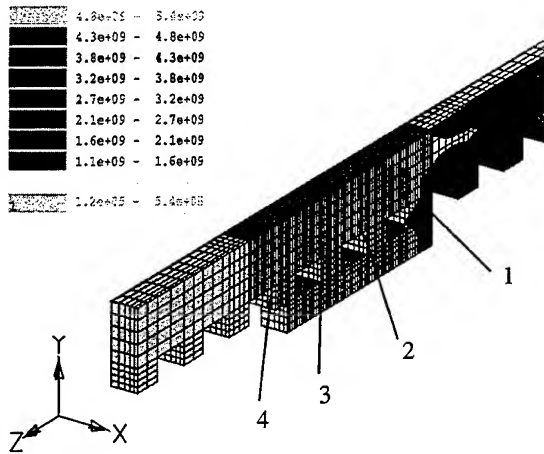


Fig. 9 Current density (A/m²) in the projectile 1, the contact-studs and the rail at the current maximum ( $t = 200 \mu s$  see Fig. 8)

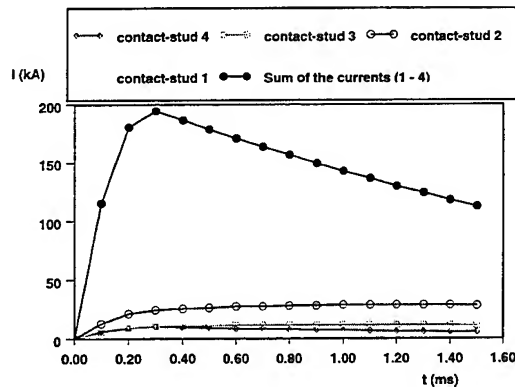


Fig. 10 Current flowing through the contact-studs 1, 2, 3 and 4

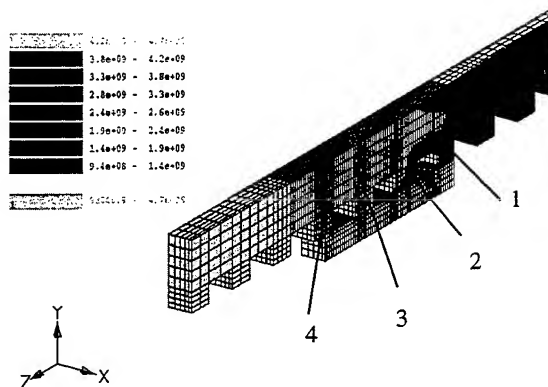


Fig. 11 Current density (A/m²) in the projectile 2, the contact-studs and the rail at the current maximum ( $t = 200 \mu s$  see Fig. 8).

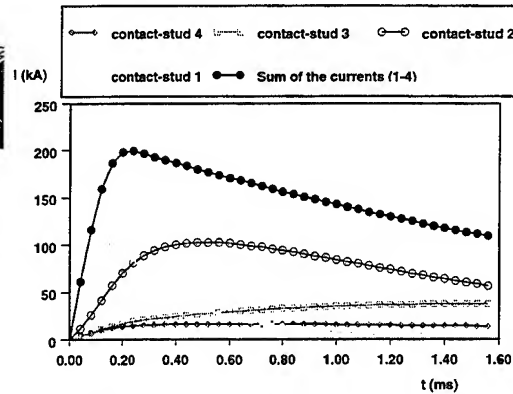


Fig. 12 Current flowing through the contact-studs 1, 2, 3 and 4

#### D. Lorentz forces acting on the projectile 2 and on the contact-studs

The calculated Lorentz force acting on the projectile 2 is shown in Fig. 13. The force acting on the contact-stud 4 (Fig. 11) is not plotted in that figure because it is too small to be seen. The maximum force acting on the projectile (at  $t = 200 \mu s$ ) is about 6.4 kN. Applying the well-known formula  $F = L'I^2/2$  the value of the apparent inductance gradient  $L'_3$  can be deduced and is about  $0.32 \mu H/m$ . For this simulation the contact-studs width  $l$  was large compared to the distance  $e$  between them so the value of  $L'$  is reduced.

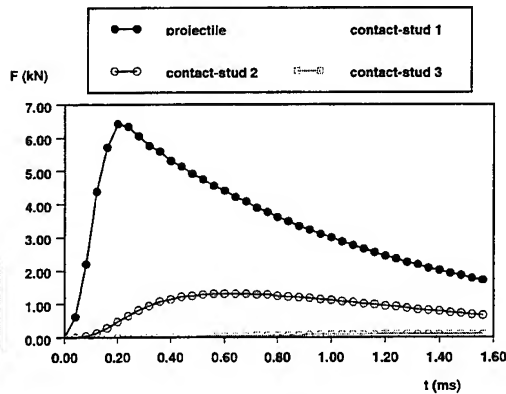


Fig. 13 Lorentz force acting on projectile 2 and on the contact-studs

#### V. CONCLUSIONS

In this paper we compared the classical railgun with the contact-studs provided railgun. The latter allows us to increase the injected current because the railgun caliber is increased while the projectile

diameter remains low and so the projectile mass.

A 3D electromagnetic numerical simulation has shown that the current can be distributed along the contact-studs by choosing the appropriate armature materials: bad conductor (e.g. Ti) at the rear end and good conductor (e.g. Cu) in the front part of the projectile

#### REFERENCES

- [1] F. Jamet, V. Wegner, P. Lehmann, "Lanceurs électriques et projectiles hypervéloces. Analyse technico-opérationnelle synthétique", ISL Report ISL - R 110/94, 1994
- [2] K. Darée, "A computational study of railgun performance at different calibers", in: Proceedings of the 1st European Symposium on EML Technology, Delft, The Netherlands, 1988
- [3] P. Lehmann, H. Peter, "Some remarks concerning the optimization of a railgun system", IEEE Transactions on Magnetics, **31** (1995) 546
- [4] "Lanceur électrique à rails munis de plots", French Patent N° 95 116 38
- [5] F. Jamet, P. Lehmann, V. Wegner, "Power conditioning requirements for electric guns", in: Proceedings of the 1st Conf. on All Electric Combat Vehicle (AECV), Haifa, Israel, May 1995
- [6] K. Darée, "Modellierung von DES Railguns mit Hilfe eines iterativen Runge-Kutta-Nystroem-Verfahrens", ISL Report ISL - N 606/88, 1988
- [7] B.E. MacNeal, "MSC-EMAS Modeling guide", The MacNeal Schwendler Corporation, June 1991
- [8] P. Lehmann, A.-G. Schmitt, "Theoretical study of the internal ballistics of an electromagnetically launched long-rod penetrator", Proceedings of the 5th European Symposium on EML Technology, Toulouse, France, 1995

# **On Electromagnetic 3-Dimensional Effects in Square-bore and Round-bore Rail Accelerators**

Arnold Schoolderman

Pulse Physics Laboratory  
TNO Prins Maurits Laboratory

visiting address: Schoemakerstraat 97, 2628 VK Delft, the Netherlands

mailing address: P.O. Box 45, 2280 AA Rijswijk, the Netherlands

fax: +31 15 2621268, phone: +31 15 2697011

## **Summary**

The influence of the geometry of the rail and armature cross section on the current distribution near the rail-armature interface and on the accelerating force on the armature in square-bore and round-bore accelerators is investigated by means of 3D computer simulations. The inductance gradient of the accelerators considered is calculated from the Lorentz force and from the energy equation. The stability of the armature for rotation in a round-bore accelerator is studied, too.

## **1. Introduction**

In electromagnetic launch research, a profound understanding of the magnetic field, the current density and the temperature distribution in the rails and the armature during acceleration is essential for the design of efficient rail accelerators and armatures. The study of these fields in 3 dimensions requires a large computational effort. Therefore, in most studies on electromagnetic launching, a 2-dimensional representation of the accelerator and the armature has been considered, assuming that 3-dimensional effects are of minor importance.

In this paper, a number of 3-dimensional effects is addressed and their influence on the current distribution in the armature and the accelerating force on the armature is studied by using the 3-dimensional electrothermal computer code MEGA, developed by the University of Bath. In section 2 the current distribution across the rail-armature interface in square-bore accelerators is studied for a number of armature width and rail width combinations. For round-bore accelerators the influence of different rail cross sections on the magnitude of the accelerating force on the armature is studied in section 3. The assumption of the inductance gradient being constant during a transient current is checked for the square-bore and round-bore accelerators considered. In section 4 the influence of a small armature rotation in round-bore accelerators on the armature torque and on the armature stability is investigated and compared with experimental results. All simulations are performed for zero armature velocity, but the effects studied here will also occur during electromagnetic launch.

## **2. Influence of rail and armature width on the current distribution, the inductance gradient and the accelerating force in square-bore accelerators**

At the Pulse Physics Laboratory, electromagnetic launch experiments are performed with a 2.37 m, 20 mm square-bore dipole rail accelerator. In this accelerator, launch packages with multi-fibre solid brush armatures have been accelerated arc-erosion free from standstill to a velocity of 1175 m/s. The U-shaped copper fibre armatures used in these experiments have a rail-armature interface length of 15 to 30 mm. Because of the confinement structure of the fibre armatures, the width of these armatures was limited to 13 mm. To reach a higher transition velocity, the armature width was increased to 15 mm. For these armatures, the average current density and the average Joule heating rate

are 15% and 30% lower, respectively. Hence, one expects a higher transition velocity for similar launch parameters (current profile, launch package mass, etc). A number of experiments has been performed with these wider fibre armatures. However, no increase in the transition velocity was found. This can only partially be explained by the slightly higher mass of the launch package with the 15 mm wide armature.

In order to find an explanation for the disappointing results of these experiments, a number of 3D computer simulations has been performed to calculate the current density in monolithic U-shaped solid copper armatures with widths of 10, 14 and 18 mm in a square-bore rail accelerator. The rail height is 10 mm and the distance between the rails is 20 mm. Rail widths of 18, 22 and 30 mm are considered. In Table 1 the armature width and rail width combinations and the identification labels for the simulations are given. The Figures 1a and 1b show the armature and rail geometry used in the simulation with the 18 mm width armature and 30 mm width rail (simulation #1). The armatures considered in the simulations #1, #2 and #3 have equal masses, the armature masses in the simulations #4 and #5 are lower, proportional with the armature width. Because of the limitations of the computer programme only armatures at zero velocity are considered. The effects studied here at zero velocity will also occur during electromagnetic launch, although their influence on the current and force distributions in the rails and the armatures will be affected by the velocity skin effect.

Table 1 Armature width and rail width combinations and simulation identification labels.

| armature width (mm) | rail width (mm) | label |
|---------------------|-----------------|-------|
| 18                  | 30              | #1    |
| 18                  | 22              | #2    |
| 18                  | 18              | #3    |
| 14                  | 30              | #4    |
| 10                  | 30              | #5    |

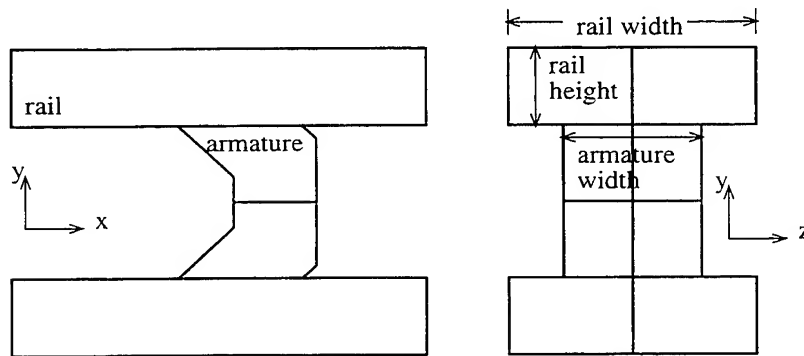


Figure 1 Rail and armature geometry used in simulation #1: the x-y plane on the left, the z-y plane on the right.

The current used in the simulations is shown in Figure 2. The current rises in 0.5 ms with a slope of 600 kA/ms to its maximum value of 300 kA.

The Figures 3a, 3b and 3c show the current density  $|J|$  at  $t = 0.52$  ms along the z-direction in the armatures with widths of 10, 14 and 18 mm, just below the rail-armature interface at three positions in the forward direction, i.e. at the trailing side of the armature, at the middle of the armature and at the leading side of the armature. From these Figures it is clear that the maximum values of the current densities in the three armatures are not linearly dependent on the armature width during the transient current. Wider armatures do not lead to proportionally lower maximum values of the current density.

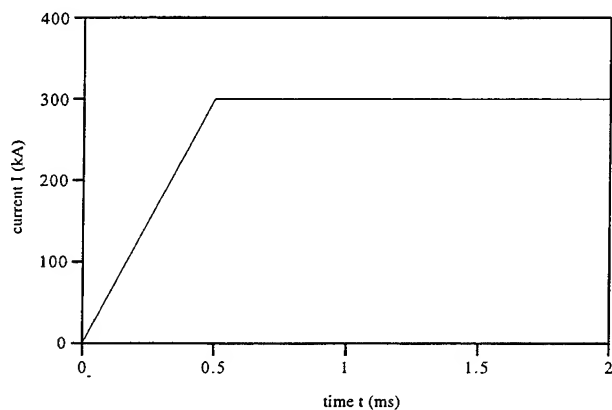


Figure 2 Current versus time, used in the simulations.

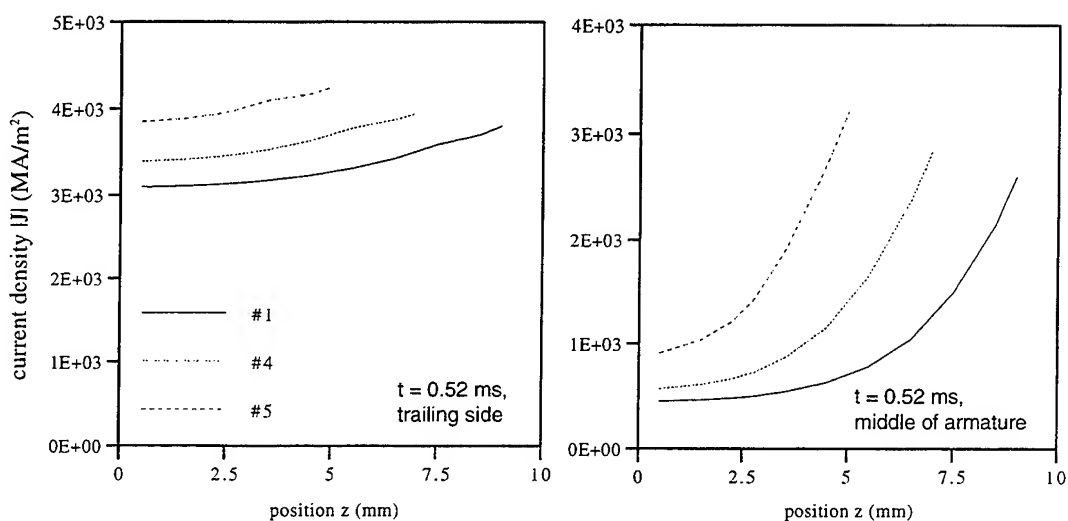


Figure 3a,b Current density in the armature just below the rail-armature interface at the trailing side of the armature (left) and in the middle of the armature (right) at  $t = 0.52$  ms.

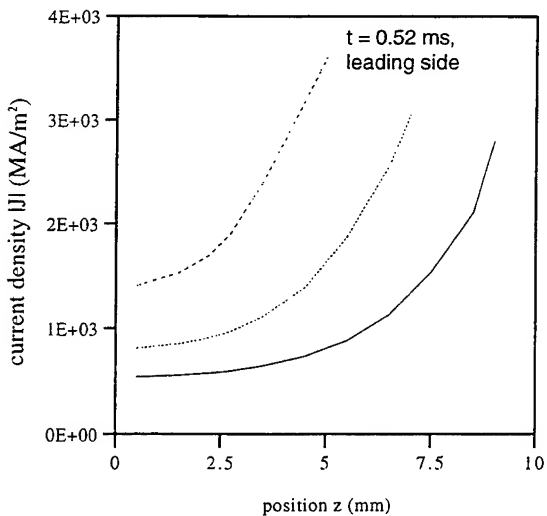


Figure 3c Current density in the armature just below the rail-armature interface at the leading side of the armature at  $t = 0.52$  ms.

In order to study the effect of the width of the rails and the armature on the accelerating force on the armature, the total Lorentz force  $F_L$  in the forward direction on the armature is calculated according to the equation (1).

$$F_L = \left( \int_{V_a} J \times B dV \right) \cdot i_x \quad (1)$$

Here,  $i_x$  is the unit vector in the forward direction and  $V_a$  the volume of the armature. Figure 4 gives the total Lorentz force on the armatures in the forward direction as a function of time and the Lorentz force on the armatures per unit armature volume, i.e. the average Lorentz force density in the armature. The highest acceleration is obtained with the rail-armature combination considered in simulation #5. For a fixed armature width, the accelerating force and the average armature force density increase with decreasing rail width. For a fixed rail width, the accelerating force and the average force density increase with decreasing armature width. Hence, the 15 mm wide fibre armature experienced a lower accelerating force in the launch experiment than the armature with a width of 13 mm. This (partially) explains the disappointing experimental results with the wider fibre armatures.

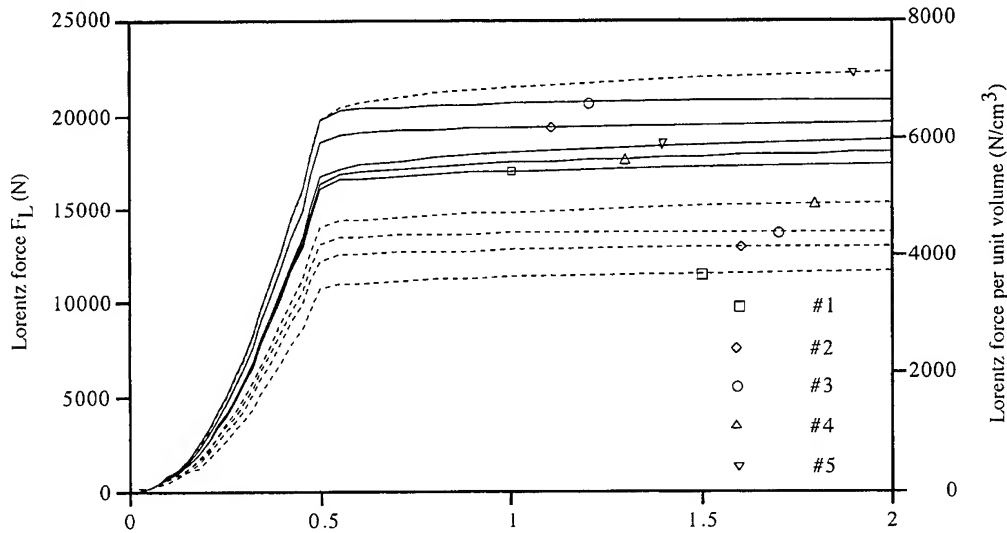


Figure 4 Lorentz force on the armatures in the x-direction (solid lines) and Lorentz force on the armatures per unit armature volume (dotted lines).

The inductance gradient  $L'$  of the rail accelerator can be calculated in two ways. From the well-known formula for the Lorentz force on the armature in the forward direction, one obtains

$$L' = 2F_L / I^2 = \frac{2}{I^2} \left( \int_{V_a} J \times B dV \right) \cdot i_x \quad (2)$$

The inductance gradient can also be calculated by taking the gradient in the forward direction of the inductance  $L$ . The inductance is given by the energy equation

$$L = \frac{2}{I^2} \int_V H \cdot B dV \quad (3)$$

Here, the gradient is evaluated at 2.5 cm behind the armatures. In Figure 5 the inductance gradient calculated according to these two methods is shown. The inductance gradient is not constant during a transient current, because its value is determined by the current distribution in the conductors. The two methods for the calculation of the inductance gradient give different results. Because in the long-time limit the values of the inductance gradient calculated from the energy equation approach the dc values, in the remainder of



this paper  $L'$  will be calculated from the energy equation. The dc values for the rail geometries considered in the simulations are given in Table 2 [1].

Table 2 *dc values for the inductance gradient.*

| label      | $L' \text{ dc } (\mu\text{H/m})$ |
|------------|----------------------------------|
| #1, #4, #5 | 0.51                             |
| #2         | 0.59                             |
| #3         | 0.63                             |

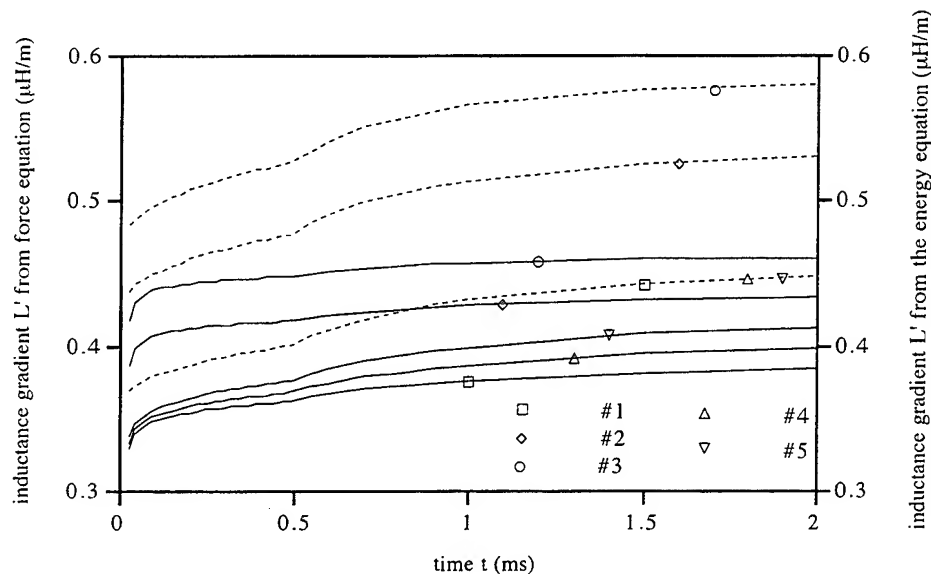


Figure 5 *Inductance gradient calculated from the Lorentz force on the armatures (solid lines) and inductance gradient calculated from the energy equation (dotted lines).*

### 3. Influence of the rail cross section for round-bore accelerators on the accelerating force

The Pulse Physics Laboratory is involved in a large project for the development of a solid armature for arc-erosion free acceleration up to 2.5 km/s in a 90 mm round-bore accelerator. Up to now, small-scale experiments have been performed at the Laboratory with the 20 mm square-bore accelerator. This accelerator will be provided with a round bore with a caliber between 20 mm and 25 mm to use it for small-scale experiments. In order to calculate the Lorentz force on the armature, a number of computer simulations have been performed for different rail cross sections for a round-bore accelerator with a calibre of 22 mm. Figure 6 shows the four rail and armature geometries considered in the simulations. These geometries are labeled #b, #c, #d and #e. The rails and the armatures are assumed to be made of copper. The rail cross section of geometries #d and #e is obtained by down-scaling the rail cross section of the 90 mm round-bore accelerator, present at the Center for Electromechanics at Austin, Tx [2]. In the simulations, the monolithic armatures, which are 1 cm long, have zero velocity. The armature width is 11 mm for geometries #b, #c and #d, for geometry #e the armature width is 15.6 mm. Since these armatures don't have the U-shape of the square-bore armatures considered in the previous section, it can be dangerous to compare the results of these simulations with the results presented in section 2. The current shown in Figure 2 was used in the simulations. The Lorentz force on the armatures in the forward direction and the Lorentz force per unit armature volume are shown in Figure 7. The highest Lorentz force and the highest Lorentz force per unit armature volume are found for geometry #b.

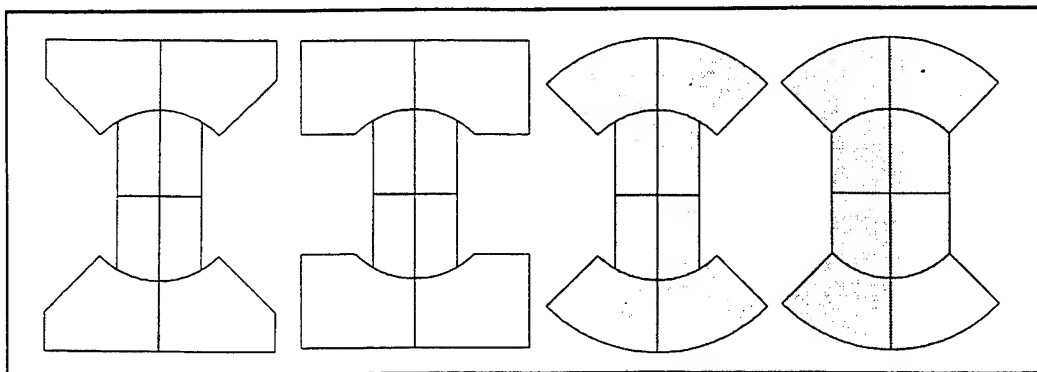


Figure 6 Round-bore rail accelerator and armature cross sections #b, #c, #d and #e (from left to right).

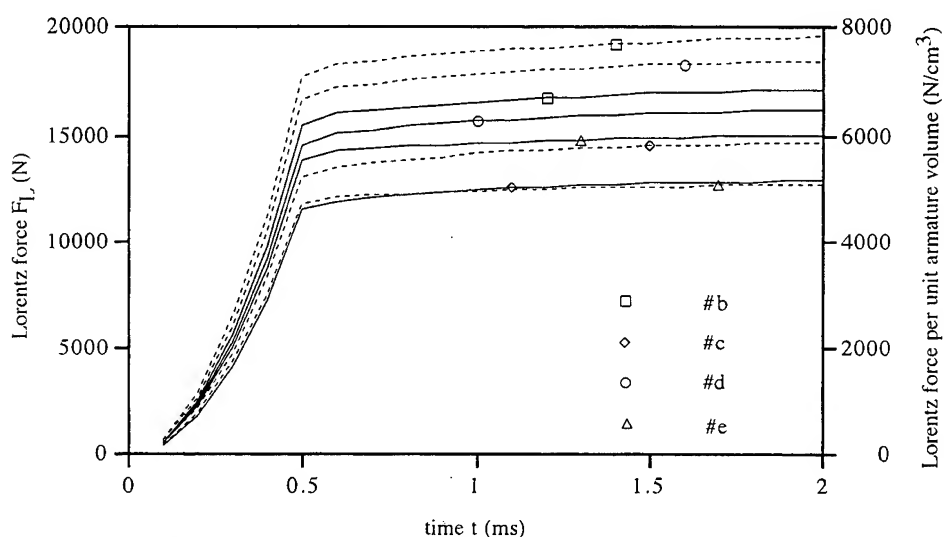


Figure 7 The Lorentz force (solid lines) and the Lorentz force per unit volume (dotted lines) on the armatures in the forward direction.

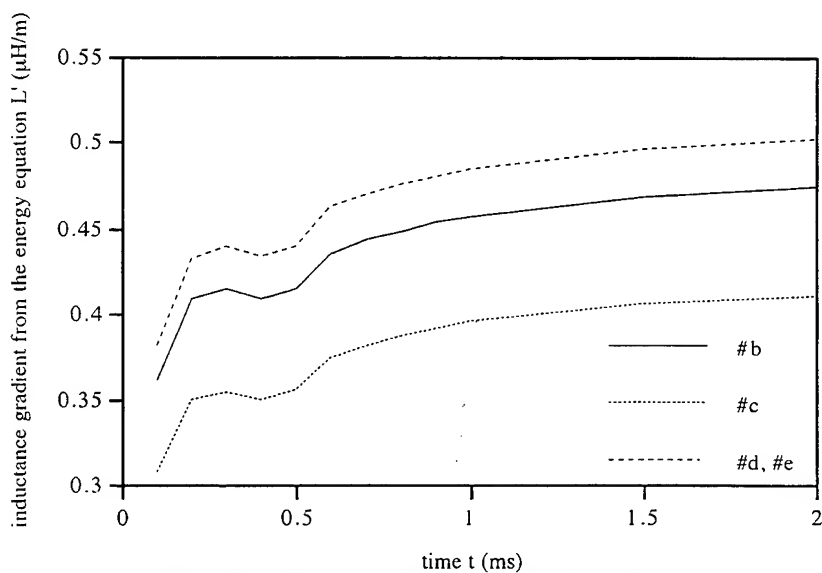


Figure 8 The inductance gradient calculated from the energy equation.

The inductance gradient  $L'$  for the different rail and armature geometries is calculated from the energy equation (3) and plotted in Figure 8. Experimentally it has been checked that the inductance gradient of geometry #b is indeed higher than that of geometry #c [3]. Although the geometries considered in simulations #d and #e have the highest value for the inductance gradient, the armature accelerated in the rail accelerator with the rail cross section from simulation #b experiences the highest acceleration.

#### 4. Influence of rotation of armatures in round-bore accelerators on the stability of the armature

In the literature, experimental evidence for rotation of armatures during electromagnetic launch in round-bore rail accelerators has been reported [4]. A consequence of rotation of the armature during the launch can be a reduction of the rail-armature contact area and consequently higher current densities at this contact area, higher Joule heat rates and probably melting at the solid rail-armature contact at a lower launch package velocity than without rotation of the armature, can occur. Especially in fibre armatures made of electrically insulated fibres an early transition of the armature to a hybrid one is expected when the armature is rotated during launch, because the fibres which make no contact with the rails, can't carry current.

In order to get an impression of the torque on monolithic armatures which are rotated over a small angle, two simulations have been performed: one with a rotation of  $5^\circ$  and one with a rotation of  $10^\circ$ . The cross section of the copper armature and the copper rails is depicted in the Figure 9 for an armature rotation of  $10^\circ$ . The bore diameter is 22 mm. The armature length is 4.5 mm and its width is 14.1 mm. The current shown in Figure 2 was used.

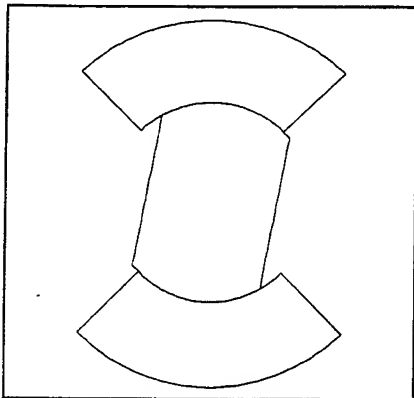


Figure 9 Rail and armature cross section. The armature rotation angle is  $10^\circ$ .

In Figure 10, the torque in the forward direction on the armature at rotation angles of  $5^\circ$  and  $10^\circ$  is shown. The torque becomes larger when the angle of rotation is larger. This agrees with the experimentally determined torque by Challita et al [4]. When it is assumed that the torque scales approximately with the product of the bore size and the square of the current, the values for the torque calculated in the simulations presented here can be compared with the values measured by Challita et al. For a rotation angle of  $10^\circ$  the scaled value from the simulation and the measured value are 1400 Nm and 720 Nm, respectively. The lower value measured in the experiment is probably due to friction. From these results it can be concluded that when an armature is rotated over a small angle during launch in a round bore accelerator, the angle of rotation will increase. A possible consequence can be an early transition of the solid armature.

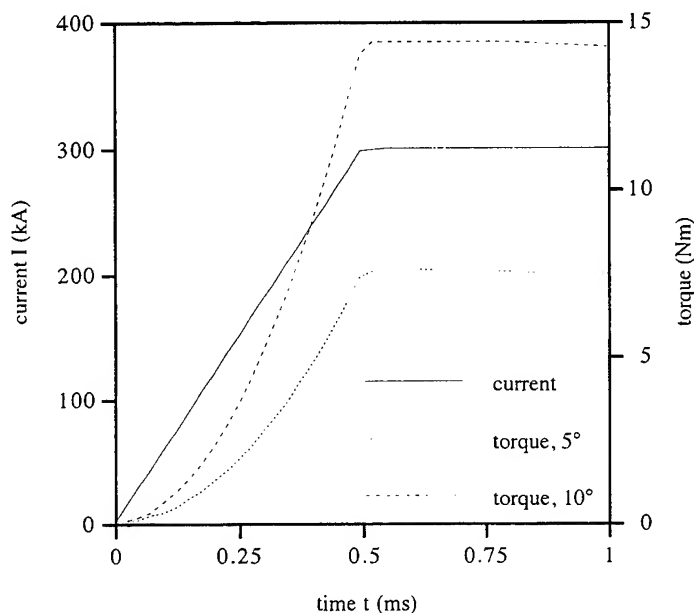


Figure 10 The torque on the armature at rotation angles of  $5^\circ$  and  $10^\circ$ .

## 5. Conclusions

From 3D computer simulations of rail accelerators and armatures at zero velocity it is found that, for transient currents, the maximum current density in an armature can be decreased by increasing the armature width. However, the decrease of the maximum current density is less than proportional to the increase of the armature width. The accelerating Lorentz force on the armature depends not only on the rail geometry but also on the armature geometry, e.g. the armature width. Armatures with a small width experience a higher accelerating Lorentz force per unit armature volume than wider armatures when the same rail geometry and rail width are used. Probably, there exists an optimum armature width which combines a low maximum current density and Joule heating rate, and a high accelerating Lorentz force. The calculation of the inductance gradient from the energy equation and from the Lorentz force gives different results.

Four rail and armature cross sections for round-bore accelerators are studied. It is found that the rail cross section which yields the highest value for the inductance gradient, doesn't result in the highest accelerating Lorentz force on the armature.

An armature which is accelerated in a round-bore accelerator and which is rotated over a small angle, experiences a torque which will increase the angle of rotation. The torque on the armature increases when the angle of rotation increases. This will result in instable behaviour of the armature and possibly an early armature transition because of the decrease of the electrical contact surface between the armature and the rails.

## 6. References

- [1] F.W. Grover, "Inductance calculations", Dover Publications Inc, 1946, equation (20), chapter 5.
- [2] R.C. Zowarka Jr et al., "9 MJ laboratory gun and range at the University of Texas at Austin", IEEE Trans. Mag. 25 (1989) p. 653-661.
- [3] T. Huijser, private communication, October 28, 1996.
- [4] A. Challita et al., "Analysis of rotational forces in round bore railguns", IEEE Trans. Mag. 31 (1995) p. 123-127.

## HIGH-CURRENT ARC EROSION OF EXPLOSIVELY COMPACTED Mo/Cu AND W/Cu ELECTRODES

G. A. Shvetsov, V. I. Maly, A. G. Anisimov, S. V. Stankevich,  
A. V. Solovov and T. S. Teslenko

Lavrentyev Institute of Hydrodynamics Russian Academy of Sciences,  
Siberian Division, Novosibirsk, 630090, Russia

### Summary

The paper presents the results of an experimental study of the erosion of tungsten-copper and molybdenum-copper electrodes produced by the method of explosion compacting of powders. The W, Mo, and Cu content in the composites varied from 0 to 100%. The erosion resistance of W/Cu and Mo/Cu electrodes was compared with the erosion resistance of electrodes made of pure copper, molybdenum and tungsten. The experimental results show that in a certain range of electric-pulse parameters ( $I_{\max}=180$  kA,  $t_{\max}=50$   $\mu$ s,  $\int Idt=15$  C and  $\int I^2 dt=1.7 \cdot 10^6$  A<sup>2</sup>·s) the erosion of W/Cu and Mo/Cu compacts is smaller by approximately a factor of 3 than the erosion of pure molybdenum and tungsten and is smaller by approximately a factor of 10 than the erosion of pure copper. The mass loss has a flat minimum for molybdenum and tungsten content of about 20 to 80 vol.%. Experimental dependences of the mass loss on the electric-discharge energy in the interelectrode gap, the results of metallography and X-ray studies of the electrodes before and after tests are given. The experimental results indicate that the tested composites are of interest for some pulsed power and industrial applications.

### Introduction

An analysis of the physical phenomena and processes limiting the kinematic characteristics and the multishot life of railguns shows that erosion of materials and associated effects are among the most important factors. In recent years these problems have been the particular concern of many scientists working on the problems of EML Technologies. At the Lavrentyev Institute of Hydrodynamics considerable attention has been given to the study and development of composites produced by the explosive welding method (bimetallic and multilayer materials) and by the explosive powder-compacting method [1]. The materials produced by these technologies have been studied in order to analyze the potentials of their use for a variety of pulsed power devices including EM launchers. Experimental and theoretical studies [2,3] have shown that the materials produced by these technologies, with their unique potentials of producing composites with different physicochemical properties, can offer certain advantages over other technologies.

The present paper is an extension of a previous work [3] and reports the results of tests on the erosion of explosively compacted Mo/Cu and W/Cu electrodes in high-current arc discharges.

## Production of composite electrodes

The tested electrode (Fig. 1) was a cylinder, with a working part 6 mm in diameter, fabricated from a composite produced by explosive compacting of tungsten, molybdenum and copper powders and their mixtures. Explosive compacting was performed, as in [1], in steel cylindrical capsules with outside diameter 18 mm and inside diameter 10 mm with a steel rod 3 mm in diameter on the axis of the capsule. An 6GV ammonite located coaxially around a capsule was used as an explosive. The charge density was  $0.9 \text{ g/cm}^3$ , and the detonation velocity was 3.8 km/sec.

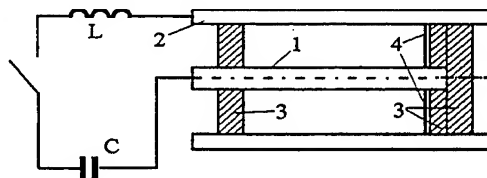


Fig.1. Coaxial accelerator model. 1 is the tested electrode, 2 is the outer electrode, 3 is insulator, and 4 is initiating foil.

The experiments were performed with tungsten powders of two fractions  $2\div 9 \mu\text{m}$  and  $20\div 60 \mu\text{m}$ , each of which was mixed with a copper powder in various volume percent proportions. The molybdenum-particle size was  $5\div 10 \mu\text{m}$ . The same copper powder with a particle size of  $10\div 30 \mu\text{m}$  was used in all experiments. Mixing was produced in a planetary mill.

The initial and final densities of the mixtures in a capsule varied with variation in the percent proportion of tungsten, molybdenum and copper, as is shown in Fig.2.

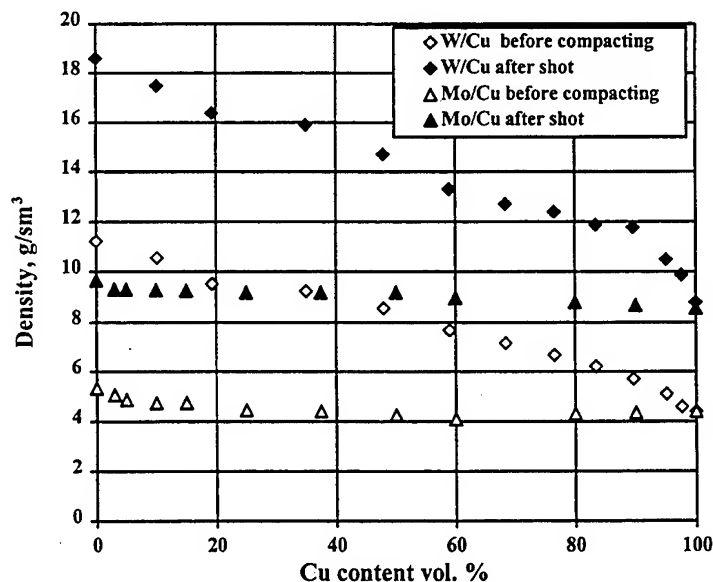


Fig.2. Density of W/Cu and Mo/Cu mixture before and after compacting vs. the volume copper content.

After explosive compacting and preliminary mechanical treatment, the specimens were subjected to heat treatment in a vacuum furnace at  $T=850^{\circ}\text{C}$ . The final mechanical treatment included grinding of the cylindrical working part of the specimens, after which the specimens were dried and degassed in a vacuum drying oven.

### Experimental results and discussion

The erosion of the electrodes was measured on a coaxial accelerator model under conditions of a high-current  $H$ -pressed discharge (Fig. 1). A capacitor bank with a capacity of  $3.4 \cdot 10^{-3}$  F and voltage of 5 kV was a power source. A discharge was initiated by an explosion of a thin foil 4. The magnitude of current in the discharge did not exceed 300 kA.

The erosion of the electrodes was determined from the mass loss by weighing the electrodes before and after the experiments. The experiments showed that the dependence of the mass loss on  $\int I^2 dt$  agrees with the data on the erosion of materials under conditions of high-current  $H$ -pressed discharge in plane geometry [4]. Technologically, however, experiments on erosion in coaxial geometry are simpler.

The relative erosion resistance of the electrodes was determined by comparison of the mass loss for the same magnitude of current and discharge duration ( $I_{\text{max}}=180$  kA,  $t_{\text{max}}=50$   $\mu\text{s}$ ,  $\int I dt=15$  C and  $\int I^2 dt=1.7 \cdot 10^6$   $\text{A}^2 \cdot \text{s}$ ). In the case of a central electrode made of copper, the mass loss was 32 mg under the above-described conditions. Figure 3 shows the experimental results. For Mo/Cu and W/Cu compacts, the dependence of the relative mass loss on the content of the high-melting components is as follows. Erosion decreases sharply by approximately a factor of 10 in the range of 0÷20%, stabilizes in the range of 20÷80%, and increases in going to pure molybdenum and tungsten.

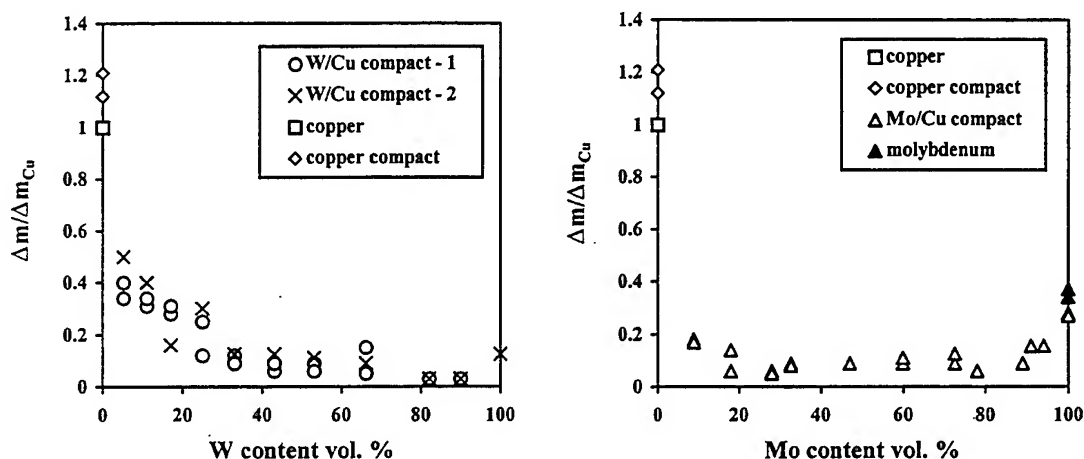


Fig.3. The relative erosion resistance of the Mo/Cu and W/Cu electrodes.  
W/Cu compact: 1 - ( $2 \div 9 \mu\text{m}$ ), 2 - ( $20 \div 60 \mu\text{m}$ ).

No differences between W/Cu composites with different fractions of the tungsten powder were found in the experiments performed. Figure 3 gives the results for  $2\div 9\text{ }\mu\text{m}$  and  $20\div 60\text{ }\mu\text{m}$  tungsten, the copper-particle size being  $10\div 30\text{ }\mu\text{m}$  in both cases.

A series of experiments was performed to study the dependence of mass loss on the electric-discharge energy released in the interelectrode gap. In the experiments, the current and voltage in the interelectrode gap were measured. Experiments were performed with electrodes made of copper and molybdenum and with Mo/Cu electrodes produced by explosive compacting of powders. Figure 4 shows the dependence of mass loss on  $\int I^2 dt$  for the indicated materials: Cu, Mo and Mo/Cu compacts (40% Mo and 60% Cu). In the studied range of energies, the dependencies of  $\Delta m$  on  $\int I^2 dt$  are nearly linear. For copper and molybdenum electrodes, the slopes of the erosion "straight lines" agree with the data obtained previously for plane electrodes [4]. The slope of the dependence of  $\Delta m$  on  $\int I^2 dt$  in experiments with Mo/Cu electrodes is much smaller. This fact is of interest, although the question of whether this dependence is preserved for higher energies remains open.

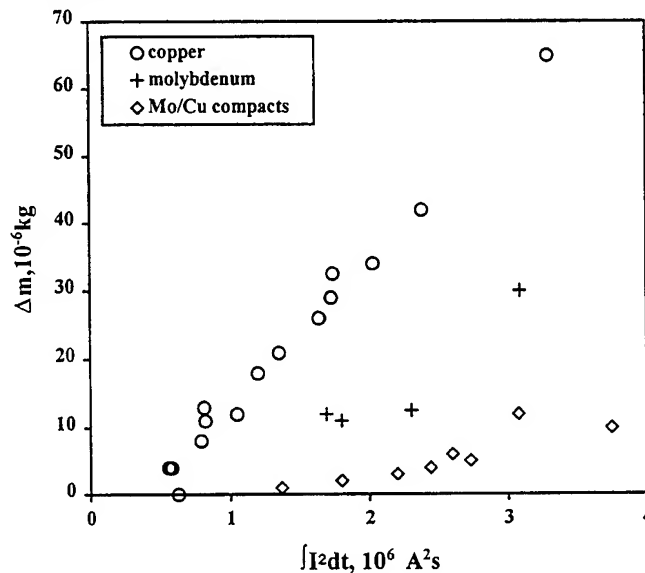


Fig.4. The dependence of mass loss on  $\int I^2 dt$  for Cu, Mo, and Mo/Cu compacts (40% Mo and 60% Cu).

A metallographic study of sections of the composites after electric discharge shows that the appearance of the surface depends on the specimen composition. For specimens of 100% Mo and 100% Cu, melting of the surface, splashing of the melt, and, in the case of copper, large drops were observed. The thicknesses of the melted Mo and Cu layers were  $15\text{ }\mu\text{m}$  and  $70\text{ }\mu\text{m}$  accordingly. The material under the melt was heated and had a smaller hardness than the material at depth.

Specimens of composition of 50 vol. % Mo+50 vol. % Cu also have drops, and splashes of melt on the surface, and the melt was predominantly composed of copper. Under such a melted layer, there was a  $30\text{-}\mu\text{m}$  thick layer with a higher Mo content in comparison with the starting material at depth. This layer enriched with Mo had higher



porosity. The copper from this layer passed into the melt on the surface and constituted the major portion of the ablated material.

Composites consisting of 75 vol. % Mo and 25 vol. % Cu also had porous drops of melted copper on the surface. The material immediately under the melt was the same as the material at depth, although microhardness measurements show that there is a thin layer ( $<10\text{ }\mu\text{m}$ ) with a hardness increased to 450 Hv; the average microhardness of the structure at depth of the material was 300 Hv. Obviously, in this case, only the copper of a very thin layer emerged on the surface and was removed.

The structure of W/Cu compacts with a fine fraction of W ( $2\div 9\text{ }\mu\text{m}$ ) was qualitatively similar to those of Mo/Cu compacts with similar sizes ( $5\div 10\text{ }\mu\text{m}$ ) of Mo particles.

A solidified porous layer of a copper melt with individual large (up to 1 mm) round hollow drops on the surface was observed in the erosion trace of 90% Cu+10% W electrodes. The composition of the drop material is the same as that of the starting composite, i.e., in both cases, about the same amount of W particles was observed in the copper base. With an increase in the W content ( $>20\%$ ), the amount of large drops (to  $200\text{ }\mu\text{m}$ ) was smaller, and the melted porous layer ( $30\div 50\text{ }\mu\text{m}$ ) on the surface of the erosion trace contained primarily copper, in which tungsten conglomerates ( $5\div 10$  diameters of the starting particles) were rarely found. A tungsten-rich layer  $10\div 20\text{ }\mu\text{m}$  thick was present within the erosion trace directly below this layer deep.

As the initial W percent content of the W/Cu compacts increased from 20% to 80%, the thickness of the melted porous copper layer on the surface of the erosion trace decreased. Large W conglomerates of irregular shape were observed in some places inside the copper melt. A tungsten-rich layer was observed immediately on the surface of the erosion layer for the initial W content of 80%. The copper melt in this case was completely removed from the surface of the electrodes.

In W/Cu compacts with large ( $20\div 60\text{ }\mu\text{m}$ ) W particles, an erosion trace with a smoother surface without layers enriched with copper and tungsten was found. These compacts, however, have a large number of pores, particularly, for W content of  $>90\%$ . The amount of copper, in this case, is too small to fill all these pores between large tungsten particles, and the compacting regime did not make it possible to deform all hard tungsten particles. The hardness of W/Cu compacts with large W particles turned out to be higher than that of compacts with small ( $2\div 9\text{ }\mu\text{m}$ ) W particles, from which we were unable to fabricate electrodes with a content of  $W>95\%$  because of the large amount of cracks. The irregularities on the surface on which an electric discharge was applied are more smoothed than in Mo/Cu composites [3], and the amount of melting traces is smaller.

Thus, in an H-pressed discharge, the material from W/Cu electrodes with a tungsten content of 20% and 80%, is removed in the initial proportion of the starting components; at low W content, it is mainly removed as large ( $500\div 1000\text{ }\mu\text{m}$ ) drops, and at high W content, as particles whose sizes are close to the sizes of the powders of the mixture. When the W content is ( $20\div 80\%$ ), primarily the copper that is present as a continuous melt on the surface of the erosion trace is removed from the W/Cu electrodes. The tungsten in the melted layer is segregated as conglomerates, which are partly removed, and partly remain near the surface of the erosion trace and form a continuous layer in places.

In the production of electrodes by the method of explosive compacting, deformation and hardening of material particles take place. This is the case not only for soft copper but also for harder molybdenum and tungsten particles. This effect cannot be achieved by static compacting methods. It is impossible, however to detect these hardening of particles by microhardness measurements, since the hardness of the composites depend on composition and varies proportionally with the hard-phase content, the spread of values being large because of residual porosity and nonuniform strength of contacts among particles. Therefore, the only method that makes it possible to estimate the effect of deformation is the x-ray measurement of the residual microdeformations of the crystal lattice  $\Delta a/a$  ( $a$  is the lattice parameter), which is based on analysis of broadening of x-ray diffraction lines [5]. The values of microdeformations  $\Delta a/a$  measured by this method in continuous one-phase metals usually correlate with hardening. The x-ray method allows one to determine the levels of residual microdeformations for each individual component of the composite.

Studies have shown that microdeformations are introduced both in the stage of mixing of powders in the mill and in explosive compacting. Tungsten and copper powders are hardened most greatly in the mill (up to  $\Delta a/a=1.6 \cdot 10^{-3}$ ), and molybdenum to a lesser extent ( $\Delta a/a=1.1 \cdot 10^{-3}$ ). In subsequent explosive loading, microdeformations of tungsten and molybdenum increase to  $1.75 \cdot 10^{-3}$  and  $1.3 \cdot 10^{-3}$ , respectively, and  $\Delta a/a$  of copper can both increase and decrease due to heating in explosive compacting, as was observed in composites of a copper powder with a fine tungsten powder. The subsequent annealing of thus produced electrodes decreased only the hardening of the copper component of the composites, and the molybdenum and tungsten frameworks remain hardened.

The improvement in the erosion resistance of the compacts in the middle range of compositions, i.e., from 20 to 80 vol.% of each component is apparently caused by the formation of frameworks in the composites, i.e., particles of each component are bound. Indeed, with a content of less than 20%, the particles are surrounded by the other material and cannot function as effective heat removal in the case of copper or as a strong high-melting matrix of molybdenum or tungsten. Nevertheless, more plastic copper penetrates more readily into small gaps, and, therefore, with 10% copper in mixtures of W/Cu and Mo/Cu, the bonding of the copper particles is not yet lost, owing to which high erosion strength is preserved up to relatively small copper amounts in the composite electrodes.

### Conclusion

The described experiments show that the erosion of explosively compacted Mo/Cu and W/Cu electrodes for certain magnitudes of current and discharge duration can be smaller severalfold than the erosion of pure molybdenum or tungsten. These data indicate that the compacts hold much promise for various pulsed power devices.

Subsequent studies will be concerned with the influence of some technological parameters and processes on the final physical properties of composites and with the behavior of compacts under extreme operating conditions of railguns.

## References

- [1] G.A.Shvetsov, V.I.Maly, Yu.L.Bashkatov et al. "New materials and technologies for railguns", Proc. 5th European EML Technology Symposium, Toulouse, France, 1995, paper N 91.
- [2] G.A.Shvetsov, S.V.Stankevich "Critical current density in railguns with composite electrodes", *IEEE Trans. on Magn.*, vol. 31, no. 1, 1995, pp. 237-242.
- [3] G.A.Shvetsov, V.I.Maly, A.G.Anisimov, S.V.Stankevich, A.V.Solovov, and T.S.Teslenko "Erosion of explosively compacted Mo/Cu electrodes in high-current arc discharges", Proc. 8<sup>th</sup> Electromagnetic Launch (EML) Symposium, Baltimore, MD, April 21-24, 1996.
- [4] G.A.Shvetsov, A.G.Anisimov, S.V.Stankevich, V.I.Maly, N.V.Gubareva, T.M.Sobolenko, and V.P.Chistyakov "Interaction between plasma piston and railgun electrodes", Proc. 8<sup>th</sup> IEEE international Pulsed Power Conference, San Diego, C A., 1991, pp. 771-777.
- [5] S.S.Gorelik, L.N.Rastorguev, Yu.A.Skakov "X-ray and electronoptical analysis", Moscow, "Metallurgiya", 1970, p. 145.

# On scaling relations for hypervelocity electromagnetic launch processes

Marcel Koops and Arnold Schoolderman

Pulse Physics Laboratory, TNO Prins Maurits Laboratory, Delft, the Netherlands

mailing address: P.O. Box 45, 2280 AA Rijswijk, the Netherlands

visiting address: Schoemakerstraat 97, 2628 VK Delft, the Netherlands

phone: +31152697011, fax: +31152621268

**Summary**—In this paper, a set of fundamental scaling relations for hypervelocity electromagnetic launch processes is presented. These relations are based on the electrical circuit equations, the magnetic and heat diffusion equations, the equation of motion and the constitutive equations. The analysis includes Joule heating and frictional heating as source terms for the heat diffusion equation and temperature-dependent material properties. The feasibility of scaling and its consequences are discussed in terms of scaleable and non-scaleable aspects. The scaling relations derived provide the guidelines for performing scaled experiments. Examples of lumped parameter and finite element simulations of full scale and small scale hypervelocity launch experiments are presented.

## 1. INTRODUCTION

Large calibre electromagnetic launchers require pulsed power facilities capable of delivering energies to the breach of several tens of mega-Joules to accelerate launch packages to hypervelocities. At this moment, only a few of such facilities exist. However, the development of large calibre armatures for KE launch packages is not limited to those laboratories having access to large pulsed power sources and large calibre rail accelerators as meaningful launch experiments can be performed at smaller scale. Moreover, performing electromagnetic launch experiments at smaller scale is interesting, because it will lead to a reduction in costs. At the Pulse Physics Laboratory, performing small scale experiments will be inevitable for the development of a large calibre, low voltage, solid armature, capable of launching efficiently a large calibre launch package to a muzzle velocity of about 2500 m/s without arc erosion. To establish a successful development path, the existence of fundamental scaling relations is of value. Then, the performance of a solid armature in the small calibre launch process can be used to predict the performance of a similar armature in the large calibre launch process.

In the literature on electromagnetic launch technology only a few authors have paid attention to scaling. Railgun performance at different calibres was studied by Dareé using one-dimensional, electrical circuit analysis [6]. The behaviour of plasma armatures in different calibres has been treated by Jackson et al. [3] and Thornhill et al. [4], [5], including valuable experimental data. The scaling problem addressed by Pappas et al. in [1] deals with the ability to predict current distribution in a solid armature at low velocity and extrapolate these results to higher velocities. In [2], Hsieh and Kim have treated the scaling of the electromechanical behaviour of solid armatures. These authors provide a useful scaling criterion. Here, a general treatment of the scaling problem is given, which includes the cases described by others. New options are introduced for performing scaled launch experiments based on a different approach of the scaling criteria.

Thermal and electromechanical loading of the solid armature are important parameters in the failure mechanisms of the electrical contact with the rails which induce transition to a hybrid armature. The temperature rise in the armature as a result of Joule heating depends upon the acceleration profile in a complex way. Due to the velocity skin effect, the current distribution changes with mass and material properties as well as with armature current.

In this paper, a set of fundamental scaling relations is presented which is based on the electrical circuit equations, the magnetic and heat diffusion equations, the equation of motion and the constitutive equations. The analysis includes Joule heating and frictional heating as source terms for the heat diffusion equation and temperature-dependent material properties. The feasibility of scaling and its consequences are discussed in terms of scaleable and non-scaleable aspects. The scaling relations derived provide the guidelines for performing scaled experiments. Examples of lumped parameter and finite element simulations of full scale and small scale hypervelocity launch experiments are presented. Results of static experiments are presented which have been performed to validate the applicability of the scaling relations for electromagnetic launch experiments.

## 2. DERIVATION OF SCALING RELATIONS

2.1. Scaling relations are derived from the fundamental equations governing the electrothermal and mechanical behaviour of the armature and the rail accelerator during electromagnetic launch, i.e. Maxwell equations, the magnetic diffusion equation, the thermal diffusion equation and the momentum equation:

Maxwell equations (displacement current is omitted):

$$\nabla \times \frac{\mathbf{B}}{\mu_0} = \mathbf{J} \quad (\text{Ampère's Law}) \quad (1)$$

$$\nabla \times \mathbf{E} = -\frac{\partial \mathbf{B}}{\partial t} \quad (\text{Faraday's Law}) \quad (2)$$

Ohm's Law:

$$\mathbf{J} = \bar{\bar{\rho}}_e^{-1} \cdot [\mathbf{E} + \mathbf{v} \times \mathbf{B}] \quad (3)$$

From eq. (1) through eq. (3), the magnetic diffusion equation is derived:

$$\nabla \times \left[ \bar{\bar{\rho}}_e \cdot \left( \nabla \times \frac{\mathbf{B}}{\mu_0} \right) \right] - \nabla \times [\mathbf{v} \times \mathbf{B}] = -\frac{\partial \mathbf{B}}{\partial t} \quad (4)$$

Energy balance equation:

$$\nabla \cdot \bar{\bar{\kappa}} \cdot \nabla T - c_v \mathbf{v} \cdot \nabla T = c_v \frac{\partial T}{\partial t} - \mathbf{J} \cdot \bar{\bar{\rho}}_e \cdot \mathbf{J} \quad (5)$$

Momentum equation:

$$\nabla \cdot \mathbf{S} + \mathbf{J} \times \mathbf{B} = \rho_m \mathbf{a} = \rho_m \frac{\partial^2 s}{\partial t^2} \quad (6)$$

where  $\mathbf{B}$  is the magnetic induction,  $\mathbf{J}$  is the current density,  $\rho_e$  is the resistivity tensor,  $\mu_0$  is the vacuum magnetic susceptibility,  $t$  is the time,  $\mathbf{v}$  is the velocity of the moving conductors,  $\mathbf{E}$  is the electric field,  $\mathbf{S}$  is the stress tensor,  $\rho_m$  is the mass density,  $c_v$  is the specific heat per unit volume,  $\bar{\bar{\kappa}}$  is the thermal conductivity tensor and  $T$  is the temperature,  $\mathbf{a}$  is the acceleration of the launch package and  $s$  is the displacement in the direction of the velocity  $\mathbf{v}$ .

We introduce a geometrical scaling factor  $g$  and a time scaling factor  $\tau$ :

$$x' = gx, y' = gy, z' = gz \quad (7)$$

$$t' = \tau t$$

Hence,

$$\nabla = \frac{\nabla}{g}, \quad \frac{\partial}{\partial t} = \frac{1}{\tau} \frac{\partial}{\partial t'} \quad (8)$$

The primed quantities refer to the full scale experiment. The position- and time-dependency of the quantities will be omitted from the notation in the remainder of the paper, e.g.  $\mathbf{S}(x', y', z', t')$  will be denoted by  $\mathbf{S}'$  and  $\mathbf{S}(x, y, z, t)$  by  $\mathbf{S}$ .

Scaling requires that the equations are invariant. From eq. (4), one finds the scaling relations for the resistivity and velocity:

$$\bar{\bar{\rho}}_e' = \frac{g^2}{\tau} \bar{\bar{\rho}}_e, \quad \mathbf{v}' = \frac{g}{\tau} \mathbf{v} \quad (9)$$

Next, we introduce scaling factors  $\chi$  for the specific heat per unit volume and  $\eta$  for the temperature:

$$c_v' = \chi c_v, \quad T' = \eta T \quad (10)$$

Substitution in eq. (5) gives:

$$\bar{\bar{\kappa}}' = \frac{\chi g^2}{\tau} \bar{\bar{\kappa}}, \quad \mathbf{J}' = \frac{\sqrt{\chi \eta}}{g} \mathbf{J}, \quad i' = \sqrt{\chi \eta} g i \quad (11)$$

Substitution of (11) in eq. (1) yields:

$$\mathbf{B}' = \sqrt{\chi \eta} \mathbf{B} \quad (12)$$

The momentum equation (6) gives:

$$\rho_m' = \frac{\tau^2 \chi \eta}{g^2} \rho_m, \quad \mathbf{S}' = \chi \eta \mathbf{S} \quad (13)$$

Important parameters like acceleration, velocity and displacement scale according to:

$$\mathbf{a}' = \frac{g}{\tau^2} \mathbf{a}, \quad \mathbf{v}' = \frac{g}{\tau} \mathbf{v}, \quad s' = g s \quad (14)$$

The consequence of the scaled acceleration profile is that the total launch package mass  $m$  must be scaled:

$$m' = g \tau^2 \chi \eta m \quad (15)$$

The mass density  $\rho_m$  can be considered as the average mass density of the launch package.

2.2. The criterion used by Hsieh and Kim [2], which states that the temperature and stress distributions in the small scale experiment and in the full scale experiment should be the exact images, is one of the scaling criteria considered in this paper. Hence, the stress tensor  $\mathbf{S}$  and temperature  $T$  must be invariant under scaling:

$$\begin{aligned} \mathbf{S}'(x', y', z', t') &= \mathbf{S}(x, y, z, t) \\ T'(x', y', z', t') &= T(x, y, z, t) \end{aligned} \quad (16)$$

For these scaling conditions to be fulfilled,  $\chi$  and  $\eta$  must be equal to 1. The difference with the work of Hsieh and Kim lies in the fact that, in our equations (4) through (6), we have used the Eulerian formalism, in which velocity is stated, explicitly. We find that scaling relations that comply with eq. (16), only exist when we allow the material properties to scale. The scaling relations for the material properties for this case are listed in Table I. If these conditions are fulfilled, the current density and current scale according to:

$$J = \frac{J}{g}, \quad i = g i \quad (17)$$

TABLE I

SCALING OF MATERIAL PROPERTIES FOR  $\mathbf{S}=\mathbf{S}$  AND  $T'=T$

| parameter                     | small scale    | full scale                      |
|-------------------------------|----------------|---------------------------------|
| specific heat per unit volume | $c_v$          | $c_v$                           |
| resistivity                   | $\bar{\rho}_e$ | $\frac{g^2}{\tau} \bar{\rho}_e$ |
| thermal conductivity          | $\bar{\kappa}$ | $\frac{g^2}{\tau} \bar{\kappa}$ |
| mass density                  | $\rho_m$       | $\frac{\tau^2}{g^2} \rho_m$     |

Eq. (16) is only one of the scaling conditions that can be imposed on the electromechanical system. Different scaling conditions lead to different sets of requirements for the scaling factors  $g$ ,  $\tau$ ,  $\chi$  and  $\eta$ . Consequently, different scaling relations for the launch parameters are obtained. A more complete list of scaling conditions is given in Table II.

2.3. An important implication of the scaling relations is that exact guidelines are given for the scaling of the current pulse form. The problem of how to construct a small scale current pulse from a known full scale current pulse can be addressed by scaling the complete pulse forming network. By recognising that the breech voltage scales by a factor  $\sqrt{\chi \eta} g^2 / \tau$ , a unique scaling is obtained by multiplying all voltage nodes of the circuit by this same factor. For a basic LCR circuit (e.g. capacitor bank), the scaling relations are given in Table III.

In practice, scaling of a complete pulse forming network will not be very likely and we must rely on other methods to generate the required scaled current pulse.

2.4. Interesting conclusions can be drawn by applying the scaling relations to the launch parameters. It can be easily shown that the inductance gradient of the rail accelerator is invariant under scaling (the inductance gradient of the rail accelerator is only geometry-dependent [7]). It is important to note that the length of the rail accelerator in the small scale experiment can be  $g$  times smaller than the full scale version. The kinetic energy is independent of the time scaling factor  $\tau$ . A list of scaling relations for relevant launch parameters is given in Table IV.

A very useful aspect of these scaling relations is the fact that three parameters that characterise the quality of the launch process are invariant under scaling, i.e. launch efficiency, total efficiency and armature Figure Of Merit. These parameters are defined by:

$$\begin{aligned} \eta_{\text{launch}} &= \frac{\text{kinetic energy of the launch package}}{\text{energy input at the breech}} \\ \eta_{\text{total}} &= \frac{\text{kinetic energy of the launch package}}{\text{energy stored in the pulsed power source}} \end{aligned}$$

$$FOM = \frac{\text{kinetic energy of the launch package}}{\text{energy dissipated in the armature}}$$

The electrothermal action absorbed by the armature scales according to:

$$A' = g^2 \tau \chi \eta A \quad (18)$$

TABLE II  
SCALING CONDITIONS

| invariant quantities               | scaling factor relations                    |
|------------------------------------|---|
| $S' = S \wedge T' = T$             | $\Rightarrow \chi = 1 \wedge \eta = 1$      |
| $J' = J \wedge T' = T$             | $\Rightarrow \chi = g^2 \wedge \eta = 1$    |
| $S' = S \wedge J' = J$             | $\Rightarrow g = 1 \wedge \chi = \eta^{-1}$ |
| $\dot{S}' = \dot{S} \wedge T' = T$ | $\Rightarrow \chi = \tau \wedge \eta = 1$   |
| $S' = S$                           | $\Rightarrow \chi = \eta^{-1}$              |
| $T' = T$                           | $\Rightarrow \eta = 1$                      |
| $J' = J$                           | $\Rightarrow \chi \eta = g^2$               |
| $\dot{S}' = \dot{S}$               | $\Rightarrow \chi \eta = \tau$              |
| $a' = a$                           | $\Rightarrow \tau = \sqrt{g}$               |
| $v' = v$                           | $\Rightarrow \tau = g$                      |
| $s' = s, x' = x$                   | $\Rightarrow g = 1$                         |
| $\bar{\rho}_e' = \bar{\rho}_e$     | $\Rightarrow \tau = g^2$                    |

TABLE III  
SCALING RELATIONS FOR THE PULSE FORMING NETWORK

| parameter                         | small scale | full scale                |
|-----------------------------------|-------------|---------------------------|
| capacitor of capacitance C        | C           | $\frac{\tau^2}{g} C$      |
| inductor of inductance L          | L           | $g L$                     |
| resistor with resistance R        | R           | $\frac{g}{\tau} R$        |
| charging voltage of the capacitor | $V_{ch}$    | $\frac{g^2}{\tau} V_{ch}$ |

TABLE IV  
SCALING RELATIONS FOR THE ELECTROMAGNETIC LAUNCH PROCESS

| parameter                          | small scale     | full scale                                |
|------------------------------------|-----------------|---|
| bore width (calibre)               | d               | g d                                       |
| mass                               | m               | $g \tau^2 \chi \eta m$                    |
| displacement, position             | s, x            | g s, g x                                  |
| velocity                           | v               | $\frac{g}{\tau} v$                        |
| acceleration                       | a               | $\frac{g}{\tau^2} a$                      |
| jerk                               | $\dot{a}$       | $\frac{g}{\tau^3} \dot{a}$                |
| muzzle energy                      | $E_{kin}$       | $g^3 \chi \eta E_{kin}$                   |
| pulse duration                     | $\Delta t$      | $\tau \Delta t$                           |
| armature current                   | i               | $g \sqrt{\chi \eta} i$                    |
| rate of change in armature current | $\dot{i}$       | $\frac{g \sqrt{\chi \eta}}{\tau} \dot{i}$ |
| inductance gradient rail           | L'              | L'  |
| resistance gradient rail           | R'              | $\frac{1}{\tau} R'$                       |
| armature resistance                | $R_{arm}$       | $\frac{g}{\tau} R_{arm}$                  |
| electrothermal action              | A               | $g^2 \tau \chi \eta A$                    |
| launch efficiency                  | $\eta_{launch}$ | $\eta_{launch}$                           |
| armature FOM                       | FOM             | FOM                                       |
| total efficiency                   | $\eta_{tot}$    | $\eta_{tot}$                              |
| stress rate                        | $\dot{S}$       | $\frac{\chi \eta}{\tau} \dot{S}$          |

### 3. APPLICATION OF THE SCALING RELATIONS

The scaling relations are useful for the extrapolation of the results of launch experiments with small scale armatures to the performance of large calibre armatures. By choosing values for  $g$ ,  $\tau$ ,  $\chi$  and  $\eta$ , different aspects of large scale armatures can be studied at smaller scale. The scaling factor  $g$  is not a free choice, since it depends on the ratio of the bore widths of the full scale and small scale rail accelerator. The objective of the small scale launch experiments to be performed, determines the required scaling conditions. From Table II, the required scaling factor relations can be found for the selected scaling conditions. In practice, the applicability of the scaling relations will be limited to a few cases where realistic values are found for armature current, launch package mass and velocity in both full scale and small scale launch experiments. In this section, we will discuss the feasible cases of scaling.

Invariance of the current density is an interesting case, but appears to be impractical when the temperature should be invariant, too. Without this second condition, the case described by Pappas et al. is found [1]. The criterion of Hsieh and Kim is a practical one and is considered in detail here. Another

criterion of practical importance states that temperature and stress rate should be invariant under scaling. This case will also be considered.

### 3.1. Invariant current density

3.1.1. A special case of  $J'=J$  is  $g=1$ . Then  $v'=v/\tau$  and  $m'=\tau^2 m$ . This is the case described in [1], although the authors did not consider the influence of the temperature, specific heat, rail material and launch mass, explicitly. In this case, the geometry and size of the armature and the rail accelerator stay unaltered. This type of scaling is useful to compare the performance of different materials, only. Because  $g$  and  $\tau$  are uncoupled,  $\tau$  is the only significant scaling factor.  $\tau$  is determined by the resistivity ratio of the materials that are compared in the two experiments.

This case for instance can be used for predicting the behaviour of a light weight Al armature at high velocity by testing a heavy Cu armature at low velocity ( $m_{Al}=\tau^2 m_{Cu}$  and  $v_{Cu}=\tau v_{Al}$  with  $\tau=\rho_{Cu}/\rho_{Al}=0.63$ ,  $\chi=c_{v,Al}/c_{v,Cu}=0.68$  and  $\eta=1/\chi$ ). The kinetic energy is the same in both experiments. The temperature at equal current density is 1.47 times higher for Al.

3.1.2. More important is the comparison of the performance of armatures at different calibres, i.e.  $g>1$ . For  $\chi=g^2$ , one has  $T=T'$ , in addition to  $J'=J$ . Only the case  $\tau=1$  is feasible, as other options are unrealistic:

for  $\tau>1$ :  $m'>g^3 m$  and for  $\tau<1$ :  $v'>g v$ . A disadvantage of this case is:  $\rho_c'=g^2 \rho_c$  and  $i'=g^2 i$ .

### 3.2. Invariant temperature and stress distribution

So far, the scaling factors  $g$  and  $\tau$  are independent. To prevent an extreme ratio for the mass in the full scale and small scale experiment, the value of  $\tau$  should be kept small. Choosing  $\tau=g^2$  as in [2] is impractical, since then the mass scales according to  $g^5$ .

Three interesting cases exist, for which  $\chi=1$  and  $\eta=1$ :  $i'=g i$

3.2.1.  $\tau=g$ :  $v'=v$  and  $m'=g^3 m$

The muzzle velocity in the small scale and full scale launch experiment are the same. Acceleration is  $g$  times higher and the jerk is  $g^2$  times higher in the small scale experiment. The ratio of the masses is still high.

3.2.2.  $\tau=1$ :  $v'=g v$  and  $m'=g m$

The time is invariant under scaling, which makes it easier to apply the same pulsed power source for both experiments. The large difference in velocity and acceleration profile is a disadvantage. Resistivity scales with  $g^2$ , while the mass only scales with  $g$ .

3.2.3.  $\tau=\sqrt{g}$ :  $v'=\sqrt{g} v$  and  $m'=g^2 m$

The acceleration in the small scale and full scale experiment are the same. Velocity and mass scaling is still practical. Jerk in the full scale launch experiment is lower than in the small scale launch experiment.

The scaling factor relations in 3.2.1 and 3.2.2 are limiting cases for the invariance of temperature and stress distribution.

### 3.3. Invariant temperature and stress rate distribution

Due to the high stress rates involved in electromagnetic launch experiments, the strength of materials is expected to be depending on strain rate rather than strain. Again, two limiting cases exist.

3.3.1.  $\tau=\sqrt{g}$  and  $\chi=\sqrt{g}$ :  $v'=\sqrt{g} v$ ,  $m'=g^{5/2} m$  and  $i'=g^{3/2} i$

The acceleration in the small scale and full scale experiment are the same. Velocity and mass scaling is feasible. The armature current in the small scale experiment is much lower than in the full scale experiment.

3.3.2.  $\tau=1$  and  $\chi=1$ :  $v'=g v$ ,  $m'=g m$  and  $i'=g i$

In fact, this is the same case as 3.1.2.

### 3.4. Invariant temperature distribution

Relaxing the condition for the mechanical load leads to a more flexible scaling procedure. Since for most high resistivity materials  $\chi < 1$  when copper is used in the small scale experiment, the following cases are interesting:

3.4.1.  $\chi=1/\sqrt{g}$ :  $i'=g^{3/4} i$   $\wedge$   $S'=1/\sqrt{g} S$

a.  $\tau=\sqrt{g}$ :  $v'=\sqrt{g} v$  and  $m'=g^{3/2} m$

b.  $\tau=g$ :  $v'=v$  and  $m'=g^{5/2} m$

3.4.2.  $\chi=1/g$ :  $i'=\sqrt{g} i$   $\wedge$   $S'=1/g S$

a.  $\tau=\sqrt{g}$ :  $v'=\sqrt{g} v$  and  $m'=g m$

b.  $\tau=g$ :  $v'=v$  and  $m'=g^2 m$



In practice,  $\chi$  will be determined by the material with the appropriate resistivity. As long as  $\chi$  is in the order of 1, scaling of mechanical load will not be a limiting factor.

The cases  $\tau=g$  and  $\tau=1$  are considered as the practical limits of scaling electromagnetic launch experiments. The launch mass should scale with a factor between  $g$  and  $g^3$ . We have chosen the case  $\tau=\sqrt{g}$  for our small scale experiments, which reduces the velocity for the small scale experiment by a factor of  $\sqrt{g}$  and leaves the acceleration unaltered. Then, the launch mass is still within practical limits if  $\chi$  is in the order of 1 (cases 3.2.3, 3.3.1, 3.4.1a and 3.4.2a). Due to limitations of our pulsed power supply, we search for materials that meet the scaling factor relations described in cases 3.2.3 and 3.3.1.

The results of simulations of the electrothermal behaviour of a small scale and full scale fibre armature, using a 2D finite element code [11], are shown in Fig. 1 and Fig. 2. These figures show the validity of the scaling relations when rail and armature materials are applied with material properties which obey the relations in Table I. The material for rail and armature in the small scale experiment is copper and the geometrical scaling factor is chosen as  $g=4.5$ . Current is used as input data for the simulations. Fig. 1 shows that the velocity and time axes are scaled by a factor  $\sqrt{4.5}$  for both experiments. Fig. 2 shows that the skin depth  $\delta$  in the armature is a factor 4.5 larger in the full scale experiment and is time-shifted. The maximum temperature in the armature is the same and occurs at the scaled positions in the armatures, but is also time-shifted.

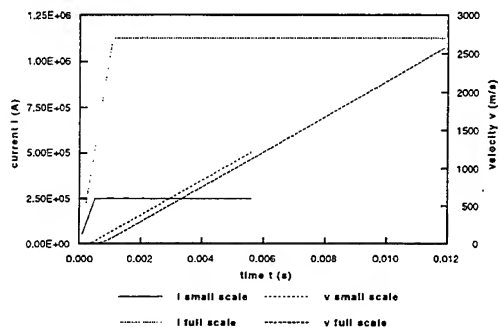


Fig. 1 Current-time profile and velocity-time profile of the simulated small scale and full scale launch ( $g = 4.5$ ,  $\tau = \sqrt{g}$  and  $\chi = 1$ ).

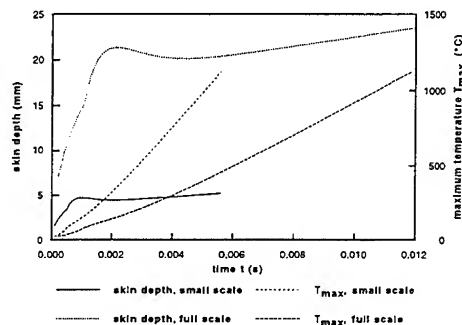


Fig. 2 Skin depth and maximum local temperature-time behaviour during the simulated small scale and full scale experiment ( $g = 4.5$ ,  $\tau = \sqrt{g}$  and  $\chi = 1$ ).

#### 4. EXAMPLES OF SCALED LAUNCH PROCESSES

Using the scaling relations for an LCR circuit in Table III, lumped parameter simulations (Pspice) of full scale and small scale launch experiments have been performed. The specifications of the ARDEC 52 MJ capacitor bank facility [8], [9] have been used in an example of a simulation of a full scale experiment. Fig. 3 through Fig. 5 show that by applying the scaling relations to a pulsed power source, a small scale version of the current pulse is constructed which leads to an exactly scaled launch process. In this example,  $g=4$ ,  $\tau=\sqrt{g}=2$  and  $\chi=1$  were chosen. The full scale launch package mass was set to 2.4 kg which leads to a mass of 150 g for the small scale launch package. The results show that the maximum current for the small scale experiment is 1/4 of the maximum current of the full scale experiment. The velocity scales by a factor 2, e.g. 1250 m/s vs. 2500 m/s at the muzzle. The acceleration is the same in both experiments and the displacement plot in Fig. 5 shows that the launch packages leave the muzzle at 2 m and 8 m, respectively.

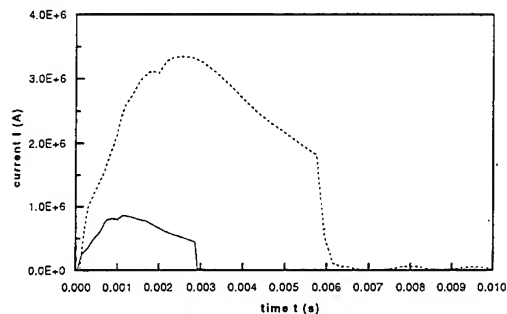


Fig. 3 Current-time profiles for a simulated full scale (dashed) and a 1/4-scale launch process ( $g = 4$ ,  $\tau = 2$  and  $\chi = 1$ ).

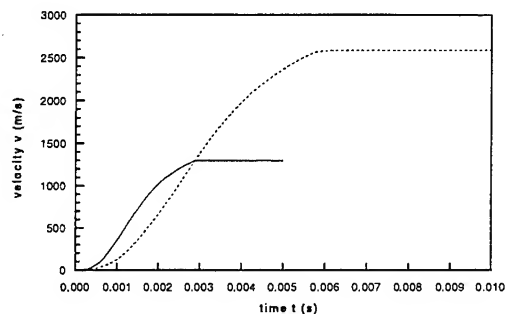


Fig. 4 Velocity-time profile obtained in a simulated full scale (dashed) and 1/4-scale launch process ( $g = 4$ ,  $\tau = 2$  and  $\chi = 1$ ).

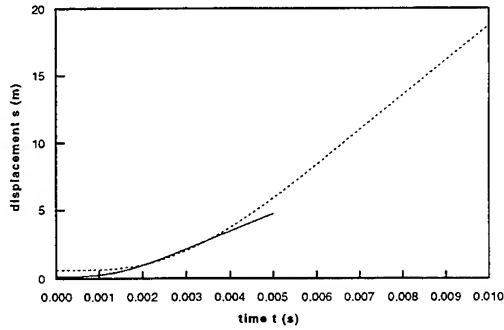


Fig. 5. Displacement-time profile in a simulated full scale (dashed) and 1/4-scale launch process ( $g = 4$ ,  $\tau = 2$  and  $\chi = 1$ ).

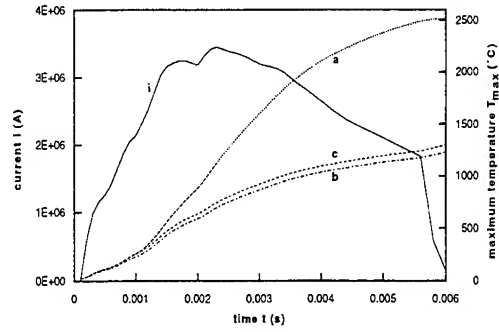


Fig. 6. Effect of deviations from exact scaling relations on the maximum temperature in the armature ( $g = 4.5$ ,  $\tau = \sqrt{g}$  and  $\chi = 1$ ): curve 'a': exact scaling, curve 'b': Cu rails, curve 'c': Cu rails and deviant thermal conductivity.

## 5. DEVIATIONS FROM EXACT SCALING

Deviations from exact scaling can be expected due to the practical and physical limitations of existing large calibre rail accelerators, pulsed power sources and material properties.

Effects of such deviations on the maximum temperature obtained in the full scale armature have been studied by 2D-simulations of the electrothermal behaviour of armatures in full scale experiments based on a small scale experiment with Cu rails and a Cu fibre armature in a 20 mm square bore rail accelerator. For the full scale experiment, the scaling factors were chosen as  $g=4.5$ ,  $\tau=\sqrt{g}$  and  $\chi=1$ . Fig. 6 shows the results of these computer simulations. The current pulse of Fig. 3 has been used as input data. The solid curve labelled 'a' is the calculated maximum temperature in the armature when the exactly scaled material is applied. For the small scale experiment, the melting temperature of Cu is exceeded. The rails of most existing large calibre rail accelerators are made of Cu and it is likely that this cannot be changed. Curve 'b' is the calculated maximum temperature when Cu is used as the rail material in both experiments. The final temperature obtained in the armature drops by a factor of two compared with curve 'a'. The current density at the interface appears to be lower. Curve 'c' is obtained when, in addition to Cu as rail material, the thermal conductivity of the full scale armature scales as  $\kappa' = \kappa g^{3/2}$  instead of  $\kappa' = \kappa g^{-3/2}$ . This can be expected since the thermal conductivity of a metal is related to its resistivity by the Wiedemann-Franz Law [12]:

$$\bar{\kappa} = \frac{\pi^2}{3} \left( \frac{k_B}{e} \right)^2 T \bar{\rho}_e^{-1} \quad (19)$$

The lower heat conduction results in a slightly higher temperature in the full scale experiment.

From the 2D computer simulations with Cu rails and a Cu fibre armature, it is found that applying the scaling relations to the armature material only and not to the rail material has a positive effect on the maximum temperature obtained in the full scale armature. In addition, this will also have a positive effect on the launch efficiency. Deviation from the scaling relation for the thermal conductivity has only a small effect on the temperature.

The temperature effects of deviations from the exactly scaled current pulse profile have been studied, but appear to be of minor importance as long as the total electrothermal action is unchanged. A deviating  $\partial i / \partial t$  does not have a large effect on the electrothermal behaviour of the armature, but results in a different stress rate (and jerk).

For the selection of material pairs for scaled launch experiments, the scaling relations for the resistivity and heat capacity constitute the most significant selection criteria.

## 6. DEFORMATION OF THE SOLID ARMATURE

The armature shape is known to have a large effect on the current distribution at the electrical contact with the rail. Therefore, the deformed shape of the armature in the small scale and full scale experiment should be identical. So far, the scaling relations have been derived for solids. Deformation of a solid is a function of the stress. For isotropic, perfectly elastic materials, a linear relationship exists between stress and strain:

$$\bar{\bar{\epsilon}} = \frac{1}{2G} \mathbf{S} - \frac{\nu}{Y} (tr \mathbf{S}) \mathbf{I} \quad (\text{Hooke's Law}) \quad (20)$$

where  $G = \frac{Y}{2(1+\nu)}$

with  $Y$  is Young's modulus,  $G$  is shear modulus and  $\nu$  is Poisson's ratio. From eq. (20) it is clear that for an invariant shape of a solid armature, the moduli of the materials should scale with  $\chi\eta$ . Eq. (20) oversimplifies the mechanical behaviour of armatures, since it is valid for infinitesimal strains, only. For large strains, which are likely to occur, scaling relations have not been derived. In general, the strain tensor  $\epsilon$  must be invariant under scaling and the stiffness matrix  $\mathbf{C}$  must scale with  $\chi\eta$ :

$$\mathbf{S} = \mathbf{C} \cdot \bar{\bar{\epsilon}} \quad (\text{generalised Hooke's Law}) \quad (21)$$

The internal stress distribution and stress rate distribution cannot be exact images in the full scale and small scale experiment at the same time, since the stress rate scales according to:

$$\dot{\mathbf{S}}' = \frac{\chi\eta}{\tau} \dot{\mathbf{S}} \quad (22)$$

Dynamic stress-strain curves deviate from quasi-static material behaviour. The strain rate is important for the mechanical behaviour of the launch package, since non-linear material behaviour can be expected at the stresses and strain rates involved in electromagnetic launches. Viscoelastic material behaviour of e.g. glass-fibre epoxy parts can still comply with the scaling relations if an additional scaling requirement for the material viscosity is fulfilled:

$$\mu' = \frac{1}{\tau} \mu \quad (23)$$

TABLE V

SCALING RELATIONS FOR MECHANICAL MATERIAL PARAMETERS

| parameter        | small scale  | full scale            |
|------------------|--------------|-----------------------|
| Young's modulus  | $Y$          | $\chi\eta Y$          |
| shear modulus    | $G$          | $\chi\eta G$          |
| Poisson's ratio  | $\nu$        | $\nu$                 |
| stiffness matrix | $\mathbf{C}$ | $\chi\eta \mathbf{C}$ |
| viscosity        | $\mu$        | $\frac{\mu}{\tau}$    |

## 7. SCALEABLE AND NON-SCALEABLE EFFECTS

The validity of the scaling relations derived strongly depends on the influence of the effects that are not included in the equations. In general, all linear electromechanical effects are included in the scaling relations. Some non-linear effects are also included, for instance the temperature-dependency of material properties  $mp$ , when these behave according to:

$$mp'(T') = f(g, \tau, \chi, \eta) mp(T)$$

An example is the temperature-dependency of the electrical resistivity  $\rho_e(T) = \rho_{e,0} (1 + \alpha T)$ . Other non-linearities, such as the rate effects on material behaviour, are non-scaleable (e.g. strain-rate).

The effects of applying the scaling relations to a part of the system, e.g. the armature, are not described by the scaling relations and must be studied, separately.

Preload force and frictional heating are scaleable when certain conditions are fulfilled. The preload force on the electrical contact with area  $A_C$  and normal unit vector  $\hat{n}$  is:

$$\mathbf{F}_p = \int_{A_C} \mathbf{S}_p^T \cdot \hat{n} da \quad (24)$$

The contact stress  $\mathbf{S}_p$  on the armature must have the same value in the small scale and full scale experiment. The pressure on the electrical contact during launch consists of an electromechanical and a preload contribution. Since the electromechanical part scales with  $\chi\eta$ , one finds:

$$\mathbf{S}_p' = \chi\eta \mathbf{S}_p \quad (25)$$

Therefore, the preload force must scale as:

$$F_p' = g^2 \chi \eta F_p \quad (26)$$

The friction force constitutes an extra heat source at the interface, which is given by:

$$q_{fr} = c_{fr} \mathbf{S}^T \cdot \hat{\mathbf{n}} |\mathbf{v}| \quad (27)$$

Using Eqs. (24) and (26), we find that the total heat flux due to friction scales according to:

$$q_{fr}' = \frac{g}{\tau} \chi \eta q_{fr} \quad (28)$$

where it is assumed that the coefficient of friction  $c_{fr}$  is unchanged under scaling.

Gouging is probably an important effect that violates our scaling relations. As far as the phenomenon of gouging is understood to date, it is strongly velocity-dependent. This would make the results obtained in small scale experiments at lower velocity insufficient accurate to predict the behaviour of full scale armatures. However, the aspects of hypervelocity sliding could be investigated in launch experiments with a separate set of scaling relations for which  $\tau=g$  is required.

## 8. EXPERIMENTAL VALIDATION

Although the scaling relations have been derived from first principles, a validation of the applicability in practice is useful. To check our assumptions, we have performed static experiments in an armature test bed [10]. The results of magnetic induction measurements for two different calibres have been compared. The small scale experiment was performed with a 20 mm square bore geometry with Cu rails and armature. The large scale experiment was performed with a 40 mm square bore geometry with CuZn ("brass") rails and armature. Thus, the geometrical scaling factor  $g=2$ . In Fig. 7 and Fig. 8, the resistivity  $\rho$  and specific heat  $c_v$  of CuZn alloys are shown as a function of the alloying compound Zn [13]. The brass alloy used in our experiments was CuZn39Pb3. Fig. 7 shows that the specific heat  $c_v$  has almost the same value for both materials ( $\chi=0.96$ ). The resistivity, shown in Fig. 8, complies with the scaling relations if the time scaling factor  $\tau$  equals  $\tau = \rho_{Cu} / \rho_{CuZn} g^2 = 0.97$ .

In the experiments, a flat top current pulse was used (50 kA for the small scale and 100 kA for the large scale experiment). The rise time of the large scale current was 0.97 times that of the small scale current. The inductance gradient  $L'$  was checked to be the same for both geometries. Fig. 9 shows the magnetic induction  $\sqrt{\chi} B$  at  $t=0.5$  ms for the small scale experiment, where the armature axis has been stretched by a factor  $g=2$ , and  $B'$  at  $t'=0.5 \tau$  ms for the large scale experiment. The relative positions -1 and +1 correspond with the trailing and forward edge of the armatures. Fig. 10 is the magnetic induction plot  $\sqrt{\chi} B$  at  $t=1.5$  ms for the small scale and  $B'$  at  $t'=1.5 \tau$  ms for the large scale experiment. The results show that within experimental accuracy  $B'=\sqrt{\chi} B$ , in accordance with the scaling relations.

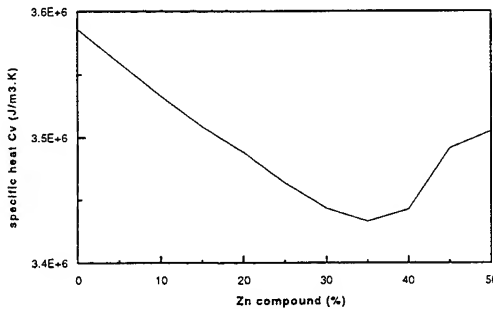


Fig. 7 Heat capacity for CuZn alloys as a function of Zn percentage [13].

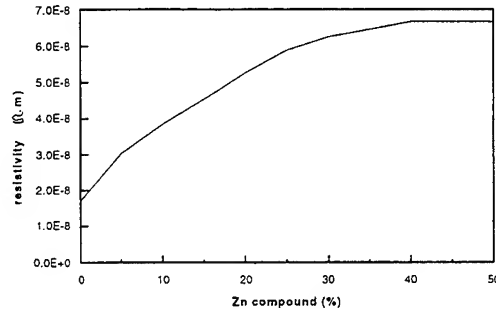


Fig. 8 Resistivity for CuZn alloys as a function of Zn percentage [13].

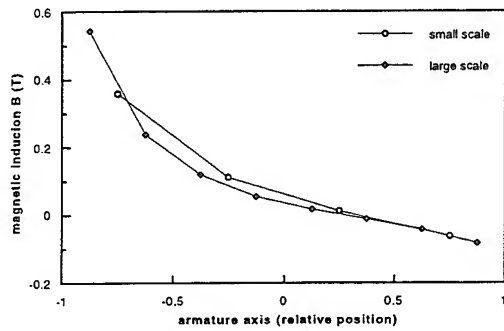


Fig. 9 Magnetic induction  $\sqrt{\chi} B(x)$  at  $t = 0.5$  ms and  $B'(x')$  at  $t = 0.5\tau$  ms versus relative position in the armature.

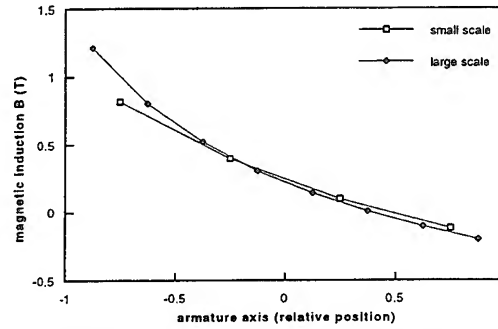


Fig. 10 Magnetic induction  $\sqrt{\chi} B(x)$  at  $t = 1.5$  ms and  $B'(x')$  at  $t = 1.5\tau$  ms versus relative position in the armature.

## 9. CONCLUSIONS

It is shown that certain performance aspects of large calibre armatures can be studied at small scale by applying scaling relations. These relations are derived from the fundamental equations which describe the electromagnet launch process. Four scaling factors are introduced:  $g$  for geometrical scaling,  $\tau$  for time scaling,  $\chi$  for scaling of the specific heat per unit volume and  $\eta$  for temperature scaling. Critical design parameters, such as launch efficiency, total efficiency and armature Figure Of Merit, are invariant under scaling according to the method presented in this paper.

The most important scaling criterion is the condition for which the temperature distribution in the small scale and full scale experiment are the same ( $\eta = 1$ ). Invariance of the stress or stress rate distribution is not required, since small deviations from exact scaling are allowed for these distributions. The scaling relations for the resistivity and the heat capacity per unit volume are the most significant guidelines for the selection of the armature and rail materials in scaled launch experiments. Thermal conductivity plays a minor role.

For small scale experiments at the Pulse Physics Laboratory, a geometrical scaling factor  $g=4$  and time scaling factor  $\tau=\sqrt{g}$  are chosen. Therefore, materials for the large calibre armatures have to be found for which the value of the resistivity must be eight times that of copper, when copper fibre armatures are used in the small scale launch experiments. The specific heat of such a material is in general lower than that of copper ( $\chi < 1$ ). Its melting temperature must at least be equal to that of copper. For example, the resistivity and melting temperature of refractory metals are within the interesting range.

## ACKNOWLEDGEMENT

The authors acknowledge Timo Huijsers for his contribution to the experiments.

## REFERENCES

- [1] J.A. Pappas, M.D. Driga, and W.F. Weldon, "Physical scale modeling to predict current diffusion in solid armatures," *IEEE Trans. Magn.* **25** (1989), 408 - 411.
- [2] K.T. Hsieh and B.K. Kim, "Scaling relations on an electromechanical system," *Procs. 5th Eur. Symp. on EML Techn.*, April 10 -13, 1995, Toulouse, France.
- [3] G.L. Jackson, M.M. Tower, and C.H. Haight, "Scaling relationships for plasma driven railguns," *IEEE Trans. Magn.* **25** (1989), 252 - 255.
- [4] L.D. Thornhill, J.H. Batteh, and D.M. Littrell, "Scaling study for the performance of railgun armatures," *IEEE Trans. Plasma Sci.* **17** (1989), 409 - 421.
- [5] L.D. Thornhill and J.H. Batteh, "Scaling laws for plasma armatures in railguns," *IEEE Trans. Plasma Sci.* **21** (1993), 289 - 297.
- [6] K. Dareé, "A computational study of railgun performance at different calibers," *Procs. 1st Eur. Symp. on EML Techn.*, September 13 -14, 1988, Delft, the Netherlands.
- [7] F.W. Grover, "Inductance Calculations, Working Formulas and Tables", Dover Publications Inc., New York, 1946.
- [8] T. Coradeschi, G. Colombo, A. Davis, R. Puterbaugh, T. Bernhardt, C. Dobbie, P. Gaywood, E. Harris, and I. McNab, "52 MJ Electric Gun Test Facility", *IEEE Trans. Magn.* **29** (1993), 923 - 928.
- [9] D.I. Chang, Kien Luu, L. Tran, T. Coradeschi, and B. Long, "Performance of the 52 MJ power supply at the Electric Armaments Research Center", *IEEE Trans. Magn.* **31** (1995), 22 - 25.
- [10] M. Koops and W. Karthaus, "Test bed for the evaluation of solid armature concepts," *Procs. 5th Eur. Symp. on EML Techn.*, April 10 -13, 1995, Toulouse, France.
- [11] A.J. Schoolderman, "Performance predictions for electromagnetic launching with multi-fibre solid brush armatures and resistively layered rail accelerators," *IEEE Trans. Magn.* **31** (1995), 651 - 656.
- [12] N.W. Ashcroft and N.D. Mermin, "Solid State Physics", Holt-Saunders, Philadelphia, 1979 (ISBN0-03-049346-3).
- [13] K. Dies, "Kupfer und Kupferlegierungen in der Technik", Springer Verlag, Berlin, 1967 (in German).

## APPARENT ENHANCED BURN RATES OF SOLID PROPELLANTS DUE TO PLASMAS

Clive R Woodley, Steve Fuller

WX6 Gun Systems Department, Weapons Systems Sector,  
Defence Research Agency Division, Defence Evaluation and Research Agency,  
Fort Halstead, Sevenoaks, Kent TN14 7BP, United Kingdom

**Abstract:** The Defence Evaluation and Research Agency (DERA) is investigating a number of different electrothermal gun concepts which utilise solid propellants. One of these concepts is known as current injection (CI). In the CI concept, electrical energy is discharged in a combustion chamber through two electrodes which are connected by a fuse wire. These electrodes are located inside the combustion chamber. The CI concept can be used to ignite the charge of solid propellant, and/or to augment the combustion of the solid propellant. Anomalous enhanced gas generation rates have been identified for some propellants after the electrical discharge has ceased. Methods of quantifying the enhanced gas generation rates have been developed and used to compare the results from different tests and propellants.

### INTRODUCTION

The internal ballistics of guns firing conventional solid propellant charges is a very mature research area. Most gun/charge systems are highly optimised and it is difficult to obtain substantial increases in muzzle velocity with conventional charge designs. To increase substantially the muzzle velocity of a gun, it is necessary to broaden the shot base pressure versus shot travel profile, ie by quickly attaining a high pressure and then sustaining that maximum pressure as long as possible, subject to constraints on muzzle blast and barrel pressure. In order to sustain the maximum pressure, it is necessary to increase the gas generation rate from the propellant. This increase can be achieved by increasing either the burning surface area of the propellant or the propellant burn rate. Therefore, there is a strong interest in the development of advanced charge concepts such as layered propellants in which a fast burning propellant is surrounded by a slower burning propellant. Other concepts include travelling charge concepts which have been considered for direct fire applications and programmed splitting propellants in which the propellant breaks up, in a controlled manner, after a predefined fraction of propellant has burned.

However, all of these methods present risks in that the manufacturing tolerance on the propellants needs to be very tightly controlled. If it is not, then, for the example of layered grains, the faster burning layer might start burning too early in the internal ballistic cycle, possibly before peak pressure has been achieved. This could lead to dangerously high

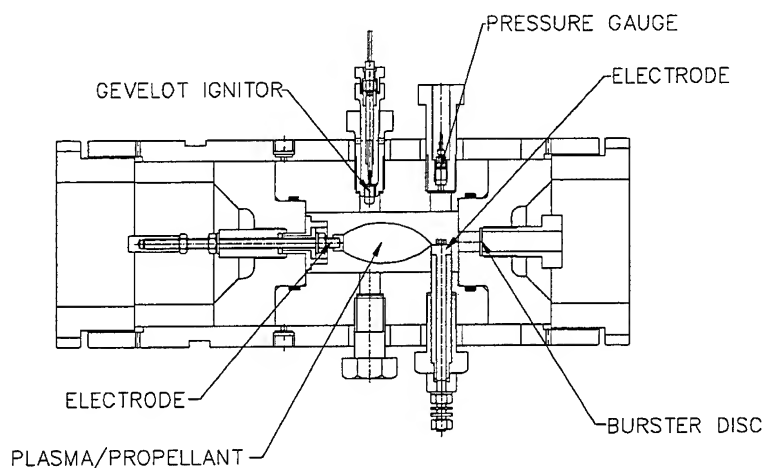
pressures in the gun chamber. An alternative to using the aforementioned methods of increasing the gas generation rates could be to use some form of electrical energy to increase the gas generation rate of a homogeneous propellant. Probably the easiest way in which electrical energy can be used to affect propellant combustion is to create a plasma in the combustion chamber. In the UK, the CI concept is being investigated which can create a plasma in the combustion chamber. The use of plasmas to increase gas generation rates of propellants has been reported by a number of different research workers (references 1-3) who have also proffered explanations for the increases. These explanations include radiative heating of the propellant (sub-surface heating), worm holes, erosive burning and propellant break-up.

This paper describes the analyses of some closed vessel firings, conducted under a range of different conditions, that were carried out for the CI concept using propellants which are of different chemical compositions. To date, tests have been conducted using three triple base propellants, six nitramine enriched double/triple base compositions and three next generation low vulnerability ammunition (LOVA) propellants. The analyses show substantially different behaviour between the propellants.

## DESCRIPTION OF EXPERIMENTS

Figure 1 shows the vessel that was used for the CI experiments. The electrodes are shown at the left-hand side and the bottom right-hand corner of the vessel; on the right-hand side a burster disk is shown. In the experiments reported in this paper, a burster disk was not used and the right-hand side of the vessel was sealed. Also shown in figure 1 are two pressure gauges and a Gevelot igniter (a 30mm gun charge igniter). A Gevelot igniter contains nearly 1g of gunpowder. The electrical energy is provided by a capacitor-based pulse forming network (reference 4). The CI vessel has a volume of 400cc approximately.

Fig. 1: CURRENT INJECTION VESSEL



ETN-784

A large number of experiments have been conducted using different propellants. Table 1 shows a selection of the propellants used and indicates the main constituents of each propellant. NQ is a triple base propellant.

Composition 1 is a double base propellant which is enriched with RDX, a nitramine. Compositions 2 and 3 are triple base propellants with added

RDX. The LOVA propellant is a CAB (cellulose acetate butyrate) based LOVA propellant. The HELOVA propellant is a high energy LOVA (HELOVA) propellant which contains a

curable energetic binder. Composition 1 has been used in most of the experiments and these have attempted to determine the effect of electrical power, electrical energy and initial propellant temperature on the deduced gas generation rates.

Table 1 - Propellant compositions

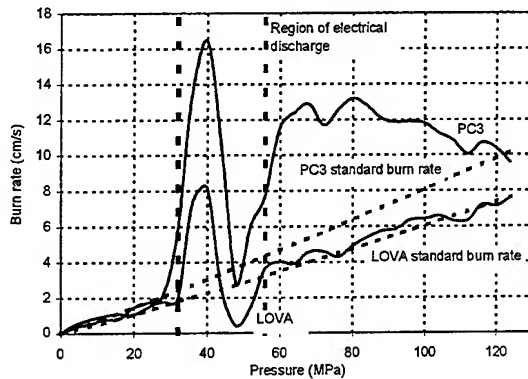
|                       | NQ | Comp<br>1 | Comp<br>2 | Comp<br>3 | LOVA | HELOVA |
|-----------------------|----|-----------|-----------|-----------|------|--------|
| NC                    | x  | x         | x         | x         | x    |        |
| NG                    | x  | x         | x         | x         |      |        |
| RDX                   |    | x         | x         | x         | x    |        |
| Picrite               | x  |           | x         | x         |      | x      |
| Carbamite             | x  | x         | x         | x         |      |        |
| Inert plasticiser     |    | x         |           | x         | x    |        |
| Energetic plasticiser |    |           |           |           | x    | x      |
| PolyNIMMO             |    |           |           |           |      | x      |
| Isocyanate            |    |           |           |           |      | x      |
| HMX                   |    |           |           |           |      | x      |
| CAB                   |    |           |           |           | x    |        |

## ANALYSIS OF MEASURED DATA

In all of the firings, transient histories of combustion pressure, plasma current and voltage were recorded. The pressure-time measurements were analysed using a code called BRLCB, version 3.0 (reference 5). This code enables the thermal effect of any electrical energy that is discharged to be taken into account. Therefore, any enhanced gas generation rates that are deduced by the BRLCB analysis are due to other effects, such as erosive burning or radiative heating, and not due to extra thermal energy contributed by the electrical source. However, BRLCB can not distinguish between increased gas generation rates due to geometric changes in the propellant grain or those due to changes in the burn rate. One of the assumptions in the BRLCB code is that propellants burn in parallel layers and do not break-up. The main purpose of the BRLCB code is to calculate the burn rate of a propellant at various pressures and it is this that has been selected as the means of comparison of different tests that are reported in this paper. Therefore, although the graphs discussed below show the variation in burn rate with pressure, what the BRLCB code is actually deducing is a variation in gas generation rate. The authors have merely portrayed the variation in gas generation rate as a variation in burn rate.



Fig. 2: EXPERIMENT ET053 TEST 3 & ET063 TEST 13 - 48g PROPELLANT, 26kJ EE



The authors have reported previously the effects of plasmas on different propellants (reference 6) under a range of different conditions. Figure 2 shows typical results for propellant composition 3 (PC3) and the LOVA propellant. In both tests, 48g of propellant were ignited by means of a Gevelot igniter and, when the pressure in the combustion chamber had reached about 30MPa, 26kJ of electrical energy were discharged

into the vessel using a 26μH inductor in the capacitor bank module. The vertical dotted lines in figure 2 indicate the pressure region over which the electrical discharge took place.

Both propellants exhibit enhanced burn rates during the electrical discharge. However, after the electrical discharge has ended the burn rate behaviour of the two propellants is substantially different. The burn rate of the LOVA propellant reverts back to the standard burn rate law (indicated by the dashed line) whereas PC3 continues to burn at a faster rate than its standard burn rate law. PC1 and PC2 behave in a similar manner to PC3. The HELOVA propellant behaves in a similar manner to the LOVA propellant. Reference 6 reported that interrupted burning vented vessel tests using PC1 showed no evidence that fracturing of the propellant was occurring.

The main findings from the work reported in reference 6 are as follows: (1) a faster, higher power pulse produced greater EGGR than slow, lower power pulses; (2) the greater the ratio of electrical energy to charge mass (electrical energy density), the greater the amount of gas generation rate enhancement; (3) tests in which up to about 30kJ of electrical energy were discharged in order to ignite the propellant did not show PEDEGGR (this finding suggests that there is a threshold value for the electrical energy to cause PEDEGGR); (4) taking into account the temperature variation of the burn rate coefficient, the initial temperature of the propellant had little effect on the deduced gas generation rates.

## QUANTIFICATION OF ENHANCED GAS GENERATION RATES

Fig. 3: EXPERIMENT ET025 TEST 4 - 48g PC1, 27kJ EE

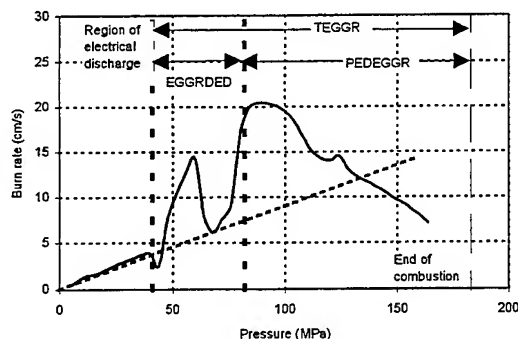


Figure 3 shows a typical graph of burn rate versus pressure for propellant composition 1 (PC1) under test conditions similar to those stated above for figure 2. Three 'measures' of the enhanced gas generation rates have been defined. The first of these quantifies the enhanced gas generation rates during the electrical discharge (EGGRDED). The second 'measure' quantifies the

post electrical discharge enhanced gas generation rates (PEDEGGR). The third 'measure' quantifies the total enhanced gas generation rates (TEGGR). The regions of the burn rate profile over which these measures are calculated are shown in figure 3. The method of calculation of each measure is described below.

The standard burn rate law for the propellant is used to calculate the burn rate coefficient for the test in which electrical energy was discharged. The resultant burn rate coefficient profile should be a straight line at a constant value, assuming that there is no discontinuity in the standard burn rate profile for that propellant. The burn rate coefficient profile is integrated with respect to pressure over the appropriate pressure range. The integrated burn rate coefficient is then divided by the pressure difference of the range to determine a pressure-averaged burn rate coefficient over the appropriate pressure range. The resultant mean burn rate coefficients that are calculated are then divided by those from tests in which no electrical discharge took place to determine a unitless quantity which indicates the level of enhancement in the burn rate coefficient. A value of two indicates that the average burn rate coefficient over the appropriate pressure range is twice that of the standard burn rate coefficient.

## EFFECT OF ELECTRICAL POWER AND ENERGY ON EGGR

In experiment ET051, a number of tests were conducted using the CI concept for PC1 to investigate the effect of electrical power and energy on the levels of EGGRDED, PEDEGGR and TEGGR. These tests were all conducted under similar conditions except for the amount of electrical power and energy that were discharged. Figure 4 shows the variation in the three quantities with maximum electrical power. For each of the three EGGR measures, a linear trend line was fitted and plotted. The equation and correlation coefficient of each trend line are also plotted. High correlations exist between all three EGGR measures and the maximum electrical power. Figure 5 shows the variation in the three quantities with electrical energy. Fitted trend lines show that there are also high correlations between the EGGR measures and the electrical energy. There is no indication that either the electrical power or the electrical energy is the dominant effect.

Fig. 4: VARIATION IN EGGR MEASURES WITH ELECTRICAL POWER - 48g PC1

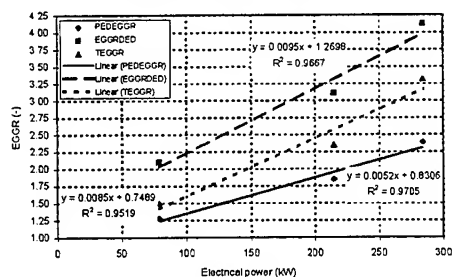
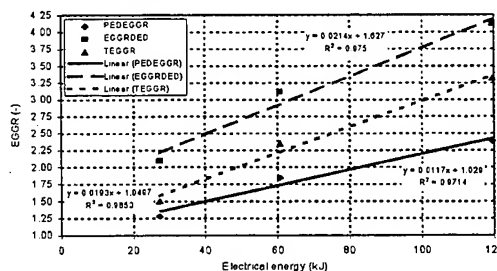


Fig. 5: VARIATION IN EGGR MEASURES WITH ELECTRICAL ENERGY - 48g PC1



## THRESHOLD FOR PEDEGGR

Reference 6 reported that the analysis of some tests indicated that there was a threshold value required of the electrical energy or power for EGGR to occur when the propellant

was ignited using electrical energy. Experiment ET051 contained a number of tests in which different amounts of electrical energy were used to ignite 48g of PC1. In test 1, 29kJ of electrical energy, at a maximum power of 44kW, were used to ignite the propellant. PEDEGGR were not exhibited. In test 2, 72kJ of electrical energy, at a maximum power of 94kW, were used to ignite the propellant. PEDEGGR were exhibited (figure 6) and the level of PEDEGGR was calculated to be about 1.38. Further tests need to be conducted in order to determine, assuming that they exist, the threshold values of the electrical energy or power for PEDEGGR to occur.

Fig. 6: EXPERIMENT ET051 TEST 2 - 48g PC1, 71.7kJ EE

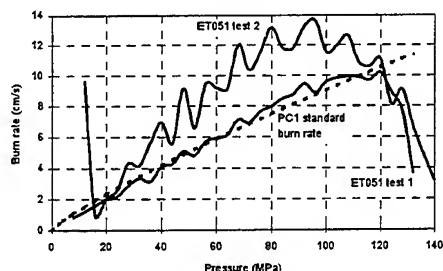
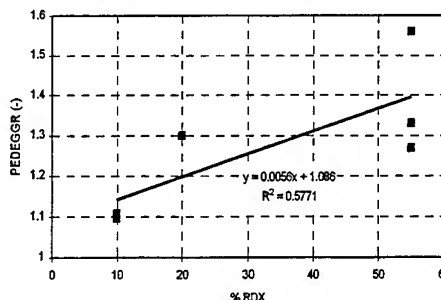


Fig. 7: VARIATION IN PEDEGGR WITH PERCENTAGE OF RDX

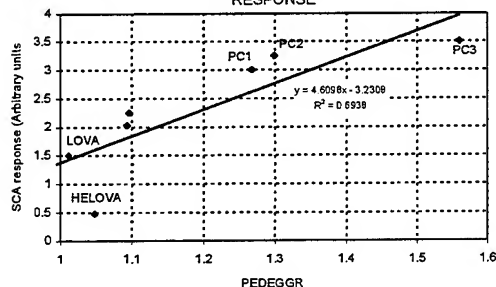


## EFFECT OF PERCENTAGE OF RDX ON PEDEGGR

In reference 6 it was speculated that the percentage, by mass, of RDX contained in a propellant was, in some manner that was not understood, responsible for the level of PEDEGGR that was observed. However, it was also noted in reference 6 that the LOVA propellant, which contained RDX, exhibited a normal level of PEDEGGR. Figure 7 shows the variation with PEDEGGR with the percentage of RDX for all the non-LOVA propellants which have been investigated to date. Although there is an indication that the level of PEDEGGR increases with the percentage of RDX contained in a propellant, the correlation coefficient of the trend line is low.

## CORRELATION BETWEEN PEDEGGR AND SHAPED CHARGE ATTACK RESPONSE

Fig. 8: CORRELATION BETWEEN PEDEGGR AND SCA RESPONSE



It was noted that the propellants, such as PC1, PC2 and PC3, which exhibited PEDEGGR are much more sensitive to mechanical shock waves than the LOVA and HELOVA propellants. Therefore it is possible that the PEDEGGR are a feature of the more sensitive propellants although other explanations are also possible. The findings reported above for PC1 are consistent with this

hypothesis; a strong mechanical shock wave would be produced for a high electrical energy density plasma and high electrical power. It is also feasible that there would be a threshold

above which PEDEGGR occur. It is known that the burning behaviour of RDX propellant can be influenced by a mechanical shock wave (reference 7). Figure 8 shows the correlation between the level of PEDEGGR for a number of propellants and their shaped charge attack response. There is a reasonable correlation between the two quantities. In particular, if the result for the HELOVA propellant is removed from the calculation of the trend line, the  $R^2$  value increases to about 0.8. Removal of the HELOVA result could be justified on the grounds that physically the propellant is very different from the others; the HELOVA propellant is very elastic rather than 'brittle'. Further experiments are planned to investigate this possibility further, including the testing of PC1 which has been deliberately subjected to mechanical shock waves.

## DISCUSSION AND CONCLUSIONS

From a control viewpoint, it is more desirable to have a propellant exhibit a high level of EGGRDED than a high level of PEDEGGR, even though with PEDEGGR one is practically getting 'something for nothing'. Except for PC3, the highest level of TEGGR is exhibited by the LOVA propellant. The level of TEGGR is high for the LOVA propellant because it exhibits a very high level of EGGRDED. This fact is encouraging because the vulnerability of propellants such as PC3 will prevent them from ever being used other than for experimental purposes. Therefore, with propellants, such as the LOVA propellant, which do not exhibit PEDEGGR, there exists a feasible opportunity for electrical power or energy to be used to control the combustion of such propellants.

Results that have been obtained so far indicate that there are strong correlations between the electrical energy/power and the level of PEDEGGR. Further work needs to be conducted to establish whether the electrical energy or the electrical power is the dominant effect. The results from this work should give some indication of the plasma properties that might be causing the PEDEGGR.

Weak correlations have been established between the PEDEGGR level exhibited by a propellant and the percentage of RDX it contains.

A weak correlation has been established between the PEDEGGR level exhibited by a propellant and its response to shaped charge attack. Furthermore, there is evidence of a threshold level of the electrical power/energy for PEDEGGR to occur. Therefore it has been conjectured that a propellant's sensitivity is, in some way that is not yet understood, linked to the level of PEDEGGR exhibited. Although the correlation is weak, this explanation for the anomalous EGGR after the electrical discharge has ended can not yet be eliminated.

Other explanations for the enhanced burn rate behaviour of the propellants are feasible. For example, radiative heating of the propellant due to the high temperature plasma will undoubtedly have an important effect on the burn rates. Key properties of the propellants that need to be investigated include their absorption characteristics.

Gun firings using PC1 are planned to investigate whether that propellant exhibits EGGR under typical gun firing conditions.

## ACKNOWLEDGEMENTS

The work reported here forms part of the UK ETC gun research programme; a collaborative programme undertaken by the DERA and Royal Ordnance. The efforts of the DERA ETC research team members in conducting the experiments reported here are gratefully acknowledged. Mr D Debenham of WX4 Department, DERA, is thanked for his advice on the propellants used. Mr W F Oberle, of the US Army Research Laboratory is also thanked for supplying the DERA with a copy of BRLCB and for giving advice on the use of the software.

## REFERENCES

1. C R Woodley & S R Lumley, 'DRA Modelling activities in electrothermal-chemical guns', 15th International Symposium on Ballistics, Jerusalem, May 1995.
2. W Oberle et al, 'Investigations into the combustion behavior of propellants interacting with an electrically generated plasma', 15th International Symposium on Ballistics, Jerusalem, May 1995.
3. R J Lieb & C J Gillich, 'Morphology of Extinguished Monolithic JA2 Grains Fired in a 30-mm Solid Propellant Electrothermal-Chemical (SPETC) Gun', ARL Technical Report ARL-TR-606, US Army Research Laboratory, Aberdeen Proving Ground, MD, November 1994.
4. B Augsburger et al, 'DRA 500kJ multi-module capacitor bank', IEEE Transactions on Magnetics, Volume 31, number 1, January 1995.
5. W F Oberle & D E Kooker, 'BRLCB: A Closed-Chamber Data Analysis Program: Part I - Theory and User's Manual', ARL Technical Report ARL-TR-36, US Army Research Laboratory, Aberdeen Proving Ground, MD, January 1993.
6. C R Woodley & S Fuller, 'Apparent Enhanced Burn Rates of Solid Propellants Due to Plasmas', 16th International Symposium on Ballistics, San Francisco, 23-28 September 1996.
7. J Fellows, private communication, WX4 Department, DRA Fort Halstead, UK.

© British Crown Copyright 1997/DERA

Published with the permission of the controller of Her Britannic Majesty's Stationery Office.

A Civilian Application of Coil Launchers Technology—  
Elevators for High-Rise Buildings

Zivan Zabbar, Enrico Levi, and Leo Birenbaum  
Polytechnic University  
Department of Electrical Engineering  
Six Metrotech Center  
Brooklyn, NY 11201

Abstract

Electromagnetic coilgun technology offers a number of promising spin-offs, such as earth-to-orbit launchers, Maglev, and cordless-contactless elevators. This paper deals with the latter. At the Polytechnic, the Linear Induction Launcher (LIL) was successfully developed: a projectile, enclosed in a cylindrical conducting sleeve, is accelerated by a long coaxial array of coils energized in polyphase fashion. This occurs while the projectile within is completely levitated. For application to the cordless elevator, the long coaxial array of coils (the energized primary motor winding) is positioned vertically, and the short aluminum sleeve (the secondary) surrounds the coils. The moving sleeve has to be cut longitudinally, in order to allow for mechanical support of the interior primary. The coils are energized at industrial frequency (e.g., at 50 or 60 Hz).

In one realization, a cluster of four vertical coaxial coil arrays extends over the height of the elevator shaft. Four short secondary sleeves are attached to the outer walls of the elevator car at the corners. In addition to providing propulsion and braking forces in the vertical direction, this unusual choice for the topology of the air-cored linear induction motor has a number of other advantages: (1) it allows clearance of an inch or more between the parts in relative motion, and (2) it provides strong lateral guidance. Special positive action activators are provided for opening or closing the doors, for stopping the car at the various floor levels, and in case of interruption of supply power. This system thus overcomes limitations which, in present elevator systems, are set by the weight of the cords and by irregularities in the lateral guides, and which create difficulties in deep mine shafts and in high-rise buildings. This paper presents a preliminary design of a complete system.

## A Civilian Application of Coil Launchers Technology— Elevators for High-Rise Buildings

Zivan Zabar, Enrico Levi, and Leo Birenbaum  
Polytechnic University  
Department of Electrical Engineering  
Six Metrotech Center  
Brooklyn, NY 11201

### 1. Introduction

With conventional raising and lowering devices, the length of the vertical shafts, such as are found in deep mines and in high-rise buildings, is limited by the weight and vibrations of the ropes, by variations in the alignment of the steel tee-rail guides due to wear and tear, and by joints and vibrations of the shaft itself. Use of ordinary iron-cored, linear motors with planar air gaps can eliminate the ropes but not the guides, because such motors cannot provide the necessary guidance. The reason is that the force of attraction between the primary and the secondary structures increases as the air-gap length (clearance) decreases. As a result, a small perturbation which decreases the clearance, leads to physical contact between the parts in relative motion. Another problem is that it is not practical to have larger clearance than about a quarter of an inch.

Earlier, at the Polytechnic, we gained experience with air-cored linear induction motors and successfully developed and tested a coilgun called a Linear Induction Launcher (LIL). The coil gun had a 60-cm-long barrel, and achieved design performance by accelerating a 137-gram projectile to a muzzle velocity of 476 m/s, with an average acceleration of over 19 kGee's [1]. During the whole transit within the barrel, the projectile was completely levitated. This latter feature has prompted us to propose applications to civilian use, such as to magnetically-levitated (Maglev) trains [2], to earth-to-orbit (ETO) satellite launchers [3], and in the present paper, to elevators.

The LIL consists of a linear coaxial array of circular coils energized in polyphase fashion, so as to create a traveling electromagnetic wave. This array serves as the primary of an air-cored induction motor. The secondary is a cylindrical sleeve of conducting material, such as aluminum, that envelops the projectile; thus, in the coilgun, the sleeve is located inside the energized coils. In the proposed uses, on the other hand, the sleeve would be located outside the energized coils. It must therefore be cut longitudinally, in order to allow for mechanical support of the coils within. Also it would be considerably thicker and heavier.

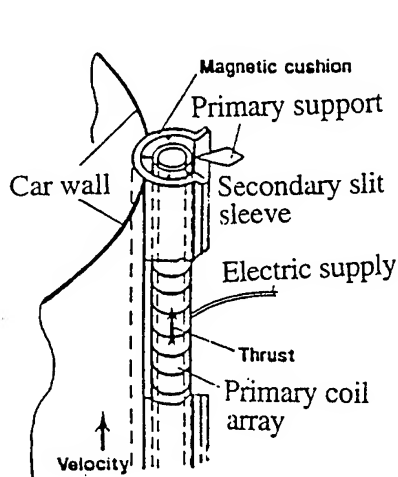


Fig. 1. Close-up of a motor element.

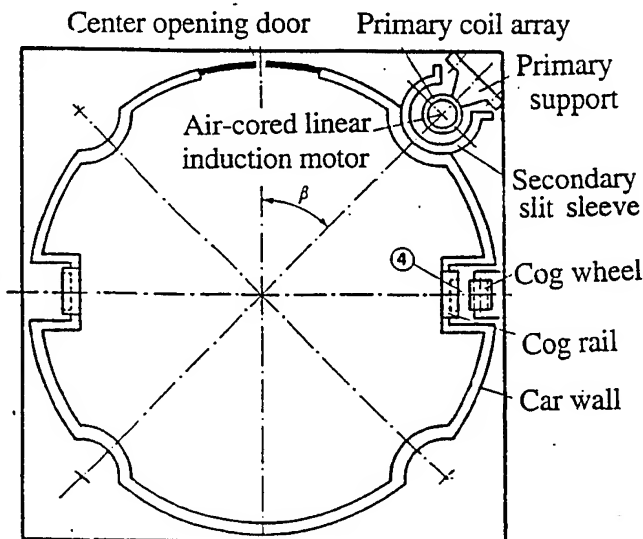


Fig. 2. Sketch of proposed elevator system.

## 2. Propulsion and Guidance System

A motor element for the cordless and contactless elevator is shown schematically in Fig. 1. The coil array (primary) is fixed to the wall of the shaft by supports. It extends over the whole height of the elevator shaft. It is divided into sections which are energized sequentially. The secondary slit sleeves are short and attached to the car walls. A number of such motor elements (four in the case of Fig. 2) constitute the elevator drive.

The motor element operates as a linear induction motor and as such provides for propulsion and, when the sequence of the phases is inverted, for braking. It also serves as a magnetic cushion which provides lateral guidance. The source of this cushioning action is a radial stress which results from the interaction between the azimuthal currents in the coils and the longitudinal component of the magnetic flux density. As shown in Fig. 3, the asymmetry generated by the opening angle  $\alpha$  of the slit sleeve, and by the displacement  $d$  between the axes of the coil array and of the slit sleeve, produces a net force  $f_s$ . This is a restoring force, because it opposes the sense of the displacement. Its magnitude is a function of the slip  $s$  between the traveling electromagnetic wave and the slit sleeves, and it is of the same order of magnitude as that of the propelling force.

This arrangement of the motor serves four main purposes:

- (1) it decouples the size and geometry of the energized coils from the size and geometry of the car.
- (2) it allows the needed power to be supplied without reaching



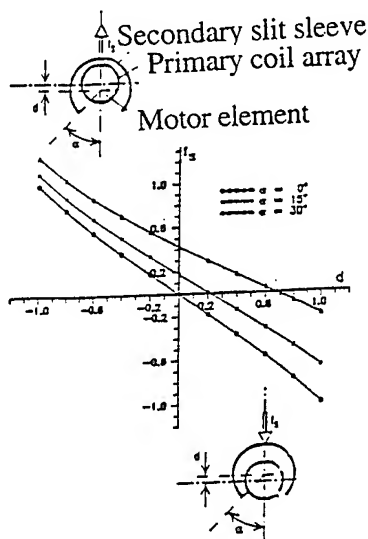


Fig. 3. Transverse force vs. displacement between axes, with sleeve opening-angle  $\alpha$  as a parameter.

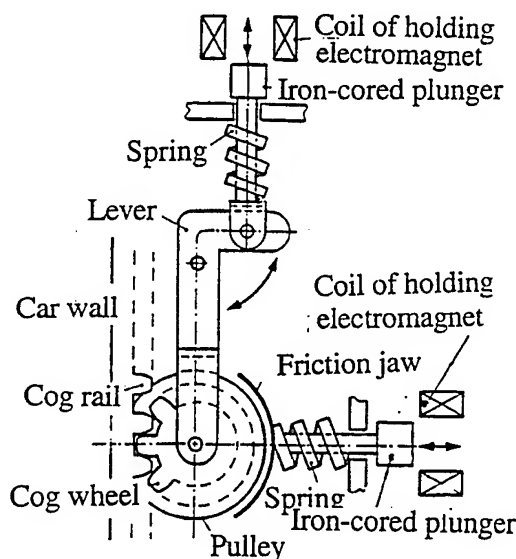


Fig. 4. Floor-stopping brake.

dangerously high voltages, since coil groups within a motor element can be connected electrically in parallel.

(3) it permits specified ratios of guidance to propelling forces by selecting the proper slot opening angle, as can be deduced from Fig. 3, and

(4) it reduces investment costs by allowing modular construction.

The special topology of the motor, with its cylindrical air gap, presents several advantages:

- (a) it develops force components which are strong enough to provide lateral guidance, as well as vertical propulsion and braking; the centering forces in the motor elements and their symmetrical distribution around the car afford great lateral stability;
- (b) the coaxial arrangement of the primary and secondary results in the confinement of the magnetic flux to the interior of the sleeve, and in the consequent proximity of all portions of the magnetic flux path to the exciting currents. This permits the elimination of iron cores without increasing unduly the size of the magnetizing current needed to establish the magnetic field, and without increasing unduly the exposure of passengers to the magnetic field.

- (c) in each turn, all portions of the current-carrying conductors contribute to the generation of useful forces. This leads to relatively high efficiency with a minimum of material stresses, physical dimensions, and cost of the apparatus.
- (d) the main functions of propulsion and guidance are performed while leaving a relatively large clearance between the parts in relative motion.
- (e) the presence of massive secondary sleeves also solves the problem of high compliance and lack of damping which plague other air-cored systems.
- (f) the asynchronous mode permits the operation at variable speed during acceleration and deceleration while utilizing ordinary constant frequency supplies and without the need for expensive power conditioning apparatus. It also allows for high acceleration and emergency braking.

A preliminary design for an elevator is presented in the Appendix.

### 3. Stopping at Floors

A major problem with ropeless hoist drives relates to stopping the car at floor levels. Here, the car is slowed down and brought to a halt by inverting the sequence of the drive phases, thus changing the direction of the propelling force in the appropriate section. A cog-rail/cog-wheel arrangement then locks the car at the exact level. For this purpose, two sides of the car wall are provided with a rail with cogs that engage cog wheels located at the desired floor as indicated in Fig. 2.

This arrangement is shown in Fig. 4. When the coil of the upper electromagnet is deenergized, the spring rotates the lever clockwise, and pushes the cog wheel forward toward the cog until it comes into contact with the rail and holds it there. At the same time, the coil of the lower electromagnet is also deenergized and its spring pushes the friction jaw forward toward a pulley which is solidly coupled to the cog wheel, and thus prevents its motion, and consequently the motion of the car. To permit running of the car between floors both coils must be energized; the iron-cored plungers are attracted against the action of the springs, thus releasing the cog-wheel/cog-rail engagement. A similar kind of operation governs opening and closure of the gate and hatchway doors, as indicated in Fig. 5. The spring holds the door closed when the coil of the electromagnet is deenergized. Energization of the coil attracts the iron-cored plunger and the consequent rotation of the lever opens the doors. Thus, at the exact floor level, positive action is ensured by having cog wheels, brakes and doors operated automatically by springs. This arrangement also provides emergency braking and closure of the doors in the case of interruption of the power supply.

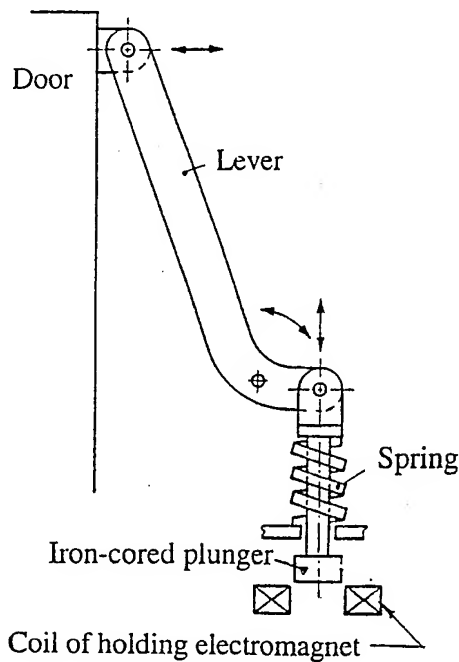


Fig. 5. Door opening arrangement.

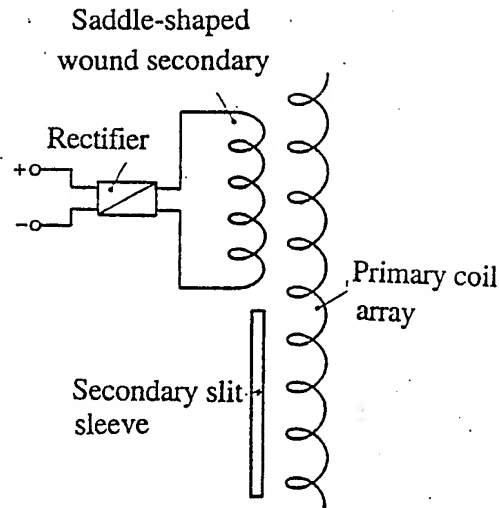


Fig. 6. Auxiliary power supply.

#### 4. Auxiliary supply

Another problem associated with ropeless hoist drives is the contactless supply of auxiliary power for lighting, air conditioning, and controls to the car. This is solved by adding at the end of each slit sleeve, a short saddle-shaped wound section which is attached to the car and is coupled electromagnetically as a secondary to the energized primary coils. As indicated in Fig. 6, it operates as a linear version of the wound-rotor induction machine. The frequency of its output is at slip-frequency  $sf$ , where  $s$  is the slip of the car past the electromagnetic wave traveling along the primary, and  $f$  is the primary frequency. Since the speed of the car, and with it the slip, vary with time, the output of the wound secondary is rectified by a rectifier. The energy thus transferred to the car must be stored in order to make this power supply an uninterruptible one.

In small installations, one can use a chemical battery. At present, their storage capacity, expressed in terms of specific energy, does not exceed about 100 kilojoule per kilogram weight (0.012 kWh/lb) [4]. Specific energies at least three times higher can be achieved with electromechanical energy storage [3]. With this arrangement, the dc output of the rectifier is transformed to ac in an adjustable-frequency inverter and fed into a synchronous machine which, operating in the motoring mode, drives a flywheel. The energy thus stored in kinetic form is "discharged" when the synchronous machine, acting now as a generator, is connected to the electrical load of the car.

## References

- [1] Z. Zabbar, X. N. Lu, E. Levi, L. Birenbaum and J. Creedon, "Experimental Results and Performance Analysis of a 500 m/sec Linear Induction Launcher (LIL)," IEEE Trans. on Magnetics, Vol. 31, No. 1, Jan. 1995, pp. 522-527.
- [2] "Air-Cored, Linear Induction Motor for Magnetically Levitated Systems," U.S. Patent No. 5,270,593, to E. Levi and Z. Zabbar, Dec. 1993.
- [3] Z. Zabbar, E. Levi and L. Birenbaum, "Air-Cored Linear Induction Motor for Earth-to-Orbit Systems," presented at the 3<sup>rd</sup> International Symposium on Magnetic Suspension Technology, Dec. 13-15, 1995, Tallahassee, Florida.
- [4] *Standard Handbook for Electrical Engineering*, D. C. Fink and H. Wayne Beaty, eds., McGraw-Hill Book Company, New York, 1987.

Appendix  
Preliminary Design

Performance Specifications [4]

|                           |  |
|---------------------------|--|
| Weight of loaded car      | $W = 3 \text{ tonnes (6614 lbs)}$              |
| Maximum speed:            | $v = 12 \text{ m/s (2,360 ft/min)}$            |
| Power:                    | $P = Wgv = 353 \text{ kW}$                     |
| Acceleration:             | $a = 3.0 \text{ m/s}^2 (9.8 \text{ ft/s}^2)$   |
| Retardation:              | $a_r = -4.0 \text{ m/s}^2 (13 \text{ ft/s}^2)$ |
| Emergency braking:        | $a_e = -19.6 \text{ m/s}^2 (2 \text{ Gee's})$  |
| Automatic leveling speed: | $v_l = v/10 = 1.2 \text{ m/s (236}$            |
| ft/min)                   |  |
| Air-gap clearance         | $c = 0.051 \text{ m (2")}$                     |

The conveyance is pressurized to avoid objectionable rapid changes of air pressure. A preliminary design yields the following dimensions for the motor elements

|                            |   |
|----------------------------|---|
| <u>Primary coils</u>       | $OD_1 = 0.248 \text{ m (9.76")}$                    |
|                            | $ID_1 = 0.208 \text{ m (8.18")}$                    |
| Material:                  | aluminum  |
| Weight:                    | $38.6 \text{ kg/m (29.95 lb/ft)}$                   |
| <u>Passive secondaries</u> | $OD_s = 0.39 \text{ m (15.35")}$                    |
|                            | $ID_s = 0.35 \text{ m (13.78")}$                    |
| Material:                  | aluminum  |
| Weight:                    | $4 \times 135 \text{ kg (4} \times 297 \text{ lb)}$ |

where OD represents outside diameter and ID represents inside diameter. The energy needed for the electrical load of the conveyance is stored in the flywheel motor/generator set with specific energy of 236 kJ/kg (0.03 kWh/lb), a conservative estimate.

# Physics of Plasma-Fluid Interaction - Key to a Complete Numerical Model of the ET-Gun

Karl Darée, Dieter Hensel and Klaus Zimmermann  
French-German Research Institute Saint-Louis, 68301 Saint-Louis, France

**Abstract:** Energy transport between a plasma and a working fluid is by radiation, conduction and convection. Comparing computational and experimental results, strong indications were found for a predominantly radiative transfer enhanced by deformations of the plasma-fluid interface. A new version of the ISL code, ETK1C, accounts for this enlargement of the effective arc surface and models the whole system from the electrical circuit to the projectile.

Three different situations have been studied: discharges without any liquid material, liquid inside and liquid outside the plasma generator. With an empty discharge tube, the arc surface is not perturbed. With liquid in the discharge tube, surface enhancement factors of the order of 30 give excellent agreement with experimental data, both for shots in the gun and shots in a closed vessel. Computations for a plasma jet interacting with liquid outside the plasma generator indicate a less significant perturbation of the jet surface. For shots at moderate energy, a considerable fraction of the external liquid appears to be accelerated in condensed phase together with the projectile.

## I. INTRODUCTION

The propelling gas in an ET-gun is generated by energy transfer from a hot plasma to some evaporable, condensed material. The first theoretical models describing this process were based on the conception of a wall-stabilized arc [1], [2], [3]. A vapour layer [4] between plasma and wall was considered in some of these descriptions [1], [5]. It was soon recognized as indispensable to couple the arc models with interior ballistics in order to determine the pressure history at the front end of the plasma generator. Codes offering such a treatment in closed form have meanwhile become available [5], [6] and have been successfully applied to the simulation of shots fired with an empty, ablating polyethylene tube as a plasma source [5], [7].

Introducing working fluid into the gun - preferentially into the discharge tube itself, - the efficiency of the gun could be improved [8], but the theoretical description of the plasma-fluid interaction remained unclear until recently. Comparing results from the ISL code ETK1, version A, to

experimental data, strong evidence was given for a preponderance of radiative energy transfer over transfer by convective mixing of plasma and vapour [9]. An additional vapour-plasma mass flow proportional to the radiated power had to be introduced to reproduce the measured arc resistances. The conclusion was that the radiating surface is increased by turbulence and, maybe, by the formation of liquid droplets.

In the meantime a new version ETK1C of the ISL code has become operational. It works with a radically reduced set of free parameters by modelling the electrical circuit (ETK1A required the measured power as an input) and by replacing the extra vapour-plasma mass flow (with its critical influence on the plasma resistance) by a nearly constant enlargement factor for the arc surface.

ETK1C will be briefly presented in section II. Section III is devoted to the comparison of computed results to experimental ones obtained under quite different conditions (shots with and without liquid, shots in a gun and in a closed vessel, liquid inside and outside the plasma generator). Our concept of arc surface enlargement will turn out to be successful in all investigated situations and to allow conclusions on the physics of plasma-fluid interaction.

## II. NUMERICAL MODEL ETK1C

ETK1 is a one-dimensional interior ballistics code with spatial resolution in axial direction including a model of the arc section, which is sketched in Fig.1. The plasma is treated as a cylindrical blackbody radiator of average temperature  $T$  surrounded by concentric layers of vapour (temperature  $T_v$ ) and working fluid (or ablating wall material). The radiated intensity  $\sigma T^4$  is absorbed in the plasma boundary layer (absorption coefficient  $A_p$ ), in the vapour ( $A_v$ ) and in the condensed material ( $A_w$ ). Heat transfer by conduction and convection can be modelled by defining non-zero transfer coefficients  $c_{pv}$  and  $c_{vw}$  for plasma-vapour and vapour-fluid transfer. Mass flows  $\dot{m}_v$  and  $\dot{m}_p$

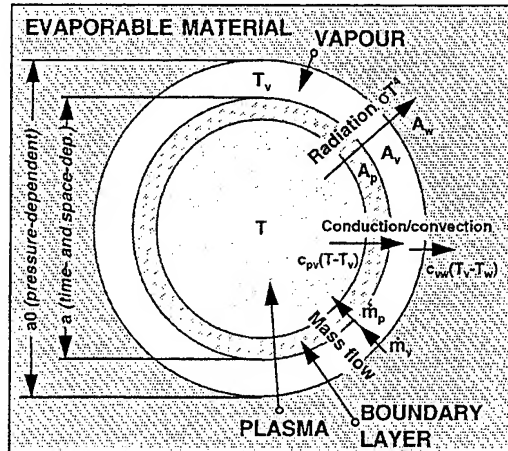


Fig.1: Arc model of ETK1

are released by the absorbed radiation and by the conductive-convective transfer. The thickness of the vapour layer  $0.5(a_0-a)$  is determined by these mass flows in radial direction, the vapour flow in axial direction (assumed as stationary), the computed pressure  $p(z)$  ( $z$  is the axial coordinate) and the average vapour temperature  $T_v$ , which has to be estimated (usually  $T_v=4000$  K). The inner tube diameter  $a_0(z)$  is space-dependent and is approximately computed from the bulk modulus of the condensed material, the local pressure and the time-integrated, ablated mass at the position  $z$ . The arc diameter  $a(z)$  is immediately obtained from  $a_0$  and from the thickness of the vapour layer.

The most important features of ETK1 are compiled in Tab.I. To increase the speed of the computation, the equations of state (pressure  $p$  and internal energy  $\varepsilon$ ) and the electrical conductivity  $\sigma_{el}$  were determined in advance and tabulated as functions of density and temperature. The radiation absorption coefficients were obtained from computed plasma opacities [10] and, in the case of  $A_p$ , from a radiation transport code [5], [11]. They are strongly temperature-dependent. The pressure dependence is less critical; it is sufficient to guess an average pressure before each run of ETK1.

ETK1 starts with reading the usual shot parameters (gun geometry, projectile mass, barrel length). For the timestep, a time-split MacCormack method is applied. We compute in every mesh point  $z_n$  the energy flow and the corresponding mass flows. As indicated above, the arc diameter is determined from the mass conservation for the vapour and from the pressure-dependent tube diameter  $a_0$ .

| PREPARATIVE WORK   |                            |   |
|--|----------------------------|---|
| Generate tables $p(\rho, T)$ , $\varepsilon(\rho, T)$ , $\sigma_{el}(\rho, T)$<br>$A_p(\rho, T)$ , $A_v(\rho, T)$ , $A_w(\rho, T)$ |                            |   |
| INPUT OF SHOT DATA   |                            |   |
| TIME STEP  |                            |   |
| for each $z_n$   | Energy flow                | Radiation, conduction and convection  |
|  | Mass ablation              | Rates $\dot{m}_p$ and $\dot{m}_v$ depending on energy flow                  |
|  | Vapour layer, arc diameter | Approx. solution of mass conservation for vapour, pressure-dep. tube radius |
|  | Hydrodynamics              | Solution of cons. eqs. (MacCormack)   |
| for each $z_n$ in arc  | Arc heating                | From current, local conductivity, arc diameter                              |
| once per step  | Arc resist. $R_p$          | Integration over arc length   |
|  | Current                    | From circuit, $R_p$ and $\partial R_p / \partial t$                         |
|  | Projectile motion          | From extrapolated pressure  |
| OPTIONS  |                            |   |
| Arc surface enlargement (time-dependent)   |                            |   |
| not used: Moving arc   |                            |   |
| Limitation of evaporable mass  |                            |   |
| Simulation of burst plate  |                            |   |
| Projectile starting pressure $> 0$   |                            |   |
| Delayed boiling of working fluid   |                            |   |

Tab.I: ETK1C - overview

Within the arc section, ohmic heating is computed from the instantaneous current and from the resistance  $dR_n$  of mesh number  $n$  depending on the local conductivity and on the arc diameter. This is a new feature, which was not available in the old code version A, where the given electrical power was evenly distributed along the arc. The arc resistance  $R_p$  is easily obtained as the sum of all  $dR_n$ . The current is computed by the subroutine CIRCE, which is the essential innovation in the code version C. CIRCE models a RLC-circuit with crowbar diode and uses as an input the plasma resistance  $R_p$  and its temporal derivative.

As an option, a time-dependent surface enlargement factor can be introduced to describe deviations from the ideal, cylindrical arc surface originally assumed in our model (see Fig.1). It is the primary aim of the present work to study the influence of this factor and, by comparison with experimental data, to give informations on its magnitude under different experimental conditions. Some additional options are available with ETK1C and are quoted in Tab.I. They are not switched on for the present computations.

### III. SIMULATION OF REAL SHOTS AND DISCUSSION

Computational results will be presented for four representative shots covering the range of experimental conditions studied at our institute. The four shots are characterized in Tab.II. Three of them were fired in a small gun (calibre 12 mm, projectile mass 5 g), one in a closed vessel. With 100 kJ stored, the energies fed into the arc varied between 36 and 67 kJ. Methanol was used as a

| Shot | Gun | Vessel | CH <sub>3</sub> OH (2 g)<br>in cap. outside | Energy<br>(kJ) |
|------|-----|--------|---|----------------|
| 1    | x   | -      | - -   | 36             |
| 2    | x   | -      | x -   | 63.6           |
| 3    | -   | x      | x -   | 66.9           |
| 4    | x   | -      | - x   | 37.4           |

Tab.II: Selected shots

working fluid; in shot 1 there was only ablation from the PE walls of the discharge tube. The experimental geometries are sketched in Fig.2.

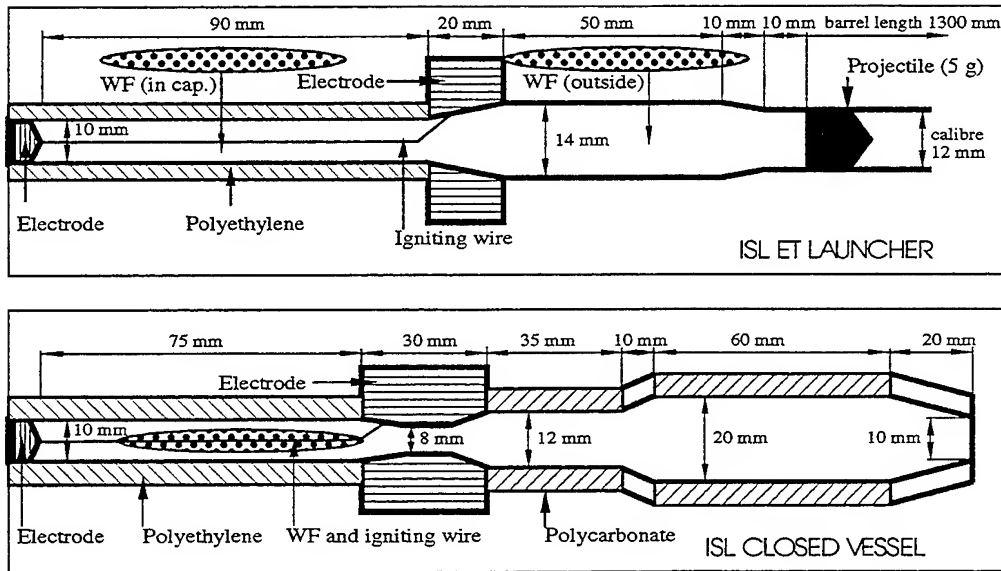


Fig.2: Geometry of ISL experimental apparatus (gun and closed vessel)

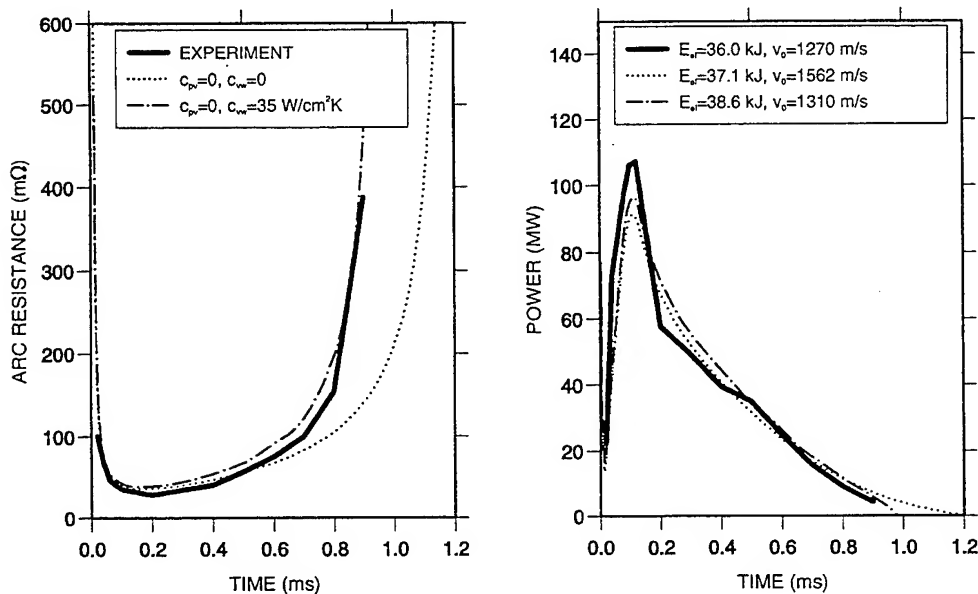


Fig.3: Shot 1, experimental and computational results for arc resistance and electrical power



Fig.3 shows experimental results for the arc resistance and the electrical power dissipated in the arc section of the ISL ET gun during shot 1 (thick, solid lines). Neglecting conductive and convective transport towards the tube walls, the dotted lines have been computed with ETK1C. There is good agreement with the experimental results for the first 0.5 ms, but the computed discharge burns longer than the observed one. Introducing a vapour-wall heat transfer coefficient of reasonable magnitude, the agreement between the measured and the computed data (dash-dotted lines) is considerably improved. No other free parameter has entered this computation. With regard to the plasma temperature of more than 20000 K, the amount of lost energy (69% of the computed total energy of 38.6 kJ) is of the expected order of magnitude. The computed mass of ablated polyethylene (0.36 g) corresponds to the measured ablated mass and the muzzle velocity (1310 m/s) comes close to the experimental one (1270 m/s). Neglecting conductive-convective transfer, the computed muzzle velocity is too high (1562 m/s) as could have been expected. Summarizing it can be said that shots without additional working liquid are well understood if the heat losses by conduction and convection are accounted for in addition to the radiative losses.

Results obtained with 2 g of methanol (contained in a plastic bag) inside the discharge tube, are presented in Fig.4. The minimum arc resistance is higher by a factor of 5, the discharge duration is considerably shorter and the dissipated energy is larger in comparison to shot 1. Considering enhanced convective transfer due to deformations of the liquid surface ( $c_{vw}=150 \text{ W/cm}^2\text{K}$  instead of  $35 \text{ W/cm}^2\text{K}$  for shot 1) is not sufficient to explain the experimental results; the computed arc resistance (thin, solid line) is by far too small, the pulse duration too long and the muzzle velocity far below the measured one.

It is the basic idea in ETK1C to introduce a nearly constant (see dotted line in the insert of Fig.5a) enlargement factor for the radiating surface. Factors of 10, 20 and 30 have been used for computations. With a surface 30 times larger than that of the originally cylindrical arc, an excellent agreement between measured and computed resistances is obtained (dotted line in Fig.4). At the same time, the computed muzzle velocity is fully satisfactory (it should be slightly larger than the measured one as friction and gas leakage are not considered). The ablated mass corresponds to the mass of the liquid (2 g) plus 0.17 g of PE. Differences persist between measured and computed gas pressures. They are possibly due to a mechanical preload of the gauge in its mounting.

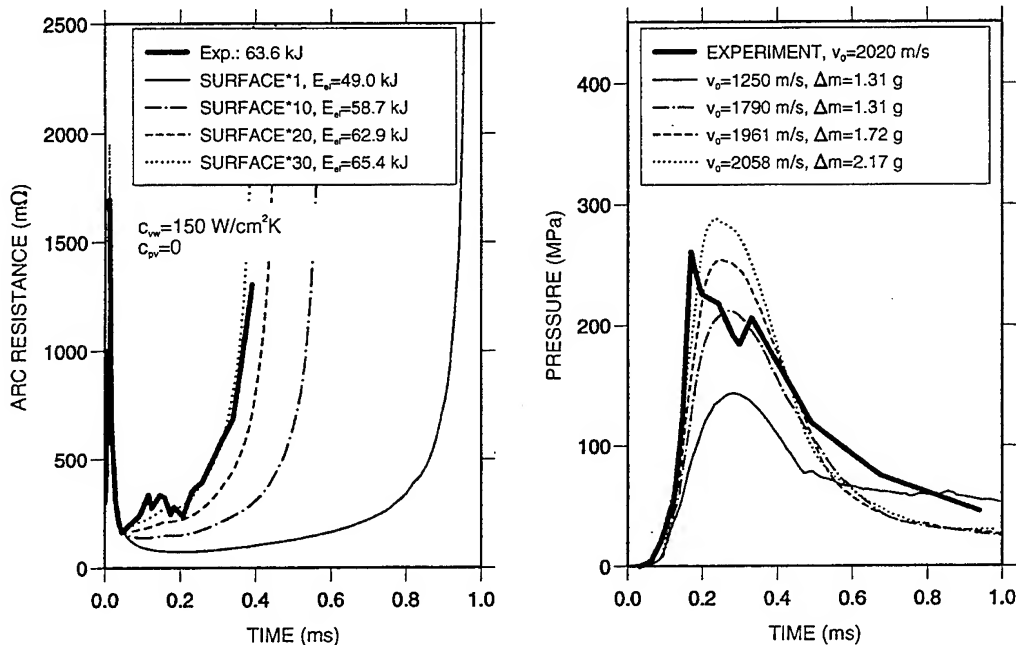


Fig.4: Shot 2, measured and computed arc resistances and pressures (at initial position of projectile)

It is interesting to test our conception of arc surface enlargement due to turbulence for the case of shot 3, which was fired in the closed vessel under the same conditions as shot 2. Repeating the computation with identical parameters but accounting for the different geometry, we obtain the dotted lines shown in Fig.5a for the arc resistance and for the electrical power. The agreement with the experiment is good for times  $>0.1$  ms. For early times, considerable improvement is achieved

by assuming a prompt onset of the arc surface perturbation (dash-dotted lines); for shot 2, a delay of  $50 \mu\text{s}$  had been assumed (see insert). The enlargement factor was 30 in both cases.

Pressures inside the arc and near the closed end of the vessel are shown in Fig.5b. The computed pressures oscillate slightly stronger than the measured ones; the magnitudes and oscillation frequencies are in good agreement as well as the ablated masses  $\Delta m$  of methanol and plastic material.

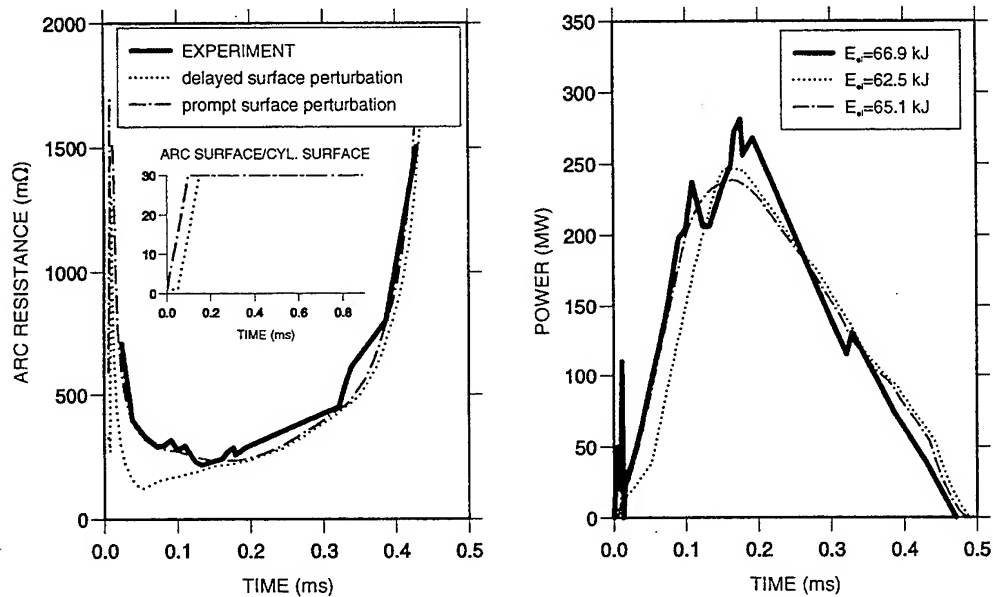


Fig.5a: Shot 3, arc resistance and electrical power. Computations for prompt and delayed arc surface perturbation.

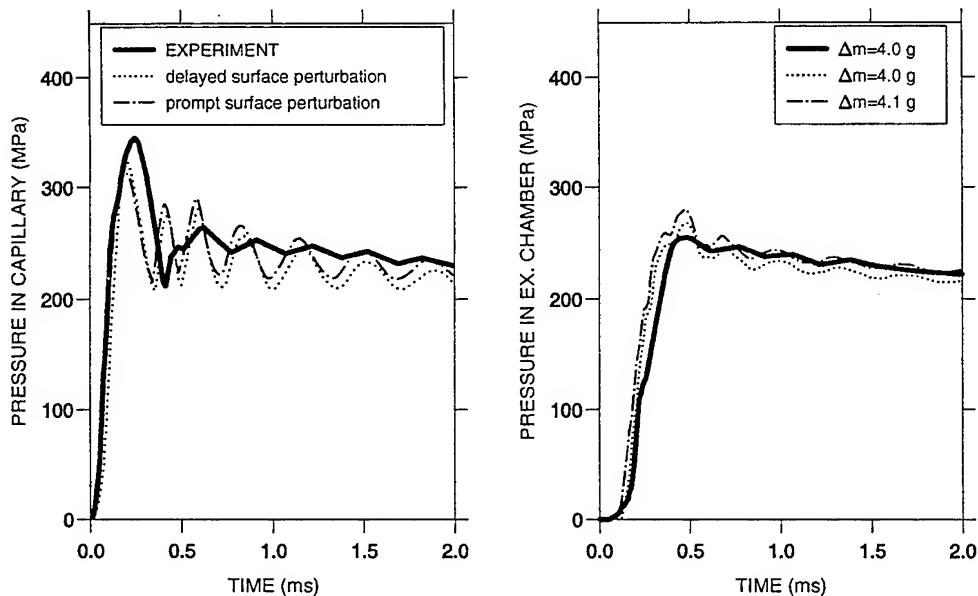


Fig.5b: Shot 3, measured and computed pressures (left: inside the discharge tube, right: near closed end of vessel)

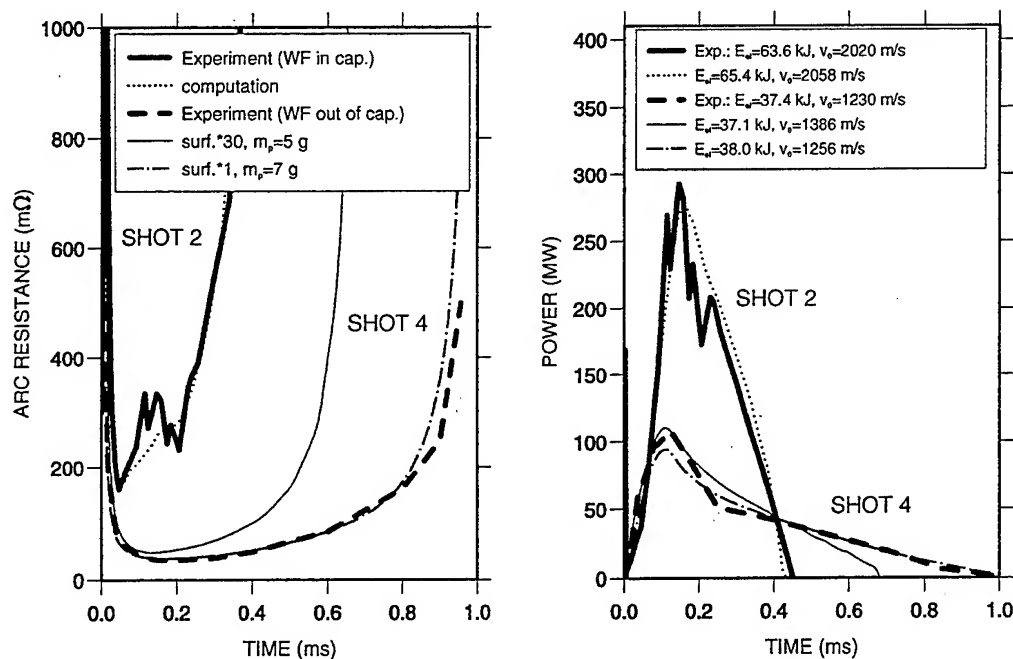


Fig.6: Comparison of shots 2 (WF in capillary) and 4 (WF outside), arc resistance and electrical power. Computations for shot 4 with and without enlarged plasma jet surface.

With working fluid outside the discharge tube (righthand position in Fig.2), the measured arc resistance (shot 4; thick, dashed curve in Fig.6) resembles, as expected, that of shot 1 without any liquid added (see Fig.3). The quite different result with liquid inside the capillary (shot 2) is shown in Fig.6 for comparison.

In a first computation, we have again assumed a surface enlargement factor of 30, which is not applied to the arc section but only to the plasma jet outside the discharge tube. The result is given as a thin, solid line. Up to a time of 0.4 ms, the resistance and, in particular, the electrical power are in satisfactory agreement with the experiment. Later, the computed resistance increases faster than the measured one and the duration of the discharge is too short by about 0.3 ms.

For a less pronounced enlargement of the radiating surface, the radiative losses diminish with the result of a higher plasma temperature and of a lower arc resistance. To study a limiting case, the plasma jet was assumed to be perfectly cylindrical (surface \*1). In this case the radiative transfer is not sufficient to evaporate the two grams of added methanol completely; only 0.6 g were ablated during the shot duration in the computation. It is therefore assumed that the methanol is accelerated together with the projectile (total accelerated mass 7 g). The computational results, shown as dash-dotted lines in Fig.6 are in nearly perfect agreement with the experiment concerning the arc

resistance, the duration of the discharge and the muzzle velocity. The computed total energy fed into the arc is close to the measured one for both types of computation.

#### IV. CONCLUSIONS

We have studied four different types of experiments in relation with electrothermal acceleration by numerical simulation of the complete system of electrical circuit, arc, interior ballistics and projectile acceleration. From a comparison with experimental results, the following conclusions on heat transport between plasma and working medium have been drawn:

- Working medium and tube walls are heated by radiation but also by a non-negligible energy flow due to conduction and convection.
- Between plasma and vapour, radiative transfer is preponderant and enhanced by deformations of the radiating surface as soon as liquid material is present as a working medium.

The first of these conclusions is a rather trivial one; it is well-known from classical ballistics that of the order of 30% of the total energy are lost by conductive-convective transfer to the tube walls. In the case of the ET gun, the losses (about one half radiative, the other convective) are of the order of 70% of the total energy without liquid,

55% with liquid outside and 40% with liquid inside the discharge tube.

Without a working liquid, convective transfer between vapour and tube walls is sufficient to explain the experiments. There is no indication for an enlargement of the arc surface; the geometry is well-defined by the solid walls.

With liquid inside the plasma generator, the assumption of a thirty-fold increase of the radiating surface excellently reproduces the experimental results in the gun as well as in the closed vessel. A small temporal delay of the surface deformation is stated in case of the gun. The magnitude of the effective, radiating surface concluded from the simulations can be explained by a strong perturbation of the liquid by turbulence, by blow-out of liquid from the discharge tube and, eventually, by a formation of droplets. It is remarkable that a constant surface enlargement factor (preceded by a linear growth over a time of 100  $\mu$ s) is sufficient to explain the experiments. This could be an indication that droplet formation and evaporation, which should introduce some time-dependence, are not of crucial importance.

When the liquid is outside the plasma generator, there is certainly some perturbation of its surface, but a less pronounced one than with liquid inside. The comparison of computations and experiments has indicated an enlargement of the plasma jet surface by a factor of clearly less than thirty. The influence of the plasma jet perturbation on the simulation results is not sufficient to quote an exact number here. Direct visualization by X-ray techniques could help to improve the model.

Concluding, it can be said that the processes governing heat transfer from the plasma to the working medium have been identified and, to some extent, quantified. This will be helpful in designing models for convective transfer and arc surface deformation in future two- and three-dimensional codes. On the experimental side, the interaction of the arc plasma with inert powders should be investigated in order to determine - as for liquids - the effective surface for radiation absorption. It is expected that the theoretical description of gun powder ignition by a plasma can profit from an investigation of this type.

## REFERENCES

- [1] P. Kovitya and J.J. Lowke, „Theoretical predictions of ablation-stabilised arcs in cylindrical tubes“, *J.Phys. D17*, 1197 (1984).
- [2] A. Loeb and Z. Kaplan, „A theoretical model for the physical processes in the confined high pressure discharges of electrothermal launchers“, *IEEE Trans. Magnetics* **25**, 342 (1989).
- [3] J.D. Powell and A.E. Zielinski, „Capillary discharge in the electrothermal gun“, *IEEE Trans. Magnetics* **29**, 591 (1993).
- [4] A.D. Stokes and L.J. Cao, „Ablation arcs I: arcs in ice“, *J. Phys. D22*, 1697 (1989);  
A.D. Stokes, H. Sibilski and P. Kovitya, „Ablation arcs II: arcs in plastic materials and in boric acid“, *J. Phys. D22*, 1702 (1989).
- [5] K. Darée, D. Hensel and N. Silvestre, „Eindimensionale Modellrechnungen zum elektrothermischen Beschleuniger des ISL“, Report *R 127/94*, ISL, Saint-Louis (1994).
- [6] E. Jacob, S. Bouquet and B. Tortel, „A global theoretical approach for the electrothermal gun: scaling laws and a 0-D time-dependent model“, *IEEE Trans. Magnetics* **31**, 419 (1995).
- [7] E. Jacob, S. Bouquet, P. Noiret, L. Véron, S. Roux, K. Darée, D. Hensel and K. Zimmermann, „Experiments and modelling of high energy ET-gun shots: comparisons between ISL and CEA approaches“, Proc. 5th Europ. Symp. on EM Launch Technology, April 10-13, 1995, Toulouse, France.
- [8] K. Zimmermann, J. Raupp, D. Mura and C. Steinbach, „Parametrische Untersuchung an einem elektrothermischen Beschleuniger vom Kaliber 12mm“, Report *RT 514/92*, ISL, Saint-Louis (1992).
- [9] K. Darée, D. Hensel and K. Zimmermann, „Plasma-fluid interaction and arc resistance in electrothermal launchers“, 8th EML Symp., April 21-24, 1996, Baltimore, MD, to appear in *IEEE Trans. Magnetics*.
- [10] A. Rickert, K. Eidmann, J. Meyer-ter-Vehn, F.J.D. Serduke and C.A. Iglesias eds., „3rd Int. Opacity Workshop & Code Comparison Study WorkOp-III:94“, MPI für Quantenoptik, Report *MPQ 204* (1995), Garching, Germany.
- [11] K. Darée and D. Hensel, „Modellierung der elektrothermischen Beschleunigung. Konzept und erste Ergebnisse“, Report *R 108/91*, ISL, Saint-Louis, France.

## **40mm Armature Development at the Defence Research Agency**

DC Haugh  
Defence Research Agency  
Fort Halstead, Sevenoaks, Kent, TN14 BP, UK

### **ABSTRACT**

The Defence Research Agency has an active research programme looking at electromagnetic launchers for tactical applications. Solid armature firings are conducted at both 90mm and 40mm calibres. This paper concentrates upon recent work in developing a satisfactory design of 40mm armature to allow firings at velocities up to  $2500 \text{ ms}^{-1}$  to be undertaken. Both material variants and design changes have been examined in the quest for a reliable armature, and finite element modelling has been used to predict behavioural trends and indicate the most promising approaches. The paper contains details of the modifications tried and results of actual firing trials.

### **INTRODUCTION AND DESIGN CONSIDERATIONS**

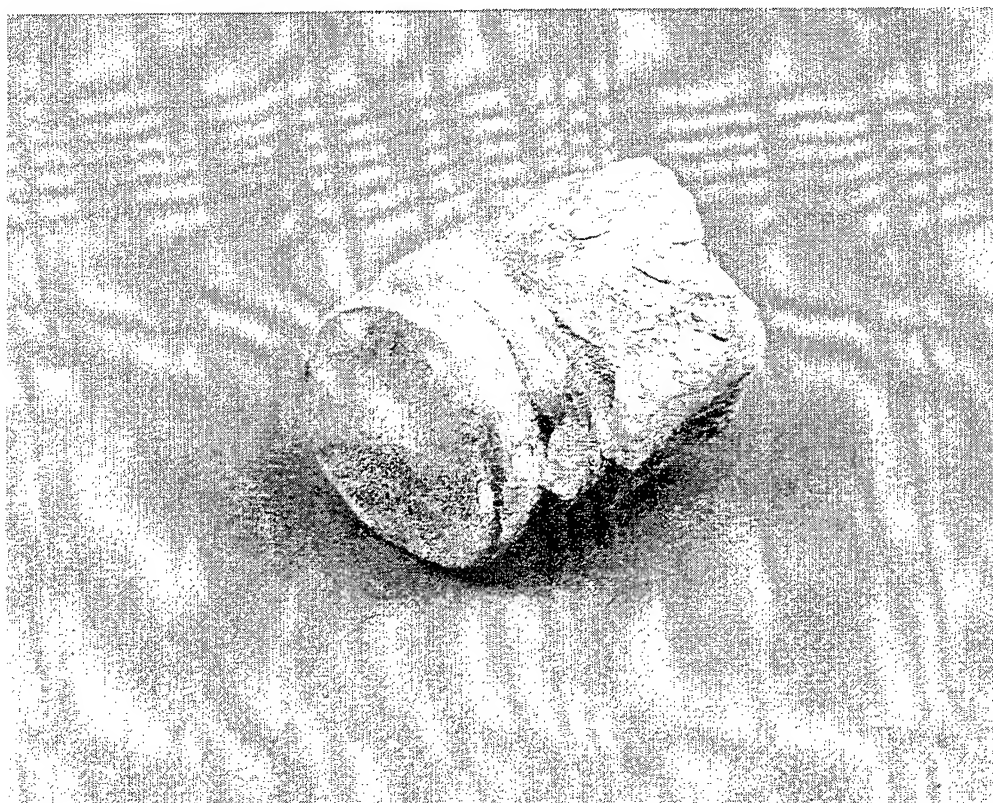
Previous papers at EML Symposia, Refs 1 and 2, have detailed the work undertaken by the Defence Research Agency in their EM gun research programme. In the most recent (Ref 1), an explanation of the methodology used by the DRA was given, and this approach has been continued in the work reported here. At the velocities of interest, ie  $>2000 \text{ ms}^{-1}$ , all 40mm solid armatures fired have transitioned to plasma, and it is felt that this phenomenon is unlikely to change with the round bore configuration currently under test. Work remains to be done in quantifying the differences between round, square or other geometry to determine the most efficient format for a railgun. There are indications that square will have advantages over round for the armature alone. These could include more uniform current flow from rail to armature and the use of concepts not applicable to a round bore. However, there could be penalties in the design of the sabot and projectile, so a full system analysis is needed to determine the actual benefits.

To date, all work has been done with base-push armatures. It is intended to carry out some tests on mid-riding concepts, but this will be reported at a later date. The results from the work presented here should be equally applicable to any other design, since the tests are aimed at identifying the particular requirements of solid armatures. It is becoming clear that the successful armature of the future will not be a simple monobloc material, but will be composed of a number of different materials, each bringing their own unique properties to a particular region of the armature. Thus, the front part, which is in contact with the projectile, needs to be strong to transmit force forwards.

In a conventional powder gun, a 'pusher plate' is used to transfer loads from the propelling gases to the projectile across the whole bore area. At 90mm calibre, this weighs in excess of 0.7kg. Any reduction in this mass results in structural failure of the plate under peak acceleration forces. A solid base-pushing armature has to fulfil a

similar function, transmitting force from the rear of the armature to the projectile. However, the armature also has to carry out a number of other duties as well. It must carry significant currents and suffer the inevitable thermal consequences, with all the strength reductions that such action brings. Therefore, it is naive to suppose that a base-pushing armature can weigh less than its powder gun equivalent. The current 90mm armature mass of over 1kg can be reduced, but not by as much as is first thought.

Solid armatures at 40mm calibre are heavier per unit bore area than 90mm armatures because of the greater thermal input to the smaller volume of metal. Recovery of fired 40mm armatures is much worse than for the larger calibre ones, since their mass and size is so much smaller. From the limited number recovered, and from examination of muzzle flash radiographs, it is clear that they suffer more bulk melting and mass loss than their larger counterparts. Fig 1 shows what remained after a typical shot at a velocity exceeding  $2000\text{ms}^{-1}$ . The mass loss was over 50%. The piece is almost unrecognisable as an armature.



**Fig. 1 Recovered 40mm armature from  $2000\text{ms}^{-1}$  firing.**

The rear portion of the armature needs to have very good electrical conductivity, especially at smaller calibres. This material property is normally inversely related to strength. It may be possible to obtain some benefits in strength without sacrificing conductivity by moving to a metal matrix alloy, but this has not yet been proven. This paper will describe some experiments using multi-material armatures in the search for increased performance.

One of the most important factors governing railgun launch performance is the production of rail defects. This tends to occur around the transition region from solid-solid contact to a plasma arc. Gouges are also seen at other places in the bore, but are worst in the region where the contact type is changing. Once transition has occurred, the efficiency falls due to the greater electrical resistance, but this effect is not the most significant. The hot plasma gases can severely affect the armature structure in a number of ways. The pressure can lead to failure in the seal between projectile and gun, sometimes with catastrophic effects on both. Erosion of the armature material from random positions can increase in-bore balloting, as can one-sided plasma forces. If solid armatures are to transition, then efforts need to be made to try and control this phenomenon.

## FIRING TRIALS AND DISCUSSION

Refs 1 and 2 detailed the earlier DRA work at 40mm calibre. In that time, preliminary experiments were conducted to try and identify the materials properties required of solid armatures. They showed that conductivity was the paramount parameter at this calibre, though not the only one. Thus, A7075 alloy was replaced by A6082. This had lower strength but better conductivity. Taking a further step to pure aluminium proved to be a retrograde step, since the lack of strength became the prime issue. Unless otherwise stated, all armatures discussed here were manufactured from A6082 alloy. It was also becoming clear that different properties were needed in different parts of the armature. A schematic is shown in Fig. 2.

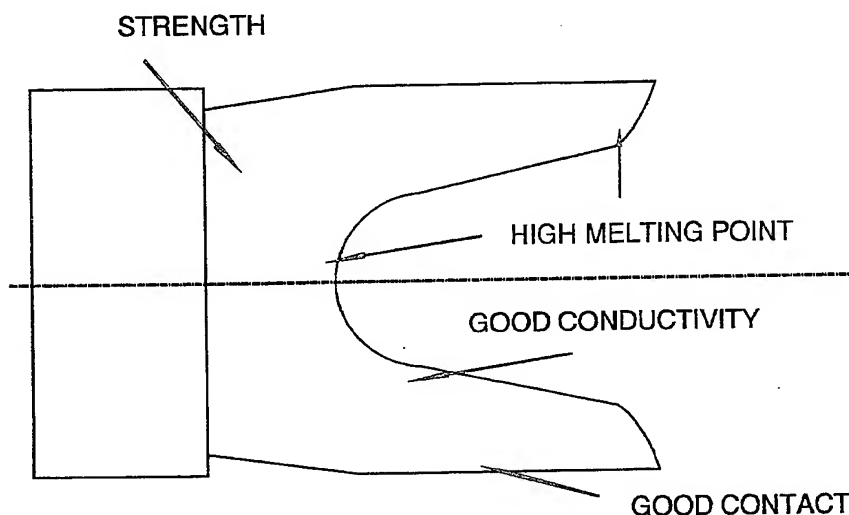


Fig. 2 Armature property requirements.

Two firings were therefore undertaken using a simple two piece armature. This employed A7075 for the forward portion, and pure aluminium for the rear. The first armature was made by shrink fitting the two parts together. Unfortunately, this failed in-bore at peak pressure, and exited the gun in pieces at a much lower velocity than predicted. A stronger interface joint was required. The second armature was made by friction welding the two halves together. This was fired successfully at  $1618\text{ms}^{-1}$ , leaving behind the usual residue of smeared aluminium on the rail surfaces. Data for the 40mm shots is given in Table 1.

**Table 1. Summary of 40mm Firing Data.**

| Shot # | Description                    | Mass (kg) | Velocity ( $\text{ms}^{-1}$ ) | $I_{\text{peak}}$ (MA) | Notes                         |
|--------|--------------------------------|-----------|-------------------------------|------------------------|-------------------------------|
| 54     | 2 part shrink fit              | 0.381     | 1506                          | 1.3                    |                               |
| 57     | 2 part friction weld           | 0.345     | 1618                          | 1.04                   |                               |
| 58     | Cone taper legs                | 0.343     | 1694                          | 1.04                   |                               |
| 59     | ditto                          | 0.344     | 1699                          | 1.04                   |                               |
| 60     | ditto                          | 0.356     | 2463                          | 1.51                   |                               |
| 61     | ditto                          | 0.355     | 2380                          | 1.36                   |                               |
| 64     | full proj mass-slack interface | 0.409     | 2101                          | 1.0                    | New 8 metre gun, CuCr rails   |
| 65     | ditto                          | 0.411     | 2139                          | 1.17                   |                               |
| 66     | ditto                          | 0.407     | 1908                          | 0.93                   |                               |
| 80     | full proj mass-good interface  | 0.412     | 2114                          | 1.15                   |                               |
| 81     | ditto                          | 0.412     | 2123                          | 1.15                   |                               |
| 82     | Steel rod through armature     | 0.253     | 1774                          | 0.83                   |                               |
| 83     | as for #81                     | 0.411     | 2596                          | 1.2                    |                               |
| 84     | ditto                          | 0.411     | 2369                          | 1.15                   |                               |
| 85     | ditto                          |           |                               |                        | No divotting to date on rails |



All the early DRA solid armatures had the legs profile milled so that on loading into the gun, they had the maximum surface area contact with the rails. This was an expensive and time consuming operation, and trials were next conducted with a simple turned cone design on the legs to produce the required interference. This meant that at shot start, only part of the armature surface was in contact with the rails.

Four shots were fired sequentially, at velocities from  $1700\text{ms}^{-1}$  to  $2463\text{ms}^{-1}$ , and at peak accelerations beyond 100 kilogeeks. Comparison of the data with that from the earlier more costly design variants showed them to be indistinguishable. Attempts were also made to obtain in-bore Doppler tracking data to complement the normal B-dot signals, with a view to identifying the early shot start situation more clearly. The small calibre meant that aligning the radar beam was critical and good results were not always obtained.

Round masses for the above shots were approximately 0.35kg. The forebody was a simple turned aluminium alloy mass bolted to the armature. Designs of fully discarding long rod projectile packages were some 70 grams heavier than this armature proof shot. It was clear that in order to fire 40mm APFSDS projectiles at velocities exceeding  $2500\text{ms}^{-1}$ , the existing hardware would be inadequate. The launcher was therefore extended from five metres to eight metres in length, and the rail material was improved. Previous rails had been made from plain C101 copper, which had poor strength, and therefore poor resistance to rail gouging. The new eight metre long rails were manufactured from copper-chromium alloy, which was considerably harder than its predecessor. Continuous lengths were not readily available in the UK, so two abutting pieces were electron beam welded together to produce the single long rail stock.

With the new long gun, all round masses were of the order of 0.42kg. A representative mass was designed to simulate the full projectile both in terms of mass and wheelbase of the contact positions. Three shots were fired at velocities around the  $2000\text{ms}^{-1}$  mark. The longer launcher meant that peak accelerations could be lower than before. With a peak current of 1MA, a velocity of  $2101\text{ms}^{-1}$  was obtained with the first shot. Muzzle X-rays revealed evidence of plasma blow-by forward of the armature, with some arcing from the forebody to the launcher. The second shot, fired with only a quick cleaning of the bore using dry rags, aimed for the same velocity but with a greater peak current pulse. Similar results were observed.

The armatures in the above shots transitioned to plasma within the launcher before shot exit. The third shot was fired at a lower velocity, to try and determine an onset velocity for sealing failure. At  $1908\text{ms}^{-1}$ , results again showed a failure of the band connecting the armature to the forebody. For these shots, the interface between the two components was somewhat flexible. An error in machining meant that there was some axial play between the two pieces, but no radial movement was possible. At that time, and even now, it is not possible to be positive about the rigidity required between armature and forebody (or projectile). It is not clear how the two parts act and react during the launch process in-bore. More trials are needed to identify this factor.

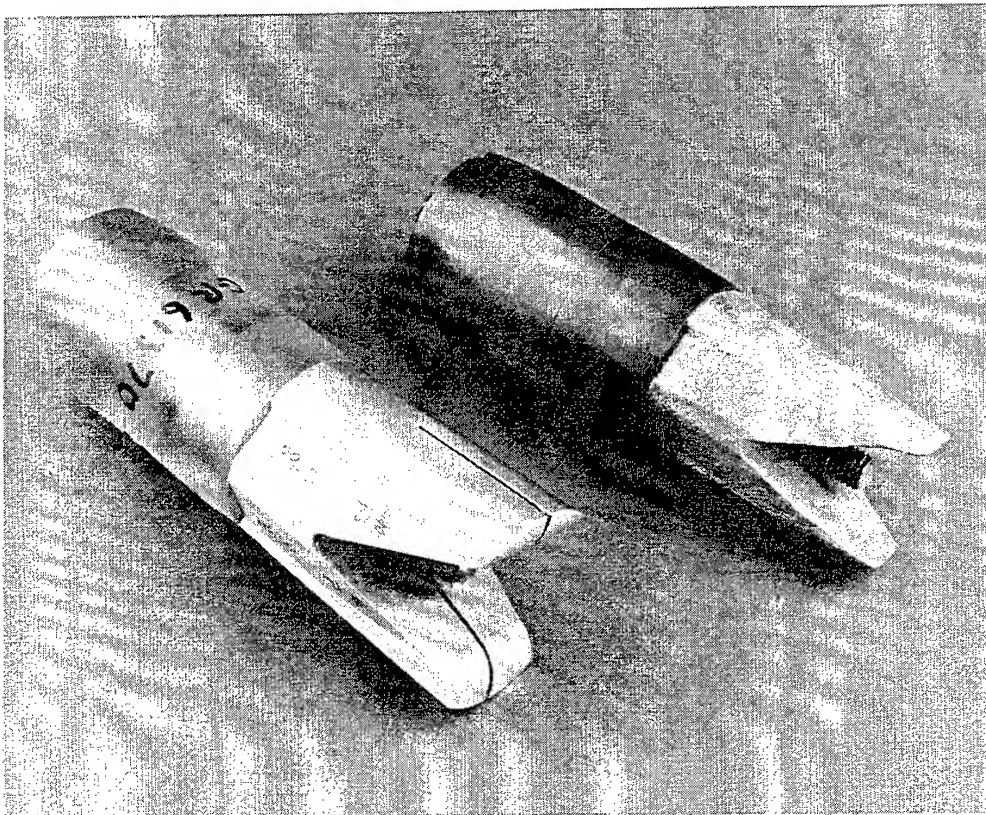
The most significant observation from these three firings was the complete lack of rail gouges after the shots. With plain copper rails, gouges were observed every time an armature transitioned and exceeded about  $1400\text{ms}^{-1}$ . This benefit, though not wholly unexpected, has led to increased rail life, and helps to positively explain the formation of rail gouges as a purely mechanical effect. Further examination of this area of work is beyond the scope of this paper, but may be presented in the future.

A repeat series of firings was undertaken with forebodies correctly machined. This produced a flight package with a relatively stiff interface. Four shots were fired at velocities exceeding  $2000\text{ms}^{-1}$ . Two had velocities around  $2100\text{ms}^{-1}$  and two about  $2500\text{ms}^{-1}$ . The first two performed well, with no signs of plasma leakage, and velocities close to predicted levels. At the higher velocities, however, the forebodies suffered physical damage in-bore. During the first shot, the body fractured and was observed to arc from a velocity of about  $2200\text{ms}^{-1}$ . In the second firing, the body bent, and plasma formed at around  $2150\text{ms}^{-1}$ .

During this firing series, an additional novel shot was fired. Though the DRA programme has concentrated upon base pushed designs, it has long been recognised that a mid-riding sabot-armature concept could have benefits for some package designs. Accordingly, an armature was designed with a steel rod passing centrally through it. The centre of a solid armature carries the greatest current, so its removal could give problems with modified current flow, perhaps even through the replacement rod. The rear protruding rod also sits in the centre of any plasma arc formed after transition, and is obviously susceptible to thermal attack. The trial was the first in a series planned with increasing complexity as designs move towards a real-life situation with discarding sabot/armature segments.

The package was fired at a conservative velocity of  $1774\text{ms}^{-1}$ , and excellent diagnostics were obtained. However, the fired package was recovered down range and is shown in Fig. 3 together with an unfired one. The material loss from the armature is clear, but the steel rod, which was painted before firing, suffered virtually no damage. This result bodes well for future shots with mid-riding armature designs.

The poor sealing of the centring bands at high velocities in the above trials led to a redesign of this component. There is very little space to incorporate any extra sealing flanges or the like, but a small flare was added to the rear of the centring band. When loaded into the bore, this squeezes into the space between the front taper of the armature and the rail. Consideration is also being given to adding a similar feature to the front projectile band, to help reduce balloting forces.



**Fig.3 New and recovered 40mm armatures.**

To date, only one shot has been fired with the modified centring band. Preliminary analysis of the data looks promising, with a velocity of  $2200\text{ms}^{-1}$  being achieved. A bore insulator failure prevented further firings on that occasion, and may have clouded the results of the new band. There was no sign of any plasma leakage (secondary B-dot peaks) but the muzzle X-rays showed that the band had broken in-bore, allowing some minor arcing to the thread portion of the armature. This was confirmed when the fired armature was recovered later in the day.

## CONCLUSIONS

The DRA 40mm firings have demonstrated many times that launching projectiles at high velocities at medium calibre is very demanding upon the armature. All shots have demonstrated significant mass loss from the rear of the armatures, with transition at velocities below  $2000\text{ms}^{-1}$ . A simplified manufacturing route has been shown to work satisfactorily under a wide variety of launch parameters. Construction of multi-material armatures has also been shown to be feasible, and it is very likely that future optimized armatures will be so made.

Controlling transition of solid armatures is well acknowledged as necessary, but it is proving difficult to achieve this. The interaction between armature and launcher cannot be under-rated in this respect, since bore expansion leads to premature armature failure and transition. Stiffer launcher structures may well have a greater effect than design changes to armatures alone. Stiffer structures come at a significant cost in terms of money and design effort, but to achieve the highest velocities they are becoming more and more important. The days of the copper/plastic launcher are numbered. High performance demands top of the range materials and designs.

## ACKNOWLEDGEMENTS

The author is indebted to the many members of the EM gun experimental team based at Fort Halstead and Kirkcudbright for their part in producing the data presented in this paper. The work was funded by the UK MOD Corporate Research Programme, TG1. Discussions with staff at IAT have been invaluable in eliminating many abortive routes which could have been tried.

## REFERENCES

- 1 Launching tactically configured solid armature projectiles from large and medium calibre railguns - results from the DRA test programme.  
D.J.Kirkpatrick and D.C.Haugh  
8th EML Symposium, 1996
- 2 Recent firings at the DRA 32MJ Kirkcudbright facility.  
D.C.Haugh, D.J.Kirkpatrick, A.P.J.Argyle, M.D.Bennett  
5th EEMLS Symposium, 1995

© British Crown Copyright 1997/DERA

Published with the permission of the controller of Her Britannic Majesty's Stationery Office.

# 3D Softly Coupled Electromagnetic/Thermal/Structural Analysis Using MEGA-DYNA3D

C. Leyden, R. Critchley and J.A. Downey  
Defence Research Agency  
Fort Halstead WX6  
Sevenoaks, Kent TN14 7BP

**Abstract** - This paper details research being performed at the DRA on the simulation of railguns using a soft coupling of the transient electromagnetic-thermal code MEGA with the structural mechanics code DYNA3D. The coupling of the codes has been enhanced by making use of the existing facility within DYNA3D to accept nodal temperature information. The MEGA code has been modified to allow transfer of nodal temperature information to DYNA3D and subsequent simulation of thermal softening. Details of the validation tests of this technique and the results of numerical simulations of real armature firings are shown.

## INTRODUCTION

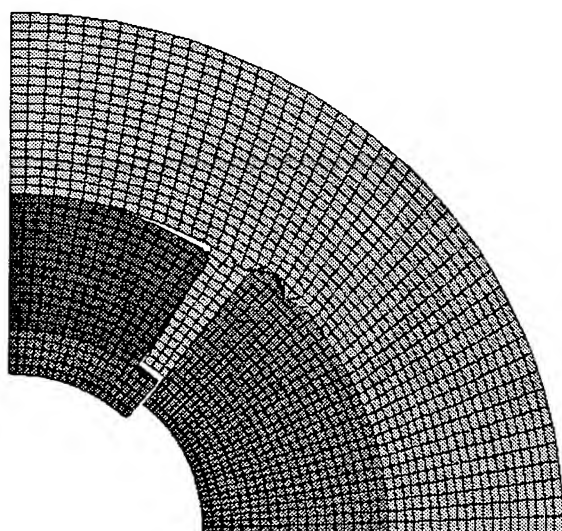


Fig. 1 Composite barrel (MEGA-DYNA3D)

Initial versions of MEGA-DYNA3D allowed engineers at the DRA to accurately transfer electromagnetic force distributions in a railgun from MEGA to DYNA3D [1,2]. The usefulness of this soft coupling was demonstrated in the analysis of electromagnetic gun barrels. Previously, a uniform pressure distribution was assumed to represent the body forces generated in a rail/armature. However, this approach proved to be deficient since it could not accurately predict the displacement of insulators adjacent to the rails. For example, a composite barrel suffered a catastrophic failure at the

Kirkcudbright EML facility in Scotland as a result of a collapsed core. Earlier analysis of the barrel did not indicate that the barrel would fail. However, analysis using MEGA-DYNA3D clearly showed gaps developing between insulators and rail (Fig. 1) which would allow plasma leakage and arc damage to occur.

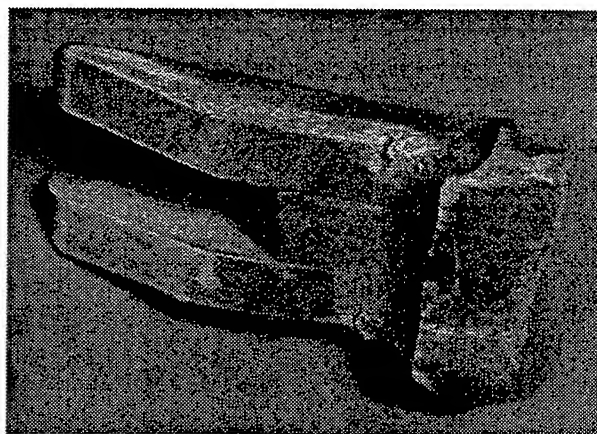


Fig. 2 Recovered armature (Kirkcudbright EML facility)

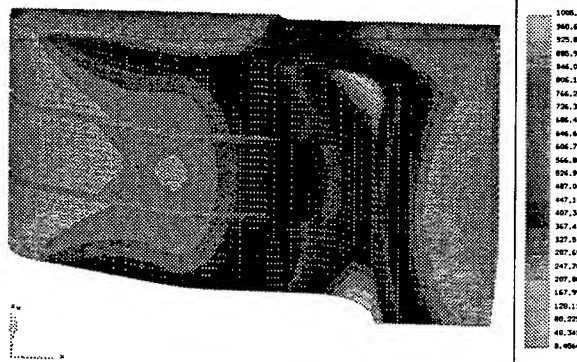


Fig. 3 Temperature in armature (MEGA)

MEGA has also been used successfully to predict the thermal hot spots that occur in armatures during a railgun firing [3]. Recovered armatures from Kirkcudbright exhibited melt regions around the inside root of the armature (Fig. 2). Simulations using MEGA displayed the same high temperature regions (Fig. 3). Furthermore, armatures that have

been recovered and sliced through their centre indicate electric current paths that are remarkably similar to model predictions.

These and other examples demonstrate the successful application of MEGA-DYNA3D but unfortunately there were obvious weaknesses in this implementation. Although armature failures were predicted by MEGA due to extensive melting at the root regions, there have also been unsuccessful firings that MEGA-DYNA3D was not able to forecast. Results from stress analysis did not show significant differences between armatures that survived and those that failed. It was believed that the material response of the armature was not being modelled accurately due to the fact that thermally dependent material models were not being used. To develop better material models would first require that nodal thermal data as well as nodal force data be transferred from MEGA to DYNA3D. The implementation of the coupling was carried out along the lines of the existing TOPAZ3D-DYNA3D link by the developers of MEGA at the University of Bath. The revised code was then evaluated by comparing results to an analytical solution and a TOPAZ3D-DYNA3D computer model.

#### ANALYTICAL SOLUTION

From Timoshenko [4] analytical expressions for the thermal strains induced in a variety of dynamic and steady state situations relating to cylinders and plates can be found. Any of these solutions can be used to validate the MEGA-DYNA3D thermal link or the corresponding TOPAZ3D-DYNA3D link.

The situation studied here will be the case of a cylinder with a concentric circular hole which has a fixed temperature of 100°C on the inner surface and a fixed temperature of 0°C on the outer surface (i.e. a constant temperature gradient is defined). Since the analytical solution is for the case of an infinitely long cylinder, convergence studies were performed to determine the minimum length of cylinder to be modelled. Furthermore, since the analytical solution assumed a steady state situation where the material constants such as thermal conductivity do not play a part, we can optimize the solution speed by increasing the conductivity to 500 times that of C101 copper. This meant that the problem time could be reduced from 1s to 5ms.

The chosen geometry was a cylinder 0.05m long with an inner radius of 9.5mm and an outer radius of 25.25mm. Reference [4] states that for the steady state case the axial stress,  $\sigma_z$ , on the inner surface is,

$$(\sigma_z)_{r=a} = \frac{\alpha ET}{2(1-\nu)\ln\frac{b}{a}} \left( 1 - \frac{2b^2}{b^2-a^2} \ln\frac{b}{a} \right) \quad (1)$$

and on the outer surface,

$$(\sigma_z)_{r=b} = \frac{\alpha ET}{2(1-\nu)\ln\frac{b}{a}} \left( 1 - \frac{2a^2}{b^2-a^2} \ln\frac{b}{a} \right) \quad (2)$$

where,

- a = inner radius of cylinder
- b = outer radius of cylinder
- $\alpha$  = coefficient of thermal expansion
- E = Young's modulus
- T = temperature on the inner surface
- $\nu$  = Poisson's ratio

Thus, we obtain a value of -210MPa for the axial stress on the inner surface and 111MPa on the outer surface.

#### TOPAZ3D-DYNA3D MODEL

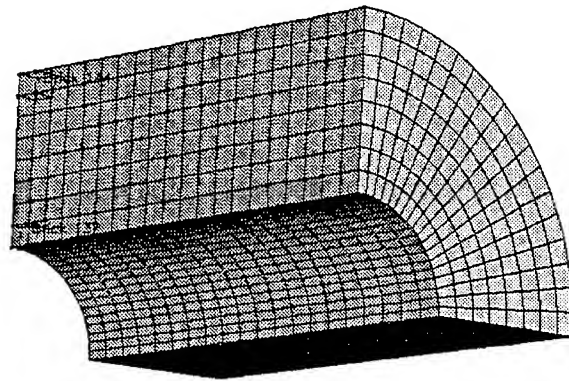


Fig. 4 Elements 144 and 137 (TOPAZ3D-DYNA3D)

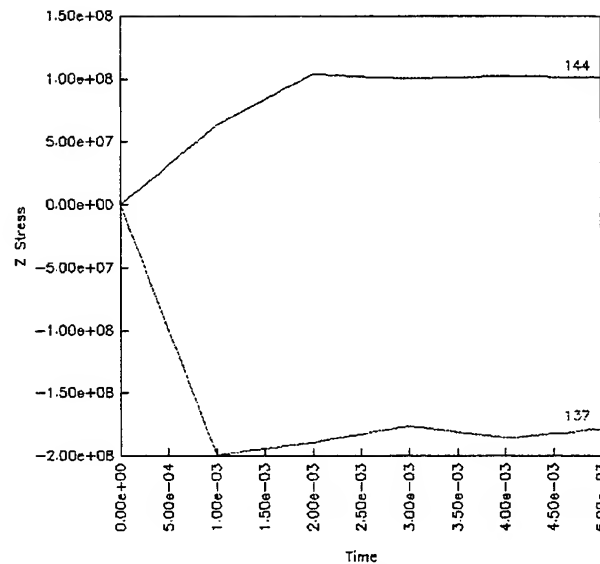


Fig. 5 Axial stress in elements 144 and 137 (TOPAZ3D-DYNA3D)

The temperatures at various states in TOPAZ3D plotfiles can be read in by DYNA3D to allow an analysis of thermal strains. The finite element model consisted of 8 x 18 x 20 brick elements. Reference [4] reveals that the maximum tangential and axial stress occurs at the inner and outer surfaces of the cylinder. Therefore mesh elements 144 and 137 (Fig. 4) were

chosen to generate a time history plot. The converged late time solution was identical on the two platforms that were used to run the benchmark - a Cray YMP 8i and a Sun SPARCcenter 2000. It was found that the axial stress,  $\sigma_z$ , on the inner and outer surfaces was -180MPa and 111MPa respectively (Fig. 5 & Fig. 6). Thus the TOPAZ3D solution for the given mesh was 10 - 13% in error compared to the analytical solution. Since the CPU time required to solve this problem was 24,186s on the SPARCcenter, further mesh convergence studies were not performed.

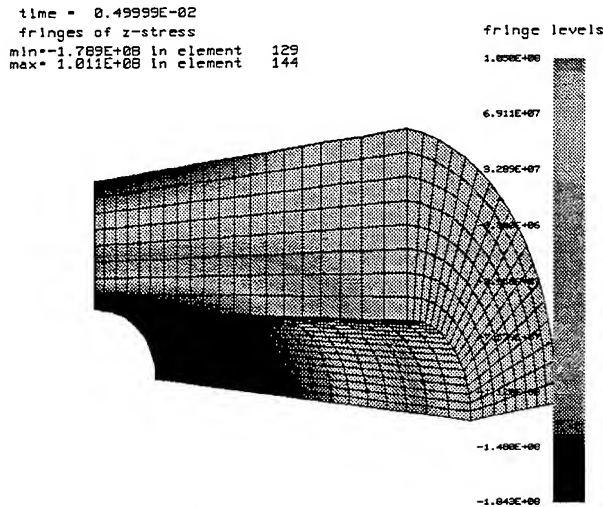


Fig. 6 Axial stress in cylinder (TOPAZ3D-DYNA3D)

TOPAZ3D predictions for the temperature distribution in the cylinder compared satisfactorily with the analytical solution.

#### MEGA-DYNA3D MODEL

The geometry, mesh density and initial temperatures were identical to that used in the TOPAZ3D-DYNA3D case. Thermal conductivity was assumed to be 500 times greater than C101 copper, thereby reducing the time required to converge to the steady state solution. The analysis also utilized a 1/4 symmetry representation to shorten computational time. In this analysis the heat distribution in the cylinder was first calculated by MEGA and then nodal temperature information was exported to a file readable by DYNA3D.

The axial stress,  $\sigma_z$ , was calculated to be -176MPa on the inner surface and 109MPa on the outer surface (Fig. 7). These values are very close to those produced by TOPAZ3D-DYNA3D and indicate that discrepancies between the analytical results and the finite element based results may relate to mesh dependency issues. It should be simple to verify if this is indeed the case by re-running both sets of models with finer meshes.

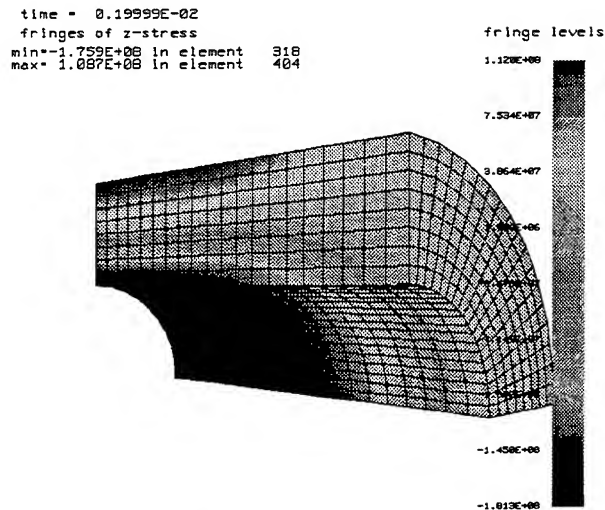


Fig. 7 Axial stress in cylinder (MEGA-DYNA3D)

#### ARMATURE SIMULATIONS

To test the effectiveness of MEGA-DYNA3D for investigating the material response of armatures, results from simulations were compared to a 25mm square bore railgun shot. A square bore barrel was chosen as it was easier to mesh accurately in finite element pre-processors. The launch package consisted of a 7075 aluminium armature of mass 18.7gm attached to the rear of a tufnol cylindrical insulator. The insulator incorporated a metallic insert at the front to increase the total mass of the package to 249.9gm. The applied current pulse attained a peak of 692kA in 0.38ms. The muzzle velocity of the package was 247ms<sup>-1</sup> but the armature broke at 1ms - its arms fused to the ETP copper rails. The objective of this exercise was to determine if computer simulations could have predicted the demise of the armature.

The MEGA model consisted of 175,592 brick elements. Using a time step of 0.02ms required a computational time of 42hrs on a Sun SPARCcenter 2000. The predicted temperatures at 1ms indicated that some melting would occur at the inside root region of the armature (Fig. 8) but it was not extensive enough to suggest that the shot would fail.

The first structural analysis of the armature transferred only nodal force information from MEGA to DYNA3D. The MEGA air elements were not required in DYNA3D and the rail elements were also ignored in order to reduce computational time. This resulted in a DYNA3D mesh of 4,704 brick elements which required 16hrs of CPU time on the SPARCcenter. DYNA3D material type 3 (isotropic elastic-plastic) was used to model the 7075 aluminium armature with the following data set.



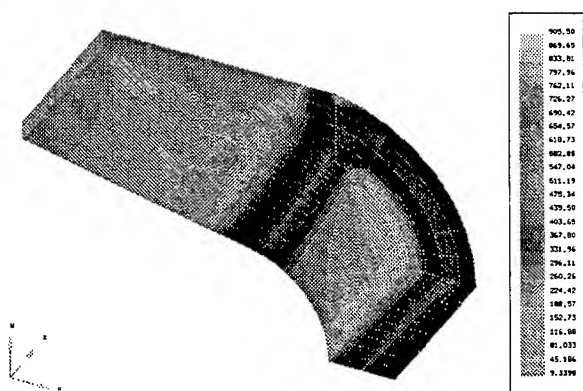


Fig. 8 Temperature in armature at 1ms (MEGA)

Density,  $\rho = 2,800 \text{ kgm}^{-3}$   
 Young's modulus,  $E = 72.3 \text{ GPa}$   
 Poisson's ratio,  $\nu = 0.30$   
 Yield stress,  $\sigma = 580 \text{ MPa}$   
 Hardening parameter,  $\beta = 1.0$

Clearly, the effective (von-mises) stress and plastic strain plots at 1ms (Fig. 9 & Fig. 10) contain no indications that the armature will fail. The peak stress is 232MPa, well below yield, and there is no plastic strain at all.

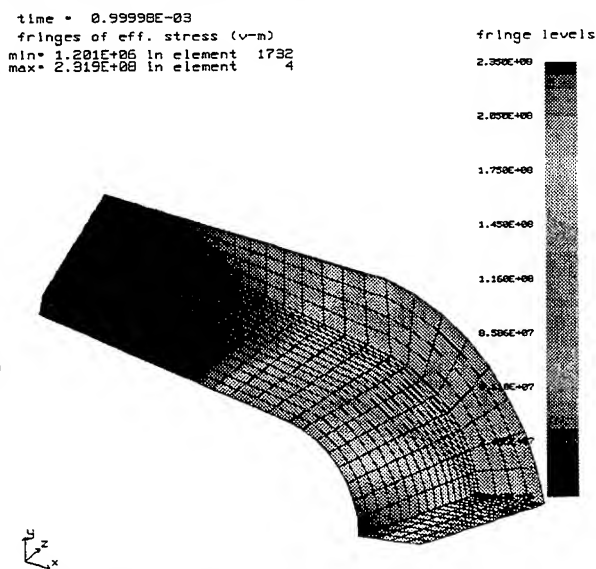


Fig. 9 Effective stress at 1ms (MEGA-DYNA3D, non-thermal)

To test the idea that thermal softening plays an important role in armature failure required modifying MEGA-DYNA3D to transfer nodal thermal as well as nodal force data between the codes. MEGA could now be used to create a DYNA3D compatible file containing temperature information for the armature. DYNA3D material type 4 (thermo-elastic-plastic) was used in the next series of simulations. One model was run

with no thermally dependent material data in order to compare the results using material type 3 with material type 4. There was, as expected, no discernable difference between the two calculations. The armature material data was then modified by specifying values for yield stress,  $\sigma_T$ , versus temperature,  $T$ .

$\sigma_0 = 580 \text{ MPa}$ ,  
 $\sigma_{100} = 538 \text{ MPa}$ ,  
 $\sigma_{150} = 445 \text{ MPa}$ ,  
 $\sigma_{200} = 310 \text{ MPa}$ ,  
 $\sigma_{250} = 145 \text{ MPa}$ ,  
 $\sigma_{300} = 62 \text{ MPa}$ ,  
 $\sigma_{400} = 20 \text{ MPa}$ ,  
 $\sigma_{2500} = 20 \text{ MPa}$

No coefficient of thermal expansion,  $\alpha$ , values were introduced in order to determine the effect of thermal softening in isolation. Thermal strain would be looked at separately.

time = 0.99998E-03  
 fringes of eff. plastic strain  
 min = 0.000E+00 in element 1732  
 max = 0.000E+00 in element 1792

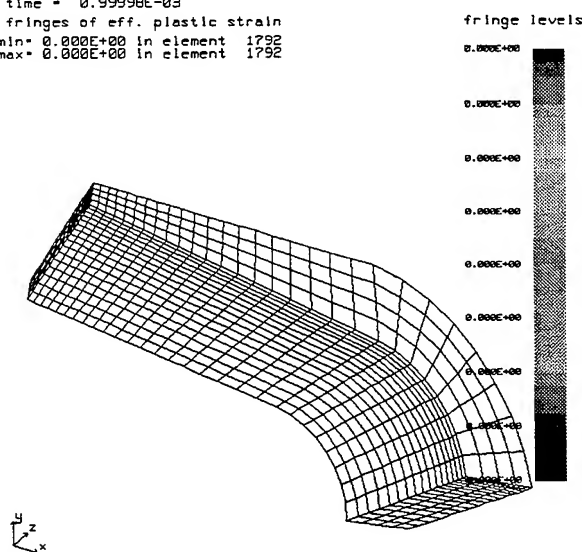


Fig. 10 Effective plastic strain at 1ms (MEGA-DYNA3D, non thermal)

The effective stress and effective plastic strain plots at 0.6ms (Fig. 11 & Fig. 12) now clearly indicate that the armature will fail. The peak stress has risen to 350MPa and the peak strain is 223%. The time of 0.6ms is earlier than the experimentally observed time of failure. However, this was probably due to the fact that the rail was not modelled in DYNA3D. With the rail in place, it is possible that the model would show material softening propagating from the outside of the armature towards the centre, which would have delayed the onset of armature failure. It is hoped that further models will verify this.

Another model was solved using the original non-thermal material data but including values for the thermal coefficient of expansion versus temperature. Although the results are not as significant as for thermal softening, they are still very different



from those obtained from the non-thermal model. At 1ms the effective stress and plastic strain was 580MPa and 1.60% respectively.

time = 0.59997E-03  
fringes of eff. stress (v-m)  
min= 1.862E+06 in element 1732  
max= 3.496E+08 in element 17

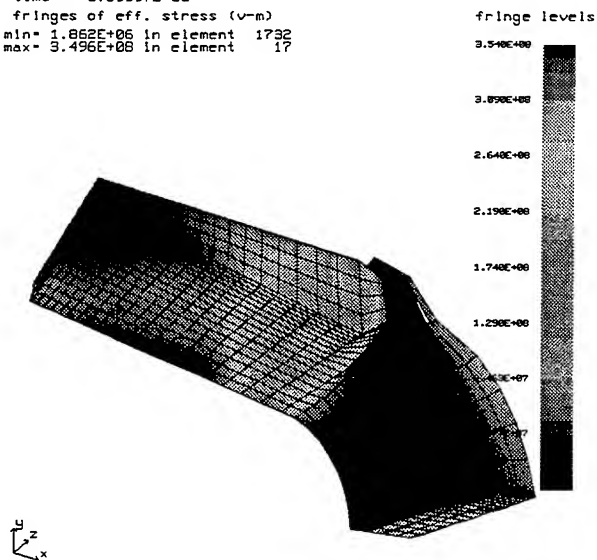


Fig. 11 Effective stress at 0.6ms (MEGA-DYNA3D, thermal softening)

time = 0.59997E-03  
fringes of eff. plastic strain  
min= 0.000E+00 in element 1792  
max= 2.294E+00 in element 1710

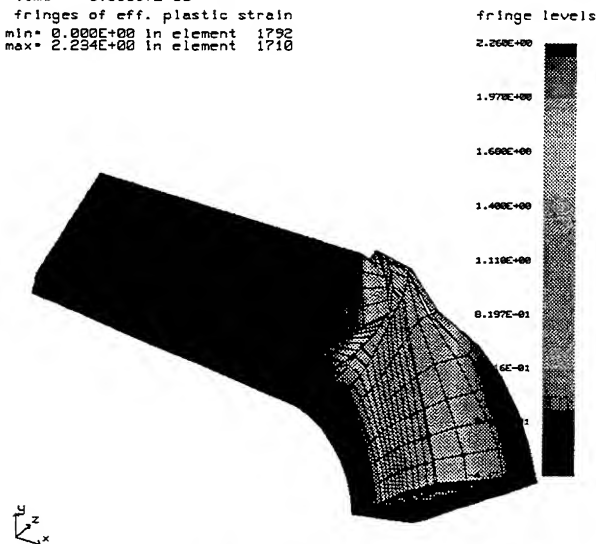


Fig. 12 Eff. plastic strain at 0.6ms (MEGA-DYNA3D, thermal softening)

## CONCLUSIONS

Overall, the benchmark tests give confidence that both TOPAZ3D-DYNA3D and MEGA-DYNA3D can be used to provide meaningful results. However, previous studies have shown that mesh quality does affect finite element predictions and that a number of models may have to be solved to ensure that results have converged to an optimum solution.

It is very clear from these results that to model an armature accurately requires that thermal softening is taken into account

and that future work should include verifying and improving thermal material models in DYNA3D.

## REFERENCES

- [1] R. Critchley and C. Leyden, "The use of coupled EM-hydro finite element techniques for the design of railguns", IEEE Trans. Magn., vol. 31, no. 1, January 1995, pp. 576-581.
- [2] G. Hainsworth, D. Rodger, P.J. Leonard, and C. Leyden, "Finite element modelling of magnetic compression using coupled electromagnetic-structural codes", IEEE Trans. Magn., vol. 32, no. 3, May 1996, pp. 1050-1053.
- [3] A.P.J. Argyle and C. Leyden, "The use of the MEGA electromagnetic-thermal finite element code in predicting thermal behaviour of large calibre EM armatures", Proceedings of the 5th European Symposium on Electromagnetic Launch Technology, Toulouse, France, April 1995.
- [4] S. Timoshenko, "Theory of elasticity", McGraw-Hill Book Company, Inc., New York and London, 1934.

# Factors Influencing Choice of Bore Geometry for Rail Launchers

Richard A. Marshall

Institute for Advanced Technology, The University of Texas at Austin  
4030-2 W. Braker Lane, Austin, TX 78759, USA

**Summary**—There are two fairly evenly divided schools of thought on whether “square” or “round” is the better geometry to employ for rail launchers. The question is examined from the point of view of research launchers as well as of fieldable launchers. A dozen or so criteria are examined and the conclusion is reached that “square” is better for research launchers. The same conclusion is reached for fieldable launchers but the case is not quite so clear cut.

## I. INTRODUCTION

There is no obvious answer to the general question, what is the best geometry for rail launchers. Should they be designed with round bores, square (or more correctly “rectilinear”) bores, or should some more complex geometry be used. The answer is, “it depends” on what is required of the launcher. Is it a research device or a device that must be fieldable? Should it be maintainable or is it a throwaway item, and so on. The simplistic view, that a rail launcher is just another type of gun and so should also have a round bore like any other gun, is not helpful.

In what follows, the basic geometries round and square, are examined. Other geometries are also possible, rectangular and hexagonal, to name but two. These are not discussed further here. The geometries we consider are shown in Fig. 1.

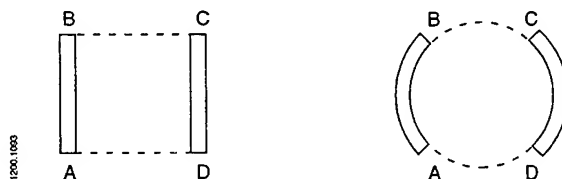


Fig. 1. The geometries are similar in that the inside rail corners A, B, C, D for both form squares. Both have areas of one square unit with rails being 0.1-unit thick.

### A. The Propelling Force

Obviously, the main difference between railguns and ordinary guns is the differences in their propulsive mechanisms. A discussion of the specifics is helpful.

The analogue of propellant gas pressure in an ordinary gun is magnetic pressure but the concept must be used with caution. Clearly, there is no “pressure” on the insulating spacers that keep the rails in place. The force experienced by the armature which drives the launch package is the Lorentz or “ $\mathbf{J} \times \mathbf{B}$ ” force which acts only on the current carrying elements of the launcher. This leads to the well known lumped parameter force law,  $F = L' I^2 / 2$ , where  $L'$  is, as usual, the inductance gradient of the launcher.

A major challenge in designing railguns is the handling of the necessarily high currents. It is therefore clear that current should be minimized. This means that  $L'$  should be made as large as is reasonable and so we discuss this first.

## B. The L-Prime Issue

### The simple breech-fed launcher

It turns out that for "reasonable" rail launcher geometries, the  $L'$  values are quite similar. Because magnetic field lines must close, adequate space between the "horns" of the rails must be provided for the magnetic flux to leave the bore, flow around behind the rails, and return to the bore. In Fig. 2, (a), (b), and (c) have reasonable geometries, while that of (d) does not.

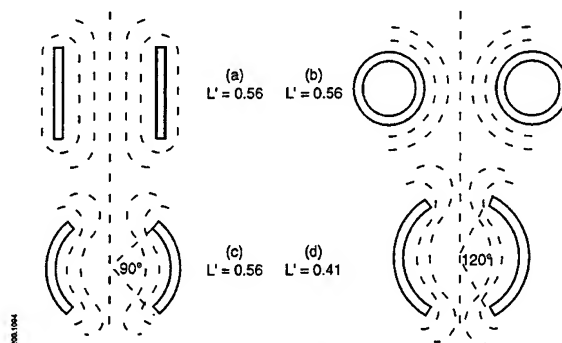


Fig. 2.  $L'$  values ( $\mu\text{H/m}$ ) for four railgun geometries shown. Field lines are indicated.

In computing the values of  $L'$  [1, 2] rail thicknesses have been taken as 1/10th of the bore size. Note that  $L'$  is geometry dependent only. It is not size dependent. In case (b), the distance between the rails has been taken as equal to the rail diameters. (It is believed that Hansler in his rail launcher work in Germany during WW II used round rails successfully.)

It is interesting to note that the two, square and the round rod pair cases (a and c) have the same  $L'$ , 0.56 [3]. Note that the penalty of reducing the throat areas between the horns in case (d) is to reduce  $L'$  by 27%. If the horns are brought closer together,  $L'$  falls further.

Concerning the necessity for magnetic flux to be able to return freely around behind the rails, the author did an (unreported) experiment in Australia to test this. The inductance gradient of a rail-pair 6m long with geometry similar to (a) above was measured and found to be  $0.56 \mu\text{H/m}$ . It was then encased outside the bore with Ferrite which has a high magnetic permeability. Inductance gradient was again measured and found to be  $0.90 \mu\text{H/m}$ , an interesting if not surprising result, showing that reducing the magnetic circuit's reluctance increased  $L'$ . This indicates that the placing iron (laminated as in a transformer) along the length of the launcher can be designed to provide an augmenting field of perhaps as much as several tesla.

Because the  $L'$  for the square and the round rod pair geometries are the same, it is evident that the choice of which is the better of the two depends on factors other than  $L'$ .

### The augmented launcher

One possible strategy for increasing  $L'$  is to increase the field in the gun's bore by using field augmenting turns. From examination of Fig. 3 it can be seen that, for a given current, the use of one augmenting turn increases the propelling force by about a factor rail launcher of three.

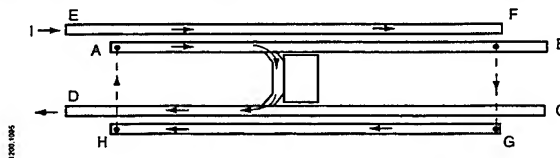


Fig. 3. Schematic of a rail launcher with one augmenting turn in series with the main rails.

The reasoning is as follows. The field at the armature is created by current in the main rails, AB and CD, and also by the current in the augmenting rails, EF and GH. The field produced at the armature by the augmenting rails is twice that produced by the main rails because it "sees" the augmenting rails both behind it and in front of it, while it only "sees" the main rails behind it. (Remember the "four caliber rule," [4]: ninety nine-percent of the driving field in a simple rail launcher is produced by current in the four caliber lengths of rail adjacent to the armature.) So if the rails are thin and close together, the field produced by current in the augmenting rails will be twice that produced by the main rails, thus demonstrating the proposition.

### C. Forces in Gun Barrels and Rail Launchers

At the risk of stating the obvious, the difference as far as internal forces are concerned between ordinary gun barrels and rail launchers is the following. Ordinary gun barrels must withstand the pressure of the propellant gasses. Locally, this produces forces in all directions as indicated in Fig. 4(a). The barrel is not much more than a simple pressure vessel and the logical way to restrain these forces is to use a round structure like a barrel. (Early gun barrels were just that; fabricated using staves and hoops.)

The forces in a rail launcher are quite different. There are electromagnetic repulsion forces pushing the rails apart as indicated in Fig. 4(b). The restraint required for each rail acts in one direction only. Further, the restraining members must be magnetically transparent; they must allow the magnetic field between the rails to exit freely. This means that solid metal cannot be used. The restraint must be electrically nonconducting in the down-launcher direction so that induced eddy currents do not prevent exit of the field.

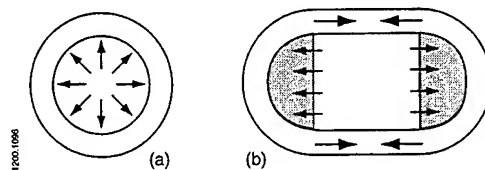


Fig. 4. Forces in a gun barrel (a), and in a rail launcher (b). The launcher rails of arbitrary shape are shown cross hatched.

### D. Armature Types

In order to generate the propelling force in a rail launcher, it is clear that current must be carried from one rail to the other in an "armature." There are three basic types of armature.

#### The metallic contact armature

For military use, solid nonarcing armatures are the armature of choice, provided that they can be made to remain nonarcing up to the velocities required (3.5km/s for the anti-tank application) and do not cause unacceptable rail damage. The metallic contact armature is one in which the armature makes smooth metal-on-metal (non-arcing) electrical contact with the rails. For military use, this is the preferred type of armature because it is the most efficient. Until recently, "rail gouging" [5] has been a possible problem. Recent work has shown that by suitably choosing rail material and design, the gouging velocity limit for aluminum armatures has been increased above 2.8km/s.

#### The hybrid armature

The hybrid armature is one in which the current is carried most of the way from rail-to-rail in a metallic conductor, but in which current is transferred from rail to armature via a "plasma brush." This is described as an "arcing contact." When smooth metal-on-metal contact changes to arcing contact, "transition" is said to have occurred.

Hybrid armatures do not produce gouging if very high velocities are required, it may be necessary to transition to hybrids below the gouging threshold velocity. It is not known at present if this is an area requiring special effort.

#### The plasma armature

The plasma armature is one in which current is conducted from rail to rail entirely by plasma. The propulsion force on the launch package is provided by plasma pressure on its rear face. Historically, much work has been done with plasma armatures but they are of little interest for military applications of rail launchers because they are highly resistive. The voltage drop across them is high, being hundreds of volts rather than the ten or twenty volts dropped across metallic contact armatures. The energy deposited in them causes rail damage and reduced propulsive efficiency.

### *E. Research Rail Launchers*

Returning to the topic, what geometry should be used for rail launchers, the answer depends in part on the particular application being considered. In the case of research rail launchers, the answer is clear. They should have square bores. The reasons for making this assertion are the following.

#### Rails as a diagnostic tool

The rails themselves are an important diagnostic. Their appearance after one shot enables much to be learned about the processes that occurred during the shot. It is therefore desirable to use rails only once. A further point in favor of flat surfaces is that they are easier to examine after a shot than curved ones. When examining gouges for example, it is simpler to define a reference surface when it is flat. For optical microscopy of the rail face, lighting is more easily controlled on flat surfaces, and so on.

#### Experimental costs

Because rails are used only once, the cost of a rail pair is an issue. It is desirable to use rail material in the as-supplied run-of-the-mill form without having to either machine it before use or to order special shapes. Rail faces are usually sanded and cleaned before a shot and this is more easily done with flat surfaces. Time taken to install rails for a shot and removing them after a shot is also a factor. The simpler the design of the rail launcher, the less time consuming it is to work on.

#### Uniformity of field

Finally, one strong point in favor of square bores for research rail launchers is that because the magnetic field between the rails is quite uniform, it is simpler to design armatures and to understand what is going on within an armature during a shot. There are fewer uncertainties in the armature region in square bores than in round bores. This is particularly important when trying to understand what physical processes are involved. The uncertainties introduced by field nonuniformity are much reduced when analyzing results of experiments.

### *F. The Fieldable Rail Launcher*

In the real world, as distinct from the laboratory world of pure and applied research, many factors must be considered before making the choice as to what launcher geometry should be used. Many of the arguments brought forward by the proponents of the two main geometries, round bore and square bore, have been incomplete, or the issue has been prejudged. In what follows, we attempt to put the pluses and minuses in perspective for the launcher geometries being considered.

### The pulsed power supply

An overriding factor in the choice of launcher geometry is the nature of the power supply that is going to power the launcher. It is tacitly assumed that rotating energy stores such as the compensated pulsed alternator or pulsed disk alternator will be used. It is also assumed that a simple rail launcher will be used with its  $L'$  of around  $0.5 \mu\text{H/m}$ . If rotating energy stores do eventually become the power supply of choice, then it might be that a high  $L'$  launcher like the augmented launcher should be used. The lower current required might simplify machine design and construction. Remember that for a given launcher duty, maximum energy to be delivered is fixed, so reducing current will require increased voltage. This may be desirable from the machine point of view. Trading lower current for higher voltage would certainly be desirable if capacitors were ever to become the store of choice.

### Current per unit rail height

The more severely an object is treated, the shorter its life becomes. Current per unit rail height is a good measure of how severely the interface between armature and launcher rail is treated [6]. In the case of the simple breech-fed FTP launcher, current densities are being driven to  $50\text{kA/mm}$  of rail height. This is a very high value and it is possible that acceptable rail life cannot be obtained when using current densities this high. It is quite likely that a current density of half that is as far as one would like to go to achieve a reasonably engineered launcher. This can only be done by increasing  $L'$ . If this is done by using single turn augmentation, to give a three-fold increase in  $L'$ , then current (and current per unit rail height) is reduced to reciprocal square root three, 58%, for a given force. This is a reasonable gain but it does have a price. The restraining forces required to hold the rails in place increases a given armature force, so the barrel mass will increase also. Only a specific system design would tell if the cost is worth the gain.

### Heat rejection

A general problem with rail launchers is that heat is generated resistively in the rails and this heat must be removed in some way. Minimizing the distance from the rails to the outside world allows more heat to be removed by simple conduction. Reduced current can allow reduced current density in the rails. This will reduce resistive heating. There is no obvious connection between bore geometry and heat rejection.

### Bore sealing

The statement has been made that "round is natural for bore sealing." The metal-on-metal armature requires no seal. Sealing is so unimportant that the top and bottom of the launcher can be left open as can its breech. It is possible that some kind of local sealing may be required for the hybrid armature but general sealing of the bore is not required. Plasma armatures require general sealing but their use has been ruled out as discussed above. (Note, however that the plasma armature of the small square bore Melbourne, Australia rail launcher was successfully sealed using square "tulip" seals [7].) Bore sealing is a nonissue for fieldable rail launchers.

### Launch package rotation in bore

It was observed occasionally in a recent program that round launch packages in round bore rail launchers could rotate sufficiently to move the armature contacts partly off the rails [8]. If this becomes a recurrent problem, then some steps would have to be taken to prevent rotation from occurring. Such rotation can occur in a simple round bore launcher but cannot occur in a square bore rail launcher.

### Launcher maintenance

Launcher maintenance has been raised as an issue and it could become one whether or not the "100 war rounds" life is reached or not. The contention is that round bores can be readily honed while the process of refurbishing damaged square bore require the slower and less accurate "broaching" process. In this

context, note that rail launcher barrels are a fabricated entity, not something that is machined from one piece of material like an ordinary gun barrel, so even the apparently simple honing process is not all that simple. The hone stones must cross and recross the discontinuities between rail and insulator. The fact is that because rail launchers are fabricated in the first place, they could at some appropriate stage in their life be re-fabricated if that were economically reasonable. This is a less costly process with square bore launchers.

#### Stability of bore shape

No rail launcher can possibly have the same mechanical stability as regular gun barrels. They require rails separated by insulators contained in some suitable fabricated structure. With repeated firings, it is likely that rail launchers experience some movement and creep of rail-to-insulator interfaces. Over time, it is likely that the original mating of these faces will change a little from what it was when the gun was originally assembled. This is likely to matter more for a round bore launcher because the rail surfaces and insulator surfaces are initially aligned. In a square bore launcher these surfaces are already "misaligned" by 90 degrees. Any small movement will be immaterial. It is likely that launch packages and armatures should be able to tolerate such distortions in both bore shapes.

#### Sabot mass

At first sight it would look as if rail launchers designed for some particular duty and having the same bore areas would have the same sabot mass for square bore as for round bore. It could be however that there would be some mass penalty in the square case because of the lack of azimuthal symmetry although this is by no means certain. Certainly the structural codes required to design square sabots would be more complex than for round sabots. But note that codes for round bore rail launcher sabots will be different from those that already exist for regular powder guns because the driving force is not azimuthally symmetrical.

#### Sabot separation

The issue of sabot separation arises because of the thought that rail launchers may have to have two petals rather than four. This might well be the case for mid-riding armatures but is not the case when base-push armatures are used. Four petals can be used in this case just as they are in powder guns. But in any case, this issue has little bearing on which bore shape is the more appropriate.

#### Cost and ease of manufacture

The cost of rail launchers that are to be fielded is not such an important issue as it is for experimental launchers in which the rails are used only one time, but it is something worth thinking about. The component parts required to assemble a rail launcher will cost less when they can be used in the "as supplied" condition. Special processes and extra machining can be costly. If there is nothing much to drive the choice of round or square, cost should certainly be a factor.

#### Armature simplicity

As is stated above, the magnetic field between the rails in the armature position is quite uniform in a square bore launcher. This makes the armature problem less severe and anything that helps the armature helps the whole system. The armature is the system's most critical component. The distribution of current and strength of the magnetic field in the armature region is difficult to compute with certainty even with the best computer codes available. To compound the problem by using anything but the simplest geometry only makes sense if by any chance there should be other overriding factors involved. This says that square is better than round.

### Rail complexity

To date, the prevailing view has been that the rails of a rail launcher will have the same cross section and will be made of the same material(s) along their whole length from breech to muzzle. It should be kept in mind that the duty required of the rails vary greatly along the launcher's length. For example, in a breech-fed system the rails near the breech must carry higher currents for longer times than rails near the exit end of the launcher. For this reason it may well be desirable to have reduced rail cross sectional areas near the muzzle. This would mean that a simple extrusion for a rail could not be used as supplied. Machining would be required. Another issue is that the armature start position may require special rail treatment. It is possible also that it will be necessary to trip armature transition somewhere along the launcher. This will also require special rail treatment. All of these things are more easily accomplished with flat rails than with round bore rails.

### Launch package guidance

The two prime functions of the rail launcher are same as for any gun. The first is to provide the propulsive force. The second is to give in-bore guidance to the package to get acceptable repeatability of launch to get acceptable accuracy. It may not be good to use the surfaces of the rails to provide guidance if it can be avoided because some damage to them may be hard to avoid. Round bore guns provide some guidance on the insulators, but good guidance may require a more advanced geometry than either round or square.

### *G. Other Considerations*

If rotating machines turn out to be unsatisfactory as energy stores for the rail launchers required by the Army, then other options must be examined. The two front runner candidates are capacitors and flux pumps [9]. Most of the rail launchers around the world are powered by capacitors so there are no mysteries about them and their use. Because they can discharge their energy so rapidly, it is necessary to slow their discharge down by using inductors and it is likely that some of this inductance required can be put to good propulsive use by using it to power augmenting turns in the rail launcher. Unfortunately, capacitors at the present state of the art are too heavy and bulky for convenient mobile use, but that situation could change.

Flux pumps also require inductance in series with them to smooth out the spike that they produce at the end of their compression stroke. As with capacitors, some or all of this inductance might be made to perform dual duty by having it power augmenting turns.

Specific system designs studies would have to be made because augmenting turns do not make low energy loss inductors. Their resistance tends to be high.

## II. CONCLUSION

There is no doubt that square is the best bore shape to use for research launchers.

For the first generation of fieldable rail launchers, it also seems clear from the considerations examined above that the use of flat rails is to be preferred to the use of curved rails, i.e., "square" is to be preferred over "round." It is the author's opinion that, on balance, square is the preferred geometry for the first fieldable rail launcher. Because there is no compelling reason to employ the round bore geometry, it would seem more practical to go with the simpler square geometry.

## III. ACKNOWLEDGMENT

This work was supported by the U.S. Army Research Laboratory under contract DAAA21-93-C-0101.



#### REFERENCES

- [1] Kerrisk, J. F., "Current distribution and inductance calculation for railgun conductors," Los Alamos National Laboratory Report LA-9092-MS, October 1980.
- [2] Sadedin, D. R., "Electric propulsion and pulse power generation," PhD Thesis, Monash University, November 1985.
- [3] Parker, J. V., unpublished computer codes.
- [4] Marshall, R. A., Barber, J. P., "The 10km/s, 10kg railgun," *IEEE Trans. Mag.*, vol. 27, pp. 21-27, January 1991.
- [5] Persad, C., "Solid armature performance: a progress review 1980-1990," *IEEE Trans. Mag.*, vol. 33, no. 1, pp. 134-139, January 1997.
- [6] Marshall, R. A., "The OAT armature experiments," IAT Report IAT.R 0072, July 1995.
- [7] Marshall, R. A., "Structure of plasma armature of a railgun," *IEEE Trans. Mag.*, vol. 22, no. 6, pp. 1609-1612, November 1986.
- [8] Challita, A., Bauer, D. P., Hanlin, G. A., Noel, A. P., Hisle, R. E., and Jackson, G., "Analysis of rotational forces in round bore railguns," *IEEE Trans. Mag.*, vol. 31, no. 1, pp. 123-127, January 1995.
- [9] Marshall, R. A., "The distributed energy store railgun, its efficiency, and its energy store implications," *IEEE Trans. Mag.*, vol. 33, no. 1, pp. 582-588, January 1997.





## **LATEST RESULTS OF THE TRILATERAL FRANCE-GERMANY-THE NETHERLANDS COOPERATION**

First of all, I would like to thank Germany and the Netherlands for asking France to present the work of our three countries on electric guns. I hope that my presentation will be accurate and will show that closer links will be necessary among researchers in this field in order to achieve technological progress.

\* \* \*

Franco-German cooperation dates from 1986. This agreement was based on an exchange of information concerning research and technology in the field of electric guns for military applications. In 1991, a new agreement was signed for a period of five years. Its extension is scheduled for the end of 1997.

In 1993, France and Germany signed a bilateral agreement with the Netherlands limited to rail guns and energy storage.

### The 1991 agreement

The 1991 Franco-German cooperation programme was divided into six sub-programmes, each one being bi-national and controlled by a country:

SP1: operational and integration aspects

SP2: rail guns

SP3: coil guns

SP4: electrothermal guns

SP5: hypervelocity projectiles

SP6: energy storage and switching

The programme under discussion is limited to the chemical electrothermal gun with low electrical energy. It obviously complements the Franco-German work done at ISL on rail guns, energy storage and switching.

There were several operational targets, mainly anti-tank warfare and air defence. Sub-programme 1 was in charge of studying the system in order to assess the potential of electric guns in the fields considered. It took into account the technical results of the other sub-programmes and its aim was to establish a future projection.

The studies were divided between France and Germany. The same applied for the production of demonstrators.

The technical aims were as follows:

- rail gun at ISL: 10 MJ, 1 kg, 2600 m/s (capacitor bank)
- electrothermal gun at TZN: 30 MJ, 3.2 kg; 2,300 m/s (capacitor bank)
- coil gun at ETBS/Bourges: 3-5 MJ, 4.5 kg, 400-500 m/s (capacitor bank)

TNO has a 6 MJ, square 20 mm bore, 2,000 m/s rail gun (homopolar generator)

## Results

### Operational interest

The interest of electromagnetic guns is due to the fact that, in principle, they are not limited by theoretical physical considerations while the performance of conventional powder guns is considerably reduced in excess of 1,800 m/s. The higher velocity can either destroy heavier armour in anti-tank warfare or offer the prospect of a higher kill probability in air defence combat.

In anti-tank warfare, simulations have led to the definition of an APFSDS projectile capable of destroying the future threat and the definition of the corresponding guns.

Rail guns appear to be the best launchers for anti-tank and air defence applications. Their projected efficiency is high and the energy necessary for a round is lower. The problem of the electrical contact between the rails and the frame of the sabot at velocities of more than 2000 m/s and currents reaching several MA still has to be solved.

An efficiency of 50% could be achieved at calibres of 80 mm for high velocities.

At ISL, we have demonstrated that a projectile can be fired at more than 2,000 m/s without any contact problem.

Although coil guns have an interesting potential, there are many problems: definition of the projectile, supply of the coils and mechanical resistance of the coils when the current passes through them. In view of the results at present, this futuristic technology cannot be ruled out as yet.

TZN reached 2,300 m/s with its electrothermal gun. However, it should be noted that efficiency is poor, that it decreases when the velocity of the projectile increases. Levels of

2,500 to 3,000 m/s are not easy to reach and an efficiency of 25% to 30% is possible at 2,200 m/s. The energy necessary for firing a round is a handicap.

Chemical electrothermal guns are interesting. Unfortunately, the possibility of their development towards high velocities is limited.

The studies of the interest of electric launchers in air defence have not been completed. They are much more difficult than those done on anti-tank warfare. Certainly, the high velocities possible with small projectiles suggest that they could rival middle calibre guns. But, since the gap between these two technologies has not been studied in depth, it cannot be concluded that this new technology is interesting.

The high energies possible could lead to new projectile concepts. But wouldn't this be to the detriment of the energy stored? I think that rail guns used in air defence could only be developed if this technology was used in anti-tank combat.

### Energy storage - Pulse forming

The main handicap of electric guns that can be used operationally is energy storage and switching. We have seen that firing a round requires some 60 MJ and that, in anti-tank warfare, it would be necessary to fire two or even three rounds one after the other. A look at the unit necessary to store 30 MJ at present show the tremendous amount of work that still has to be done.

The Franco-German studies have concentrated on the potential use for the power section of capacitors or superconducting coils. These pulse forming networks have to be associated with an energy storage which could be a rotating machine.

The progress achieved in the volumic energy of the capacities is not enough. Values of around  $2 \text{ MJ/m}^3$  to  $5 \text{ MJ/m}^3$  can be achieved but the levels required are 10 times higher. Studies done by TPC in France using new dielectric materials with industrial processes should enable this target to be reached in 10 to 15 years time.

Superconducting coils are studied for storage applications in the civilian market. In order to be used as a power supply for electric launchers, the superconductive state has to be maintained during the delivering of pulses which are between 2 and 5 ms. Some studies have been conducted by the Magnet Motor Company in Germany, based on the use of NbTi technology.

A demonstrator of 1 MJ has been built which is characterized by an energy density of  $7 \text{ MJ/m}^3$ . As the NbTi technology is limited, a new storage facility of 4 MJ using Nb<sub>3</sub>Sn superconducting material has been developed. It will deliver 20 kA pulses and it is characterized by an energy density of  $28 \text{ MJ/m}^3$ .

In the field of the energy storage section, Magnet Motor has more than 10 years of activity on the development of rotating machines based on the magneto dynamic storage (MDS). Machines storing energy of 78 MJ exist today. They are characterized by a specific energy of 37 MJ/t. Must it be repeated that the anti-tank application requires an energy storage for a salvo of about 200 MJ and a power of 10 - 20 GW.

The research activities on the pulse forming for the power section have shown that the use of semiconductors as switching components presents a great interest. ISL, in a partner relationship with ABB, has developed thyristors for blocking voltages of 12 kV and carrying up to 100 kA in pulsed applications.

## Cooperation with the Netherlands

This trilateral cooperation concerns rail guns, storage and switching.

The work on rail guns concerns the improvement of performance and is based on modelling. The work on storage and that on switching are complementary to those of the Franco-German work. The path followed is storage through induction which requires the development of an opening switch and storage by means of the battery.

## Future work

Anti tank combat remains the dominant operational application. However, the technology of electric guns is handicapped by energy storage and commutation.

For the short term, chemical electrothermal guns with low electrical energy appear to be interesting.

Power ignition via plasma provoked by an electrical discharge, then control of its combustion seems to be a solution for improving powder guns. The electrical energy necessary for firing a round would be a maximum of 3 MJ to be delivered in 1 to 4 ms.

Taking into account a salvo of three rounds and losses, the energy to be stored would be 1,5 to 10 MJ. Research should be done, firstly on the pulse forming network, including the storage and switching components and, secondly on powder ignition and combustion.

Although the energy requirement is lower than that of electromagnetic guns, storage in the vehicle is not yet accessible. The same applies to work on the ignition-powder couple which should not be minimized.

This is the path which Germany is considering extending until 1999, involving the Rheinmetal/TZN company and the Diehl company. France will be associated with Giat Industries and SNPE.

For the long term, rail guns seem to be a promising path dedicated to ISL.

Since the electrical energy required per round in the anti-tank application is 60 MJ (power of several tens of GW) and the energy necessary for three rounds has to be stored in a volume of 2 m<sup>3</sup>, the target volumic energy is 90 MJ/m<sup>3</sup>. Efforts will have to be concentrated on the field of energy and power storage components.

Many nations have realized this. In terms of the RTP4 on pulsed electrical energy sources in the context of the electrical engineering CEPA 16, six nations expressed their interest. In the context of NATO, the LTSS 47 or Electric Pulse Power System should render its conclusions at the end of the year.

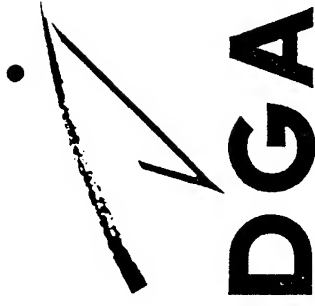
## Conclusion

For the last 10 years, the Franco-German capacity in terms of electric guns, with which the Netherlands has become associated, has achieved significant results in the field of rail guns and in that of energy storage and switching.

The main problem is still that of power or energy storage which will have to be solved if we want to satisfy both military and civil requirements.

The ETC remains a short-term solution. Whether or not it deserves to be supported will be seen quickly.

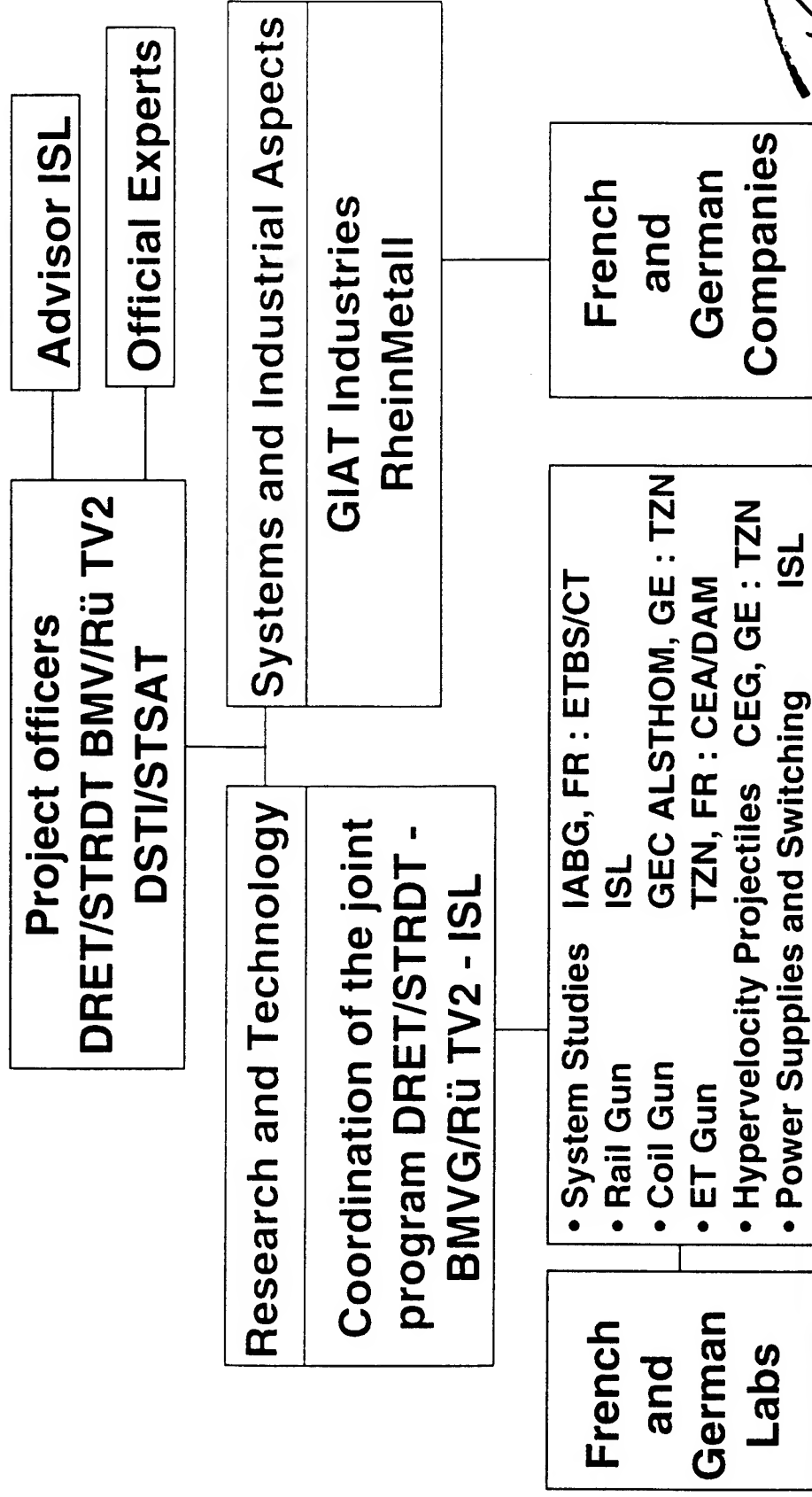




**EML 97**

# **Last results of trilateral cooperation France-Germany-Netherlands**

# French - German Program on Electromagnetic Launch Technology



# ELECTRIC LAUNCHERS

## Systems - Integration

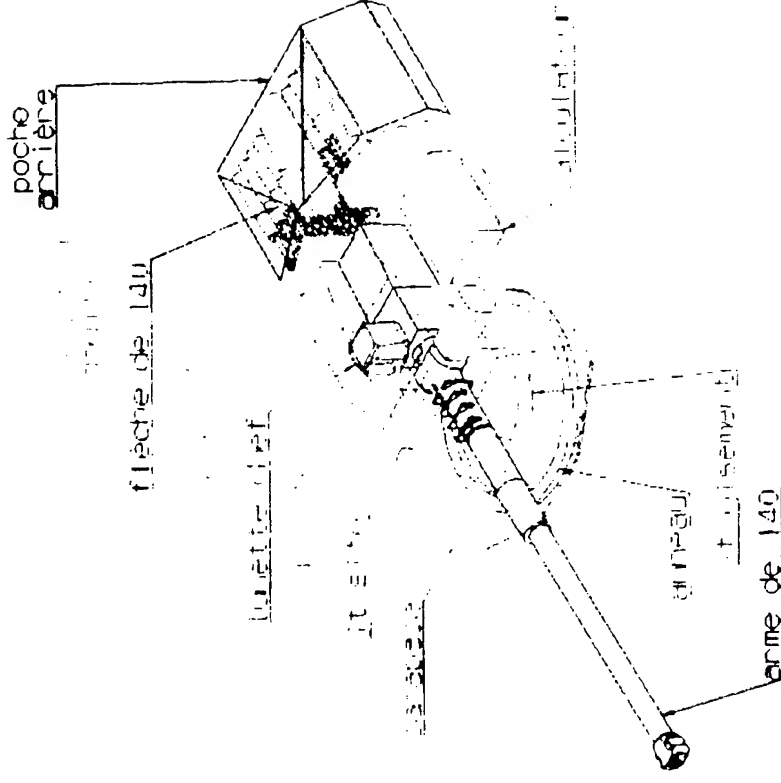
### Electrothermal - Chemical Armament

#### ■ Turret :

- Plasma burner
- 40 ammunitions

#### ■ Armament :

- Cal : 140 mm
- Velocity : 2200 m/s

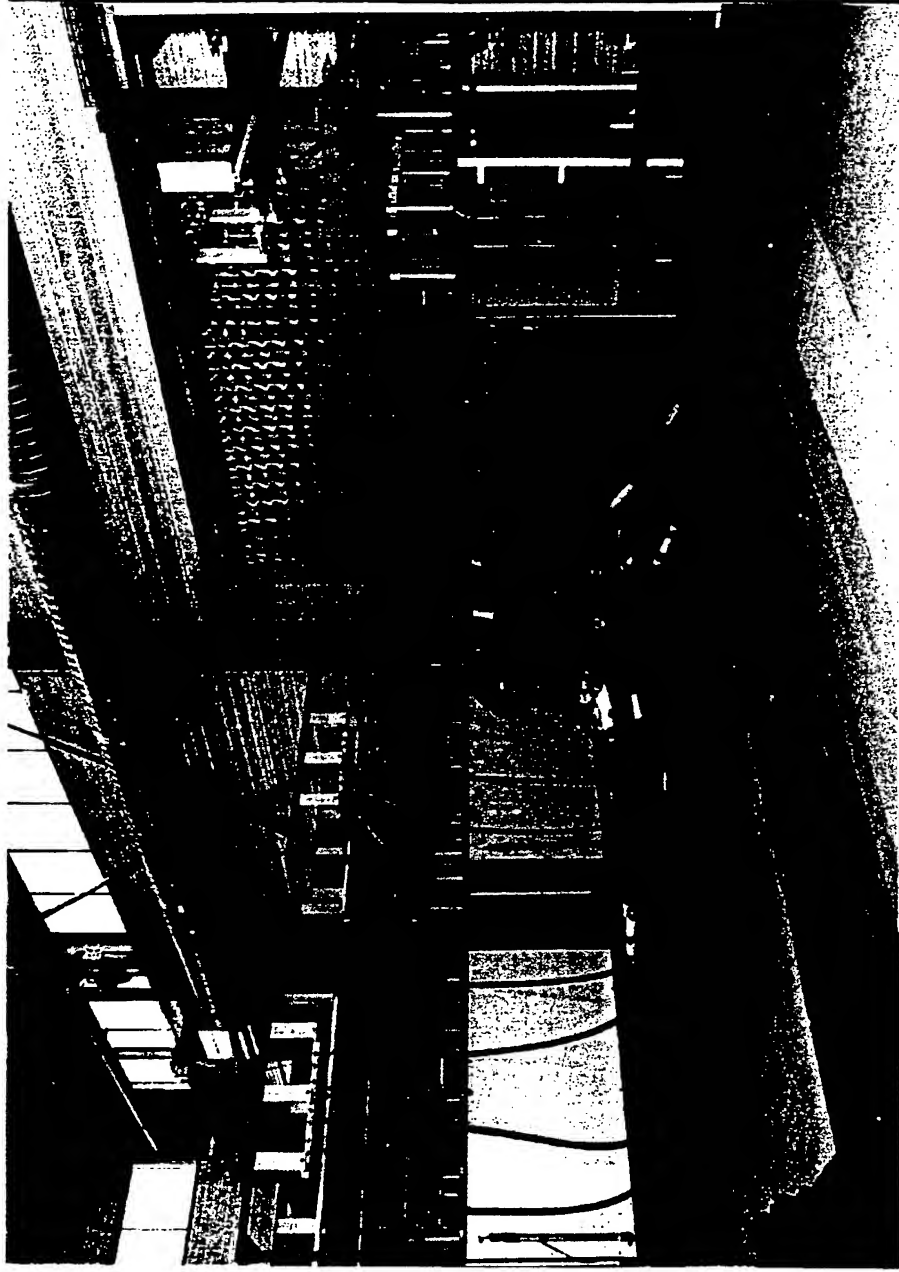


# Electrical energy storage requirement for one shot

|                            | ET   | ETC  | RAIL | COIL |
|----------------------------|------|------|------|------|
| $M_p$ (kg)                 | 5.5  | 5.5  | 5.5  | 5.5  |
| $M_s$ (kg)                 | 3    | 3    | 4    | 4    |
| $M_t$ (kg)                 | 8.5  | 8.5  | 9.5  | 9.5  |
| $V_m$ ( $\text{ms}^{-1}$ ) | 2500 | 2500 | 2500 | 2500 |
| $E_m$ (MJ)                 | 26   | 26   | 30   | 30   |
| $\eta$ (%)                 | 25   | 20   | 45   | 50   |
| $E_e$ (MJ)                 | 105  | 43   | 67   | 60   |

✓

# GEC ALSTHOM Three-Coil Prelauncher

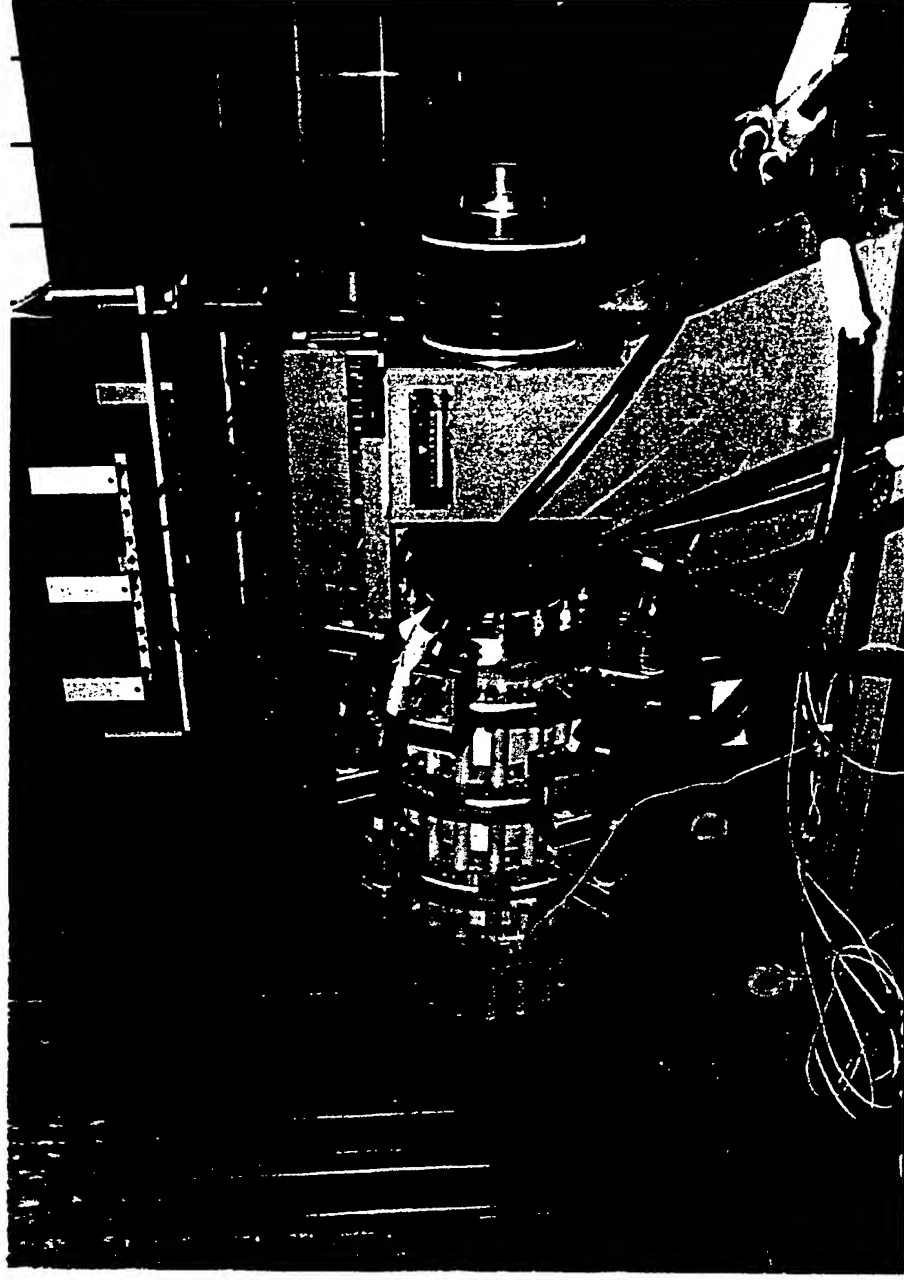


EML 97

DGA/DSA/SPART - C.C. - 97/05 - 5/20

 **DGA**

# GEC ALSTHOM Three-Coil Prelauncher



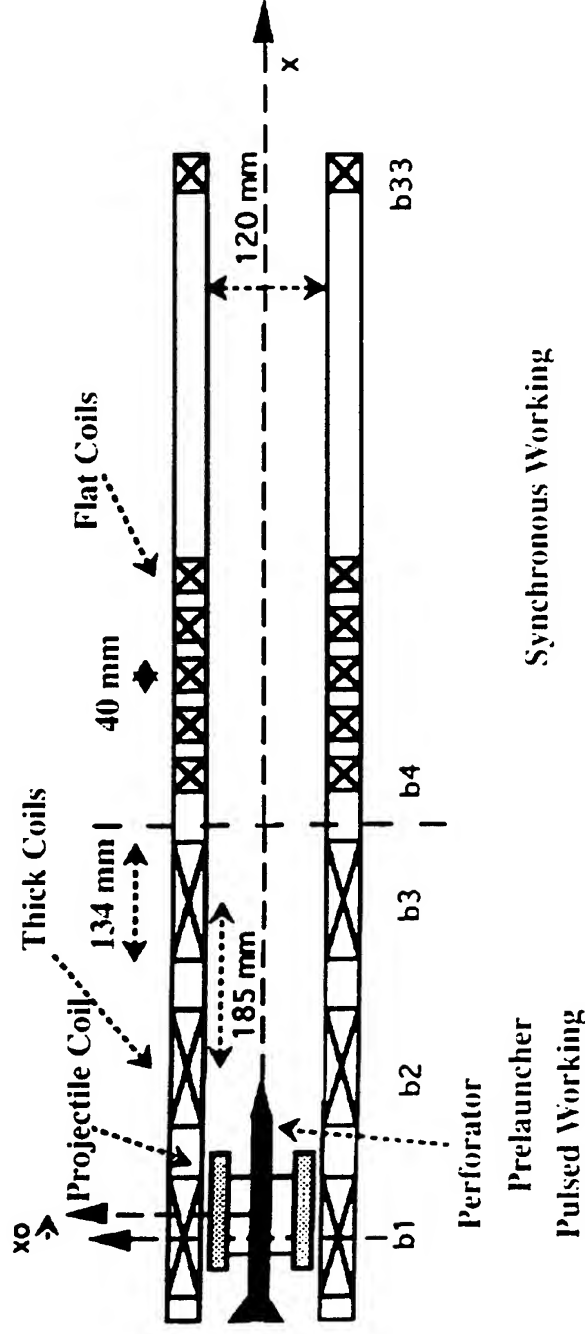
EML 97

DGA/DSA/SPART - C.C. - 97/05 - 6/20

  
**DGA**

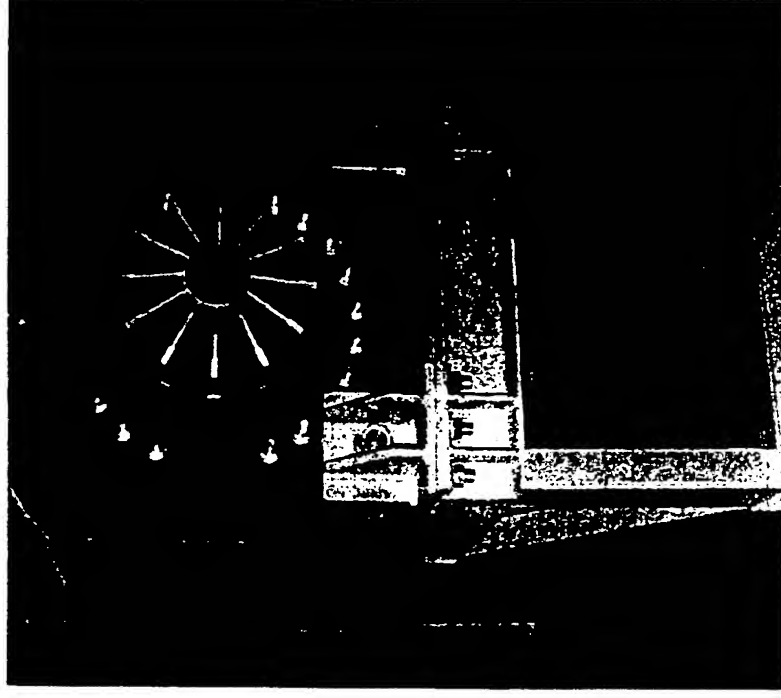
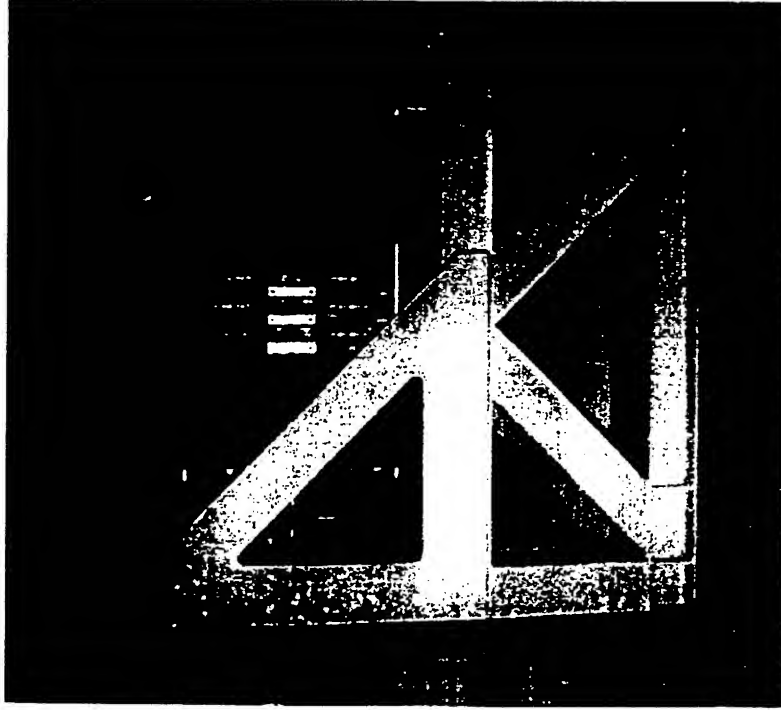
# GEC ALSTHOM Electric Induction Launcher

## *Thirty-Three-Coil Launcher*



Schematic Diagram

# MAGNET MOTOR Three-Stage Toroidal Experimental Accelerator



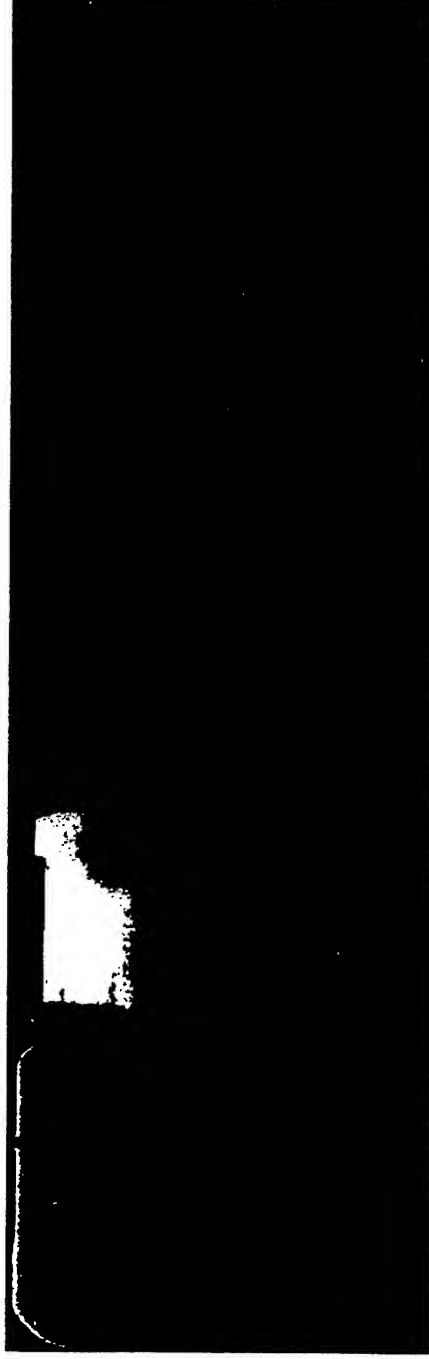
Complete Stator Integrated in its Frame (left) and with Translator (right)





# RHEINMETALL TZN Electrothermal Gun

105-mm-ETK



- since 1994
- 24 shootings with shooting simulator, 16 shootings with 105-mm-ETK
- $V_0 = 2120 \text{ m/s}$
- $m = 1.85 \text{ kg}$
- $\eta = 24\%$



---

## A Module (5 MJ) of the 30 MJ TZN Installation

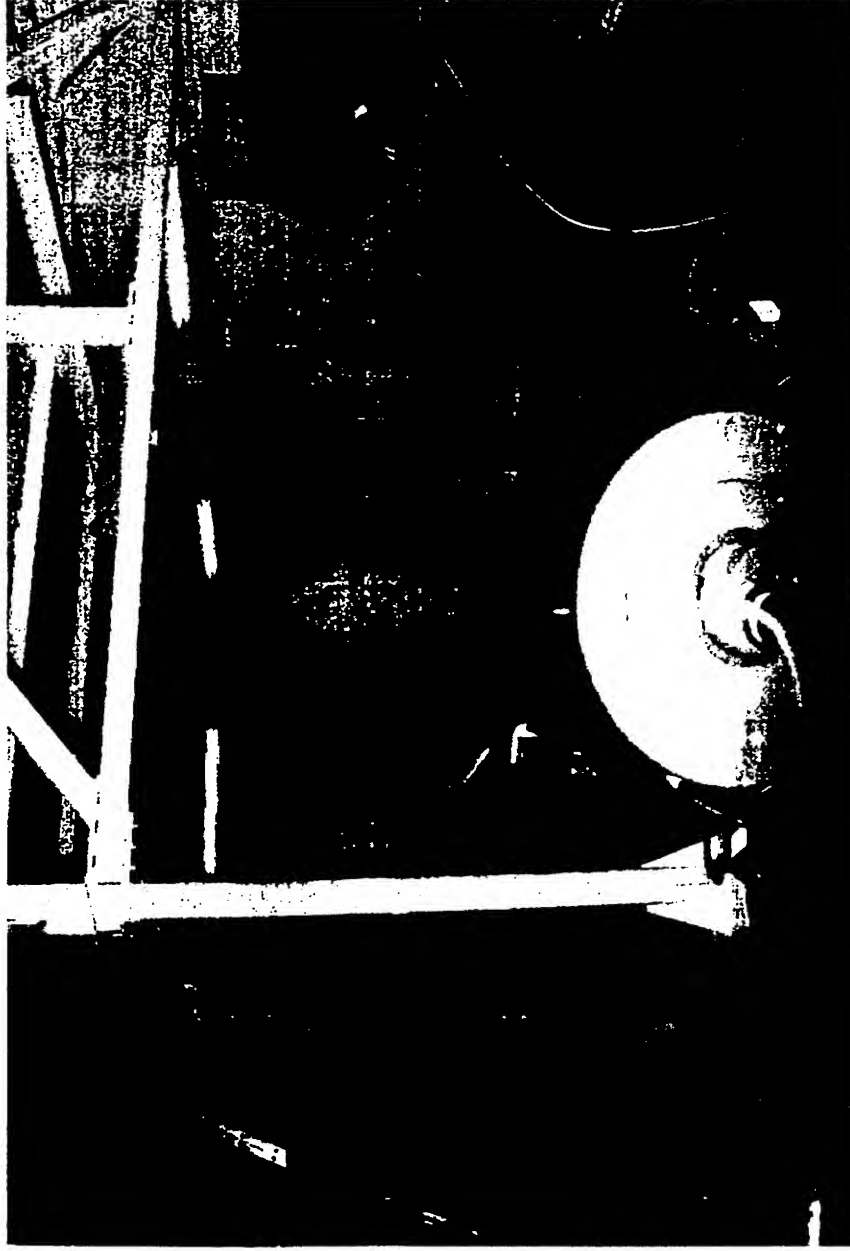


Each module is divided into four 1.25 MJ modules  
(blue frames)

 DGA

---

# General View of the X-Rays Generators and the Bomb

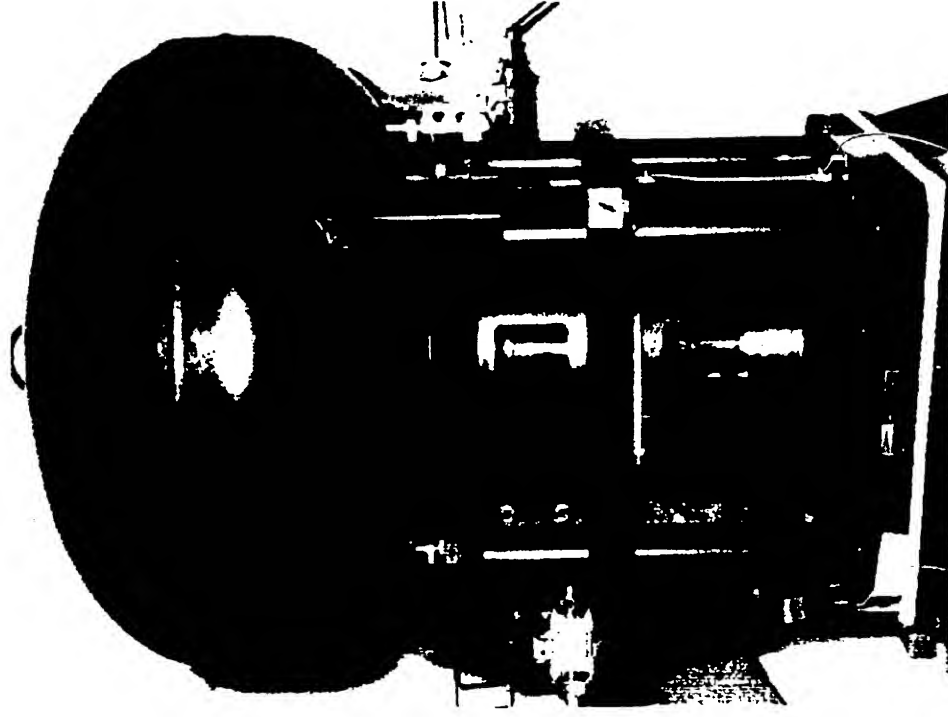


EML 97

DGA/DSA/SPART - C.C. - 97/05 - 11/20

DGA

# Detailed View of the Bomb



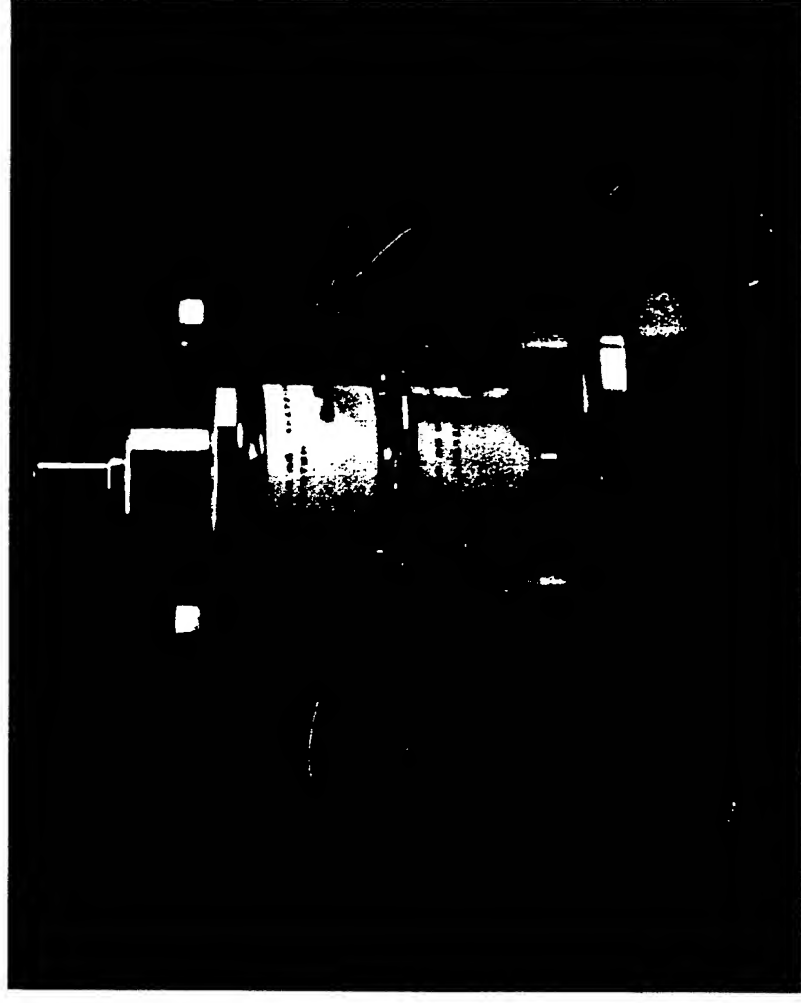
EML 97

DGA/DSA/SPART - C.C. - 97/05 - 12/20

 **DGA**

# ISL and ABB Semiconductor Switching System

- It consists of :
  - a stack of thyristors able to conduct 100 kA (blocking voltage 12 kV)
  - a stack of diodes
- This compact switching system is integrated in the 50 kJ PFN units



# ISL 50 kJ Pulse Forming Network Unit

## ■ It consists of :

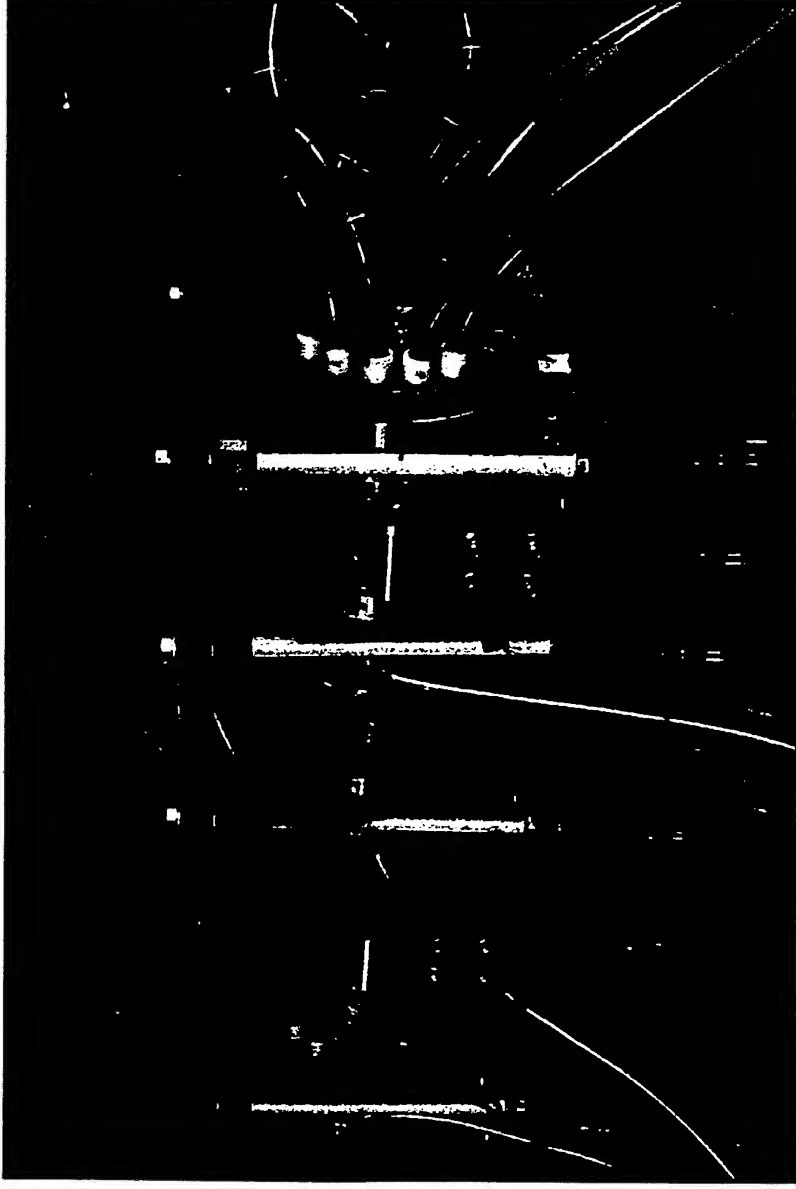
- a capacitor
- a semi-conductor switching system
- a storage inductance

## ■ 200 identical units are assembled to

form the 10 MJ Pulsed Power System of the ISL Rail gun.



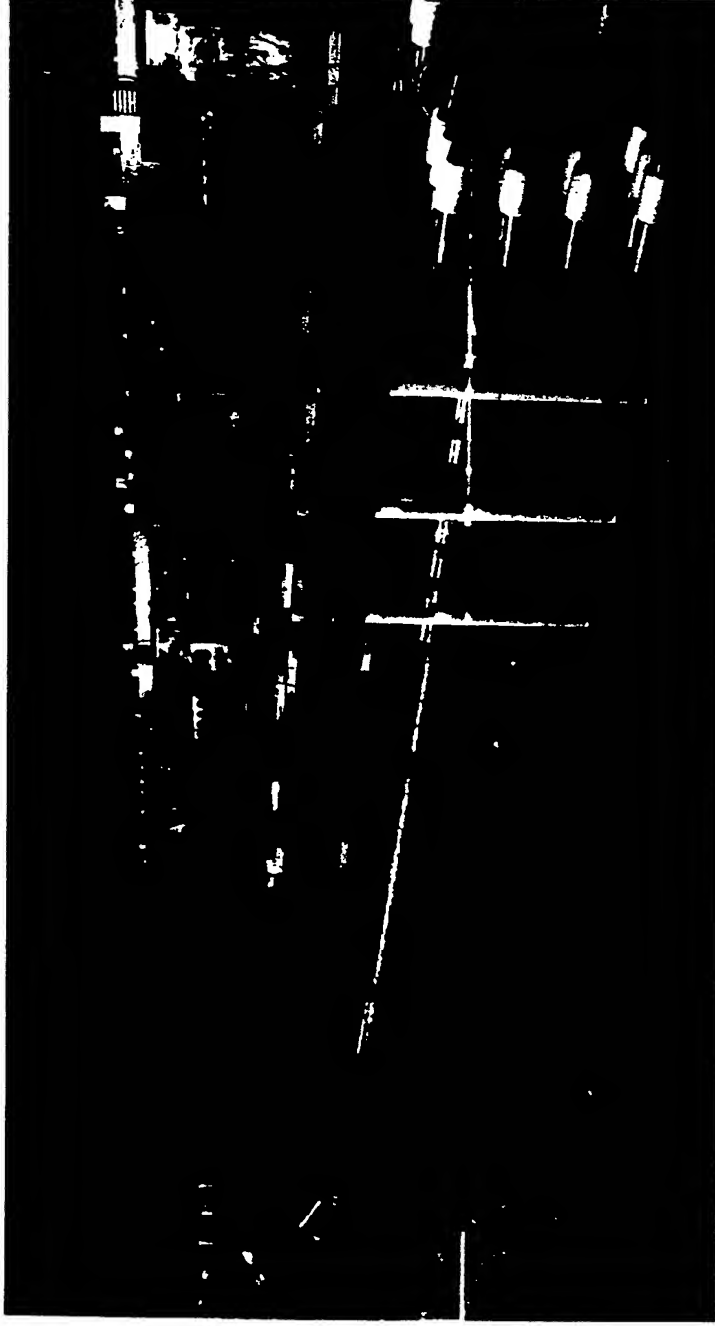
# 3 MJ Capacitor bank driven ISL Rail gun



Characterized by a Distributed Energy Storage (DES)



# 3 MJ Capacitor bank driven ISL Rail gun



- Diameter : 30 or 50 mm
- Length : 3 m
- Current : 2 MA
- Breech fed





# TNO Netherlands Contribution

## ■ Specific Agreement Nr. 1 "Electric Rail Accelerators"

- 1. Armature and rail accelerators
  - solid and hybrid armatures
- 2. Diagnostic
  - electromagnetic, optical and ballistic measuring methods
- 3. Physical descriptions (modelling)
  - 2 and 3D, time mechanical computer codes for rail accelerator response
  - 2 and 3D, time dependant electromechanical/electrothermal computer codes for armature response

# TNO Netherlands Contribution

## ■ Specific Agreement Nr. 2

### "Energy Storage and Switching"

- 1. Inductive storage systems
  - energy storage in normal and superconducting coils
  - SMES research for generation of pulsed currents
- 2. Semiconductor opening switches
  - series and parallel connected resonant counterpulse switch systems for fast interruptions of Mega ampere currents
- 3. Fast discharge batteries for generating high current pulses
  - lead acid bipolar batteries for generating high current high energy pulses

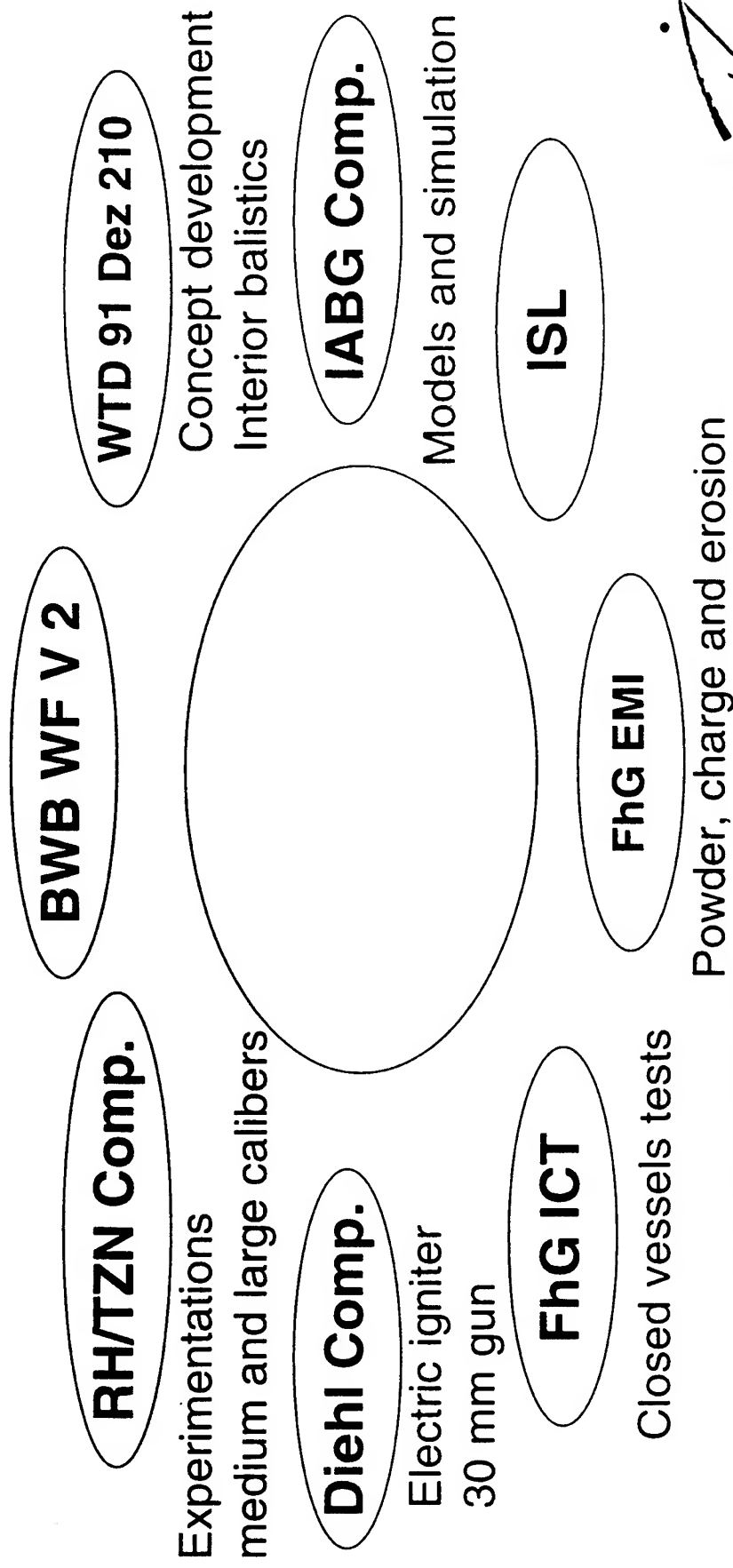




# Overview of the German ETC-Activities

*Members of the national ETC/HYPEC*

*Working Group*



# Electric Guns Alimentation

| Main Storage  | ETC | Stored Energy | Delivered Power | Tension   | Current     |
|---------------|-----|---------------|-----------------|-----------|-------------|
|               |     |               |                 |           |             |
|               | ETC | 20 - 100 MJ   | 0.1 - MW        | 500 V     | 0.2 - 2 kA  |
|               | EM  | 0.5 - 1 GJ    | 10 - 40 MW      | 500 V     | 20 - 80 kA  |
| Power Storage | ETC | 0.5 - 3 MJ    | 0.1 - 1 GW      | 5 kV      | 25 - 250 kA |
|               | EM  | 50 - 70 MJ    | 10 - 20 GW      | 5 - 10 kV | 2 - 5 MA    |

# Experiments with Brush Armatures<sup>1</sup>

H. Peter, R. Charon

French-German Research Institute ISL  
5 rue du Général Cassagnou  
F 68301 Saint Louis

**Abstract-** We present experimental results obtained with a 15 mm square bore railgun powered by a 500 kJ capacitive energy source. Fibre brushes consisting of Cu-Cd wires with 40  $\mu\text{m}$  diameter are integrated as an armature in the sabot. From the tested sabot materials (metals, plastic, reinforced plastic) glass-fibre reinforced plastic gives the best results.

With a good electric contact between rails and armature we realized the following values:  $I_{\text{max}} = 540 \text{ kA}$ ,  $j_{\text{max}} (\text{armature}) = 10 \text{ GA/m}^2$ ,  $T_{\text{max}} (\text{armature}) = 1000^\circ\text{C}$ ,  $\gamma_{\text{max}} = 2 \cdot 10^6 \text{ m/s}^2$ ,  $v_0 = 1450 \text{ m/s}$  with  $m_p = 30 \text{ g}$ . A Heavy-metal penetrator of 17 g can be accelerated up to 910 m/s; the sabot stays intact.

The experimental findings can be described by a simple bulk parameter model. The simulation allows for a ranking of relevant parameters: temperature dependance of resistivity, skin- and velocity skin effect, armature materials, projectile mass, friction at the beginning of acceleration.

The rail surface temperature at the interface between rail and armature is strongly influenced by the armature design. The armature temperature can be kept below the melting point by a proper choice of brush material.

**Introduction-** Many theoretical and experimental investigations show that multi-fibre solid brush armatures are well suited for railgun operation, see for example [1-4] and the references mentioned therein. A high ratio contact area/apparent contact area, even in the position of rest, low friction, and a perfect electric contact are the main features of this type of armature [5]. In addition, a compensation for rail separation and an easy achievable influence on current distribution are possible.

Small caliber railgun experiments are necessary to study in detail the complex phenomena at the rail armature interface and to evaluate different concepts [6, 7].

The present paper has to be seen as a succession of [7] at a higher current level. We present the experimental set-up, the armature design and give some illustrative examples.

**Experimental set-up-** The following table gives an overview of relevant railgun parameters [8]:

|                      |                      |  |               |
|----------------------|----------------------|--|---------------|
| <u>Railgun:</u>      | calibre:             | square bore;                                       | 15 mm x 15 mm |
|                      | rails:               | Cu-Cr or Cu;                                       | 15 mm x 15 mm |
|                      | inductance gradient: | $L' = 0.46 \mu\text{H/m}$                          |               |
|                      | acceleration length: | 1.3 m  |               |
|                      | rail support:        | bolted GRP bars; side and breech end open          |               |
| <u>Power source:</u> | capacitor bank:      | 3 units  |               |
|                      | unit:                | 8 capacitors with 385 $\mu\text{F}$ in parallel    |               |
|                      | energy/unit:         | 154 kJ at 10 kV                                    |               |
|                      | switch/unit:         | spark gap; semiconducting diodes as crowbar switch |               |
|                      | inductance/unit:     | 4 $\mu\text{H}$                                    |               |
|                      | current leads:       | coaxial cables (2 or 3 cables/unit)                |               |
|                      | trigger mode:        | single, together, or time delayed                  |               |

A variation of the current amplitude is possible by changing the loading voltage, by different trigger modes (variation of rise time), and by reduction of ohmic losses in the coaxial cables.

<sup>1</sup> This work was supported by the French and German Ministries of Defence under contracts.

## Experiments and results

**General remarks-** Our brushes are made from strengthened Cu-1%Cd fibres with a diameter of 40  $\mu\text{m}$ . To establish a good electrical contact between armature and rails the rail support has to be as stiff as possible. The fibre bundle length must be greater than the calibre in order to compensate for the inevitable rail separation under load, which is usually in the order of 1%. These requirements are documented by flash radiographs in Fig. 1-3. Two fibre brushes are fastened at the rear end of a piece of Polycarbonate, not to be seen on the photos. In Fig. 1 contact is lost 400  $\mu\text{s}$  after trigger. Bundles with overlength show a poor definition of contact area after loading, when the end faces are perpendicular to the bundle axis, Fig. 2. Together with inertial forces a bad contact definition results in a non negligible reduction of contact area, Fig. 3.



Fig. 1: Metallic contact lost

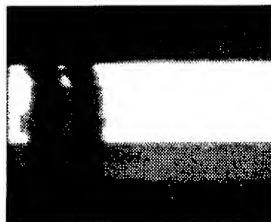


Fig. 2: Poor definition of contact area

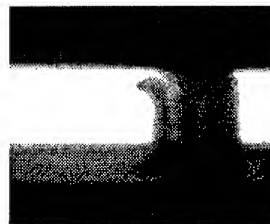


Fig. 3: Reduction of contact area

Rail separation and reduction of contact area are strongly dependent on current amplitude. Fig. 4, 5 show current and muzzle voltage for two different shots with a peak current of 180 kA and 330 kA, resp.

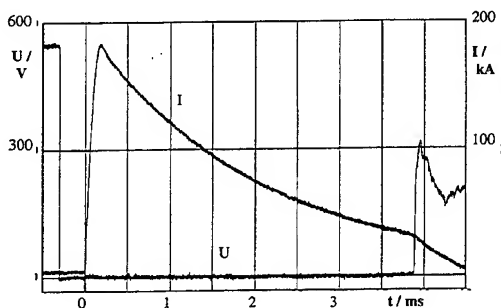


Fig. 4: Current and muzzle voltage vs. time

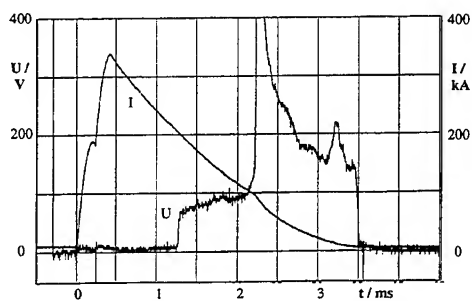


Fig. 5: Current and muzzle voltage vs. time

In Fig. 5 the sharp increase in muzzle voltage up to 80 V indicates the transition into arcing. Flash radiographs taken during free flight reveal that the arcing process leads to a very high amount of brush erosion, Fig. 7; whereas erosion is low in case of metallic brush contact, Fig. 6.

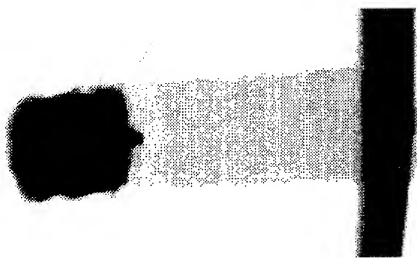


Fig. 6: Flash X-ray picture; free flight;  $I_{\text{max}} = 180 \text{ kA}$

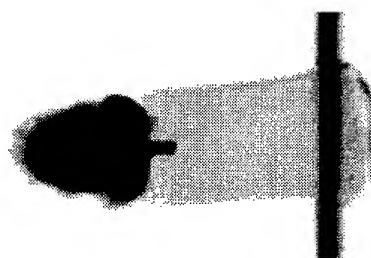


Fig. 7: Flash X-ray picture; free flight;  $I_{\text{max}} = 330 \text{ kA}$

One remarkable property of brush armatures has to be mentioned explicitly: although the railgun is open at the side, we never observe precursors passing the arcing projectile. The arcs always remained fixed at the brush end faces.

The rear end fixed brush armatures in push mode fail at higher currents and accelerations.

**Modified multi-fibre armature-** A better force distribution inside the sabot and an appropriate definition of the contact surface can be achieved by a modified armature design, Fig. 8, 9.

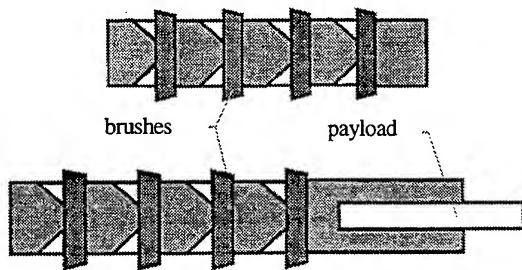


Fig. 8: Principle of an integrated armature without and with payload

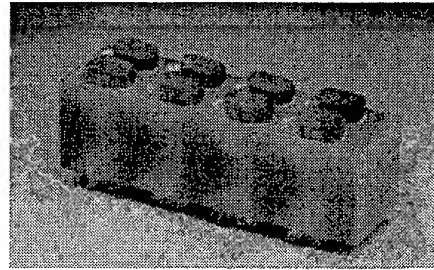


Fig. 9: Photo of the armature

The brushes are placed in two rows of boreholes (diameter 5 mm) in a piece of glass-fibre reinforced plastic, true to calibre size. On both ends of the holes there is a milled reserve volume in which the overlong fibres can be bent during the loading process. The bending force determines the contact load and at the same time the amount of friction against the rails. To avoid the geometric effect of Fig. 2 there is an angle of approximately  $10^\circ$  between the brush end faces and the GRP sabot. The fabrication of the end faces is made in a special containment with the help of a milling machine.

The following table gives a few parameters characterizing this kind of armature:

| shot number | projectile mass / g | $I_{\max}$ / kA | $U_{\text{muzzle}}$ / V                                   | $v_{\text{muzzle}}$ / $\frac{\text{m}}{\text{s}}$ |
|-------------|---------------------|-----------------|---|---|
| 37          | 34.3                | 510             | $< 3 \text{ V}$   | 1330  |
| 39          | 29                  | 540             | $< 3 \text{ V up to } t_1$<br>$< 20 \text{ V up to } t_f$ | 1450  |
| 40          | 50.5                | 540             | $< 5 \text{ V up to } t_f$                                | 1095  |
| 41          | 34.9                | 540             | $< 3 \text{ V up to } t_1$<br>$< 20 \text{ V up to } t_f$ | 1515  |
| 43          | 64.9                | 540             | $< 4 \text{ V up to } t_f$                                | 910   |

The structure of the armature of the five shots is identical, two rows of 4 boreholes each, the filling factor is about 75%.  $t_1$  is on the order of 1.5 ms,  $t_f$  designates the shot out time.

Fig. 10 shows current and muzzle voltage for shot 37, Fig 11 a flash radiograph of the armature at muzzle exit time, Fig. 12 a free flight flash X-ray picture taken from above.

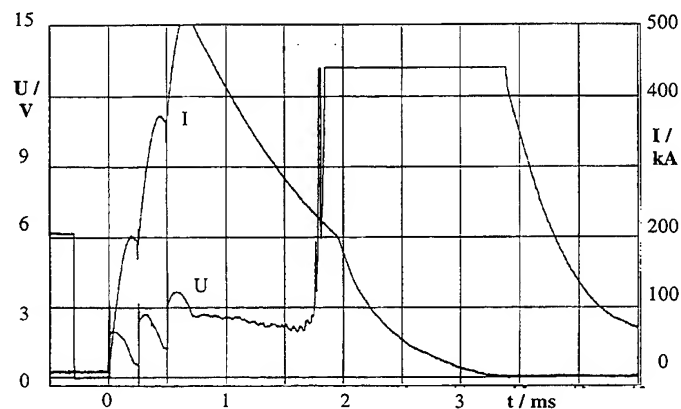


Fig. 10: Current and muzzle voltage vs time for shot nr. 37,  $I_{\max} = 510 \text{ kA}$

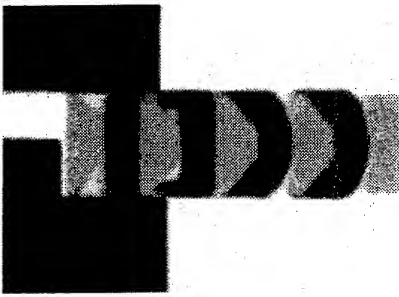


Fig. 11: Projectile at muzzle exit

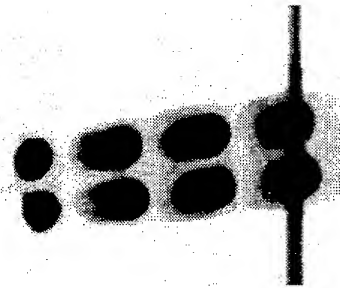


Fig. 12: Projectile during free flight

In Fig. 11 we see, that the metallic contact to the rails still exists; we observe the deformed brushes indicating the current distribution in the brush configuration. A distinct beginning of erosion on the rear end of the first fibre bundle has to be stated.

This kind of erosion is greater at higher currents, cf. muzzle voltage for shot 39 in the table.

A sabot with payload and an armature is shown in the flash radiograph in Fig. 13 before shot. The payload is a 17 g heavy metal rod with a length to diameter ratio of 7.5. This projectile was fired in shot 43; Fig. 14 to 16 show the result.

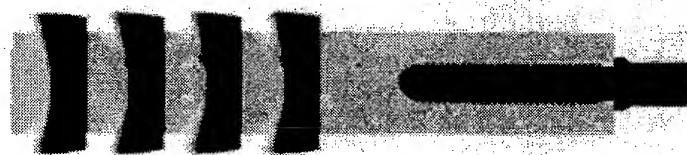


Fig. 13: Flash radiograph of a projectile before shot

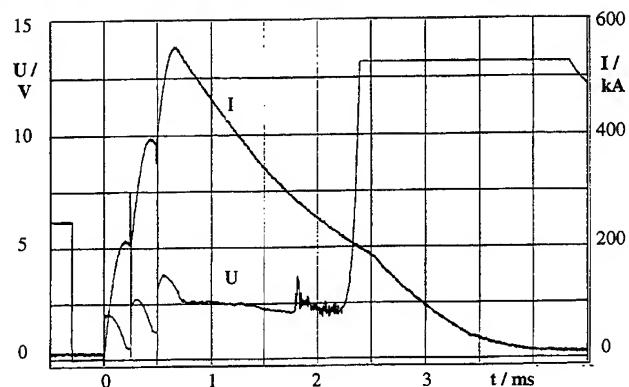


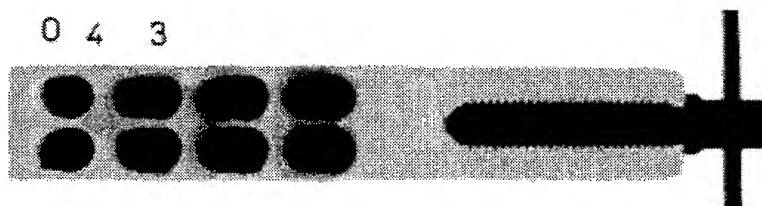
Fig. 14: Current and muzzle voltage vs time; shot nr. 43;  $I_{max} = 540$  kA



Fig. 15: Flash radiograph of the projectile at muzzle exit time, shot nr. 43



Fig. 16: Flash X-ray picture during free flight



From Fig. 15 we learn, that loss of contact at the first fibre bundle due to erosion does not provoke a dramatic armature failure. Even at a maximum acceleration of  $1.1 \cdot 10^6 \text{ m/s}^2$  the sabot remains intact.

### Discussion

- The armature temperature is an essential parameter. In Fig. 17 we state a thermal destruction of the sabot. The sabot was made from Polyamid-Imid (Torlon); the thermal load in the rear fibre brushes was too high, the resulting gas generation from ablated material inside the boreholes leads to an overpressure and mechanical failure.
- Another important parameter is the temperature at the contact area. In Fig. 18 we show a projectile, which is slit over its whole length. In this case the quality of the end faces of the fibre bundles (the smoothness) was not sufficiently good and subsequently the power input into the resulting arc was too high.
- The fabrication process, the end face treatment of the fibres, and the proper choice of material are therefore of paramount importance for a good armature.

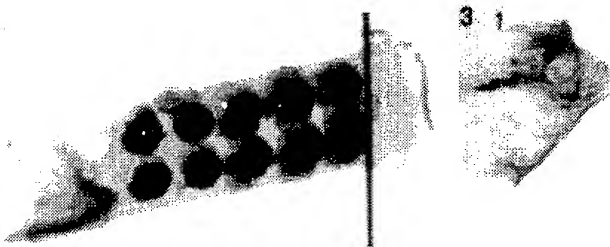


Fig. 17: Sabot made from Polyamid-Imid;  $I_{\text{max}} = 450 \text{ kA}$



Fig. 18: Brushes with poor end face treatment;  $I_{\text{max}} = 450 \text{ kA}$

- Sabots made from metals with brushes reaching from rail to rail have no advantages in comparison with GRP material. They have higher densities; when the brushes are not insulated against the sabot, axial leak currents can occur leading to moments and a resulting balloting of projectiles. In this case the main advantages of brushes are lost.

- Between a maximum current of 200 kA and 540 kA the rail surface is slightly changing. At low values no surface transformations can be observed. At higher rates a faint change in reflectivity is established some time after the shot. This change occurs in case of pure copper as well as in case of Cu-Cr. The transformation is more pronounced at the breech end, Fig. 19, than at the muzzle, Fig 20.

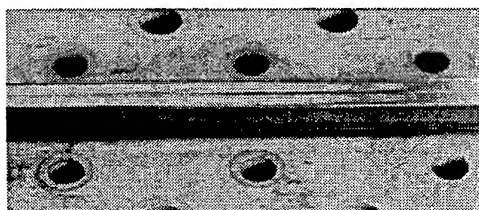


Fig. 19: Rail surface after the shot; breech end



Fig. 20: Rail surface after the shot; muzzle end

**Simple model for armature description-** We assume the current to be distributed equally in the two rows of brushes. With this symmetry it suffices to calculate one row only. The four brushes are treated as ohmic resistances with the specific resistivity of Cu-Cd ( $\rho = 20 \text{ n}\Omega\text{m}$ ) and a temperature coefficient  $\alpha = 0.0033 \text{ /K}$ . The rail sections between the brushes are supposed to have an inductance  $L'1$  ( $l$  is the inter-brush distance) and a resistance  $R_s$  in series.  $R_s$  contains the classic skin resistance as well as a velocity dependent term. From the total current  $I$  ( $I_{\text{max}} = 500 \text{ kA}$ ) we calculate the armature velocity for a given projectile mass as function of time. Then the partial currents, temperatures and resistances are determined simultaneously. The numbering 1-4 is to be understood from the rear to the front end of the four brush armature. In Fig. 21 and 22 the current and temperature distributions are shown.

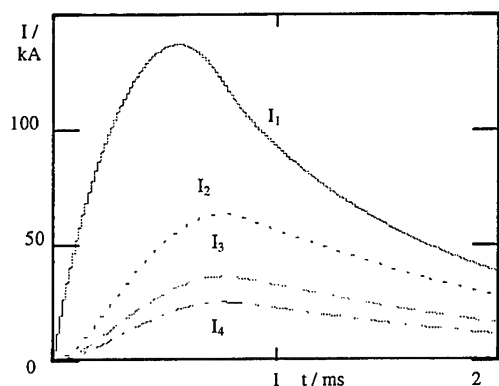


Fig. 21: Current distribution in the 4 brushes

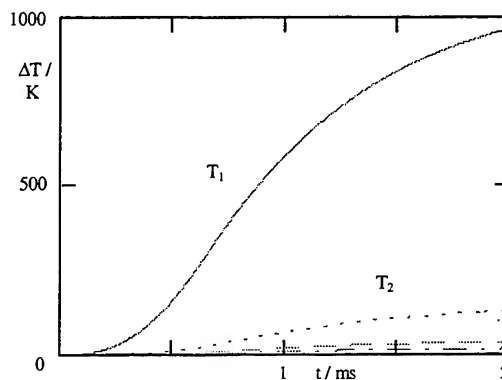


Fig. 22: Temperature distribution in the 4 brushes

The strong disparity in the current distribution corresponds to the deformation of the brushes in Fig. 11. In Fig. 23 the first brush is divided in 4 resistances and one can see the temperature distribution in this brush. The calculated temperature together with an additional friction term is sufficient to melt the rear part of brush 1 at the contact, cf. Fig. 11. Fig. 24 shows the resistance of the rail segment between brush 1 and 2 and the evolution of brush resistance  $R_1$  as function of time. Up to beginning of motion at  $t_s$ ,  $R_s$  decreases as skin depth grows, afterwards it increases due to the velocity skin effect.

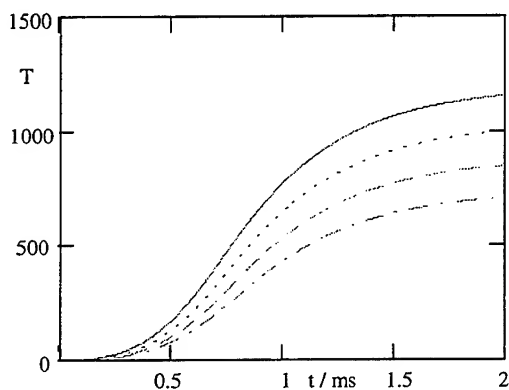


Fig. 23: Temperature distribution in brush 1, divided in 4 segments

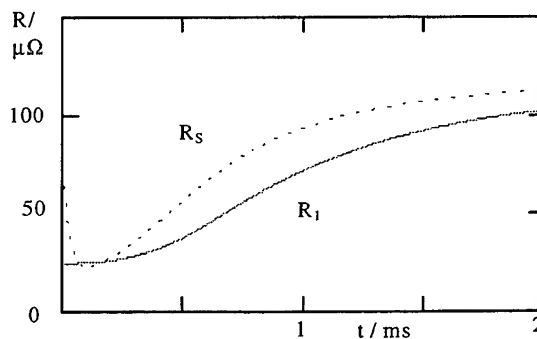


Fig. 24: Brush ( $R_1$ ) and rail segment resistance ( $R_s$ )

A detailed analysis reveals that the maximum temperature  $T_1$  in brush 1 can be slightly lowered by increase of projectile mass and by retarding the projectile start time  $t_s$ . The most important influence on brush temperature is given by geometric brush dimensions and by the choice of material. In Fig. 25 a calculated temperature distribution is shown with brush 1 made from CuSn6 ( $\rho = 130 \text{ n}\Omega\text{m}$ ,  $\alpha = 0.7 \cdot 10^{-3} \text{ /K}$ ) and brush 2-4 made from Cu-Cd. The temperature reduction is evident.

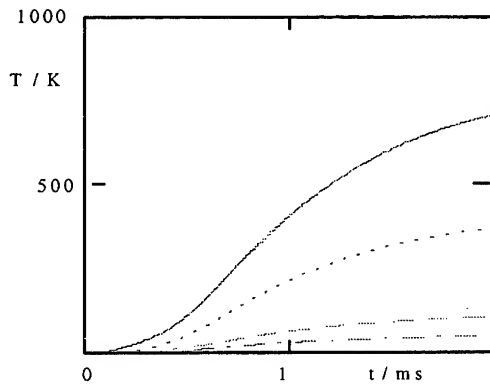


Fig. 25: Temperature distribution, 1 x CuSn6 + 3 x CuCd brushes

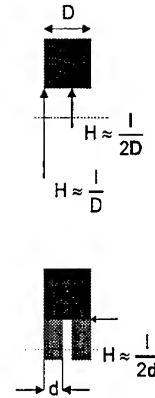


Fig. 26: Rail geometry

According to Fig. 22 the brush temperature cannot be responsible for the change of the rail surface at the beginning of the acceleration. The current induced heating of the rails can be approximated by

$$T \approx \frac{1}{c_V} \int_0^{t_0} \rho j^2 dt, \quad j = j_x = \frac{\partial H_z}{\partial y}, \quad \delta = \sqrt{\frac{\rho}{\mu_0}} t, \quad \bar{j} = \frac{H}{\delta},$$

with heat capacity  $c_V$ , resistivity  $\rho$  and current density  $j$ . The upper integration limit is given by the time in which the armature has traveled its own length.  $H$  denotes in usual notation the magnetic field,  $\delta$  the skin depth and  $\bar{j}$  the average current density. A strongly simplified assumption on the velocity induced switching of the magnetic field  $H$  delivers the surface temperature  $T$

$$H = H_0 \sqrt{\frac{t}{t_0}}, \quad T \approx \frac{1}{c_V} \mu_0 H_0^2 t.$$

The melting temperature of Cu,  $T = 1083^\circ\text{C}$ , will be reached in this approximation independently from  $t_0$  and  $\rho$  at a magnetic field strength of  $H_0 \approx 50 \text{ kA/mm}$ .

On the rail surface  $H_0$  is on the order of  $H \approx I/2D$ , at the edges  $H \approx I/D$ , and at the interface between armature and rail  $H \approx I/2d$ , cf. Fig. 26. With a brush diameter of  $d = 5 \text{ mm}$  and 500 kA total current the above given limit is exceeded, when the brush filling factor is taken into account.

**Conclusion-** Brush armatures need a well defined containment. The brushes must have a greater length than the calibre in order to compensate for the small rail separation under load. The fabrication of the end faces is crucial, a small angle between rails and end face surface is advantageous for a good geometric definition of the contact surface. The most important parameter is the temperature of the armature; by a proper choice of fibre material one can either alter the current distribution or support higher temperatures (ex.: Fe). In either case there is a strong interaction between metallic fibre brushes and the surrounding sabot material. Due to its thermal and mechanical properties glass fibre reinforced epoxy is a good candidate for making sabots.

In case of brush armatures friction, projectile mass, and starting time  $t_s$  are of minor importance. With the help of a simple model the armature can be designed.

To arrive at higher velocities there are two options:

- 1) Accept erosion, make the armature long enough, so that disastrous arcing can be avoided.
- 2) Lower temperature at the first brushes or choose material with higher melting temperatures.

Both possibilities are under investigation at ISL at the moment.

## References

- [1] W. H. Lupton, P. Reichner  
Ultrahigh speed fiber brush design and tests  
Wear, **78**, 139, (1982)
- [2] D. Kuhlmann-Wilsdorf  
Theoretical speed and current density limits for different types of electrical brushes  
IEEE Transactions on Magnetics, **22**, 340, (1984)
- [3] W. Karthaus, W. A. de Zeeuw, W. J. Kolkert  
Erosion-free electromagnetic acceleration of solid brush armatures with rail launchers  
Proc. 3rd Europ. Symp. on EML Technology, London, 1991
- [4] W. Karthaus, M Koops  
Results of experiments performed with multi-fibre solid brush armatures  
Proc. 4th Europ. Symp. on EML Technology, Celle, 1993
- [5] H. Peter, R. Charon  
Der Kontakt zwischen Schiene und metallischer Strombrücke bei einem Schienenbeschleuniger  
ISL - R 111/95
- [6] M. Koops, W. Karthaus  
Test bed for the evaluation of solid armature concepts  
Proc. 5th Europ. Symp. on EML Technology, Toulouse, 1995
- [7] H. Peter, R. Charon, J. P. Chabrierie  
Metallic railgun armatures  
Proc. 5th Europ. Symp. on EML Technology, Toulouse, 1995
- [8] H. Peter, R. Charon, C. Gauthier, J. Wey, W. Wenning  
Untersuchungen zum Zusammenwirken von Nutzlasten mit Treibkäfigen und Armaturen von Geschossen für Schienenbeschleuniger. Experimenteller Teil  
ISL - RT 508/96

# Experiments to Measure Gouging Threshold Velocity for Various Metals Against Copper

Francis Stefani and Jerald V. Parker

Institute for Advanced Technology, The University of Texas at Austin  
4030-2 W. Braker Lane, Austin, TX 78759

**Summary**—Hypervelocity gouging is a form of damage that can occur to surfaces in sliding contact at high relative velocity. Gouges, which are in the form of teardrop-shaped craters, have been observed on rocket sled tracks, in light gas gun barrels, and in the bore of railguns. One aspect of gouging that has not been adequately explained is the existence of a minimum velocity (or threshold velocity) for a given material pair below which gouging does not occur. This paper reports a series of experiments to test the hypothesis that the onset of gouging is governed by the hardness of the harder material and by the density and sound speed of both materials. In the tests, samples of various metals were accelerated to 2.2 km/s while in direct sliding contact with CD110 copper rails. The samples were carried in a Lexan forebody, modified to apply normal loads of 40 - 80 MPa to the sample/rail interface. The portion of the armature directly in line with the samples was cut away to avoid contaminating the gouge track. Visual inspection of the resulting gouges was used to establish a gouging threshold for each metal. The tests were conducted in the 40 mm square bore electromagnetic launcher at the Institute for Advanced Technology. Metals tested include 1015 steel, silver, molybdenum, pure copper, tungsten, nickel, magnesium, and 7075 aluminum. The results of the experiments show the existence of a straight line fit between hardness of the harder material and the shock pressure for a normal collision at the gouging threshold velocity.

## I. INTRODUCTION

Hypervelocity gouging (henceforth simply "gouging") is a form of damage that can occur to surfaces that are in sliding contact at high relative velocity. Gouges are in the form of tear-shaped craters along the velocity vector, such as shown in Fig. 1.

Damage from gouging in solid armature railguns is usually so severe that the useful life of rails is limited to a few shots. Unfortunately, the present understanding of gouging is not complete enough to identify clear solutions to the problem: there are no predictive models of gouging, and the existing database is too small to guarantee the success of empirical solutions.

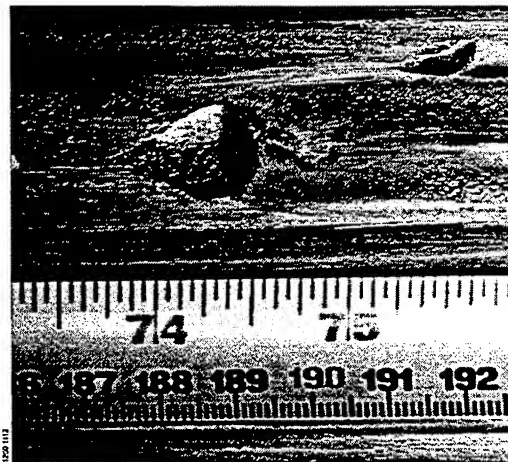


Fig. 1. Typical hypervelocity gouges produced by aluminum sliding on copper.

Certain aspects of gouging have come to be understood through operational experience with railguns and rocket sleds. Gouging is a threshold phenomenon, in that, for any given material pair there is a threshold velocity below which gouging does not occur. For example, the gouging threshold for aluminum on ETP copper rails is widely reported to be 1.4 km/s, independent of launcher or armature design. Material hardness is known to affect the gouging threshold with harder materials being more resistant to gouging.

There is a long history of research into the gouging problem, dating back to the 1960's, when gouges were first reported on the rocket sled at Holloman A.F.B. The first systematic investigation of gouging was undertaken by researchers at Ohio State University to find out why damage to the rocket sled tracks often occurred when the sled was operated above 1.5 km/s [1].

The OSU researchers studied evidence from the rocket sled range and from gouges produced in their laboratory using a light gas gun. They inspected recovered rocket sled slippers and found gouges similar to those on the tracks, from which they inferred that the gouging process is symmetrical in the slider and in the track. They found that gouges can be initiated by 3rd particle debris, such as grains of sand on the track, but that this was not the only possible initiation mechanism as it cannot explain the creation of gouges in the laboratory. In the end, they concluded that most gouges are caused by the interaction of microscopic asperities which begins with the formation of a contact weld such as occurs in adhesive wear.

The first paper devoted exclusively to gouging in railguns was published in 1982 by Barber and Bauer [2]. Like the OSU researchers, they attributed gouging to the interaction of micro-asperities. They emphasized that gouging is a hypervelocity phenomenon, that occurs when the impact induced stress is equal to the ultimate strength of the materials. The gouging threshold velocity, they concluded, is determined by asperity impact velocity, angle of impact, material densities, and shock speeds.

Gouging has also been investigated numerically by researchers at Sandia National Laboratory using 2D and 3D versions of the hydrocode CTH [3,4]. Their simulations exhibit many of the physical features of gouges, including the threshold-like behavior of the process. A key feature of the Sandia approach is the view that gouging is an instability and, as such, what matter are the conditions that determine whether or not the instability grows. In one of the studies, a 100 micron diameter piece of debris between the slider and glider is used as an initiating perturbation. The authors show that similar results are obtained for other size initiators [3]. The simulations show reasonably close agreement with the limited database on gouging. However, to obtain these results, assumptions have to be made about the setup of the problem whose meaning is not clear physically.

## II. RATIONALE FOR EXPERIMENTS

The experiments we performed are based upon many of the ideas put forth in earlier work. Our hypothesis is that gouging occurs when interactions between slider and glider create stresses that exceed the strength of the harder material. We believe that various initiation mechanisms exist, but that the details of these are unimportant.

The idea that the strength of the harder material governs the onset of gouging is key to our approach. The rationale is as follows. If asperities on the surfaces of the slider and glider are interacting and the harder material doesn't fail, the process is simply that of abrasive wear: the hard material produces a score track in the soft material, but not a gouge. If, on the other hand, the interaction occurs at a velocity such that stresses exceed the yield strength of the harder material, then a portion of the hard material will be dislodged and joined with the initiator. This increases the interaction with the soft material leading to even higher stresses and a runaway process that produces a macroscopic gouge.

To test this explanation of gouging it is necessary to demonstrate that a relationship exists between the stresses generated during the formation of a gouge and the strength of the stronger material. There are two difficulties associated with direct measurement of this relationship. The first difficulty is determining the stresses, which cannot be measured directly and cannot be calculated given the present uncertainties in

modeling high strain rate processes and failure. A second difficulty is identifying an appropriate measure of material strength that governs gouging, since the mode of failure is also presently unknown.

Given the difficulties associated with determining the actual stresses, we tested instead for a correlation to a knowable stress. If the relative velocity of the slider and glider are known, it is possible to accurately place an upper bound on the pressure generated in any interaction. This is the pressure that would be generated if the surfaces collided in a normal impact. This value, the normal planar shock pressure, is related to the density and shock speed of both materials. Although normal shock pressures at gouging velocities greatly exceed the yield strength of the materials, it is reasonable to believe that there might be a consistent relationship between this limiting value and the actual pressures involved in the formation of gouges. This would be the case if the same relative distribution of stresses occurred in the formation of all gouges, regardless of materials, a reasonable assumption given the remarkable similarity of gouges made under widely differing conditions. Ultimately, this assumption is supported by the experimental data.

The second source of ambiguity noted above comes from not knowing the exact failure mechanism involved in gouging. A number of failure criteria are used in the study of friction and wear, including ultimate tensile strength, yield strength, hardness, and elastic strain energy capacity ( $H^2/2E$ ). Other criteria, such as spall strength, dynamic tensile strength, and strain-to-failure, are used in the study of high-strain-rate processes. We chose to use hardness because the process by which hardness is measured is similar to the process by which gouges are created. Hardness is a measure of the stress required to create a cavity in a continuous material, and depends on the stress-strain behavior of the material and the final strain to failure [5,6]. Also, unlike ultimate tensile strength, which is a macroscopic average, hardness measures strength on the length scale at which gouges initiate. A final advantage of using hardness is that measurements can be made directly on our machined samples.

### III. DESIGN OF EXPERIMENTS

The experiments consisted of a series of six railgun launches in which samples of various materials were tested in sliding contact with copper rails to establish gouging threshold velocities. The tests were conducted in the 40 mm square bore launcher at the Institute for Advanced Technology. In the tests, the samples were accelerated to 2.2 km/s while in direct contact with CD110 copper rails.

The samples were carried in a forebody, shown in Fig. 2, that consists of a polycarbonate block containing two sample-holders. The sample size is 1cm x 2cm x 2mm. Sample holders made out of 7075 aluminum are used to distribute the acceleration forces so the polycarbonate does not fail. An interference fit of approximately 0.25 mm between the samples and the rails produces normal loads of 40 - 80 MPa at the sample/rail interfaces. In order to avoid contaminating the gouge track, the portion of the armature directly in line with the samples was cut away.

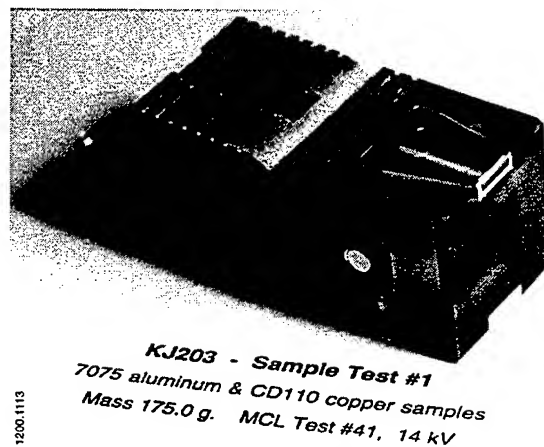


Fig. 2. Armature and forebody used in gouging experiments.

Because the objective was to establish the effects of shock pressure and hardness on gouging threshold velocity, we tested materials with differing values of acoustic impedance and hardness. Acoustic impedance is the product of density and sound speed, and defines a material's capacity for generating shock pressures. Figure 3 shows the range of combinations spanned by our test matrix, which includes:

- soft materials with low acoustic impedance (Mg and graphite)
- moderately hard materials with low acoustic impedance (7075 Al and Ti)
- soft materials with high acoustic impedance (Ag, Cu, and 1015 steel)
- very hard materials with high acoustic impedance (80% Au/20% Cu, W, 4340 Steel).

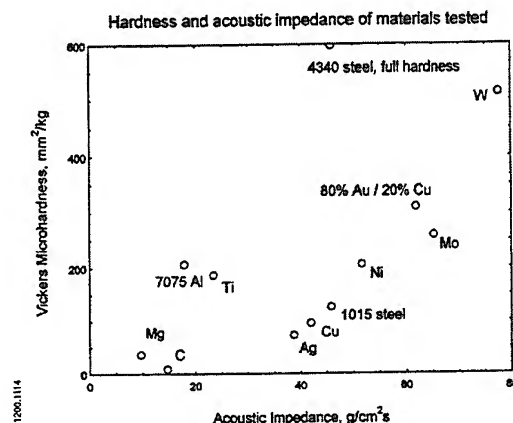


Fig. 3. Hardness and acoustic impedance of materials tested.

#### IV. RESULTS AND DISCUSSIONS

Results from the 12 tests are summarized in Table 1. A new set of rails was used for each test. After the launch the rails were removed and inspected to establish the location at which gouging began. The first column of data is the velocity of the sample at the location of first gouges. The velocities were computed using a b-dot analysis program that solves for a best fit to the probe data, subject to physics-based constraints.

The error bars in velocity reflect the level of uncertainty in locating the first gouges. For harder materials the transition to gouging was reasonably sudden, and the onset of gouging was clearly discernible. The uncertainty in the location of the first gouges was typically  $\pm 5$  cm. For the softer materials, in particular face-centered cubic metals, the sample tracks often included a transition region that contained adhesive wear damage, making it more difficult to establish the exact location of the first gouges. The uncertainty in the location of the first gouges was typically  $\pm 10$  cm. The uncertainty associated with the b-dot analysis was on the order of  $\pm 1$  cm for all tests.

The second column of tabulated data is the normal planar shock pressure corresponding to the threshold velocity. The shock pressures were found by graphically matching acoustic impedance for the material pairs, using shock data from Los Alamos [7,8].

The hardness measurements shown in the table were made on machined samples using two Vickers microhardness testers; one with a 3 kg weight for 10 seconds, the other with a 1 kg weight for 10 seconds. The measurements made in the 1 kg microhardness tester are systematically higher by about 10%, possibly reflecting the effects of surface hardening from machining. The hardness of the copper samples was slightly higher than the hardness of the copper rails possibly for the same reason.



TABLE I. SUMMARY OF TEST RESULTS

| MATERIAL               | THRESHOLD<br>VELOCITY<br>[M/S] | NORMAL<br>PLANAR<br>SHOCK<br>PRESSURE<br>[GPA] | VICKERS<br>HARDNESS<br>1 KG, 10 S<br>[KG/MM <sup>2</sup> ] | VICKERS<br>HARDNESS<br>3 KG, 10 S<br>[KG/MM <sup>2</sup> ] |
|------------------------|--------------------------------|--|--|--|
| 7075 ALUMINUM          | 1300 ± 0                       | 16.3 ± 0                                       | 208 ± 17   | 206 ± 7  |
| CD110 COPPER SAMPLE    | 746 ± 50                       | 14.9 ± 1.25                                    | 109 ± 3  | 96 ± 2   |
| 80% Au / 20% Cu        | 1,346 ± 75                     | 35.7 ± 2.6                                     | 340 ± 13   | 309 ± 13   |
| 1015 STEEL             | 977 ± 110                      | 20.4 ± 3.5                                     | 143 ± 8  | 126 ± 7  |
| SILVER                 | 770 ± 90                       | 15.8 ± 1.9                                     | 75 ± 2   | 73 ± 2   |
| MOLYBDENUM             | 1,268 ± 30                     | 32.3 ± 0.8                                     | 296 ± 17   | 258 ± 8  |
| NICKEL                 | 996 ± 70                       | 22.2 ± 1.7                                     | 207 ± 11   | 205 ± 17   |
| TUNGSTEN               | 1,474 ± 45                     | 46.3 ± 1.9                                     | 581 ± 47   | 513 ± 33   |
| TITANIUM               | 1,420 ± 55                     | 23.0 ± 1.0                                     | 218 ± 17   | 186 ± 10   |
| MAGNESIUM              | INCONCLUSIVE                   | -  | 48 ± 4*  | 37 ± 4   |
| GRAPHITE               | INCONCLUSIVE                   | -  | 15 ± 4*  | 9 ± 3  |
| 4340 STEEL, FULLY HARD | 1,878 ± 90                     | 44.3 ± 3                                       | 541 ± 27   |  |
| CD 110 COPPER RAILS    |                                |  | 88 ± 2   | 82 ± 3   |

\* 100gf for 10 seconds

In order to benchmark our experiment we began by testing samples of 7075 aluminum and CD110 copper, materials for which the gouging threshold is already known (albeit only approximately in the case of copper). For both materials, the measured gouging threshold velocity agreed well with the accepted values of 1,400 m/s and 600 m/s [9]. Figure 4 is an X-ray of the launch package in flight after it left the muzzle, showing that the samples remained intact for the duration of the launch.

Two of the tests (magnesium and graphite) were deemed inconclusive because no gouges were produced. These were the softest materials we tested and it is possible that the samples wore excessively. In the muzzle X-rays for this test, there is no trace of the magnesium sample, and the graphite sample appears to have worn flush with the sample holder.

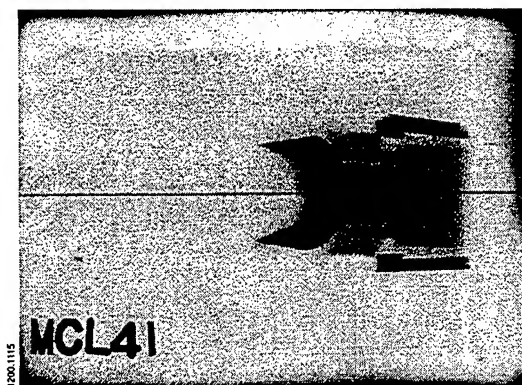


Fig. 4. X-ray of launch package in flight after leaving muzzle. The test samples (copper top, aluminum bottom) and sample holders are beginning to separate due to aerodynamic forces.

Figure 5 is a plot of the data in the last three columns in the table. With the exception of the data points for 7075 aluminum, there is a reasonably good straight line fit to the data. This supports the existence of a relationship between shock pressure at the gouging threshold velocity and hardness. Relatively large uncertainty in the measurements is due in large part to the statistical nature of the gouging process and the fact that we chose to test many materials once rather than fewer materials repeatedly. The horizontal error bars for each data point reflect our uncertainty in locating the onset of gouging *in a single trial*.

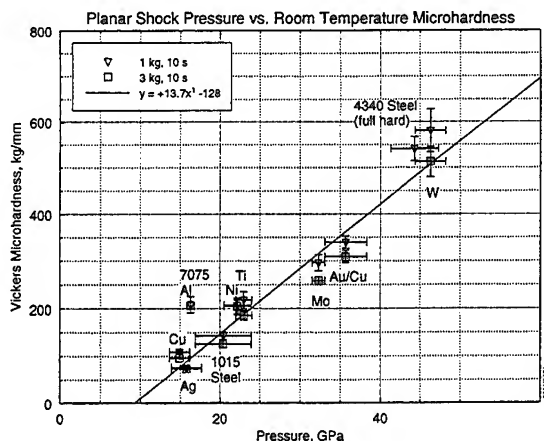


Fig. 5. Planar shock pressure at gouging threshold velocity vs. room temperature hardness.

The failure of 7075 aluminum to fit the trend may be the result of thermal softening in the bulk of the aluminum sample from intense frictional heating. The net effect would be a lowering in actual hardness at the gouging threshold, bringing the data for aluminum more in line with the other data. Although the same frictional heating exists for all the tests, aluminum is particularly susceptible, because the 7075 alloy loses 50% of its tensile strength for a temperature rise of only 200°.

Evidence suggests that thermal softening occurred in some of the other tests, albeit only locally. For some of the samples, the onset of gouging was preceded by the formation of needle-like gouges. These are gouges that did not form the characteristic tear-shape, ending with a crater lip. We believe these gouges began like normal gouges, but did not grow because the bulk of the sample was harder than the high spot that initiated the gouge. This process is also seen where high spots in the samples left score tracks early in the launch that eventually deteriorated into limited, near gouge-like damage before the gouging threshold was reached.

We believe a similar process occurred late in the launch with the 4340 steel. The samples created uncharacteristically shallow, barely perceptible gouges after having traveled almost two meters, farther than any other sample. The shallowness of the gouges, we believe, was caused because the samples only failed in a thin surface layer that had annealed. A second possibility, however, makes it difficult to draw conclusions from this test. The steel was tested in the same launch package as the graphite sample, which wore away. The wear may have resulted in decreased pressure at the steel/rail interface and precluded the possibility of forming deep gouges.

While the curve fit shown in Fig. 5 does not lie within the error bars at all points, it nevertheless demonstrates the existence of a correlation between shock pressure and hardness. For example, this correlation can explain the relative gouging velocities of nickel and titanium. Because they have approximately the same hardness they should gouge at the same pressure, about 22 GPa. Nickel, by virtue of being twice as dense as titanium, can generate higher shock pressures, and must therefore have a correspondingly lower gouging threshold velocity (1 km/s vs 1.4 km/s). By this type of reasoning it is possible to predict the approximate gouging threshold velocities for other materials, including materials that we did not test. All that is required is shock data for the materials and knowledge of the hardness of the harder material.

#### V. ACKNOWLEDGMENT

This work was supported by the U.S. Army Research Laboratory under contract DAAA21-93-C-0101.

#### REFERENCES

- [1] K. F. Graff, B. B. Dettloff, and H. A. Bobulski, "Study of High Velocity Rail Damage," Department of Engineering Mechanics, Ohio State University Research Foundation, Air Force Missile Development Center, Holloman Air Force Base, New Mexico, November 1968.
- [2] J. P. Barber and D. P. Bauer, "Contact Phenomena at Hypervelocities," *Wear* (1982), Vol. 78, pp. 163-169.
- [3] L. M. Barker, T. G. Trucano, and A. R. Susoeff, "Gun-barrel Gouging by Sliding Metal Contact at Very High Velocities," *IEEE Transactions on Magnetics*, Vol. 25, No. 1, January 1989, pp. 83-87.
- [4] L. M. Barker, T. G. Trucano, and J. W. Mumford, "Surface Gouging by Hypervelocity Sliding Contact at Between Metallic Materials," Sandia Report SAND 87-1328 UC-34, Sandia National Laboratories, September 1987.
- [5] R. F. Bishop, R. Hill, and N. F. Mott, "The Theory of Indentation and Hardness Tests," *Proc. Phys. Soc.* Vol. 57, No. 147, 1 May, 1945.
- [6] S. J. Bless, W. Gooch, S. Satapathy, J. Campos, and M. Lee, "Penetration Resistance of Titanium and Ultra-hard Steel at Elevated Velocities," presented at the 1996 Hypervelocity Impact Symposium, Saint Louis, France, October 1996.
- [7] J. R. Assay, and M. Shahinpoor, *High Pressure Shock Compression of Solids*, Springer-Verlag, New York, 1993, pp. 30-34.
- [8] S. P. Marsh, *LASL Shock Hugoniot Data*, University of California Press, 1980.
- [9] J. P. Barber, R. A. Marshall, and P. Muttik, "Projectile and Current Behavior in ANU Railgun," ARA Meeting held at Naval Ordnance Laboratory, MD, October 1974.

## About Localization of Electrical Current in Sliding Metal Contact

A.P. Glinov, V.A. Frol'tsov, M.A. Bykov  
B.S. Schastnykh, A.K. Kondratenko and A.E. Poltanov

Troitsk Institute for Innovation & Fusion Research  
TRINITI, Troitsk, Moscow Reg., Russia, 142092  
Phone: ( 095)334-06-81, Fax: ( 095)334-51-58  
Email: glinov.@fly.triniti.troitsk.ru, kondrat.@fly.triniti.troitsk.ru

**Abstract.** The physical problem of the electric current distribution for high-velocity sliding metal contact in railgun is solved taking into account the influence of the contact electric resistance. For a vast region of physical parameters of contact pairs materials and armature velocities the approximate formula offered formerly for estimation of the localization of the high current density is verified by the numerical simulation. The distributions of current density and electric potential drop along the armature are calculated for various contact materials. On the base of the experimental data our calculation procedure has enabled to evaluate the contact electrical resistance for some pairs of materials.

### 1. Introduction

At development and optimization of electromagnetic launchers for macrobodies it is important to have the computing programs enabling to carry out numerical experiments on simulation of some work aspects in similar facilities. One of the basic problems constraining the development of such engineering with solid metal armature is deterioration of the solid metal contact caused by high-velocity current skin-effect [1]. Therefore it is important to know the real distribution of electrical current in the sliding contact zone. But it is impossible without the account of losses of magnetic flux in the rail-armature zone of sliding. The adequate physical simulation of the current localization with the help of  $\alpha$ -spot [2] in such narrow, about 10  $\mu\text{m}$ , zones represents a rather difficult task. The simplified method of simulation is offered by G. Sherclif [3]. It consists of simulation the contact region by infinite thin mathematical discontinuity of a tangent component of the electrical field intensity. This discontinuity is proportional to the current density with the constant of proportionality  $R$ , which is named as contact electrical resistance per unit of square.

In our work the method of the parameter estimation  $R$  is offered. It is based on comparison of theoretical results which were obtained in the present work and of the experimental data [4] about distribution of the contact current density. The results of the parameter definition  $R$  would be to compare with the data for the contact pair *Cu-Al* [5,6]. Our theoretical analysis has enabled to define the admissible boundaries of use of the approximate formula, which was obtained in [7]. This formula is intended for estimations of localization zone of contact current in the large region of physical characteristics of materials in the rails and the armature.

### 2. Formulation of the Problem

We'll analyze a distribution of electrical current in a vicinity of contact zone at the rear of the armature where the current density is maximum. We'll consider the stationary two-dimensional formulation and homogeneous isotropic rails and armature. The obtained asymptotic solution will be true at rather high velocities of launching  $V$ :  $t \gg \lambda / V$ ,  $\lambda_v \ll \lambda \ll a$ ,  $\lambda_v = D_r / V$ . Here  $t$  - time,  $a$  - the length of the armature in direction of moving,  $D_r$  - the diffusivity of magnetic field in rails,  $\lambda$  - the size of current skin zone on the contact at the rear of the armature.

We'll use the coordinate system, connected with the moving body. In the region of the upper rail (fig. 1) the problem leads to the definition of the  $z$  - component of the magnetic field induction  $B$ .

$$\frac{\partial B}{\partial x} + \lambda_v \frac{\partial^2 B}{\partial y^2} = 0, \quad B(x, 0) = B_s(x), \quad B(a, y) = 0 : x < a, y > 0 \quad (1)$$

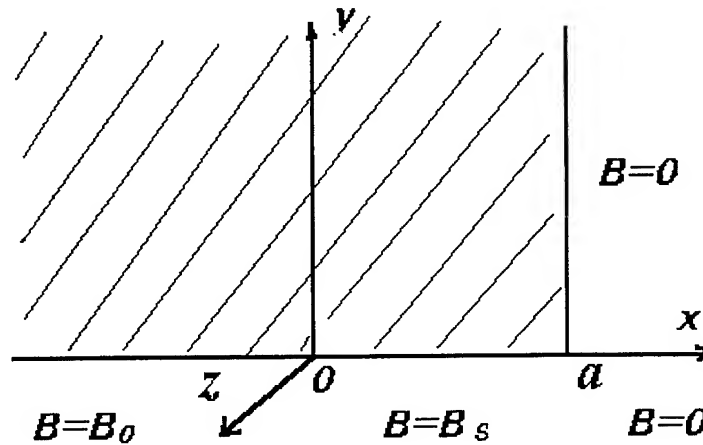


Fig. 1 Geometry of problem and the boundary conditions in the rail

For the lower rail the picture of current distribution is symmetric. The condition of absence of the currents leakage to infinity closes the formulation of problem about the diffusion of the magnetic field in the rails. In the region of the armature it will be (fig.2):

$$\Delta B = 0, \quad B(0, y) = B_0, \quad B(a, y) = 0, \quad B(x, 0) = B_s, \\ \frac{\partial B(x, -b/2)}{\partial y} = 0 : 0 < x < a, -b < y < 0 \quad (2)$$

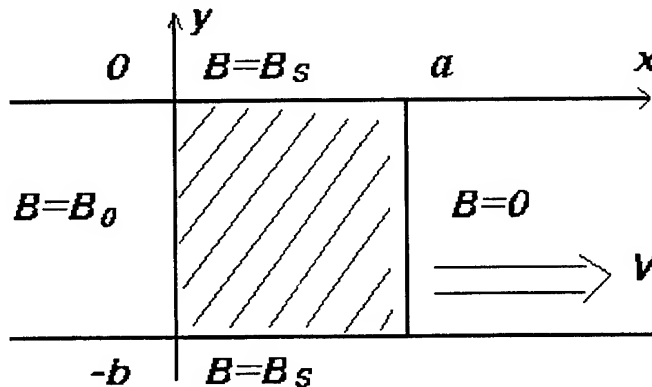


Fig. 2 Geometry of the armature and the boundary conditions.

### 3. Construction of Solution and Analysis of Results

For the solution of the problem in the region of the rails we used the sine Fourier transformation with respect to  $y$ .

$$\tilde{B}(v, x) = \sqrt{2/\pi} \int_0^{\infty} B(x, y) \sin vy dy$$

Thus from (1) we obtained

$$\frac{d\tilde{B}}{dx} = \lambda_v v (\tilde{B} - \sqrt{2/\pi} B_s), \quad \tilde{B}(v, a) = \tilde{B}(v, \infty) = 0 \quad (3)$$

We solved (3) by the method of parameters variation and obtained

$$\tilde{B}(v, x) = v \lambda_v \sqrt{2/\pi} \int_x^a \exp[-\lambda_v v^2 (p-x)] B_s(p) dp \quad (4)$$

Thus if  $p < 0$  it is necessary  $B_s$  to replace by  $B_0$ .

We found the magnetic field  $B=B_r$  in the upper ( $y > 0$ ) rail, applying the inverse sine Fourier transformation and [8]:

$$\begin{aligned} B_r(x, y) &= \sqrt{2/\pi} \int_0^\infty \tilde{B}(v, x) \sin vy dv = \\ &= \int_a^x \operatorname{erfc}\left(\frac{y}{2\sqrt{\lambda_v}(p-x)}\right) \frac{dB_s(p)}{dp} dp, \\ \operatorname{erfc}(x) &= \frac{2}{\sqrt{\pi}} \int_x^\infty \exp(-x^2) dx \end{aligned} \quad (5)$$

Below we'll build the solution of problem in the region of the armature. The variable  $B=B_a$  is being sought as  $B = G + H + (1-x/a) B_0$ . Then for  $G$  and  $H$  we have obtained

$$\Delta G=0, \quad G(0, y)=0, \quad G(a, y)=0, \quad G(x, 0)=B_s, \quad \partial G(x, -b/2) / \partial y=0 \quad (6)$$

$$\Delta H=0, \quad H(0, y)=0, \quad H(a, y)=0, \quad H(x, 0)=B_0(x/a-1), \quad \partial H(x, -b/2) / \partial y=0 \quad (7)$$

The equations (6), (7) are solved by the method of variables separation and by the expansion of inhomogeneous boundary functions in the Fourier series on the eigenfunctions of the homogeneous equations. It'll result in

$$B_a(x, y) = \sum_{n=1}^{\infty} A_n (e^{\pi n(y+b)/a} + e^{-\pi n y/a}) \sin(\pi n x / a) + B_0(1-x/a), \quad (8)$$

$$A_n = [(2/a) \int_0^a B_s(x) \sin(\pi n x / a) dx - 2B_0 / \pi n] / [1 + \exp(\pi b n / a)]$$

We'll unite together the general solutions obtained above for the rails and the armature on the contact at  $y = 0$ . We'll supply  $B$  with the indexes "a" and "r" accordingly for the armature and the electrodes. After that the conditions of bringing into coincidence taking into account the contact resistance  $R$  [4] will be

$$D_a \frac{\partial B_a}{\partial y} - D_r \frac{\partial B_r}{\partial y} = \frac{R}{\mu_0} \frac{\partial^2 B_s}{\partial x^2}, \quad B_s = B_r = B_a \quad (9)$$

$$\frac{\partial B_r(x, 0)}{\partial y} = \frac{I}{\sqrt{\pi} \lambda_v x} \int_x^a \frac{B'_s(p)}{\sqrt{p-x}} dp \quad (10)$$

$$\frac{\partial B_a(x, 0)}{\partial y} = \sum_{n=1}^{\infty} C_n \sin \frac{\pi n x}{a}, \quad C_n = A_n \frac{\pi n}{a} (e^{\pi b n / a} - 1) \quad (11)$$

The equations (9-11) and the boundary conditions  $B_s(0) = B_0$ ,  $B_s(a) = 0$  give required integro-differential boundary problem for the definition of the contact field  $B_s$ . It is possible to show that  $B_s = B_0(1-x/a)$  will be true either for ideally conducting rails ( $D_r = 0$ ) or for strongly resistant electrical contact ( $R = \infty$ ). More complicated tests, in particular, for small either  $D_a$  or  $R$ , and the method of numerical solution of the boundary problem (9-11) are represented in [9].

In [7] the approximate evaluation for the current skin size  $\lambda$  along contact at the rear of the armature is obtained:

$$\frac{\lambda}{\lambda_v} = 1 + (e-1) \left( \frac{D_a}{D_r} \right)^2 + \left( \frac{R}{\mu_0 \rho_r \lambda_v} \right)^{2/3}, \quad D_{r,a} = \rho_{r,a} / \mu_0, \quad \mu_0 = 4\pi 10^{-7} \text{ H/m} \quad (12)$$

Here  $\rho_{r,a}$  - specific electric resistances accordingly for the rail materials and the armature.

This formula has found the confirmation in unique specially made experiment on research of metal contact crisis in railgun with the bronze rails and the aluminium armature [10]. In this case the scale  $\lambda$  had served for the current density estimation. And the coefficients of specific electrical resistance of the rails materials and the armature had depended on temperature  $T$  which was calculated from the Joule heat from the equation of local balance heat taking into account the current change during time  $t$ . We had taken  $R \sim 0.1 \div 0.3 \text{ nOhm}\cdot\text{m}^2$  from [5,6] in order to process the experiment [10].

In present work the theoretical result [7] as the approximate formula (12) is compared with the numerical simulation results of the boundary problem (9-11). The scale  $\lambda$  is the distance between the rear of the armature on the contact in the direction of moving and the point where the magnetic field falls in  $e$ -times. The results of computation are represented in fig. 3.

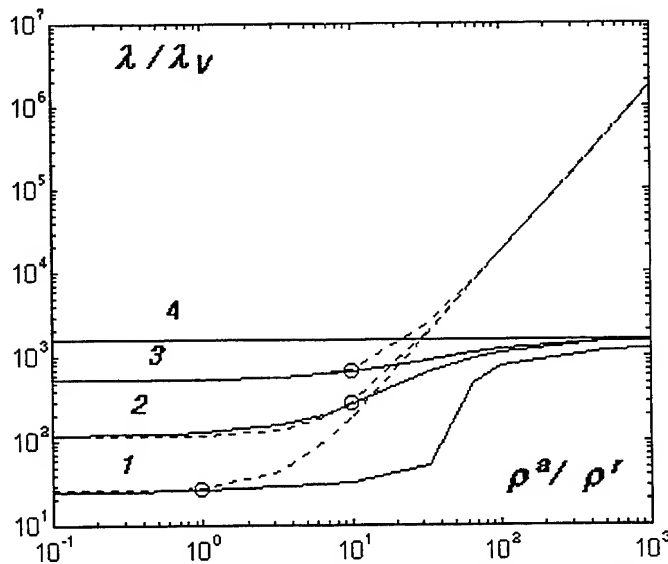


Fig. 3 The scale  $\lambda$  of contact current localization vs.  $\rho_a/\rho_r$  for the different  $R$ : 1-  $R = 0.01 \text{ nOhm}\cdot\text{m}^2$ ; 2-  $0.1$ ; 3-  $1.0$ ; 4-  $\infty$ . The latter corresponds to  $\lambda = a/e$ . The solid lines are computation, the dashed ones are the theoretical estimation.  $V = 1 \text{ km/s}$ ,  $b = 1 \text{ cm}$ ,  $a = 2 \text{ cm}$

The circles on this figure are the boundaries when the difference between theoretical estimation and computing results is 16 %. The mentioned difference can

become stronger with the increase of the ratio of the armature specific resistances to the rails specific resistances. It is explained by that the theoretical estimation [7] which was obtained in asymptotic approximation  $\lambda \ll a$ . It is formally  $a = \infty$ . If the length of the armature is limited then during the contact current smoothing the electrical current can reach also the right armature boundary if the value either  $R$  or  $\rho_a / \rho_r$  increases. Then  $\lambda$  becomes of the order of  $a$  and our model can't be used. The analysis of fig. 3 shows that the formula (12) suits for current skin estimations in sliding metal contact in the armatures with the length about a few centimeters and moderate contact resistances  $R \leq 1.0 \text{ nOhm}\cdot\text{m}^2$  and good electro-conducting armatures  $\rho_a / \rho_r \leq 10$ .

Similarly we take from [4] the experimental data of the distribution of current in the zone of high-velocity solid metal contact ( $V = 650 \text{ m/s}$ ) for the set of the contact pairs (1- bronze - aluminum, 2- steels - aluminums, 3- copper - titan) and plot the graphs of the normalized current densities  $j_y / j_y^{\max}$  (fig. 4). This normalized current densities obtained from numerical computation by asymptotic model of current skin. In our case:  $\rho_{\text{bronze}} = 0.15 \text{ }\mu\text{Ohm}\cdot\text{m}$ ;  $\rho_{\text{Ti}} = 1.2 \text{ }\mu\text{Ohm}\cdot\text{m}$ ;  $\rho_{\text{Cu}} = 0.018 \text{ }\mu\text{Ohm}\cdot\text{m}$ ;  $\rho_{\text{steel}} = 50 \text{ }\rho_{\text{Cu}}$ ;  $\rho_{\text{Al}} = 0.024 \text{ }\mu\text{Ohm}\cdot\text{m}$ .

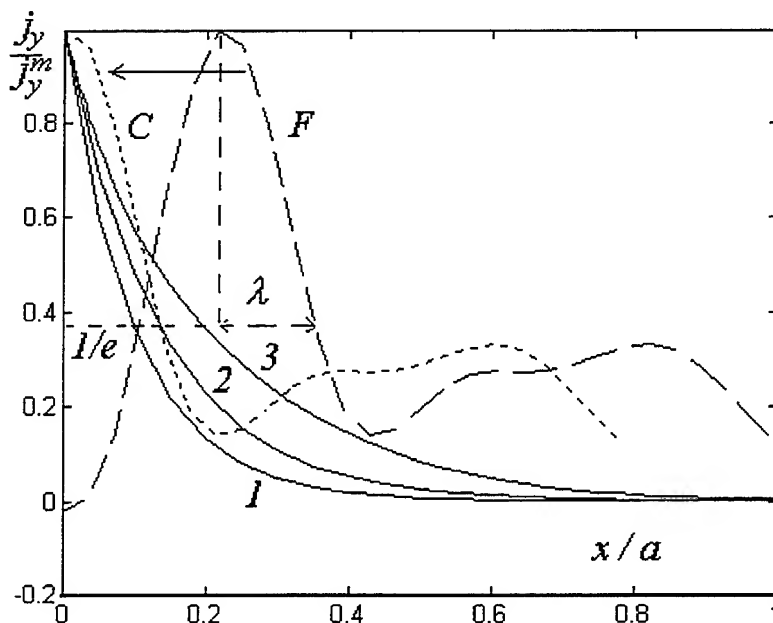


Fig. 4 The distribution of contact current density. The solid lines correspond to calculated data for the variants 1-3. The dashed lines are the experimental curves for variant 2, where: F - the factual data [4], C - the data from [4] superposed in the current density maxima point with the results of numerical computations.

The scale  $\lambda$  was found from the experimental data [4] for the estimation of the contact electrical resistance magnitude  $R$ . The scale  $\lambda$  characterizes the size of diminish of the current density at the rear of the armature along the contact surface (fig. 4). For the mentioned above contact pairs variants  $\lambda / a$  equals accordingly 0.10; 0.14; 0.23. From these data it is possible to find the sought data for the pointed variants: 1 -  $R = 1.6 \text{ nOhm}\cdot\text{m}^2$ , 2-  $R = 6.3 \text{ nOhm}\cdot\text{m}^2$ , 3-  $R = 4.4 \text{ nOhm}\cdot\text{m}^2$ . It can be done with the help of



iterative method using curves like in fig. 4 and taking  $R$  derived from the formula (12) as initial approximation.

By our estimations the contact pressure in the experiments [4] was about 300 atm. The failure of solid metal contact wasn't observed thus the heat of the armature wasn't too strong. We neglect the heat influence over the parameter definition  $R$  in the considered variants. For the experimental values  $\lambda$  in the variants 1,2 the left part of (12) dominates over  $(D_a/D_r)^2$ . In variant 3 the dependence of  $D_a$  of the temperature is weak.

The typical picture of electrical current distribution in railgun taking into consideration the contact resistance looks like (fig.5).

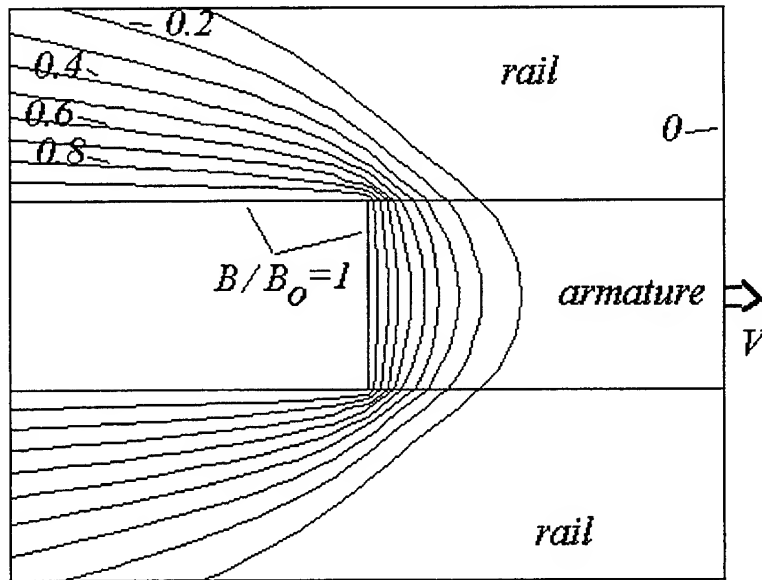


Fig. 5 The current streamlines for variant 2.

The experimental method [4] for the definition of the distribution of contact current density based on rather nontrivial mathematical calculation of the magnetic probes indications is rather complicated.

We analyze also an other approach to the experimental diagnostics in the contact zone founded on electrical probes indications. We locate potential sensors (1 and 2) in the rails at the distance  $h$  from the sliding surface (fig. 6).

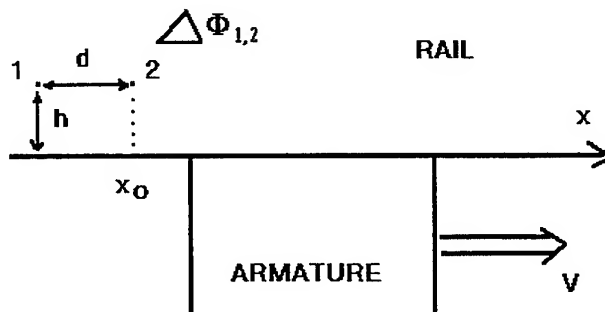


Fig. 6 The picture of electrical probes location.

The voltage drop between points 1 and 2 is:

$$\Delta\phi_{1,2} = \int_1^2 E_x dx = - \frac{\rho_r}{\mu_0} \int_1^2 \frac{\partial B}{\partial y} dx$$

Here  $E_x$  is the  $x$  - component of electric field intensity. It is possible to show that

$$\Delta\phi_{1,2} / J = \frac{\rho_r a}{B_0 \sqrt{\pi} \lambda_v} \int_{x_0-d}^{x_0} f(x) dx$$

$$f(x) = \int_c^D e^{\frac{-h^2}{4\lambda_v(p-x)}} \frac{B'_s(p)}{\sqrt{p-x}} dp$$

Here  $J = B_0 / \mu_0$  - current per unit of rails width . If  $x \leq 0$  :  $C=0$ ,  $D=a$ . If  $x \geq a$  :  $C=D$ . When  $0 < x < a$  :  $C=x$ ,  $D=a$ .

The results of estimations are represented in fig. 7 with  $a = 2$  cm,  $b = 1$  cm,  $V=1$  km/s,  $\rho_a = \rho_r = 10$  nOhm·m<sup>2</sup>,  $d=1$  cm,  $h = 1$  mm.

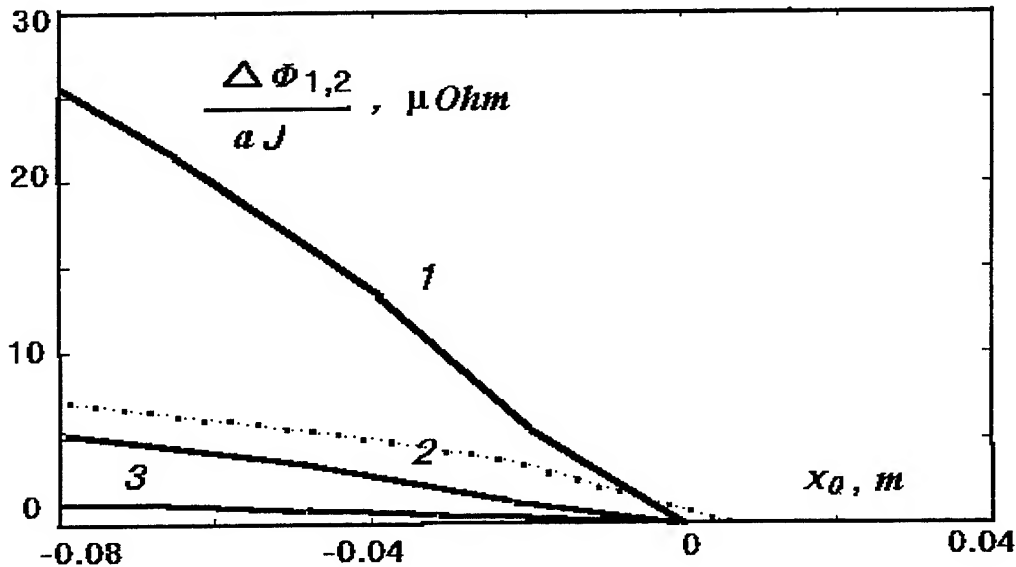


Fig. 7 The effective electrical resistance between the sensors 1, 2 in rails: 1 -  $R = 0.01$  nOhm·m<sup>2</sup>; 2 - 0.1; 3 - 1.0.

The change of potential difference (of the electrical resistance) between the points of measure 1, 2 is observed in this case at the various contact resistances  $R$  depending on the sensors location characterized by  $x_0$ -coordinate. The dotted line marks the variant  $h = 0.4$  mm,  $R = 0.1$  nOhm·m<sup>2</sup>.

It is realised that the voltage drop in rails more strongly responses upon the change of the  $R$ - parameter magnitude than the contact current density. The last quantity is obtained in experiments from the indications of magnetic probes by numerical inversion of the integrated convolution operator. This problem is mathematically incorrect and requires a special regularization. To get information about voltage drop in rails doesn't require complicated mathematical calculations. The method of the  $R$ -parameter definition based on measurements of electrical potential distribution in rails perhaps will be more convenient due to the reasons which were already mentioned.

The amplitude of  $\Delta\phi$  falls at the decrease of contact resistance. It is explained by the follow reasons. The large  $R$  tends to disperse the contact current along the normal to surface of sliding. And it diminishes the longitudinal potential difference. It is necessary to notice that the signal intensivity of  $\Delta\phi$  will be much higher (fig.7) when the sensors are close to the surface of sliding ( $h \rightarrow 0$ ). It follows also directly from the observation of the dependence  $f(x)$ , defining the value of  $\Delta\phi$ , because at  $h=0$  the exponential little term tends to 1 at moderate  $h$ .

#### 4. Conclusion

The solution of the physical problem about the distribution of electrical current in a vicinity of sliding solid metal contact in two-dimensional stationary formulation is constructed. It has enabled us to fulfil the theoretical evaluation of the precision of the approximate formula offered formerly for the definition of the zone size of current concentration. The method of estimation of the contact resistance  $R$  in rail launchers with a solid metal armature is considered. The application of the suggested method to the processing of the earlier made experiments has enabled us to estimate the  $R$ -parameter for several contact pairs in typical conditions for electromagnetic launchers. For improvement of the obtained results and for processing of the considered method it is necessary to fulfil the test experiments in a railgun with such contact electrode pairs, i.g.  $Cu - Al$ , for which the value  $R$  is known.

#### References

1. A.P. Glinov, N.M. Kolyadin, A.E. Poltanov et al. / Materials of 2-th All-Union Seminar on Dynamics of High Current Arc Discharges in Magnetic Field, Novosibirsk, 4-6 December, 1991, Novosibirsk, 1992, p.315-339. (in Russian)
2. R. Holm. "The Electrical Contacts", Moscow, I L, 1961 (in Russian)
3. G. Sherclif "Course of Magnetic Hydrodynamics", Moscow, Mir, 1967 (in Russian)
4. A.K. Kondratenko, M.A. Bykov, B.S. Schastnykh, A.P. Glinov, A.E. Poltanov "The Study of Sliding Contact in Railgun with Metal Armature"/ 8-th EML Symp., USA, Baltimore, 24-26 April, 1996, paper No. 56H.
5. J.P. Barber, Yu.A. Dreizin "Model of Contact Transitioning with Realistic Armature/Rail Interface" / 7-th USA EML Symp.
6. J.P. Barber, A. Chalita, B.L. Maass, L.E. Thurmond / IEEE Trans. Magn. , Vol. 27, No. 1, 1991, pp. 228-232.
7. A.P. Glinov, N.A. Farkova "About Influence of Contact Resistance on Current Skin in Railgun"/ 5th European Symp. on EMLT, Toulouse, France, April 1995, paper No.14
8. I.N. Bronshtein, K.A. Semendyaev "Handbook on Mathematics for Engineers and Students", Moscow, Nauka, 1980 (in Russian)
9. A.P. Glinov, V.A. Frol'tsov "About Method for Finding of Contact Electrical Resistance in Railgun with Metal Armature" / Preprint TRINITI, No.0024-A, Moscow, CNIATOMINFORM, 1996, 16p. (in Russian)
10. A.P. Glinov, L.G. Kotova, Y.A. Halimullin "About Crisis of High Speed Metal Contact in Railgun" / 5th European Symp. on EMLT , Toulouse, France, 10-13 April, 1995, paper No. 14.

# Investigation of Transverse Striations on Aluminum Rails

Leslie C. Woods and Andrew Yeoh

Institute for Advanced Technology, The University of Texas at Austin  
4030-2 W. Braker Ln. Suite 200, Austin, Texas 78759-5329

**Summary**—The ohmically-heated, liquid layer between the rails and solid armature of a railgun has a key role in the onset of transition, so understanding its nature is important. Experiments in which both the rails and the armature are made of aluminum, show periodic, transverse striations in the rail surface, with a wave length varying between 0.5 mm and about 5 mm. Apparently the melted aluminum at the contact surface has solidified into waves with their crests at right angles to the motion of the armature. It is conjectured that these waves are generated by an instability in the sheared fluid layer separating the rail and armature, at a point just to the rear of the armature. While layers of uniform vorticity adjacent to a rigid wall are known to be linearly stable, there is a non-linear, secondary instability capable of generating the observed waves. This instability can also cause 'filamentation,' namely the ejection of thin filaments of vortical fluid from regions of high curvature. That the observed crests are rather steep, appears to be due to this phenomenon.

## I. INTRODUCTION

During an electromagnetic launch, bore deposits are usually left behind by the armature. In the case of an aluminum armature, a primarily aluminum deposit is found on the recovered rail conductors, regardless of the rail conductor material. The general nature of these deposits have been previously reported [1,2]; typically one sees a smooth-appearing layer (though microscopically rough) that averages 20- $\mu$ m thick. It should be noted, however, that these results originated from either a monolithic or a laminated armature, with equal spacing between the conducting and insulating laminates. More particularly, the armature conductor(s) spanned the rail height almost completely in the above experiments.

The observations and resulting theory presented in this paper are due to *not* using the entire rail conductor height during the launch. Specifically, only 40% of the rail conductor height about the longitudinal centerline of the rail was in contact with the armature. The initial reason for this geometry was to enable a 12.7-mm x 25.4-mm armature to be launched from a 25.4-mm square bore in order to obtain higher exit velocities. Higher velocities were attained, but then transverse striations on the rails, lying orthogonal to the velocity vector, were also observed. These striations occurred when an Al 7075-T6 armature was launched on Al 6061-T6 rails, and were not found with other rail conductor materials.

## II. EXPERIMENTAL ARRANGEMENT AND RESULTS

These experiments were conducted at the Institute for Advanced Technology Laboratory. The testbed used was the rebuilt OAT or Okaloosa Armature Tester coupled with a 3-MJ power supply from the former Thunderbolt program [3]. In the first experiment, the testbed was cored to produce a rectangular bore measuring 12.7-mm high x 25.4-mm wide (the larger being the rail-to-rail dimension). Due to testbed constraints, the rail height was maintained at 31.8 mm, of which 12.7 mm was in contact with the armature. The armature used for this experiment is depicted in Fig. 1. It had six adjacent 2-mm thick Al 7075-T6 laminates which produced a 12-mm stack held together by an Al 6061-T6 pin and a polycarbonate bore rider. The total mass of this package was 19.00 grams.

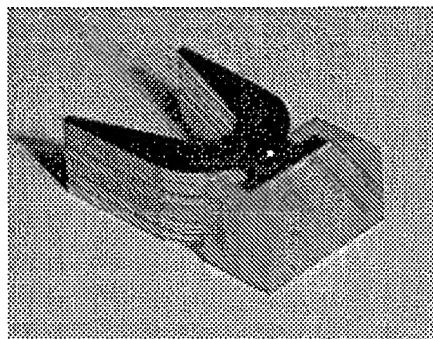


Figure 1. 12.7-mm high x 25.4-mm wide armature used in the first experiment.

For the second experiment, a 25.4-mm square bore was used. However, the six Al 7075-T6 laminates were arranged in a manner similar to the first experiment and is illustrated in Fig. 2. The initial mass of this armature was 26.70 grams.

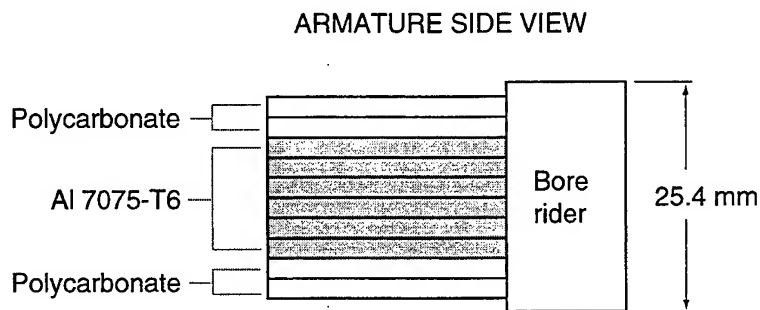


Figure 2. Schematic side view of the 25.4 mm x 25.4 mm armature used in the second experiment.

In both cases, Al 6061-T6 rails were used and a driving current with a 450-kA peak propelled the armatures. Because of the initially smaller mass, the first armature attained an exit velocity of  $\sim 2.0$  km/s, while the second armature reached  $\sim 1.8$  km/s. Transition occurred almost immediately (several centimeters beyond  $x = 0$  cm) and transverse striations were observed soon after the location of armature transition on the recovered rails. Figures 3 and 4 are photographs depicting the transverse striations formed by the armature deposit from each of the experiments.

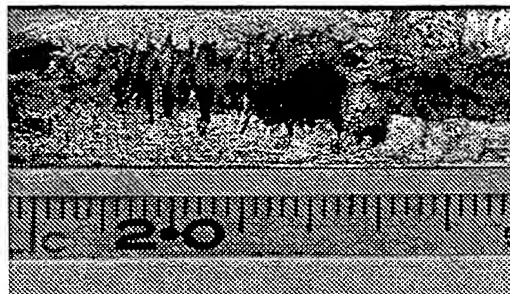


Fig. 3. Transverse striations about the  $x = 20$  cm location; armature velocity was  $\sim 850$  m/s at this location. Photograph from the positive Al 6061-T6 rail of the first experiment.

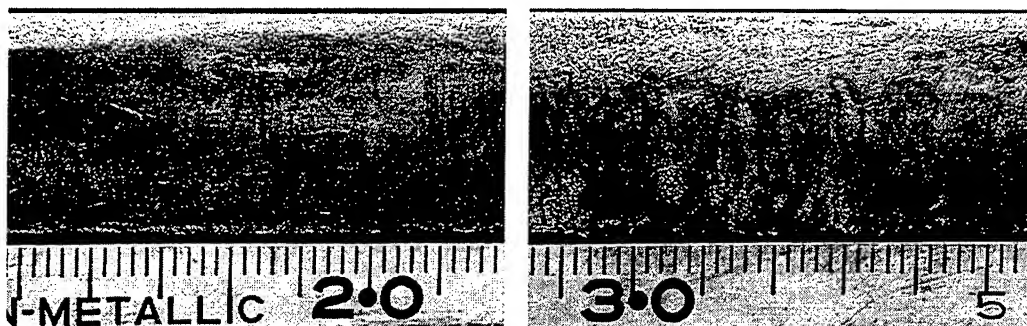


Figure 4. (a) Fine transverse striations starting from the  $x = 15$  cm location and (b) coarse transverse striations about the  $x = 30$  cm location. The armature velocities were  $\sim 825$  m/s and  $\sim 1140$  m/s respectively. Photographs are from the negative Al 6061-T6 rail of the second experiment.

It should be noted that the striations are by no means symmetrical, i.e. they do not appear on both rails simultaneously. Closer inspection of the striated deposit revealed the presence of spherical cavities within the layer—an indication that the aluminum fluid flow prior to solidification was turbulent in nature, and/or the aluminum may have been boiling. Figure 5 is a low-magnification micrograph depicting a cluster of spherical cavities.



Fig. 5. Clusters of spherical cavities within the deposit layer suggests turbulent mixing during the moment of solidification.

An analysis of these striations show that the peak-to-peak distance generally increases with the velocity of the armature. The wavelengths range from 0.5 mm to greater than 5 mm, but not necessarily in that order, i.e. a 1-mm wavelength can be found in a region displaying primarily 2.5-mm striations. The thickness of the deposit was also measured to vary from several microns thick at the valleys of the striations to greater than 200- $\mu$ m thick at the peaks.

### III. THE SOLIDIFICATION TIME

It is a reasonable assumption that the waves observed on the aluminum rail are generated by an instability in the highly sheared fluid layer leaving the interface at the rear of the armature. Vortex sheets are well known to be unstable, a phenomenon termed the 'Kelvin-Helmholtz' instability. Classic examples are observed in the wing-tip streamers generated by high-flying aircraft in supercooled, atmospheric conditions and in the generation of waves at the free surface of a liquid, over which a gas is flowing. But these flows are *linearly* unstable, whereas sheared flow past a rigid wall is stable to linear perturbations. There is a more subtle destabilizing mechanism, as we shall describe shortly.

Viscosity very slowly eliminates the fluid shear, but as we shall show, in the conditions of the experiment, long before this can happen, heat is lost to the rail and the liquid aluminum solidifies. To verify

these statements, we need the time  $t_v = h^2/\nu$  for the kinematic viscosity  $\nu$  to remove the shear in a layer of thickness  $h$ . With the typical value,  $\nu = 5.7 \times 10^{-7} \text{ m}^2/\text{s}$  for molten aluminum and the measured layer thickness of  $h = 50 \text{ } \mu\text{m}$ , we find that  $t_v \sim 4.4 \text{ ms}$ . We shall find below that the time for the solidification of the layer is much smaller than this, so we can ignore the effects of viscosity for the liquid layer.

There remains the possibility that the layer solidifies before the non-linear instability that we shall discuss below, has had time to develop a substantial perturbation on the fluid surface. So we need an estimate for the solidification time  $t_s$  for the molten liquid to give up its heat to the solid rail surface.

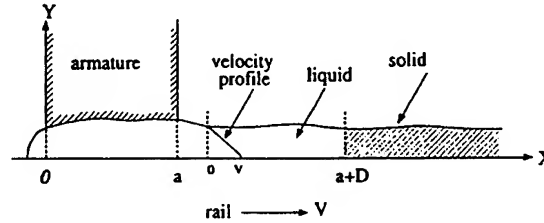


Fig. 6. Solidification Distance,  $D$ .

In Fig. 6 we show an armature extending over a contact distance  $a$ , measured in the direction of motion. The mixture remains liquid on the rail surface, until a distance  $(a + D)$  measured from the leading edge of the armature. We term  $D$  the solidification distance. Denote by  $T_m$ ,  $T_0$  the melting temperature and the laboratory temperature, and let  $\lambda_r$  denote the rail thickness. The surface  $y = 0$  separates the liquid phase from the solid phase. Ignoring ohmic heating in the rail, we find that its temperature is approximately

$$T - T_0 = (1 - y/\lambda_r) (T_m - T_0) \quad (-\lambda_r < y < 0). \quad (1)$$

Let the rail be moving with velocity  $V$  relative to the armature in a direction along the  $OX$ -axis. Also let  $\kappa_r$  denote the thermal conductivity,  $\rho$  the density and  $L_m$  the enthalpy of fusion. In the range  $a < x < \infty$ , the aluminum layer is not ohmically heated and viscous heating is negligible. Hence, in steady conditions, the energy equation becomes

$$0 = \kappa_r \frac{\partial^2 T}{\partial y^2} + \rho L_m \left(\frac{1}{2} V\right) \delta(x^*) \quad (x^* \equiv a + D), \quad (2)$$

where  $\delta(x)$  is the delta function, the liquid/solid interface in the layer being at  $x = a + D$  and having an average velocity of  $\frac{1}{2}V$  relative to the liquid layer.

First we integrate across the liquid layer to get

$$0 = \kappa_r \frac{\partial T}{\partial y} \Big|_{y=0}^{y=h} + \frac{1}{2} \rho h L_m V \delta(x^*). \quad (3)$$

At  $y = 0$ ,  $\frac{\partial T}{\partial y} = -(T_m - T_0)/\lambda_r$ ; at  $y = h$ ,  $\frac{\partial T}{\partial y} \approx 0$ , since we shall ignore losses to the air. Hence

$$\frac{\kappa_r}{\lambda_r} (T_m - T_0) = \frac{1}{2} \rho h L_m V \delta(x^*). \quad (4)$$

Next we integrate from  $x = a$  to  $x = a + D$ . This gives the solidification distance

$$D = \frac{\rho L_m}{2\kappa_r(T_m - T_0)} \lambda_r h V \approx 3 \times 10^3 \lambda_r h V, \quad (5)$$

where we have used the values (in MKS units)  $\kappa_r = 251$ ,  $\rho = 2410$ ,  $L_m = 3.97 \times 10^5$ ,  $T_m - T_0 = 635$ . In the experiment,  $V = 850$  m/s,  $\lambda_r = 6.35$  mm,  $h = 50$   $\mu$ m and therefore from (5),  $D \approx 809$  mm. The solidification time,  $t_s \equiv D/V$ , is therefore about 0.95 ms. This time is to be compared with the growth time of the non-linear shearing instability, to be described below.

#### IV. INSTABILITY OF FINITE AMPLITUDE WAVES IN A SHEARED FLUID

The instability in a sheared fluid has a long history that started with Kelvin and Helmholtz. They considered vortex sheets, and their work was extended by Lord Rayleigh [4] to sheets of finite thickness. Rayleigh's unstable sheets were free to distort sinusoidally, maintaining constant width. The greatest growth rates are found at wave lengths,  $\lambda$ , equal to about eight times the thickness  $h$  of the sheet. His linear theory showed that infinite sheets adjacent to rigid walls were not unstable, at least to small displacements.

Consider the case of a sheet of thickness  $h$ , in which the fluid velocity decreases uniformly from a value  $V$  directed along the positive  $x$ -axis, on the solid surface  $y = -h$ , to zero on  $y = 0$ . The resulting vorticity is  $\omega = V/h$  and each fluid element spins with an angular velocity  $\zeta = \frac{1}{2}\omega$ . The wall moves with the velocity  $V$ , although as we shall ignore viscosity, this is not an essential element. Above  $y = 0$  the flow is irrotational. Rayleigh adopted a theorem due to Helmholtz that stated that the effect of an element  $dA$  rotating with an angular velocity  $\zeta$ , is to produce, at a point whose distance from the element is  $r$ , a transverse velocity  $q$ , such that

$$q = \frac{\zeta dA}{\pi r}. \quad (6)$$

It is not difficult to show that waves of length  $\lambda$  on the surface  $y = 0$  will propagate with a velocity  $c$  given by

$$c = \frac{V}{\epsilon} (1 - e^{-\epsilon}) \quad \left( \epsilon \equiv \frac{4\pi h}{\lambda} \right). \quad (7)$$

These are called Kelvin-Helmholtz waves; they have neutral stability. In recent years, with the aid of computers, this work has been extended to the non-linear regime [5,6]. For a general survey, Saffman's monograph [7] may be consulted.

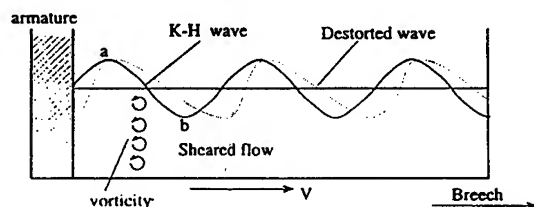


Fig. 7. Kelvin-Helmholtz waves.



The configuration of interest here is that of a *semi*-infinite sheet, extending from the rear of the armature at  $x = 0$  to the breech at (say)  $x \sim \infty$ . As illustrated in Fig. 7, the K-H waves will propagate away from the armature, but the presence of the armature boundary changes the stability of these waves. Consider, for example, the effect of an small increase in the wave amplitude at the point  $a$  of the wave closest to the armature. A second-order effect of this modulation will be to reduce the strength of the vorticity  $\omega$ , and as this effect is convected with the local fluid velocity, it is evident from (6) that the reduced spin of the fluid elements immediately downstream of the point  $a$  will tend to *increase* the amplitude of the perturbation at  $a$ . In an infinite wave pattern, perturbed over all waves, this tendency would be balanced by an increase in the spin at the trough of the wave immediately upstream of  $a$ . Our conclusion is that the presence of the armature—which suppresses upstream changes—induces an instability in the naturally occurring K-H waves in the layer behind the armature. We have not attempted to quantify this phenomenon, since there are other non-linear effects to take into account. The flow pattern is rather complex. Just as in the linear theory for free vortex sheets, there should be a value of the ratio  $\lambda/h$  at which the growth rate of the instability is a maximum and so we expected the observations to show that  $\lambda/h = \alpha$ , where  $\alpha$  is roughly constant. And certainly the longer waves occurred where the layer was thickest, but no clear value of  $\alpha$  emerged.

Pullin [5] shows that convecting free vortical boundaries are quickly distorted by differential motions. For large enough wave amplitude, the valleys in the wave pattern tend to move faster than the peaks, a phenomenon one can also trace to the influence of the distorted vorticity distribution, as indicated in Fig. 7. If this process occurs in the aluminum layer, we would expect to find the crests of the waves to be thicker towards the muzzle end of the rail. This is observed to be the case in Fig. 4(a), although at another station nearer the muzzle, the opposite wave inclination appears.

Pullin also shows that the time scale  $t_w$  for the distortion of the primary wave is approximately the same as the wave's period

$$t_w = \frac{4\pi}{\omega} (1 - e^{-\varepsilon})^{-1}.$$

In a typical railgun observation, with  $h = 50 \mu\text{m}$ ,  $\lambda = 800 \mu\text{m}$  and  $\omega = V/h = 850 / (50 \times 10^{-6}) = 1.7 \times 10^7$ , we get  $t_w = 1.3 \mu\text{s}$ , which is somewhat less than the solidification time calculated above, i.e. the waves have time to develop.

Finally we should mention the phenomenon of filamentation studied by Pullin et al. This is the tendency of small bumps on surfaces separating regions of differing vorticity to steepen and form points of high curvature, from which spring thin filaments of vortical fluid. There is some evidence of this with the aluminum waves, the crests of which sometimes have a rough 'Christmas tree' edging.

## V. CONCLUSIONS

It is not easy to draw firm quantitative conclusions from the experiments, because of the variability of the ratio  $\lambda/h$ . The thickness  $h$  changes over an order of magnitude from one part of the rail to another. That the various non-linear instabilities we have cited are involved in the process, we have no doubt. The evidence about the direction of cresting is a little confusing, but that filamentation is occurring seems convincing. It seems unlikely that aluminum rails have any practical value, except perhaps to be a means of studying the very complicated liquid metal boundary between armatures and rails.

## VI. ACKNOWLEDGMENT

This work was supported by the U.S. Army Research Laboratory under contract DAAA21-93-C-0101.

#### REFERENCES

- [1] Persad, C. "On the Nature of the Aluminum-on-Copper Armature/Rail Interface." Paper No. 88a in the Proceedings of the 5th European Symposium on Electromagnetic Launch Technology, Toulouse, France, April 1995.
- [2] Persad, C., Yeoh, A., Prabhu, G., White, G., and Eliezer, Z. "On the Nature of the Armature/Rail Interface: Liquid Metal Effects." *IEEE Trans. Mag.*, vol. 33, no. 1, pp. 140-145, January 1997.
- [3] Parker, J., Snowden, P., and Berry, D.T. "New Electromagnetic Launcher Facility at the Institute for Advanced Technology." Paper No. 12 in the Proceedings of the 5th European Symposium on Electromagnetic Launch Technology, Toulouse, France, April 1995.
- [4] Rayleigh, Lord. *Scientific Papers*. 1880, vol. 1, pp. 474-87, and 1887, vol. 3, pp. 17-23.
- [5] Pullin, D. "The Non-Linear Behavior of a Constant Vorticity Layer at a Wall." *J. Fluid Mech.*, vol. 108, pp. 401-21, 1981.
- [6] Pullin, D. I., Jacobs, P. A., Grimshaw, R. H. J. and Saffman, P. G. "Instability and Filamentation of Finite-Amplitude Waves on Vortex Layers of Finite Thickness." *J. Fluid Mech.*, vol. 209, pp. 359-384, 1989.
- [7] Saffman, P. G. *Vortex Dynamics*. Cambridge University Press, 1995.

## Investigation of the metal contact crisis in a railgun with sectioned rails

Yu. A. Kareev, L. G. Kotova, A. T. Kuharenko, Yu. A. Halimullin  
Troitsk Institute for Innovation and Fusion Research (TRINITI)  
142092, Troitsk, Moscow Region, Russia

*Abstract* — There are discussed in detail the experimental results of the new method proposed by authors earlier which allows to obtain the non-arc acceleration regime with a larger value of the metal armature velocity than is realized in traditional railguns.

### I. Introduction

The armature metal contact crisis in railguns with directing rails arises from the velocity skin current effect. Connected with this event is the evaporation of a thin layer of the armature contact surface in a high magnetic field region. This evaporation leads to an increased voltage drop across the interface between the armature and the rail and is followed by arc ignition. The armature transition velocity corresponding to the time, when the contact transitions, depends weakly on the current and its period [1]. There are methods resulting in an increase of the transition velocity: the use of rails with a resistive layer [2 - 5] and the use of muzzle feed railguns [6 - 8]. These methods are based on the idea of decreasing the thickness of the skin layer.

In this work we continue an investigation of a new method proposed by us [9] to increase the transition velocity termed as the Dynamic Current Distribution (DCD) method. It consists of current localization in narrow regions of the contact that are forced to move opposite to the velocity. This is done periodically along the armature contact surface by sections in the surface of the rail. Thus, there arises the effect of DCD over all the contact surface of the armature.

The performance of a railgun with resistive rails has been experimentally investigated. The processing of experimental results was carried out using the physical and mathematical model [9] of the armature acceleration process. The results of this investigation are presented in the following parts of the report.

### II. Experimental installation and experimental data

#### A. Experimental installation

The experiments were carried out with the installation consisting of a capacitor bank ( $C=0.075$  F,  $U=5$  kV), the railgun and the diagnostics. The latter allowed measurement of the railgun current, the muzzle voltage, the armature position with help of magnetic probes placed with definite interval along the trajectory of flight.

The railgun contains the sectioned rails (pos.1), made from copper alloy, and aluminium armature (pos.2) which are shown in fig. 1. The rails surface consists of alternating insulating and conducting strips - teeth (pos.3). The insulators are made from polymer with boron nitride filler. The full length of a rail is 850 mm and the

breach section with a length of 200 mm is not sectioned. The armature has sizes  $d = h = 10$  mm,  $l = 18$  mm. Its mass  $M = 4.5$  g. The rail has constant sectioning along length  $a/l = 0.4$ . The lateral insulator walls of the railgun bore are made from the fiber-glass laminate.

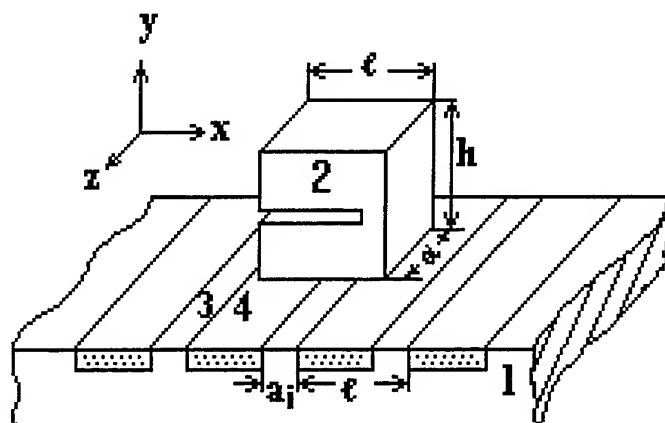


Fig.1. The appearance of sectioned rail in the railgun.  
1 - metallic rail, 2 - armature, 3 - tooth, 4 - insulator.

#### B. Description of the experiment and the measurements results

With help of the powder preliminary accelerator the armature acquired the velocity  $V_0$ , which was not measured. The current was supplied to the rails  $100 \mu s$  before the armature came to the first section. The current and voltage profiles on the railgun muzzle end are presented in fig. 2.

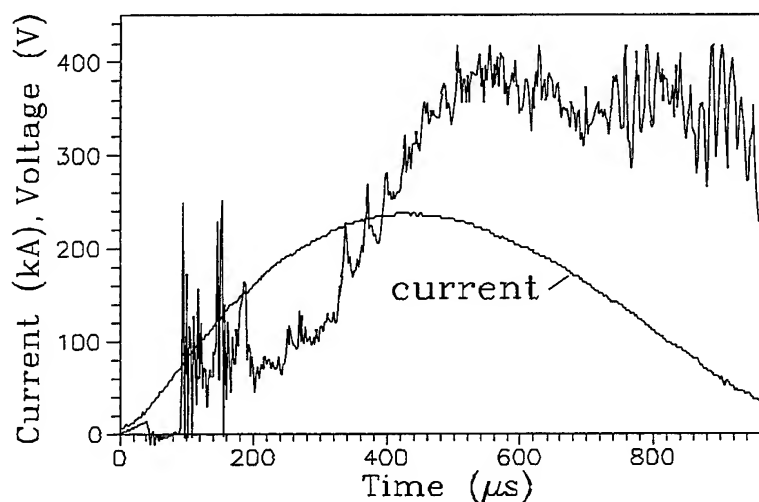


Fig.2. The railgun current and muzzle voltage profiles with sectioned rails for  $a_i/l = 0.4$ . The initial armature velocity is 614 m/s (powder acceleration).

The current reaches the maximum value 230 kA at time 450  $\mu$ s. The voltage has the characteristic leaps stipulated for a passage of the armature from section to section of the rail. The maximum voltage reached 400 V with metallic type of contact. In fig. 3 there are presented the current profiles in sections 14 and 15 at the moment when the armature passes them. Metallographic analysis has shown the presence of micro destruction in the corners of all sections that confirms the existence of spark discharges analogous to the collector sparking in electric machines. The moments when the armature passes the magnetic probes installed along the rails are shown in fig. 4 by 5 squares.

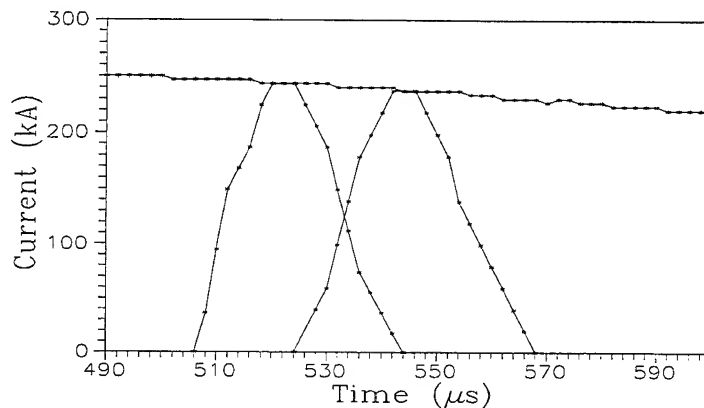


Fig.3. The currents profiles in the 14th and 15th tooth of the railgun electrode with sectioned rails for  $a_i/l = 0.4$ . The initial armature velocity is 614 m/s (powder acceleration).

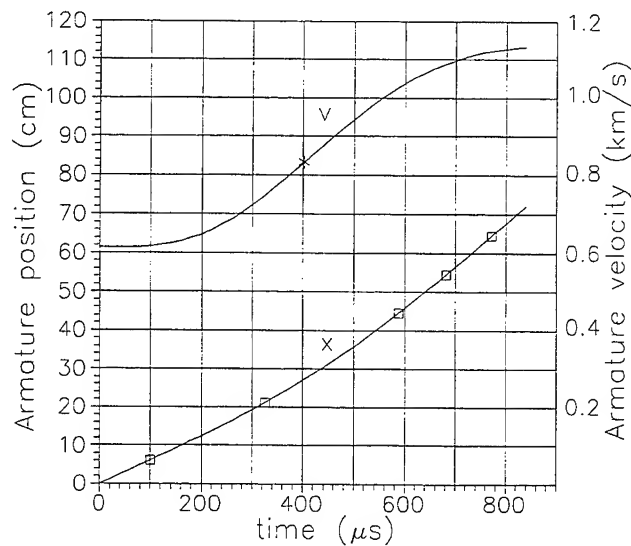


Fig. 4. The dependence of the armature position (X) and the velocity (V) versus time.

### III. Discussion of the results

The analysis of the experimental data has shown that without taking into account the friction force between the armature and the sectioned rails it is impossible to reproduce a trajectory of the armature in the railgun with help of calculations. To determine correctly the friction force we have used the recommendations [3] for a definition of a pressing force  $F_y$  of our armature to the rails,  $F_y = 2.11 \cdot L' \cdot I^2 / 2$ , where  $L'$  and  $I$  are the railgun inductance per unit length and the railgun current, respectively. Thus, the armature movement equation has a form  $dV/dt = L'_{eff} \cdot I^2 / (2 \cdot M)$ , where  $L'_{eff} = L' \cdot (1 - 4.22 \cdot \alpha)$ , and  $\alpha$  is the coefficient of friction. Solving the movement equation for  $V_0 = 614$  m/s and  $L'_{eff} = 1.82 \cdot 10^{-7}$  H/m, we have been successful to reproduce the armature movement trajectory which is represented in fig. 4. Here is presented the time dependence of the armature velocity, too. It is seen that the armature was accelerated up to the velocity 1140 m/s. The point \* on the curve for the velocity corresponds to the armature transition velocity for continuous rails. This velocity is  $V_* = 830$  m/s. Investigating the state of the sectioned rails contact surface we have not discovered tracks of high current arcing.

Mathematical model of the heat calculation of the armature contact surface and the rail teeth is presented by us in [9]. In this report we shall write the calculation formulae and give the explanations for its. Let us make use of the notation presented in fig.1 and define the optimum sectioning of the rail as the sectioning in which the tooth size  $a_i$  equals to  $\delta_i$ , where  $\delta_i$  is the width of the skin layer in the tooth. With the non-optimum sectioning of the rail  $\delta_i < a_i < l$ . The current density in the  $i$ -tooth and adjacent to it the thin layer of the armature contact surface is  $j_i = I_i / (\delta_i \cdot d)$ , where  $I_i$  is the current value in the railgun at the time when the armature places above the  $i$ -tooth. For the optimum sectioning of the rail  $\delta_i / l = g [(1 + 4/g)^{0.5} - 1] / 2$  and for the non-optimum sectioning of the rail  $\delta_i / l = [g (1 - a_i / l)]^{0.5}$ , where  $g = D_{ri} / (V_i \cdot l)$ ,  $D_{ri}$  is the field diffusion coefficient in the rail tooth,  $V_i$  is the armature velocity at the time when the armature passes the  $i$ -tooth. The heat of the  $i$ -tooth is  $Q_{ri} = \mu \cdot D_{ri} \cdot j_i^2 \cdot \tau_{ri} = \mu (j_i \cdot \delta_i)^2 = \mu (I_i / d)^2$ . Here  $\tau_{ri} = (1 - a_i) / V_i$  is the time of the current flowing in the  $i$ -tooth,  $\mu$  is the magnetic permeability. The energy emitting in the volume unit of the armature contact surface thin layer in passing every the  $j$ -tooth is  $Q_{aj} = j_j^2 \cdot \tau_{aj} / \sigma_{aj} = (I_j / d)^2 / (\delta_j \cdot \sigma_{aj} \cdot V_j)$ , where  $\tau_{aj} = \delta_j / V_j$  is the time of heating,  $\sigma_{aj}$  is the armature conductivity. Thus, the energy of the armature contact surface thin layer after passing the  $i$ -tooth will be  $Q_{ai} = \sum_{j=1}^i Q_{aj}$ .

In fig. 5 the heat calculation results in a thin layer of the armature contact surface versus time are presented. The heat is normalized to the value of the aluminium evaporation heat  $Q_{ev} = 31.3$  GJ/m<sup>3</sup>. The curve (1) corresponds to the sectioned rails used in the experiments and the curve (2) to the sectioned rails with the optimum tooth sizes  $a_i$ . The values of the relative heat 0.053 and 0.086 correspond to the beginning and the end of the melting process with the temperature 658° C.

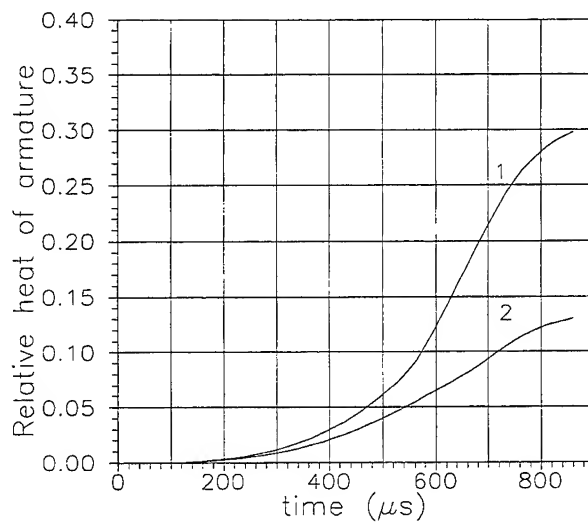


Fig. 5. The dependence of the ratio of the heat on the armature contact surface to the evaporation heat versus time.

The value of the relative heat of 0.216 corresponds to the beginning of the evaporation with the temperature  $2447^{\circ}\text{C}$ . As seen from the conduct of curve (1) at time  $700\ \mu s$  the armature contact surface reaches the evaporation temperature but actual evaporation does not occur. Note that in a traditional railgun a crisis arrives at  $400\ \mu s$  (see fig. 4). With optimum sectioning of rails it is possible to decrease the contact surface heat considerably as seen from curve 2.

In fig. 6 there are presented the calculation results of the temperature ( $T$ ) and the optimum tooth size ( $a_i$ ) versus the section number. The level of temperatures is quite moderate. The tooth sizes  $a_i$  are in reasonable limits.

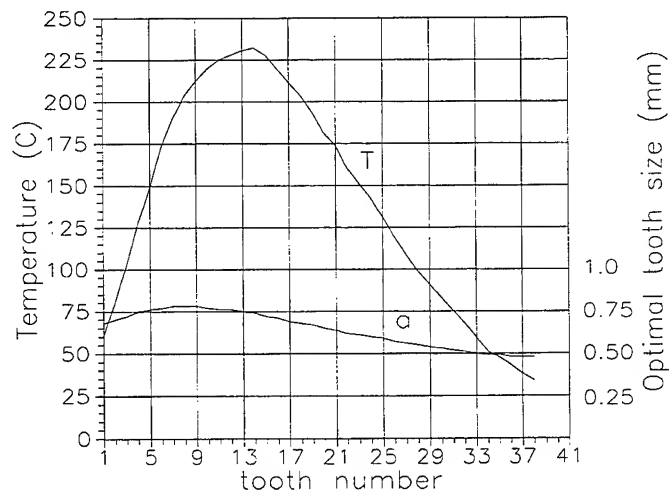


Fig. 6. The dependence of the temperature ( $T$ ) and optimal size of tooth ( $a$ ) versus its number.

#### IV. Conclusion

The experiments and above presented calculations have shown that a conception of DCD is correct. If in a traditional railgun, because of the velocity skin current effect, the transition of a metallic contact occurred at an armature velocity of 830 m/s, then in the railgun with sectioned rails, realizing the conception DCD, the transition of a metallic contact has not been discovered. The total length of the rails could therefore be used for armature acceleration and a velocity of 1140 m/s at the exit of the railgun was obtained.

#### References

- [1] V. P. Bazilevski, Yu. A. Kareev, R. M. Zayatdinov, "Electroconductivity crisis of high speed metal contact", Proceedings of II All-Union Conference on high current arc discharge dynamics in magnetic field (Novosibirsk, 4-6 December 1991), Novosibirsk, 1992, pp. 285-304.
- [2] G. C. Long, W. F. Weldon, "Limits to the velocity of solid armature in railguns", *IEEE Trans. Magn.*, Vol. 25, No. 1, pp. 347-352, January 1989.
- [3] A. P. Glinov, A. V. Kurilov, Preprint of Kurchatov Atomic Energy Institute, No. 5478/1, Moscow 1992.
- [4] Yu. A. Dreizin, "Solid armature performance with resistive rails", *IEEE Trans. Magn.*, Vol. 29, No. 1, pp. 797-803, January 1993.
- [5] Yu. A. Kareev, L. G. Kotova, A. T. Kuharenko, Yu. A. Halimullin, "Investigation of the metal contact crisis in railgun with resistive rails", Proceedings of 5-th European Symposium on Electromagnetic Launch Technology, Toulouse, 10-13 April 1995, No. 22.
- [6] M. Cowan, "Solid armature railguns without the velocity-skin effect", *IEEE Trans. Magn.*, Vol. 29, No. 1, 1993, p. 385.
- [7] O. V. Fatyanov, V. E. Ostashev, A. N. Lopirev, A. V. Ulianov, "Electromagnetic railguns configurations", *Thermophysics of High Temperature*, Vol. 31, No. 3, pp. 462-468, June 1993.
- [8] Yu. A. Kareev, R. M. Zayatdinov, "Transition conditions for solid armatures in railguns with muzzle current feed", *IEEE Trans. Magn.*, Vol. 31, No. 1, 1995, pp. 180-182.
- [9] I. S. Glushkov, Yu. A. Kareev, L. G. Kotova, A. T. Kuharenko, Yu. A. Halimullin, "Investigation of techniques to increase armature transition velocity", *IEEE Trans. Magn.*, Vol. 33, No. 1, 1997.



# Numerical modelling of the internal ballistics of an electrothermal launcher.

Y. Jordan, J. M. Lombard, F. Caillau.

GIAT Industries,  
7, route de Guerry, F-18.023 Bourges, FRANCE

O. Vallée.

Centre Universitaire de Bourges  
Université d'Orléans - UFR Faculté des Sciences - GREMI  
BP 403, rue Gaston Berger, F-18.028 Bourges cedex, FRANCE.

## SUMMARY

We describe the present state of development of a 0 - D model of an electrothermal launcher resulting from the combination of the PFN and plasma burner modules developed by CEA with the interior ballistics module developed by GIAT Industries, which model the phenomena in the chamber and in the tube, respectively.

This last module is presented here with assumptions and preliminary results. A first comparison of calculated and experimental ( $\leq 4$  MJ) results is exposed, and permits a partial validation of the assumptions. Reasonable agreement with typical experimental results is noted although there is a difference of time scale.

This comparison with experiment is encouraging and underlines the need to improve and develop our hypothesis and exploit the available experimental results to validate the model.

## NOMENCLATURE

### Variables

|       |  |               |                               |
|-------|--|---------------|-------------------------------|
| Q     | : energy ;                               | $\rho$        | : density ;                   |
| U     | : internal energy ;                      | M             | : molar mass ;                |
| H     | : mean molar enthalpy ;                  | S             | : area ;                      |
| h     | : convective heat transfer coefficient ; | v             | : velocity ;                  |
| $L_v$ | : molar latent heat of vaporisation ;    | t             | : time ;                      |
| N     | : number of moles ;                      | $Nu_D$        | : Nusselt number ;            |
| p     | : pressure ;                             | $Re_D$        | : Reynolds number ;           |
| T     | : temperature ;                          | Pr            | : Prandtl number ;            |
| V     | : volume ;                               | $\varepsilon$ | : emissivity of a grey body ; |

### Subscripts

|        |                     |        |                          |
|--------|---------------------|--------|--------------------------|
| cap    | : capillary ;       | pl     | : plasma ;               |
| $H_2O$ | : water ;           | w      | : tube wall ;            |
| b      | : projectile base ; | i or j | : i-th or j-th species ; |

### Superscripts

|    |                |     |              |
|----|----------------|-----|--------------|
| cc | : convective ; | rad | : radiative. |
|----|----------------|-----|--------------|

## INTRODUCTION

Within the framework of sub - program 4 of the Franco - German co-operation on electrical launchers, GIAT Industries developed in co-ordination with CEA, a numerical model to compute the performance of an electrothermal gun containing water as working fluid.

Within the framework of its work on ETL (ElectroThermal Launcher) financed by *Direction de la Recherche et de la Technologie* (DRET), CEA developed and validated the LET0D [1 - 2] code that simulates the PFN (Pulse Forming Network) and the plasma burner. GIAT Industries focuses its interests on the interior ballistics (geometrically limited on one side by the plasma torch exhaust and on the other by the projectile base) to complete the above model ; the complete model of ETL contains three parts : the CEA modules (PFN and plasma torch) and the interior ballistics (IB) module presented here.

In this module, we made significant modifications to our older model [3] including, among others, the computation of the evolving thermodynamical properties of the gas phase during the shot. We present here the hypotheses made in this module, a first comparison with experimental results carried out in weapon configuration at the end of 1996 within the framework of the joint effort with CEA, and the possible evolution of our model towards to a validation stage.

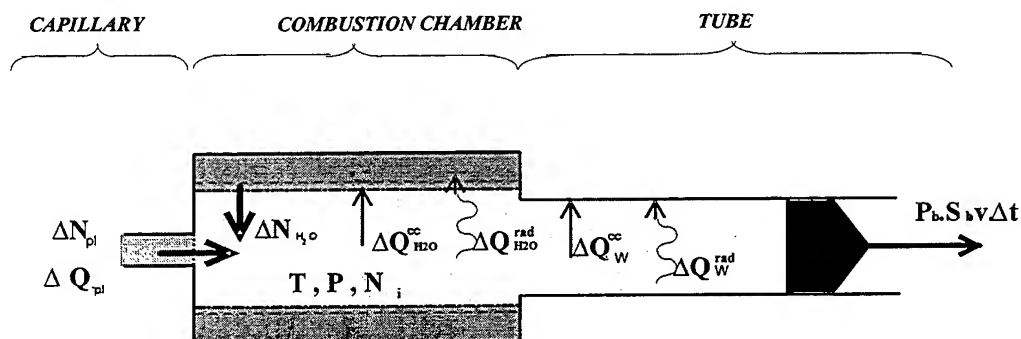
## DESCRIPTION OF THE INTERIOR BALLISTICS MODULE.

This module is a global (0 - D) model of interior ballistics that uses the Lagrange assumption to calculate the pressure and velocity distribution of the gas phase along the chamber and the tube. The projectile motion is computed from the momentum conservation equation taking into account the pressure at its base.

We made some hypotheses, a priori, to build the model.

Between the torch exhaust and the projectile base, we distinguish three elements : a gas phase, a liquid phase and the tube.

We have schematically represented these elements with their interactions in figure 1.



**Figure 1** : Physical phenomenon of the interior ballistics.

## ELEMENTS AND INTERACTIONS CONSIDERED IN THE IB MODULE.

### The gas phase

The gas phase is considered to be in thermodynamical equilibrium and to verify the Debye - Hückel model which modifies the ideal gas equation because of the Coulombian interaction. The thermodynamical properties (EOS, energy, entropy, ...) are determined by the physical statistics.

Its composition and temperature, considering the mass and energy balances, are computed by maximising its entropy by using a modified Downhill - Simplex optimum-seeking method [4].

### The working fluid.

Considering the existing tests of visualisation on working fluid ablation and those we carried out earlier [5], the working fluid seems generally to develop an annular configuration in the combustion chamber. Consequently, we considered the working fluid simply as the cylinder represented on figure 1 with a surface  $S_{H_2O}$  gas / fluid interface. The temperature of the water was chosen constant and equal to  $T_0 = 300$  K. The working fluid is ablated by the incident thermal flow (radiative and convective). This results in vaporisation followed by heating to a temperature  $T_1 = 400$  K before perfect mixing with the gas phase.

### The tube wall

The tube wall is fixed and has a uniform temperature near 300 K which is determined by the ratio of the received heat to the thermal capacity of the complete tube.

### The plasma torch / gas phase interaction

The plasma is limited to the first ionisation and its flow is given by the relation :

$$\frac{\Delta N_{pl}}{\Delta t} = \frac{\rho_{pl}}{M_{pl}} S_{cap} \sqrt{\frac{2(P_{pl} - P)}{\rho_{pl}}} \quad [E - 1]$$

The number of plasma moles transferred during  $\Delta t$  is perfectly mixed with the gas phase, adding the energy :  $\Delta Q_{pl} = \Delta N_{pl} \cdot H_{pl}(t)$

### Gas phase / working fluid and wall interaction

The radiative flow to the working fluid and the tube coming from the gas phase is considered as that of a grey body of emissivity  $\varepsilon = 0,5$  ; so the radiative heat received by the Y medium (tube or working fluid) during  $\Delta t$  is :  $\Delta Q_Y^{rad} = \varepsilon \cdot \sigma \cdot T^4 \cdot S_Y \cdot \Delta t$

The heat transfer coefficient is estimated using the COLBURN equation with averaged Reynolds and Prandtl numbers corresponding to the working fluid in the chamber at the exhaust plasma flow velocity, and for the tube with the Lagrange assumption :

$$Nu_D = 0.023 Re_D^{0.8} Pr^{1/3} \quad [E - 2]$$

To take into account the gradients near the surfaces, the MacAdams rule is used ; it depends, for the calculation of interfacial properties (except  $C_p$ ), on the definition of a film temperature, the mean of the gas and the X medium temperatures. The heat transferred to the fluid or the tube wall by convection is  $\Delta Q_X^{cc} = h(T - T_x) \cdot S_X \cdot \Delta t$ .

The heat received at the interface by the working fluid generates its vaporisation and its heating to  $T_1$ . As a consequence, the number of moles of water vaporised during  $\Delta t$  is :

$$\Delta N_{H_2O} = \frac{\Delta Q_{H_2O}^{cc} + \Delta Q_{H_2O}^{rad}}{(L_v + H_{H_2O}(T_1) - H_{H_2O}(T_0))} \quad [E - 3]$$

and the associated volume released to the gas phase is :  $\Delta V_{H_2O} = M_{H_2O} \cdot \frac{\Delta N_{H_2O}}{\rho_{H_2O}}$ .

#### Conservation relations for the gas phase.

The matter conservation equation is clearly valid. The energy balance corresponds to the following expression for the variation of the energy balance :

$$\begin{aligned} \underbrace{U_{gas}(t + \Delta t) - U_{gas}(t)}_{\text{Internal energy change gas phase}} &= \underbrace{H_{pl}(t) \cdot \Delta N_{pl} + H_{H_2O}(T_0) \cdot \Delta N_{H_2O}}_{\text{Energy of the plasma and the water entering the gas phase during } \Delta t.} \\ &+ \underbrace{E_{kin}(t) - E_{kin}(t + \Delta t)}_{\text{Kinetic energy change.}} - \underbrace{(P(t) \cdot \Delta V_{H_2O} + P_B(t) \cdot S_t \cdot \Delta X)}_{\text{Work exerted against pressure.}} - \underbrace{[\Delta Q_W^{rad} + \Delta Q_W^{cc}]}_{\text{Losses to the tube wall.}} \end{aligned} \quad [E - 4]$$

We specify that the kinetic energy variation is that of the moving mass formed by the projectile, the gas phase and the working fluid. The work exerted against pressure is that of the mean pressure on the volume released by the working fluid ablation on one side, and that of the base pressure due to the projectile motion on the other side.

The differentiation of this equation gives, with  $\Delta f = f(t + \Delta t) - f(t)$  :

$$\begin{aligned} \Delta U_{gas} &= \left( \frac{\partial U_{gas}}{\partial T} \right)_{N_i, V} (T(t), V(t + \Delta t), N_i(t + \Delta t)) \cdot \Delta T + \sum_j \left( \frac{\partial U_{gas}}{\partial N_j} \right)_{N_{i, i \neq j}, V, T} (T(t), V(t + \Delta t), N_i(t)) \cdot \Delta N_j \\ &+ \left( \frac{\partial U_{gas}}{\partial V} \right)_{N_i, T} (T(t), V(t), N_i(t)) \cdot \Delta V \end{aligned} \quad [E - 5]$$

By grouping corresponding terms in [E-4] and [E-5], we get the relation [E-6] where the term on the left of the equation corresponds to the variation of the internal energy of an adiabatic system of volume  $V(t + \Delta t)$ , and the term on the right to a perfectly defined value. The system temperature and composition is determined (using a modified Downhill - Simplex method) by the entropy maximisation of the gas phase and the energy balance.

$$\begin{aligned} &\left( \frac{\partial U_{gas}}{\partial T} \right)_{N_i, V} (T(t), V(t + \Delta t), N_i(t + \Delta t)) \cdot \Delta T + \sum_j \left( \frac{\partial U_{gas}}{\partial N_j} \right)_{N_{i, i \neq j}, V, T} (T(t), V(t + \Delta t), N_i(t)) \cdot \Delta N_j = \\ &H_{pl}(t) \cdot \Delta N_{pl} + H_{H_2O}(T_0) \cdot \Delta N_{H_2O} + E_{cin}(t) - E_{cin}(t + \Delta t) - (P(t) \cdot \Delta V_{H_2O} + P_B(t) \cdot S_t \cdot \Delta X) \\ &- [\Delta Q_W^{rad} + \Delta Q_W^{cc}] - \left( \frac{\partial U_{gas}}{\partial V} \right)_{N_i, T} (T(t), V(t), N_i(t)) \cdot \Delta V \end{aligned} \quad [E - 6]$$

This method shows good agreement with plasma equilibrium computations from the literature and indicates that it is reasonable to determine the equilibrium solely with predominant species. In the following computations, we only consider the 9 species :  $H_2O$ ,  $H$ ,  $C$ ,  $O$ ,  $H^+$ ,  $C^+$ ,  $O^+$ ,  $e^-$  and  $C_2H_4$  (vapour coming from the plasma torch).

The numerical scheme of integration is an explicit Eulerian, with an adaptive time step.

## COMPUTED AND EXPERIMENTAL RESULTS.

In our computations, we considered a shot start pressure of 40 MPa and then no drag force.

The input data for the PFN and the capillary model are those used for the shots by CEA.

The code has been calibrated with available experimental results in a weapon (250 to 750 kJ) and in closed vessels (250 kJ) of 30 mm, and then applied, without modification, to GI / CEA experiments in 30 mm carried out in 1996 for energies from 1 to 4 MJ.

The input data for the computations and the experimental shots (shot number, projectile mass, working fluid mass, tube length and initial PFN voltage) are given in table 1.

**Table 1 :** Input data for 250 kJ to 4 MJ shots.

| Electrical energy | Shot n° | Projectile mass (g) | Working fluid mass (g) | Tube length (m) | Initial voltage (kV) [PFN] |
|-------------------|---------|---------------------|------------------------|-----------------|----------------------------|
| 250 kJ.           | 169     | 49,1                | 20                     | 0,25            | 11,1 [1]                   |
| 1 MJ.             | 113     | 48,0                | 20                     | 1,0             | 22,0 [1]                   |
| 2 MJ.             | 120     | 49,0                | 40                     | 3,0             | 18,6 [3]                   |
| 3 MJ.             | 114     | 60,0                | 54                     | 3,0             | 21,3 [3]                   |
| 4 MJ.             | 115     | 132                 | 77                     | 3,0             | 21,1 [3] + 22,2 [1]        |

N.B. : The PFN 1 and 3 contain respectively 4 & 12 RLC cells ; for the 4 MJ shot, the PFN 1 was boosted after 850  $\mu$ s.

The characteristic values (maximum current  $I_{max}$ , minimum resistance  $R_{min}$ , maximum pressure  $P_{max}$  and discharging voltage  $U_{disc}$  in the plasma torch, projectile exit velocity  $v$  and discharging time  $\tau$ ) of the computed (**bold**) and experimental (*italic*) results are given in table 2.

**Table 2 :** Typical results for the 250 kJ to 4 MJ shots.

| Num. / Exp. | $I_{max}$ (kA)   | $R_{min}$ (m $\Omega$ ) | $v$ (m/s)          | $P_{max}$ (kbar)   | $\tau$ (ms)        | (CH <sub>2</sub> ) <sub>n</sub> ablated (g) | $U_{disc}$ (kV)  |
|-------------|------------------|-------------------------|--------------------|--------------------|--------------------|---|------------------|
| 250 kJ      | <b>122 / 122</b> | <b>40,0 / 28,0</b>      | ***                | <b>1,30 / 1,45</b> | <b>0,43 / 0,41</b> | <b>0,85 / 0,89</b>                          | <b>4,5 / 4,0</b> |
| 1 MJ.       | <b>294 / 300</b> | <b>20,0 / 20,5</b>      | <b>1810 / 2130</b> | <b>2,33 / 3,28</b> | <b>0,45 / 0,40</b> | ***   | <b>6,1 / 6,1</b> |
| 2 MJ.       | <b>264 / 241</b> | <b>17,3 / 16,7</b>      | <b>2530 / 2620</b> | <b>2,03 / 1,95</b> | <b>1,28 / 1,28</b> | ***   | <b>4,6 / 4,1</b> |
| 3 MJ.       | <b>311 / 309</b> | <b>15,5 / 19,5</b>      | <b>2560 / 2480</b> | <b>2,87 / 4,19</b> | <b>1,29 / 1,17</b> | ***   | <b>4,9 / 6,0</b> |
| 4 MJ.       | <b>534 / 485</b> | <b>11,2 / 15,6</b>      | <b>2160 / 2180</b> | <b>3,33 / 4,24</b> | <b>1,25 / 2,09</b> | ***   | <b>6,0 / 7,6</b> |

N.B. : A short circuit occurred during the 4 MJ shot.

The ablated masses of PE for the 1 to 4 MJ shots are not available.

### 250 KJ.

For this shot, the results correspond to a closed vessel shot ; the maximum pressure is a radial one in the plasma burner. Generally speaking, computed and experimental results are quite close.

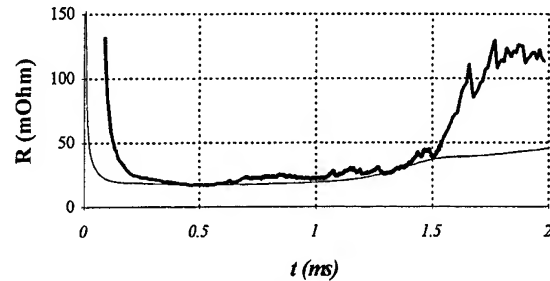
### 1 TO 4 MJ SHOTS.

For these shots realised in a 30 mm gun tube, the experimental maximum pressures given in table 2 are Crusher readings (only indicative) except for the 2 MJ shot where the given pressure is that of the base of the projectile one deduced from the projectile motion determined by IDL. Experimental and computed results are again close, except for the Crusher pressures.

Only the experimental results from the IDL measurement for the 2 MJ shot permit a refinement of the comparison of experiment & computation. This is generally limited to current and voltage curves and sometimes to the total mass of ablated material.

We compare the experimental (bold) and computed (fine) resistance versus time for a 2 MJ shot in figure 2.

This figure underlines the good agreement for the minimum resistance during the shot and shows a time difference of nearly 0,1 ms with the plasma setup.

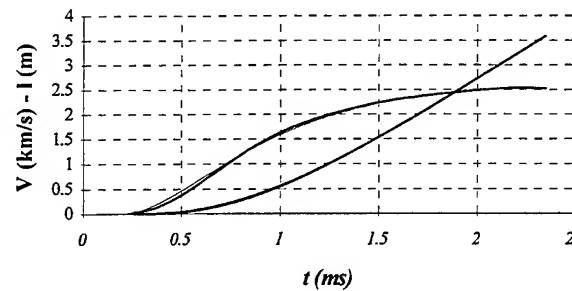


**Figure 2** : Plasma resistance - 2 MJ shot.

In figure 3, we show the experimental (bold) and computed (fine) projectile displacement and velocity.

Experimental results being plotted with an advance of 0,1 ms. With this advance, experimental and computed results are :

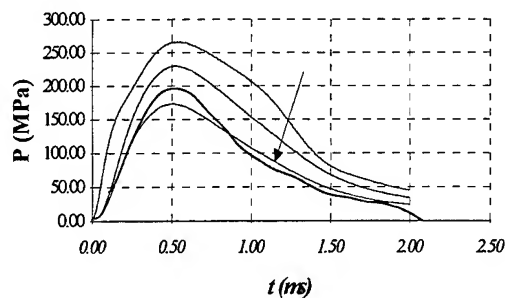
- merged for projectile motion (1 curve) ;
- very close for projectile velocity.



**Figure 3** : Projectile position and velocity - 2 MJ shot.

In figure 4, we have plotted the computed (fine) and experimental (bold) base pressure with a time advance of 0,1 ms according to the above remarks.

The upper curve of the computed pressures corresponds to the mean pressure in the capillary, the next to the mean pressure in the combustion chamber and the lower curve to the base pressure, the arrow indicates the instant (1.1 ms) at which all the fluid was vaporised.



**Figure 4** : Pressures in the ETL - 2 MJ shot.

Between 0,35 and 0,80 ms, the experimental base pressure is greater than the computed one. A possible explanation of this difference could be that experimental ablation is faster than we assumed.

## DISCUSSION - CONCLUSION

A comparison of computation & experiments shows reasonable agreement for current, voltage, discharging time and projectile velocity. The agreement is quite remarkable, considering the simple hypothesis used.

We assumed that the time difference between experimental and computed results in the plasma torch is due to the simple model of the plasma initiation. This is not embarrassing since quite good agreement with the plasma resistance in the torch and with the projectile velocity is observed.

Considering the remark on figure 4, an adapted ablation rate should allow one to match the base pressure estimated by IDL. A realistic adaptation consists in determining the ablated water fractions for each of the following interactions : radiative, convective and mechanical.

This shows that the most sensitive point is the one concerning the plasma / matter interaction since there are not enough significant results available.

The model validation will necessitate an evaluation in the future work of the different elements used as well as improving them to improve the computation/experiments agreement. These elements are :

- the plasma resistance model (improvement of the electron/neutral collision contribution to the plasma resistance) ;
- the introduction of the double ionisation ;
- the plasma/matter interaction with or without vapour shield :
  - for the WF : thermal aspects (convective, radiative) and mechanical (dragging) ;
  - for the PE : convective aspect, radiative and mechanical ( PE compression).

## REFERENCES.

- [1] **Jacob E., Bouquet S., Tortel B.,** *A global theoretical approach for the electrothermal gun : scaling laws and a 0 - D time dependent model*, IEEE Trans. Mag., Vol. 31, n° 1, Jan. 1995.
- [2] **Jacob E., Aussel A., Bouquet S., Hermeline F.,** *Electrothermal launcher modelling in CEA*, 5th Europ. Symp. on EML Technology, 1995, 105.
- [3] **Caillau F., Jordan Y., Jacob E., Bouquet S., Vallée O.,** *Modelisation of interior ballistics of an electrothermal launcher*, 5th Europ. Symp. on EML Technology, 1995, 105.
- [4] **Press W. H., Flannery B. P., Teukolsky T. A., Ketterling W. T.,** *Numerical Recipes, the Art of Scientific Computing*, Cambridge University Press, 1989, 702 p.
- [5] **Caillau F., Collin M.,** *Closed Vessel Experiments for Electrothermal Gun Investigation*, 5<sup>th</sup> Eur. Symp. on EML Tecnol., 1995.

## ACKNOWLEDGEMENTS.

This work has been carried out within the framework of a thesis to which the *Conseil Général du Centre* (to which we particularly want to express our acknowledgements) contributes. We are very grateful to CEA for its financial and scientific support for the study presented here. We more particularly express our gratitude to Mr Jacob and Mr Bouquet for the work done together to link the numerical programs.

# Investigation of the Performance of Rail Conductor Materials

Chadee Persad, Shaun Phillips, Andrew Yeoh, Jonathan Stolk and Zwy Eliezer  
Institute for Advanced Technology, The University of Texas at Austin  
4030-2 W. Braker Lane, Suite 200, Austin, Texas 78759-5329

**Summary**—Solid armature railguns have been found to be more efficient than plasma armature railguns in laboratory experiments for launching useful payloads at up to 3 km/s. These launchers use armatures that are accelerated from rest by a high-current pulse. This study draws upon experimental results obtained using a 25-mm square bore launcher. The experimental focus is the post-shot condition of the rail contact surface after a single launch experiment. The performance of rails made of molybdenum, copper-chromium alloy, and unalloyed copper is compared. A liquid metal layer forms between the aluminum armature and the rail during the very early stage of launch. The rail contact surfaces are observed to have different areal coverages of resolidified liquid metal. Measurements of the spatial evolution of these coverages as a function of current are reported. It is proposed that the behavior can be interpreted in terms of the known Mode III shear failure at the support of a moving beam. Molybdenum and copper-based alloys both have development potential as rail conductor materials. Some of the pertinent materials technology developments are reviewed.

## I. INTRODUCTION

There is a need to improve the damage resistance of rail conductors and to increase the lifetime of rail conductors. Multi-shot service conditions in which similar forces are applied to structures at different temperatures demand expanded launcher design and materials selection space. One structure degrading mechanism is rail heating. Joulean heating of the rail conductors increases the rail resistivity and the energy dissipated in the launcher structure. Elevated temperature operation reduces allowable operating stress levels and increases the size and mass of rail conductors.

For many minimum-mass armature designs constructed of aluminum alloys, there is the need to know precisely how the current and the resulting Lorentz force is distributed in the armature. The heated armature which has undergone plastic deformation can be a more mass-efficient projectile driver. If during the early current pulse, the current is non-uniformly distributed, the resultant accelerating force can perturb and misalign the early trajectory. Such misalignments and uneven heating produce launch package overstress and bore interactions which have been observed to damage rail surfaces.

The research is described in three sections. In Section 1, the experimental part of the study presents observations of the armature/rail interface in cases where three different rail materials were tested with a common aluminum alloy armature. Regions of recovered rails corresponding to the rising-current, early phase of launch were examined. Section 2 proposes that the initial armature motion resembles a dynamically loaded beam — a model developed by other workers. As motion begins there is a shearing of the armature material near the armature/rail interface. A Mode III beam-support failure is observed. Section 3 provides a general assessment of rail materials performance. The potential for improved rail conductor materials is provided through a review of reported research on these materials.

## II. DESCRIPTION OF THE RESEARCH

### A. Section 1: *Experimental Study*

This experimental procedures section is divided into three topics: materials description, test and evaluation procedures, and post-test evaluation and analysis results.

### B. *Materials Description*

Three rail materials were tested: Unalloyed Copper C11000, Copper-Chromium Alloy C18200, and Molybdenum. For the baseline laboratory rail conductor tests we have employed unalloyed "electrolytic



tough pitch" (ETP) copper {C11000}. ETP copper contains approximately 0.03% oxygen and a minimum of 99.0% copper. In the commercial busbar grades, the material was supplied in the half-hard temper. The commercial busbar designated "182 RWMA Class II" was the copper-chromium alloy used for these experiments. The molybdenum was made from commercial-purity powder-metallurgy plate stock. Rails were supplied cut from 0.25-inch thick rolled plate, with the longitudinal rolling direction matching the long dimension of the rail. The relative values of electrical conductivity and strength for the three rail materials are shown graphically in Figure 1.

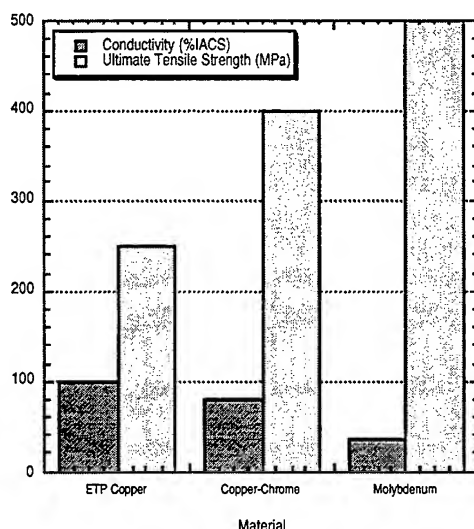


Fig. 1. Relative values of conductivity and strength for the three materials studied.

The ETP copper and the copper-chromium alloy rail conductors were supplied by Copper & Brass Sales, CA. The molybdenum rails were supplied by Phillips Elmet Inc., MA. The rail conductor sizes were 1.25 in x 0.25 in with rectangular cross sections. They were cut in 60-inch lengths and drilled and tapped to accommodate muzzle voltage probes. The rail conductor surfaces were lightly scrubbed with a nylon foam pad wetted with ethyl alcohol, followed by an alcohol rinse and air drying.

### C. Test and Evaluation Procedures

**EML Test Bed** — The test bed used was the Okaloosa Armature Tester (OAT). OAT was a 1.2-m long, 25-mm square bore launcher designed for armature/rail physics and materials studies. It was powered by a 4.8 MJ capacitor/inductor pulsed power supply, described elsewhere [1]. For these tests, current pulses with nominal 600 kA peaks were employed. These tests examined rail behaviors and the current-carrying limits of these aluminum armatures. The MCA 1.01 armature designed by Price and Yun [2] was used in these tests. In these experiments the armature mass was 24 g and it pushed a polycarbonate slug with a mass of 16 g. The armature configuration is shown in Figure 2a. The typical current pulse shape is shown in Figure 2b.

### D. Post-Test Evaluation and Analysis

The rails were recovered after each experiment for evaluation. Qualitative assessments of the materials transfer between the armature and rail conductors were performed using a low power stereoscopic optical microscope. Photomicrographs were taken of the rail surface at the point of armature motion initiation. The molybdenum rails were observed to crack at discontinuities in their supports. SEM fractography was used to determine the nature of the fracture process. Optical profilometry was used to measure wetting angles of the deposits. The details of this method have been described in our previous work [3].

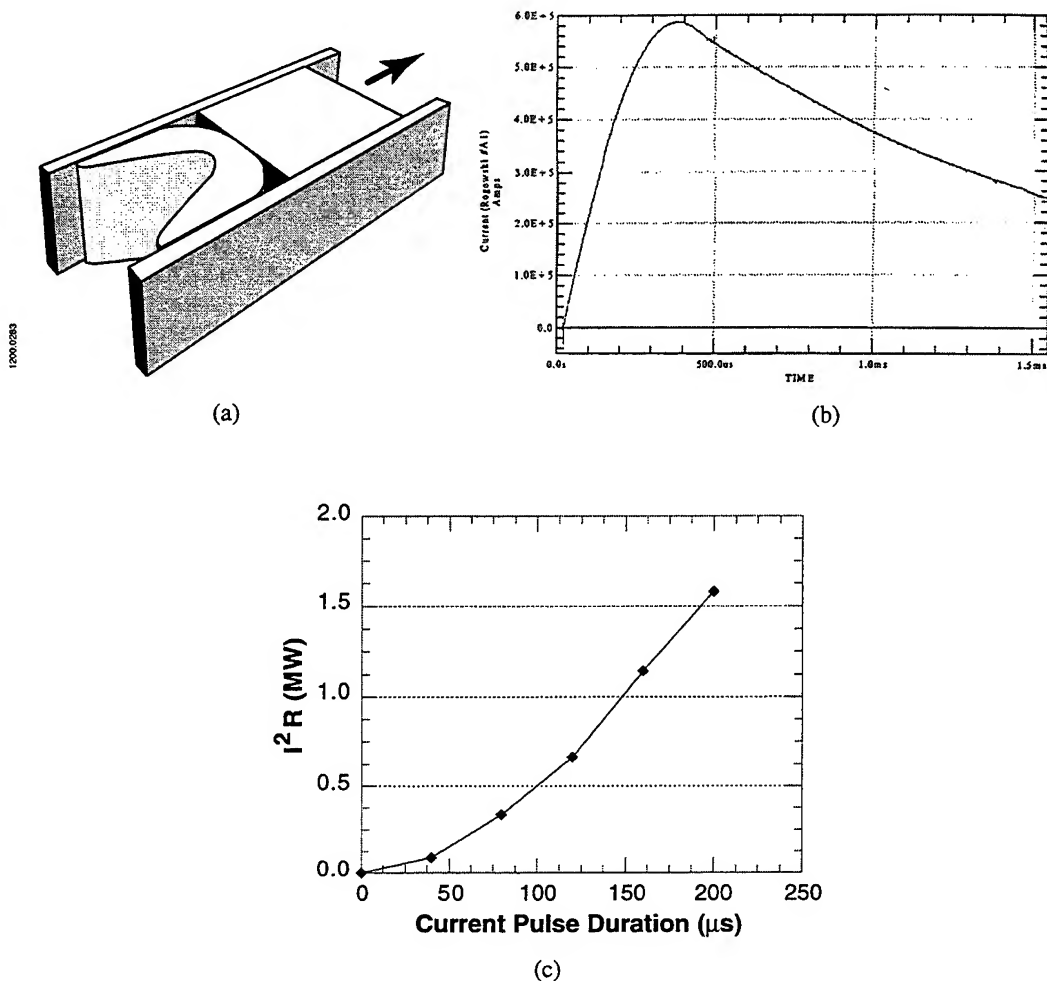


Fig. 2. a) The monolithic aluminum armature MCA 1.0.1 used in the tests studied; b) current pulse shape typical of the tests studied; c) interface power dissipation versus current pulse duration plot for the ETP copper rail studied.

### III. RESULTS AND DISCUSSION

#### E. Performance Data from Test

Test data show the measured current profile, as shown in Figure 2b for the unalloyed copper rail. In Figure 2c these data are used in an extended analysis to produce the power dissipation trace. The method is briefly outlined here. Data measured by Jamison are used [4]. The armature interface resistance during a current pulse was measured with a stationary armature clamped between unalloyed copper rails. Those measurements concluded that for the MCA 1.01 design "each contact that the armature makes with the rail acts as a 7 microhm resistor." Using this measured value of interface resistance, the instantaneous power dissipation is approximated by the product of the current squared and this measured value of the resistance. The resistance is assumed to have a constant value.

The area under the  $I^2 R$  vs.  $t$  curve in Figure 2c is the interface energy dissipated. The calculated energy value for the unalloyed copper rail is 121 J. This energy dissipation data is used to set upper-bound estimates on the melted mass loss of aluminum at one armature/rail interface. The specific enthalpy contributions are first identified. The latent heat of fusion of aluminum is 397 J/g, and the specific heat is 0.9 J/g-K at 300 K [5]. If the energy dissipation at the interface is assumed to heat the aluminum alloy from 300 K to 850 K to initiate melting and then to melt it, an estimated total of 892 J/g is required to just

melt the aluminum alloy. For each degree the liquid is heated, an additional 1.18 J/g will be expended. A conservative 100 K of liquid heating is assumed providing an additional enthalpy contribution of 118 J/g. Summing these contributions it is calculated that the total energy expended to produce one gram of 950 K liquid aluminum is 1010 J. Using these data we estimate that during the first 200 microseconds of this launch cycle, 121 milligrams of liquid aluminum is produced on each rail. This calculation assumes that all the energy dissipated in the interface resistance is used to heat and melt the aluminum that is left on the rail. Measurements of corresponding deposit volumes, which have been made, are being corrected for porosity and the presence of the more dense alumina as a reaction product. These data will be incorporated into a thermophysical wear model for aluminum armatures.

#### *F. Evidence on the Recovered Rail*

A typical set of photomicrographs of the recovered rails is shown in Figure 3. These depict the deposit left during the first 5 mm of armature travel. In Figure 3a, a fairly uniform smearing of aluminum-rich debris onto the copper rail is evident. Figures 3b and 3c give comparable images of the aluminum transfer on the copper-chromium alloy rails and on the molybdenum rail.

The appearance of the copper rail surface in the vicinity of the transferred aluminum is different from the case of a copper wire armature [6]. In that case it was observed that at the start position a heat affected zone surrounded each of the contact locations. This zone was marked by a brown oxide forming about half a millimeter around each contact footprint. The indication is that the process of melting the aluminum alloy, which begins at about 850 K, leads to a limit in the temperature rise on the rail surface and a reduction in the extent of temperature-induced oxidation. A second reason proposed is the reduced delay time before initial armature motion of an aluminum armature compared to a copper armature. This reduced time is associated with the energy deposition time needed to melt the aluminum compared with that needed to melt copper. This early melting behavior provides the interface lubricant and reduces the frictional force that must be overcome by the ready-to-move armature.

The wetting and spreading interactions between the liquid aluminum and the rail were assessed using optical profilometry, stereomicroscopy, and digital image analysis. Measured wetting angles from the edge profiles of the resolidified aluminum at the  $X = 0$  location ranged from 1.1 degrees to 1.7 degrees for aluminum on ETP copper. Values of 1.6 to 4.5 degrees were measured for aluminum on copper-chromium alloy. For molybdenum, the values were 3.7 to 6.9 degrees. For optimum wetting, small wetting angles are desirable. Thin, poorly-adherent deposits have been observed to detach spontaneously.

Spreading of liquid aluminum prior to resolidification was assessed for the baseline ETP copper rail conductor. The deposits were found to spread out to a far greater extent on the unalloyed copper than the deposits on the other two rail conductors. It is suggested that this spreading is promoted by the relatively higher temperature of the spreading liquid aluminum front. Current flow in the unalloyed copper is more concentrated near the skin of the conductor during the initial phase of the pulse and has been shown to modify the surface through skin effect heating [7]. A further increase in the temperature at the edges of the spreading liquid metal is thought to be due to the exothermic reaction between liquid aluminum and the native surface copper oxide [3].

The deposits on the molybdenum rail conductor did not spread as readily as the deposits on the other rail conductors. A possible reason is that the molybdenum rail has a higher surface roughness compared to the other rail materials, as is evident in Figure 3. This allowed the molybdenum rail conductor to "trap" the liquid aluminum and affect its spreading behavior relative to the other rail conductors.

The values of these angles are normally interpreted in terms of surface energy interactions. It is apparent that the roles of surface oxides and surface topography are important for these warm rail substrates. Before the aluminum deposit resolidifies, the temperature distribution in the rail substrate also influences the thickness, area of spread, and the residual stress patterns that exist in the deposit layers.

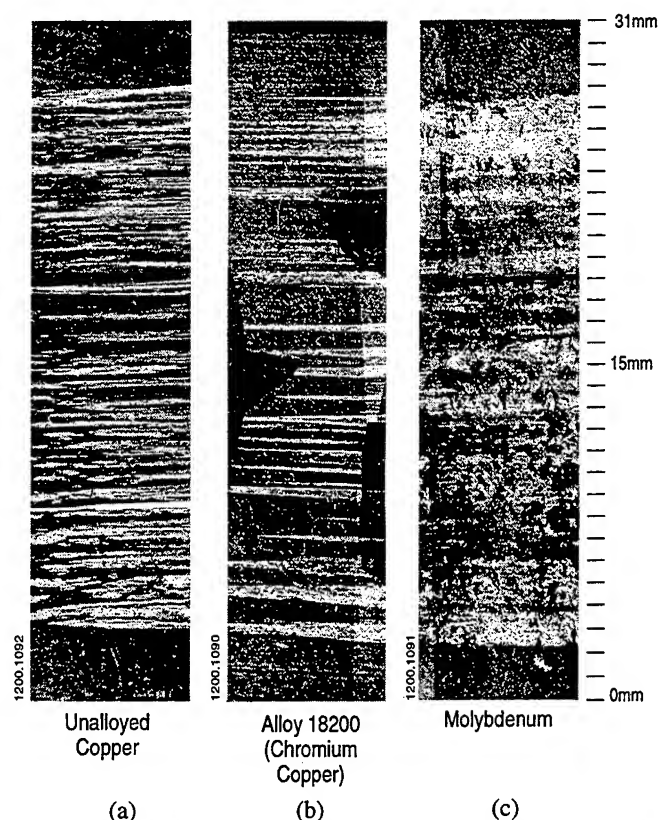


Fig. 3. Photograph of armature start-up region of each rail contact surface studied. Rail material from left to right: ETP copper, copper chromium alloy C18200, and molybdenum. Aluminum is transferred to the rail and appears as a resolidified deposit. The armature motion is left-to-right.

### G. Section 2: Armature as a Beam in Motion

A new interpretation of the observed interface phenomena at armature startup is proposed. The armature is treated as a loaded beam clamped between the rail supports. Shearing of the softening armature surface at the armature/rail interface is the mechanism that allows the armature to begin its motion. The residue left on the rail surface reflects the Menkes and Opat [8] Mode III behavior for an impulsively loaded beam. This description shall be referred to as the MO beam analysis.

The arrangement that we have studied is the case in which the rails in the physical model of a simple rectilinear railgun launcher support and guide the moving beam. The end-supported beam material is the hot aluminum armature. It experiences transverse shear failure adjacent to the rail surface supports. Figure 4 is a simplified physical representation of the armature located between two planar rail surfaces. AB and A'B' are the line contacts along which current is transferred and location at which shearing occurs. BC and B'C' are insulator/conductor interfaces free of current flow.

Preliminary conceptual analysis of the potential for applying this MO approach to armature/rail systems has been researched. The electromagnetic loading on an armature does not closely mirror the uniformly distributed impulsive velocity model that is used in standard beam analysis [9]. However, it is interesting for armature scaling discussions to note that Jones [9] found that the threshold velocity loading for the onset of Mode III shearing is constant for a given beam material, independent of rectangular beam length and thickness. Details of the start-up behavior observed in a 25-mm launcher are expected to be similar to those for larger launchers with equivalent current densities.

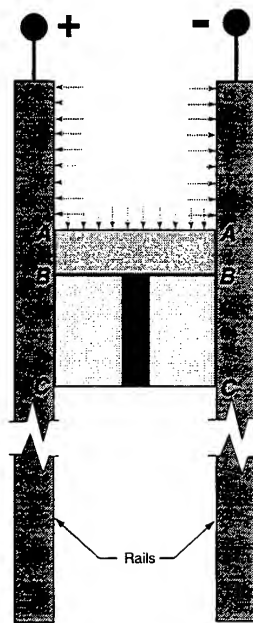


Fig. 4. Illustration of the Menkes and Opat Mode III behavior for an impulsively loaded beam.

In state-of-the-art EM launch analysis, numerical analysis tools do now allow for a complete description of the actual force distributions within the armature body at the start of armature motion. It becomes immediately apparent from simple analyses that nearly perfect symmetric loading of these short beams with enlarged ends is necessary for stable operation of the simple C-shaped armatures such as those employed in this research. Predictive trends for start-up behavior based on force distribution analysis of more complex armature designs are also possible using this approach. For example, this MO treatment of impulsively loaded beams has also been applied to the case where the beam is a sandwich structure in which the inner core has different shear properties [9].

In addition to the current-path dependence of the calculable element-by-element accelerating force vectors within the armature body, there is one additional contributor to the way in which end constraint of an armature beam evolves. As the beam body temperature rises due to Joulean heating, the temperature at the end rises even faster. This faster temperature rise can be assumed to be due to the larger interfacial resistance at the armature/rail interface. The net result is that the local shear strength of the beam material decreases rapidly due to temperature-induced softening. In the limit, there is a change of phase of the aluminum at the interface. The aluminum armature surface melts, the melt is ejected, and the beam begins to move.

The controlled failure of the armature contact face depends on many geometric, test, and material parameters. Drake and Rathmann [10] argue that the simple one-dimensional solutions underestimate the Joule heating near the bore surface. Precise knowledge of the rail temperature will be important in determining how long the armature remains at rest after the current pulse is initiated. In earlier work on molybdenum rails with Mo armatures, pulse-to-pulse variations of 50 microseconds elapsed time prior to motion were observed by Wright [11].

#### *H. Section 3: Development Potential of Molybdenum and Copper-Chromium*

Both molybdenum and copper-chromium alloy C18200 have been used as rail conductors in laboratory launchers. The performance of these conductors has been linked with barrel design in a recent patent by Dreizin [12]. Molybdenum has a high melting point, specific elastic modulus and thermal conductivity. It

has a low specific heat. Molybdenum and its alloys are produced either by vacuum-arc casting or by powder metallurgy (P/M) techniques [13]. The Mo rail stock used in this work was made by P/M techniques.

Molybdenum and copper-based alloys both have development potential as rail conductor materials. One arrangement that has been proposed is that where the copper alloy forms the substrate and the molybdenum alloy is the surface layer that contacts the armature [14].

### *I. Fractography of Molybdenum*

Typical scanning electron fractographs of the rail sections that failed are shown in Figure 5. The fracture mode appears to be principally intergranular. The embrittlement is attributed to oxide impurities originating in the surfaces of the powders used for the P/M processing. Similar fracture features have been observed in our earlier work on molybdenum alloy powders [15].

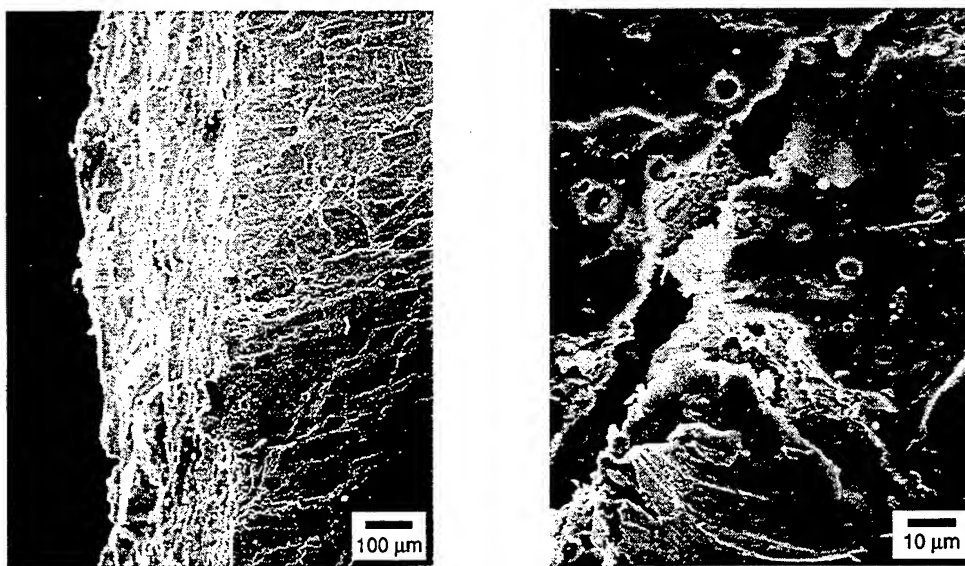


Fig. 5. Scanning electron micrographs of the fracture surfaces of molybdenum rail.

### *J. Improved Ductility Molybdenum*

Poor ductility and low toughness continue to limit the use of molybdenum alloys. When the material is worked by rolling, anisotropic texturing produces near zero ductility in the short transverse direction. Brittle behavior is frequently observed in welded and in recrystallized structures [16, 17]. In the powder-metallurgy molybdenum, the most common cause of intergranular embrittlement is the segregation of oxygen and nitrogen to grain boundaries. Indications are that small additions of carbon, titanium, boron and rhenium enhance grain boundary cohesion in these alloys. Molybdenum-base alloys include the carbide-strengthened, solid-solution, combination and dispersion-strengthened P/M alloys. These more advanced alloys are yet to be evaluated for rail conductor applications.

Control of tensile stress components during unloading after exposure to temperatures above 400 K appears to be important in avoiding fracture [18]. It may be necessary to apply an "autofrettage" type operation such as that described by Perl [19, 20] to the contact surface of the molybdenum to achieve the desired stress control. This 400 K temperature is associated with the lower threshold for dynamic recovery in molybdenum. Koval et al. [18] also looked at the effects of loading sequences. In the load/unload/repeat load sequences that they studied, fracture was observed to initiate as a set of microcracks on the free surface. Some of these cracks were blunted. In body-centered-cubic metals such as Mo, blunting is associated with dislocation mobility near the crack tip [21]. Dislocation densities and mobilities can be manipulated and enhanced using the dispersion-strengthening approaches described by Shields [13].

### *K. Development Potential of Copper-Chromium Alloys*

One of the most popularly used resistance welding electrode materials is copper-chromium (Cu-0.85wt%Cr). Such materials are required to have high thermal and electrical conductivity along with good mechanical properties. This is a fairly mature alloy technology. A brief review of pertinent copper-chromium alloy development work over the last twenty-five years is outlined here. From this work it is apparent that the controlled supersaturation of copper with chromium can lead to materials with a range of hardnesses and conductivities. Because this is a well-established alloy, the processing technology can be customized to meet the bulk properties for long-length (up to 10 m) rail conductors. Electrical conductivities in the range of 10% IACS to 80% IACS and tensile strengths of 300 MPa to 500 MPa are achievable.

Various hardness/electric conductivity combinations are obtained in supersaturated solutions of chromium in copper. Simmen [22] tabulated these values and showed that the highest hardness is obtained by metasaturation, that is, quenching from liquid state.

Kovacs et al. [23] made resistivity measurements at a temperature of 495 °C in Cu-Cr base alloys. They found that the deviation from Matthiessen's rule that relates resistivity to solute content is highly sensitive to nucleation and growth processes. Solute chromium atoms increase resistivity. As the chromium is precipitated and as the precipitates coarsen, the resistivity is observed to decrease.

Szablewski and Kuznicka [24] found that melt spinning allowed an increase in the chromium content in solid solution from the maximum equilibrium solubility of 0.8 atomic percent to more than three atomic percent. In this melt-spun state, the variation of resistivity as a function of the chromium content was observed to be a simple linear extension of the relationship obtained for Cu-Cr alloys after solid-state quenching. The measurements on aged ribbons indicate that their conductivity changes from about 10% IACS in the melt-spun condition to a maximum of 60% IACS in the overaged condition. The resistivity of melt-spun alloys is controlled by the spacing between chromium atoms in solid solution, whereas the resistivity of these alloys after aging is controlled by the spacing between precipitated chromium-rich particles, both of these spacings being much smaller than the mean freepath of electrons in copper.

Correia et al. [25] studied Cu-Cr alloy powders that were produced by water atomization, and were consolidated by warm extrusion, after canning and degassing. A banded structure was observed in the extruded material. A two-fold increase in the tensile properties, with respect to the conventionally processed Cu-Cr alloys, was obtained. This type of approach may lead to strength levels that are adequate for high performance launchers.

The tribological behavior of these alloys has also been studied. Saka et al. [26] investigated the effect of the second-phase particle structure on the wear properties of precipitation-hardened copper-chromium alloys. The hardness of these materials was found to increase initially with the aging time and then to decrease; the maximum value was reached after about 100 min. of aging at 500 °C. Metallographic examination of worn specimens indicated that the wear process proceeded by subsurface deformation, crack nucleation, and crack propagation, i.e., by delamination.

### IV. CONCLUSIONS

The start-up behavior of an armature is aided by the presence of a lubricant. It is found that an aluminum armature melts at the armature/rail interface and produces an auto-lubricating action. Tests and measurements on recovered rails made of three different conductor materials show that the surface topography and oxide chemistry play a role in the spread of the liquid metal lubricant.

A new interpretation of the observed interface phenomena is proposed. The armature is treated as a loaded beam clamped between the rail supports. Shearing of the softening armature surface at the armature/rail interface is the mechanism that allows the armature to begin its motion. The residue left on the rail surface reflects the Menkes and Opat Mode III behavior for an impulsively loaded beam.

It is concluded that none of the three materials tested is ideally suited for application as a monolithic rail conductor. Of the materials tested, the copper-chromium alloys have the greatest development potential. The unalloyed copper, though an excellent electrical and thermal conductor, is deficient in mechanical properties such as hardness. Molybdenum conductor stock processed by powder metallurgy, though hard, has insufficient fracture toughness.

From the review of previous research and the observed performance of these conductor materials, it is clear that the strength and conductivity requirements for these alloys are not a sufficient specification. The role of surface-originating cracking and the resistance to crack propagation are also important in predicting the multicycle behaviors. These topics are the subject of our ongoing rail materials performance research.

#### ACKNOWLEDGMENT

This work was supported by the U.S. Army Research Laboratory under contract DAAA21-93-C-0101.

#### REFERENCES

- [1] M. Matyac, F. Christopher, K. Jamison, C. Persad, and R. Marshall, "Railgun Performance Enhancement from Distribution of Energy Feeds," *IEEE Transactions on Magnetics*, Vol. 31, No. 1, p. 332, Jan 1995.
- [2] J. H. Price and H. D. Yun, "Design and Testing of Integrated Metal Armature Sabots for Launch of Armor Penetrating Projectiles from Electric Guns," *IEEE Transactions on Magnetics*, Vol. 31, No. 1, p. 219, Jan 1995.
- [3] C. Persad, A. Yeoh, G. Prabhu, G. White and Z. Eliezer, "On The Nature of the Armature/Rail Interface: Liquid Metal Effects," *IEEE Transactions on Magnetics*, Vol. 33, No. 1, pp. 140-145, Jan 1997.
- [4] K. A. Jamison, unpublished personal communication re: monolithic armature testing, October 15, 1993.
- [5] H. Y. Hunsicker et al., *Properties of Pure Aluminum, Metals Handbook*, Vol. 2, Materials Park, Ohio: ASM International Press, 1993, p. 1099.
- [6] C. Persad, R. Marshall, R. Allen, A. Barton, D. Wright and Z. Eliezer, "A Comparison of the Wear Behaviors of Six Elemental Wire Conductors," *IEEE Transactions on Magnetics*, Vol. 31, No. 1, p. 746, Jan 1995.
- [7] C. Persad and D. R. Peterson, "High Energy Rate Modification of Surface Layers of Conductors," *IEEE Transactions on Magnetics*, MAG-22, pp. 1658-1661, Nov 1986.
- [8] S. B. Menkes and H. J. Opat, "Broken Beams," *Exp. Mech.*, Vol. 13, p. 480, 1973.
- [9] N. Jones, "Plastic Failure of Ductile Beams Loaded Dynamically," *J. Eng. Ind.*, Vol. 98, pp. 131-136, 1976.
- [10] P. A. Drake and C. E. Rathmann, "Two-Dimensional Current Diffusion in an EML Rail with Constant Properties," *IEEE Transactions on Magnetics*, MAG-22, pp. 1448-1452, Nov 1986.
- [11] D. Wright, MS Thesis, The University of Texas at Austin, 1994.
- [12] Y. A. Dreizin, Electromagnetic Launcher with Advanced Rail and Barrel Design, United States Patent # 5,183,863, Jan 16, 1996.
- [13] J. A. Shields, "Molybdenum and its Alloys," *Advanced Materials & Processes*, Vol. 142, No. 4, p. 28, Oct 1992.
- [14] M. M. Holland, P. D. Eggers, S. Guinto, R. D. Stevenson, and G. Colombo, "Advanced Railgun Experimental Test Results and Implications for the Future," *IEEE Transactions on Magnetics*, Vol. 29, No. 1, p. 419, Jan 1993.
- [15] D. R. Ervin, D. L. Bourell, C. Persad, L. Rabenberg, "Structure and Properties of High Energy, High Rate Consolidated Molybdenum Alloy TZM," *Materials Science & Engineering A: Structural Materials: Properties, Microstructure and Processing*, Vol. A102, No. 1, p. 25, Jun 1988.
- [16] K. Tsuya and N. Aritomi, *J. Less-Common Metals*, Vol. 15, p. 245, 1968.
- [17] R. Kishore and A. Kumar, *J. of Nuclear Materials*, Vol. 101, p. 16, 1981.
- [18] A. Y. Koval, E. P. Pechkovskii, E. P. Polishchuk, "Effect of Relaxational Treatment on the Fracture of Molybdenum," *Strength of Materials*, Vol. 27, No. 7, p. 411, 1995.
- [19] M. Perl, "Basic Concept and Numerical Simulation (An Axisymmetric Stress Release Method for Measuring the Autofrettage Level in Thick-Walled Cylinders, Part 1)," *Journal of Pressure Vessel Technology*, Vol. 116, No. 4, p. 384, Nov 1994.
- [20] M. Perl, "Experimental Validation (An Axisymmetric Stress Release Method for Measuring the Autofrettage Level in Thick-Walled Cylinders, Part 2)," *Journal of Pressure Vessel Technology*, Vol. 116, No. 4, p. 389, Nov 1994.
- [21] R. Change, "Fracture in Metals," *Int. J. Fract. Mech.*, Vol. 6, pp. 111-116, 1970.
- [22] B. Simmen, "Effect of Different Degrees of Supersaturation of Copper Chromium (0.7% CR) Solid Solutions on Maximum Hardness and Conductivity Values Obtainable by Aging," *Neue Huette*, Vol. 14, No. 3, pp. 168-71, March 1969.
- [23] I. Kovacs, G. Szenes, E. Nagy, "Investigation of the Nucleation Process in Cu-Cr Base Alloys," *Phys. Status Solidi (A) Appl Res*, Vol. 15, No. 2, p. 573-577, Feb 1993.
- [24] J. Szablewski, B. Kuznicka, "Electrical Properties of Rapidly Solidified Cu-Cr Alloys," *Materials Science and Technology*, Vol. 7, No. 5, pp. 407-409, May 1991.
- [25] J. B. Correia et al., "Microstructure and Properties of Water Atomized and Extruded Cu-Cr Alloy Powders, Materials Science & Engineering A: Structural Materials: Properties, Microstructure and Processing," *Proceedings of the 7th International Conference on Rapidly Quenched Materials*, Aug 13-17 1990, Stockholm, Sweden, Vol. A133, Pt. 1, pp. 265-269, Mar 1991.
- [26] N. Saka, J. J. Pamies-Teixeira, N. P. Suh, "Wear of Two-Phase Metals," *Wear*, Vol. 44, No. 1, pp. 77-86, Aug 1977.



# ADVANCED LOW COST RAILS AND ARMATURES FOR RAIL LAUNCHERS

Richard A. Marshall

Institute for Advanced Technology, The University of Texas at Austin  
4030-2 W. Braker Lane, Austin, TX 78759

**Summary**—Experiments are being conducted in a small rectangular bore (25 mm rail-to-rail by 12-mm high, nominal length one meter) railgun using laminated rails and a new armature concept, the “pseudo-liquid” armature. Presented are some of the results obtained in these experiments. A second aspect of this work is the design of the railgun itself. It is arranged so that it can be used with simple breech current feed or with one turn of series augmentation. Because the gun has what amounts to an open top, some in-bore diagnostics are simplified, and rails can be replaced with a minimum of effort.

## I. INTRODUCTION

When investigating armature-to-rail contact performance at zero velocity in the “ZeeVee Tester” [1] it was necessary to use flexible rails to enable a known initial force to be applied to the armature-to-rail contacts. The flexibility was obtained by using rails made up of eight 0.8-mm thick copper laminations instead of the normal solid 6.4-mm thick solid copper rails. The arrangement of the apparatus is shown in Fig. 1.

In the course of conducting the experiments described in Reference [1], even with currents as high as 200 kA using armatures 25-mm high, it was observed that there was no sign of the passage of current through the interface between the rear face of the bore lamination and the front face of the adjacent lamination. This is a surprising result. Making the reasonable assumption that the current was well distributed between all eight rail laminations at some distance back from the armature, then most of the current (seven-eighths of it) must pass across this interface quite close to the armature.

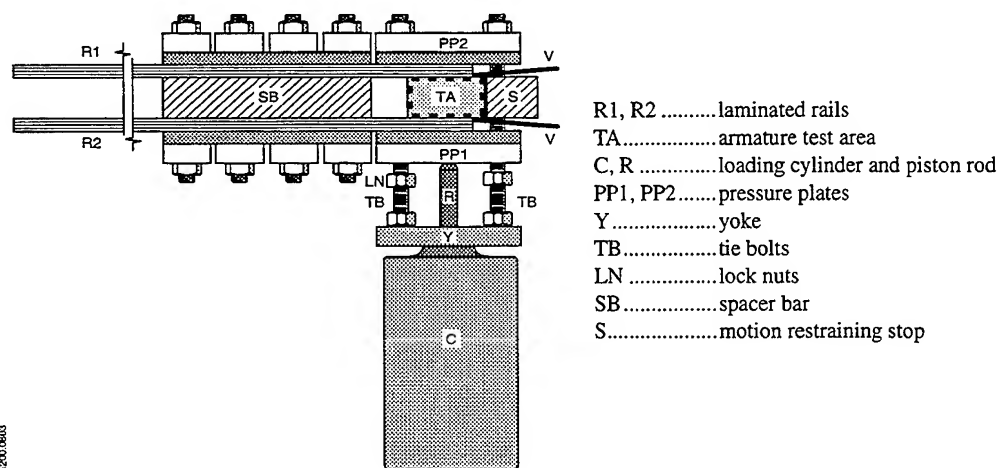


Fig. 1. The ZeeVee Tester. The laminations are simply clamped together. They are not soldered or welded together in any way.

It is logical to then say, if laminated rails perform so well at zero speed, then they should perform even better in a real railgun where the contact heating is spread along the length of the rails and not at a fixed location. It was decided that this matter was worthy of further study.

In order to be sure that it is rail structure and rail materials that are being tested, it is necessary to have armatures that behave in a repeatable manner. For these reasons, the work reported here is divided between armature design and behavior, and rail behavior. Of necessity the results obtained are for particular armature/rail combinations. The two cannot be separated easily.

#### A. The AUG-OAT railgun

The test bed used to test the behavior of laminated rails was the AUG-OAT (augmented Okaloosa armature tester, [2]) railgun shown in Fig. 2.

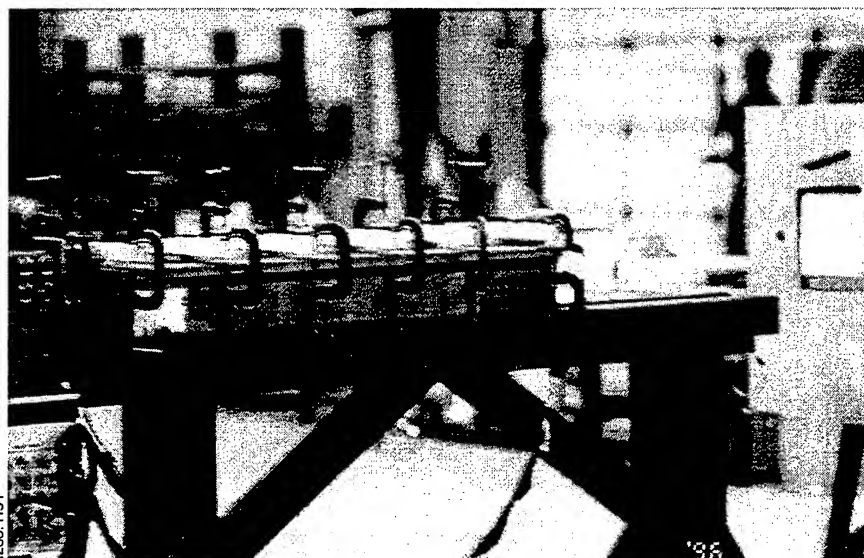


Fig. 2. The AUG-OAT railgun. The gun has a clamped-in-place "see-through" top to facilitate observation of the armature in-bore during a firing.

An incidental benefit of using the laminated rails is the ease with which they can be configured. The best way to make the muzzle cross-over is to bend the rails outwards and to clamp the cross-over conductor to them. The rails are easily bent making this process simple. Similarly, it was simple to bend a "crank" into one of the main rails at the breech to reduce the size of the cross-over "hoop." This minimizes the amount of the reaction force that the hoop must carry. The crank which is more robust than the cross-over hoop carries the bulk of the reaction force. Use of laminated rails has made this geometry simple to implement.

Test have also been conducted with the AUG-OAT railgun de-augmented. The reason for doing this was to get reliable muzzle voltage data. It is not simple to obtain such data from an augmented railgun because to do so, it is necessary to subtract two large voltages that are very nearly equal.

### *B. Laminated copper rails tested with monolithic armature*

The behavior of monolithic armatures made of 7075 aluminum on the laminated copper rails was different from their behavior on solid copper rails. For these tests, the AUG-OAT railgun had not been configured as described above and it was necessary to conduct the tests with one rail only being laminated. The other was the normal solid rail. While not the purpose of this arrangement, it did enable direct comparison between armature behavior on laminated and solid rails to be made. There were two significant differences in the behavior of the laminated rail.

First, when transition occurred from metal-on-metal sliding contact to hybrid contact, it occurred in a gradual and benign manner. There was little of the arc damage and rail "bronzing" normally seen at transition.

Second, gouging did not occur on the laminated rails in two of the three shots, even though severe gouging occurred on the solid rail. Velocity achieved was 1.9 km/s. The usually observed gouging threshold for aluminum on copper is 1.4 km/s. In the one shot where gouging did occur, the gouges were non-typical. There was one large gouge (at 1.1 km/s) followed by a scatter of very small gouges.

It is probable that the dramatic improvement in gouging behavior is a result of the difference in the bulk mechanical properties of the two rail constructions. In order for gouges to form, the rail material must be rigid enough in compression to allow the high pressure required for gouge initiation. The compression modulus of a laminated rail must be a lot less than for a rail made of one piece of metal. The "give" of a laminated rail surface would be expected to inhibit the start of a gouge.

There will also be some differences in electrical properties between the two rail constructions. This is likely to play a part in the benign transition observed. Electrical experimental results are discussed further below.

### *C. The desirability of using laminated rails*

The non-gouging behavior and benign transition obtained with laminated rails show how such a simple change in rail construction can dramatically change the armature-to-rail contact behavior. The simple laminating technique indicates that materials other than copper can be experimented with at low cost by simply mechanically holding rail layers together. They do not have to be welded together or be co-extruded. There are other rail face materials that look promising [3].

### *D. The "pseudo-liquid" armature*

Because the 7075 aluminum armatures did not behave in a repeatable enough manner, it was decided to experiment with an armature of quite a different type—the "pseudo-liquid" (PSL) armature. The logic is as follows.

In an ordinary powder gun, the propelling medium, the hot gas, has zero strength except in the compression direction. When asking the question, "What is the near analogue of this in a railgun?" one gets the following answer. First, the armature can hardly be thought of as a gas but it can be thought of as a liquid. The next step would be to use armatures made of liquid metal. These would provide a fairly uniform pressure over the base of the launch package in much the same way that gas pressure does in an ordinary gun. The problem with this is that because the liquid is Rayleigh-Taylor unstable, it would have to be confined in some manner to make it stable. This problem does not arise in an ordinary gun because gas under pressure extends from the base of the package to the gun breech. No instabilities are involved.

The next logical development of the idea is to use an assemblage of filaments [4, 5, 6] that can be thought of as behaving to some degree like a liquid—a “pseudo-liquid.” The filaments have strength in tension, in the rail-to-rail direction, and in their trailing arms along the rails, but would be small enough in diameter so that they would have low strength in bending. Because of the low bending strength, initial contact between armature and rail would have to be provided by some mechanical means. Later in the pulse the force can be provided electromechanically. Figure 3 shows the arrangement.

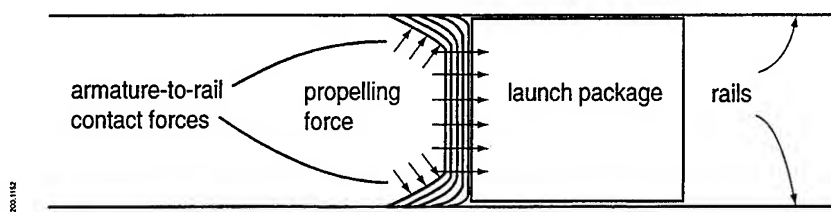


Fig. 3. The “pseudo-liquid” armature in principle.

#### E. Test at zero velocity

A two-layer version of this armature concept using “thick” wires has been tested successfully in the ZeeVee Tester. The armature used is shown in Fig. 4.

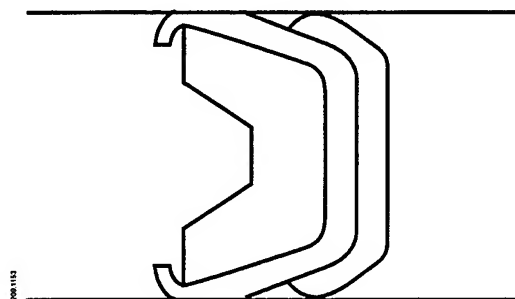


Fig. 4. The armature used in the ZeeVee Tester. It consisted of two layers each having five 1100 (pure) aluminum wires 2 mm square.

In this test the initial armature-to-rail contact was provided by the Lexan spring shown. Peak current was 191 kA. The armature actioned out at  $52,000,000 \text{ A}^2\text{-s}$ . Dividing this by the area, we get  $32,500 \text{ A}^2\text{-s/mm}^4$  for the specific action. This is right at the Tucker and Toth [7] value for action to the end of melt for aluminum. It's difficult to believe this result; however, remember that the Tucker and Toth work was done by exploding wires in very short times. Their process was adiabatic. We can get significant heat loss during a pulse. Our process is not adiabatic.

#### F. Tests with armature motion

The first PSL armature design is shown in Fig. 5. For ease of manufacture, the armatures were made using four layers of 1-mm thick 1100 aluminum. The change was made from use of the 2-mm square wires because use of the wire was awkward.

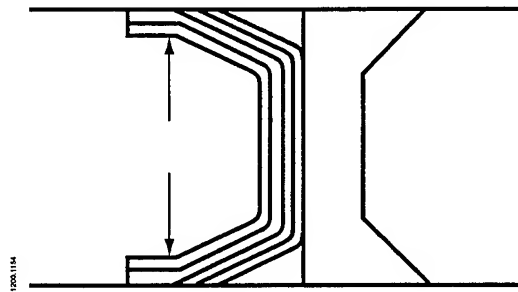


Fig. 5. The four-layer PSL armature. The shaped front piece is a low mass Lexan bore rider.

This armature was "started" by forcing its arms into contact with the rails as indicated by the arrows using a Lexan spring. The spring remained behind as the armature moved off down the gun, the necessary contact force then being provided electromagnetically.

As has been stated often, muzzle voltage gives a good indication of volt drop rail-to-rail across the armature. In an augmented gun this is no longer true because the muzzle voltage has induced voltages added to the rail-to-rail voltage. For this reason, a series of experiments was conducted in which the gun was de-augmented by replacing the augmenting rails with non-conducting spacers. The first shot was conducted using an armature as shown above in Fig. 5, and solid copper rails. It transitioned almost immediately because the reduced field without the augmentation was not high enough to give adequate EM contact force. To rectify this situation, an armature was made with longer arms as shown in Fig. 6.

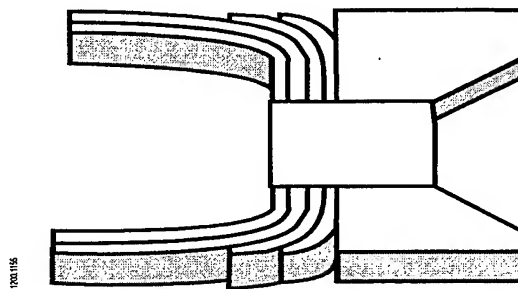


Fig. 6. The four-layer PSL armature with arm lengths increased.

This armature ran reasonably well but was still somewhat uncertain in its performance, so a further refinement was added. The "travelling spring" was added as shown in Fig. 7. This armature ran reasonably well in a reasonably repeatable manner, and it has been used for all the most recent experiments in the un-augmented AUG-OAT railgun.

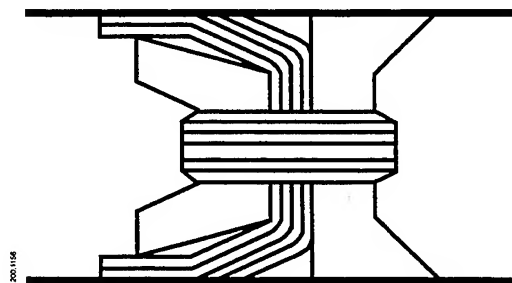


Fig. 7. The PSL armature with the "travelling contact-forcing spring" bound to it.

### G. Comparison of performance with solid and laminated rails

A final experiment done in this series was with the PSL armature run on solid and on laminated rails with the railgun not augmented so that muzzle voltages could be obtained and compared. As can be seen in Fig. 8, it was significantly different in the two cases, being 15% higher for the laminated rail experiment than for the solid rail experiment. The result shows that rail resistance at the armature contact area is higher for the laminated rail than for the solid rail as might be expected. The result shows that it took about one extra volt to drive the current into the armature from the laminated rail than for the solid rail.

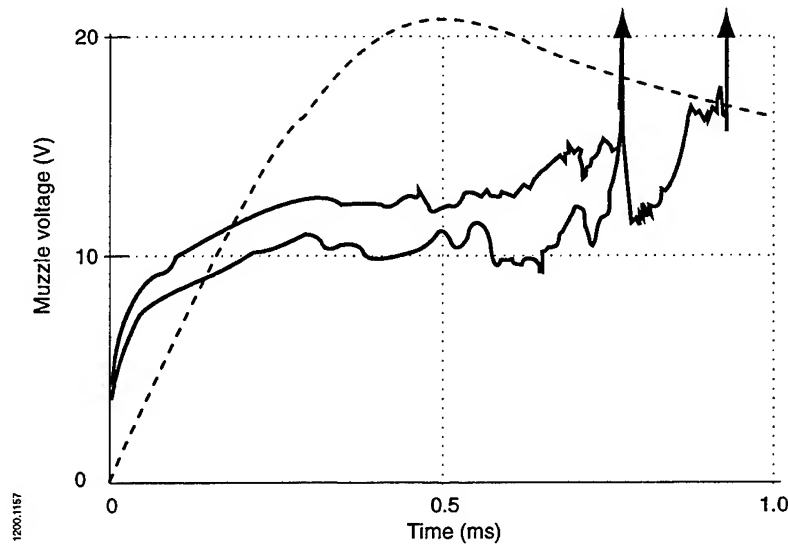


Fig. 8. Muzzle voltage vs. time for the PSL armature running on solid copper rails (lower curve) and laminated copper rails (upper curve). Current vs. time shown dashed, arbitrary scale. Peak current 208 kA for both cases.

Rail appearance after the shots showed that the armature-to-rail behavior was quite similar. Rail appearance also showed that the armature ran more smoothly on the laminated rail than on the solid and ran for longer before it transitioned. Transition points are shown by the up-arrows in the figure. For both, transition was momentary only. Both recovered to run smoothly again after 0.05 ms.

## II. DISCUSSION

We have shown that a small railgun of simple construction can be used easily for obtaining experimental results over a wide range of conditions. Rails made up of laminations are just as readily used as are solid rails. This leads the way to the use of laminated rails consisting of materials other than just copper.

An incidental result is that armature and rail behavior was a lot better when the gun was augmented. For the parameters used in these experiments, quite strenuous efforts failed to completely prevent transition when the gun was not augmented, while in the augmented gun, simpler armatures (having no "travelling spring") performed with no transition.

#### ACKNOWLEDGMENT

This work was supported by the U.S. Army Research Laboratory under contract DAAA21-93-C-0101.

#### REFERENCES

- [1] R. A. Marshall, "Current Carrying Capacity of Solid Armatures for Railguns at Zero Speed," *IEEE Trans. Mag.*, Vol. 33, No. 1, January 1997. In that paper, the apparatus is called the "armature rail contact tester" or ARCT. It is now renamed the "zero velocity tester" or ZeeVee Tester.
- [2] R. A. Marshall, C. Persad, K. A. Jamison, and M. J. Matyac, "Observation of Solid Armature Behavior," *IEEE Trans. Mag.*, Vol. 31, No. 1, pp. 214-218, January 1995.
- [3] F. Stefani and J. V. Parker, "Experiments to Measure Hypervelocity Gouging Threshold for Various Metals against Copper," 6th European Symposium on EM Launch Technology, The Netherlands, May 1997.
- [4] E. Thompson, "How the Carbon Brush Came into Use," *The Electrical Engineer*, Vol. 18, No. 335, October 1894.
- [5] D. P. Ross, G. L. Ferrentino, and F. J. Young, "Experimental Determination of the Contact Friction for an Electromagnetically Accelerated Armature," *Wear*, 78, pp. 189-200, 1982.
- [6] W. Karthaus, W. A. de Zeeuw, and W. J. Kolkert, "On the Design and Testing of Solid Armatures for Rail Accelerator Applications," *IEEE Trans. Magn.*, Vol. 27, p. 308, January 1991.
- [7] T. J. Tucker and R. P. Toth, "EBWI: A Computer Code for the Prediction of the Behavior of Electrical Circuits Containing Exploding Wire Elements," Sandia Laboratories Report No. SAND 75-0041, Sandia, New Mexico, April 1975.

## Effects of the initial conditions on the results of launch experiments with fibre armatures

W. Karthaus, M. Koops, T. Huijser

TNO PML-Pulse Physics Laboratory

Mailing address : P.O. Box 45, 2280 AA Rijswijk, the Netherlands

Visiting address : Schoemakerstraat 97, 2628 VK Delft, the Netherlands

Phone : + 31 15 2697011, Fax : + 31 15 2621268

### Summary

Launch experiments with multi-fibre armatures conducted under apparently the same conditions result quite often in different values of the transition velocity. It is assumed that poor electrical armature-rail contact results in early arcing. A better quantitative control of the initial mechanical condition seems therefore to be necessary. The armature-rail contact resistance in the initial phase of a launch process is mainly determined by the preload force. To be able to perform a series of experiments under the same initial conditions, a method for the determination of the preload force is necessary. Results of a 2D mechanical finite element model of the rail accelerator to simulate its static mechanical behaviour show the optimal location for measuring the stress condition in the armature region of the rail accelerator to control the armature preload force. A fibre-optic strain sensor has been developed to measure the mechanical stress condition. A priori knowledge of the stress-strain behaviour of the fibre armatures is required to determine the preload on the electrical contacts. A test set-up to determine the value of mechanical parameters of the fibre armatures was used. The 2D mechanical model of the rail accelerator is verified with experiments in the armature test bed (ATB). A simple optical method to determine the departure time of the armature during a launch experiment has been developed to establish the current at which the launch package starts moving. In this paper a summary is given of the development of a method for controlling the initial conditions of a launch experiment. A measurement set-up used to determine the value of mechanical parameters of the multi-fibre armatures, and a fibre optic displacement sensor to measure the preload on the armature for controlling purposes is described too.

### Introduction

Armature research at the Pulse Physics Laboratory is directed towards non-arcing electrical contacts for solid armatures at as high as possible velocities, followed by a controllable transition to hybrid armatures with either liquid or vapour or plasma boundary layers at the rail/armature interface. To this end a programme of launch experiments is executed. Much attention is paid to establish equal experimental conditions under which a certain armature concept is tested. It is tried to reproduce from one experiment to the other the armature oversize with respect to the rail to rail distance, launch package mass, mechanical preload of the rail accelerator and the current pulse shape. An overview of results of a series of launch experiments with a launch package of 36 gram provided with a multi-fibre copper armature (18 gram) is presented in table 1.

Table 1 Overview of results of a series of launch experiments with multi-fibre Cu armatures

| exp. nr | $v_{\text{trans.}}$ (m/s) | $v_{\text{muzzle}}$ (m/s) | $\eta_{\text{trans.}}$ (%) | $I_{\text{max.}}$ (kA) | $I_{\text{dep.}}$ (kA) |
|---------|---------------------------|---------------------------|----------------------------|------------------------|------------------------|
| E-510   | 945                       | 1230                      | 27.3                       | 316                    | 233                    |
| E-516   | 999                       | 1210                      | 27.4                       | 319                    | 169                    |
| E-512   | 841                       | 1250                      | 27.3                       | 317                    | 148                    |
| E-523   | 1176                      | 1254                      | 29.3                       | 306                    | 228                    |

where :  $v_{\text{trans.}}$  = velocity at which the muzzle voltage begins to increase rapidly

$v_{\text{muzzle}}$  = muzzle velocity

$\eta_{\text{trans.}}$  = launch efficiency at transition defined as the ratio of kinetic energy and the energy commutated into the rail accelerator

$I_{\text{max.}}$  = peak current

$I_{\text{dep.}}$  = current level at launch package departure



As can be seen from the table, there is quite a difference in transition velocity obtained in this series of experiments. One reason for the difference can be the different armature-rail contact resistance values in the initial phase of the launch process. The measurement of the preload force dependence of the rail-armature contact resistance, shows how critical the preload force on the armature is for the initial conditions of a launch experiment [5]. Improper contact force can lead to a relative large contact resistance, resulting in an increased heating of the armature-rail surface during the acceleration process.

The thought of improper contact force was enhanced by some results of static experiments performed with the armature test bed (ATB), a 50 cm version of the 2.37 m rail accelerator [1,2]. It demonstrates what can happen when an fibre armature is not properly compressed in the rail accelerator. For a series of experiments the armatures were provided with small Rogowski coils so that current in the rear- and leading half could be measured in order to see amongst others the influence of the armature material on current diffusion. The ATB was hooked-up to the 400 kJ capacitor [2]. As an example results of a copper and a molybdenum multi-fibre armature each 10 mm long are presented. The armatures were placed in the same G10 housing and carbon fibre confinement structure, as used in our launch experiments. The launch packages were blocked in the ATB so that no movement could occur. The data presented in figure 1a show the total current and the current in the rear- and leading half of a Cu multi-fibre armature as a function of time. The sum of the two currents equals the total rail current. As can be expected under the conditions mentioned, the current starts flowing initially mainly in the rear part of the armature followed shortly by current flowing in the leading part.

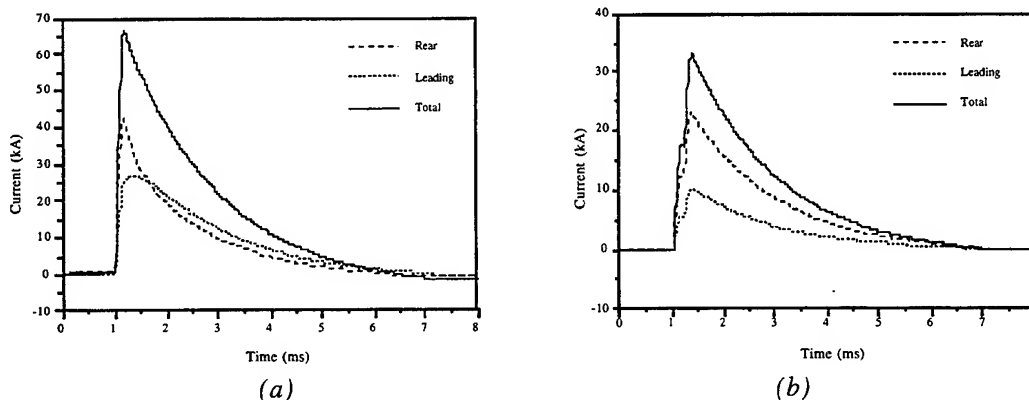


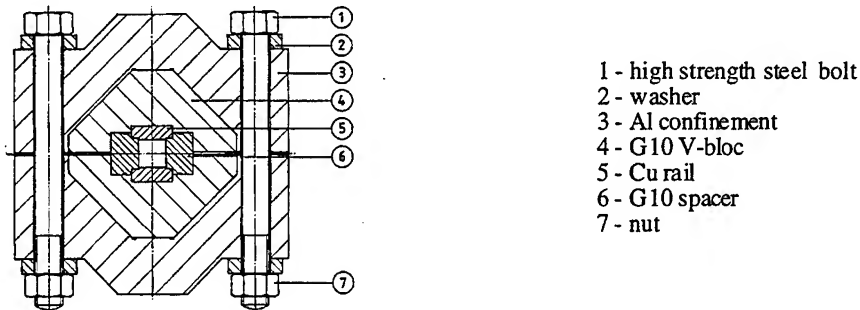
Figure 1 Total current and currents in the rear and leading part at stand still as a function of time in (a) Cu multi-fibre armature and (b) Mo multi-fibre armature.

The data of the current measurement in the rear- and leading half of a Mo multi-fibre armature is presented in figure 1b. The sum of the two currents equals the total rail current. The current profile is as expected. Because of the higher resistivity of the Mo and the relative short length of the armature the current profiles should be nearly equal in both parts. However, two congruent current pulse shapes are visible differing much in absolute values, which can be explained by the difference in contact resistance of the leading part of the armature caused by an improper mechanical preload.

The mechanical initial conditions in our launch experiments are controlled by the armature oversize and the preload exerted by the rail accelerator. A better control that means a quantitative control on the initial mechanical conditions for launch experiments seems necessary. As a result, it was decided to study the mechanical stress conditions of an armature prior to an experiment and develop a simple measuring method to better control the initial mechanical conditions for launch experiments. The easiest way is to measure the stress in the rail accelerator just above the armature. A fibre optic method was selected and the development of the method and the first results are presented.

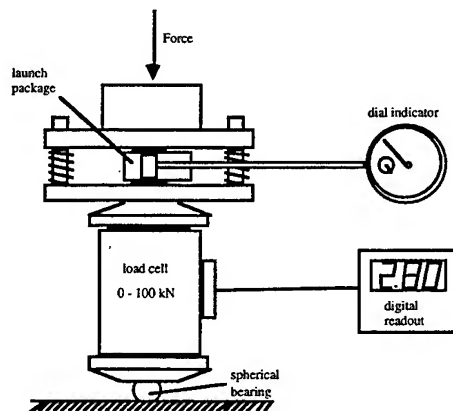
### ***COSMOS/M FE - Code simulation***

A 2D description of the rail accelerator has been made with the Finite Element Code COSMOS/M to simulate the static mechanical behaviour [3]. The Cross-sectional view of the 2.37m, 20 mm square-bore rail accelerator is presented in figure 2. The rail accelerator consists of two parallel Cu conductors and G-10 spacers embedded in a G-10 structure forming the inner parts. Two high strength Al blocks provided with a V-shaped slot serve as a confining structure. The parts are bolted together with high-strength steel bolts.



**Figure 2**      *Cross-sectional view of the 2.37 m rail accelerator.*

In order to simulate the mechanical response of multi-fibre armatures, the bulk mechanical parameters like the Young's modulus have to be known. Therefore, a set-up to measure the (static) stress-strain behaviour of multi-fibre armatures has been designed and made operational.



**Figure 3**      *Set-up for the stress-strain measurements.*

The test set-up, see figure 3, consists of a thick stainless steel bottom plate, a calibrated load-cell to measure the applied force, a fixture of two parallel steel plates which contains the object to be measured and a dial indicator to measure the displacement. The force is applied by means of a hydraulic press. The results of a series of compression/relaxation experiments with a Mo multi-fibre armature (length 20mm, height 15mm) and a Cu multi-fibre armature (length 10mm, height 15mm) are presented in the graphs of figure 4. The compression is displayed as function of the applied force.

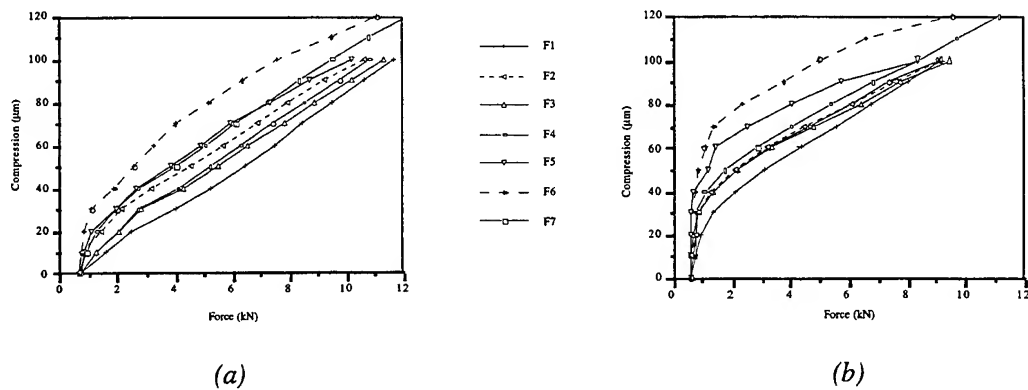


Figure 4 Results of a series of compression/relaxation experiments with (a) a Mo multi-fibre armature and (b) a Cu multi-fibre armature.

where : F<sub>1</sub> = compression of the armature in steps of 10 μm and time in-between measurement readings is about 10 seconds  
 F<sub>2</sub> = after decompression of the armature, the measurements were repeated as F<sub>1</sub>  
 F<sub>3</sub>/F<sub>4</sub> = as F<sub>1</sub>; after each increment the pressure is measured directly (F<sub>3</sub>) and measured after waiting for 3 minutes (F<sub>4</sub>).  
 F<sub>5</sub> = After 10 minutes compression at 100 μm, the armature is unloaded in steps of 10 μm. Time between measurement readings is 5 minutes.  
 F<sub>6</sub> = After 30 minutes compression at 120 μm, the armature is unloaded in steps of 10 μm. Time between measurement readings is 30 minutes.  
 F<sub>7</sub> = as F<sub>4</sub>

After a certain period of unloading, relaxation of the armature is noticed. The residual deformation of the Mo armature after the compression experiment is less compared to the Cu one. From these experiments a Young's modulus of 7.0 kN/mm has been deduced for the molybdenum fibre armature. This value is used in the FE simulations.

The results of the COSMOS/M simulation of a static situation where a Mo armature is clamped inside the rail accelerator is presented in the next figures. The load of the bolts on the aluminium confinement structure is deduced from a torque of 200 Nm and the armature has an oversize of 120 μm. For symmetry reasons only one quarter of the cross section is presented.

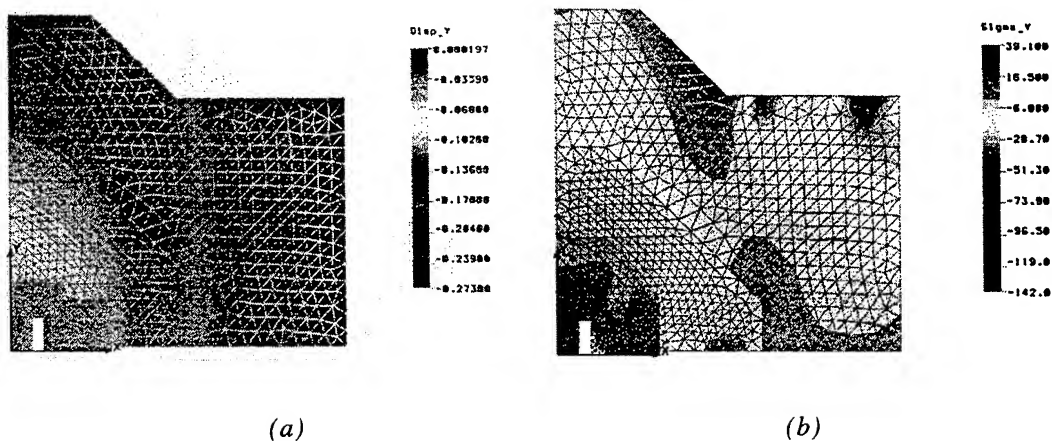
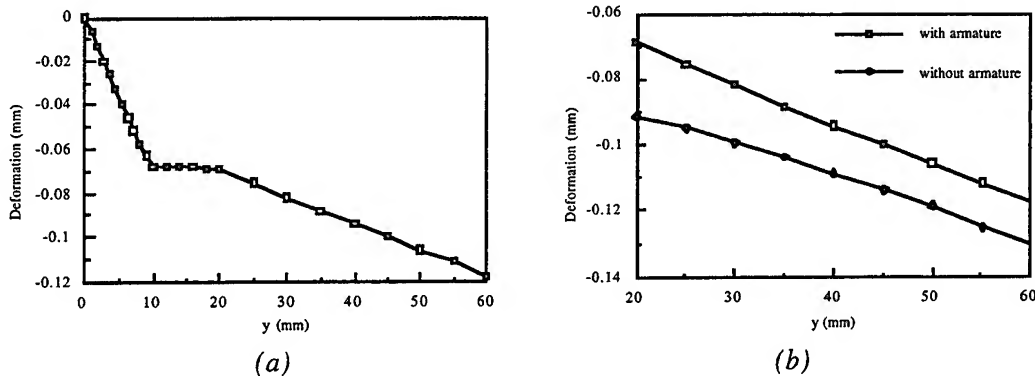


Figure 5 COSMOS/M static displacement distribution (a) and static stress distribution (b) in a cross-section of the rail accelerator and a Mo multi-fibre armature.

The calculated deformation along the axis of symmetry (y-axis, relative distance) of the rail accelerator with an Mo armature in place is presented in figure 6a. As can be seen the deformation of the armature and the G10 V-bloc is linear along the axis of symmetry. The deformation of the rail is very little.



**Figure 6** Calculated deformation of the rail accelerator along the axis of symmetry: (a) Mo multi-fibre armature (0 - 10mm), rail (10 - 20mm), G10 V-bloc (20 - 60mm), and (b) the G10 V-bloc with and without armature.

For comparison the calculated deformation along the axis of symmetry of the G-10 V-bloc with and without a molybdenum armature placed in the accelerator is shown in figure 6b.

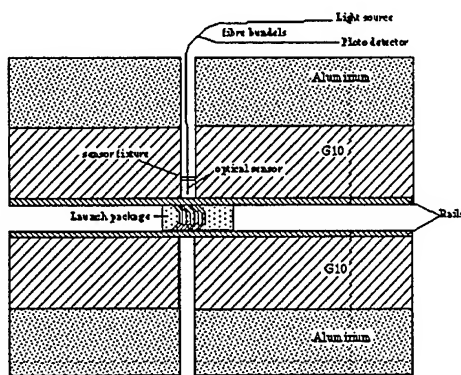
The results of the simulations with the 2D FE model support the idea of application of a simple mechanical model along the axis of symmetry. The G10 V-bloc, the insulators (spacers), and the armature can be represented as a linear spring and the rail is assumed to be absolute stiff. If such a simple model is applicable the initial mechanical status of the armature can be controlled by for instance the measurement of the compression of the G10 V-bloc above the armature prior to an experiment.

### Measuring method

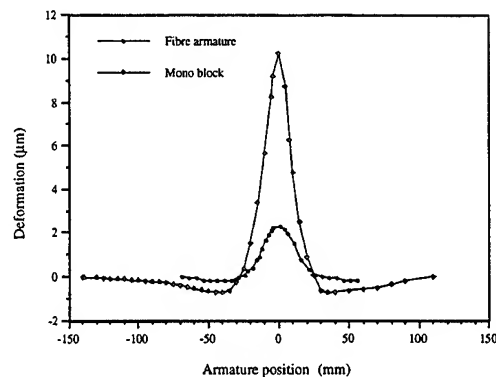
An optical displacement sensor is tested for application of the measurement of the deformation of the G10 V-bloc above the armature, see figure 7a. Such a sensor consists basically of two bundles of fibres fitted in one housing, one bundle emitting light and the other receiving light from a reflecting surface. The intensity of the reflected light is a measure of the distance between reflecting surface and the sensor. More about the measuring principle is described elsewhere [4]. The sensor is fixed in the G10 V-bloc 10 mm above the rail surface, so that the deformation of 10 mm G10 above the rail surface can be measured.

### Results of experiments

To test the measuring method with the optical displacement sensor and get an impression of the length in axial direction over which the armature has an influence on the stress distribution in the rail accelerator, experiments were performed with the ATB. An optical displacement sensor was fixed in the G10 V-bloc 10 mm above the rail surface. A launch package provided with a 10mm long Cu multi-fibre armature and a solid piece of copper (size and shape equal to the armature) were pushed over a certain distance through the ATB and the deformation of the G10 V-bloc was measured. The bolts of the ATB have been torqued to 200 Nm. The graph in figure 7b presents the results of measurements of the compression of 10 mm G10 above the rail as function of the armature position relative to the optical displacement sensor. The Cu mono-bloc used in this experiment had an oversize of 70µm relative to the rail distance that was measured before insertion and the Cu multi-fibre armature had an oversize of 60µm. As can be seen the influence of the presence of the armature on the static stress distribution extends to several armature lengths.



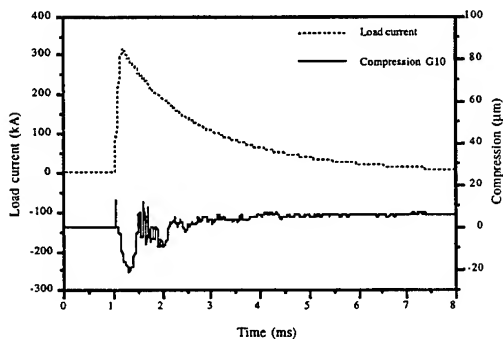
(a)



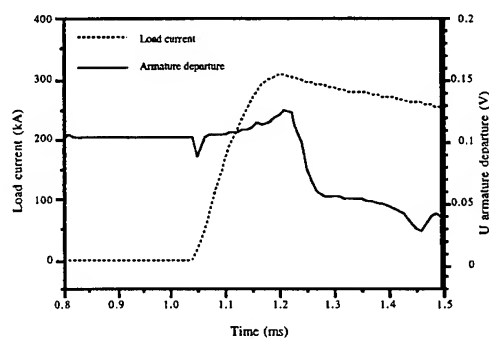
(b)

Figure 7 Measurement set-up with a fibre optic displacement sensor in the armature test bed (a) and measured deformation of the G10 V-bloc as function of the armature position relative to the optical sensor (b).

To get an impression of the change of deformation of the G10 V-bloc under electrodynamic circumstances and the current level at which the armature starts to move, dynamic experiments - that means armatures are loaded with a current pulse - have been performed with the ATB, too. The ATB was hooked-up to the 400 kJ capacitor bank for these experiments. Launch packages were inserted in the ATB under the displacement sensor in the G-10 V-bloc and insulating stopping blocs were placed at a short distance in front, allowing motion only over about 3 cm. Results of a 300 kA peak current experiment with a launch package provided with a Mo multi-fibre armature are presented in the following figures. Figure 8a presents the total current pulse and the deformation of 10mm G10 V-bloc above the rail surface as function of time. As a result of the electrodynamic force, deformation of G10 takes place, followed by a distinct decrease in deformation.



(a)



(b)

Figure 8 (a) Armature current and deformation of the G10 V-bloc as a function of time and (b) armature current and reflected light signal (armature departure) as function of time.

Another indication for the mechanical stress conditions in the initial phase of the launch process is the current level at which the launch package starts to move. To measure the onset of motion of the armature another optical method has been tried out. The launch package was provided with a small strip (2 mm) Al reflecting tape at the side. An optical displacement sensor as described above was placed in the G-10 rail spacer adjacent to the reflecting strip. By movement of the launch package in other words moving of the reflecting strip, its surface changes in reflectivity, resulting in a change in the output signal of the sensor. Figure 8b shows the armature current and reflected light signal from the

“departure” sensor as a function of time of the same experiment. Launch package motion starts at the steep decrease of the reflected light signal. The time between maximum and minimum value of the light signal yields an average launch package velocity of about 30 m/s.

The point in time where the light signal in figure 8b shows a clear change coincides very well with the moment (just after peak current) in figure 8a at which deformation of the G10 starts decreasing, indicating the launch package departure. The difference between the values of the deformation signal prior to the current pulse and at the end of the current pulse is an indication of the difference in compression of the G10 “with” and “without” armature in the ATB as the armature moved about three centimetres. The measured difference is a relaxation of about 5  $\mu\text{m}$ . From figure 6b a relaxation of about 2.5  $\mu\text{m}$  can be estimated from the simulations at  $y=20\text{mm}$  and  $y=30\text{mm}$ .

The optical displacement sensor appeared to be an useful instrument to measure the compression of the G-10 above the armature for controlling the preload of the armature by adjustment of the bolt torque. Stress-strain measurements of the multi-fibre armature show a linear force-strain dependency. However, relaxation effects occur inside the armatures which makes interpretation of the absolute values difficult. The control of the preload force will therefore be on a comparative basis for a series of launch experiments. The sensor will be further developed and dedicated for application in the 2.37m rail accelerator in the near future.

The armature “departure” sensor gave good results in the ATB experiments. An improved version is in use now with the launch experiments. Instead of one Al strip, a “bar code” of four 3mm wide Al strips, 3mm apart is fixed on the side of the launch packages. An example of a data recording during a launch experiment is presented in figure 9.

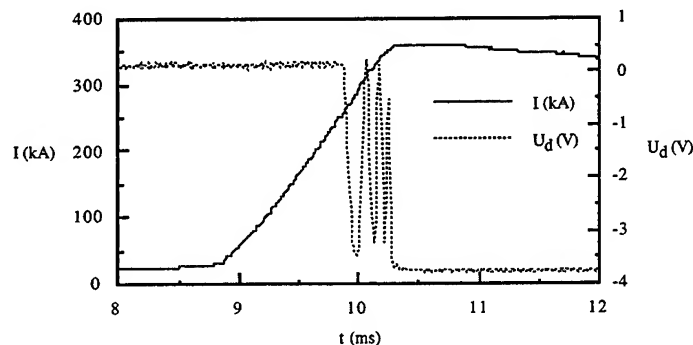


Figure 9 Armature current  $I$  and reflected light signal  $U_d$  (armature departure) as a function of time registered during a Cu multi-fibre armature launch experiment with the Hyper Velocity Launch-set up.

The current at which the launch package starts moving can easily be deduced from the data. Furthermore a good impression of the initial movement of the launch package can be obtained. A velocity increase of  $14 \pm 1$  m/s per 3mm armature travel is measured for this experiment.

#### Concluding remarks

- The initial mechanical conditions of rail accelerator-armature combination for a launch experiment influence the results of launch experiments. Although a direct relation between the transition velocity, and the current at which the launch package starts moving (an indication for the mechanical prestress) has not been found, a quantitative control of the initial mechanical conditions is necessary. So far, the initial mechanical conditions are controlled by the armature oversize and the preload exerted by the rail accelerator by means of a controlled torque of the bolts.

- 2D mechanical finite element simulations of the static situation show the possibility of a simple method to control the initial condition by measuring the deformation of the rail accelerator material above the armature.
- A fibre optic displacement sensor has been developed as an instrument to measure the compression of a rail accelerator component for controlling purposes of the mechanical preload of the armature. For measuring the absolute stress values, more study is necessary.
- Stress-strain measurements of the multi-fibre armature show a linear force-strain dependency. However, relaxation effects occur which makes interpretation of the absolute values difficult.
- A simple method has been developed to determine the "departure" time e.g. the current at which the launch package starts moving.

#### *References*

- [1] M. Koops, "Design of an armature test bed", presented at the 11<sup>th</sup> Meeting of the Electric Launcher Association, 13 - 16 September 1994, Minneapolis, USA
- [2] M. Koops, W. Karthaus, "Test bed for the evaluation of solid armature concepts", Proc. 5<sup>th</sup> Eur. Symp. on EML technology, April 10 - 13 1995, Toulouse, France
- [3] J. van de Kerkhof, "Mechanische spanningsanalyse van het armature testbed", stageverslag Technische Hogeschool Eindhoven, 23 Januari 1995 (in Dutch)
- [4] T. Huijser, M. Koops, "Optical sensor for measuring rail displacement in a rail accelerator during electromagnetic launch", Proc. 5<sup>th</sup> Eur. Symp. on EML technology, April 10 - 13 1995, Toulouse, France
- [5] M. Koops, T. Huijser, W. Karthaus, "Design and evaluation of carbon fibre-reinforced launch packages with segmented, copper and molybdenum fibre armatures", Proc. 8<sup>th</sup> EML Symp., April 21-24 1996, Baltimore, USA

#### *Acknowledgement*

The contributions of J. Starrenburg, T. van Leeuwen and J. van de Kerkhof to this work are gratefully acknowledged.

## Electrothermal Acceleration of Microparticles.

E.Ya. Shcolnikov, I.L. Kolensky, S.P. Maslennikov, A.V. Melnik, N.N. Nechaev, A.V. Chebotarev, S.M. Bakhrakh\*, S.P. Egorshin\*, A.N. Tarasova\*, S.A. Shaverdov\*.

Moscow State Engineering Physics Institute (technical university), 115409, Moscow, Kashirskoye Shosse 31.

\* Russian Federation Nuclear Centre - All Russian Scientific Research Institute of Experimental Physics, 607200, Sarov, Nizhny Novgorod region.

### Abstracts.

Analysis carried out on the basis of the developed theoretical model has shown that the conventional acceleration method, realized in the electrothermal launcher by the plasma flow quasi-stationary region, couldn't be applied for microparticles with dimensions from tens ns to some  $\mu$ s due to their uncontrolled heating up to the evaporation temperature. For this reason it is suggested to use the flow region that follows the head shock-wave and permits to realize the acceleration with high efficiency. Techniques of forming such regions are considered and microparticle dynamics is analysed in the space between the launcher barrel and the substrate. The regions of microparticles acceleration and deceleration are found. For the experimental research a test installation was developed. It includes some specific units such as the discharge gap with the discharge triggering block as well as the microparticles injector (the dosage unit).

### I. Introduction.

At present certain efforts are undertaken to obtain high quality wear and heat-proof coatings made of fine-grained powder materials including crystal corundum powder which consists of nanometers dimension particles. With that purpose it is necessary to put into effect acceleration of microparticles with such dimensions. Moreover, strict monitoring of the acceleration temperature regime as well as the composition and pressure of surrounding media is required. The microparticle velocity should be very high (more than 1 km/s) in the process of their interaction with substrates. Conventional technologies of obtaining powder coatings such as gas-burning, detonation and plasmatron ones are not able to meet such requirements. As it was shown in [1] the use of electrothermal launchers for microparticle acceleration has some substantial virtues among which there are obtaining much more higher particle velocities, possibility of the temperature regime adjustment and acceleration regime variation. In this connection the electrothermal method of acceleration is appeared to be promising for obtaining coatings out of fine-grained powder materials.

At the same time the specific character of the problem connected with very small dimensions of microparticles leads to the necessity of reconsidering the method of acceleration in the quasi-stationary flow part, that was analysed in [1]. Also it necessitates to study the flow and microparticles dynamics in the space between the barrel and substrates to be coated.

### II. Theoretical model.

In contrast to macroparticles acceleration, when projectiles block the electrothermal launcher barrel, acceleration of microparticles occurs in the high velocity plasma flow, that is formed as a result of pulse discharge and freely propagates



along the launcher barrel. In that case some effects influencing the plasma flow pulse become apparent. Among them one can select the turbulent friction as well as intense pulse exchange between plasma flow and microparticles. The latter prevents analysis of their dynamics independently from each other.

The developed theoretical model that takes into account these effects describes the flows dynamics and microparticles acceleration in three regions: a) in pulse discharge region, where the high velocity flow is being formed; b) inside the barrel, where microparticles acceleration and heating are realised; c) in the open space between the barrel and the substrate. The model description for the first and second regions is presented in [1]. It includes one-dimensional nonstationary equations of hydrodynamics that account for the dielectric ablation inside the discharge gap, the flow turbulent friction against the channel walls, the plasma radiation, the flow retardation by microparticles and the resistive heating of plasma by the discharge current. They are supplemented with the equation describing heat exchange between the flow and microparticles, the particle movement equation and Kirchhoff equations for the discharge circuit, consisting of the capacitive store element, discharge gap and the circuit stray resistance and inductance.

For description of microparticles dynamics in the space between the barrel and the substrate where it is necessary to take into account the flow distribution in space the corresponding nonstationary two-dimensional hydrodynamics equations are used.

In all cases values of the plasma inner energy, its electric and thermal conductivity and viscosity are taken from special tables [2], formed out of thermodynamics parameters and transfer coefficients for real gases. Numerical algorithms are composed on the basis of completely conservative patterns for the solution of hydrodynamics equations by means of adaptive movable calculation meshes.

### III. Microparticle acceleration technique.

As soon as the high current discharge is initiated the head shock wave is being generated inside the launcher channel. Its propagation results in flowing of the gas located in the barrel. Immediately after this flowing the plasma flow follows which can be called as the flow quasi-stationary part. It is formed by the gas heated by pulse discharge and streaming out of the discharge gap. The products of dielectric ablation in the discharge gap also can join the plasma flow.

Typical values of the plasma flow temperature are tens of thousands degrees that makes practically impossible to accelerate microparticles of micrometer and sub-micrometer dimension range due to their quick evaporations. That is illustrated by Fig.1, where velocities of corundum microparticles with 1 micrometer diameter are plotted against the plasma flow temperature. The plasma flow density is  $1 \text{ kg/m}^3$  and it is propagating along the barrel with velocity  $2 \text{ km/s}$ . Note that for typical flow temperature values corundum microparticles having been heated up to melting temperature acquire velocity not exceeding 10 % of the flow velocity, the characteristic acceleration length value being equal several millimetres whereas the acceleration time equals several microseconds.

Data of Fig.1 correspond to the case without ablation. The situation is getting worse if there is an ablating dielectric in the discharge gap. It can be explained by increased plasma density due to its enrichment by ablation products that results in the radiation losses decrease and hence in the flow temperature growth.

So, acceleration of micrometer and submicrometer range particles captured by the flow quasistationary region is accompanied by uncontrolled heating of the particles till their evaporation. The process takes place during very short period so that microparticles are not able to gain appreciable velocities.

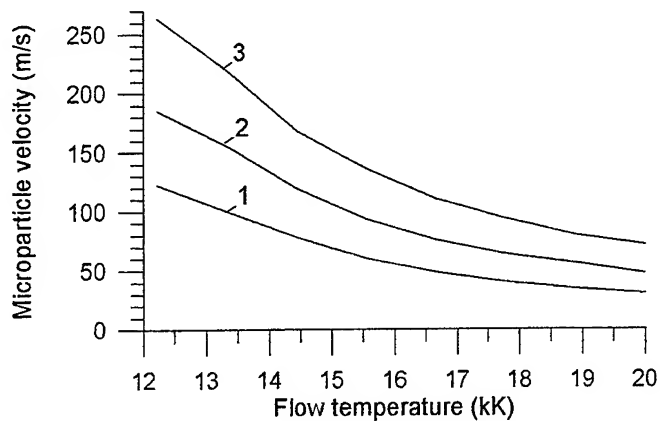


Fig. 1 Microparticle velocity versus flow temperature. 1. beginning of microparticles melting; 2. end of melting; 3. beginning of evaporation.

At the same time the space distribution of the flow density and temperature inside the barrel has rather specific character that is shown in Fig.2. It can be seen that in the head part of the flow there is a small length region that is characterised by increased value of density and lower temperature as compared to the flow main part. That region is formed by the head shock-wave and is expanded with time as a result of supplementation of gas existing in the barrel. The most typical values of the flow density and temperature in this region (so called "cork") are correspondingly  $5 \div 7 \text{ kg/m}^3$  and  $2 \div 5 \text{ kK}$  in case with no ablation. Otherwise (with ablation of the dielectric) the density value can be increased  $2 \div 3$  times whereas the temperature changes only slightly.

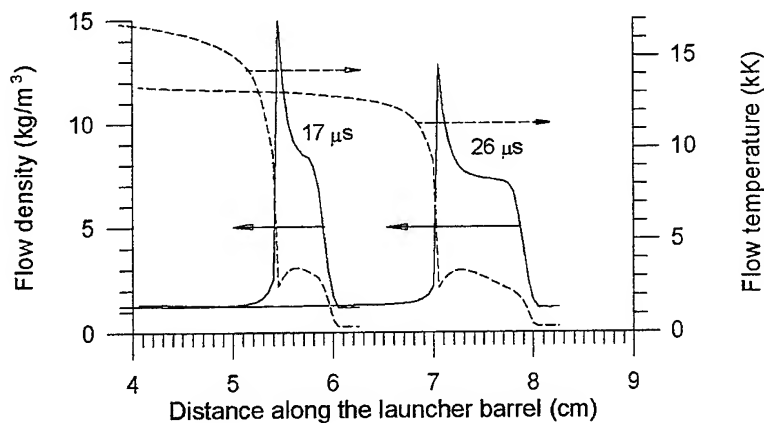


Fig. 2 Density (solid curves) and temperature (dotted curves) distributions along the launcher barrel at the time moments  $17 \mu\text{s}$  and  $26 \mu\text{s}$ .

Microparticles acceleration efficiency in this part of the flow could be significantly higher than in its quasistationary part. It is connected with the fact that the temperature of gas compressed by the shock-wave is substantially lower than that of plasma generated in the discharge gap. Moreover its value is close to the required temperature of accelerating particles and can be adjusted by means of changing the head shock-wave intensity (i.e. by changing the energy deposition power into the discharge). The increased gas density in the "cork" that follows the shock-wave front contributes to microparticles effective acceleration as well as to diminishing of their path in gas media (slipping in the flow).

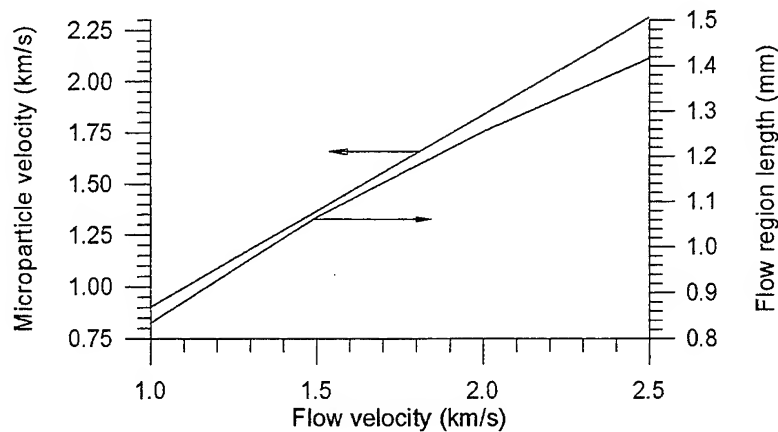


Fig. 3 Microparticle velocity and flow increased density region length as functions of flow velocity.

This is also valid if the acceleration regime is chosen so that microparticles don't leave the increased density region during all time of acceleration that is if the movement of microparticles is synchronised with that of the "cork". The conditions for the capture of corundum microparticles with diameter 1 micrometer by the "cork" are illustrated in Fig.3, the flow density and temperature being equal to  $7 \text{ kg/m}^3$  and  $3 \text{ kK}$  correspondingly. Here the length of microparticle slipping with respect to the flow (i.e. "cork" length required for microarticles acceleration) is plotted against the flow velocity at the moment of particles complete melting. In addition, values of microparticles velocities which they gain in the process of acceleration at indicated conditions are presented in that figure. In contrast to microparticles acceleration by the quasistationary region of the flow in this case particles have enough time to reach velocities equal more than 90 % of the flow velocity. In the process microparticles are "slipping" with respect to the flow by about several millimetres. At the same conditions if the diameter of microparticles increases their velocity is practically not changed whereas the "cork" length linearly increases and reaches 1 cm for microparticles with diameter  $5 \mu\text{m}$ .

#### IV. Forming of the flow increased density region.

The problem of forming the gas layer ("cork") compressed by the shock-wave in the electrothermal launcher channel includes several aspects. In the first place, for succesful acceleration of microparticles this gas region should be formed so that its linear dimensions exeeded the maximal value of microparticle free path length in that region. The linear dimensions are determined by the distance that the shock-wave would pass along the channel as well as by the degree of gas compression in the region under consideration. Secondly, by the moment, when the "cork" of required dimensions is formed, its velocity and gas temperature should satisfy optimal conditions for particles acceleration, which in turn are determined by technological requirements to the coating process. For obtaining coatings with high adhesion coefficients the microparticle velocity should be as high as possible. The coating microstructure greatly depends on the accelerated microparticles temperature.

Such requirements could be partially met by means of time shaping of the head shock-wave intensity that is directly connected with proper choice of the pulse power supply parameters, configuration of the discharge gap and the launcher barrel geometry as well as the position of microparticles injection.

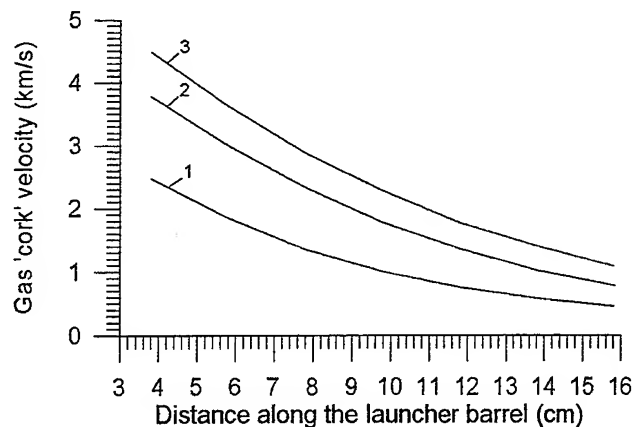


Fig. 4 Gas 'cork' velocity versus distance along the launcher barrel at various energy deposition: 1. 200 J; 2. 1000 J; 3. 2000 J.

The velocity variation of the flow increased density region with distance along the barrel is shown in Fig.4. Here we have the discharge gap length 2 cm, its diameter and that of the barrel 6 mm. The energy from the store have been deposited into the discharge steadily over 10 s period. It is clear from Fig.4 that if the energy deposition into the discharge is augmented from 200 J up to 2 kJ the "cork" velocity at the discharge gap output increases from 2.5 km/s up to 5 km/s. At the same time the substantial drop of the "cork" velocity in the process of its propagation along the barrel is observed, the drop being larger with increased level of energy deposition. This effect appears to be connected with the dissipation of the flow pulse due to the turbulent friction that increases proportionally to the gas velocity squared and, in addition, with autonomous movement of the head shock wave due to the quick speedy pressure drop in the discharge region. In case under consideration the increase of the energy deposition by one order results in the flow velocity growth only by two times. It indicates to the necessity of time shapping of the energy deposition into the discharge. Such procedure permits to minimize the retarding influence of the turbulent friction on the flow velocity as well as to provide the shock-wave propagation with small attenuation and to decrease the net energy deposition into the system. The latter is especially important under the condition of launcher repetitive regime.

#### V. Microparticle and flow dynamics beyond the barrel.

Analysis of microparticle and flow dynamics in the space between the barrel butt and the substrate was carried out with the following assumptions. At the moment  $t = 0$  the steady state gas flow is generated at the barrel butt-end. The flow with density  $5 \text{ kg/m}^3$ , temperature 3000 K and velocity 2 km/s is streaming into the mentioned above space, where there is room temperature and atmospheric pressure. At some distance from the barrel the cylindrical substrate with diameter 10 mm is placed coaxially with the barrel. Microparticles are injected into the barrel-substrate space together with the flow, their velocity being equal to that of the flow. The moment of particles injection with respect to that of the flow is considered to be variable. Such assumptions permit to model the real process, where particles caught into acceleration regime inside the barrel by the gas "cork" are streaming out of the barrel together with the gas flow.

Some results of the modelling are presented in Fig.5. Here the media density distribution along the symmetry axis is shown at various time moments. The substrate is placed at distance 3 cm from the barrel butt. Microparticles of

corundum powder with diameter  $3\text{ }\mu\text{m}$  are injected  $15\text{ }\mu\text{s}$  after the flow starts streaming out of the barrel. Positions of a microparticle are marked on the abscissa, where its velocity and corresponding moment are given.

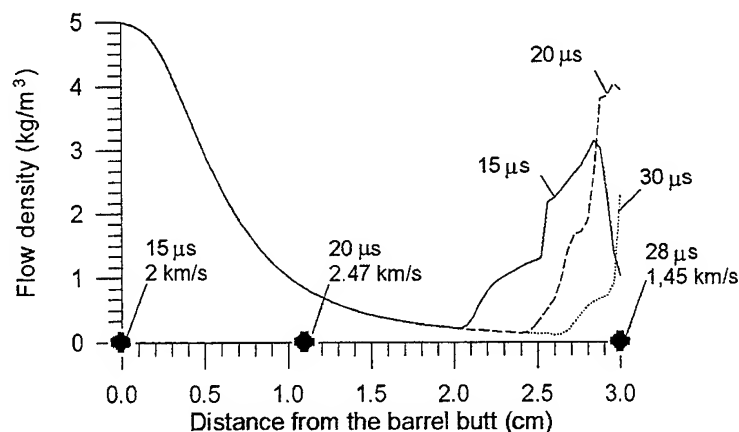


Fig. 5 Flow density distribution along the central axis in the space beyond the barrel butt.

As soon as the flow streams into the space beyond the barrel it starts to expand and, as seen from Fig.5, the media density in the space between the barrel butt and the shock-wave front drops drastically. In less than  $15\text{ }\mu\text{s}$  after streaming out starts the shock wave reaches the substrate and the air layer with increased density begins to be formed in the vicinity of the substrate. But with time this layer thickness and density diminish and toward  $35\text{ }\mu\text{s}$  the air density in the layer gets equal to the atmospheric one. The flow streaming out of the barrel is accomplished by its acceleration. So, along the system axis the flow velocity is increased from  $2\text{ km/s}$  up to  $3.2\text{ km/s}$  in  $10\text{ }\mu\text{s}$  after leaving the barrel, when the flow front advanced by  $1.5\text{ cm}$ . Further on however the velocity begins to decrease.

Microparticles captured by the flow initially get acceleration, their velocity increases from  $2\text{ km/s}$  up to  $2.5\text{ km/s}$  but afterwards their intense deceleration begins. It can be explained by some factors. One of them is the existence of backward flows reflected from the substrate. Microparticles get additional deceleration in the gas layer at the substrate surface. In the case under consideration the velocity of microparticles drops till  $1.45\text{ km/s}$ .

Thus the choice of the distance from the barrel butt to the substrate determines substantially the microparticle velocity at the substrate and hence the coating quality. It should be also noted that this choice has to be made with accounting for not only microparticle acceleration dynamics inside the barrel and beyond it but also for heating of the substrate by the incident flow.

## VI. Experimental installation.

For the purpose of experimental studies an experimental installation was developed on the basis of the electrothermal launcher. It consists of a capacitive store block, a discharge gap, a discharge triggering unit, a barrel and a microparticles injector.

For the launcher efficiency improving, i.e. for the flow velocity increase with diminished energy deposition into the discharge region it is necessary to decrease the deposition time. The latter condition stipulated the choice of the discharge circuit parameters and discharge unit construction. S, condensers with low value of

capacitance ( $12\ \mu\text{F}$ ,  $25\ \text{kV}$ ) and small stray inductance ( $40\ \text{nH}$ ) were chosen as the capacitive store unit. Nevertheless high value of the discharge circuit characteristic impedance could result in oscillating character of the discharge current. For the current to be aperiodic we have to increase the resistance of plasma in the discharge gap at the expense of enlarging the gap length. For this purpose a three-electrode system is provided in the discharge unit construction. The corresponding electric circuit is presented in Fig.6.

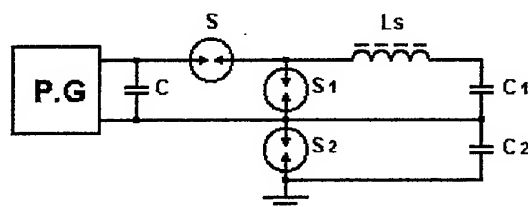


Fig. 6 Schematic of the launcher discharge circuits.

For triggering the main discharge gap  $S_2$  the plasma, which is produced in the additional gap  $S_1$ , is used. In turn for triggering the gap  $S_1$  the magnetic switch  $L_s$ , high voltage pulse generator PG and pulse sharpening spark-gap are used [3]. Such construction permits to trigger the discharge in the main gap with its length varying up to  $5\ \text{cm}$  that is adequate for obtaining aperiodic discharge current.

The collector, discharge gap and discharge triggering unit are constructively combined in a unified block where Rogowsky coil and high voltage divider to be used for measurements of the current in the discharge circuit and the discharge voltage are also placed. The launcher barrel and the powder dosage unit are fastened to this unified block.

Injection of a pre-set portion of microparticles into the launcher barrel and obtaining the suspension presents a rather complicated problem in this case. The point is that powders consisting of micrometer and submicrometer dimensions particles, especially dielectric powders (including ceramics), constitute wad-like states - agglomerates. Herewith for smaller microparticles the adhesion force between them is stronger. For that reason the application of dosage units which are commonly used in detonation guns and plasmatrone is not possible. For breaking the agglomerates in our installation the technique of powder pseudo-liquefaction is used that is based on the drift of particles in electric fields, ultrasonic oscillations action on particles and generation of turbulent curls. The agglomerates destruction is a result of their colliding either with each other or with other microparticles or with camera walls. So the uniform cloud of microparticles with dimension about  $1 \div 3$  diameters of the barrel is obtained during powder portion injection. The cloud mass equals several mg.

The experimental research program includes the study of the flow composition, measurement of velocities and temperatures of the flow and microparticles. At present measurements technique is being tested. The results of experiments would be published later.

## VII. Conclusion.

Acceleration of powder material microparticles with micrometer and submicrometer dimensions in the flow increased density region allows to obtain high velocities of microparticles with possibility to provide real control of their heating regime. At the same time the realisation of acceleration regimes to be applied for microparticles of different materials and different dimensions requires the selection

of the discharge region configurations and dimensions, the store parameters, the stored energy level, the position of injection, the distance between the barrel butt and the substrate. Those parameters could be determined on the basis of the optimisation analysis.

The experiments that is now under way would show if the proposed theoretical model was adequate. The point is that the hydrodynamic description of interaction between the flow and microparticles with dimensions less than 1 micrometer could be non-correct because the gas molecule free path length is comparable with the dimension of microparticles.

#### References.

1. E.Ya. Shcolnikov, A.V. Chebotarev et al. "Acceleration of Powder Materials in an Electrothermal Launcher", IEEE Transactions on Magnetics, vol 31, Jan. 1995, pp 758-763.
2. S.A. Vasiljevsky, I.A. Sokolova. "Non-ideal and ideal property of multicomponent plasma of air", Non-equilibrium processes in gases and low temperature plasma. International school seminar. Minsk 1992.
3. E.Ya. Shcolnikov et al. "Discharge initiation system in electrothermal launcher", Proceedings of XVI International Symposium on Discharges and Electrical Insulation in Vacuum, Moscow, 1994. pp 52-53.

# The Angle Point and Velocity Skin-Effect Roles at Different Stages of Electromagnetic Launch.

M.P.Galanin, V.V.Savitchev\*

Keldysh Inst. of Applied Math., Russian Academia of Science; Miusskaya sq., 4, Moscow, 125047, Russia.  
Fax: (095) 972-0737. E - mail: galan@applmat.msk.su.  
\*N.E.Bauman Moscow State Technical University

## Summary.

In this work we emphasize the role of electromagnetic field singularities in the metal contact destruction. Mainly the singularities are connected with geometry factors. The velocity magnitudes at which the armature evaporation takes place (contact "crisis") were stated in dependency on different characteristics using numerical simulation method. To state the problem of simulation correctly and obtain comparable results it is to point out the method of singularity smoothing. It was shown in the launch beginning the magnetic diffusion plays the main role, but after velocity  $\sim 100$  m/sec the importance of the velocity compression of current layer becomes dominant. The possibility of critical velocity rise depending to form and friction was shown.

## Introduction. Statement of the problem.

Due to great amount of complicated interconnected phenomena a physical model of contact zone between moving conductors (rail and armature) has not been formulated finally. The numerous investigations stated (see [1-5]) that as the armature velocity rises the character of current flow changes: 1. metallic (potential drop of some volts), 2. quasimetallic or microarcing (tens of volts) and 3. arcing (hundreds of volts). For practical purposes it is desirable to move point of transformation from 1 to 2 ("crisis" contact point) into area of much greater velocities.

In the works [6-8] we already investigated this problem. We have developed and realized the computer code for problem investigation in two - dimensional approach. The details of the used numerical algorithm are contained in [8]. The "critical" velocity magnitudes were obtained in dependency on different problem parameters. Here we aim at investigation of the problem from other point of view and emphasize the role of singularity points in metallic contact destruction.

We use the next physical model. At acceleration a metal armature is heated by friction and joule heating. It fuses at melting temperature and with achieving of boiling the boiling mass escapes from contact zone, creating cavern. We call critical the velocity, at which the boiling takes place. The problem is solved in two-dimensional case.

The work was supported by Russian Foundation of Fundamental Researches (project N 96-02-16842).

## § 1. The model of acceleration process.

The model comprises Maxwell system of equations in mhd-approximation for two components of electric field in longitudinal direction and one component of magnetic field in



transversal, equations for temperature and armature motion (see for details [6-8]). Further we shall use  $T$ -temperature,  $T_m$  and  $T_b$ -melting and boiling ones,  $Q_{fr}$ -specific friction heat power. The current  $I(t)$  is specified.

One half of typical railgun cross section is shown in Fig. 1. We use right forward side of armature and arbitrary back one. We denote the angle (greater than  $\pi$ ) between armature back side and rail as  $\varphi_0$  ( $\varphi_0 = 1.5\pi$  on Fig. 1).

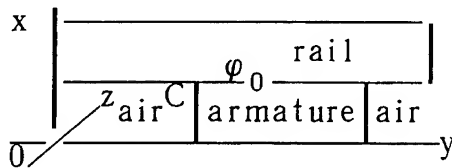


Fig. 1.

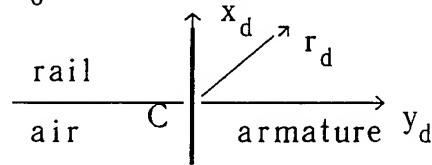


Fig. 2.

The armature velocity  $u_a$  is determined by the equation

$$m u_{a,t} = \int_A [\mathbf{j} * \mathbf{H}]_y dV - F_{fr}, \quad u_a|_{t=0} = u_{a,0}, \quad (1)$$

$$F_{fr} = \int_{S_a} f_{fr}(\mathbf{r}, T) dS, \quad f_{fr} = (k_0(T) + k_v(T)v^\beta) \int_A [\mathbf{j} * \mathbf{H}]_x dV / S_a,$$

where  $m$ -armature mass,  $A$ -its region,  $F_{fr}$ -friction force,  $S_a$ -contact surface,  $f_{fr}(\mathbf{r}, T)$ -friction force surface density,  $k_0(T)$  and  $k_v(T)$ -friction coefficients,  $\beta$ -parameter ( $|\beta| \leq 1$ ). We consider  $k_0$  and  $k_v$  are zero at  $T > T_m$ . We used the power  $Q_{fr} = f_{fr} u_a \delta(x - x_0)$  on  $S_a$ , where  $\delta(x - x_0)$ -Dirac-function,  $x_0$ -contact point. The  $Q_{fr}$  is concentrated on  $S_a$ .

## § 2. The examples of simulations and their discussions.

### 2.1. The main set of problem parameters.

We present below results of calculation runs under different conditions. The main set of parameters we used are following: caliber-1 cm, rail thickness-1 cm, rail height-0.5 cm, current in time 0.2 ms linearly increasing saturation value 0.5 MA. Initial  $T$  is  $17^\circ\text{C}$ ,  $\langle h \rangle = 3.06 \cdot 10^{-2}$  cm ( $\langle h \rangle$ -side length of right grid triangle with average square), initial velocity is equal to zero. The Cu rail and Al armature were the main pair of materials. Variations will be pointed specially.

### 2.2. On the velocity skin-layer structure.

To investigate the structure we present some results about the magnetic field diffusion depth. Fig. 2 describes the paths for Fig. 3, which shows the depth versus time in the case of rail with 1.2 mm Ni-Cr layer. Fig. 3,a,b,c show time evolution of points with  $H = 0.5 H_0$  at lines orthogonal to rail, going under angle  $\pi/4$  to it and along rail. These lines pass through the C point.

It is clearly seen the diffusion wave passes through Ni-Cr layer very quickly (less than 0.01 ms). Further it moves much slower in Cu. But as the velocity rises the diffusion depth decreases. This process becomes dominant from the time near 0.09 ms and velocity about 200 m/sec. The layer compression is the strongest in  $y$ -direction. The

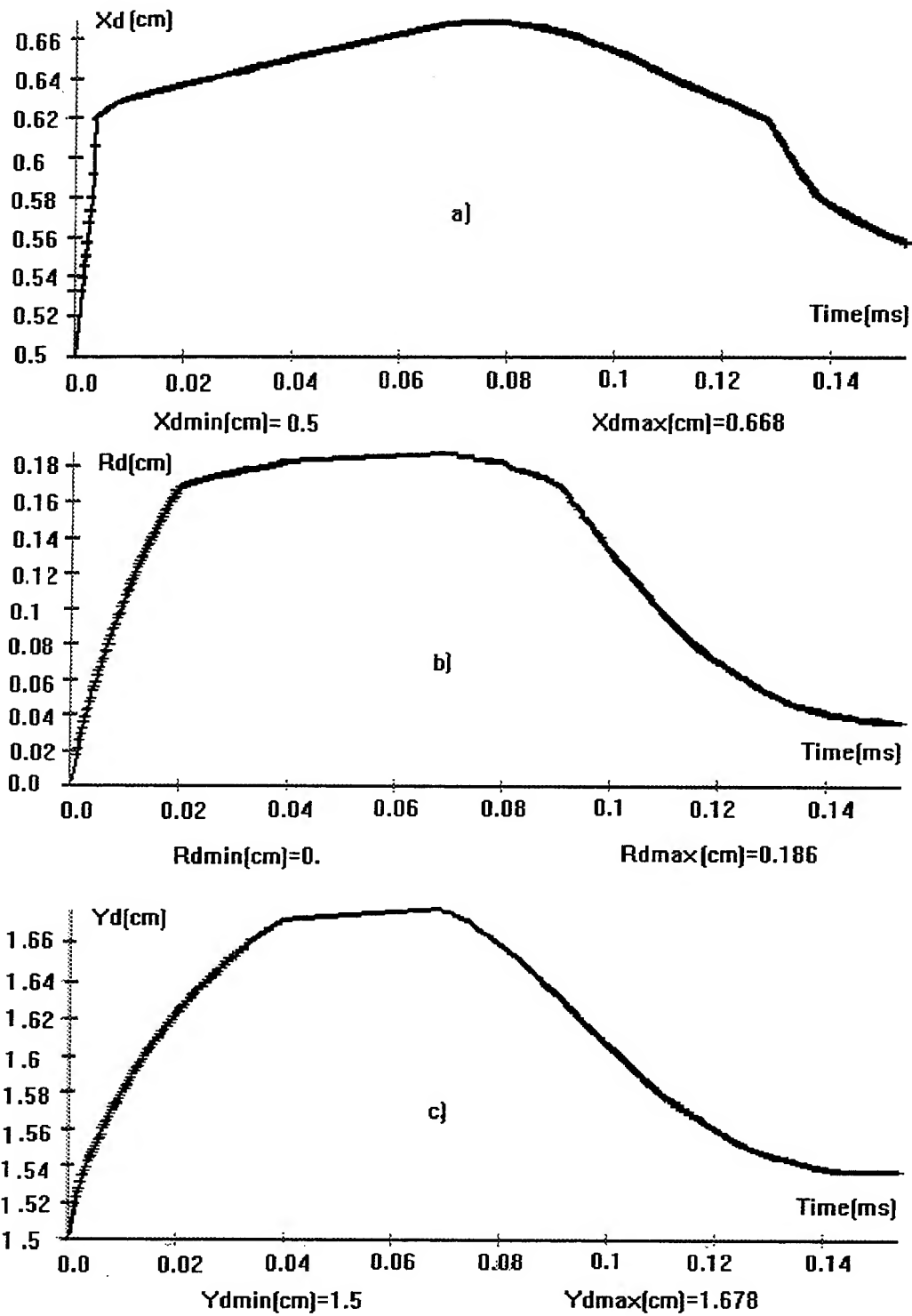


Fig.3. The time evolution of points with  $H=0.5H_0$  on lines, passing through C point:  
a)- orthogonal to rail; b)-under angle  $45^\circ$ ; c)- along rail.

Fig. 3 confirms that diffusion plays main role at low velocities but velocity compression becomes dominant at higher velocity. We point out in this variant the armature melting starts at  $t \approx 0.1 \mu\text{s}$  and critical velocity of 1170 m/sec was achieved at  $t = 0.154 \mu\text{s}$  (see. [6,7]).

Fig.3 shows the compression of layer with magnetic field on y - direction too. In the most of skin-layer models this effect is not taken into consideration. But this compression is able to describe data [9] about existence of some optimal resistive layer thickness. See also our results [7] for critical velocity values at different Ni-Cr layers.

### 2.3. Simulation runs with rest armature.

It is acknowledged that diffusion is very sensitive to angle points. To demonstrate it in clear form we remind the results [6-8] for magnetic field diffusion from inter-rail space with rest armature (here the velocity skin-layer is absent absolutely) and different  $\varphi_0$ . The problem solution contains singularity depending on used angle  $\varphi_0 > \pi$ . We calculated time interval  $t_0$  before  $T_b$ . The results shown the  $t_0$  decreases when  $\varphi_0$  rises as a rule.

The analytical expression for joule heating in angle point shows the boiling must begin immediately at  $t = 0$ . But solving a problem numerically we obtain only some approach of precise solution because of finite approximation. Partially, it is naturally to suppose the numerical joule heating action corresponds to analytical one averaging over square  $O(r_0^2)$ . Here the value  $r_0$  must be of used grid dimension.

Under this assumption the approximation results of simulation data by analytical expression gave correlation coefficient 0.99998 and parameter  $r_0 = 3.063 \cdot 10^{-2} \text{ cm}$ . It coincides with the  $\langle h \rangle$  ideally. The result for case  $\langle h \rangle = 4.477 \cdot 10^{-2} \text{ cm}$  shows the rising  $\langle h \rangle$  leads to corresponding increase of  $t_0$  according to stronger spreading of heat source.

The situation is typical for problems in regions with angle points (for electrodynamics-see [10], for elasticity-see [11] and so on). At the same time the physical heat source has finite value. Thus it is necessary apriori to point out the method, which smooths (regularizes) the solution near angle point. It is desirable this method has physical sense. The specification of curvature radius near angle is one from such methods. The concrete  $\langle h \rangle$  value can be obtained, for instance, from the comparison of experimental and calculated data about critical velocity value. We made such comparison in [6,7], the used  $\langle h \rangle$  value is it's result. There are other methods of course.

### 2.4. Simulation runs with different friction and angles.

Here we investigate the joint action of diffusion and velocity compression. The simplest way for it is to take into account the friction (1). The friction acts in two ways. First, it decreases the acceleration and leads to the growth of angle points importance. Second, it causes

friction heating. In this section we present the data about friction influence for different angles. Here only  $k_0(T) \neq 0$  at  $T < T_m$  in (1).

Table 1.

| $k_0$ | $\varphi_0^\circ$    | 225   | 270   | 315   | 351   |
|-------|----------------------|-------|-------|-------|-------|
| 0.0   | $t_o, \text{ ms}$    | 0.12  | 0.127 | 0.135 | 0.131 |
|       | $v_c, \text{ m/sec}$ | 577   | 685   | 829   | 795   |
| 0.2   | $t_o, \text{ ms}$    | 0.137 | 0.137 | 0.142 | 0.135 |
|       | $v_c, \text{ m/sec}$ | 494   | 516   | 623   | 677   |
| 0.35  | $t_o, \text{ ms}$    | 0.164 | 0.153 | 0.154 | 0.139 |
|       | $v_c, \text{ m/sec}$ | 375   | 370   | 446   | 587   |
| 0.5   | $t_o, \text{ ms}$    | ----- | 0.181 | 0.179 | 0.143 |
|       | $v_c, \text{ m/sec}$ | ----- | 64.6  | 170   | 477   |

In the calculation we didn't observe the liquid film, originated by friction only. It needs much smaller  $\langle h \rangle$  value for its calculation. Moreover the film creation leads to friction vanishing [12]. The further heating without electricity is possible only as result of viscosity forces. It corresponds to other problem statement. Here the heating, melting and boiling are results of friction and current flow common action.

It is noticeable the  $k_0$  value influences on  $v_c$  greatly. It is possible to obtain any velocity from 0 to  $v_c$  at  $k_0=0$  by changing  $k_0$  and providing constant angle. It is well seen at  $k_0=0$ , the  $\varphi_0$  value influences on  $v_c$  unlike the case with  $v=0$ . Different explanations of this fact are possible. It may be associated with the difference between  $H$  on armature back side and contact surface. This difference creates additional  $r$ -component of current, inversely proportional to  $(\varphi_0 - \pi)$ . The correlation coefficient calculation for this data and supposed dependency on  $\varphi_0$  is 0.93. It is possible too this effect is connected with studied in [13] influence of resistive layer between armature and rail. The presence of this layer leads to spreading of skin-layer proportional to  $(\varphi_0 - \pi)$ . The liquid film might be such resistive layer.

The analogous results were obtained in [14] (without friction) when studying the dependence of critical time on  $\varphi_0$ . The results substantially depended on materials.

But higher values of  $k_0$  lead to changing of such behavior. The singularity role becomes crucial and  $t_o$  decreases with angle growth. It is also obvious that the friction force in form (1) leads to its great dependence on armature shape and  $k_0$ . So, in the case of  $k_0=0.5$  and  $\varphi_0=225$  this

friction model gave absurd results with  $v < 0$ . On the other hand, in rectangular armature  $[j \cdot H]_x \approx 0$ , therefore the friction will be negligible. Thus the results for critical velocity  $v_c$  can alter accordingly to concrete  $f_{fr}$  form.

So, the process time is result of this effect and one, described in p.2.3. Hence we obtain some optimal angle for armature back-side. This angle depends on friction force and materials (see [14]).

#### 2.5. Simulation of evaporation wave motion.

It is of great interest to investigate the next stage after "crisis" point. Here we present the results for evaporation wave along contact zone simulation.

If there is no arcing then all armatures becomes identical relative to  $\varphi_0$  at stage of evaporation. All armatures have the same angle  $\varphi_0 = 2\pi$ . This variant is the worst among all angles, if we don't take into account the difference of materials. The  $\langle h \rangle$  value is of great importance here. It must be of real split thickness between conductors.

Fig. 4 shows level lines for  $H$  and  $T$  at main set of problem parameters for 4 time moments after "crisis". We remind the  $H$  level lines are the current lines here. It is well seen after some time the initial form of back side doesn't play any role. Fig. 5 shows time evolution of point with 0.9 of maximum  $T$  value along the contact zone after melting beginning. It demonstrates the point motion has not form of  $t^{0.5}$  type, which is typical for phase transition boundary in diffusion or heat-conductivity process. It is connected with presence of point heat source in phase transition region. The time dependency has character, changing in time accordingly to reconstruction of geometry. The mean velocity of evaporation wave motion is about 6 cm/sec. So, the wave passes 10-cm armature during  $1.5 \mu s$ , which is about to common time of launch.

#### Conclusion.

1. The problem of existence of continuous metal contact between armature and rail in electromagnetic launchers was investigated. The influence of singularity points on the results was studied.
2. The calculation runs confirmed great role of angle points in reaching of metal contact "crisis". For correct statement of mathematical model it is need to choose some method of regularization for obtaining finite values.
3. Due to singularity the solution results depend substantially on  $\langle h \rangle$  parameter, which corresponds to curvature radius near singularity and split thickness between conductors. Therefore the  $\langle h \rangle$  specification is one of possible regularization method. In this case the  $\langle h \rangle$  specification is an integral part of the problem statement analogously other geometry characteristics.
4. The concrete  $\langle h \rangle$  value can be result of special investigations. It is possible to obtain this parameter from experimental and calculated data about critical velocity.
5. The investigation of obtained dependence of critical velocity and time shows in the beginning of launch the diffusion of magnetic field and angle magnitude play the

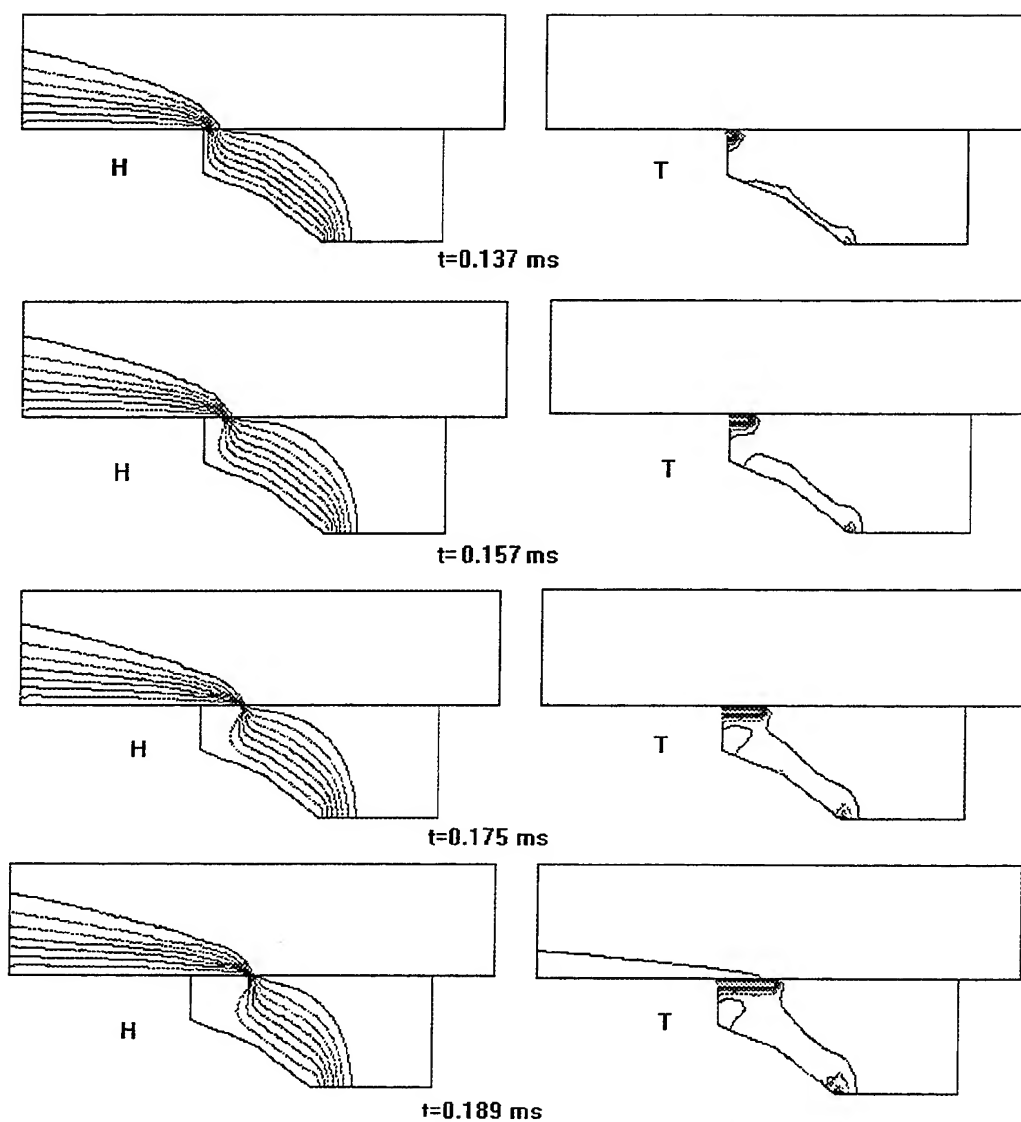


Fig. 4. The level lines of H (left) and T (right) in different times  $t$  after "crisis".

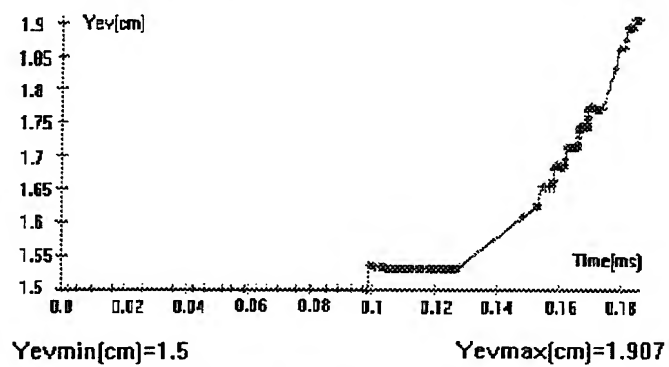


Fig. 5. The time evolution of point with 0.9 of maximum T along the contact zone after "crisis".

main role, but after the velocity near 100 m/sec - the velocity skin - layer. The character of singularity changes.  
6. The variation of materials, angles and friction makes possible to increase the critical velocity.

#### References.

1. G.C.Long, W.F.Weldom. Limits to the Velocity of Solid Armatures in Railguns, IEEE Trans. on Mag., 1989, v. MAG-25, N. 1, pp. 347-352.
2. J.C.Nearing, M.A.Huerta. Skin and Heating Effects of Railgun Current, IEEE Trans. on Mag., 1989. V. MAG-25. N. 1. P. 381-386.
3. J.P.Barber, A.Challita. Velocity Effects on Metal Armature Contact Transition, IEEE Trans. on Mag., 1993, v. MAG-29, N. 1, pp. 733-738.
4. A.P.Glinoff, N.M.Kolyadin, A.E.Poltanoff et al. Railgun metal contact crisis with transition to arc discharge investigation // Mater. of II All-union Seminar on Dynamics of Strong-Current Arc Discharge in Magn. Field, V.E.Nakoryakoff (Ed.), Novosibirsk, Inst. of Heat Phys., 1992, pp. 315 - 339. (In Russian).
5. V.P.Bazilevskii, R.M.Zayaddinoff, Yu.A.Kareeff. High-velocity metal contact electroconductivity crisis // Ibid, pp. 285 - 303. (In Russian).
6. M.P.Galanin, A.V.Plekhanov, V.V.Savitchev. The Investigation of Metal Contact Conditions for Electromagnetic Launch of Solid Armatures in Railgun// Proc. of 5th European Symp. on Electromagnetic Launch Technology, April 1995. Toulouse, France. Rep. N 76. 9 pp.
7. M.P.Galanin, A.V.Plekhanov, V.V.Savitchev. The Investigation of Metal Contact Behavior at Electromagnetic Launch of Conducting Armatures // Teplophysica Vysokih Temperature, 1996, v. 34, N 2. Pp. 293 - 298. (In Russian).
8. M.P.Galanin, Yu.P.Popov. Quasistationary Electromagnetic Fields in Nonhomogeneous Media. Mathematical Modeling.-M.: Nauka. Physmatlyt, 1995, 320 pp (In Russian).
9. Y.A.Kareev, L.G.Kotova, A.T.Kuharenko et al. Investigation of the Metal Contact Crisis in Railgun with Resistive Rails // Proc. of 5th European Symp. on Electromagnetic Launch Technology, April 1995. Toulouse, France. Rep. N 22.
10. G.Fickera. The Asymptotic Behavior of Electric Field and Electric Charge Density near Singular Points of Conducting Surface // Uspekhy Math. Nauk, 1975. V. 30. N. 3 (183). P. 105 - 124. (In Russian).
11. V.Z.Parton, P.I.Perlyn. Methods of Mathematical Theory of Elasticity. - M.: Nauka. 1981. (In Russian).
12. M.P.Galanin, A.D.Lebedev, V.V.Savitchev, B.A.Uryukov. The analysis of contact surfaces melting process at solid armature launch // Prepr. of Keldysh Inst. of Appl. Math., 1996. N 53. 19 p. (In Russian).
13. J.P.Barber, Y.A.Dreizin. Model of Contact Transitioning with "Realistic" Armature - Rail Interface // IEEE Trans. on Magn., 1993. V. MAG-29. N. 1. Pp. 96-100.
14. A.J.Schoolderman, W.A. de Zeeuw, M.Koops. Electro-thermal Design Aspects of Transitioning Solid Armatures // IEEE Trans. on Magn., 1993. V. MAG-29. N. 1. Pp. 865-870.

# The analysis of contact surfaces melting process at solid armature launching.

M.P.Galanin\*, A.D.Lebedev, V.V.Savitchev, B.A.Uryukov

\*Keldysh Inst. of Applied Math., Russian Academia of Science; Miusskaya sq., 4, Moscow, 125047, Russia.

Fax: (095) 972-0737. E - mail: galan@applmat.msk.su.  
N.E.Bauman Moscow State Technical University

## Summary.

The main purpose of the work is the investigation of the contact melting phenomenon and appearance of a liquid film as a result of friction. It can lead to the loss of solid contact and its transition into a plasma one. In the work the investigation of heat transfer on contacts and the stresses on them allowed to establish the conditions of liquid film creation, its existence and features and, hence, the time of contact surface melting. The theoretical analysis has shown that the origination of the liquid film leads to a sharp decrease of the friction force compared with "dry" friction, so the friction can be neglected in armature launch simulation.

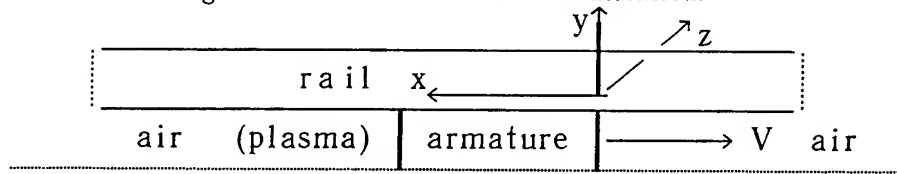


Fig. 1.

## Introduction. Statement of the problem.

The work is dedicated to analysis of the processes on the contact surfaces of electromagnetic launchers of the railgun type [1-3]. One half of a typical railgun crossing is shown on Fig. 1. The electromagnetic launch of a solid armature with metallic contact has some advantages over a plasma one [1]. Unfortunately, at velocities  $V \sim 1$  km/sec almost always the metallic contact regime transforms into a plasma contact. Currently, it is acknowledged that the transition of a contact from metallic into plasma is the result of great set of physical phenomena. Among them there are velocity skin - effect, conductors friction and many others (see also [4, 5]). These factors lead to melting and evaporation of contact surfaces and thus to contact losing. This work is dedicated to analysis of contact melting and creation of a liquid film at the contact surface as a result of friction.

The work was supported by Russian Foundation of Fundamental Researches (project N 96-02-16842).

## § 1. Heat-exchange on railgun surfaces.

The armature sliding creates the heat  $q = k_{fr} \sigma_n V$  on the contact surface, where  $k_{fr}$  - friction coefficient,  $\sigma_n$  - normal stress,  $V$  - relative velocity. Due to little interaction time we shall suppose that the transversal dimensions of the heated region are small. In this way it is possible to obtain some simple solutions. Further we



shall use the contact temperature:

$$T_0 = 2 \sqrt{2} q / (\sqrt{\pi} (B_1 \sqrt{V/x} + B_2 \sqrt{t})). \quad (1.1)$$

This temperature was derived in [6]. Here index 1 relates to the wall (rail), 2-to the armature,  $B_i = \sqrt{\lambda_i \rho_i c_i}$ ,  $\rho$  -density,  $c$ -heat capacity,  $\lambda$ -coefficient of heat conductivity. The temperature is calculated so that  $T_0(x=0)=0$ .

## § 2. The conditions for liquid film origination.

We denote melting temperature as  $T_m$ . To obtain approximate values we shall consider the homogeneous cylinder of  $l$  length and the tangential stress, corresponding to the beginning of surface layers shift, that is equal  $1/2$  of the time resistance to shift  $\sigma_T$ :  $\sigma_T = k_{fr} \sigma_n = 0.5 \sigma_T$ . We consider an Al armature inside the bore with a constant acceleration and zero initial velocity.

Table 1  
Melting boundary position (mm)

|        | graphite<br>6470<br>acceleration, m/sec <sup>2</sup> | Al<br>21200         | Fe<br>10200         | Cu<br>33100 | W<br>15500          | V,<br>km/sec |
|--------|--|---------------------|---------------------|-------------|---------------------|--------------|
| $10^7$ | $6,8 \cdot 10^{-3}$                                  | $7,7 \cdot 10^{-2}$ | $1,7 \cdot 10^{-2}$ | 0,20        | $4,1 \cdot 10^{-2}$ | 1,41         |
| $10^6$ | $2,3 \cdot 10^{-2}$                                  | 0,28                | $6,0 \cdot 10^{-2}$ | 0,73        | 0,14                | 0,45         |
| $10^5$ | $8,5 \cdot 10^{-2}$                                  | 1,09                | 0,22                | 3,06        | 0,55                | 0,14         |

Table 2  
Time of melting beginning (sec)

| material | graphite<br>acceleration, m/sec <sup>2</sup> | Al                   | Fe                   | Cu                   | W                    |
|----------|--|----------------------|----------------------|----------------------|----------------------|
| $10^7$   | $1,40 \cdot 10^{-5}$                         | $1,86 \cdot 10^{-5}$ | $1,52 \cdot 10^{-5}$ | $2,19 \cdot 10^{-5}$ | $1,69 \cdot 10^{-5}$ |
| $10^6$   | $6,48 \cdot 10^{-5}$                         | $8,62 \cdot 10^{-5}$ | $7,05 \cdot 10^{-5}$ | $10,2 \cdot 10^{-5}$ | $7,83 \cdot 10^{-5}$ |
| $10^5$   | $30,1 \cdot 10^{-5}$                         | $40,0 \cdot 10^{-5}$ | $32,8 \cdot 10^{-5}$ | $47,2 \cdot 10^{-5}$ | $36,3 \cdot 10^{-5}$ |

Table 3  
Time of melting beginning for different  $V_0$  (sec)

| material | graphite<br>velocity, km/sec | Al                   | Fe                   | Cu                   | W                    |
|----------|------------------------------|----------------------|----------------------|----------------------|----------------------|
| 0,1      | $4,84 \cdot 10^{-5}$         | $11,4 \cdot 10^{-5}$ | $6,24 \cdot 10^{-5}$ | $18,7 \cdot 10^{-5}$ | $8,52 \cdot 10^{-5}$ |
| 0,5      | $1,94 \cdot 10^{-6}$         | $4,55 \cdot 10^{-6}$ | $2,50 \cdot 10^{-6}$ | $7,46 \cdot 10^{-6}$ | $3,41 \cdot 10^{-6}$ |
| 1,0      | $4,84 \cdot 10^{-7}$         | $11,4 \cdot 10^{-7}$ | $6,24 \cdot 10^{-7}$ | $18,6 \cdot 10^{-7}$ | $8,52 \cdot 10^{-7}$ |
| 1,5      | $2,15 \cdot 10^{-7}$         | $5,06 \cdot 10^{-7}$ | $2,77 \cdot 10^{-7}$ | $8,29 \cdot 10^{-7}$ | $3,79 \cdot 10^{-7}$ |
| 2,0      | $1,21 \cdot 10^{-7}$         | $2,84 \cdot 10^{-7}$ | $1,56 \cdot 10^{-7}$ | $4,66 \cdot 10^{-7}$ | $2,13 \cdot 10^{-7}$ |

Table 1 shows the calculational results for the melting boundary position relative to the front point of the contact surface after the first 10 cm of the path with different accelerations and rail materials. We used  $T_m = 1070$  K,  $\sigma_T = 7,54 \cdot 10^7$  N/m<sup>2</sup>. The values of B parameter (in w sec<sup>1/2</sup>/m<sup>2</sup>K) are represented in Table 1 under the

material. The last column contains the velocity of the armature at this time. It is well seen in all cases nearly all contact surface fuses very quickly, especially at maximal acceleration. Table 2 represents the values  $t_0$  - time of melting beginning for the same conditions, as in Table 1. Table 2 shows the melting begins at velocities of some ten or one hundred m/sec after passing only a few mm. In real railguns the initial velocity  $V_0$  is  $10^2$ - $10^3$  m/sec. Table 3 represents data about  $t_0$  for different initial velocities at conditions analogous to Table 2. From the Table it is seen the armature passes only a few millimeters or less before beginning of contact surface melting.

### § 3. The stresses on contact surface.

The previous data related to big and specified tangential stresses on contact surface. Here we want to calculate the friction on contact surface. Let's study the acceleration of the homogeneous armature of  $l$  length. The stress on bore walls is result of acceleration, friction heating, joule heating and hot gas on ends.

I. We begin from the longitudinal stresses calculation, originated by the electromagnetic acceleration. We use the next equation of motion for unit volume of accelerated armature, regarding armature material as an incompressible liquid (or elastic body [7]) :

$$\rho \frac{dV}{dt} = \frac{\partial}{\partial x} \left( p + \frac{B^2}{2\mu_e} \right) - f_{fr}, \quad (3.1)$$

where  $\rho$ -density,  $p$ -longitudinal stress, analogous to pressure in liquid,  $f_{fr}$ -friction force per unit square,  $B$ -magnetic induction,  $\mu_e$ -magnetic permeability. We suppose all values depend on  $x$  only and  $B$  has only one nonzero component in the  $z$ -direction (see Fig. 1).

At analyzing (3.1) we shall assume also that all points of the elastic body move with the same velocity and acceleration (see also quasistationary approximation [7]). Then if  $f_{fr}$  depends on time only and as  $\rho = \text{const}$ ,

$V=V(t)$  we can integrate (3.1) over the length. Thus we obtain

$$p = p_0 \left( 1 - \frac{x}{l} \right) + p_1 \frac{x}{l} + \frac{B_1^2}{2\mu_e} \frac{x}{l} - \frac{B^2}{2\mu_e},$$

where  $p_0$  is external pressure at the front armature boundary,  $p_1$  is external pressure at the rear boundary (at  $x=l$ ),  $B_1$  is magnetic induction at the same place.

Using the Maxwell equation  $\mu_e j = -\partial B / \partial x$  [8] (here  $j$  is  $y$ -direction component of current density) it is possible to obtain  $B$ , if  $j$  is known. Therefore it is possible to obtain longitudinal stress distribution. As an example let's take electric current uniformly distributed between  $x_1$  and  $x_2$  ( $x_2 > x_1$ ). The current density is equal to  $-j_0$ . Then we can obtain the next stress distribution:

$$\begin{aligned}
p &= p_0 \left(1 - \frac{x}{l}\right) + p_1 \frac{x}{l} + F_g/S \frac{x}{l} \quad \text{at } 0 \leq x \leq x_1, \\
p &= p_0 \left(1 - \frac{x}{l}\right) + p_1 \frac{x}{l} + F_g/S \left[\frac{x}{l} - \left(\frac{x - x_1}{x_2 - x_1}\right)^2\right] \quad \text{at } x_1 < x < x_2, \\
p &= p_0 \left(1 - \frac{x}{l}\right) + p_1 \frac{x}{l} + F_g/S \left(\frac{x}{l} - 1\right) \quad \text{at } x_2 \leq x \leq l.
\end{aligned}$$

Here  $F_g$  is the total electromagnetic force, acting on the armature,  $S$  is its cross - section square.

In reality there are different variants of relationships between  $p_1$  and magnetic pressure  $p_m = F_g/S$ . For instance,  $p_m = 0$  in a plasma armature. Then the longitudinal stresses are compressible ( $p > 0$ ), and their distribution is linear. If a metallic armature is used (all current flows through the body) then  $p_1 \ll p_m$ , and the  $p_0$  is negligible compared to magnetic pressure. In this case the stress distribution is nonlinear. In the front part the stresses are compressible increasing with  $x$ . They are maximal at some point  $x_m$ , equal to zero at  $x = x_0$ , and remain tensile up to the end. The mean longitudinal stress is equal

$$\langle p \rangle = \frac{1}{l} \int_0^l p \, dx = \frac{p_0 + p_1}{2} + \frac{F_g}{S} \left( \frac{x_1}{3} + \frac{2x_2}{l} - \frac{1}{2} \right). \quad (3.2)$$

II. Here we want to calculate the stresses which are result of armature heating. Let's study the next model problem about two cylinders. One of them simulates the armature, the other - the railgun bore. We consider the temperature distribution is given and depends on radius  $r$  only. The cylinders are in contact along all the internal cylinder lateral surface (at  $r = R$ ,  $R_0$  is external radius of external cylinder). We aim to determine the stresses, particularly, radial stress on the contact.

Supposing the displacement vector  $u$  has only a radial component and depends on radius only we obtain [7]:

$$\frac{d}{dr} \left( \frac{1}{r} \frac{d}{dr} (ru_r) \right) = C \frac{dT}{dr}, \quad C = \frac{\alpha}{3} (1 + \mu_0)/(1 - \mu_0).$$

Here  $\mu_0$  is Poisson coefficient,  $\alpha$  is expansion coefficient,  $E$  is elasticity modulus,  $\alpha_1 = \alpha/3$  is linear expansion coefficient.

Solving this equation with the boundary conditions we obtain the stresses and displacement. We represent the result expression for the radial stress at  $r = R$ :

$$\sigma_{rr}|_R = b S (K_1 D_1 + K_2 D_2)/(D_1 + D_2), \quad (3.3)$$

where  $K_1$  and  $K_2$  are some constants, depending on the contact temperature  $T_0$ ,  $\langle T \rangle$  and  $\langle T' \rangle$  (mean temperatures of internal and external cylinders correspondingly),  $D_1$  and  $D_2$  are constants, depending mainly on geometry,  $b$  is an expression, depending on  $E$  and  $\mu_0$ . We calculate the temperature so that  $T(R_0) = 0$  (see for details [9]).

We can simplify the expression (3.3) if we take into

account the heat processes scale. As  $\langle T \rangle \sim T_0 \delta / R$ , where  $\delta$  is the heated zone scale, then at small interaction time we can neglect the mean temperature compared with the contact one.

As a result we obtain the approximate expression:

$$\sigma_{r,r}|_R \sim N E \alpha_1 T_0 / (1 - 2 \mu_0), \quad (3.4)$$

$$N = \left[ \frac{1 - \mu_0}{1 - \mu_0} \frac{C}{C} + 1 - 2 \mu_0 \right] / \left[ \frac{b}{b} + (1 - 2 \mu_0) \left[ 1 + \frac{R^2}{R_0^2} \left( 1 - \frac{b}{b} \right) \right] \right].$$

To take into account the common influence of mechanic and heat phenomena it is needed to add the transversal stresses, originated at acceleration, into (3.4). Then

$$\sigma_n \approx \frac{N}{1 - 2 \mu_0} (E \alpha_1 T_0 + \mu_0 \langle p \rangle). \quad (3.5)$$

#### § 4. The calculation of melting beginning time.

We shall study the next simplified problem. Let the armature move in a cylindrical channel containing four segments. Two of them are electrodes and the others are isolating walls. The armature has an initial velocity  $V_0$ . We use the equation of motion in the ordinary form:  $M \frac{dV}{dt} = 0.5 L_x I^2 - F_{fr}$ , where  $M$  is the armature mass,  $L_x$  is inductance gradient,  $I$  is current.

The friction consists of the armature interaction with electrodes (index e) and isolating walls (index w):

$$F_{fr} = (k_{fre} \Pi_e \sigma_{ne} + k_{frw} \Pi_w \sigma_{nw}) l,$$

where  $k_{fr}$  is friction coefficient,  $\Pi$  is the fraction of cross-section perimeter, occupied by electrodes or walls.

Using (3.5) we obtain (for electrodes and walls):

$$\sigma_n = m (n T_0 + \langle p \rangle), \quad m = \frac{N \mu_0}{1 - 2 \mu_0}, \quad n = \frac{E \alpha_1}{\mu_0}.$$

Neglecting  $p_1$  and  $p_0$  we obtain (3.2) in the form:

$$\langle p \rangle = \beta F_g / S, \quad F_g = \frac{L_x}{2} I^2, \quad \beta = \frac{x_1 + 2 x_2}{3 l} - \frac{1}{2}.$$

We use (1.1) for  $T_0$  determination:

$$T_{0e} = \sqrt{\frac{8}{\pi}} \frac{q_e}{B_e \sqrt{V/\sqrt{x}} + B/\sqrt{f}}, \quad T_{0w} = \sqrt{\frac{8}{\pi}} \frac{q_w}{B_w \sqrt{V/\sqrt{x}} + B/\sqrt{f}}$$

Here  $B$  parameter for armature is written without index.

$$q_e = k_{fre} V \sigma_{ne}, \quad q_w = k_{frw} V \sigma_{nw}.$$

As in [6] we take for calculations the friction coefficient equal to  $k_{fr0}$  at  $V < V_*$  and proportional to  $V^{-0.4}$  at higher  $V$ .

These equations were solved numerically simultaneously with electric circuit equations. The time of melting beginning was determined. We used Al armature, graphite and Cu walls. We varied the initial velocities, velocity of current rise and dimensions. Almost in all cases at nonzero initial velocity ( $V_0 > 10^2$  m/sec) the melting of

the contact surface began practically at the entrance of railgun bore. At the same time the tangential stresses on the contact were higher than  $\sigma_T$  in almost all cases.

#### § 5. The conditions for liquid film existence.

The liquid film created at the contact can exist at sufficiently high heat flux originated by friction. The flux must be equal to the sum of the flux for wall heating ( $q_1$ ), for maintaining a constant melting boundary temperature (equal to  $T_m$ ) ( $q_2$ ) and for creation of a liquid film ( $q_m$ ), which escapes from the contact zone.

After the film formation the process of heat generation changes. Now it is the result of kinetic energy dissipation of melted metal moving relative to the solid boundaries. Supposing linear velocity distribution across the film we obtain the tangential stress is constant on thickness and is equal to

$$\sigma_T = \mu V / \Delta, \quad (5.1)$$

where  $\mu$  is viscosity of liquid,  $\Delta$  is its thickness.

Then the power of the heat source is equal to  $q = \mu V^2 / \Delta$ . When analyzing the heat transfer the next characteristics were obtained:

$$q_1 = \frac{\alpha_1 \lambda_1 T_0}{\delta_1}, \quad \delta_1 = \sqrt{\frac{2 \alpha_1 \lambda_1 x}{\rho_1 c_1 K_1 V}}, \quad q_2 = \frac{\alpha_2 \lambda_2 T_m}{\delta_2}, \quad \delta_2 = \sqrt{\frac{2 \alpha_2 \lambda_2 t}{\rho_2 c_2 K_2}},$$

where  $\delta_1$  and  $\delta_2$  are depths of heated zones in wall and armature,  $\alpha_i K_i = \pi/4$ ,  $T_0$  is wall temperature.

Thus the heat flux  $q_m$  is equal to  $\rho r_m d\Delta/dt$ , where  $\rho$  is the density of liquid metal,  $r_m$  is the specific heat of melting.

I. The wall temperature can be estimated by the following way. Solving the stationary equation for  $T$

$$\lambda \frac{\partial^2 T}{\partial y^2} + \mu \left( \frac{\partial V}{\partial y} \right)^2 = 0 \quad (5.2)$$

with the appropriate boundary conditions at  $y=0$  ( $T=T_m$ ) and  $y=\Delta$  ( $q=q_1$ ) we derive the wall temperature (using

$$(1.1) \text{ and neglecting } B_2 \sqrt{t}) \quad T_0 = \frac{T_m + \mu V^2 / 2 \lambda}{1 + \frac{\Delta}{\lambda} B_1 \sqrt{\pi V / 8 x}}.$$

The relation shows an upper limit for film thickness, when the temperature is just under the melting one:

$$\Delta_{lim} = \sqrt{2 x / \pi V} \mu V^2 / B_1 T_m. \quad (5.3)$$

That is at  $\Delta < \Delta_{lim}$  there is no cooling and crystallization of liquid film. If  $\Delta > \Delta_{lim}$  the source power is not enough for flux into wall. It leads to crystallization near the wall. In this case the boundary conditions near wall change. The temperature becomes equal to  $T_m$ . The crystallization generates specific heat of melting, in-

creasing the heat flux into wall. The film thickness becomes less, increasing the dissipative energy. So, the phase transitions (melting and crystallization) supply film control. Once formed it must be maintained by the dissipative processes and phase transforms.

II. At the same time the armature mass diminishes continuously due to wiping off liquid film by the moving wall. At linear velocity distribution and weakly changing film thickness along the length ( $x$  is mean longitudinal film coordinate) the flow rate of mass (per unit film thickness) is equal to

$$G = 0.5 \rho V \Delta. \quad (5.4)$$

The flow rate of heat is  $dQ/dt = \int_0^\Delta \rho v (cT + \frac{v^2}{2}) dy$ , where  $v$  is local velocity in the film  $v = Vy/\Delta$ . Using the (5.2) solution, under this assumptions we derive

$$\frac{dQ}{dt} = \rho V \Delta \left\{ \frac{V^2}{6} + cT_m \frac{1 + \frac{\chi}{2} + \frac{2}{3}\theta(1 + \frac{\chi}{4})}{1 + \chi} \right\}, \quad \chi = \frac{\Delta}{\lambda} \sqrt{\frac{\pi V}{8x}} B_1, \quad \theta = \frac{\mu V^2}{2\lambda T_m}.$$

Dividing to the film length  $l$ , we obtain the corresponding heat flux ( $q_r$ ).

Dividing (5.4) by the length  $l$  and density  $\rho$ , we obtain the corresponding decrease of the film thickness, which must be compensated by the spreading of the body due to internal stresses. Dividing (5.4) by the armature radius we obtain the velocity of relative spreading of the body which is needed for taking away compensation ( $D=2R$ )  $d\epsilon/dt = V\Delta/(Dl)$ . The relative spreading diminishes normal stresses on the contact:

$$\sigma_n = m (n T_m + \langle p \rangle) - \epsilon E.$$

At the moment when the  $\sigma_n$  becomes equal to zero, split between body and wall originates. Then the friction vanishes. If the armature spreads further then the process can restart when the armature will contact with the wall.

III. The final relations for film thickness can be written in the next form. If the conditions of film existence are satisfied then its thickness can be calculated from the equation

$$q_1 = q_2 + q_m + q_r + q, \text{ or } \frac{d\Delta^2}{dt} = 2 \frac{\lambda T_m}{\rho r} [2\theta - \chi \frac{1+\theta}{1+\chi} - \chi \sqrt{x/Vt} \frac{B_2}{B_1} - \frac{Re}{3} \frac{\Delta^2}{l^2} (\theta + 3 Pr \frac{1 + \frac{\chi}{2} + \frac{2}{3}\theta(1 + \frac{\chi}{4})}{1 + \chi})] \quad (5.5)$$

where  $Re = \rho V l / \mu$ ,  $Pr = \mu c / \lambda$ . The equation (5.5) must be solved with the initial condition  $\Delta=0$  at  $t=t_0$ . This equation describes the melting process and crystallization. But in the case of crystallization at  $T_0 < T_m$  the complex  $(1+\theta)/(1+\chi)$  must be changed to 1.

#### Conclusion.

The theoretical investigation and results of large set of numerical simulations for liquid film features permit

to draw some main conclusions.

1. In the most of variants the film thickness was between 1 - 10  $\mu$ . 2. The external conditions (initial inductance and velocity) acts weakly on the time of film origination and its dynamics. 3. In all simulation variants the temperature  $T_0$  on the moving boundary was less then  $T_m$ , that is the film solidified at contact. 4. After a long time the film thickness becomes almost constant. It's upper limit can be estimated from the relation  $\Delta_{\max} \sim 2\sqrt{\frac{2x}{\pi V}} \frac{\mu V^2}{B_1 T_m}$ . This one is twice the limit  $\Delta_{\lim}$  from (5.3). 5. In this case we can estimate the friction. Using  $\Delta_{\lim}$  as  $\Delta$  we obtain  $F_{fr} = B_1 T_m \sqrt{\frac{2I}{V}}$ . The force doesn't depend on viscosity and is inversely proportional to the velocity. 6. The little variation of normal pressure  $\sigma_n$  on the contact surface gives evidence of stable film existence. 7. The main conclusion is the next: the liquid film origination leads to a sharp decrease of the friction force compared with dry force. So, it can be neglected in simulations.

#### References.

1. V.B. Geleznyi, A.D. Lebedev, A.V. Plekhanov. The actions on armature launch dynamics in railgun // Mater. of II All-union Seminar on Dynamics of Strong-Current Arc Discharge in Magn. Field, V.E. Nakoryakoff (Ed.), Novosibirsk, Inst. of Heat Phys., 1992, pp. 5-32. (In Russ.).
2. A.D. Lebedev, B.A. Uryukov. The high pressure impulse plasma accelerators. Novosibirsk, Inst. of Heat Phys. 1990. 290 pp. (In Russ.).
3. M.P. Galanin, Yu.P. Popov. Quasistationary Electromagnetic Fields in Nonhomogeneous Media. Mathematical Modeling.-M.: Nauka. Physmatlyt, 1995, 320pp (In Russ.).
4. M.P. Galanin, A.V. Plekhanov, V.V. Savitchev. The Investigation of Metal Contact Behavior at Electromagnetic Launch of Conducting Armatures // Teplophysica Vysokih Temperature, 1996, v.34, N2. Pp. 293-298. (In Russ.).
5. A.P. Glinoff, N.M. Kolyadin, A.E. Poltanoff et al. Railgun metal contact crisis with transition to arc discharge investigation // Mater. of II All-union Seminar on Dynamics of Strong-Current Arc Discharge in Magn. Field, V.E. Nakoryakoff (Ed.), Novosibirsk, Inst. of Heat Phys., 1992, pp. 315-339. (In Russ.).
6. B.A. Uryukov, A.D. Lebedev, K.K. Mylyayev. The influence of processes at contact surfaces on metallic armature launch dynamics // Ibid, P. 33-71. (In Russ.).
7. S.P. Tymoshenko, G. Gudier. The theory of elasticity. - M.: Nauka. 1975. 576 p. (In Russ.).
8. I.E. Tamm. The basis of electricity theory. M.: Nauka. 1966. 624 p. (In Russ.).
9. M.P. Galanin, A.D. Lebedev, V.V. Savitchev, B.A. Uryukov. The analysis of contact surfaces melting process at solid armature launch // Prepr. of Keldysh Inst. of Appl. Math., 1996. N 53. 19 p. (In Russ.).

# Numerical Simulation of Mechanical Effects in Composite Sabots for Railguns by the Finite Element Method

C. Müller

French-German Research Institute of Saint-Louis (ISL)  
5, rue du Général Cassagnou, F-68301 Saint-Louis Cedex, France

**Abstract:** In electromagnetic railgun experiments at ISL, the composite-projectiles are accelerated up to 2000 m/s with a maximal acceleration of  $7 \times 10^6 \text{ m/s}^2$ . The forces' maximum typically will have been achieved after 200  $\mu\text{s}$ . One consequence of this dynamic load is a strain-velocity in the order of  $\dot{\epsilon} = 2000 \text{ s}^{-1}$ , a rate at which also metals are giving up their static properties.

The aim of the research at ISL is the construction of a sabot made of fiber reinforced material adapted for the dynamic bearing. FE simulations should support the construction process, as well as they allow a detailed investigation of micromechanical effects occurring during the acceleration. The most important problem of the numerical simulation of composites under dynamic bearing is the material model. We show in this paper, that the classical homogenized laminate models, well known for static analysis, don't meet the needs of dynamic simulation. To develop an appropriate material model for railgun sabots, we made quasistatic experiments with a specific sabot geometry as well as dynamic investigations with simple cylinder specimens. Lateral support (no radial strain) of a specimen increases its strength up to two times the strength of a non supported one. The system answer still remains linear elastic, only little internal delamination occurs.

Tests in a Split Hopkinson Pressure Bar test facility proofed the maximum strain as the principal failure criterion for dynamic bearing. Whereby the maximum strain depends of the instantaneous strain-rate. Higher the strain-rate is, higher the maximum failure strain will be.

By doing this we show that the viscous properties of the matrix are fundamental for the mechanic behavior of composites under dynamic bearing. So when the material fails, the stress is beyond the static failure stress. Also experiments with real sabots have shown, that failure occurs a relatively long time after the stress has achieved its maximum.

## 1 Introduction

The physical principle of a railgun is shown in figure 1.

The railgun consists of two conducting rails and a conducting projectile. The current in the rails generates a magnetic field  $B$  and yields by interacting with the current of the projectile the LORENTZ-forces. The LORENTZ-force can be described by the equation  $\vec{F} = I(\vec{l} \times \vec{B})$ , where  $l$  is the length of the current bridge and  $I$  is the current which crosses the armature [6], [9].

One method to augment the actual load factor of electromagnetic railguns is to decrease the sabot's mass. Furthermore, railguns are working with accelerations up to  $7 \times 10^6 \text{ m/s}^2$  and also the sabot must be built of a strong material.

Fiber reinforced polymers perfectly combine the advantages of low density with those of high toughness.

Due to their high specific strength and capability of being tailored to meet precise specifications concerning stiffness characteristics, there is a great deal of interest to be able to simulate numerically a certain geometry under dynamic loading. A consequence of dynamic loading in railguns is a strain rate in the order of  $\dot{\epsilon} = 2000 \text{ s}^{-1}$ , a rate at which also metals give up their static properties.

We know that there will also exist a limit in strain-rate for composites where they change their dynamic behavior.

Typical theoretical investigations of the modulus of composites are dealing with

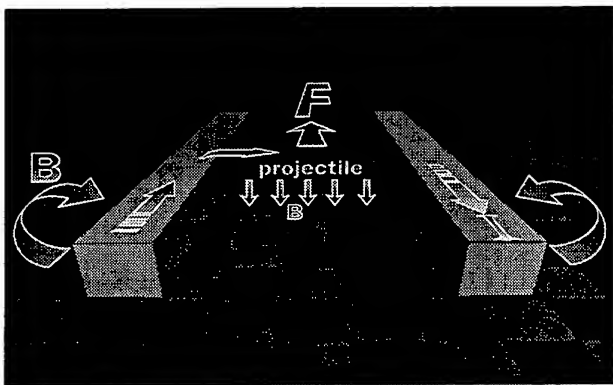


Figure 1: Physical Principle of a Railgun



rates in the range of  $10^{-4} \leq \dot{\epsilon} \leq 10^{-2} \text{ s}^{-1}$ , a so called quasistatic loading [2], [7].

Studies of dynamic behavior are rare and they typically treat a specific relatively simple geometry like thick plates [8] which are notched. Other investigations were made by Bruck et al. [1]. They use a magnetic flyer plate to generate a short duration pulse ( $< 1 \mu\text{s}$ ) on a carbon-fiber/epoxy laminate.

Figure 2 shows the sabot for the 30 mm railgun prestudy Pegasus. It is a cylinder with a length of 70 mm and a diameter of 29 mm. The 7.5 mm holes contain the brushes which apply the force. We only know the total force by measuring the current in the rails. In the described railgun, one can calculate the total force by:

$$F = \frac{1}{2} L' I^2$$

$L'$  is the gradient of inductivity and the value is in the range of  $0.44 \mu\text{H/m}$ .  $I$  represents the total current.

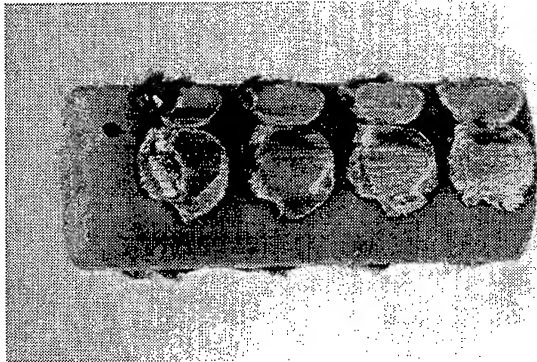


Figure 2: Sabot Prestudy PEGASUS after a shot

For prestudy PEGASUS the rise time of the current is about  $250 \mu\text{s}$ . The distribution of the current in each brush depends on the material of the brush (we are using iron, nickel and copper fibers), but the true current distribution is not known. It only can be evaluated with respect of their specific resistance that increases with temperature.

Figure 3 shows the calculated forces which are based on a computed current distribution. All the material investigations are based on figure 3.

The second chapter deals shortly with the used materials. In the third chapter we elucidate the quasistatic behavior of the sabot made of the material TE 630 and we will study the influence of the boundary condition of no radial strain as well as those of notching. The fourth chapter is dedicated to treat the dynamic properties of laminates in Split Hopkinson Pressure Bar tests as well as numerical investigations. Finally chapter five concludes the presented results.

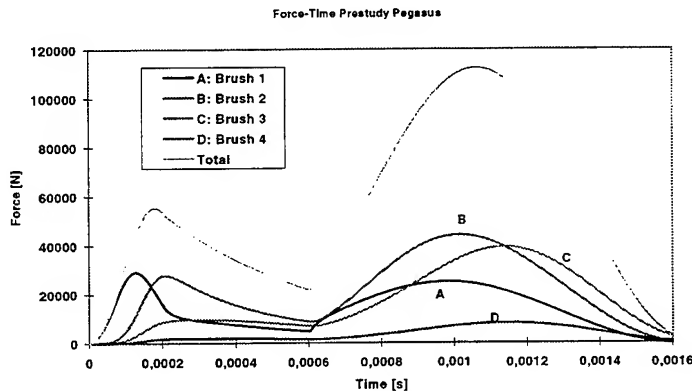


Figure 3: Calculated Forces

## 2 Materials

For the experiments we used different materials.

To have a representative selection of fiber reinforced materials, we chose the materials presented in table 1.

Quasistatic experiments with the special sabot geometry were made only with TE 630. This material has orthotropic properties.

| Designation | Producer             | Materials/Structure  |
|-------------|----------------------|--|
| TE 630      | Permal/France        | E-glass fiber/epoxy laminate (90° woven tissue)  |
| ME 730      | Permal/France        | E-glass fiber/epoxy laminate (long fibers randomly distributed)  |
| CFK         | Lerc/France (Vendor) | HR-carbon fiber/epoxy laminate (90° woven tissue with orientated structure: 84 % in axial yarn, 16 % in transverse yarn) |
| Lexan       | General Electric     | Polycarbonate, not reinforced  |
| QE 22       | Fraunhofer/IFAM      | Magnesium with 20 % Saffil fibers ( $Al_2O_3$ ), planar isotropy   |
| WE 54       | Fraunhofer/IFAM      | Magnesium with 20 % Saffil fibers ( $Al_2O_3$ ), planar isotropy   |

Table 1: Used Materials

### 3 Quasistatic Investigations

#### 3.1 Pressure Tests with Specimens „Prestudy PEGASUS“

For a first approach we made static investigations with a model with the geometry of the sabot. In order to test different specimens under multiple conditions in the tensile testing-machine we had to replace the last brush-hole by a shoulder with the projected surface of the cylindrical boring. The pressure piston applies the total force on the shoulders. In figure 4 we can see a specimen after the test. As a boundary condition we put the specimen in a thick-wall steel tube which prevents the sabot of radial strain.

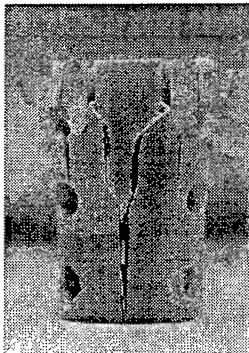


Figure 4: Specimen "Pressure-3" after the Test

The left diagram of figure 5 describes the quasistatic behavior of supported specimens. It is remarkable that lateral support increases the toughness to about twice the non-supported toughness (figure 5, right). Only little variation of curvature in the stress-strain curve has been observed. This means, and the appearance of the specimen allows the conclusion, that an internal delamination of the specimen occurs. Nearby the holes a little cracking has been observed. Globally seen, the specimen did not fail (figure 6).

The maximum pressure force was 250 kN, the machine's limiting force. So we only can estimate maximum endurable pressure to be 20% about the in figure 5 (left) shown.

The non-supported specimens are showing up to  $\epsilon > 2.3\%$  a curvature that seems like perfect plastic strain. A closer examination, however, reveals that buckling occurs. The inner-specimen forces (i.e. essentially the friction forces between matrix and tissue) are in equilibrium with the outer forces up to the moment where the specimen totally cracks.

In the railgun, the tube encloses the sabot with a little gap of 0.25 mm around it. The brushes support the sabot. This case correlates with the gun-tube-supported specimens. At the other end of the spectrum, the force in the pressure test was applied only on the shoulders. In reality it acts upon each brush so that we have

approached the worst case with the quasistatic tests.

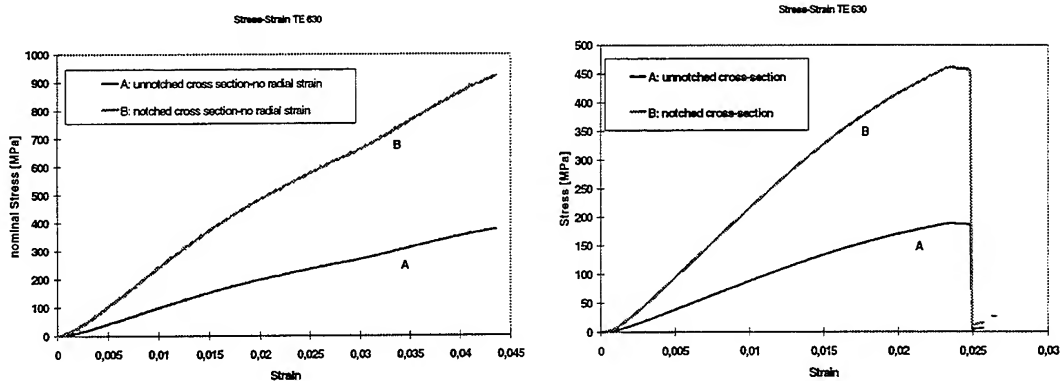


Figure 5: Stress-Strain Diagrams of notched Specimen, no radial strain in the left Diagram

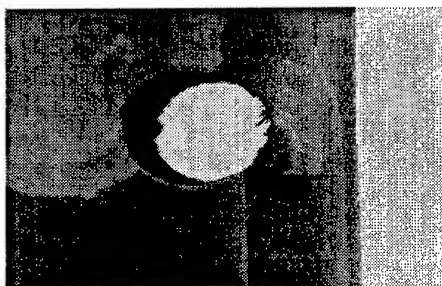


Figure 6: Specimen "Pressure-3" in detail

### 3.2 Results of Nonnotched Experiments

On the other hand the experiments were made with two different specimen-types: one notched with the brush's holes the other without them to study in detail the influence of the notches. From applications like e.g. screws and shafts [5], we know that holes, nicks and indentations influence the material's strength. On both sides of the holes resides the maximum of compressive stress. Figure 7 shows that the stress in the notched cross section is twice the stress in the unnotched cross-section. It also reveals, how important the stress concentration around the notches is. The curves represent an average stress. We know, like Lemmon and Blacketter [4] showed, that for laminates

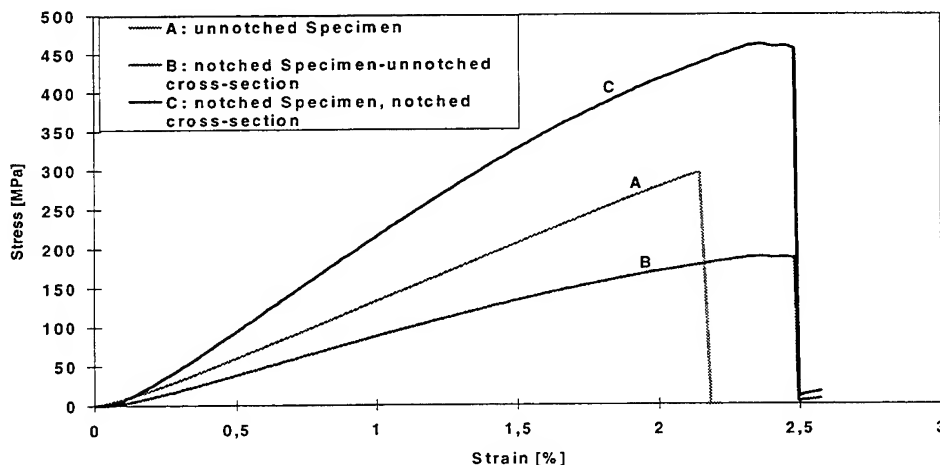


Figure 7: Strength Comparison between Notched and Unnotched Specimens

St. Venant's hypothesis only can be applied very far away from the application point of the forces.

With help of figure 7, we define a notch factor:

$$\delta = \frac{\sigma_{F,un}}{\sigma_{F,n}} \approx 1.7$$

where  $\sigma_{F,un}$  is the failure-stress of the unnotched and  $\sigma_{F,n}$  that of the notched specimen. It describes the influence of the local concentration of the stress. In our case, the unnotched specimen fails with a stress 1.7 times that of the notched specimen. Designing a projectile we must respect the stress concentration by assuming an average stress  $\delta$ -times higher than that calculated according to St. Venant's hypothesis.

### 3.3 Results of the Quasistatic Numerical Investigations

These examinations were made with the valuable help of Mr. Neumann from WIM (Wehrwissenschaftliches Institut für Materialuntersuchungen) in Erding/Germany. The laboratory disposes of the implicit code ANSYS for quasistatic calculus.

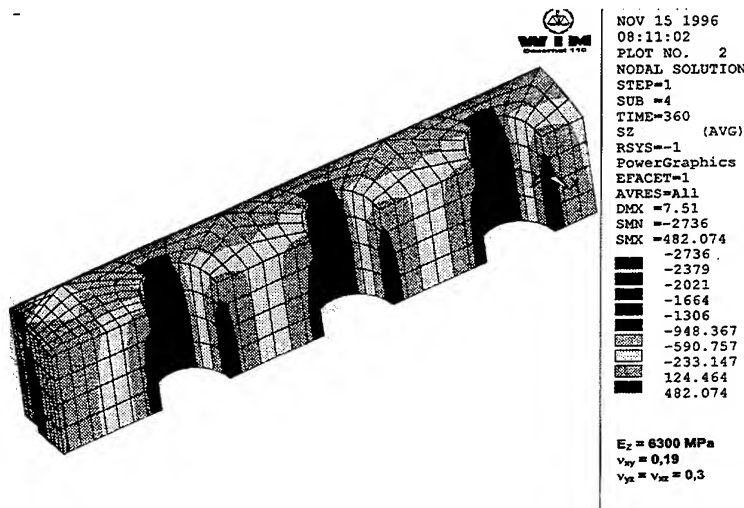


Figure 8: Model "Pressure-1" with Radial Strain

Figure 8 shows the stress  $\sigma_{zz}$  in MPa of a laterally non-supported specimen. The stress repartition correlates well with the stresses in the right diagram of figure 5.

## 4 Dynamic Examinations

Material behavior is a function of multiple variables. For dynamic investigations the strain rate is the most important one.

The accelerations in railguns drive the strain rates to values up to  $\dot{\epsilon} = 2000 \text{ s}^{-1}$ . The deformation passes from an isothermal to an adiabatic process. So, the internal energy increases very fast and in the case of extreme strains one can have a phase transition. In some experiments the projectiles do not survive. Besides a mechanical degradation also the following processes will have an influence on failure.

- The current causes a high temperature in the brushes. There could be a phase transition of the brushes' material from solid to gas-phases with a gain in volume. The „material gas“ cannot escape, so the gas-pressure cracks the sabot.
- The current heats the brushes and by thermal conductivity, convection and heat radiation it indirectly heats the sabot. Thus, the sabot has a loss in material toughness. The material is no

more strong enough to support the forces as more as the decreasing toughness occurs when the forces are reaching their maximum.

- The deformation work heats the sabot and the aforementioned effects will occur.

#### 4.1 Experimental Results of Split-Hopkinson-Pressure-Bar Tests

Aim of this investigation was to ascertain the matrix' influence of the toughness of the laminate. We know very little about the failure criteria of laminates for high strain rates. Gibson and Plunkett [2] made analytical and experimental efforts to find the internal damping and elastic stiffness of E-glass fiber-reinforced epoxy beams under flexural vibration. They have found out, that damping and stiffness are independent of amplitudes as long as they do not exceed the fracture strain amplitude. The matrix material fails in a brittle fashion under tension at a level governed by the tensile strength of the material and the strain concentration. For Gibson and Plunkett, fracture occurs for a specific to a material ratio of stress and strain. Their investigations were made in a frequency spectrum from 0 to 500 Hz.

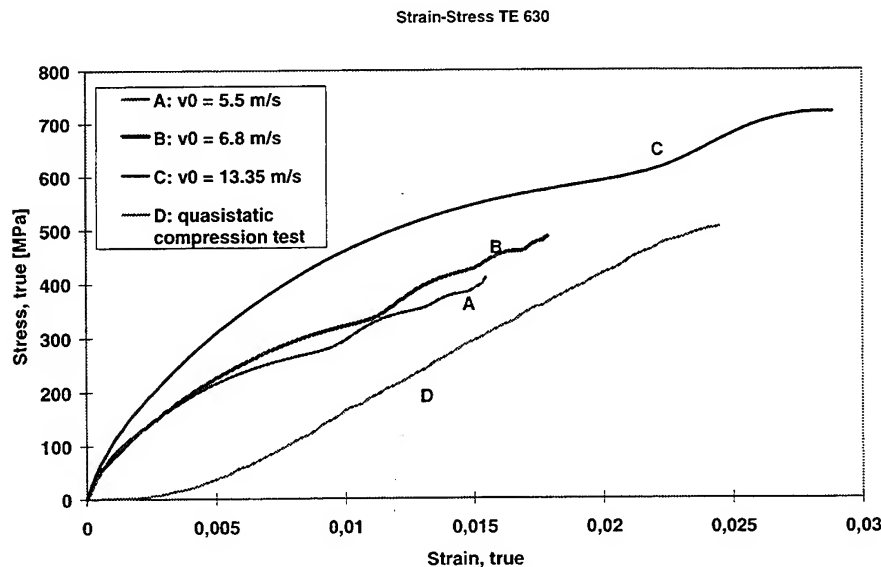
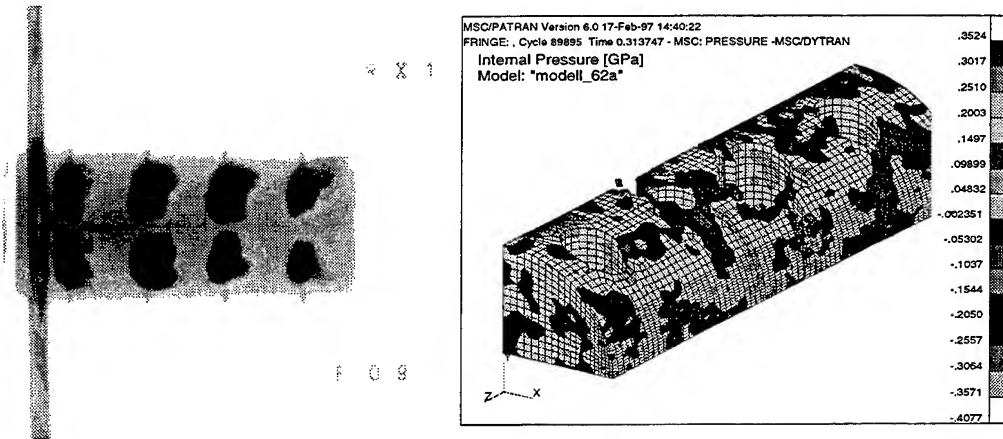


Figure 9: Hopkinson-Results for TE 630

One can establish that the dynamic strength is higher than the quasistatic (Figure 9) and it is a function of the initial strain-rate. The average strain-rate of the third test is  $\dot{\epsilon} \approx 900 \text{ s}^{-1}$ . The failure stress has a value of  $\sigma_F = 720 \text{ MPa}$  with a failure strain of near  $\epsilon_F = 2.4 \%$  (quasistatic:  $\sigma_F = 460 \text{ MPa}$ ,  $\epsilon_F = 2 \%$ ). We must remark, that only the specimen C and D are failing. The velocity of the Hopkinson-projectile is with  $v_0 = 5.5 \text{ m/s}$  and  $v_0 = 6.8 \text{ m/s}$  too low to crack the specimen A and B.

Furthermore the Hopkinson experiments affirmed the strain as main failure criterion. In static investigations stress and strain are, like for isotropic materials, coupled by HOOKE's law (in the elastic range of the considered material). Due to the viscosity of the matrix, the strain rises with a time delay to the stress. Thus stress and strain are no longer coupled by a linear function. The failure strain is a history function, that means, it is dependent upon the instantaneous strain-rate. The higher the strain-rate is, the higher the failure strain will be. So when the material fails, the stress is beyond the static failure stress. Experiments with real sabots have shown, that failure occurs a relatively long time after the stress has achieved its maximum.

#### 4.2 Comparison between Numerical Results of Model „modell\_62a“ and Experiment „Prestudy PEGASUS“



**Figure 10: Flash-X-Ray-Picture of Shot F09 of Prestudy PEGASUS in Free Flight(left)**

The calculation shown in figure 10 is based on the calculated force distribution of figure 3.

For numerical investigation we work with a 3D-FE code for transient use. The model, which was baptized „modell\_62a“, is constituted of about 70,000 finite elements with a general edge length of 0.7 mm. Only HEXA-elements were used. The time step of the calculation is given, as usual for explicit codes, by the program itself. As consequence of the explicit code and an anisotropic material model (a classical homogenization formulation), many problems in view of a numerically stable and useful analysis are encountered.

Impellusco and Murakami [3] alleviated these difficulties by setting different switches in the program (like e.g. artificial viscosity and hourglass damping) and above all by a fine meshing. According to the Users' Manual for MSC/DYTRAN, extreme cases of hourglassing are caused by coarse meshes. The only solution is to refine the meshes. Thus the calculation time increases.

In order to save computing time, only a quarter of the symmetrical model was built. The setting of symmetrical boundary conditions allows this measure.

The calculation time of the model shown in figure 12 to time  $t = 0.31$  ms, was about 100 hours on an Alpha 400 workstation.

Easily we can see in figure 10 that relatively big parts of the sabot, mainly around the second boring failed. The borings are counted from the rear of the sabot and the shot direction is parallel to the coordinate frame's z-axis.

If one compares the two pictures of figure 10, one reveals a big gap between numerical and experimental results for the prestudy PEGASUS and its FE-model „modell\_62a“. Furthermore the calculation is based, as aforementioned, on the calculated forces of figure 3, where the calculated forces only correlate in the slope with the measured force. This points out, that the real projectile in the shot F09 supported higher forces than the model. Nevertheless the first one did not fail.

So, the used material model is yet not elaborated enough to simulate in detail the mechanical effects of fiber reinforced laminates under dynamic loading during acceleration in railguns.

## 5 Summary and Conclusions

We have shown that the quasistatic behavior of anisotropic materials depends on the boundary conditions. With the boundary condition of no radial strain, we were able to achieve more than twice the compression strength of a unsupported specimen. There are some internal cracks, but globally seen, the supported specimen do not fail.

Also nicks, indentations and holes have a big influence on the material strength, because, like for isotropic materials too, nearby these geometric discontinuities maximal values of stress will be reached. It is a good approximation to design a sabot with an average stress of  $\delta$ -times higher of that, which would occur in an unnotched cross section.

The dynamic investigations have elucidated, that the material toughness increases with an increasing strain rate.

A future work will be the elaboration of material models of laminates under dynamic loading. One way to do so is to simulate Split-Hopkinson-Pressure-Bar experiments step by step. This progression will reveal, until comparing the numerical and the experimental results, the nexus of matrix, fiber and boundary conditions.

## 6 References

- [1] Bruck, H.A.; Epstein, J.S.; Perry, K.E. Jr.: Dynamic Characterization of Short Duration Stress Pulses Generated by a Magnetic Flyer Plate in Carbon-Fiber/Epoxy Laminates, 1n: 1995 Society for experimental Mechanics Spring Conference, Grand Rapids, June, 12-14, 1995
- [2] Gibson, R.F.; Plunkett, R.: Dynamic Mechanical Behavior of Fibre Reinforced Composites: Measurement and Analysis, in: Journal of Composite Materials, Vol. 10, No. 4, pp. 325-351, 1976
- [3] Impelluso, Th.J.; Murakami, H.: A Homogenized Continuum Model for Fiber-Reinforced Composites and its Applications, in: Zeitschrift für Angewandte Mathematik und Mechanik (ZAMM), Vol. 75, No. 3, pp. 171-188, 1995
- [4] Lemmon, R.K.; Blacketter, D.M.: Stress Analysis of an Orthotropic Material under Diametral Compression, in: Experimental Mechanics, Vol. 36, No. 3, September 1996, pp. 204-211
- [5] Niemann, G.: Maschinenelemente Band I, Konstruktion und Berechnung von Verbindungen, Lagern, Wellen, Berlin et al.: Springer, 1981
- [6] Peter, H.; Wenning, W.; Scherrer, A.: Analyse des Elektromechanischen Verhaltens eines Schienenbeschleunigers, ISL-Report No. RT 504/93, ISL Saint-Louis, 1993
- [7] Puck, A.: Zur Beanspruchung und Verformung von GFK-Mehrschichtverbund-Bauelementen, Teil 1: Grundlagen der Spannungs- und Verformungsanalyse, in: Kunststoffe, Bd. 57, Heft 4, 1967
- [8] Sun, C.T.; Potti, S.V.: Modelling of Dynamic Penetration of Thick Section Composite Laminates, in: 36th AIAA/ASME/ASCE/AHS/ASC Structures, Structural Dynamics and Materials Conference and AIAA/ASME Adaptive Structures Forum, Vol. 1 No. 95-1203, pp. 383-393, 1995
- [9] Wey, J.; Lehmann, P.; Peter, H.: Analyse des premiers résultats obtenus avec le lanceur de la préétude PEGASUS; ISL-Report No. RT 503/94, ISL Saint-Louis, 1994

## Experimental study of the current distribution in a multi-armature projectile

A. - G. SCHMITT<sup>\*</sup>, R. CHARON, D. ECKENFELS, F. HATTERER and J. WEY

French-German Research Institute of Saint-Louis

5 rue du Général Cassagnou - F 68301 SAINT-LOUIS Cedex - France

**Abstract** --- In the powder guns, the accelerating forces are applied through the sabots mainly near the rear end of the projectile. Consequently we can observe a tension at the rear and a compression at the front. That leads to some difficulties when accelerating long rods penetrators characterized by  $L/D \geq 30$  (buckling). An advantage of the rail-guns is the possibility to distribute the current, and as a result the accelerating forces, along the projectile. The distribution can be achieved with a multi-armature sabot, the impedance corresponding to each armature being determined to assume ideally the equality of the space and time distribution of the forces.

In order to study that distribution of the forces, we have made some measurements of the current distribution in a multi-armature projectile in a stationary experiment. It has been made by injecting a current pulse whose peak intensity ranged from 10kA to 50kA, with a rise time of about 240  $\mu$ s. First, we have analyzed the current distribution between two armatures made of a copper-cadmium alloy. Each armature was made of metallic fiberbrushes, in order to ensure a good contact between the rails and the projectile. We obtained a current distribution of 70% of the total current in the rear armature and 30% in the front one. The study of the distance influence showed the rise of the delay between the two currents when the distance between the two armatures increases. Next, in order to improve the distribution, the first armature was replaced with iron fiberbrushes, and we observed that the current distribution was reversed (30% of the total current in the rear armature, and 70% in the front one). Finally, a projectile with four brushes armatures has been accelerated in our EMA3 facility, with a peak of current of 540 kA, and the results were compared to the numerical simulation.

### I. INTRODUCTION

The railguns offer an advantage compared to the powder guns that is the possibility to distribute the accelerating forces along the projectile. By this way, we can avoid some mechanical stresses that can appear in the projectile during the acceleration when the forces are only applied at the rear side. In latter case, some strains can be observed, like bending or buckling, especially when accelerating long rods penetrators with fineness ratios greater than 30.

To distribute the forces and the current along the sabot, we have divided it in several armatures. By determining the right impedance for each of them, our aim is to achieve the equality of the space and time distribution of the forces.

We have started this study with a projectile made of two armatures. In the first experiment, which served as reference, the projectile and the rails were milled in the same piece of copper to have a perfect contact. Next, the armatures were made of copper fiberbrushes which ensure the good contact at the rail-projectile interfaces. The influence of the distance between the two armatures was studied too. The third test was led with two different materials for the fiber brushes. Next the projectile was made of four fiberbrushes armatures. It has been tested in a dynamical experiment, and the results were compared to the numerical simulation.

### II. PROJECTILE MADE OF TWO ARMATURES

We have chosen to start this experiment with a projectile made of two armatures because we wanted to analyze the current distribution and the contact between the rails and the projectile, when the armatures are made of fiberbrushes, for a simple case. Figure 1 shows a scheme of the facility for the first part of this study.

The experiment was made with a square bore railgun. The rails made of copper have 365 mm in length and a 15 mm x 15 mm section. The caliber is 15 mm x 15 mm. The power supply provided a current pulse reaching a maximum of 50 kA for a load voltage of 10 kV. For each step of the experiment, we have measured the current going through the two armatures and the total current with Rogowski probes, the voltage between the



rails at the two armatures and the muzzle voltage [1]. We call the nearest armature to the power supply A1, and the other one A2. The corresponding currents and voltages are noted  $I_1$ ,  $I_2$  and  $I_{tot}$ , and  $U_1$ ,  $U_2$  and  $U_{muzz}$ .

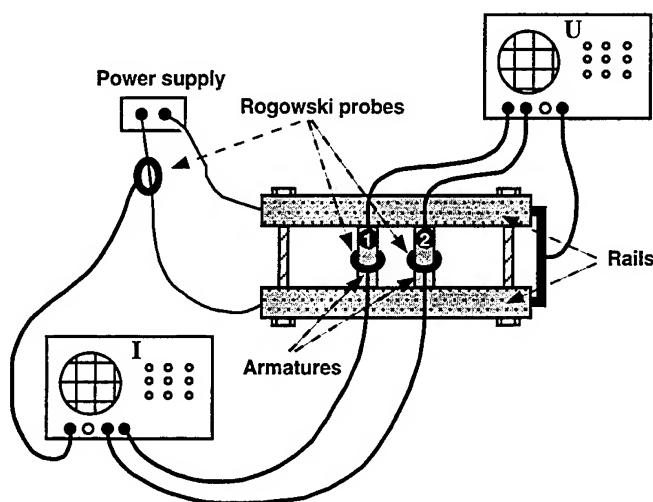


Figure 1 Scheme of the facility with two armatures at rest

#### A. Perfect contact

In order to get some reference results, the first experiment was done with a facility in which the contact between the rails and the two armatures is perfect. The best solution to obtain a perfect contact was to mill the rails and the projectile in the same piece of copper. The size of the two armatures were chosen so that the caliber of the railgun is equal for all these experiments (15 mm x 15 mm), and the section of each of them is the same as the total one of an armature made of fiberbrushes (see §II.B. ). Table 1 gives the current distribution in the two armatures for different current pulses. We observe a constant ratio of 83.5% of the total current in A1 and 16.5% in A2 at the time of the peak of the total current for the five different load voltages.

| Load voltage                        | U=2000V     | U=4000V     | U=6000V     | U=8000V     | U=10000V    |
|-------------------------------------|-------------|-------------|-------------|-------------|-------------|
| $I_{tot}$ max (0.24 ms)             | 9.6 kA      | 19.4 kA     | 29.5 kA     | 39.4 kA     | 49.9 kA     |
| $I_1$ max (0.24 ms)                 | 8.0 kA      | 16.2 kA     | 24.8 kA     | 33 kA       | 42 kA       |
| $I_2$ max (1.4 ms)                  | 2.3 kA      | 4.8 kA      | 6.8 kA      | 9.8 kA      | 12.3 kA     |
| % ( $I_1/I_{tot}$ - $I_2/I_{tot}$ ) | 83.5 - 16.5 | 83.5 - 16.5 | 83.5 - 16.5 | 83.5 - 16.5 | 83.5 - 16.5 |

Table 1 Current distribution in the two armatures for five different load voltages ( perfect contact)

#### B. Fiberbrushes contacts

Then we reproduced the same measurements with two armatures made of metallic fiberbrushes [2]. Each armature is made of two brushes enclosed in the same body in glassfiber reinforced plastic (GRP) as shown in figure 2. The material of the fiberbrushes is a copper-cadmium alloy. Each brush has 5 mm of diameter, and we assume that 80% of the volume is filled with the metallic fibers. The distance between the two armatures is 10 mm.

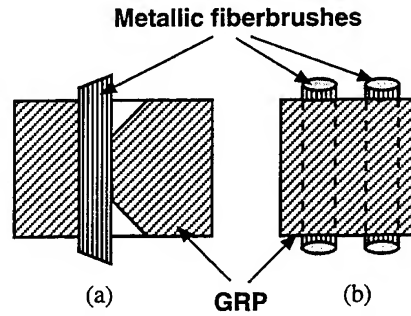


Figure 2 Schemes of an armature with two fiberbrushes (section (a) and front view (b))

In table 2, we can observe that the ratio of current in A1 and A2 is still constant for each load voltage, but different from the case of a perfect contact. Indeed, we get now about 67% in A1 and 33% in A2 at the time of the peak of the total current. Compared to the perfect contact case, the current distribution has changed and more current flows in A2. Figure 3 shows the current distribution between two fiberbrushes armatures for a load voltage of 2 kV.

| Load voltage                        | U=2000V | U=4000V | U=6000V | U=8000V     | U=10000V |
|-------------------------------------|---------|---------|---------|-------------|----------|
| $I_{tot,max}$ (0.24 ms)             | 9.7 kA  | 19.5 kA | 29.8 kA | 39.9 kA     | 50.4 kA  |
| $I_1$ max (0.24 ms)                 | 6.5 kA  | 13.2 kA | 19.8 kA | 26.9 kA     | 33.8 kA  |
| $I_2$ max (0.64 ms)                 | 3.9 kA  | 8.0 kA  | 12.2 kA | 16.0 kA     | 21.5 kA  |
| % ( $I_1/I_{tot}$ - $I_2/I_{tot}$ ) | 67 - 33 | 67 - 33 | 67 - 33 | 66.5 - 33.5 | 66 - 34  |

Table 2 Current distribution in the two armatures for five different load voltages ( fiberbrushes armatures)

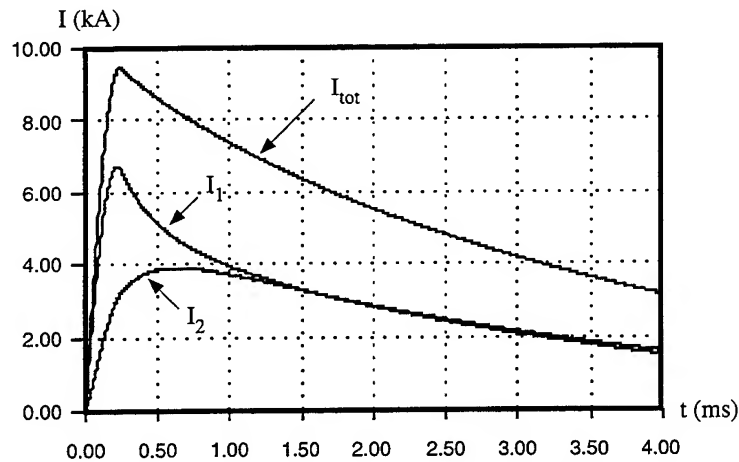


Figure 3  $I_1$ ,  $I_2$  and  $I_{tot}$  for a load voltage of 2kV (case of fiberbrushes armatures)

The impedance of the circuit changed because a contact resistance appears at the interface rail-projectile [3]. From  $I_1$  and  $U_1$  we have deduced an inductance  $L_1$  in A1 of about 8.5 nH for the case perfect contact, and 7.7 nH for the case fiberbrushes. These results lead to the resistance  $R_1$  of A1 ( $R_1 = (U_1 - L_1 dI_1/dt)/I_1$ ).

In the perfect contact case,  $R_1$  goes from about 15  $\mu\Omega$  at the peak of current to 8  $\mu\Omega$  when the current is totally diffused into the armature. In the case of fiberbrushes armatures,  $R_1$  goes from 30  $\mu\Omega$  to 19  $\mu\Omega$ . We assume that in the case of fiberbrushes armatures,  $R_1$  is the sum of the bulk resistance of the armature and both contact resistances at the two rail-projectile interfaces. Since in our study the bulk resistance of a fiberbrushes arma-

ture is the same as the one in the perfect contact case, we can write :  $R_{\text{fiber}} = R_{\text{perfect}} + R_{\text{contact}}$ . We deduce from these results that  $R_{\text{contact}}$  goes from  $15 \mu\Omega$  to about  $10 \mu\Omega$  when the current diffusion is achieved (see fig. 4). It appears that  $R_{\text{contact}}$  is a quantity that cannot be neglected because its value is in the same range as the resistance of the armature.

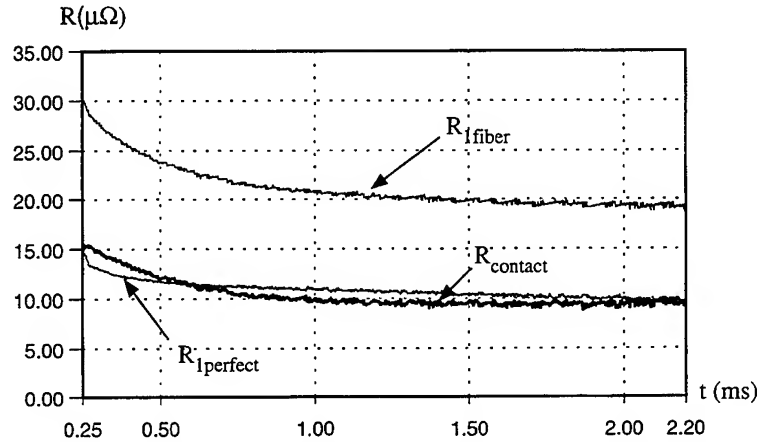


Figure 4 Resistance in Al in the case of a perfect contact ( $R_{\text{perfect}}$ ), resistance of Al and contact resistance only in the case of fiberbrushes ( $R_{\text{fiber}}$  and  $R_{\text{contact}}$ ).

### C. Distance influence

The same measurements were made for several distances between the two armatures : 15 mm, 20 mm and 25 mm. Figure 5 compares the four different  $I_1$  curves measured for a load voltage of 10 kV, and figure 6 compares the four corresponding  $I_2$  curves. On figure 7, we can see the variation of the peak of current in both armatures versus the distance between them. As we could expect, when increasing the space between the armatures, the inductance in the circuit increases too ( $L=L'd$ ,  $L'$  : inductance gradient of the rails,  $d$  : distance between the armatures). So, the current grows in A1 and drops in A2 when the distance increases. Another consequence is that it introduces an increase of the delay of the current in A2. Therefore, the greater the distance between the armatures, the later the peak of current in A2 is in comparison with the one in A1. So, in order to get a good distribution of the current in a multi-armature projectile, it is better to reduce the distance between the armatures.

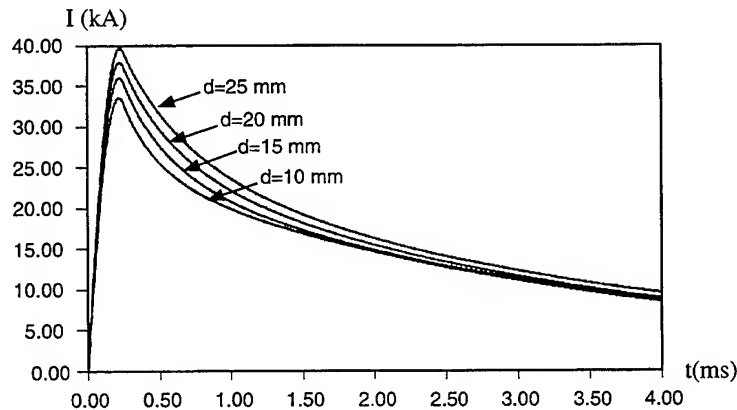


Figure 5  $I_1$  for a distance of 10, 15, 20 and 25 mm between both armatures

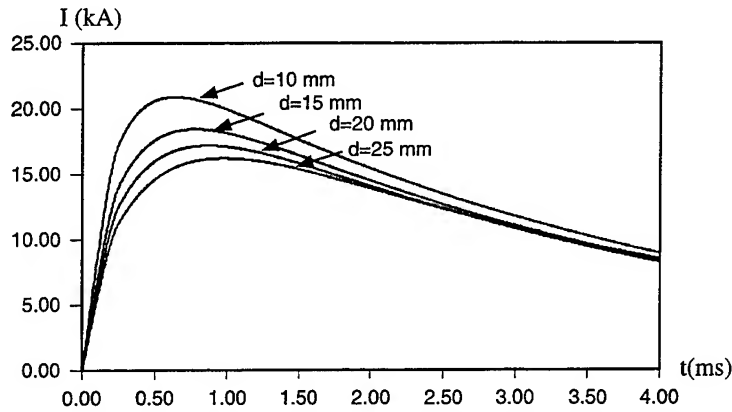


Figure 6  $I_2$  for a distance of 10, 15, 20 and 25 mm between both armatures

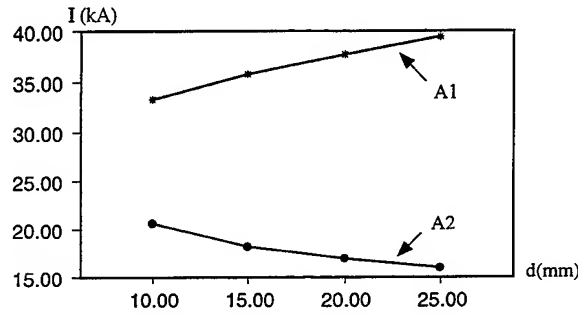


Figure 7 Variation of the peak of current in A1 and A2 versus distance

#### D. Two armatures in different materials

In order to study the influence of the resistivity on the current distribution, we have replaced A1 with an armature whose fiberbrushes are made of iron. By this way, the resistance of the first armature is now higher than the one of A2 ( $\rho_{\text{iron}} = 10.1 \cdot 10^{-8} \Omega\text{m}$ ,  $\rho_{\text{Cu-Cd}} = 2.0 \cdot 10^{-8} \Omega\text{m}$ ). Therefore, the first armature has a  $57 \mu\Omega$  resistance and the second has a  $8 \mu\Omega$  resistance.

The same measurements as before were made and table 3 gives the results for five different load voltages.

| Load voltage                                    | U=2000V     | U=4000V     | U=6000V     | U=8000V | U=10000V    |
|---|-------------|-------------|-------------|---------|-------------|
| $I_{\text{tot,max}} (0.24 \text{ ms})$          | 9.0 kA      | 19.2 kA     | 29.5 kA     | 40.1 kA | 50.7 kA     |
| $I_1 \text{max} (0.16\text{ms})$                | 2.9 kA      | 6.4 kA      | 9.7 kA      | 13.2 kA | 16.3 kA     |
| $I_2 \text{max} (0.39\text{ms})$                | 7.1 kA      | 15.1 kA     | 23.3 kA     | 31.8 kA | 40.0 kA     |
| % ( $I_1/I_{\text{tot}} - I_2/I_{\text{tot}}$ ) | 26.6 - 73.4 | 28.4 - 71.6 | 26.7 - 73.3 | 26 - 74 | 25.8 - 74.2 |

Table 3 Current in the two armatures for five different load voltages when A1 is in iron and A2 in Cu-Cd

In this new case, we can observe that the current ratio in A1 and A2 is still constant for each load voltage, but is reversed compared to the two previous cases. Indeed, now there flows more current in A2, about 73% of the total current at the time of the peak, than in A1, in which flows about 27% of the total current. Figure 8 shows the total current and the current distribution for a 2kV load voltage.

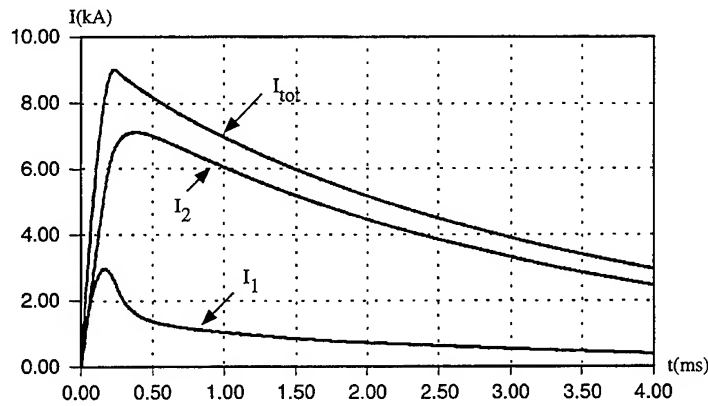


Figure 8  $I_1$ ,  $I_2$  et  $I_{tot}$  for a load voltage of 2kV

The forces  $F_1$  and  $F_2$  applied on the two armatures are the Lorentz forces :

$$F_1 = I_1 l \times (B_1 + B_{2,1}) \text{ and } F_2 = I_2 l \times B_2$$

$B_i$ ,  $i = 1, 2$  : magnetic flux density in A1 and A2

$B_{2,1}$  : magnetic flux density in A1 due to  $I_2$

$l$  : width of the armatures (caliber)

It appears that the forces in the two armatures can't be equal when  $I_1 = I_2$ . If we assume that the rails are two infinite wires (we neglect the skin effect and the proximity effect), in which flow currents in reversed direction, we obtain  $F_1 = F_2$  when  $I_1$  is about 38% of the total current and  $I_2$  is about 62% [4]. Compared to the case of A1 made of iron and A2 made of a copper-cadmium alloy, we note that we obtained a current distribution close to this result.

### III. PROJECTILE MADE OF FOUR ARMATURES

#### A. Experiment

The projectile in this part of the study is made of four pairs of metallic fiberbrushes made of a copper-cadmium alloy. The projectile has been launched with our EMA3 facility [5], which is a square bore railgun of 15 mm x 15 mm of caliber and has a DES power supply. The rails are 1.5 m long. The eight brushes have the same dimension as the ones described in the paragraph II.B., and the body is made of (GRP).

Figure 9 shows the current pulse injected in the railgun. The shot-out occurs at about 2 ms.

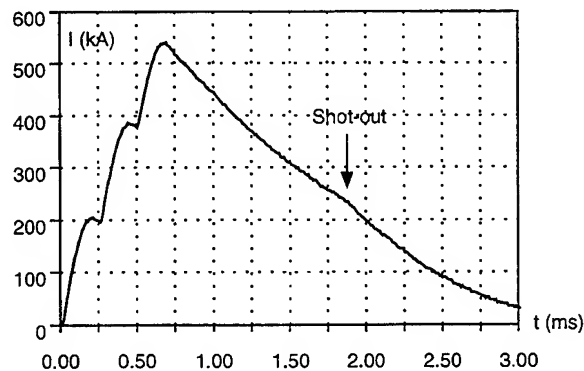


Figure 9 Current pulse injected in EMA3 facility

Figure 10 presents an X-Ray photograph of the projectile at the muzzle of the railgun. The shot direction goes from the left to the right. We call the nearest armature the power supply A1, the next A2, A3 and A4. We can observe on the photograph that A1 has melted during the launch, so there is no more contact with the rails.

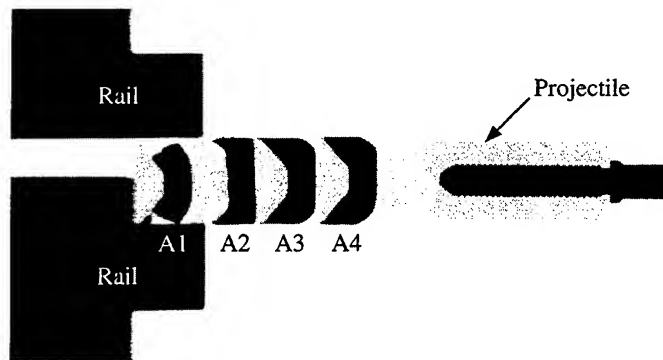


Figure 10 X-Ray photograph of the projectile at the shot-out

### B. Modelisation

We have modelised this experiment (see fig. 11 for the model of the quarter of the projectile) [6]. We have taken into account the contact resistance at the rail-projectile interface and the thermal effect [7]. In the model, we have defined the material of the first layer of element of each brush with a resistivity deduced from the contact resistance. Figure 12 shows the current distribution in the four armatures. We have obtained 60% of the total current in A1, 20% in A2, and about 10% in A3 and A4 at the time of the peak of the total current.

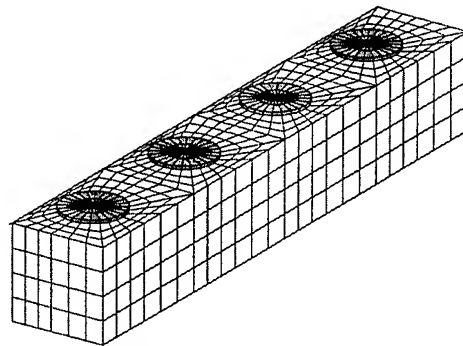


Figure 11 Model of the quarter of the projectile

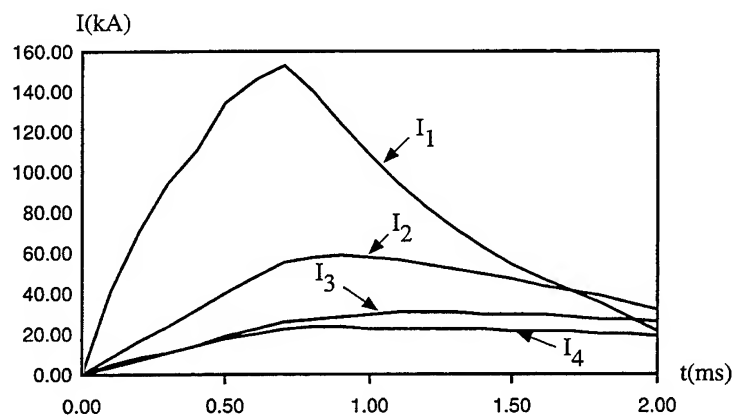


Figure 12 Current distribution in A1, A2, A3 and A4 (modelisation)

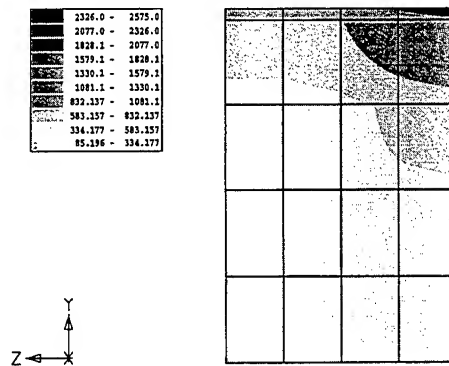


Figure 13 Temperature distribution in a cross-section of A1 at 2 ms (launch direction is Z-direction)

We have also calculated the final temperature in each brush (see fig. 13). We obtained 2000 °C, far over the melting point of copper, in a few elements of the first layer of elements of A1 (upper right part of fig. 13).

This high temperature, only due to the flow of current through the brush, lead to the melting of A1 at the rail-projectile interfaces, that explains the loss of contact of this armature that we observed on the X-Ray photograph (fig. 10).

#### IV. CONCLUSION

We have seen that for two copper-cadmium fiberbrushes armatures 70% of the total current flows in the rear armature at the time of the peak of the total current and 30% in the other one. This current distribution does not allow to have the same forces in both armatures. To improve the force distribution, we have replaced the rear armature with iron fiberbrushes whose resistance is higher than the one of a copper-cadmium armature. The latter case gave about 30% of the total current in the rear armature and 70% in the front one at the time of the peak of the total current. This result is close to the one we want to achieve to obtain the equality of the forces, that is about 40% in the rear armature and 60% in the front one. However, it remains a problem to solve that is the delay between the forces applied on each armature. We can decrease this delay in reducing the distance between the armatures, but we will never be able to suppress it. We can also increase the number of armatures. By this way, we decrease the delay, but the choice of the right material for each armature will be all the more difficult.

#### REFERENCES

- [1] D. Eckenfels, "Mesure de courant à l'aide de sondes sensibles au champ magnétique", CNAM report, 1994.
- [2] H.Peter, R.Charon, J.P. Chabrerie, "Metallic railgun armatures", Proceedings of the 5th European Symposium on EML Technology, Toulouse, France, 1995.
- [3] R. Holm, "Electric contacts, theory and application", Springer-Verlag, 1967.
- [4] P.Lehmann, V.Schirm, "Premières réflexions sur la conception d'un sabot pour perforant cinétique accéléré dans un lanceur électromagnétique à rails", ISL Report S-R 911/93, 1993.
- [5] H.Peter, R.Charon, C.Gauthier, J.Wey, W.Wenning, "Etudes de projectiles alliant charge utile, sabot et pont de courant pour lanceur à rails. Partie expérimentale", ISL Report RT 508/96, 1996.
- [6] B.E.MacNeal, "MSC-EMAS Modelling guide", The MacNeal Schwendler Corporation, June 1991.
- [7] A.-G.Schmitt, "Simulation 3D à éléments finis de l'influence de l'effet de température sur la répartition du courant dans un projectile équipé de brins filamenteux", ISL Report, to be published.

## METALLURGICAL EXAMINATION OF 90mm ARMATURES RECOVERED AFTER FIRING

G.M.G. Hainsworth and D.G. Jones  
DRA Fort Halstead, Sevenoaks, Kent. UK.

### Abstract

DERA has a unique capability to recover armatures fired from the Kirkcudbright EML facility. This paper describes a metallographic study of sections of 90mm armatures recovered from the range. Correlation with Finite Element predictions is demonstrated to a reasonable degree. The information gained from these experiments has proved to be invaluable in the design of armatures in the quest for reducing their parasitic mass.

### 1. Introduction

The DERA electromagnetic gun facility[1] launches projectiles over open moorland. This enables armatures to be recovered almost free from impact damage, by a search party, with a success rate of about 70%. Typically they are found lying on top of the grass, 500 - 900 metres down range, close to the line of firing. The armatures remain at a temperature well above ambient for a period of several hours: attempts are being made to improve the recovery, particularly of smaller armatures, using infra red detection techniques. Examination of these armatures has proved to be a valuable tool in helping to understand the in-bore behaviour.

The 90mm armatures are to the basic C type base push design, used to launch APFSDS rounds. They are machined from extruded aluminium alloy bar, either in A6082 or A7075, and heat treated to the T6, fully aged condition. Armatures examined in this paper were fired at a velocity of  $\sim 1500\text{msec}^{-1}$  with a total shot mass of 3.5kg. The legs are orientated horizontally across the barrel. The peak current is of the order of 2MA, corresponding to an acceleration of 50kGee. The residence time in the barrel is less than 10ms.

The recovered 90mm armatures closely resemble the original component, the only obvious damage apart from mild discoloration, being erosion on the outside. Hard anodising further preserves the condition of the non-contact surfaces. The bulk metal loss is of the order of 10%, corresponding to the removal of a uniform layer 4mm thick from the contact faces.

Figure 1 shows a recovered armature identifying characteristic features including:

- Severe erosion on the outer contact faces, with little or no damage on the inner surface. A thin layer of metal, apparently deposited from a liquid, accumulates in the root region.
- The erosion is much more severe on the outer fingers, as indicated by the middle finger standing proud on the inside surface compared with the adjacent parts.
- The slots between the fingers at the base region are squeezed together showing that considerable circumferential compressive forces are present in the armature. Inter-slot erosion occurs at the tips, probably due to the effects of plasma leakage.
- There is no evidence that one side of the armature is more severely affected by the launch than the other - both sides are equally damaged.
- The armature is up to 2% undersize on diameter compared with the bore when recovered.
- A fluted region forms at the edge of the armature corresponding to the edge of the rails. This extra, localised erosion is almost certainly a consequence of current flow concentrated in this region.



- Various textures form on the contact faces. Some consist of deep score marks believed to have formed as the result of unlubricated contact with the rails. Other examples exhibit marks on a much finer scale and consist of micro-ripples radiating in random directions. This effect is believed to be the result of molten metal being driven by magnetic forces. Tear drop shaped divots have been observed on some armatures. These bear a strong outward similarity to the gouges found in rails [2] except that they are reversed - with the pointed end aligned towards the muzzle.
- The legs stretch in the longitudinal direction by up to 7%. This could be a consequence of the inertial launch load applied to the legs, noting that most aluminium alloys have a very low strength at temperatures above 150°C.
- Incipient melting at the base of the outer fingers occurs at high firing energies.
- The base of the armature is unaffected by the launch although a small degree of deformation is usually found in the lip region.

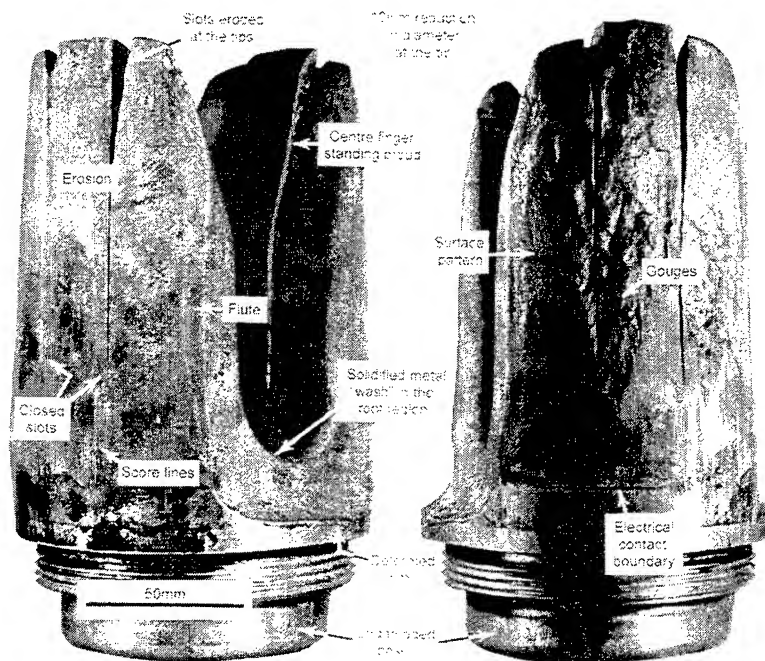


Figure 1. Example of recovered armature, showing key features resulting from launch.

## 2. Metallography

Longitudinal and transverse sections have been prepared through a number of armatures. Aluminium alloy A7075 in the T6 condition is very sensitive when etched in diluted Kellers reagent, and heated regions, indicative of high current flow, are rapidly blackened. The narrowness of the etched zones, for example, beneath the contact faces, indicates that the reduction in the resolution of the etching effect due to thermal diffusion after launch is minimal. Attempts to correlate the etching response with short term (2-4 minutes) annealing experiments have not been successful. However, the cessation of dark etching effects at the tips of regions known to liquate suggests that the dark etching response in A7075 diminishes at temperatures above 475°C. Modelling has shown that the maximum temperature in the armature drops from the melting point of aluminium to 350°C within 1 second of firing. Alloy A6082 is much less visually responsive to the etching effect in this respect. Thus, although A6082 is the preferred tactical choice because of its superior electrical conductivity, A7075 has considerable advantages in being able to readily reveal the thermal effects of firing.

Metallographic examination, figure 2, shows that the heating effect is concentrated in the outer fingers. Heating is confined to the surface skin in the root and beneath the contact faces. However, a major heating effect occurs directly across the base of the outer fingers. Liquation melting effects in the root have been described previously [3].

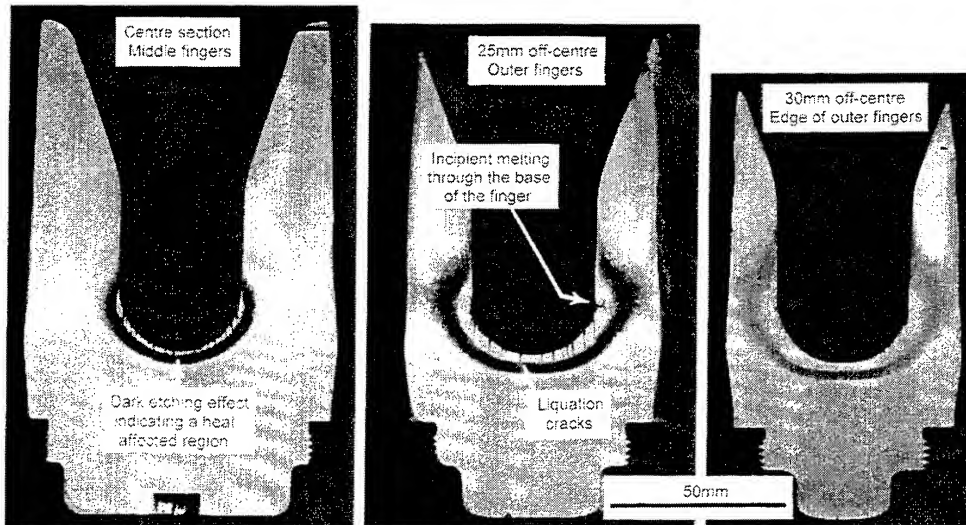


Figure 2. Sections through a recovered 90mm armature, showing the dark etching effect.

Etching effects in transverse sections show that the heating effect is concentrated in the corners of the outer fingers on the armature demonstrating that the passage of current is primarily from the corners of the rails and straight across the outer edge at the base of the armature. Under extreme firing conditions, particularly in smaller armatures, this region can fail as the result of intergranular melting. No heating effects sufficient to cause changes in the etching behaviour were found in the centre finger. This also accounts for the fact that there are minimal magnetic forces driving the central fingers outwards to maintain contact with the rail. The base is also unaffected by heat flow. The slits present a significant barrier to thermal flow and probably to the passage of current.

Hardness surveys have confirmed that the dark etching regions are significantly softer than the original material. Extensive areas have been discovered which remain unaffected and are regions where weight reduction measures will be addressed. A pattern of similar variations in hardness has been found in armatures manufactured from A6082. It is of interest that the hardness values measured in the dark etching regions, ~135HV, correspond to those developed in laboratory samples heat treated at 300°C. However, the test samples did not etch darkly. The reason for this difference in behaviour is currently under investigation.

The surface skin present in the root region of the armatures was found to be very porous, particularly in the A7075 armatures, and loosely adherent; no metallurgical bond had formed with the underlying metal. Qualitative x-ray analysis showed that the film was not enriched in solute elements from the aluminium alloy and therefore was unlikely to have originated from incipient melting. The films on the copper-free A6082 armatures, were slightly enriched with copper, suggesting an interaction had occurred with the rail. The skin was believed to have been deposited from plasma generated molten metal and condensed onto the armature at muzzle exit.

Sections through gouges in the armature showed that plastic deformation had occurred in the underlying metal, suggesting that they had formed by mechanical effects similar to that observed on rails. Any further comparison was difficult because it was thought that most of the gouge detail had been eroded between the time of formation and muzzle exit.

### 3. Modelling

Armature modelling is performed using MEGA, a coupled Electromagnetic-Thermal Finite Element code [4,5]. The technique has the capability not only of showing the current and temperature distribution but also the magnetic field and elemental forces. Solving is performed in two phases. The first runs from time zero to muzzle exit. Current then rapidly decays to zero and the solve continues to 1.3 secs, with a larger time step. It has long been known that thermal diffusion is of no significance during launch, but may be of some interest afterwards. At the point of muzzle exit, the temperature distribution throughout the armature varies from ambient to the melting point of aluminium. The second phase enables determination of whether this situation is maintained for milliseconds or minutes, which may have some bearing on metallographic effects.

Although MEGA has the capability to model velocity effects, experience has shown that standstill models bear a closer resemblance to reality. Velocity models predict severe current concentration at the rear of the legs. Similar results have been demonstrated by other codes. This theoretical effect may be counteracted by molten metal removal as the armature moves. Until we have a better understanding of the conditions at the contact surface and can incorporate these into the model, velocity effects will be ignored.

The complex geometry of round bore armatures requires the use of automatic mesh generation. At present, our experience suggests that this has not yet developed to a level satisfactory for these models. Instead, a square bore approximation is used, which can be meshed manually. In the case of 90mm armatures, this is not too far from the true geometry. Predictions should therefore be reliable in all areas except the contact face. The loss of metal due to melting and evaporation adds a further complication to the analysis in this region.

The modelling work has confirmed the temperature distribution shown by metallographic studies, figure 3. Of particular interest is the region in the root which is predicted to melt, and the hot zone at the base of the fingers. The model does not predict the relatively low current flow in the middle fingers which is believed to be a consequence of the square bore approximation adopted in the analysis. Additionally, in practice, the greater compliance of the outer fingers (because of their smaller cross section) ensures a better contact with the rail compared with the middle fingers. The electrical conductivity of the alloy has been shown to exert a significant influence on the local thermal stress. The role of the slots in modifying the heat flow can be demonstrated.

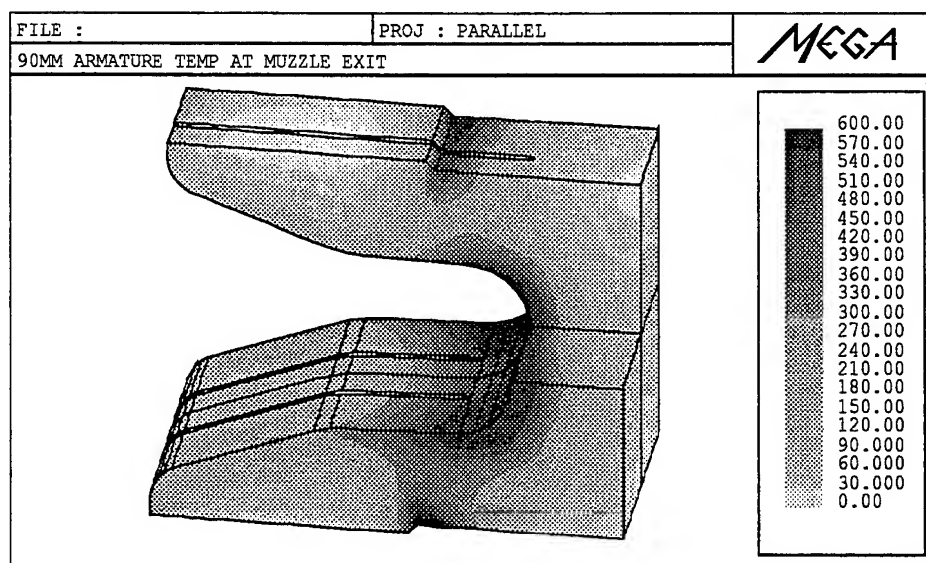


Figure 3. Armature model, showing contours of temperature at muzzle exit.

#### 4. Improvements in design

Armatures must have the capacity to carry the current whilst in-bore, but at the same time contribute the minimum parasitic mass to the launch package. Combined modelling and metallographic analysis has shown that large volumes within the present design are electrically redundant. It may be possible to reduce the mass by up to 40% without adopting sophisticated materials or manufacturing techniques. The insertion of high conductivity copper alloys into critical areas will reduce heating effects and thereby increase the current carrying capacity. Simple designs incorporating copper inserts manufactured by friction welding have been constructed and will be fired in the near future. Structural analysis of modified designs will need to be performed, to ensure mechanical integrity under launch forces.

#### 5. Conclusions

Recovered armatures contain valuable information which highlights many potential design improvements. The temperature distribution after launch, which is closely matched by that predicted by computer modelling, can be confirmed. Hence areas relatively free from electrical loading have been identified which should lead to a significant reduction in the parasitic mass of the shot. Furthermore the insertion of copper alloys into high current density regions should prove beneficial.

#### Acknowledgements

Thanks are due to the EML team at both Fort Halstead and Kirkcudbright for their efforts in recovering fired armatures. The work was funded by the UK MOD Corporate Research Programme, TG1.

#### References

- [1] D.C.Haugh, D.J.Kirkpatrick, A.P.J.Argyle and M.D.Bennett, "Recent firings at the DRA 32MJ Kirkcudbright facility", Proceedings of the 5th European Symposium on Electromagnetic Launch Technology, Toulouse, France, April 1995.
- [2] D.Munday, D.G.Jones and K.J.A.Mawella, "Metallographic studies on rails removed from the DRA EML facility at Kirkcudbright", Proceedings of the 5th European Symposium on Electromagnetic Launch Technology, Toulouse, France, April 1995.
- [3] A.Yeoh, G.Prabhu and C.Persad, "Liquation Cracking and its Effects in Aluminium Alloy Armatures", IEEE Trans. Magn., Jan 1997, to be published.
- [4] C.Leyden, R.Critchley and J.A.Downey, "3D Softly Coupled Electromagnetic/Thermal/Structural Analysis Using MEGA-DYNA3D", Proceedings of the 6th European Symposium on Electromagnetic Launch Technology, The Hague, The Netherlands, May 1997.
- [5] A.P.J.Argyle and C.Leyden, "The use of the MEGA Electromagnetic-Thermal Finite Element Code in Predicting Thermal Behaviour of Large Calibre EM Armatures", Proceedings of the 5th European Symposium on Electromagnetic Launch Technology, Toulouse, France, April 1995.

(c) British Crown Copyright 1997 /DERA

Published with the permission of the controller of  
Her Britannic Majesty's Stationery Office.

# **Systematic analysis of various electrodes in a railgun accelerator with a linear current density of $j \sim 500$ kA/cm.**

*A.P.Lototsky, A.D.Lebedev, Yu.A.Halimullin.*

Troitsk Institute for Innovation and Fusion Research (TRINITI)  
142092, Troitsk, Moscow Region, Russia

## **Abstract**

A systematic study of a group of railgun channels was made at a current density  $j \sim 400-500$  kA/cm for 4 types of erosion - resistant materials based on Cu, W and Mo, both with plasma, and with metal ("combined") current armatures. The output speed of the projectiles was more than 2,5 km/s in experiments. During tests constant checks of the sizes of the channel, acceleration dynamics and character of the current distribution were carried out. Selective metallographic analysis of electrode surface wear was carried out after each series of experiments with a given material and armature type. Results of tests with plasma armature showed that electrodes from special materials have lifetime about five or more times as long as that with copper electrodes. For tests with metal armature the size of electrode erosion greatly exceeds what is observed with a plasma armature.

## **Introduction**

During railgun (RG) operation with a plasma armature and large linear current densities, all elements of an accelerating channel undergo degradation. Main factors leading to the "wear" and following destruction of elements:

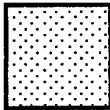
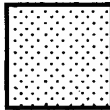

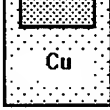

- pulse pressure - magnetic and gasdynamic;
- energy flow from a dense plasma (radiation, corpuscular and convective);
- erosion of electrodes due to current transport ( $\sim \int idt$ ).

Under the pressure action all channel elements experience elastic and plastic deformations, under the action of other two factors, the transport of mass of substance occurs. These processes are well investigated for electrode materials of copper and some its alloys [1,2]. Earlier there were conducted researches of a number of promising electrode materials [3,4], however, as a rule, results were obtained on modeling systems or in the mode of a free arc at moderate magnitude of a current density  $j < 30$  kA/mm. It is necessary to mark great difficulties originating at comparison of results on a wear of different materials, obtained on various experimental installations. Influence as the entry conditions of experiment (velocity of injection of a projectile, mode of creation of a plasma current, relation between a mass of a projectile and current amplitude etc.) and form of impulse of a current has here an effect force. For objective comparison of performances of a series of known erosion-resistant materials we conduct a large series from 37 experiments, in which the wear of electrodes as for plasma, and for the metal armatures is investigated.

## **1. Problem statement. Characteristics of a power supply and parameters of a railgun(RG).**

The described below investigations were conducted on a real RG in the working mode for five types of selected electrodes which names, composition and basic properties are presented in Table 1. The first type-electrodes of pure copper -was used as a sample for following comparisons by both quantitative characteristics of wear and qualitative picture of a behavior of a plasma strip inside a channel gap.

**TABLE 1**

| Number and type of an electrode        | 1. Copper   | 2. Copper with modifier   | 3. Stratified   | 4. On a tungsten-substrate   | 5. Combined with modifier   |
|--|---|---|---|--|---|
| Figure of a cross-section              |  |  |  |  |  |
| Structure of a material (% volumetric) | Cu (100)  | Cu (99) Al2O3 (1)   | Cu (50) Mo (50)   | W (90) Cu (10)   | Cu (56) Mo (43) LaB6 (1)  |

In Fig. 1, the principal electric circuit of a RG is presented. Parameters of electrical source and arrangement of diagnostic devices are there too.

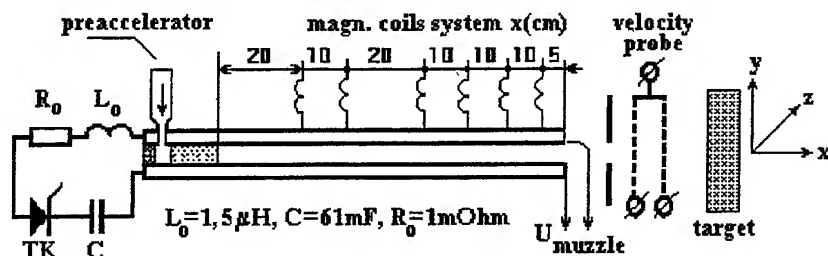


Fig.1 The principal electric circuit of test railgun.

The current commutator consisted of 60 thyristor switches, each of which turned on an assembly of 10 connected in parallel capacitors K 41-И7 ( $C=100$  mF,  $U_{\max}=5$  kV). The length of an accelerating section of a channel was 0.85 m, it had a square bore of 10x10 mm. All experiments were carried out with the use of a powder preaccelerator which provided to launch an initial assembly shown in Fig. 2 of a  $4-6 \cdot 10^{-3}$  kg mass on the length of 10 cm to the velocity of 500 m/s. After that the current was actuated, the amplitude of which reached 400-450 kA for 0,5 ms.

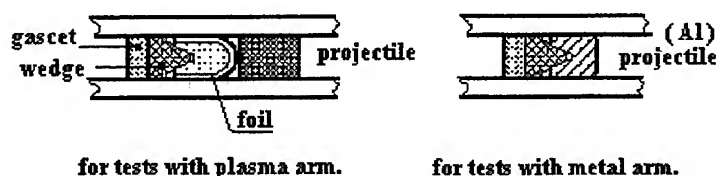


Fig.2 Initial assembly accelerated by powder preaccelerator

As a rule, the acceleration was finished through 100-150 ms after a maxima of a current and output velocity of projectile, fixed by a velocity probe exceeded 2100 m/s. Dynamics of a behaviour of a current distribution inside channel was qualitatively determined with the help of systems of differentiating magnetic probes, which are oriented on a x-component of a field and are located in 15 mm from an axes of a channel.

The electrically exploded foil for a primary formation of a plasma armature was made of beryllium bronze. The composed pad with wedging provided a reliable electric contact of a foil with rails during an acceleration in a powder preaccelerator. The aluminium projectile "swallow tail" type ensured the initial contact at tests with metallic armature. The measurement of the distance between electrodes in a channel was made with the help of a micrometer of  $10^{-5}$  m sensitivity before and after each shot. After each experimental series with a given type of electrodes and an armature, metallographic analysis of an electrode surface was performed. The longitudinal scanning of a profile was fulfilled in a mandatory order, and transversal (along axis Z) - for characteristic cuts with X-coordinates:  $X_a$  -for anode and  $X_c$  -for cathode rails.

## 2. Results of control series of experiments with copper electrodes

In a control series with the plasma armature 3 cycles was conducted. For the first cycle of an oscillogram of a current and the voltages are shown on fig. 3, and on fig. 4 signals of magnetic probes are reduced. Typical voltage drops on the plasma armature, observable through 100 μs after current switch on (after electrical explosion of a foil) is about 300 V. After the first shot the maximum increase of the interelectrode gap 0.3-0.35 was observed near the second pickup coil (see Fig. 1).

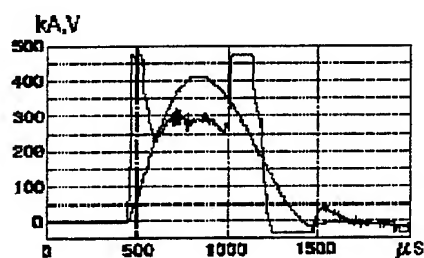


Рис.3 Current I and  $U_{\text{muzzle}}$  for Cu rails and plasma armature

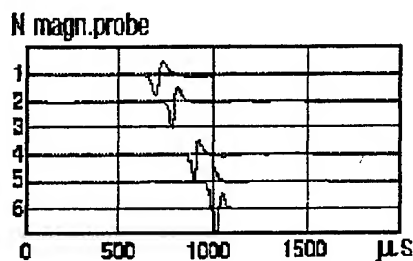


Рис.4 Signals of pickup coils for test fig,3

During the third shot, because of the residual stresses of the barrel, the PA took the projectile over practically at the beginning of the electromagnetic phase of the launch.

On fig. 5 longitudinal and transversal profiles of electrodes, obtained at metallographic scanning, are reduced.

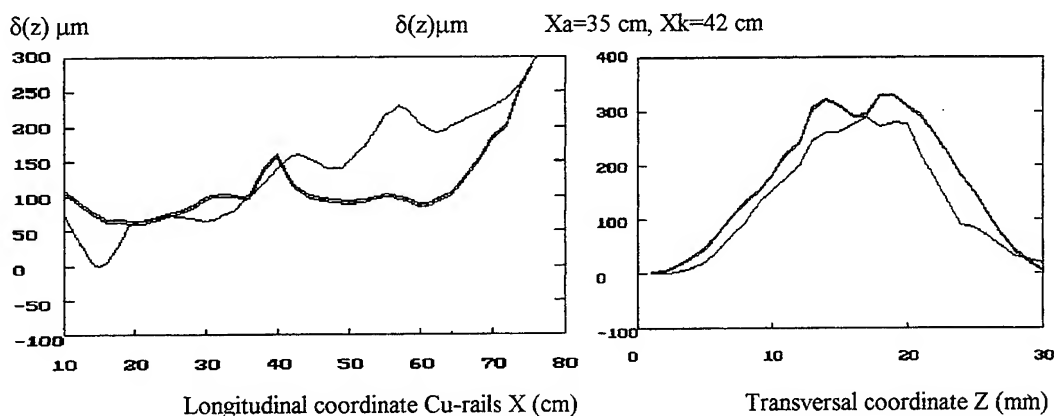


Fig.5 Rails erosion after test N3 ( Cu rails and plasma armature).

Double (or thick) the line chosen data for the anode. Uneasy to see, it is that area of a strain of rails affects not only zone of a channel, but also whole breadth of a rail. This strain is stipulated by pressure of a magnetic field, the magnitude of which at our current densities  $j > 400 \text{ kA/cm}$  exceeds a yield point for Cu. Some additional data can be received from table 2, where the report on all experiences with a plasma armature is contained.

In 1-th cycle of a control series with the metal armature an initial voltage drop made 20 V on fig. 6, but then quickly ( $t_{\text{cont}} \sim 100 \mu\text{s}$ ) increased, and contact passed through "hybrid" mode to maxima of a current.

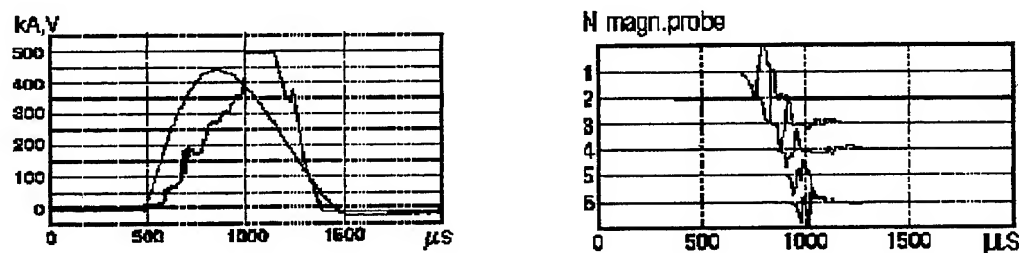


Fig.6 Current  $I$ ,  $U_{\text{muzzle}}$  and signals of pickup coils for Cu rails and metal armature

In the second test the velocity of projectile has decreased almost twice, and the initial voltage drop on contact has increased. Obviously it is that intensive erosion of a surface of a rail happened in "hybrid" contact zone at a high current density which has reduced in essential violations in the contact electric conduction in 2-th test. Profiles of wear of a surface, reduced on fig. 7 have shown, that the erosion has reduced in magnification of a size of a channel on 0,6 mm, that much more, than for a condition with a plasma armature.

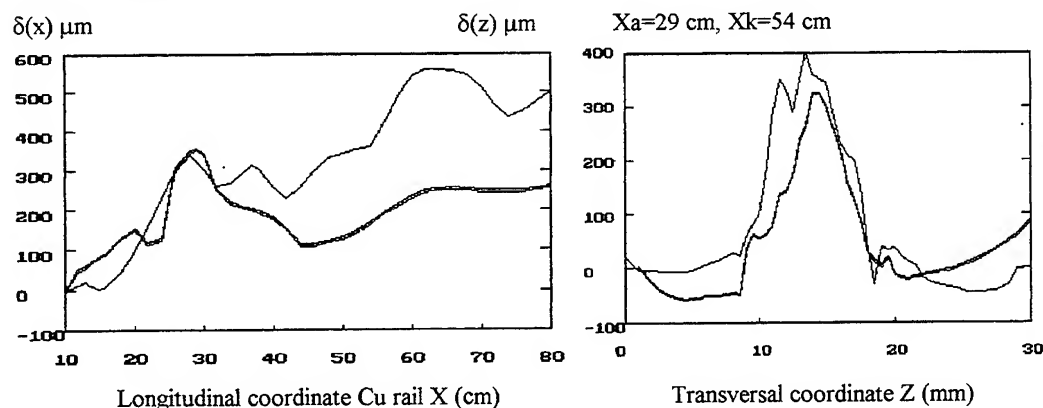


Fig.7 Rails erosion after test N25 ( Cu rails and metal armature).

### 3. Report of outcomes to test of materials

In tables 2 and 3 data, describing as test specifications, and some their outcomes are reduced. On fig. 8 and 9 outcomes of metallographic measurements for all used types of electrodes as for a boost of projectile by the plasma reinforcement (experiments in a table 2) are shown, and at acceleration of a metal anchor (table 3).

**TABLE 2**

| Shot No | Electrode type                    | Peak current, I<br>κA | Barrel caliber<br>Δz x Δy, mm | Curr. density<br>kA/mm | Muzzle<br>velocity m/s | Notes                          |
|---------|-----------------------------------|-----------------------|-------------------------------|------------------------|------------------------|--------------------------------|
| 1       | Cu                                | 415                   | 9,8 x 9,0                     | 46,2                   | 2700                   |                                |
| 2       |                                   | 412                   |                               | 45,8                   | 2600                   |                                |
| 3       |                                   | 465                   |                               | 51,7                   | 400                    | Pl. Armature<br>overtook proj. |
| 4       | Cu+Al <sub>2</sub> O <sub>3</sub> | 430                   | 9,8 x 8,5                     | 50,6                   | 2050                   |                                |
| 5       |                                   | 430                   |                               | 50,6                   | 2170                   |                                |
| 6       |                                   | 437                   |                               | 51,4                   | 2400                   |                                |
| 7       |                                   | 408                   |                               | 48                     | 2000                   |                                |
| 8       |                                   | 430                   |                               | 50,6                   | 2340                   |                                |
| 9       | Cu+Mo                             | 443                   | 9,7 x 8,5                     | 52,2                   | 2630                   |                                |
| 10      |                                   | 446                   |                               | 52,5                   | 2560                   |                                |
| 11      |                                   | 440                   |                               | 51,7                   | 2630                   |                                |
| 12      |                                   | 455                   |                               | 53,6                   | 2570                   |                                |
| 13      |                                   | 415                   |                               | 48,8                   | 540                    | Pl. Armature<br>overtook proj. |
| 14      | W+Cu                              | 446                   | 9,7 x 10                      | 44,6                   | 2500                   |                                |
| 15      |                                   | 438                   |                               | 43,6                   | 2050                   |                                |
| 16      | Diagnostic failure                |                       |                               |                        |                        |                                |
| 17      |                                   | 443                   |                               | 44,3                   | 2080                   |                                |
| 18      |                                   | 458                   |                               | 45,8                   | -                      | V not measured                 |
| 19      | Cu+Mo+LaB                         | 390                   | 10,8x9,6                      | 40,6                   | 2360                   |                                |
| 20      |                                   | 405                   |                               | 42,0                   | 2220                   |                                |
| 21      |                                   | 370                   |                               | 38,5                   | 2100                   |                                |
| 22      |                                   | 370                   |                               | 38,5                   | 2100                   |                                |
| 23      |                                   | 400                   |                               | 41,6                   | 2340                   |                                |

**TABLE 3**

| Shot No | Electrode type                    | Peak current, I<br>κA | Barrel caliber<br>Δz x Δy, mm | Curr. density<br>kA/mm | t <sub>cont</sub><br>μs | Voltage drop on<br>contact, V | Muzzle<br>velocity m/s |
|---------|-----------------------------------|-----------------------|-------------------------------|------------------------|-------------------------|-------------------------------|------------------------|
| 24      | Cu                                | 450                   | 9,2x9,6                       | 49                     | 100                     | 20                            | 2700                   |
| 25      | "-                                | 450                   | 9,2x9,6                       | 49                     | 150                     | 50                            | 1370                   |
| 26      | Cu+Al <sub>2</sub> O <sub>3</sub> | 460                   | 8,4x9,55                      | 54,5                   | 130                     | 35                            | 2500                   |
| 27      | "-                                | 450                   | 8,4x9,55                      | 52,9                   | Diagnostic failure      |                               |                        |
| 28      | Cu+ Mo                            | 460                   | 9,6x9,55                      | 47,9                   | 160                     | 30                            | 2500                   |
| 29      | "-                                | 435                   | 9,6x9,55                      | 45,3                   | -                       | -                             | 1900                   |
| 30      | W+Cu+Ni                           | 465                   | 9,4x9,8                       | 49,4                   | 180                     | 20                            | 2570                   |
| 31      | "-                                | 480                   | 9,4x9,8                       | 51                     | 240                     | 20                            | 2300                   |
| 32      | Cu+Mo+LaB <sub>6</sub>            | 435                   | 9,3x9,55                      | 46,6                   | 230                     | 30                            | 2570                   |
| 33      | "-                                | 400                   | 9,3x9,55                      | 43,0                   | 150                     | 60                            | 2130                   |
| 34      | "-                                | 415                   | 9,3x9,55                      | 44,6                   | 140                     | 30                            | 2300                   |
| 35      | "-                                | 415                   | "-                            | "-                     | 100                     | 50                            | 2000                   |
| 36      | "-                                | 400                   | "-                            | "-                     | 100                     | 50                            | ~1000                  |
| 37      | "-                                | 400                   | "-                            | "-                     |                         |                               | Proj. destruction      |



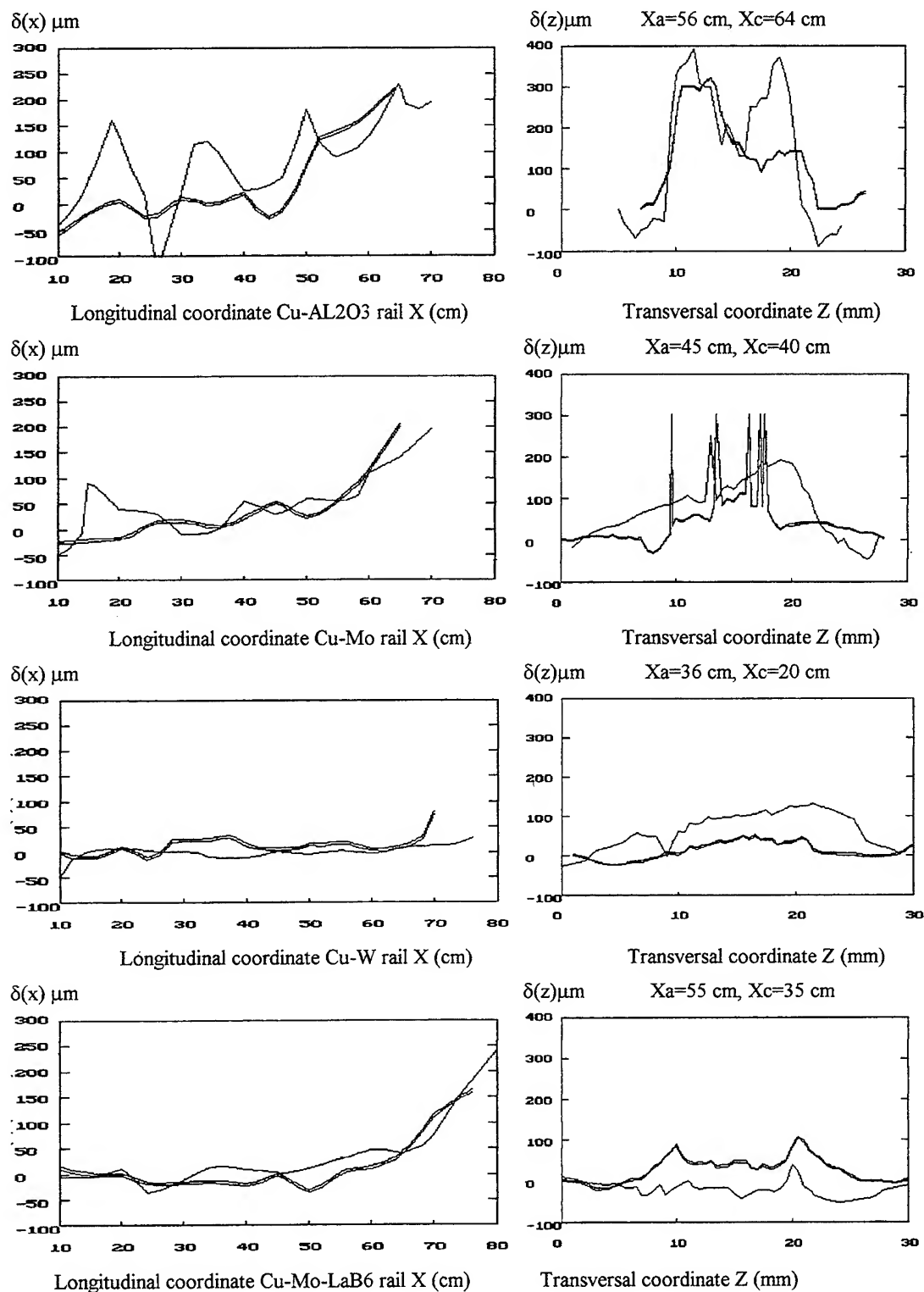


Fig.8 Results of metallographic measurements of electrode surface after tests with plasma armature for the electrode types No 2-5

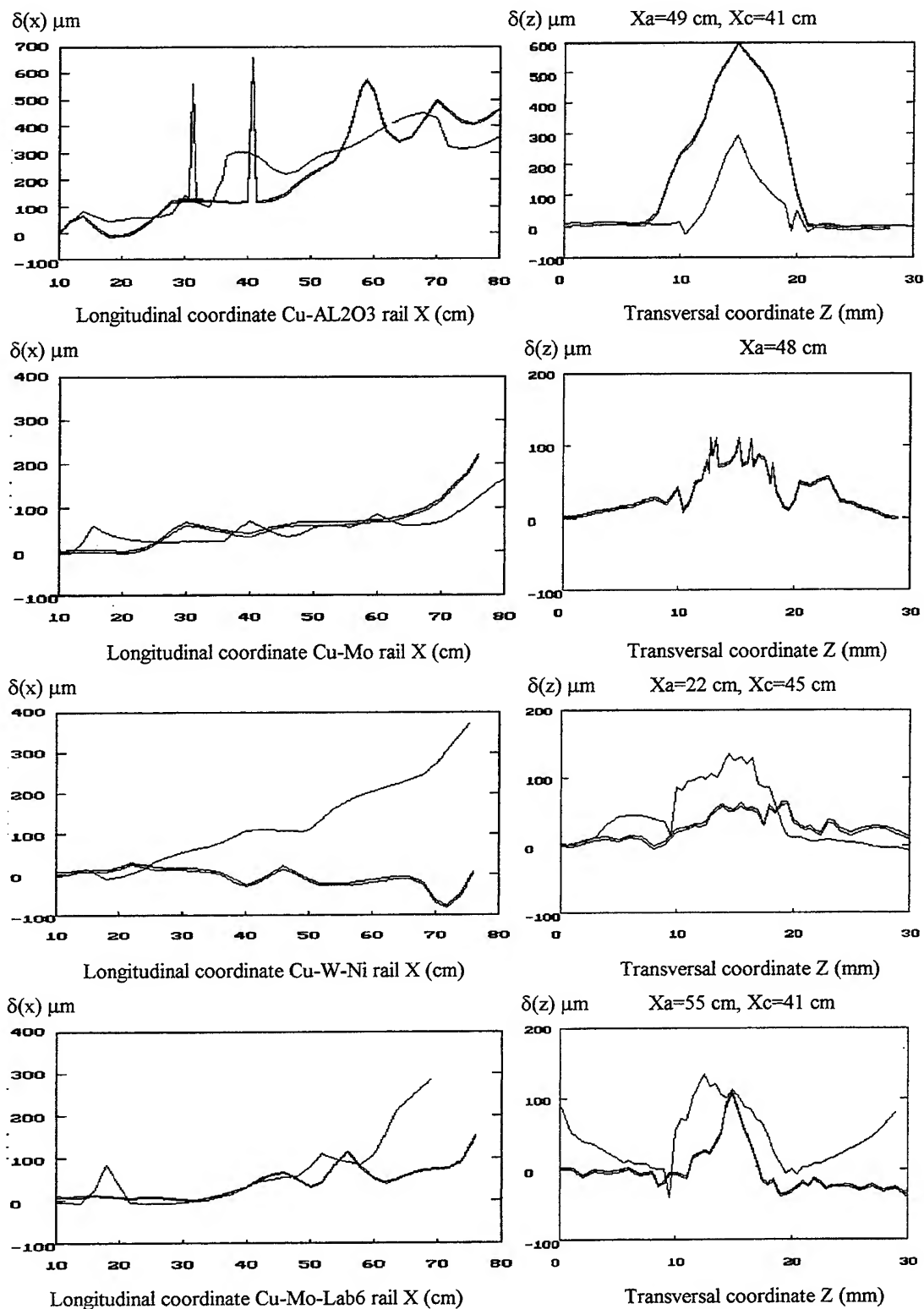


Fig.9 Results of metallographic measurements of electrode surface after tests with metal armature for the electrode types No 2-5

We have not detected any clear regularities at a comparison of a wear of electrodes of various polarity. However completely definitely it is possible to state, it is that: 1. Specific "wear" of electrodes ( $\mu\text{m}$  per shot)

channel with the plasma armature it is much less, than for electrodes of a channel with a metal anchor; 2. Use of special materials has allowed to increase resource (safe life) of a channel in 3-5 times, however this inference is fair for used current densities  $j = 40-45$  kA/mm. At smaller current densities the outcome will be different from our data.

#### 4. The basic total of tests

The carried out systematic studies of the character and value of the "wear" of the accelerator barrel showed that the use of special materials allows one to decrease considerably the destruction of barrel electrodes and increase the service life. The maximum number of shots under our increased current loads in modes with the plasma armature was equal to 5, and for certain samples of known materials this isn't a limit.

Under the circumstances of high pressure of a magnetic field, the obligatory condition of a multiple operation of the barrel is a high yield limit of material preventing mechanical deformation of working surfaces of electrodes. Only in the case of the fulfillment of this condition there is the sense to discuss electric erosion properties of rails, mechanisms and quantitative characteristics of the "wear" of electrodes connected directly with the organization of the current transport in the zone of acceleration of a projectile or metal armature. In these studies the following electrode materials were used: 1) for "sample" rails -annealed copper; as tested materials - 2) modified copper with highly dispersed additive of aluminum oxide; 3) copper with stratified reinforcement of molybdenum foils; 4) pseudoalloy of tungsten and copper (and nickel); 5) composition of copper with molybdenum modified by the additive of lanthanum hexaboride.

The tests of these materials for given variants of an armature have shown that for the projectile velocity,  $V=2.5$  km/s, the plasma armature provides much "softer" mode of destruction of railgun electrodes than a metal armature. Practically, on all of the above listed types of electrodes (except the first one), the output parameters of the accelerator ( $V>2$  km/s) were kept during the entire series of 5 shots. Here one peculiarity of the given mode of railgun operation should be noted. It consists of the fact that experimentally there is observed a clear influence of erosion properties of various materials of electrodes on the structure and dynamics of a current distribution in the plasma armature. However, this slightly affects the dynamics of acceleration and muzzle velocity of a dielectric projectile in the chosen mode of operation. Therefore (if don't take into account the dynamics of the plasma armature), as the best of tested materials, the composite Cu+Mo+LaB<sub>6</sub> and the pseudoalloy W+Cu(90%+10%) should be considered. The substantial disadvantage of the latter is the increased fragility. On fig. 10 is reduced the photos of a fragment of a surface of an electrode from a pseudo-alloy W + Cu, on which crack is visible. Such numerous cracks in direction of an axes  $z$  (across an axes of a channel) were detected after a series of experiences with the plasma armature. In consequent tests (with the metal anchor) the increased fragility was eliminated by introduction in a material structure 5 % of the component of a nickel. The mode with the metal armature at a given high current density turned out to be very hard and much more sensitive to the choice of electrode material.

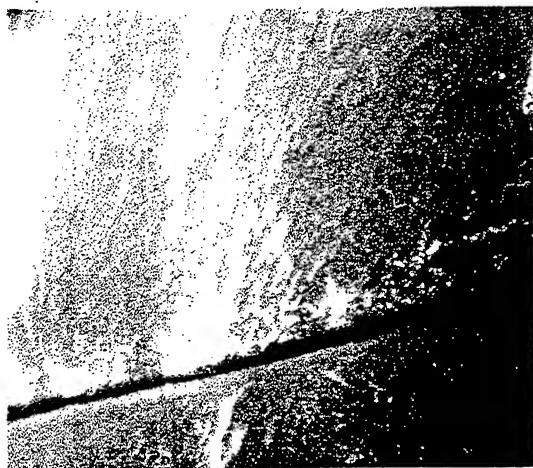


Fig.10 The split on surface of W-Cu rail. X-axis has vertical direction. The magnification of photo is equal to 10.

We observed the phase of the metal sliding contact ( $t_{\text{cont}}$  in Table 3) duration of which ( and the "critical velocity" ) depend on electric conductivity of materials of an electrode and armature. In our experiments it varied from 100 to 240  $\mu\text{s}$ . Then the phase of a hybrid, or combined, contact started, in which the level of erosion of surfaces of electrodes and armature considerably (3-4) times exceeded erosion in the case of the plasma armature. Respectively, the service life of the barrel in such mode sharply decreased (from  $n>5$  in the case of the plasma armature to 2-3). At the same time the output characteristics of acceleration decreased significantly, first of all the mass of the armature-projectile due to high erosion in the contact. Besides, spread material of the armature deposited on surfaces of the barrel walls. Because of the latter effect, in the experimental series with rails of Al<sub>2</sub>O<sub>3</sub> there was clearly observed the narrowing of the barrel.

In whole the dynamics of the mass transport in this mode is a rather complicated phenomenon which laws are not clear to us.

It can be investigated in further experiments but we didn't put this problem taking into account big difficulties of measurements of dynamics of these (likely irregular) processes.

The number of shots with a metal armature on one of the best electrode materials was maximized with the purpose of determination of the limiting service life of rails. The failure of acceleration of the metal armature occurred in the fifth shot because of the total destruction of the armature. However, it should be noted that the statement of the problem in all experiments with a metal armature isn't correct due to definitely high linear current density  $j \sim 45-50 \text{ kA/mm}$ .

In any case, advantages of operation of a railgun with a plasma armature in the given range of parameters of an electromagnetic launch are obvious for obtaining replaceable results in multiple shots.

### Inference

In the given report brief informations about the conducted trials of materials of electrodes are reduced only and basic outcomes of obtained measurements are given. The significant part of an accumulated material and, in particular, measurement on dynamics of a behaviour of the plasma armature in various channels while is not yet treated and is not thought over in a due measure.

At preparation of the report the authors recollected an intense transactions of all collective during realization of huge volume of engineering work and express gratitude to L. Kotova for carried out electrotechnical measurements, V. Afanasiev and L. Zagryidsky for preparation of installation, A. Nikolashin for preparation of a series of channels, and also to V. Lipatov and V. Akimov for the help at preaccelerator manufacture.

### References

1. T.G.Engel, M.Kristiansen, E.O'Hair, J.N.Marx. Estimating the Erosion and Degradation on Performance of ceramic and Polimeric Insulator Materials in High Current Arc Environments. Trans. Magn., v.27, No 1, p.533-537
2. E.M.Drobishevsky, B.G.Zukov, S.I.Rozov etc. Experimental study of high-power accelerating railgun discharge in FTI AN USSR. Materials 1-th all-union seminar on high current arcs in magnetic field, Novosibirsk, April 10-13, 1990 SO AN USSR, Inst. of TermoPhysic, Novosibirsk, 1990, c.268-278.
3. M.A.Bykov, N.T. Jigaylo, V.M. Nesterenko, A.E.Poltanov etc. A research of new erosion-resistive materials for railguns. Materials 2-th All-union seminar on high current arcs in magnetic field, Novosibirsk, December 4-6 1991r. 1990 SO AN USSR, Inst. of TermoPhysic, Novosibirsk, 1992, c.357-365.
4. A.G.Anisimov, N.V.Gubarev, V.I.Mali, T.M.Sobolenko, G.A.Shvetsov etc. Interaction of a plasma bunch with a surface of electrodes. Materials 1-th all-union seminar on high current arcs in magnetic field, Novosibirsk, April 10-13, 1990 SO AN USSR, Inst. of TermoPhysic, Novosibirsk, 1990, p.195-207.

# METAL PROJECTILE ACCELERATION IN MUZZLE-FED RAILGUN

*Yu.A. Kareev, A.P. Lototsky, Yu.A. Halimullin*

TRINITI, Troitsk, Russia

## Abstract

There were conducted experiments in which with the help of previously chosen barrel shape of a "muzzle-fed" type and a special armature, the velocity skin effect which destroys a metal sliding contact is suppressed. There was obtained the arc-free velocity  $\geq 2.6$  km/s followed by the spatial melting of conductors of the armature under the action of the flowing current.

## 1. Introduction.

In all known experiments with a metal armature in a railgun, when velocity becomes greater than 0.7-1.1 km/s, the loss of metallic conductivity takes place. The contact transforms into a "hybrid" and later into an arcing phase. The main role in the loss of metal conductivity is supposed to be played by the velocity skin effect; in [1] it was proposed to use a railgun barrel with a muzzle-fed current supplying (MF). Special features of the current behavior in the zone of the contact between the metal armature and the rail in MF are considered in detail in [2]. It is shown that in this case also the velocity skin effect arises leading to the deterioration of the valid metal contact. The difference is in the fact that the critical velocity depends on the rail thickness,  $d$ , as  $1/d$ . However, if to try to increase the critical velocity by decreasing  $d$ , then there could develop conditions for heating of the rail up to the melting temperature. In the case of the optimal choice of the value of  $h$  one can expect three times increase of the critical velocity in MF in comparison with one in a classical railgun barrel.

Experiments with a similar MF configuration of a barrel and a plasma armature were conducted earlier ([3], [4]) in order to find out peculiarities of its behavior. However, the latter paper states the flat conclusion that there is no prospects for the use of MF as a launcher. In our opinion, this conclusion has not enough grounds because of the results of [4] were predetermined by the unwell performance of the barrel and choice of the current mode.

The objective of this work is investigation of a specially developed MF railgun for launching a metal armature and demonstration of its potential possibility to increase the critical velocity of the contact.

## 2. The scheme of the experiment and the experimental system

For our experiments, there was chosen such a design of a MF barrel which idea was to provide additional normal pressure in the zone of the contact. The scheme of the barrel is presented in Fig. 1. Main electrode-rails guiding the armature and supplying the current into it are made of 4-mm thick plate of construction steel (Ст.3) of the thickness,  $h$ , equal to 30 mm. Plate surfaces were polished on both sides. The outer copper bus bar was of the thickness,  $\Delta Y_{de}$ , equal to 12 mm and the same width, being insulated from rails by the spacer of the thickness,  $\Delta Y_{cd}$ , equal to 0.5 mm. The electric contact between rails and bus bars in the muzzle zone was performed by mechanical pressing during the assembling process. As it will be shown below this disadvantage of the design revealed itself later. Because of the small thickness of the rail the current which flowed ahead of the armature caused the deflection of the electrode inwards caused by the magnetic field pressure in the zone of the insulating spacer. The deflection guaranteed a reliable electric contact between the rail and the conducting armature and provided necessary value of the pressure on the armature while its motion along the barrel except a short interval near the muzzle.

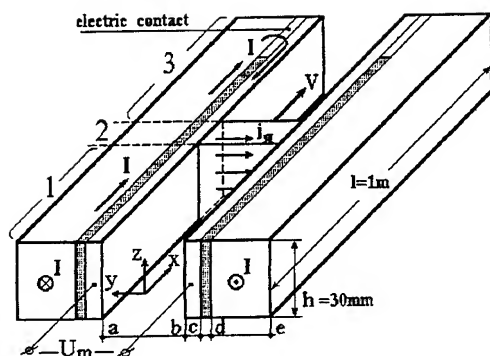


Fig. 1. The barrel of the muzzle-fed railgun

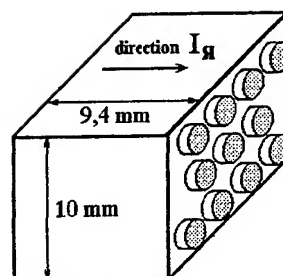


Fig. 2. The design of the armature with conducting rods.

In [5] this value was determined experimentally for the case of a motionless high current contact:  $P^* = 1 \text{ kg/kA}$ . The flexible barrel design must be in correspondence with a quite plastic armature in order to avoid the lock of a projectile inside a barrel. Therefore we used the matrix of polycarbonate with holes in which there were inserted aluminum rods-conductors of the 2 mm diameter. The armature design is shown in Fig. 2. The ends of the conductors protruded the surface of the separator by the distance of 0.3 mm. The maximum normal pressure on the surface of the separator was restricted by the yield limit of aluminum,  $s_T = 10^8 \text{ N/m}^2$ . For armatures with 11 and 8 rods which were used in experiments with the current pulse amplitude of 300 kA it was  $P^* = 0.9\text{--}1.5 \text{ kg/kA}$ . The contact of such kind must have worked reliably, at least at the part of a diagram where the railgun current was increasing. Before to choose the design and determine final dimensions of the armature and guiding rails a series of experiments was conducted on determination of the value of the barrel deformation at the current load of 100-300 kA. For improving the contact reliability, during the assembling the distance between electrodes was decreasing towards the muzzle where it was 0.1 mm. The initial acceleration of the armature up to the velocity of 900 m/s was provided by the powder accelerator, then the current was switched on. The circuitry of the power source is described in [6], here it should only be mentioned that this is an LC current source with the internal impedance significantly exceeding the impedance of the accelerating barrel.

### 3. Experimental results

The main objective of the experiments conducted is the demonstration of a fundamental possibility of the acceleration with a metal arc-free contact up to velocity  $V > 2 \text{ km/s}$  and determination of additional possibilities provided by the configuration of the MF barrel which was used. Therefore the program of experiments was mainly of a qualitative character. Two shots were made, their results and main initial data are presented in Table 1.

Table 1

| $V_0$<br>m/s | $I$<br>kA | $M_{\text{arm}}$<br>gram | $N$ of<br>conductors | $t$<br>$\mu\text{s}$ | $l$<br>m | $V_{\text{max}}$<br>m/s | $\int j^2 dt$<br>$\text{A}^4 \text{m}^{-2} \text{s}$ | $\eta$ (efficiency)<br>on the metal<br>contact* |
|--------------|-----------|--------------------------|----------------------|----------------------|----------|-------------------------|--|---|
| 900          | 300       | 2,7                      | 11                   | 400                  | 0,50     | $\sim 2000^*$           | $1,59 \cdot 10^{16}$                                 |   |
| 900          | 300       | 2,1                      | 8                    | 410                  | 0,62     | $\geq 2600^*$           | $3,2 \cdot 10^{16}$                                  | 0.22*   |

\* Note: the values marked with \* were not measured directly; their validation is discussed in the next section,  $h$  corresponds to the time interval before the loss of the contact.

The presented values of  $t$ ,  $l$  and  $V_{\max}$  are the following: the distance along the barrel which the armature passed without any indications of damage of the metal contact, velocity and time corresponding to the moment of the loss of the metal contact. The distance is measured from the point  $x_0$ , where the armature was situated at the moment of the current switching on. In Fig. 3, there are presented oscillograms of the current,  $I(t)$ , and voltages  $U_b(t)$ ,  $U_m(t)$  measured at the breech and at free ends of rails at the point  $x=0$  (see Fig. 1) in the first experiment.

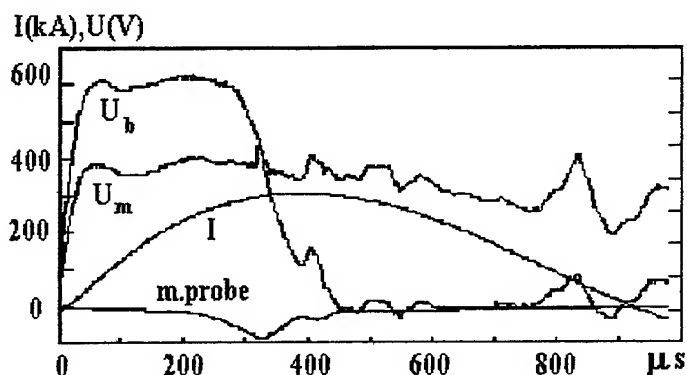


Fig. 3

Bottom oscillogram shows a signal of magnetic coil, which registered an x-component of a magnetic field on distance of 5cm from the channel muzzle. The short pulse was on the voltage oscillogram of  $U_m$  at time of 320 mks. It was consistent with electrical contact break-down in a place where current-feeder is hold down to the rail on fig.1. Because of an internal rails deflection the contact point

was moved closer to the channel muzzle and the conductivity of contact was restored. It did not affect the current circuit and armature acceleration. The next peak on the oscillogram of  $U_m$  at  $t=400 \mu s$  corresponded to the break of the armature contacts and is clearly recorded on the oscillogram of the voltage measured on the breech terminals of the railgun. Oscillograms of the second experiment qualitatively repeated the character of the described above. We don't use here quantitative data from oscillograms of  $U_b(t)$ ,  $U_m(t)$ , since their interpreting taking into account a quite complicated character of electromagnetic system of MF requires additional analysis. Besides, high values of induced EMF and voltage drops on rails don't allow one to measure the potential difference  $DU \leq 10 \text{ V}$  on contacts of the armature and rail.

In Fig. 4, there are presented photos of sections of surfaces of one of the rails of the second experiment. The surface of another rail of this pair is of totally the same character. In both experiments the loss of the metal contact occurred at the moment when the current reached its maximum value. That confirms the validity of initial considerations for the choice of design. It should be noted that both in the first and second shots the dynamics of the contact loss was of a fast-running character. In Fig. 4 one can see that on the rail surface until the point  $x=59 \text{ cm}$ , the clear traces of metallic aluminum are left. At  $x=62 \text{ cm}$  we observe the beginning of the total break of the contact with the splashing of liquid aluminum.

Analogous pictures of the first shot are not presented, but they are of the same character as in Fig. 4 with the only difference that the analogous damage of the contact corresponds to the point  $x=50 \text{ cm}$ .

Despite the fact that we had the developed technique of measurement of the muzzle projectile velocity, in this case we could not use it in a correct way because of the armature destruction in the barrel or at the muzzle.

#### 4. Some evaluations and discussion of results

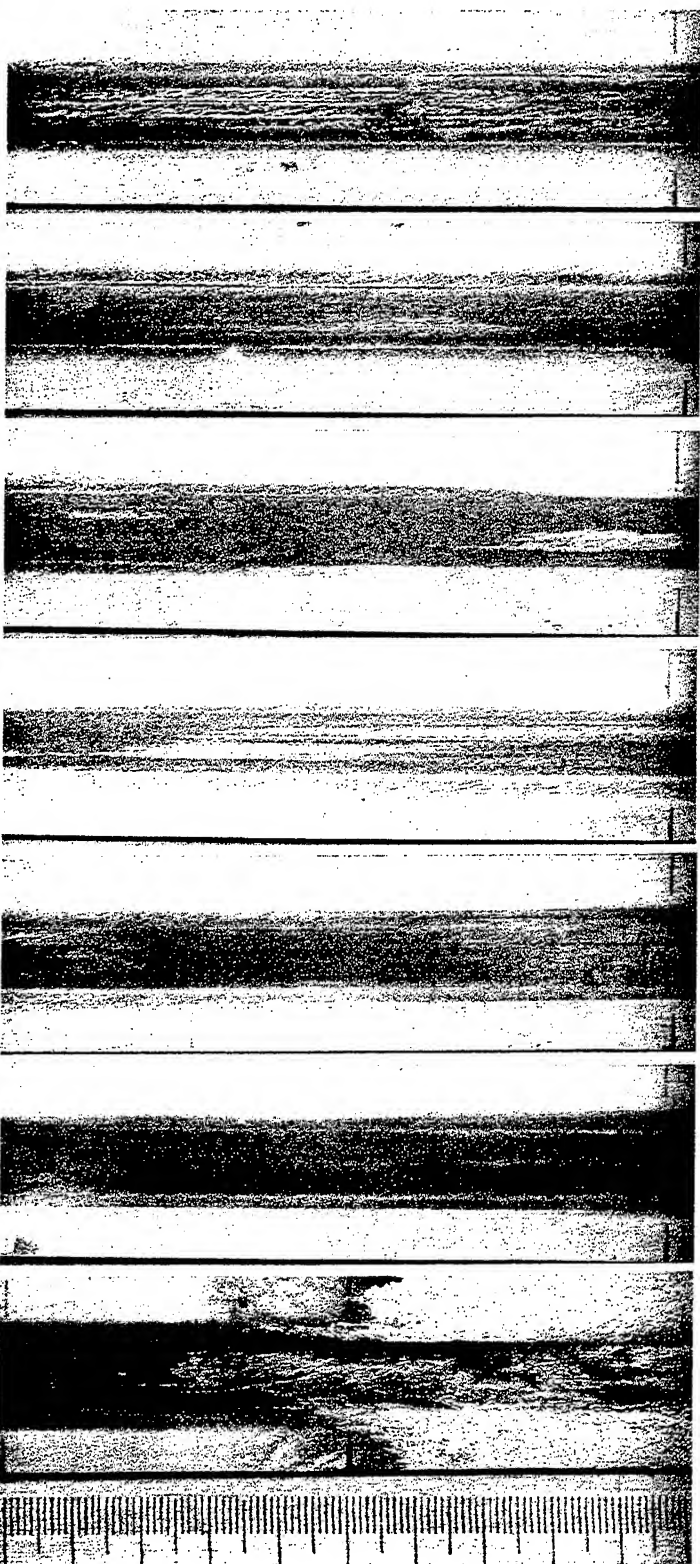
##### 4.1. Evaluations of parameters of the experiment and calculation of acceleration

For the analysis of the dynamics of acceleration one should perform evaluations of "effective" inductance per unit length,  $L'$ , of the barrel. It was calculated as the difference

**Photographs of steel rails surface from point  $x=0$  (current start)**

**0**

**10 cm**



**$x=0-10$  cm**

**$x=10-20$  cm**

**$x=20-30$  cm**

**$x=30-40$  cm**

**$x=40-50$  cm**

**$x=50-60$  cm**

**$x=60-70$  cm**

**Fig.4**



between the inductances per unit length  $L''$  and  $L'''$  of barrel sections situated in the zone 1 behind the armature in Fig. 1 and ahead in the zone 3. In this case one can neglect the fact that the pattern of current flowing in the zone 2 (which dimension is several bore calibers) is complicated and the accelerating force can be calculated as  $F=0.5L'I^2$ . The calculation of inductances was carried out with the help of a two-dimensional code for determination of a magnetic field distribution in a cross-section of complex conductors. The configuration of the magnetic field for the barrel in the zone 1 is shown in Fig. 5 (one fourth of the symmetrical cross-section). At a given current value in conductors there was determined the value of the total magnetic flux  $\Phi = BS$  and the value of  $L'$  was calculated. The following assumptions were taken:

- in the case of an iron rail in strong fields  $\mu=\mu_0(1+B_s/B_0)$ , where  $B_s$  is the saturation magnetic flux density and  $B_s \ll B_0$ , so magnetic properties of steel were not taken into account;

- the current distribution over the copper (upper) conductor corresponds to the classical skin-effect without taking into account nonlinear processes;

- the steel rail was assumed to be impenetrable for the magnetic field because of low conductivity and heating due to the flowing current.

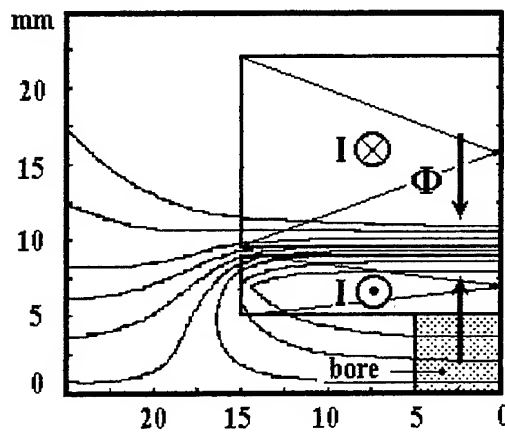


Fig. 5

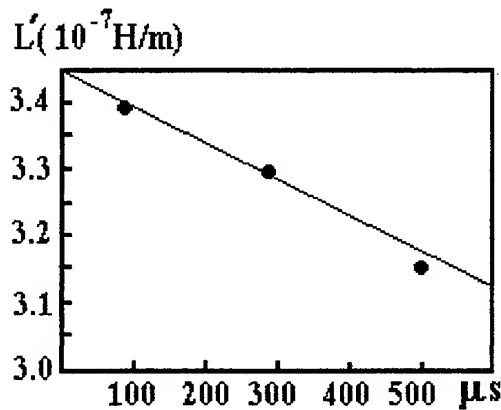


Fig. 6

In Fig. 6 values of effective inductance per unit length,  $L'$ , are shown at various moments  $t=100-1500 \mu s$ . For further calculations in the time interval which we are interested in (100-500  $\mu s$ ) this dependence was approximated by the expression  $DL=3.45 \cdot 10^{-7} (1-105t)$ .

Further the problem of acceleration when the mass,  $I(t)$  and  $L'(t)$  are given was solved numerically. We present the result for the second experiment which, in our opinion, realizes the limiting mode in the sense of the current loads on the armature.

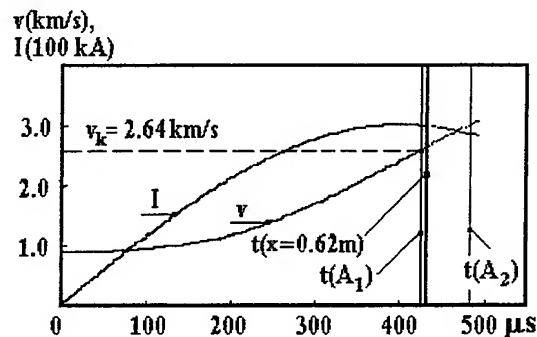


Fig. 7

contact should take place earlier (at  $t < 400 \mu s$ ) because of loss of strength of the heated conductors. Therefore the calculated magnitude of a velocity  $v=2,6 \text{ km/s}$  at a point  $x=0,62 \text{ m}$  is an underestimation of the actual magnitude. The armature kinetic energy and the energy which was supplied to the barrel  $\int U_b I dt$  were used for calculation of the efficiency,  $h$ , presented in Table 1.

#### 4.2. Calculation evaluations of the velocity skin-effect in a muzzle-fed configuration

For the analysis we used a two-dimensional numerical code allowing for simulation of development of the deterioration of the solid metal contact. There was shown in [7] that the critical velocity of the metal armature in a traditional railgun doesn't depend on the duration of the period and value of the current. It depends on the value of the parameter  $G=L'd^2/M$  [8] where  $L$ -the inductance per unit length of the barrel,  $M$ -the armature mass and  $d$ -the armature dimension in the direction of the magnetic field (the  $z$ -axis in Fig. 1). In the case of the aluminum armature with a mass of 2.7 gram the parameter  $G$  is equal to  $5.14 \cdot 10^{-9} \text{ Hm/kg}$  and when the armature mass is 2.1 g  $G=6.61 \cdot 10^{-9} \text{ Hm/kg}$ . For the current diagram presented in Fig. 3 there were calculated critical velocities in railguns with traditional and muzzle-fed current supply and the above values of the parameter  $G$ . The data are presented in Table 2.

Table 2

|                                    | Classical railgun | Muzzle-fed railgun |
|------------------------------------|-------------------|--------------------|
| $M=2.7 \text{ g}$                  |                   |                    |
| Without preacceleration            |                   |                    |
| Time of the onset of a crisis      | 318.3 $\mu s$     | 611.8 $\mu s$      |
| Critical velocity                  | 642.8 m/s         | 1960 m/s           |
| With preacceleration up to 900 m/s |                   |                    |
| Time of the onset of a crisis      | 202.7 $\mu s$     | 334 $\mu s$        |
| Critical velocity                  | 1100 m/s          | 1622 m/s           |
| $M=2.1 \text{ g}$                  |                   |                    |
| Without preacceleration            |                   |                    |
| Time of the onset of a crisis      | 301.5 $\mu s$     | 513 $\mu s$        |
| Critical velocity                  | 726 m/s           | 2091 m/s           |
| With preacceleration up to 900 m/s |                   |                    |
| Time of the onset of a crisis      | 200.9 $\mu s$     | 315.8 $\mu s$      |
| Critical velocity                  | 1151 m/s          | 1712 m/s           |

It is seen from this table that in the mode without preacceleration of the armature in the muzzle-fed railgun the critical velocity is approximately three times higher than in a traditional one. Earlier it was noted in [2]. The influence of the preaccelerator on the critical velocity for the first time was investigated in [7]. The table data on the mode with preacceleration seem to be abnormal at first sight: in a traditional railgun the critical velocity (1100 m/s) increased in comparison with the case without preacceleration (642.8 m/s) and in the muzzle-fed railgun the critical velocity (1960 m/s) decreased (1622 m/s). To explain this result, it should be noted that for the identical time diagrams of the railgun current in modes with armature preacceleration and without one the value of the velocity increment is a function of the value of  $\int I^2 dt$ . The energy released in the corner section of the armature is determined by the integral  $\int j^2 dt$ . Since in the case with a traditional railgun the preacceleration velocity equal to 900 m/s exceeds the critical velocity of 648.2 km/s then the current distribution over the armature corresponds to the case of the quasi-steady distribution, i.e. the mode of velocity skinning from the very beginning of the acceleration process. Therefore the energy of evaporation in the corner point of the armature is released at a short duration (202.7  $\mu$ s) and the velocity increase is  $1100-642.8=457.2$  m/s. In the case of the muzzle-fed railgun the injection velocity of 900 m/s is less than the critical one (1960 m/s), so the mode of the current skinning appears not in the very beginning of the armature acceleration process. This means that the evaporation energy in the corner point of the armature is released at a longer duration (334  $\mu$ s) and the velocity increase turns out to be greater ( $1622-900=722$  m/s).

Thus, the results of calculation show the possibility of development of the deterioration of the metal contact between the 2.7 g armature and the rail beginning from the moment 334  $\mu$ s when it passes the path equal to 372 mm.

#### 4.3. Discussion of experimental results

The comparison between the experimental data and the results of calculation of the dynamics of acceleration shows that in a given device during the second experiment **there were realized maximal possibilities of this barrel and solid aluminum armature**. Indeed, in our case only one of two conditions which occurred practically simultaneously in the second experiment is sufficient for explanation of the loss of metal contact :

- the melting of the armature conductors in the assumption that the current is distributed uniform over it;
- the mechanical loss of the contact because of the end of the increasing of the deflection of the leading rail inwards the barrel.

In the first experiment with 11 conductors and high armature mass the contact destruction is caused most likely by the second condition.

The experiment and calculation for the second experiment with 8 conductors turned out to be in strict frame being limited on the one hand by the quite high for this design inductance per unit length and on the other hand by the inescapable accumulation of the current integral by the armature. Attempts of alternative interpretation of results doesn't allow one to explain how the armature goes without destruction to the point  $x=0.62$  m. It seems that the velocity skin effect some peculiarities of which concerning MF configuration of the barrel were described above in these shots obviously didn't take place because of three reasons:

- the use of MF barrel increases the critical velocity threshold;
- in the case of the multi-rod design of the armature conductor the field diffuses from the rail into the body of the armature (gaps between rods), so the area of the current skinning is "scattered" over the developed perimeter of all conductors bounding the total area of the contact;
- the value of the pressure on the contact surface provides the ablation of aluminum from the contact surface into the "aluminum trace" on the rail with replacement of overheated aluminum in critical zones of the contact.

The above written doesn't deny the presence of deterioration contact phenomena in our experiments. The good surface of the rail up to the distance of 0.6 m is a strong argument in favor of arc-free acceleration but is not a reliable evidence of a solid metal contact. The use of the optical diagnostics for registration of a spark in a contact zone was inapplicable because of the presence of the powder preaccelerator; the problem of measurement of the contact voltage drop was mentioned in the previous section of this paper.

## 5. Conclusion and recommendations

In carried out experiments on acceleration of a solid metal armature in a railgun barrel of the muzzle-fed kind there was obtained the result excluding a considerable influence of the velocity skin effect on destruction of the solid metal contact. With the help of especially chosen cross-sections of rails and current supplying electrodes of a barrel authors provided high efficiency ( $\eta=0.22$ ) of acceleration of a solid armature and necessary value of the contact pressure ( $P \approx s_T$  for Al). The latter was maintained automatically and provided the "ablation" of the contact surface in the process of acceleration before the moment of spatial melting of armature conductors. There was obtained the maximum velocity of the metal arc-free contact  $V \geq 2.6$  km/s.

Further the velocity increase can be obtained in barrels of analogous type both by the increase of the relative mass of a conductor in an armature (in this experiment it was 0.4) and by the change of mutual geometry of cross-sections of barrel and armature. When velocity greater than 2.6 km/s will be achieved the influence of the velocity skin effect can turn out to be much stronger.

We are sure that the further development of the suggested configuration of a muzzle-fed railgun and continuation of this research will allow one to achieve a fast progress in solution of a resource problem of barrels operating at moderate velocities of 3-4 km/s.

Authors would like to acknowledge Dr. R.A. Marshall (UT USA) for materials of [5] presented before official publication.

## References

1. M. Cowan. Solid armature railguns without the velocity-skin effect. IEEE Trans. on magn. 1993, V.29, N1, P.385
2. Yu.A. Kareev, R.M. Zayatdinov. Transaction conditions for solid armatures in railguns with muzzle current feed. IEEE Trans. on magn. 1995, V.31, N1, P.385
3. O.V. Fatyanov, V.E. Ostashev, Ye.F. Lebedev. A Plasmodynamic discharge in MPA barrels of different directions of current supply. TVT, v.11, N4, 1993, p. 656-661. Russian.
4. J. Taylor, R. Crawford and D. Keefer. " Muzzle-fed railgun experiments with 3-d electromagnetic simulations " IEEE Trans. on Magn. 1995. V.31. N.1. P.360.
5. R.A. Marshall. Current Carrying Capacity of Solid Armatures for Railgun at Zero Speed. Report on the 8-th Symposium on Electromagnetic Launch Technology, USA, Baltimore, April, 1996.
6. A.Lototsky, Yu.Halimullin, A.Lebedev. The system analysis of a resource of electrodes in the railgun accelerator with linear density of a current  $j_{\sim 500}$  kA/cm. The report on this conf.
7. I. S. Glushkov, Yu. A. Kareev, L. G. Kotova, A. T. Kuharenko, Yu. A. Halimullin. Investigation of techniques to increase armature transition velocity. IEEE Trans. on magn., Vol. 33, No. 1, 1997 (will be published),
8. V. P. Bazilevskii, Yu. A. Kareev, R. M. Zayatdinov. Electroconductivity crisis of high speed metal contact. Proceedings of II All-Union Conference on high current arc discharge dynamics in magnetic field (Novosibirsk, 4-6 December 1991), Novosibirsk, 1992, pp. 285-304.

## RE-ESTABLISHING OF A COMPACT STRUCTURE OF A PLASMA ARMATURE IN A BARREL OF A RAILGUN

*A.P. Lototsky, L.G. Kotova, N.A. Nikolashin, Yu.A. Halimullin.*

TRINITI, Troitsk, Russia

### *Abstract*

The technology of a periodical compacting of the plasma armature in a railgun barrel for maintaining the efficiency of electromagnetic acceleration of dielectric projectiles is developed. The experiments showed that the current strip can become compact during a short section of the path equal to 10-15 cm in the barrel of a muzzle-fed railgun.

The behavior of a plasma armature in a three-stage railgun of 1 m total length is investigated. The second stage was of a muzzle-fed. The dielectric projectile of 1.5 g mass was accelerated in the barrel of 10x10 mm bore up to velocity,  $V > 3$  km/s. The dynamics of changes in the structure of a plasma armature in all stages of the railgun was investigated. Relying upon the comparison between the degrees of degradation of the armature in the first and third sections, where velocities are reasonably different, a prediction is made for the possibility of the use of barrels of a similar periodical structure for achieving high projectile velocities.

### *Introduction*

Despite the high level of velocity of a launch of dielectric projectiles of 1 g mass [1] the hope to achieve quickly hypervelocities in railguns didn't come true. Analyzing physical factors restricting operation of a railgun of dielectric projectiles with the help of a plasma armature (PA), many researchers noted disintegration of the PA with formation of parasitic current systems shunting the main discharge both in the trail of an armature and ahead of a projectile [2]. There exists a tight interconnection between delocalization of the PA and a number of physical processes, such as mismatching between a railgun and its power supply for instance and insufficient mechanical, thermal and electric strength of a barrel. Currently most research work is directed to solve the problem of disintegration of the PA with the purpose to elevate limiting velocities in a traditional (classical) railgun [3]. We are convinced that this type of research allows for a velocity level  $> 10$  km/s. The alternative possibility to suppress the discharge instability is in the use of that types of technical solutions of a barrel which facilitate the stabilization of the PA. In [4], there is investigated the railgun configuration where electrodes are divided in sections in a longitudinal direction and automatic switching off from the single current carrying bus of parts of one of the electrodes is done with the help of fuses after the armature passes them. This must prevent the possibility of flowing of a portion of the working current in the trail of the armature. In [5], there is developed a railgun with an external turn which can be fed both from a separate power source and in series with electrodes of a barrel according to a chosen connection configuration. As an option, there was considered an inverted current supply [6]. The analogous configuration was also considered in [7, 8]. It was noted that in a muzzle-fed configuration electric resistance decreases with the motion of the armature leading to the better match between the railgun and the power supply.

In order to realize successfully a muzzle-fed railgun configuration shown in fig. 1, one should take into account two factors:

- 1) generation of a strong magnetic field taking into account the current distribution over the armature;

2) the possibility of considerable deformation of the barrel along the  $y$ -axis which can lead to the change of the distance between electrodes.

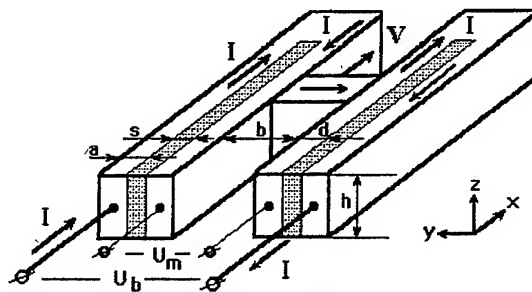


Fig. 1. The principle scheme of a muzzle-fed railgun

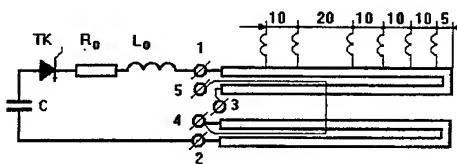


Fig. 2. The circuitry of a power source and railgun

It is obvious that both these factors are under the great influence of geometrical dimensions  $b$ ,  $d$ ,  $s$ ,  $a$ . So, the prevailing action on the rear area of the armature is exerted by the magnetic field of external electrodes. The magnetic field of internal electrodes which acts on the current in the front area of the armature is compensated with the magnetic field of external electrodes only partially, decreasing ponderomotive forces acting on the armature in direction of the  $x$ -axis. At a certain geometrical relationship between dimensions  $s$ ,  $d$ ,  $b$ , acceleration in an opposite direction is possible.

Attempts to decrease the magnitude of the decelerating force on account of optimization of geometry lead to the sharp increase of forces in  $y$ -direction due to interaction between currents of internal and external electrodes. Pulsed deformations of the barrel in this case can lock a metal armature. In the case of the PA, a dielectric projectile can be locked.

However, a presence of the accelerating ponderomotive force and its decelerating component in front of the PA develops a condition under which the discharge is getting compacted. The absence of a voltage permanently applied to the electrodes behind the PA and the flowing of a large fraction of the current in the front area also facilitate the compactness. Despite the fact that the trail is formed according to the same mechanisms as described in [2], the leakage current is low. The compactness of the structure of a PA in experiments with a railgun of UTSI is noted in [8], though one should mention a low level of a working current not exceeding 100 kA, what doesn't allow complete predicting for the area of high currents and velocities.

The number of investigations which we carried out had the purpose of realization of positive factors inherent in a muzzle-fed configuration of a railgun with a PA and consisted of three stages:

- 1) the investigation of the muzzle-fed configuration of a railgun and stability of a plasma armature;
- 2) the investigation of a combined two-stage accelerator consisting of traditional and muzzle-fed stages connected in series. In the second stage the PA is compacted with the purpose of the further use as an efficient propulsive agent;
- 3) the investigation of the three-stage accelerator, where the third usual stage is added to the previous configuration.

### *1. Experimental results of acceleration of a plasma discharge and dielectric projectile in a muzzle-fed railgun.*

It was mentioned in [2] that the biggest instability of a PA is observed when the current decreases,  $\partial/\partial t < 0$ . In the case of a classical railgun with the capacitor power supply the energy conversion into acceleration of the dielectric projectile is minimum during the period of time when

$\partial/\partial < 0$ . Therefore the objective of our experiments with a muzzle-fed railgun was determination of the stability of a PA namely on the decreasing part of the current diagram.

The electric diagram of the power supply and the railgun is presented in fig. 2, where  $C=55 \cdot 10^{-3}$  F,  $R_0=10^{-3}$  Ohm,  $L_0=1.5 \cdot 10^{-6}$  H; the active length of the railgun,  $l=0.7$  m;  $h=b=10^{-2}$  m,  $d=6s=3 \cdot 10^{-3}$  m. External electrodes of the width,  $a=12 \cdot 10^{-3}$  m are made of copper, internal ones of steel as a consequence of the requirement to have an increased mechanical strength with respect to the deflection in the  $y$ -direction.

Experiments were preceded by the static measurement of maximum values of deformations in the  $y$ -direction. With this purpose, plastic labels of indium in a lavsan insulation were installed in the barrel with a 100 mm spacing. The railgun contacts "3" and "4" were shortened. After a current discharge, new measurement of labels were conducted. The results for the maximum deformations obtained are presented in fig. 3. The marker "o" denotes experimental points. It should be noted that with the barrel length the value of  $\Delta y$  changes in the range of  $\pm 10\%$  around the average value. The dependence  $\Delta y(i_A)$  was taken into account in all experiments on acceleration of a dielectric projectile by a PA.

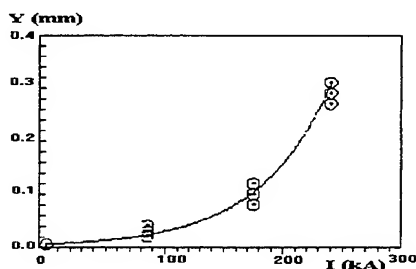


Fig. 3. The dependence of the change of the barrel dimension in the  $y$ -direction on the current amplitude

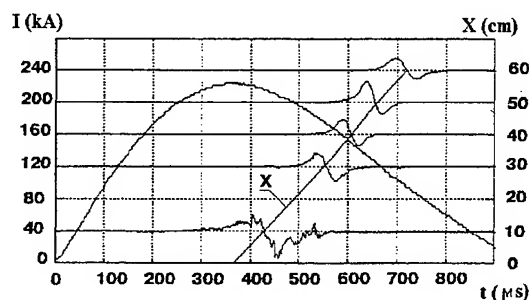


Fig. 4. The oscillogram of the current and the time dependence of the armature position in the mode of a "free arc"

We also used the characteristic feature of the pulsed deformation of the barrel with the purpose of organizing the discharge at a moment slightly later than the moment of the maximum current ( $t \approx 400 \mu s$ ). To do this, we used an ionizing conductor of the  $45 \text{ mm}^2$  cross-section installed in the barrel with the interference fit. The plastic deformation of this conductor impeded its motion along the barrel before the moment when the current had increased up to the maximum value. After the moment of the beginning of the current decrease ( $\partial/\partial < 0$ ), there appeared the gap between electrodes and the ionizing conductor which led to the barrel breakdown and formation of the discharge. Further the discharge accelerated along the barrel in the mode of a "free arc". In fig. 4, a characteristic current oscillogram with the maximum,  $i_A=220$  kA, and the dependence of the position of the geometrical center of the plasma armature on time, are presented. In the same figure, as additional information, profiles of signals from magnetic probes are presented, they were used for the determination of  $x(t)$ . The compacted character of the plasma structure is clearly seen. Its length is 6-7 cm at velocities within 1.6-2 km/s range. It can be seen in fig. 5 where the curves of the PA velocity,  $V(t)$ , and length,  $l(t)$ , vs. time are presented. Velocities were obtained by differentiating the  $x(t)$  function with respect to time. The maximum PA velocity was 2100 m/s. In an analogous mode of acceleration in a classical railgun at the same current value, the maximum PA velocity was 2960 m/s and the projectile accelerated only when the current was increasing.

In experiments on acceleration of dielectric projectiles, their dimension corresponding to  $b$  was slightly decreased taking into account the dependence  $y(l_A)$ . The gap which appears in the course of motion was compensated with an elastic shim situated behind the back side of the tandem projectile which was injected from a preaccelerator. The total mass of the tandem projectile was 5 g

at the mass of the payload of 1.4 g. In fig. 6 one can see typical oscillograms of the working current,  $I$ , voltage on input connections "1" and "2",  $U_b$ , and voltage on output connections "3" and "4",  $U_m$ . Besides, oscillogram of the voltage  $U_m$  between connections "3" and "5" which was obtained with the help of the compensation circuit shown in Fig. 2, presented too. When  $U_m$  is measured, the measurement contour turns out to be penetrated with a varying magnetic flux from external rails, that causes a counteracting electromotive force directed against the total voltage drop over the plasma armature, thus, decreasing a true time.

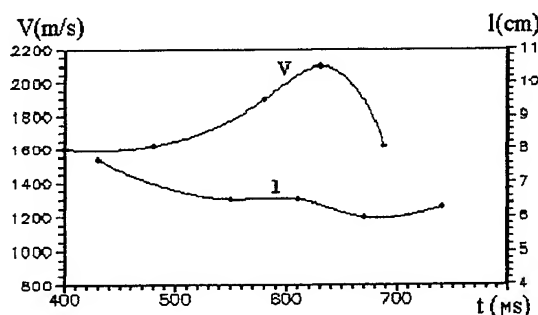


Fig. 5. The time dependence of velocity and length of the plasma armature

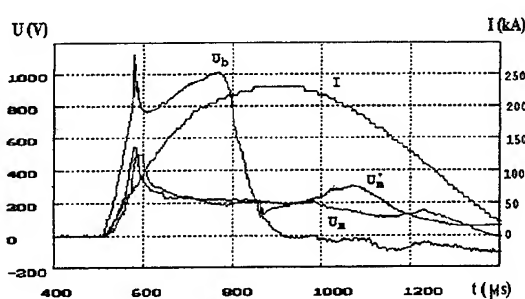


Fig. 6. Oscillograms of current ( $I$ ), voltage on the input terminals of a railgun ( $U_b$ ) and on the output terminals of a railgun ( $U_b$ ,  $U_b'$ ).

The compensation loop placed along an external perimeter of the barrel allows one to have to some extent more accurate true voltage value at the moment when the plasma armature lies under the right boundary of the loop. In our case this is the zone of location of the third magnetic probe, where the voltage drop on the PA was 280 V. The rate of the decrease of the voltage  $U_b$  is determined by two factors: the change of the sign of the current derivative and the decrease of the active railgun resistance with the motion of the PA on account of internal steel electrodes. The master plot of signals from magnetic probes and the dependence of the PA position inside the barrel is presented in fig. 7. The magnetic probe at the 0.25 m mark shows the discharge structure at the moment of its formation. It is seen that the discharge isn't localized into a compact piston. However, further with acceleration, the localization of the PA occurs and its length becomes to be about 6 cm. The payload accelerates from the injection velocity,  $V_0=500$  m/s, to the velocity of 1000 m/s at the muzzle.

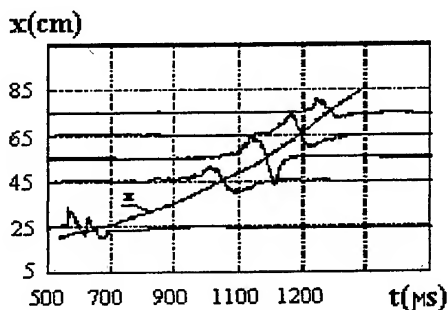


Fig. 7. The master plot of signals from magnetic probes and the time dependence of the plasma armature position.

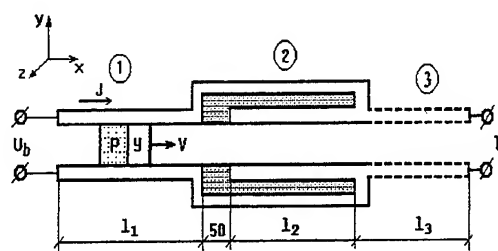


Fig. 8. The conceptual configuration of a two-cascade accelerator.



## II. Investigation of a two-cascade accelerator.

It was already stated earlier that the launch velocity of a payload is restricted in a classical railgun and the reasons of this were discussed. In brief the idea of our proposal is in following: after acceleration in a classical railgun the plasma armature should undergo some action making it compact, so it will be capable of playing the role of the plasma piston [9]. This process takes place in the second cascade of acceleration performed with a muzzle-fed configuration. Further the acceleration process can be cyclically prolonged. In our case the configuration of a two-cascade accelerator was constructed on the basis of a classical railgun shown in fig. 8. Cascades are galvanically connected and fed by the same current source. The lengths of the first and second stages,  $l_1$  and  $l_2$ , are 400 mm and 300 mm, respectively, the length of the dielectric gap between them is 50 mm. All other parameters of the barrel are analogous to parameters of a muzzle-fed barrel described in section I. In fig. 9, oscillograms of current  $I$ , and voltage  $V$ , are presented. In fig. 10 signals of magnetic probes and the dependence of the PA position in the barrel are presented. The payload of 1.4 g mass had the injection velocity of 500 m/s being between the 1-st and 2-nd magnetic probes. Delocalization of the PA in the first cascade was intentionally augmented by the use of insulation walls of macrolon, resulting in the formation of two parallel circuits (see fig. 10) and decrease of the payload velocity. The voltage  $U$  in the first cascade is the voltage on the discharge. The head portion of the PA reached the dielectric insertion at the moment of 860  $\mu$ s at the velocity of 1.62 km/s. Further, there occurred the transition of the PA into the 2-nd cascade with an increase of the discharge length. On the  $U(t)$  curve this time moment is marked with the sharp voltage leap. The current oscillogram didn't undergo noticeable changes because of the relative high value of  $L_0$ . In the muzzle-fed railgun section, the discharge was becoming more compact, this process finishing at the distance of 15-20 cm. The rate of the velocity increase was in this case lower than in the first cascade. The acceleration process completed to the time mark of 1140  $\mu$ s.

Special attention was paid to the process of transition of the PA from the first stage into the second since the problem of organizing of a plasma discharge during an initial period of the acceleration becomes much more complicated with the increase of the injection velocity. The circuitry of galvanically connected barrels with the voltage sharpening on the discharge which depends on the length of the insulation section and the velocity at the exit from the first stage allows reliable organization of the discharge in the second cascade in a wide range of velocities. It is clearly seen from the analysis of dependencies presented in fig. 11, overvoltages on the discharge,  $DU=U-U_{b1}$ , in three different experiments where  $U$ -the profile of the corresponding oscillogram at the output leads of the accelerator and  $U_{b1}$ -the voltage value at the moment when the PA reaches the dielectric interval. As a zero value of the time scale, the time of the coming of the discharge to the dielectric interval is taken.

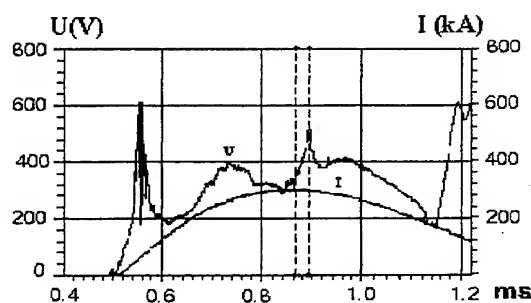


Fig. 9. Oscillograms of the current and voltage in the two-cascade accelerator.

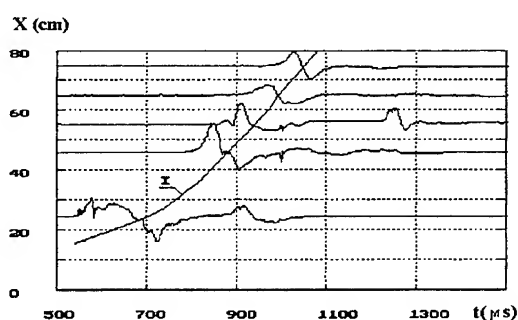


Fig. 10. The master plot of signals from magnetic probes and the time dependence of the plasma armature position.

### III. Investigation of a three-cascade accelerator

To the design of the three-cascade accelerator, for the first time a new optimized geometry of a muzzle-fed railgun was applied. The corresponding cross-section is shown in fig. 12.

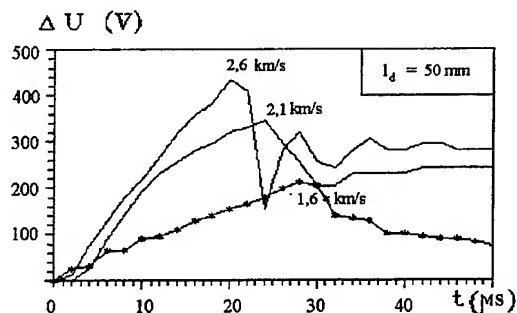


Fig. 11. The dependence of overvoltages on a dielectric interval of the accelerator (5 cm length).

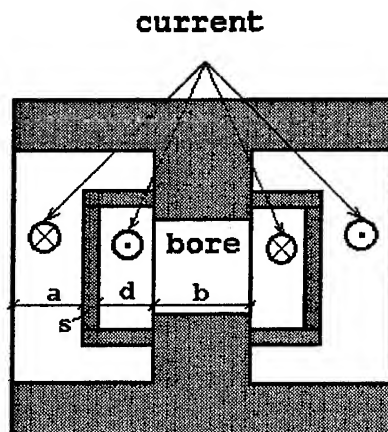


Fig. 12. The cross-section of the second cascade.

The inner electrodes are completely embedded into the body of outer ones. The thickness of dividing insulators,  $S$ , is minimized and equal to 0.5 mm. However, in this case the requirements to strength properties of the material of the inner electrodes and the construction of reinforced insulators become strict. Because of the absence of data on strength properties of a wide number of materials under pulsed loads of a characteristic duration of  $100 \mu s$ , we didn't conduct a strength calculation of a muzzle-fed design. There were carried out full-scale tests for inner electrodes made of copper and two different by design pairs of steel with a high yield strength. All tests were conducted at a feeding current amplitude of 500 kA.



Fig. 13. Inner electrodes after shots (the upper pair of copper, the middle one of steel and the lower of steel with a reinforced joint unit).

In fig. 13 photos of inner electrodes of the second cascade after tests are presented. Copper electrodes underwent plastic deformation, but the initial section of 160 mm length isn't deformed. Steel electrodes of the same design as copper ones had no plastic deformation but when they were tested there occurred the wearing of the projectile because of elastic deformations. The reinforced design of steel electrodes entirely removed the problem of pulsed deformations under the mode of tests and was performed in the three-stage accelerator shown in Fig. 8 (the third classical cascade is denoted with the dashed line). The length of cascades in an accelerator was  $l_1=250$  mm,  $l_2=210$  mm,  $l_3=335$  mm, the barrel bore was unchanged and equal to  $10 \times 10$  mm.

In the experiments, we did not use injection of the projectile into the first cascade but used the initiation of a discharge near the plugged breech of the barrel. It was done because of considerations of matching the load to the capacitance of the power source and obtaining the clearly displayed instability of the plasma discharge at a relatively low velocity level 2.5 km/s.

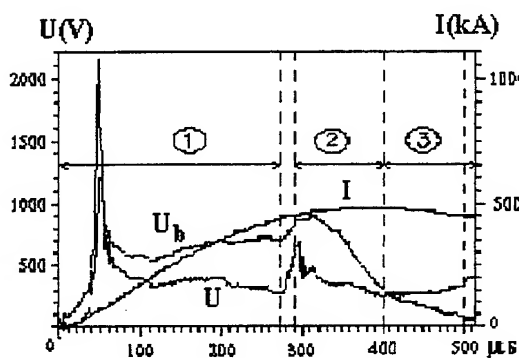


Fig. 14. Oscillograms of current ( $I$ ), voltage on the input terminals ( $U_b$ ) and output terminals ( $U$ ) of a railgun.

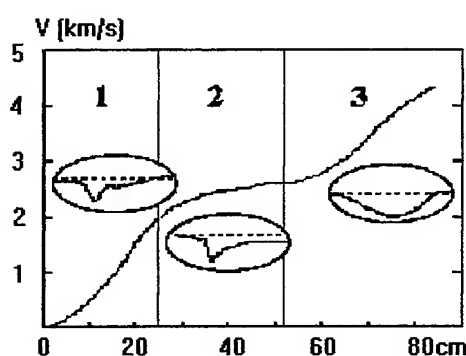


Fig. 15. The dependence of velocity and length of the plasma armature along the channel

In fig. 14 oscillograms of the current  $I$ , and voltages on the input  $U_b$ , and output  $U$ , terminals of the accelerator are shown. The dashed line shows zones characteristic for each cascade. The transition from the second cascade into the third one occurred at the  $390 \mu s$  moment and was accompanied with the change of the voltage character from decreasing to increasing  $U$ . After the exit of the PA from the accelerator at the  $500 \mu s$  moment, a restrike took place in the barrel in the zone of a joint between the second and third cascades.

The velocity diagram is presented in fig. 15. The injection into the second cascade occurred at 2.5 km/s and in the third cascade the muzzle velocity was 4.45 km/s which was facilitated by the well-compacted discharge, the profile of which is presented in the same figure. The double increase of the discharge length in the third cascade in comparison with the second one didn't lead to the break of a homogeneous structure of the discharge.

### Conclusion

The investigations performed, demonstrated new possibilities of a muzzle-fed railgun in the sense of the influence on the stability of the plasma armature. These possibilities are used for the development of an accelerator based upon a new principle allowing the re-establishing of compactness of the PA after its delocalization in a classical railgun and its transition into the next cascade. This procedure can be repeated later several times. However, in this case each following compensating cascade should be designed taking into account the level of velocity at which it operates.

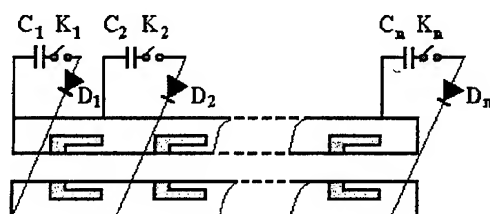


Fig. 16. The concept of a multi-cascade accelerator with a distributed current supply.

We expect that in the case of such a multi-stage accelerator the most efficient must be the power supply with a distributed current feeding based upon capacitor power sources (fig. 16). In such a configuration "classical" cascades will operate at intervals where the current increases ( $di/dt > 0$ ) and when  $di/dt < 0$ , the PA must go into the mode of re-establishing in muzzle-fed cascades. It is possible that the use of this principle will allow one to achieve launch velocities  $V > 10$  km/s which currently are not obtainable.

### References

1. E.M. Drobyshevskiy, S.I. Rosov, B.G. Zhukov, R.O. Kurakin, V.M. Sokolov. "The influence of the size of the plasma armature on efficiency of electromagnetic acceleration of a projectile". *Pisma v ZhTF*, 1991, v. 17, issue 2, p.23, Russian.
2. V.B. Zheleznyi, A.D. Lebedev, A.V. Plekhanov. "Influences on the dynamics of acceleration of an armature in a railgun". Materials of the 2-nd All-Union Seminar on dynamics of a high current arc discharge in a magnetic field. Novosibirsk, 1991, p.16. Russian
3. N. Kawashima, A. Yamori, S. Minarni, Hafiz-ur-Rahman. "Improvement of railgun projectile using higher specific weight material". *IEEE Trans. on Magn.*, 1995, v.31, n.1, p.189.
4. S. Usuba, Y. Kakudata, M. Yoshida, et al. "Performance of the discrete electrode railgun". *IEEE Trans. on Magn.*, 1991, v.27, n.1, p.611.
5. J. Tagber, R. Crawford and D. Keefer. "Experimental comparison of conventional and transaugmented railguns". *IEEE Trans. on Magn.*, 1993, v.29, n.1, p.523.
6. J. Taylor, R. Crawford and D. Keefer. "Muzzle-fed railgun experiments with 3-d electromagnetic simulations". *IEEE Trans. on Magn.*, 1995 v.31, n.1, p.360.
7. O.V. Fatianov, V.E. Ostashev, A.N. Lopyrev, A.V. Ulyanov. "Electromagnetic configurations of a railgun". *TVT*, 1993, v. 31, n. 3, p.462, Russian.
8. E. Cardelli. "Electromagnetic and thermal analysis of muzzle-fed railgun". *IEEE Trans. on Magn.*, 1995, v.31, n.1, p.113.
9. A.P. Lototsky, A.D. Lebedev, L.G. Kotova, Yu. Khalimullin. "Stability of a plasma armature in a combined two-cascade accelerator". The Seventh International Conference on Megagauss Magnetic Fields (Sarov, August 5-10, 1996). Book of Abstracts, Russia, FRNC-VNIEEF, Sarov, 1996.

# Pellet injector with the liner compression of the propellant gas

V.P. Bazilevski, Yu.A. Kareev, A.I. Kolchenko, V.P. Novikov

Troitsk Institute for Innovation and Fusion Research (TRINITI)  
142092 Troitsk, Moscow Region, Russia.

**Abstract** – Numerical and experimental investigations of the pellet injector that is a light gas gun in which the propellant gas is adiabatically compressed by the metallic liner are presented here. The movement of the metallic liner is caused by electromagnetic forces occurring during current passing through it. The experiment on accelerating the plastic pellet was carried out in the injector in which the aluminium liner compresses the propellant gas that is helium. The diameter and length of the pellet were 2 mm and 2 mm accordingly and its velocity was 2.5 km/s. The numerical experiments show that the deuterium pellet of such dimensions would be accelerated in the injector up to the velocity of 6 km/s.

## 1. Introduction

It follows from the numerical experiments that the pellet should have the velocity equal or more than 10 km/s to deliver the frozen fuel into the hot region of the big tokamak plasma cord. The best results on pellet acceleration were obtained on two stage gas guns in which the piston accelerated with the low pressure gas compresses adiabatically the gas pushing the pellet [1-3]. The maximum velocity of the pellets obtained in such injector was 3.4 km/s. The cylindrical liner accelerated by electromagnetic forces occurring during current passing through it is used in the injector proposed by us to compress the gas pushing the pellet and to keep the gas compressed for the time required for pellet acceleration. It will be shown below that on using the condenser battery with the energy of less than 1 MJ the injector concerned allows to reach such gas pulse parameters which are necessary for deuterium pellet acceleration up to the velocity equal 10 km/s.

## 2. Estimation of the pellet injector parameters

The scheme of the pellet injector is presented in Figure 1. It consists of the two steel electrodes specially made between which the cylindrical perforated metallic insert and the cylindrical aluminium liner which diameter is more than the diameter of the insert are installed. There is a hole on the axis of the one of the electrodes to place the pellet and there is a hole near the inner surface of the liner on the other electrode to puff the propellant gas. After switching on the condenser battery to the electrodes the aluminium liner moves to the radial direction, shuts off the volume occupied with the propellant gas from the gas puffing system and compresses it up to the maximum pressure  $P_M$  which value is stipulated by the correlation of the diameters of the liner and the perforated insert. During the gas compressing and keeping it in the volume  $\Omega_M$  at corresponding pressure  $P_M$  the pellet is accelerated. Compressed gas keeping for the time of the pellet acceleration is carried out by the electromagnetic forces due to the

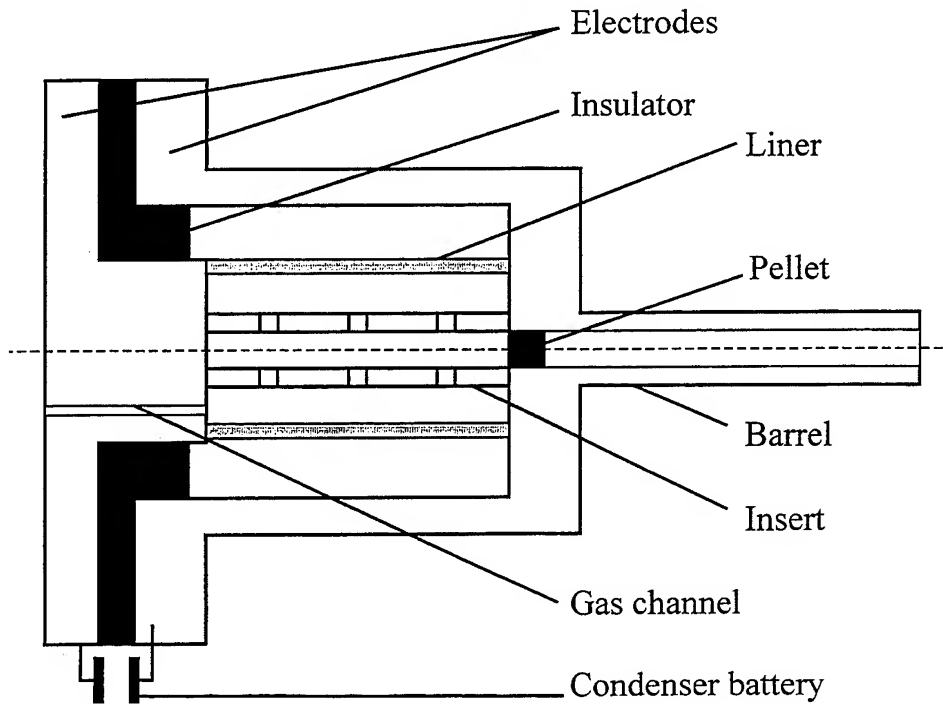


Figure 1. Scheme of pellet injector.

current of the corresponding value passing through the liner. Let us consider the injector parameters to be characterized. It is known that during the adiabatic compression of the gas its temperature  $T_g \sim \rho_g^{\gamma-1}$ , where  $\rho_g$  and  $\gamma = c_p/c_v$  - are the density and ratio of specific heats of the propellant gas. Let us have helium as a propellant gas for which  $\gamma = 5/3$ . Let us consider that the initial helium density will be increased by the compressing by  $\alpha$  times. Let us consider the initial helium temperature  $T_S = 293^\circ\text{K}$ , then the temperature of the compressed gas will be  $T_M = \alpha^{\gamma-1} T_S$ . Then the sound velocity in helium corresponding to this temperature will be  $C_M = 0.0588 T_M^{1/2} \text{ km/s} = \alpha^{1/3} \text{ km/s}$ . The analytical solution of the problem of a piston acceleration by the infinitely long gas cylinder equal to it in cross-section area is known [4]. Let us write this solution in the modified form.

$$\frac{V_p(t)}{C_M} = \frac{2}{\gamma-1} \left\{ 1 - \left[ 1 + K(t) \frac{\gamma+1}{2\gamma} \right]^{\frac{\gamma-1}{\gamma+1}} \right\}, \quad (1)$$

where  $V_p(t)$  - is the piston velocity depending on time,  $K(t) = (\rho_{gm} \cdot C_M \cdot t) / (\rho_p \cdot l_p)$ , and  $\rho_{gm}$ ,  $\rho_p$  and  $l_p$  - are the propellant gas density, piston density and its length. For uniatomic gas the formula (1) will have the form

$$\frac{V_p(t)}{C_M} = 3 \{ 1 - [1 + 0.8 K(t)]^{-0.25} \} \quad (2)$$

Let us denote  $f[K(t)] = 3 \{ 1 - [1 + 0.8 K(t)]^{-0.25} \}$  we will have the expression for definition of the piston (pellet) velocity.

$$V_p(t) = \alpha^{1/3} f[K(t)] \text{ km/s} \quad (3)$$

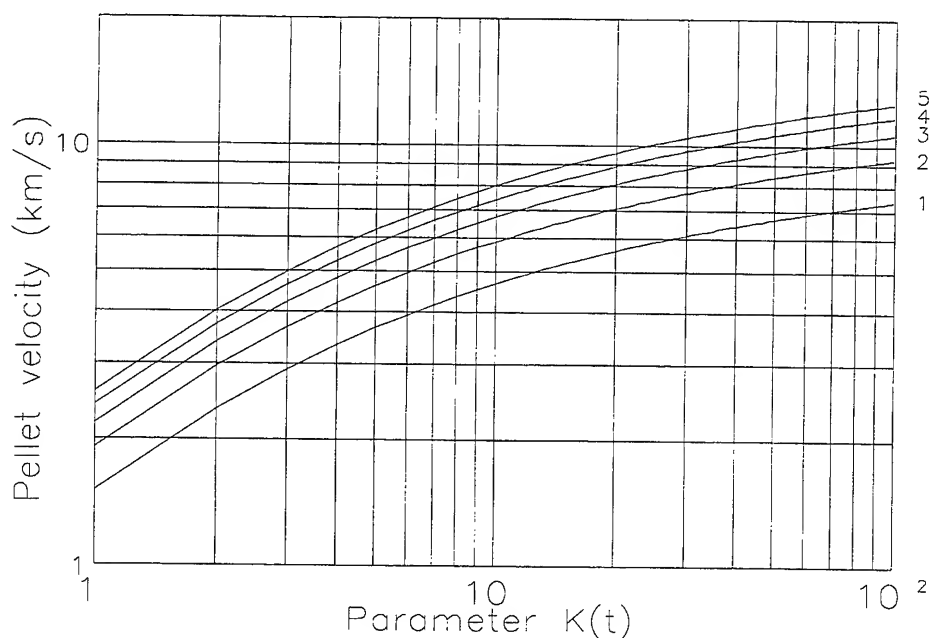


Figure 2. The dependence of the pellet velocity versus  $K(t)$  for the compressibility coefficient  $\alpha=50$  (1), 100 (2), 150 (3), 200 (4) and 250 (5).

In Figure 2 you can see the dependence of  $V_p(t)$  km/s versus  $K(t)$  for a number of fixed values of  $\alpha$ . You can see from Figure 2 that the pellet velocity reaches 10 km/s only for gas density compression up to not less than 125 times. Let us define the density of compressed gas from the expression for  $K(t)$ . For deuterium pellet with  $\rho_p l_p = 0.022$  g/cm<sup>2</sup> and keeping time for compressed gas  $t = 100$   $\mu$ s we will have  $\rho_{gm} = 0.044$  g/cm<sup>3</sup>. The pressure of the compressed gas will be  $P_M = 6.6$  kbar. To reach such parameters of the compressed gas the initial helium pressure should be  $P_S = P_M / \alpha^{5/3} = 2.1$  bar. Let us define the inner radius of the liner at the initial time as  $R_S = r_p \alpha^{1/2} = 11.2$  mm, where  $r_p = 1$  mm is the pellet radius. Let us the thickness of the liner wall  $\delta = 1$  mm. In compressed condition the outer liner radius will be  $R_f = (2R_S \delta + \delta^2 + r_p^2)^{1/2} = 4.9$  mm. Let us define the current value as  $I = 10 R_f (2\pi P_M)^{1/2} = 10 \cdot 0.49 (2\pi \cdot 6600 \cdot 10^6)^{1/2} \text{ A} \approx 1$  MA on condition that the gas pressure is equal to the magnetic pressure. Such parameters of the electric pulse can be obtained using the condenser battery whose capacity must be more than  $C = I \cdot t / U_S = 10^6 \cdot 10^{-4} / 5 \cdot 10^3 = 0.02$  F, where  $U_S$  is the voltage of the battery.

### 3. Numerical and experimental investigations of the injector

At the present time of the experimental investigation we decided the problem of the serviceably checking of the proposed scheme of the propellant gas compression. So we decided to use a plastic pellet with the density  $\rho_p = 1.14$  g/cm<sup>3</sup> to simplify the experiments. Optimal dimensions and injector parameters for experimental investigations were defined during the series of calculations. An aluminium liner was

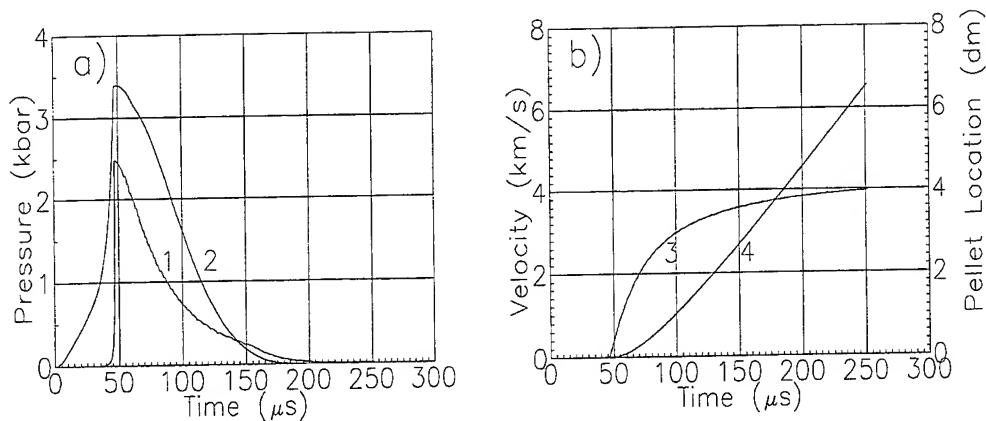


Figure 3. The dependence of the helium propellant gas pressure (1) and magnetic pressure on liner (2) versus the time, and the dependence of the pellet velocity (3) and the pellet location (4) versus the time for plastic pellet.

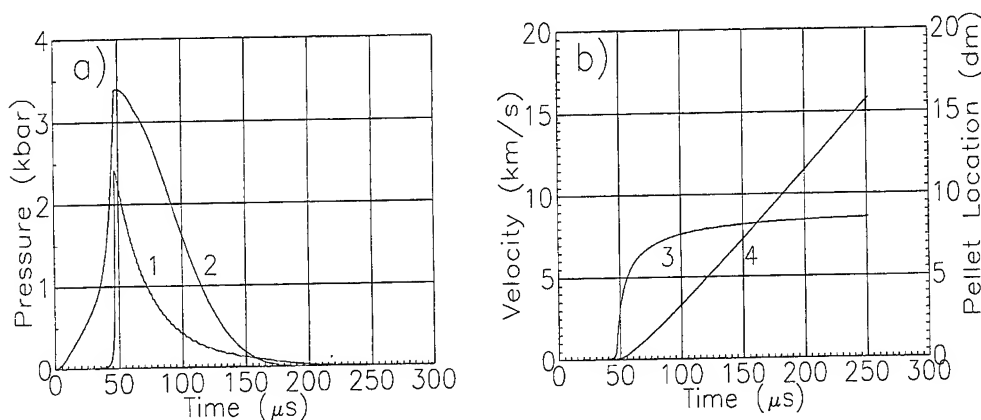


Figure 4. The dependence of the helium propellant gas pressure (1) and magnetic pressure on liner (2) versus the time, and the dependence of the pellet velocity (3) and the pellet location (4) versus the time for deuterium pellet.

chosen which length  $H_s$  is 34 mm,  $R_s = 18.5$  mm and  $\delta = 1$  mm. The initial pressure of helium propellant gas  $P_s$  is 1.1 bar. The dimensions of the cylindrical pellet are  $r_p = 1$  mm,  $l_p = 2$  mm. The power supply is a condenser battery which parameters coincide with the ones of the battery used during the experiment:  $C = 0.06$  F, accumulated energy  $W = 750$  kJ. The battery voltage was 2.1 kV in the numerical experiment. The results of the numerical investigations of the injector with plastic pellet are presented in Figure 3, and for solid deuterium pellet in Figure 4. The dependence of the helium propellant gas pressure and magnetic pressure on liner versus the time is presented in Figures 3a and 4a, and the dependence of the pellet velocity and the pellet location versus the time is presented in Figures 3b and 4b. The duration of the current pulse is 200  $\mu\text{s}$ , from which for the first 47.2  $\mu\text{s}$  the radial liner compression by the current is carried out and also the increase of the propellant gas pressure up to the



maximum value  $P_M=2.42$  kbar, which is stipulated with the dimensions of the cylindrical perforated metallic insert limited the liner movement and giving the compressibility coefficient  $\alpha=103$  is carried out. The current at that moment is about 1.2 MA and the magnetic pressure corresponding to this current is equal to 3.4 kbar. Owing to the magnetic pressure exceeds the propellant gas pressure for about subsequent 100  $\mu$ s we can see its keeping in the given volume and effective pellet acceleration as seen from Figures 3b and 4b at the acceleration length equal to 30 cm the plastic pellet has the velocity equal to 3.7 km/s, and the deuterium one -7.5 km/s.

During the experiments with the injector mentioned above the current and voltage on the liner were registered and also the photographs of the plastic pellet flight were registered by the high-speed photoregister. Before shooting the inner volume of the liner was pumped out up to the pressure 0.3 mbar and was leaked with helium up to the required pressure. The measured pellet velocity for the barrel with length equal to 30cm was 2.5 km/s and that was 1.2 km/s less than the velocity in the numerical experiment. There are several basic reasons which can promote decreasing of the pellet velocity: bad germetization of the liner endfaces, existence of microcracks in the liner material, existence of gas impurities in helium promoting to decreasing of the pellet velocity. At the same time we must point that in accordance with the calculations our injector could accelerate the deuterium pellet till the velocity of about 6 km/s.

## References

1. S.K.Combs,G.C.Barber, L.R.Baylor et al., Pellet Injector Research and Development at ORNL, in: Fusion Technology 1994.
2. S.Sudo, M.Kanno, H.Kaneko et al., High Speed Pellet Injection System "HIPEL" for Large Helical Device, in: Fusion Technology 1994.
3. J.P. Perin, A.Geraud, 3400 m/s Deuterium Pellet Injector for Tor Supra, in: Fusion Technology 1994.
4. L.D.Landau, E.M.Lifshits, Hydrodynamics, vol. VI, Moscow, "Nauka", 1988, p. 516.

## MATHEMATICAL SIMULATION OF PROJECTILE FREE MOTION IN COILGUN WITHOUT MECHANICAL LEADING ELEMENTS

Volodymyr T. Chemerys, Yuri N. Vaskovsky, Larissa N. Dynnik  
Institute of Electrodynamics, National Academy of Sciences of Ukraine  
56 Peremoga Avenue, Kyiv-57, 252680, Ukraine

**Summary** — In application to the coilgun the problem of free motion of projectile in the field of electrodynamic forces is considered. The expressions of forces and momenta affected on the conducting cylindrical projectile under influence of induced currents interaction with a pulsed solenoid field are derived. The assumption about divergence of solenoid and projectile axes in the result of both linear and angular displacement is used. The mathematical model of projectile motion in a one-stage coil accelerator is built using the magnetically coupled contours method in the cylindrical co-ordinate system. This model describes the possible transversal radial oscillations and angular oscillations of projectile in the time-varying field of solenoid excited by the capacitor discharge. The change of resistance for the elementary contours under consideration in the result of Joule's heating is taken into account. The character of projectile motion at different initial conditions was studied by the numerical investigation with the created model. The level of resulting displacement obtained by the projectile at the exit of solenoid would be less if the solenoid would be more long, center of projectile mass position would be chosen properly and if the initial velocity of projectile would not be zero. The research of center of mass position on the character of projectile motion was undertaken and its result have led to recommendation about the center of mass disposition ahead of geometrical center of conducting current-carrying shell of projectile. Numerical calculations are performed for caliber of accelerator 56 mm with mass of projectile 0.5 kg.

### 1. Introduction.

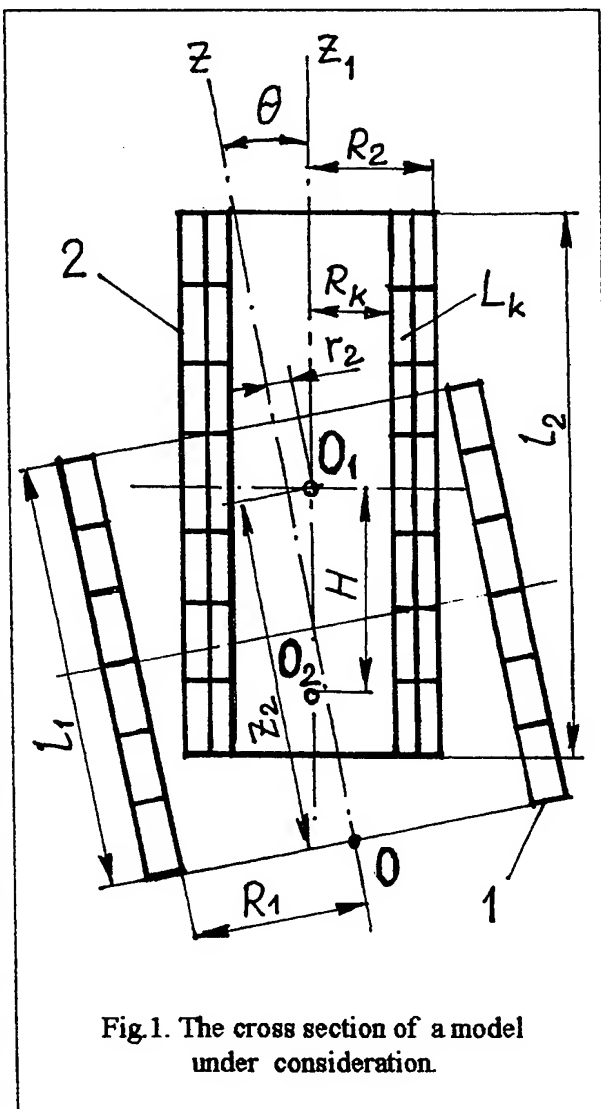
Among the possible methods of macrobody throwing by electrodynamic forces the induction method is attractive enough for development owing to negligible influence of electrical erosion process on the accelerator operation. Even at high level of energy the zone of probable destruction is concentrated on the projectile which is a body for single usage. It seems possible to defend the system of accelerating coils from the dangerous influence of strong pulsed currents and fields. But the problem of moving projectile contact with inner surface of coils is staying. Three technical approaches to resolution of this problem are possible: 1) by manufacturing of the leading barrel in the form of thin-wall tube from the solid non-magnetic and non-electroconducting material; 2) by application of the metal leading rails system made deeper partially in the body of projectile; 3) by usage of the magnetic pressure forces for motion of projectile fixation along with axis of accelerating system. Each of this approaches contains definite difficulties. There is a problem of material in the first case; complex design of barrel in the second case with necessity to mount the rail holders in the space between coils, some increasing of projectile shell electrical resistance through presence of channels for rails made on its surface in the second case; and the problem of projectile motion stability in the third case. In spite of existence of some restoring to center forces while the conducting body is accelerated by axisymmetric pulsed magnetic field, it is not simple to prevent the restlessness of projectile during motion inside of accelerator through a possible designing inaccuracy or through initial position of projectile deviations. When the mechanical leading elements is absent, a destruction of coils may be the result of a projectile restlessness. That is why this

problem is taken under consideration by different research groups [1] - [4]. This paper deals with numerical modeling of accelerated macrobody motion and studying of the restlessness evolution during interaction of projectile with primary pulsed solenoid.

## 2. A Scheme of Interaction and Electrodynamic Forces and Moments Calculation

The longitudinal cross section of coilgun under consideration is shown in Fig.1. It includes the solenoid 1 and projectile 2. The unmovable cylindrical co-ordinate system  $O, r, \varphi, z$  is connected with bottom plane of solenoid. The movable co-ordinate system  $O_1, r, \varphi, z_1$  is connected with geometric center of conducting shell of projectile 2. The instant position of projectile inside of solenoid may be given by three independent variables: the angle  $\theta$  between axes of solenoid and projectile and two co-ordinates of projectile center  $O_1$  position ( $r_2, z_2$ ) in the co-ordinate system of solenoid. The center of projectile mass  $O_2$  can differ from  $O_1$  at the non-uniform distribution of additional mass inside of conducting shell 2. The cross section of solenoid will be consider at the further analysis as the totality of the  $N$  circular elementary electrical contours with the same current  $i_1 = I w_1 / N$ , where  $w_1$  is a real number of turns of solenoid and  $I$  is a current supplied. Current-carrying shell of projectile will be presented by the  $N_d$  layers of the short-circuited elementary contours at the total numbers of them  $N_p = N_d N_q$ , where

$N_q = 2N_2 + 1$  is a number of elements along with length of shell. At the choice of the elementary contours cross section dimensions it is necessary to take into account the anticipated depth of the electromagnetic field penetration so that any dimension of element cross section would be not more then 2...3 value of skin depth.



The expressions of electrodynamic forces and moments for circular contour of small cross section (approximation of current filaments) stipulated by interaction with totality of elementary contours of solenoid were obtained using the initial expressions for the pair of non-coaxial circular contour given in [4]. The components of force can be written as

$$F_{rk} = 2 i_k R_k \sum_{j=1}^N \int_0^{\pi} B_{zj} \cos \psi d\psi; \quad (1)$$

$$F_{zk} = 2 i_k R_k \sum_{j=1}^N \int_0^{\pi} B_{rj} (\Delta R / R_k) [1 - (\Delta R / R_k) \cos \psi] d\psi. \quad (2)$$

The components of moments stipulated by the electrodynamic forces are the next:

$$M_k = -2 i_k R_k^2 \sum_{j=1}^N \int_0^{\pi} B_{rj} \cos \omega (\Delta R / R_k) [1 - (\Delta R / R_k) \cos \psi] d\psi. \quad (3)$$

Here the components of magnetic induction vector are written in accordance with [5]:

$$B_{zj} = i_j (\mu_0 / 2\pi A_1) [K + E(A_2 / A_3)];$$

$$B_{rj} = i_j (\mu_0 / 2\pi A_1) (\Delta z_j / R_k') [-K + E(A_4 / A_3)].$$

The values included:  $R_k, R_j$  are the radii of contours under consideration;  $z_j$  and  $z_k$  are their axial co-ordinates;  $K$  and  $E$  are the full elliptic integrals of the first and second kind respectively;  $\Delta z_j = z_j - z_k$ ;  $A_1 = [(R_j + R_k')^2 + \Delta z_j^2]^{1/2}$ ;  $A_2 = R_j^2 + (R_k')^2 + \Delta z_j^2$ ;  $A_3 = (R_j - R_k')^2 + \Delta z_j^2$ ;  $A_4 = R_j^2 - (R_k')^2 - \Delta z_j^2$ .

There are the forces and moments in (1) - (3) which are able to cause the contour displacement. The essential feature of analysis is the consideration of projectile as the absolutely solid body, and the forces caused its deformation were out of consideration. In this connection all the forces and moments of elementary contours in projectile were reduced to the center of its mass and were included in the equations of motion written for the center of mass. The resulting displacing radial force is

$$F_r = \sum_{k=1}^{N_p} F_{rk}, \text{ and resulting axial force is } F_z = \sum_{k=1}^{N_p} F_{zk}.$$

The resulting moment reduced to the center of mass for projectile may be written in the assumption of small value of angle  $\theta$ :

$$M_k^{cm} = M_k + (l_2 / N_q) [k - \text{int}(2hN_2)] \cdot F_{rk}, \quad k = (-N_2), N_2. \quad (4)$$

Here  $h = H / l_2$ ,  $l_2$  is an axial length of conducting shell,  $H$  is a distance between the geometric center of projectile  $O_1$  and its center of mass  $O_2$ . The parameter  $h$  is a measure of center mass displacement with respect to  $O_1$ . The range of variation for  $h$  is  $-0.5 < h < 0.5$ .

Summarized (4) on the all totality of elementary contours, the resulting moment acting on the projectile may be written:

$$M = \sum_{k=1}^{N_p} M_k^{\text{con}}. \quad \text{This moment stipulates the turn of projectile with respect to its}$$

transverse axis yielding to oscillation of the angle  $\theta$ . To be correct it is necessary to mark that the expressions given above are obtained in the assumption about small value of the angle deviation so the contours of current in the elementary conductor may be accepted practically as circular and some difference of planes for contours of solenoid and contours of projectile may be neglected.

### 3. Mathematical model

Mathematical model of coil accelerator contains the equations for the currents calculations, equation of connection with source of current, equations of motion and correlation between currents in elementary contours and their resistance. Within the frame of approach described the matrix equation for the current definition in the totality of elementary contours of projectile would be traditional in the form:

$$[L(t)](d/dt)[I] + [I](d/dt)[L(t)] + [R][I] = [U].$$

Here  $[L(t)]$  is a matrix with  $N_p \times N_p$  elements, which are the self-inductances and mutual inductances of elementary contours;  $[R]$  is a diagonal matrix of contours resistances;  $[I]$  is a matrix-column of unknown currents including current of solenoid  $i_1$ ;  $[U]$  is a matrix-column of voltages with only different from zero component which is a voltage of solenoid  $u_1$ . With energy supply from capacitor  $C$  the next equation of system is

$$du_1/dt = i_1/C, \quad u_1 = U_0; \quad i_1 = 0 \quad \text{at} \quad t = 0.$$

The matrix  $[R]$  contains the following components: a given resistance of solenoid  $\rho_1$ ; resistances of elementary contours in the projectile  $\rho_{2k} = 2\pi R_k / S \sigma_k$ , where  $S = l_2 d / N_p$ ;  $\sigma_k = \sigma_0 / (1 + \beta Q_k)$ ;  $\sigma_0$  is a coefficient of electroconductivity at  $0^\circ \text{C}$ ;  $\beta$  is a thermal coefficient for conductivity [6],  $Q_k$  is a thermal energy of a Joule's losses in the contours. This value calculation needs the next equation:

$$dQ_k/dt = \rho_{2k} i_{2k}^2,$$

$$\text{or} \quad dQ_k/dt = i_{2k}^2 (2\pi R_k / S \sigma_0) (1 + \beta Q_k); \quad k = \overline{1, N_p}.$$

The simple procedure of resistance calculation as function of heating is possible due to short-time consideration of acceleration process (within time interval near 1 ms), when the heat exchange may be neglected in the volume of massive conductors.

The equations of the projectile motion were used in the form:

$$\begin{aligned} dv_z/dt &= F_z/m; & dv_r/dt &= F_r/m; & dr_2/dt &= v_r; \\ dz_2/dt &= v_z; & d\omega/dt &= M/J; & d\theta/dt &= \omega \end{aligned}$$

with the variables used:  $v_r$  and  $v_z$  are the radial and axial components of the velocity vector;  $\omega$  is an angular frequency of projectile rotation relatively the transversal axis;  $m$  is the mass of projectile;  $J$  is a moment of inertia for a projectile. The forces of opposition to motion were not taken into attention. The system of equations given above with an initial conditions of usual kind have presented the background for a numerical investigation of projectile motion with restlessness.

#### 4. The Results of Numerical Investigations

The numerical investigations were conducted under variable initial conditions for a projectile. At the chosen dimensions of solenoid and projectile the last one could have a different initial displacements of its axis relatively of solenoid axis. The capacitor in

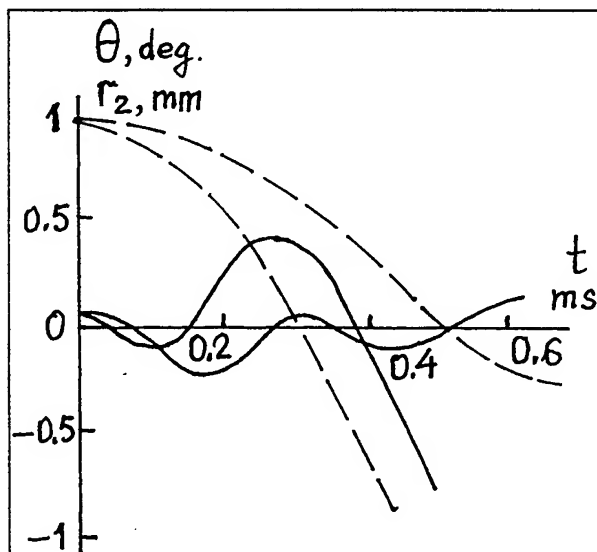


Fig.2. The parameters of deviation in time at the oscillations of the projectile without axial acceleration.

the energy store was variable also. And in the final stage of investigation the position of center of mass was variable in the projectile (parameter  $h$ ). The numerical results given in Fig.2 - Fig.4 concern the coilgun with next data: solenoid length  $l_1 = 0.08$  m; projectile shell length  $l_2 = 0.1$  m; inner radius of solenoid  $R_1 = 0.03$  m; outer radius of projectile shell  $R_2 = 0.028$  m; mass  $m = 0.5$  kg; number of turns in solenoid 24; capacity of energy store (main variant)  $c = 6.44$   $\mu\text{F}$ ; initial voltage  $U_0 = 5$  kV.

The solution of motion equations ( $\theta$  - solid line,  $r_2$  - broken line) are shown in the Fig.2 at the next initial data: the geometric centers of projectile and solenoid are

close to coinciding with small radial and angular displacement:  $\theta(0) = 0.1$  deg;  $r_2(0) = 1$  mm. Initial axial velocity was zero. This example illustrates the oscillation of projectile inside of solenoid without axial acceleration. The initial nonsymmetrical position has the sequence the impact of projectile with inner surface of coil after 0.45 ms (lines 1). While the capacity  $C$  was decreased up to 2.6  $\mu\text{F}$ , oscillations of projectile were without impact (lines 2). In the Fig.3 the next numerical result is

shown: motion was accelerated due to initial displacement of projectile center ahead on the  $0.2 \cdot l_1$  with respect to solenoid center. The others initial conditions were the same as in Fig. 2, lines 1. The center of mass position was varied in a direction to the forward butt-end of projectile shell ( $0 < h < 0.5$ ). It is seen that such a change of the center mass position does not lead to great stability of the movements of the geometric center of projectile but the angle swing may be reduced at the proper definition of parameter  $h$ .

The amplitude of the transversal oscillations of projectile center may be reduced if the initial axial velocity would be not zero. Additional factor of stability improvement is

is the proper choice of the solenoid length. In the Fig. 4 the numerical study results are shown for the accelerator with the same dimensions as in Fig. 1, but with other length of solenoid and for different meanings of initial axial velocity of projectile. The system of curves numeration in the Fig. 4 corresponds to the next data:

1 - the length of solenoid  $l_1 = 0.04$  m, initial velocity of projectile is  $v_{z0} = 100$  m/s;

2 -  $l_1 = 0.04$  m,  $v_{z0} = 200$  m/s; 3 -  $l_1 = 0.08$  m,  $v_{z0} = 200$  m/s; for all the cases 1 - 3 the initial displacement of projectile is the next:  $\theta(0) = 0$ ;  $r_2(0) = 1$  mm (only collinear displacement). For the remains curves: 4 -  $l_1 = 0.04$  m,  $v_{z0} = 100$  m/s; 5 -  $l_1 = 0.08$  m,  $v_{z0} = 100$  m/s, initial displacement for the curves 4, 5 is only angular:  $\theta(0) = 1$  deg;  $r_2(0) = 0$ . As the criterion of the projectile restlessness the new parameter of maximal deviation was introduced:

$$\delta_{\max} = \max(\delta_{\text{up}}; \delta_{\text{low}})$$

with usage of the edge points deviations of projectile shell with respect to axis of the solenoid:  $\delta_{\text{up}}$  in the upper point,  $\delta_{\text{low}}$  in the lowest point along with z-axis.

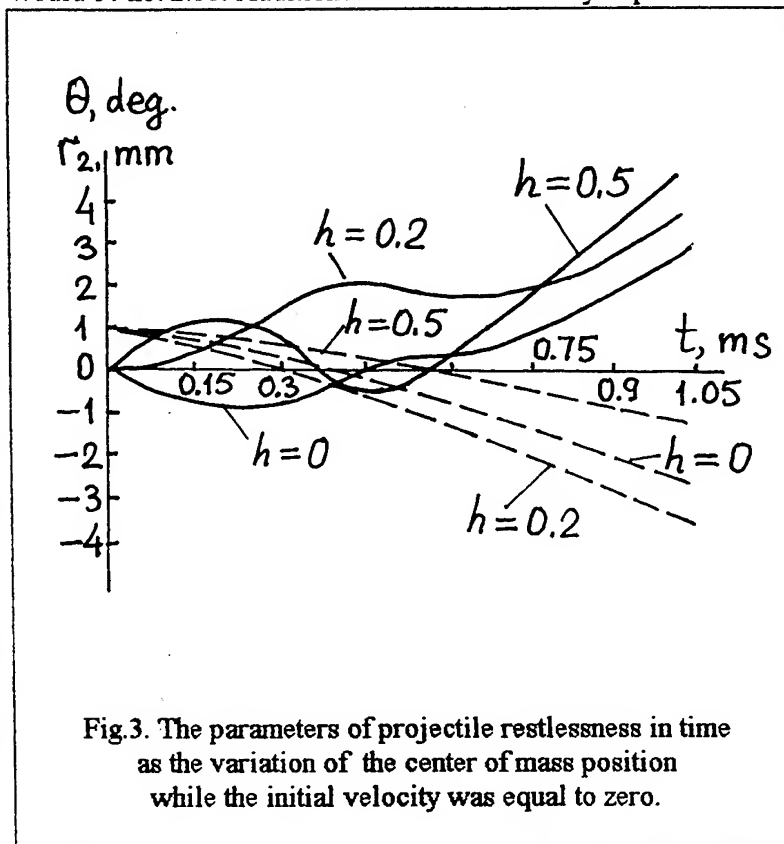


Fig. 3. The parameters of projectile restlessness in time as the variation of the center of mass position while the initial velocity was equal to zero.

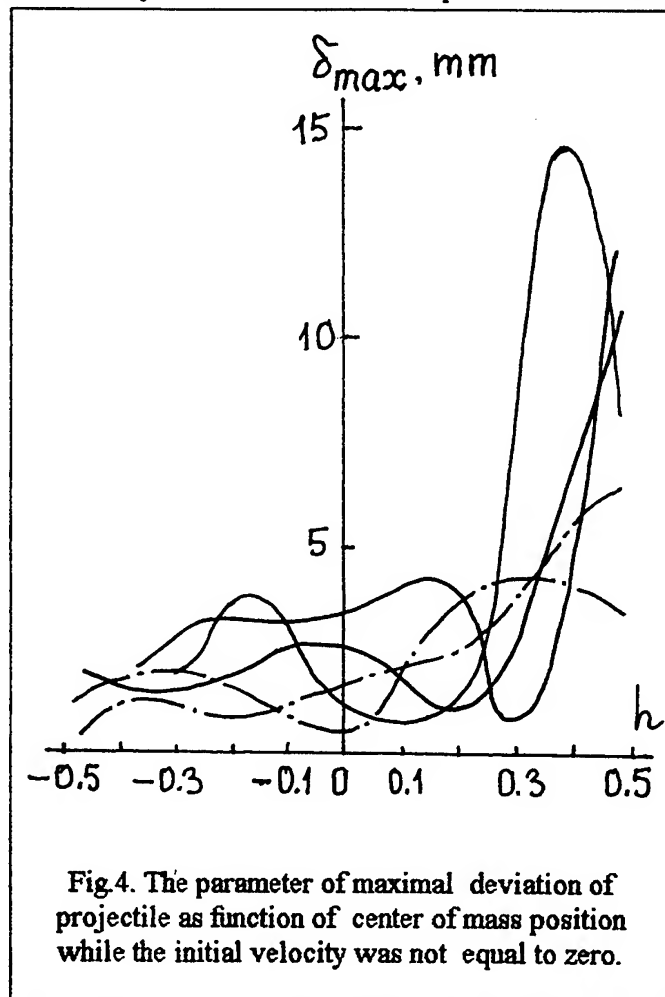
These deviations are defined as

$$\delta_{up}(t) = r_2 - l_2 (h + 0.5) \sin \theta; \quad \delta_{low}(t) = r_2 + l_2 (h + 0.5) \sin \theta.$$

It is seen in the Fig.4, that for every curve the optimal value of parameter  $h$  exists. For example, for the curve 2 the best value  $h = 0.3$ , for the curve 4 the best value  $h = 0$ . At the same time for all the cases at  $h < -0.3$  the great decreasing of the maximal deviation of projectile is observed.

## 5. Conclusion and Recommendations

The creation of mathematical model for estimation of oscillations evolution in time was connected with need to accept several simplified assumptions in the procedure of the electrodynamic interaction description for the contours having a difference of the



axes position. These assumptions have the physical background and led to numerical results which can be consider as trustworthy. The important sequence of the analysis fulfilled is the conclusion about the strong feasible oscillations of projectile near the axis solenoid even at small initial linear or angular displacement of projectile from the co-axial position inside of solenoid. It may be proved that the center of mass of projectile must be placed more close to the back butt-end of conducting shell. It may be explained by the more short length of arm for the transversal forces which are able to create the rotational momentum. The improved correction of the angle position of projectile may be made by the coercion on the forward part of

projectile with using of an additional small power solenoid because the relatively small forces are necessary to cause the turn of projectile if the force would be applied in the point remotod from the center of mass. The additional investigation may be need



to evaluate the intensity of magnetic field on this process. At any case it is out of doubts that in the very strong field the picture may be similar, and the body accelerated will be leave the zone of interaction with the transversal or the rotational momentum if the initial position of body would not be co-axial inside of a drive solenoid.

### References

1. Ki-Bong Kim, E. Levi, Z. Zabar, L. Birenbaum. *Restoring force between two noncoaxial circular coils*. - IEEE Transactions on magnetics, Vol.32, No.2, March 1996, pp.478-484.
2. Ki-Bong Kim, E. Levi, Z. Zabar, and L. Birenbaum. *In-bore projectile dynamics in the linear induction launcher, part 1: oscillations*. - IEEE Transactions on Magnetism, Vol.31, No.1, pp.484-488, January 1995.
3. Ki-Bong Kim, Z. Zabar, E. Levi, and L. Birenbaum. *In-bore projectile dynamics in the linear induction launcher, part 2: balloting, spinning and nutation*. - IEEE Transactions on Magnetism, Vol.31, No.1, pp.489-492, January 1995.
4. Yu.N. Vaskovsky. *The electromagnetic forces and moments between non-concentric circular contours of currents*. - *Tekhnicheskaya elektrodinamika* (Technical Electrodynamics), 1989, No.1, pp.22-26 (in Russian).
5. O.V. Tozony. *Electromagnetic fields calculation on the computers*. - Technique Publ., Kiev, 1967. - 252pp. (in Russian).
6. H. Knoepfel. *Pulsed high magnetic fields*. - North-Holland Publishing Company, Amsterdam - London, 1970, 392 pp.

## CURRENT DISTRIBUTION IN THE CONTACT ZONE OF RAILGUN

Volodymyr T. Chemerys, Yuri N. Vaskovsky

Institute of Electrodynamics, National Academy of Sciences of Ukraine  
56 Peremoga Avenue, Kyiv-57, 252680, Ukraine

**Summary** - The theoretical model of 2D current distribution in high current sliding contact of rail launcher is developed with detail consideration of magnetic field together with approximate presentation of transition layer in the view of thin sample of conducting medium whose initial electroconductivity is known. Dependence of electroconductivity on the local current density as for rails, as for armature and for transition layer is considered. The possible anisotropy of electroconductivity of conducting medium in contact zone is not accounted. The magnetic problem is formulated in the plane  $(x, y)$  with respect to  $z$ -component of the field strength. The movement of railgun armature is assumed having a constant acceleration (near  $5 \cdot 10^5 \text{ m/s}^2$ ) from zero or other initial velocity. The mechanical equation of armature motion, heat exchange inside of conductors and a possible rails deformation were out of consideration. The typical shape of pulsed current supply is accepted the next: linear increasing with derivative 10 MA/ms and smoothed changing to the top during 0.2 ms, linear decreasing on the top with derivative  $-0.125 \text{ MA/ms}$  during 1.0 ms, and decreasing up to zero on the back during 0.8 ms with derivative  $-1.25 \text{ MA/ms}$ . The total duration of pulsed current near 2 ms was the ground for neglecting of heat transfer. The first purpose of analysis was to investigate the influence of macrofield and average parameters of transition layer on the current distribution under armature acceleration consideration. The boundary conditions considerably were pre-defined by the two-dimension formulation of problem, but feature is in the calculation of magnetic field across the initial section of rails, which was found in the result of additional problem solution for  $y$ -component of vector potential with known current supply density in the right side. Thus the full problem consists of two parts: first of them is the calculation of  $z$ -component of magnetic strength in the beginning section of rail, and a second part is the calculation of current and Joule's losses distribution in the three areas: rail, armature and transition layer. The numerical realization of mathematical model is fulfilled by using a finite elements method. For a mesh generation the automatic program complex was used created by A.S. Tsybenko *et al.* in Kyiv Polytechnic. The peculiarities of the numerical scheme were the next: iterational method of solution in the time with coefficient of relaxation depending on the armature velocity; generation of new regular mesh in time for the armature and closing areas of rails. The results of numerical simulation which have been performed for different materials of rails and armature under conditions of different thickness and electroconductivity of transition layer and zero initial velocity of armature are given in the paper. Numerical modeling allows to conclude about efficiency of current distribution analysis and prediction in a contact zone using the conceptions of magnetic field diffusion theory if the average properties of contact layer are known.

### 1. Introduction

The problem of electrodynamic rail type accelerator creation for a hypervelocity gun systems continues to be a subject under consideration for a considerable number of researchers in different countries. At least two reasons may be found to explain this interest: 1) hypervelocity launching including electromagnetic one is staying in the list

of critical technologies in USA and NATO countries; 2) the railgun while is not studied in the full volume and it may be considered again and again as the complex and interesting subject of investigation with complicated interconnected influence of electrophysical, thermal and mechanical processes. At the same time two main problems may be named which cause the main difficulties in the practical designing of railgun: 1) a problem of the safe sliding contact provision at high velocity and mega-Amperes current; 2) a problem of transportable pulsed electric energy supply source creation.

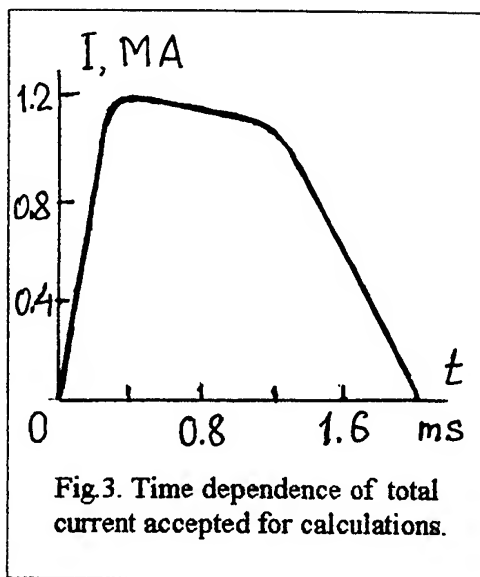
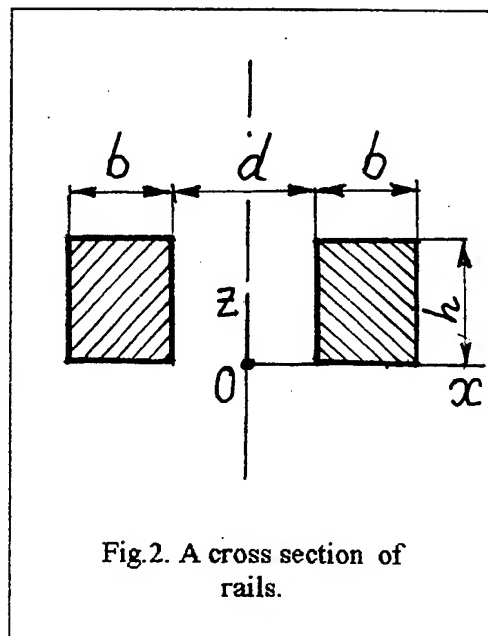
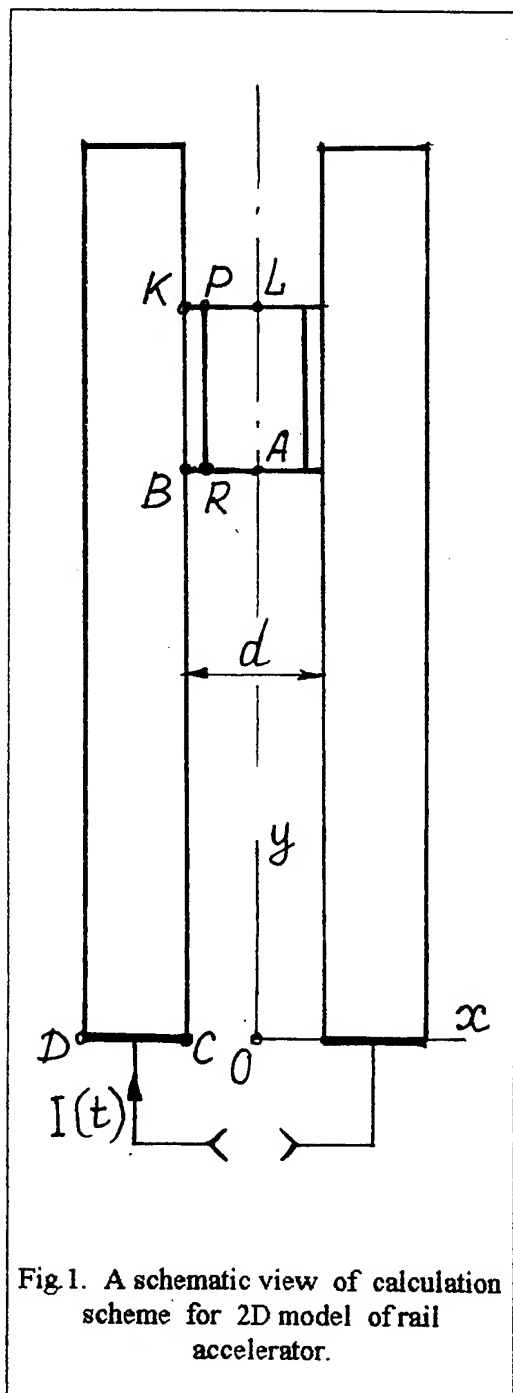
The first problem solution demands the fundamental research of electromagnetic and thermal process in common with analysis of matter and current transfer through the surface of intercontact between the moving conductors. Only first solid results storing occurs this time, nevertheless the some progress in the studying of this slowly known area may be fixed. The second problem is not trivial also. In spite of the statement done by Marilyn Freeman and Edward Schmidt [1] that Institute of Advanced Technology in University of Texas at Austin (IAT) have not found any scientific of physical limitations on the way of pulse power supply system creation for electric gun, the series difficult technical problems must be resolved before the source with acceptable specific parameters will be made. We can see the obvious achievements in the simulation of high current railgun, for example E. Cardelli work [2], which cannot however exhaust the problems inherent to this device stipulated by the presence of sliding contact. Even the results of some calculations coincide with experimental data it cannot mean to-day the building of the safe theoretical model leading always to the right results, because the accents needed with respect to contribution of different physical phenomena in the resulting picture of processes in the sliding contact are not arranged yet. In the work [2] the main attention was concentrated on the thermal melting and vapourizing of armature material in the contact zone and the numerical procedure to analyse the coupled electro-thermal transient problem, magnetohydrodynamic motion of the molten metal was neglected. The some general considerations concerning the sliding contact provision were told by one of this work authors in the paper [3]. The work presented here is devoted to the partial question of mathematic simulation of sliding contact based on the approach of electromagnetic field diffusion analysis with application of equivalent electroconductivity for transition contact layer.

## 2. Mathematic Model of Rail Accelerator

The peculiarities of current distribution and Joule's losses in the zone of electric contact between electroconducting rails and accelerated body may be investigated using two-dimensional model presented schematically in the Fig.1.

The system of Maxwell's equations for a moving electroconducting medium may be written as

$$\begin{aligned} \operatorname{rot} \mathbf{H} &= \mathbf{j} + \mathbf{j}_0; \quad \operatorname{rot} \mathbf{E} = -\partial \mathbf{B} / \partial t; \\ \mathbf{j} &= \sigma(\mathbf{E} + \mathbf{V} \times \mathbf{B}); \quad \mathbf{B} = \mu \mathbf{H}. \end{aligned} \quad (1)$$



where  $\mathbf{B}$ ,  $\mathbf{E}$ ,  $\mathbf{H}$  are the vectors of magnetic induction, electric and magnetic fields strength, respectively;  $\mathbf{j}$  is a density of induced current;  $j_0$  is the component of current density stipulated by the action of external source;  $\sigma$  is an electroconductivity coefficient for conductor,  $\mu$  is a magnetic permeability,  $\mathbf{V}$  is a velocity vector of moving conductor.

In a 2D model of the rail accelerator the next orientation of the vectors under consideration is supposed:

$$\mathbf{V} = \mathbf{e}_y V_y; \mathbf{H} = \mathbf{e}_z H_z; \mathbf{j} = \mathbf{e}_x j_x + \mathbf{e}_y j_y; \quad (2)$$

here  $\mathbf{e}_x$ ,  $\mathbf{e}_y$ ,  $\mathbf{e}_z$  are the orths of rectangular co-ordinate system.

The next equation in the partial derivatives for magnetic field strength have been obtained from (1) with account of correlations (2):

$$\frac{\partial}{\partial x} \left( \frac{1}{\mu} \frac{\partial H_z}{\partial x} \right) + \left( \frac{1}{\mu} \frac{\partial H_z}{\partial y} \right) - \sigma \frac{\partial H_z}{\partial x} = \sigma V_y \frac{\partial H_z}{\partial y}. \quad (3)$$

The components of the current density vector are defined by the first equation of system (1):

$$j_x = \partial H_z / \partial y; \quad j_y = -\partial H_z / \partial x; \quad (4)$$

In the mathematic model created the variation of the electroconductivity of material under influence of Joule's heating was taken into consideration using the known from the experimental data functional  $\sigma(W)$ , where  $W = \int ((j_x^2 + j_y^2) / \sigma) dt$  ( $J/m^3$ ) is the value of heat energy increasing in the unit of volume in the result of dissipation [4].

Due to the short time of acceleration process (near 2 ms) the adaibatic character of every element of volume heating inside of railgun conductors was assumed.

The equation (3) needs the boundary conditions. The symmetry of current distribution picture occurs if the Hall effect is out of consideration. It is enough to use for calculations only one half of railgun. Along the line  $AL$  (Fig.1) the uniform boundary condition of second type may be set:

$$\partial H_z / \partial n = \partial H_z / \partial x = 0. \quad (5)$$

The constant value of magnetic field strength

$$H = H_{int} = \text{const} \quad (6)$$

must be accepted on the internal surface of railgun conductors (along the contour  $ABC$ ).

The necessity of boundary condition in a such form follows from expression (4). In fact, normal component of current with respect to contour  $ABC$  is equal to zero, it means that the magnetic field strength is staying constant along the contour  $ABC$ . Similarly the constant value of magnetic field strength is fixed along the external surface of railgun conductors (contour  $DEFKL$ ):

$$H = H_{\text{ext}} = \text{const.} \quad (7)$$

The last condition may look as unexpected, because the equality of magnetic field strength along the all length of rails including remoted part  $EF$  follows from (7). Nevertheless the such condition application is inevitable in the 2D model, because the existence of unreal normal component of current density troughout external surface of rails into space surrounded must be assumed, if condition (7) would not be used. In general the condition (7) doesn't occur if the 3D model would be considered, in connection with possible passing of current along the rail surfaces in direction of axis  $Oz$ , i.e. perpendicularly to the vector of armature motion velocity and in parallel to the plane of armature contact with rail.

Along the line  $CD$ , where the electric contact between railgun and current source is provided, the next boundary condition of the first type is set:

$$H(x, t) = H_{\text{int}} - (I(t)/bh)(x - d/2), \quad (8)$$

where  $I(t)$  is the varying in the time accelerator's current supply, considered as known. The next correlation follows from the condition (8):

$$H_{\text{ext}} = H(b + d/2) = H_{\text{int}} - I(t)/h. \quad (9)$$

To define the boundary function  $H_{\text{int}}(t)$  the additional problem was resolved on calculation of the vector magnetic potential distribution  $A_y(t)$  in the initial cross section of accelerator rails (Fig.2). In this problem the next differential equation was considered:

$$\frac{\partial}{\partial x} \left( \frac{1}{\mu} \frac{\partial A_y}{\partial x} \right) + \frac{\partial}{\partial z} \left( \frac{1}{\mu} \frac{\partial A_y}{\partial z} \right) - \sigma \frac{\partial A_y}{\partial z} = j_0, \quad (10)$$

here  $j_0 = I(t)/bh$  is a given current density stipulated by the external source of current supply. Along the borders of cross section the uniform boundary conditions was set.

The boundary value of strength  $H_{\text{int}}(t)$  needed for the solution of main problem is calculated after solution of additional problem from the next expression:

$$H_{\text{int}}(t) = -(1/\mu_0) (\partial A_y / \partial x) \Big|_{(x=d/2, y=h/2)} \quad (11)$$

Mathematical model (3) - (11) was fulfilled numerically using the finite elements method. The triangle finite elements of the first order (symplex elements) were used to discretize the regions of calculations. Automatic program complex for a mesh generation was used created in Kyiv Polytechnic under leading of Prof. A.S. Tsybenko [5]. During the armature motion time the generated mesh of finite elements was deformed gradually along with armature coordinate varying while the all angles of

elements was more than 15 deg. If the one of the angles in the elements would reach 15 deg., the new mesh of finite elements was built.

The time derivatives included in the equations (3) - (10) were approximated by the finite differences on the two-point scheme.

### 3. The Calculation of Electromagnetic Field and Joule's Losses

The rail accelerator with the next data was under consideration in the following numerical analysis. It was accepted that the rails are made from cadmium bronze, their dimensions are the next: width  $b = 0.023$  m, height  $h = 0.023$  m also (Fig.1). Distance between rails  $d = 0.023$  m. The body accelerated (armature) is manufactured from aluminum alloy (type AL). Its dimensions are the next: the length along y-axis is equal to 0.345 m, width  $d = 0.023$  m, height along z-axis is 0.023 m also. Time sketch of the current supply pulse is presented in Fig.3 (peak value is 1.2 MA). At the calculations it was assumed, that armature was motionless at the initial time moment.

At the end of acceleration, after 2 ms time motion interval, the velocity of armature is given equal to 1 km/s. The average acceleration through the way is equal to  $500,000 \text{ m/s}^2$ .

To simplify the field analysis the linear dependence of armature velocity on the time is accepted:  $V = 500,000 t$ , and respectively quadratic dependence of a distance passed on the time:  $s = 500,000 t^2 / 2$ . As the value for estimation we can mark that the current density inside of rail is able to reach the stable meaning  $2.27 \text{ kA/mm}^2$  at the total current 1.2 MA. During numerical experiments the local Joule's losses were calculated to have the thermal energy density and corresponding values of electroconductivity coefficients for the every element of conductors under consideration.

Analysis of the current distribution in the area of moving contact of rail and armature presents the one of the most important problem in the provision of the safe operation of railgun. It is a known fact that through the sharp non-uniformity of current distribution in the contact zone the intensive electrical erosion with material of armature sublimation and electric arc appearance are observed in the tested facilities, what presents a damage of rails destruction. The multi-frequent application of railgun is impossible at such conditions.

In the papers [6], [7] the some designing measures were proposed and analysed how to decrease the current density gradient both in the contact zone and inside of the armature. Three-layer armature was investigated consisting of different metals (titanium-molybdenum-copper) with normal orientation of layers planes with respect to velocity vector.

In this work the longitudinal layer with electroconductivity low in comparison with main body of armature was inputed in the mathematic model as contact layer (area BKPR in Fig.1) and the peculiarities of current distribution in this layer were investigated for different correlation of electroconductivity in the body and in the layer. It was accepted that the thickness of the inputed contact layer less then 10% of the full width of armature. The contact of the mentioned layer of armature with rail

was supposed ideal. Thus, the inputted layer presents the generalized model of real contact transition for current passing from armature into rail. The coefficient of electroconductivity of layer was taken in  $10^3 - 10^5$  times less than for material of rails. It was found, that reduced electroconductivity of contact layer of armature yields to more uniform distribution of current density in the contact zone due to improvement of conditions for electromagnetic field diffusion into the area of contact between rail and armature.

The series of numerical experiments were performed varying the electroconductivity of the contact layer of armature. Data of current distribution obtained are shown in the Fig.4 for the next case: material of contact layer is titanium (its electroconductivity is equal to  $6 \cdot 10^5$  (1/Ohm·m) at 20 deg.C); initial electroconductivity of aluminum alloy in the armature body at 20 deg.C is equal to  $10^7$  (1/Ohm·m). The picture of Fig.3 corresponds to time motion  $t = 1.6$  ms and armature velocity  $V = 800$  m/s. The lines of equal values of current density are numbered in the Fig.4 by the next manner:

- 1 - 11.8 kA/mm<sup>2</sup>; 2 - 9.9 kA/mm<sup>2</sup>; 3 - 3.5 kA/mm<sup>2</sup>;  
4 - 1.75 kA/mm<sup>2</sup>; 5 - 0.7 kA/mm<sup>2</sup>.

It is necessary to mark, that the values of current density and picture of current distribution have a very small difference (near 1.5%) in the cases when the contact layer of armature is manufactured of titanium or the same aluminum alloy as body of armature. It is the result of heating of aluminum layer by the pulsed current. If the contact layer was supposed made from graphite whose electroconductivity is equal to  $0.25 \cdot 10^5$  (1/Ohm·m), i.e. in 24 times less than titanium, difference in the local values of current density could reach 6.3% in comparison with titanium case and 8% in comparison with aluminum case, but the non-uniformity of current distribution was the same.

The essential variation in the current distribution could be observed only if the electroconductivity in contact layer was reduced up to value 1000 (1/Ohm·m) and less. At such the conditions effect of the fast diffusion of electromagnetic field into the contact layer begins to show itself yielding to reduction of current density both at the back edge of contact layer of armature and in the contact zone in whole. The line of equal current density are shown in the Fig.5 for this case, thickness of contact layer was taken 2 mm. The manner of numbering for the lines of constant level of current density in the Fig.5 is the next:

- 1 - 10.2 kA/mm<sup>2</sup>; 2 - 8.8 kA/mm<sup>2</sup>; 3 - 3.1 kA/mm<sup>2</sup>;  
4 - 1.55 kA/mm<sup>2</sup>; 5 - 0.61 kA/mm<sup>2</sup>.

In comparison with Fig.4 it is seen, that current distribution has the great exchange. Due to increasing of depth for the electromagnetic field penetration into the contact layer material the square of effective contact between armature and rail has tendency to rise. The Fig.6 presents the calculated relative value of current density at the back edge of armature  $k_j = j/j_a$  as the function of relative electroconductivity  $k_\sigma = \sigma/\sigma_a$  of the contact layer material with respect to electroconductivity of the armature body  $\sigma_a$  (aluminum alloy). The current density  $j_a$  for the case of contact layer consisting of aluminum is taken as the basic value of current density. It is seen in the Fig.6, that the



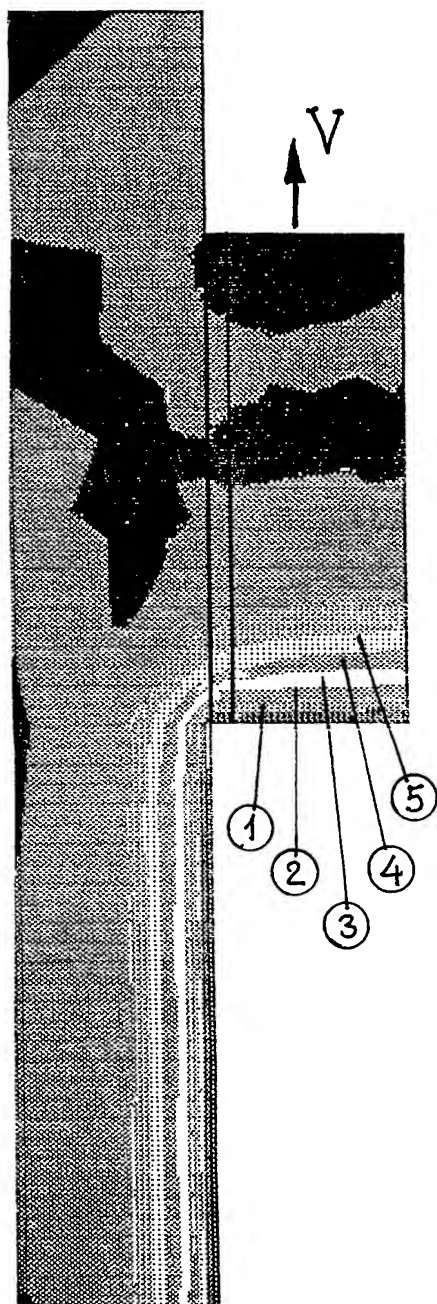


Fig.4. A picture of current distribution in case of titanium contact layer.

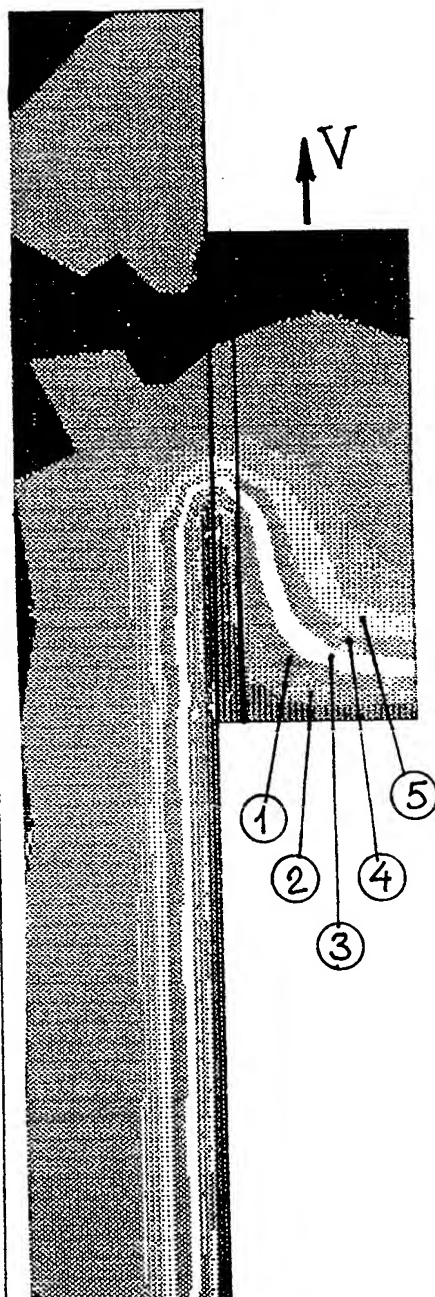


Fig.5. A picture of current distribution at low electrical conductivity of contact layer.

visible influence of electroconductivity reduction on the current density at the back edge of contact zone begins show itself at  $k_g \geq 1000$ .

The calculation fulfilled have dealt with hypothetic material of contact layer disposed on the contact surface of armature. In view of the real possibility of the current distribution control by the proper choice of electroconductive properties of armature's surface layer together with provision of the safe contact of this layer with rail it seems real to avoid a strong concentration of current density and destructions of rails caused by this concentration. It is clear, that the solid contact of such synthetic layer may be provided if this layer would be able to plastic deformation and some thermomechanical erosion during its motion between rails having the small angle of convergence. It is a

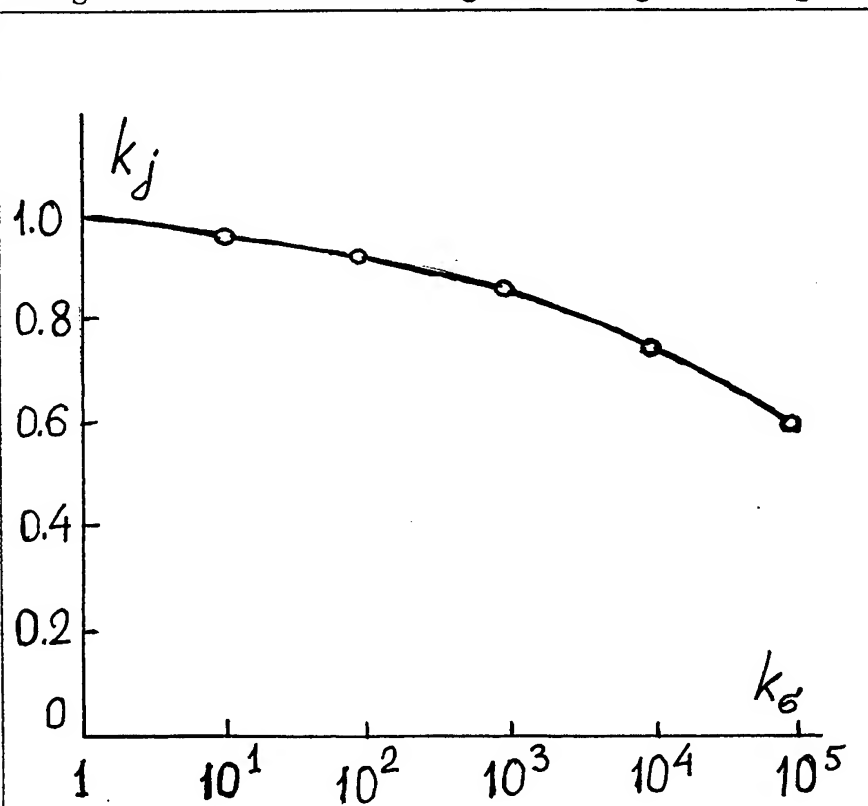


Fig. 6. Relative value of current density at the back edge of contact zone as function of its electroconductivity.

condition of the effective obturation to exclude the appearance of electric arcs and microplasma in the contact. Choice or synthesis of the suitable material which would possess the needed electrical and mechanical properties as said above, may be the one of probable keys to solution of the safe contact provision in the railgun.

The application of the layer with low electroconductivity in the zone of contact between the accelerated body and rails leads to some increasing of voltage applied to the railgun, but it may be a moderate payment for the increasing of the rails time of life.

#### 4. Conclusions and Recommendations

The approach applied which is based on the presentation of the railgun system of conductor as the totality of three bodies of different electroconductivity - rail, armature and transition layer in the zone of contact between rail and armature - with account of their electroconductivity value dependence on the local Joule's heating, may be estimated as fruitful enough to analyse the anticipated current distribution in the contact zone at the known average electrical properties of contact layer. The calculations corresponding was realized without strong problems by the finite elements method at the output velocity of projectile up to 1 km/s and may be spreaded in the area of a more high velocity after additional development of calculations scheme.

Effect observed of the current distribution improvement in the contact zone along with the essential reduction of electroconductivity in the contact layer has the sure interpretation on the base of the electromagnetic field diffusion conception. The practical consequence of the analysis performed is concluded in the expedience to search the material with proper electric and mechanical properties which would be used for current distribution improvement together with a safe obturation of the gap between rails and armature. The such material must be disposed on the contact surfaces of armature.

#### References

1. Marylin M. Freeman, Edward M. Schmidt. *Army Electric Armaments Program.* - IAT Bulletin, Winter 1996, Vol.1, pp.19-22.
2. Ermanno Cardelli. *Velocity skin-effects in railguns with solid armatures.* - The Second Intern. Sci. And Techn. Conf. "Unconventional electromechanical and electrotechnical systems", Szczecin, Poland, 1996, pp.65-76.
3. Volodymyr T. Chemerys. *Electric Gun: General Conception Discussion and Energy Supply Aspects.* - The First International Conference on All Electric Combat Vehicle (AECV), Conference Proceedings, Haifa, Israel, 1995, pp.304-314.
4. N. N. Stolovitch, N. S. Minitskaya. *The temperature dependencies of thermophysical properties of some metals.* - Minsk, Science and Technique Publ., 1975 (in Russian).
5. A.S. Tsybenko et al. *Automatic system of finite element calculations services.* - Kiev, High School Publ., 1986, 252pp. (in Russian).
6. B. Davat, Z. Ren, M. Lajoie-Mazene. *The movement in the field modeling.* - IEEE Transaction on Magnetics, 1985, 21, No.6, pp.2296-2298.
7. G. Long, W. Weldon. *Limits to the velocity of solid armature in railguns.* - IEEE Transaction on Magnetics, 1989, 25, No.1, pp.347-352.

# **INFLUENCE OF THE TEMPERATURE DEPENDENCE OF THE YIELD POINT OF RAIL MATERIALS ON THE KINEMATIC CHARACTERISTIC OF RAILGUNS**

V.P. Chistyakov

Lavrentyev Institute of Hydrodynamics, Russian Academy of Sciences,  
Siberian Division, Novosibirsk, 630090, Russia

## **Summary**

Consideration is being given to some possible conditions of material ablation from rail surfaces caused by attaining plastic flow of the material at a lower temperature than the melting point by the action (heating and friction forces) on a surface.

The possibility of this phenomenon is sustained experimentally by using steel rails. The obtained results should be taken into account in the preparation of new materials for railguns and in searches for ways of increasing a critical current density.

## **Introduction**

An understanding of the physical processes and effects constraining the body accelerations in railguns will make it possible to seek ways of overcoming these constraints. Many authors (such as [1, 2]) refer to the ablation of rail materials and insulators as one of the essential reasons for the constrained rate of launching because a material caught in an arc deteriorates plasma parameters and increases a mass launched. Next the case in point will be the interaction with metallic surfaces.

Conditions are considered as ultimate when at surfaces a melting point is achieved after which almost the whole of the melt is ablated and its part may enter the plasma because the Prandtl number for a liquid metal  $Pr \sim 1$ .

As shown in the paper [3], the limit value of a critical current calculated in case of attaining a melting point at rail surfaces is primarily affected by the heat from a moving plasma armature. Thus interaction processes are basically similar to those of acting high-velocity gas-plasma flows on materials. The ablation effects involving such actions are well studied in connection with the advancement of aeroc cosmic engineering and they are classified as follows [4]:

- 1) sublimation,
- 2) thermal decomposition,
- 3) chemical reaction with gas flow components,
- 4) chemical reaction between material components,

- 5) melting,
- 6) cracking and crushing refractory materials.

For railgun acceleration, provision should be made for

- 7) electric erosion.

Certain of these effects may occur in railgun bores.

Notice that on combined exposure (intensive heating and blow stresses) some conditions may be established when a plastic material flow starts until the melting temperature is achieved at a surface. Next, owing to high-velocity plastic shear work, the temperature will increase progressively, the viscosity will be diminished and the material may escape from rail surfaces. In this connection the process is proposed to be considered as possible mechanism providing ablation.

### Subject

Figure 1 gives temperature dependences of the static yield points -  $\tau_s$  at tangential loads for steel, copper and an iron-tungsten alloy (63% iron and 9% tungsten). The temperature dependencies data are taken from [5] for of the tensile yield points -  $\sigma_s$  and recalculated with regard to  $\tau_s \sim 0.65 \cdot \sigma_s$  for metals. Dynamic yield points will be larger at low temperatures and the differences are insignificant at high temperatures.

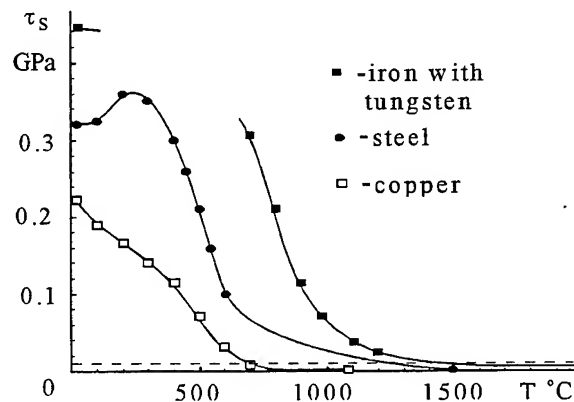


Fig. 1. Temperature dependences of static yield points for steel, copper and iron-tungsten alloy.

One can see that at nonzero shear stresses the temperature that causes the plastic flow generation will be lower than the melting point.

Let us make estimates, using a simple interaction model. Assume that the plasma armature has the length  $l$ , the density  $\rho$ , the velocity  $V$ , the pressure  $p$  and the temperature  $T_p$ , which are constant along the length. The plasma affects the surface by the thermal flow  $q$ , the pressure  $p$  and produces shear stresses  $\tau$  at the surface. In this case the interior part is extended with a heat, a flux pressure wave with the sound velocity in the material and a shear stress wave with the lateral sound velocity. Fig. 2 shows the interaction diagram.

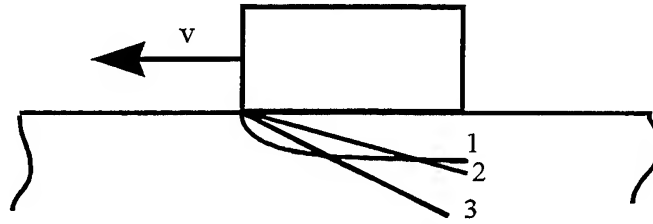


Fig. 2. The interaction diagram. 1 - isotherm, 2 - wave front of shear stresses, 3 - pressure wave front.

We take as an example the plasma density  $\rho = 30 \text{ g/m}^3$  and its velocity  $V = 5 \text{ km/s}$ . The Reynolds number will be  $\sim 10^6$  [2], and friction coefficient  $c_f \sim 0.01$  [6]. We can estimate the shear stress [2]:

$$\tau = F/s \sim c_f \cdot \rho V^2 / 2 \sim 0.01 \cdot 30 \cdot 12.5 \cdot 10^6 \sim 0.00375 \text{ GPa},$$

The dashed line in Fig. 1 denotes the obtained stress. It can be seen from the figure that for the given values of  $p$  and  $V$  the shear condition will be reached in copper at  $T \sim 700^\circ\text{C}$ , in steel at  $T \sim 1100^\circ\text{C}$  and in iron-tungsten alloy at  $T \sim 1600\div 1700^\circ\text{C}$ .

Given a higher velocity and density of the plasma, the shear stress increases and the temperature of generation a plastic flow will decrease still further. Besides, notice that the temperature addend in shear band  $\Delta T$  increases owing to high-velocity plastic shear work is proportional to shear strain  $\gamma$  and rate of shear strain  $\dot{\gamma}$  according to [7]

$$\Delta T \sim \tau (\dot{\gamma} \gamma / \lambda \rho_m c)^{1/2},$$

here  $\rho_m$  is material density,  $\lambda$  - its heat conductivity and  $c$  - heat capacity.

As an illustration, experimental results are presented for the influence of dense high-velocity gas flow in the railgun bore, cross section  $10 \times 10 \text{ mm}^2$ , on the rail surfaces made of the steel. The steel is used because a shear band can well be visualized by etching.

To produce a dense gas flow, a flat gas-cumulative charge has been used. A similar charge was used in the work [8]. A high-velocity gas flow is produced in a gap between two detonating parallel plates made of explosive. Plate thicknesses of 10mm, 15mm, and 20mm were taken, the gap between them was 10mm. The density  $\rho$  is estimated from [9] resulting in  $\sim 100 \text{ kg/m}^3$ ,  $\sim 200 \text{ kg/m}^3$  and  $\sim 250 \text{ kg/m}^3$ , respectively. The velocity  $V$  measured by high speed camera is  $\sim 8.5 \text{ km/s}$ ,  $\sim 9 \text{ km/s}$  and  $\sim 9.5 \text{ km/s}$ , and the action time is  $\sim 5 \mu\text{s}$ . To simulate the interaction of a two-phase flow with a surface in the last experiment, a gas flow is added with fine-grained graphite allowing for  $\sim 250 \text{ kg/m}^3$ . In this case the velocity decays to  $\sim 8.5 \text{ km/s}$  and the mean density is estimated at  $\sim 500 \text{ kg/m}^3$ . The shear stresses  $\tau$  ( $c_f \sim 0.01$ ) are  $\sim 0.036$ ,  $\sim 0.081$ ,  $\sim 0.146$ ,  $\sim 0.18 \text{ GPa}$  respectively.

Figure 3 shows the post-experiment microstructures of the rails cross-section.

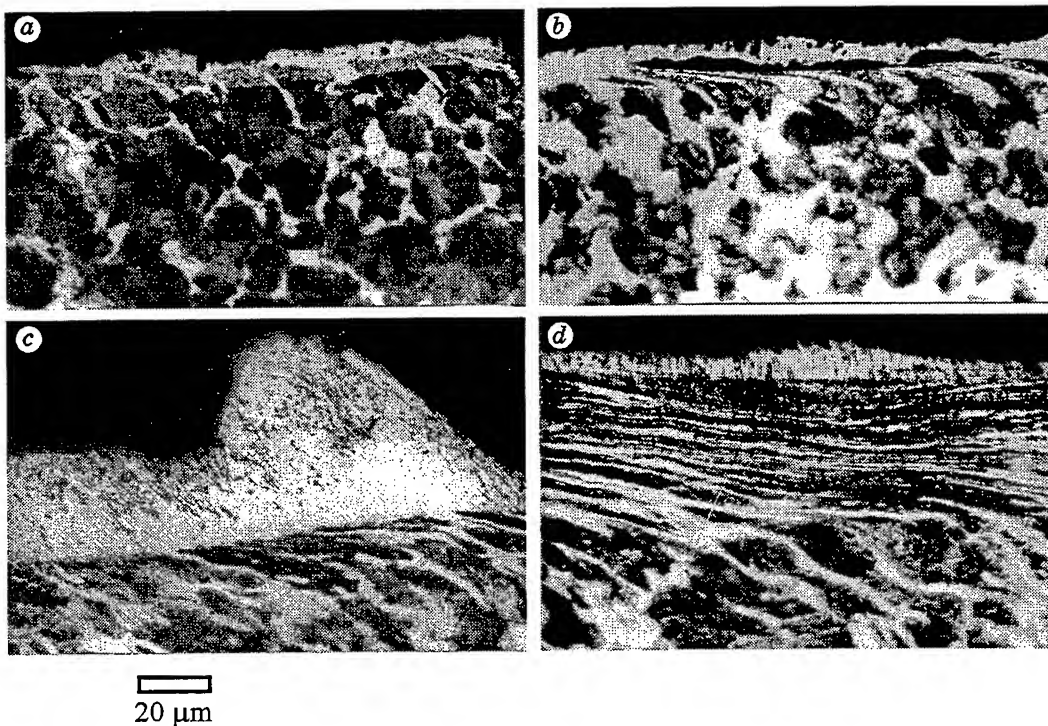


Fig. 3. Microstructures of the rail cross-sections (500  $\times$ )  
 a)  $\rho \sim 100 \text{ kg/m}^3$ , b)  $\sim 200 \text{ kg/m}^3$ , c)  $\sim 250 \text{ kg/m}^3$ , d)  $\sim 500 \text{ kg/m}^3$  respectively.

The shear bands shown here are thin,  $\sim 6 \text{ } \mu\text{m}$  in the first photograph extending with increasing shear stresses up to  $\sim 60 \text{ } \mu\text{m}$ . There are traces of molten metals at the surface. Frictional heating has likely to be added to the heat released by high-velocity plastic shear, then due to its decreasing viscosity material may escape and partially merge into the gas flow. A more comprehensive elucidation of the effect calls for further investigations.

### Conclusion

The study has shown that plastic flows are plausible in railgun accelerations caused by powerful heating and great shear stresses. For rails made of monolithic materials and at low velocities the given estimates suggest that the effect of reducing yield points is insignificant. However, with increasing plasma velocity and density this effect should be considered.

Currently some problems in the usage of different composite erosion-resistant materials are frequently discussed.

As for all the foregoing, the thermophysical properties of new materials and their temperature dependencies should be studied.

The gas-cumulative charges are useful in simulating the action of high-velocity flows.

## References

1. G. A. Shvetsov, V. M. Titov., et al. Railgun accelerators of macroparticles. Part II: Experimental Investigations, in: Proc. 4-th Int. Conf. on Megagauss Magnetic Field. July 14-17, 1986, Santa Fe USA.
2. J. V. Parker, Z. M. Parsons, C. E. Cummings, and Z. E. Fox. Performance loss due to wall ablation in plasma armature railguns. AIAA-Paper No. 1575, 1985.
3. V. P. Chistyakov and G. A. Shvetsov. "About a critical current density in railgun accelerators", J. Appl. Mech. Tech. Phys. No. 1 (1988).
4. B. I. Pankratov, Yu. V. Polezhaev, A. K. Rud'ko. Interaction of Materials with Gas Flows. Mashinostroenie, Moscow (1976).
5. A. T. Tumanov (ed.). Structural Materials. Sov. Entsyklopedia, Moscow (1965).
6. H. Shlichting. Boundary Layer Theory. McGraw-Hill Book Co., New York (1960).
7. G. L. Moss. Shock Waves and High-Strain-Rate Phenomena in Metals (ed. Meyers and Murr). Plenum, New York (1981).
8. G. A. Shvetsov, V. M. Titov., et al. Railgun powered by explosive MHD-generator, in: Ultrahigh Magnetic Fields. Nauka, Moscow (1984).
9. V. P. Chistyakov. Calculation of the gas-cumulative flow parameters, Combust. Expl. Shock Waves, No. 5 (1988).



# ETC Launcher Experiments at Seoul National University

K.H. Paek, K.J. Chung, S.T. Kim, H.J. Kwon, K.W. Whang, K.H. Chung  
Department of Nuclear Engineering, Seoul National University, Seoul 151-742, Korea

C.Y. Kim  
Department of Physics, Chungang University, Seoul 156-756, Korea

J.S. Kim, S.K. Moon  
Agency for Defense Development, Taejon 305-600, Korea

S.H. Song  
Korea Heavy Industries & Construction Co. Ltd, Changwon 641-792, Korea

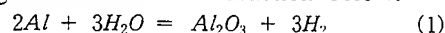
## ABSTRACT

A 20 mm bore electrothermal-chemical (ETC) launcher has been built and operated at the Department of Nuclear Engineering of Seoul National University. This paper describes the experimental setup composed of 20 mm launcher, 1.2 MJ pulse power supply and diagnostics. Some experimental results for a series of discharge tests to date are presented.

## 1. INTRODUCTION

The Department of Nuclear Engineering of Seoul National University has been conducting researches on an electrothermal-chemical (ETC) launcher. As a preliminary step of the research, a 20mm bore launcher was fabricated and tested with the goal of accelerating a 100g projectile to 2km/s muzzle velocity. The major consideration is to achieve the velocity mentioned above without damaging other parts of the launcher except cartridge assembly(cartridge, insulator and electrode) which must be replaced with a new one for each shot. Aspects like system minimization of volume and weight or multi-shot operation were of minor interest.

Aluminum powder, <50 $\mu$ m in diameter, and water mixture were used as a chemical energy source. This mixture, when energized by fast electrical pulse, undergoes rapid chemical reaction which releases thermal energy of over 15kJ per gram of the aluminum[1]. The pressure inside the cartridge assembly rises due to vaporization of water and hydrogen gas generated from the reaction below.



The launcher was powered by two 0.6MJ capacitor banks. Each capacitor bank consists of twelve capacitors of 50kJ energy capacity. Diagnostics have been prepared for four basic parameters - projectile velocity, pressure developed in the cartridge assembly, discharge current and voltage across the cartridge assembly.

Before discussing the results of some experiments obtained so far, the experimental setup is reviewed.

## 2. EXPERIMENTAL SETUP

### A. Launcher

The ETC launcher consists of a steel barrel used as earth electrode, a breech part which contains feeding electrode and support structure. A schematic of the ETC launcher is shown in Fig. 1. A test barrel for Vulcan gun which has rifling with 9

grooves was used for the ETC launcher. Bore diameter and length of the barrel is 20mm, 152cm respectively. A cartridge assembly filled with propellant is inserted into the barrel and supported by the feeding electrode of the breech part. The inside surface of the cartridge was molded with Ciba-Geigy Araldite epoxy to lengthen the discharge path. The internal volume of the cartridge is about 44ml. The cartridge assembly should be replaced with a new one between shots. The launcher is mounted on the V-block and reaction force of the launcher caused by accelerating the projectile is absorbed by oil pressure type shock absorber. The ETC launcher and the target arrangements are shown in Fig. 2.

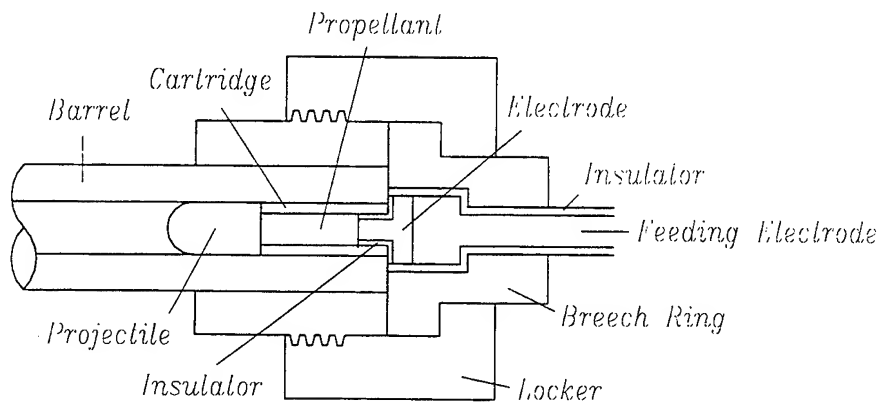


Fig. 1. Schematic of the ETC launcher.

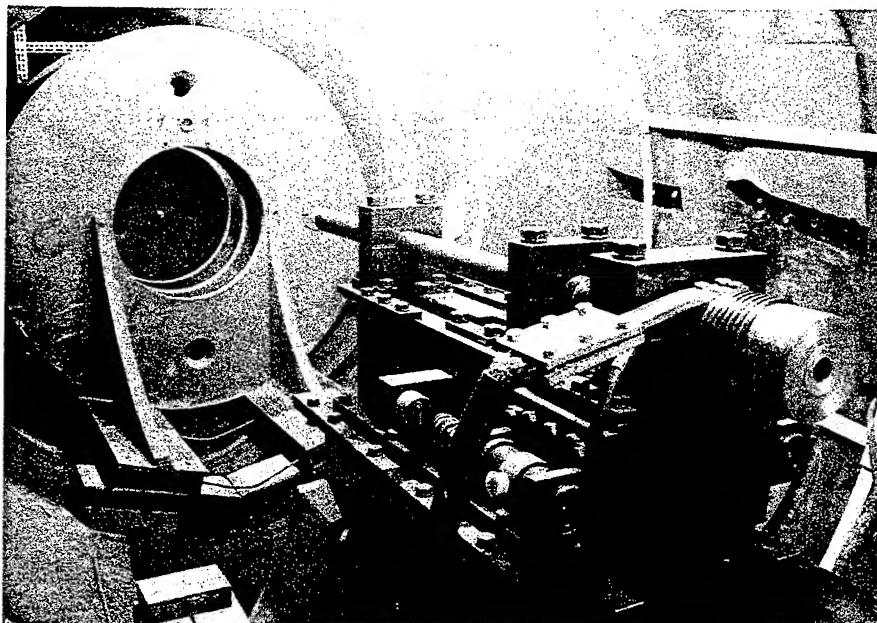


Fig. 2. View of ETC launcher and target  
(Cartridge assembly and breech part is removed for replacement)

## B. Power Supply

Two capacitor bank modules are used as a pulse power supply. Each module

consists of twelve capacitors of 50kJ energy capacity, Maxwell 32349. Charged up to maximum rated charging voltage(22kV), the modules can store 1.2 MJ of energy in total. Two modules are fired simultaneously at the time of this writing but it is planned to add another module and fire them successively.

Two types of switches are used for main closing switch, a mechanical switch or an ignitron. In the mechanical switch a triggering electrode connects two electrodes by spring expansion force. An ignitron which has maximum ratings of 300kA, 25kV, 1,500C was used in some experiments.

### C. Diagnostics

Diagnostics are currently available on four major parameters - projectile velocity, pressure, current and voltage. The projectile velocity is measured using a time-of-flight method. Two parallel He-Ne laser beams separated about 20cm and two photodiodes are used. The first laser beam passes in front of muzzle to measure muzzle velocity and exit time of the projectile. In addition to this laser diagnostics, break-wire frames separated about 24cm are also located in front of the target. A PCB M108A pressure transducer is used for measuring the cartridge pressure. To get more reliable and accurate data safely, an optical isolator will be added between the transducer and oscilloscope. Discharge current and voltage across the cartridge are measured by a Pearson 2093 current monitor and a Tektronix P6015A high voltage probe respectively. The signals are acquired and stored by Tektronix 744A, 2440 and LeCroy 9310A digital storage oscilloscopes.

## 3. EXPERIMENTAL RESULTS

10 tests were performed until now with different charging voltages and chemical compositions for propellant. Table 1 shows the summary of 10 test shots.

Table 1. Summary of 10 test shots

| Shot No. & Date | Input             |                  |   |                  |            |        | Output            |                         |                      |        |
|-----------------|-------------------|------------------|---|------------------|------------|--------|-------------------|-------------------------|----------------------|--------|
|                 | Electrical        |                  | Chemical  |                  | Projectile |        |                   |                         |                      |        |
|                 | Charge Voltage kV | Stored Energy kJ | Composition   | Stored Energy kJ | Mat.       | Mass g | Peak Pressure MPa | Projectile Velocity m/s | Projectile Energy kJ | Eff. % |
| 1<br>2/6/96     | -11               | 300              | Al(9.8g) + P <sub>2</sub> O <sub>5</sub> (26.6g) = 36.4g      | 60               | Brass      | 109.9  | 184               | Not Measured            | N/A                  | N/A    |
| 2<br>3/1/96     | -10               | 248              | Al(20.5g) + H <sub>2</sub> O(20.4g) + Graphite(14.1g) = 55.0g | 311              | Cu         | 105.9  | 136               | Not Measured            | N/A                  | N/A    |
| 3<br>3/14/96    | -15               | 558              | Al(19.7g) + H <sub>2</sub> O(22.7g) + Bentonite(9.5g) = 51.9g | 299              | Cu         | 104.6  | Not Measured      | Not Measured            | N/A                  | N/A    |
| 4<br>4/18/96    | -15               | 558              | Al(22.5g) + H <sub>2</sub> O(22.9g) + Bentonite(9.9g) = 55.3g | 341              | Cu         | 101.7  | 246               | Not Measured            | N/A                  | N/A    |
| 5<br>10/12/96   | -15               | 558              | Al(20.8g) + H <sub>2</sub> O(20.1g) + Graphite(16.0g) = 56.9g | 315              | Cu         | 105.7  | Not Measured      | Not Measured            | N/A                  | N/A    |
| 6<br>10/29/96   | +8.8              | 192              | Al(19.5g) + H <sub>2</sub> O(19.1g) + Graphite(17.0g) = 55.6g | 296              | Cu         | 102.9  | Not Measured      | 813                     | 34                   | 7.0    |
| 7<br>11/8/96    | +13.2             | 432              | Al(20.6g) + H <sub>2</sub> O(20.2g) + Graphite(16.2g) = 57.0g | 312              | Cu         | 101.8  | Not Measured      | 896                     | 41                   | 5.5    |
| 8<br>11/14/96   | +13.2             | 432              | Al(18.4g) + H <sub>2</sub> O(18.4g) + Graphite(15.3g) = 52.1g | 279              | Brass      | 110    | Not Measured      | Not Fired               | N/A                  | N/A    |
| 9<br>11/26/96   | +13.2             | 432              | Al(17.6g) + H <sub>2</sub> O(17.7g) + Graphite(14.8g) = 50.1g | 267              | Cu         | 117.1  | 73                | 214                     | 2.7                  | 0.4    |
| 10<br>11/27/96  | +13.2             | 432              | Al(16.8g) + H <sub>2</sub> O(16.9g) + Graphite(13.8g) = 47.5g | 255              | Cu         | 116.2  | Not Measured      | 1,075                   | 67                   | 9.8    |

Sufficient experimental data could not be given because diagnostics were prepared and modified in parallel with firing experiments.

Major difficulties in the experiments were preventing the highly pressurized gas in the cartridge assembly from leaking into breech part. Pressure leak not only lowers the system performance but also causes serious damage in the breech part, especially in the insulator. The cartridge assembly was modified several times during the experiments and there has been a substantial improvement in sealing of the pressure. Another problem is to keep good electrical contact between electrode in the cartridge assembly and the feeding electrode. In some experiments insulation failures occurred because of arc discharge developed in the poorly contacted surface. In those cases high discharge current flowed directly to the barrel earth without passing through propellant mixture and the velocity of projectile was very low or the projectile could not even be fired as in shot no. 8, 9. To fix this problem it is needed to modify the loading mechanism.

Fig. 3 shows time dependent pressure profiles for shot no. 1 and no. 2. Peak pressures generated are 184MPa(27kpsi) and 136MPa(20kpsi), respectively.

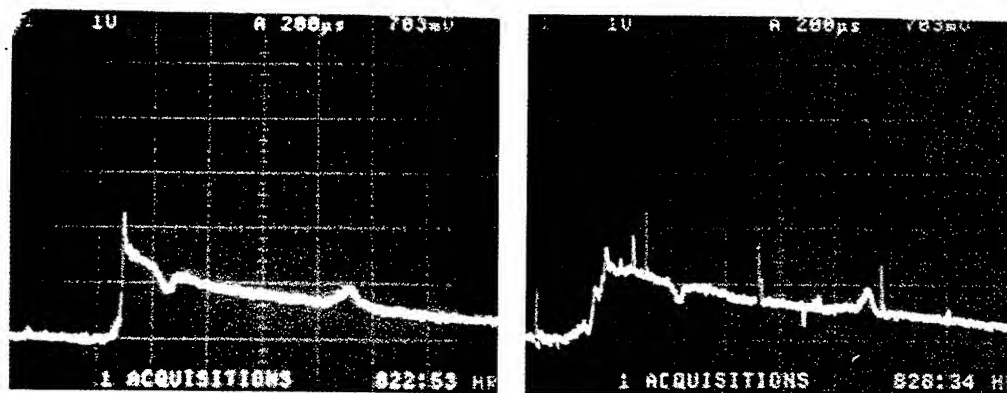


Fig. 3. Pressure profiles for shot no. 1 and 2 (200 $\mu$ s/div., 1V/div., 0.084mV/psi)

Voltage, current, input power and energy for shot no. 10 are shown in Fig. 4. The data show underdamping waveforms which are also characteristics of previous 9 shot results. The circuit inductance can be approximated to be 6.2 $\mu$ H from the result. It is shown that two thirds of electric energy dissipated in the launcher is spent in first half cycle of the discharge current, 0.6ms and one fourth of the total energy stored in capacitor bank is dissipated in other parts of the discharge circuit, mainly in the switch. The projectile velocity in this experiment is 1,075m/s and system efficiency is 9.8% assuming full reaction of the propellant.

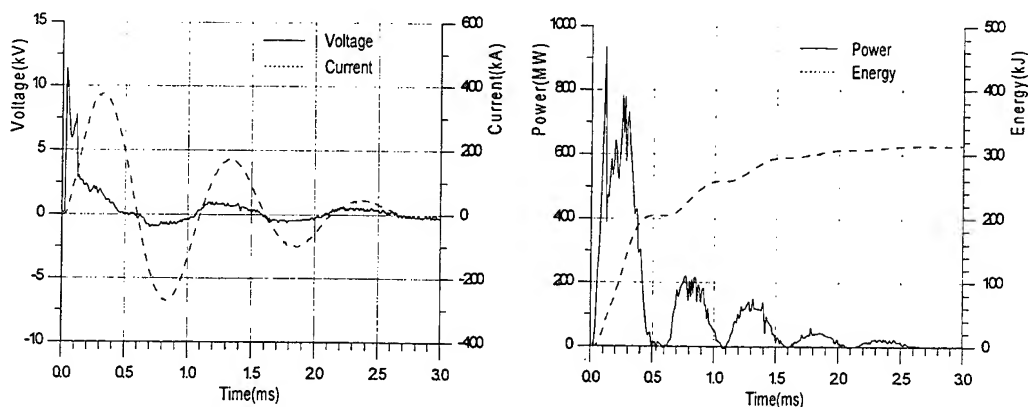


Fig. 4. Voltage, current, power and energy profiles for shot no. 10

Fig. 5 shows a 20mm thick armor plate target after 10 test shots. The target is supported by another 50mm steel plate in the backside. The target was rotated clockwise during experiments showing the projectile of 10th shot driven into the target at the left-hand.



Fig. 5. Armor plate target after 10 test shots.  
(Projectile was not fired at 8th shot)

#### 4. SUMMARY

At the time of this writing, some system components such as closing switch and diagnostics are not completely set up. The cartridge assembly and the breech part of the ETC launcher needs also some modifications and improvements. Total 10 firing experiments were performed and some important results and experiences were acquired from the experiments.

- For high pressure seal in the cartridge assembly more serious considerations on the material and geometry of the components must be given.
- To keep a good electrical contact between electrode in cartridge assembly and feeding electrode new loading mechanism is needed.
- More reliable diagnostics are needed especially for noise rejection and earth problem.

Pulse forming and use of other propellant will be the next step topics after improvements on the problems mentioned above.

#### REFERENCES

- [1] W. M. Lee, "Metal/water chemical reaction coupled to a pulsed electrical discharge," J. Appl. Phy., Vol. 69, No. 10, 15 May 1991.

**Low Power Electrothermal Enhancements to the Modular  
Propelling Charge System**

S.R.Fuller, G.F. Savell

**DRA Fort Halstead**

**Sevenoaks U K.**

**6th European Symposium on Electromagnetic Launch Technology  
The Hague, Holland  
May 1997**

**Summary**

The aim of the study reported here was to investigate the potential performance enhancements to the lower charge zones of a 155 mm artillery guns modular charge system (MCS) that might be attained by using low power electrothermal (ET) technology with a view to future capability enhancement of generic 155 mm gun systems.

This study assessed the potential performance and operation of low power ET enhancement to the MCS (electrothermal energy, when used in conjunction with chemical energy is known as electrothermal/chemical energy - ETC). Theoretical modelling was performed to investigate ignition effects, to calculate performance benefits and to estimate electrical power requirements. A full scale gun chamber simulator was built to experimentally assess the effects of an electrothermal plasma jet on the ignition and combustion of one or two Top Charge Modules (TCM), this being the module used to fire zones 3-6. The results from the full scale simulator have been compared to the existing ignition system.

**Introduction**

Practical ETC gun systems have been actively pursued by many researchers around the world for over a decade now. They consist essentially, of a conventional gun system with a means of discharging electrical energy into the gun chamber (figure 1). This energy augments the performance achievable by the propellant alone. One of the main objectives among ETC gun researchers has been to improve upon the conventional range performance. Although this is a justifiable objective, other benefits may also be feasible with the use of ET technology. One such benefit may be the use of electrical energy (EE) to eliminate some of the propellant debris that is left after firing one or two modules of a unimodular charge system. It was anticipated that additional energy, in the form of EE, could be introduced during the early stages of the charge burning cycle and that this would help to reduce the debris. In addition, a reduction in the firing intervals was expected.

**Low zone enhancement for the MCS**

**Background**

The modular charge system that is likely to be introduced into service uses one or two, single type, 'low zone' charge modules for zones one and two and the required number of 'upper zone' charge modules for zones three to six. Two different charges have therefore to be manufactured to supply a complete complement of zone charges to the vehicle.

If a single charge type, a unimodular propelling charge system (UPCS), could be used for both zones then the logistics of manufacture and supply would be much simplified.

However to obtain maximum muzzle velocity (and hence range) from a given gun, a large charge mass and large propellant ballistic size (web) must be used. If this charge is subdivided into equal increments (unimodules), the lower zones consist of relatively small propellant charge weights with large web size. This produces long firing intervals and a low peak pressure during the ballistic cycle giving rise to:

- Inconsistent muzzle velocities.
- The possibility of shot exit before all the propellant has burnt, leaving propellant debris in the bore after firing.
- An increased risk of 'stickers', (projectiles becoming stuck in the barrel).

#### **Advantages of low power ET Technology**

Electrothermal gun research has shown that a plasma is far more mobile and penetrative than conventional igniter products and ignition delays are significantly reduced.

A plasma can significantly speed up the combustion of conventional gun propellant in two ways. The first is to heat the gases already in the propellant chamber, thus speeding up the combustion process. The second is to enhance the burning rate of the propellant by a mechanism yet to be characterised but which has been seen experimentally and is being investigated at present.

It was therefore expected that the plasma would ignite charge modules far more efficiently than present igniter tubes and that the extra energy (provided electrically) would help to improve ballistic regularity and eliminate the problems of unburned propellant.

It is possible that additional benefits could be obtained by varying the electrical power profile that is delivered to the plasma generator. These benefits are:

- Improved range overlap between zone charges.
- Reduction in sensitivity to initial charge temperature leading to more accurate prediction of muzzle velocity [1].
- Increased top zone muzzle velocity.

#### **Theoretical assessment**

##### **Consideration of 155mm calibre UPCS**

An initial theoretical investigation into the UK 155 mm, Extended Range Ordnance (ERO), firing low zone charges using the MCS's top charge was undertaken to establish the possible cause of the muzzle velocity variation and also to study the propellant combustion characteristics. From this study it could be determined how best electrothermal energy could be used to provide a solution. In the theoretical computer simulations the SPETV5\_2 (Solid Propellant Electrothermal Version 5\_2) code was used.

The first calculations considered a variation in shot start pressure of between 30 MPa and 45 MPa to assess how this affected both velocity and the proportion of propellant burnt. These shot-start pressures are typical of those observed during experimental gun firings, (figure 2).

A series of calculations was then carried out to investigate the effect of poor propellant ignition. The zone 1 and 2 propellant charges were divided into five equal increments and then the moment of ignition for each was delayed by times varying from 5 ms to 15 ms, (figure 3).

From these results it is clear that shot start pressure has a significant effect on the muzzle velocity and the proportion of propellant burnt whilst ignition delays have only a slight effect. These results highlight the fact that low zone unimodular charges suffer from long firing intervals. Short delays in the ignition of various parts of a zone one or two charge will not alter this fact. However, by increasing the shot start pressure, the entire charge can begin to burn properly before the projectile moves and begins to increase the volume of the chamber.

These results have important implications for the use of ET technology with one and two TCMs. Clearly simultaneous ignition of all parts of such a charge is relatively unimportant to the eventual muzzle velocity, however, to reduce the propellant debris to a minimum, the projectile must not move before the entire charge has ignited.

#### **Thermal augmentation using electrical energy**

The next calculations undertaken were to find out the most effective way of employing the ET energy and the amount required to eliminate the problem of propellant debris. Varying amounts of electrical energy (1.25 MJ, 2.5 MJ and 5 MJ) were input into the gun model at the commencement of propellant combustion and also when the gun chamber had reached 30 MPa. This was carried out using one and two TCMs. These results are shown in figure 4.

The most obvious and easiest means of employing ET energy would be to use it to initiate the ignition process. Unfortunately, rather than increase the burn rate and reduce the quantity of propellant debris, calculations show that the ET energy simply causes the projectile to move before much of the propellant has burnt. This has the effect of increasing the amount of unburnt propellant left within the gun.

The best use of electrical energy is made when it is input after significant propellant combustion has already taken place and is ultimately found to be at the moment of shot start. A case using 5 MJ of electrical energy at 30 MPa did not quite achieve propellant all burnt before shot exit.

The figure of 30 MPa for the shot start pressure was selected as it was the lowest value seen in experimental gun firings. Calculations were conducted, increasing the shot start pressure and the amount of electrical energy discharged to achieve propellant all burnt before shot exit. This was achieved for one TCM using 6 MJ of electrical energy and a shot start pressure of 45 MPa, which is more typical of values seen during actual gun firings.

Until experimental work has been undertaken to quantify the actual effects of the electrical energy on propellant combustion during typical gun firings, the precise amount of electrical energy that will be required is uncertain. It seemed reasonable, therefore, to assume a value of 6 MJ for all future work.

#### **Electrical energy only - 1 TCM**

All of the above techniques have attempted to use electrical energy (EE) to increase the proportion of propellant burnt and provide muzzle velocity consistency. However, there is a major drawback in that the muzzle velocity of the shot has significantly increased from that obtained when using the charge alone. This is due to the extra energy being input into the gun to achieve complete combustion of the charge. One means of achieving a lower velocity would be to eliminate the chemical charge entirely and to fire the projectile using only EE. A velocity similar to that attainable with one TCM could be achieved with the expenditure of 6 MJ of EE. This technique would obviously leave no debris, although the possibility of increased gun wear would need to be investigated.

Another advantage of using EE only as a means of propulsion is that velocities below the minimum attainable with one TCM could be achieved. This would allow the minimum range at which a target could be engaged, to be reduced. The limiting factor would be the pressure at which the projectile became 'stuck' in the barrel due to frictional losses.

#### **Burn rate enhancement**

Analysis of small scale experiments [2] has shown that for certain propellants a phenomenon has been observed whereby the burn rate has increased above its expected value both during and after a plasma pulse. If use of this phenomenon could be made with TCMs then there would be two major benefits. The first is that propellant all burnt could be achieved before shot exit. The second would be that a smaller



power supply would be required and its integration into the vehicle could be more easily achieved.

Burn rate enhancement has been modelled for both one and two TCMs. Results show that if an enhanced burning rate is assumed, all burnt for both charges is easily achieved before shot exit is attained, while using only 2 MJ of electrical energy. All burnt for the zone 2 charge is achieved in a little over 3 m of shot travel. The burn rate used for this modelling exercise was assumed to have increased during the plasma pulse and for approximately 2 ms afterward. The plasma pulse was 5 ms long and an increase in the burning rate of 25% was assumed. The experiments conducted to date have actually shown enhancements of over 50%, lasting up to 10 ms after the pulse with similar electrical energy densities and so the above assumption may be somewhat conservative.

### **Experimental assessment**

#### **Ballistic simulator design**

To undertake large calibre gun firings to confirm the results obtained from the theoretical assessment would have been expensive both in terms of the manufacture of special hardware to allow a plasma generator to be fitted into a gun breech, and in range costs. It was decided instead to investigate whether a device could be built that would simulate the pressure time history of a gun firing, as predicted by modelling, no matter how the chamber pressure was generated, whether by propellant alone or by propellant and plasma generator.

An ERO gun chamber simulator was constructed (figure 5). This device consists of a central body with a series of vent holes of different diameters that become uncovered by a sliding piston as a propellant charge burns. The motion of the piston is determined by the gas pressure acting on the front of it, driving it forward. This motion is opposed by oil pressure on the rear of the piston head. The oil pressure is controlled by the discharge of oil from the chamber through a spring loaded valve. By altering the spring pre-load and the thickness of a shear disc which keeps the valve in position, the pressure at which oil starts to vent and the rate at which the oil is discharged can be controlled. Thus, control of the discharge of oil indirectly controls the motion of the piston.

Theoretical computer simulations of this device indicated that the pressure time history of a gun firing for zones 1, 2 and 3 could be simulated closely.

#### **Simulator testing**

The first round that was fired in the simulator was with one MCS TCM module with 1 kg of propellant removed. The resulting total module mass was 1.5 kg of which 1.25 kg was propellant. This round was fired to check the simulator operation. Ignition was by conventional percussion primer tube. The oil discharge pressure was kept low so that the vessel vented at a low pressure.

Good results were obtained up to the point at which the main venting of the vessel occurred. This allowed the signal to be analysed to allow comparisons to the computer prediction to be made. Adjustments were then made to the oil discharge valve, as the pressure observed in the combustion chamber was slightly lower than that expected from the calculations of the simulator operation.

The round was repeated to ensure that the changes made had the required effect. The results obtained from this second round were almost exactly as predicted.

A full TCM module was then fired in the simulator again using a conventional primer. The results were excellent, with a very good set of pressure traces being obtained (figure 6). When the vessel was dismantled no damage was observed while a small amount of propellant debris was found remaining in the chamber, something that was hoped would be seen, imitating the propellant debris left after a single TCM gun firing.

## **Comparison with ERO gun firing data**

When the results of the simulator test were compared with a real gun firing and the computer model of the simulator, a good curve fit was found (figure 7). This showed that the changes made to the oil discharge valve for the half module firing were also valid for a full module firing.

## **Plasma charge ignition**

Having achieved a successful conventional ignition firing of the simulator, a plasma ignition firing was attempted. The electrical energy pulse used to ignite the charge was the same as that used during an earlier series of plasma generator tests. These had been conducted to ensure that the plasma generator was robust enough to allow a discharge of 6 MJ over a period of 6 ms and were successfully completed.

The simulator pressure traces obtained were very good. However, only 1.7 MJ of the electrical energy had been transferred into the plasma generator.

Upon inspection, a connection between the capacitor bank and the simulator was found to be damaged due to an electrical short that had occurred. This had allowed a proportion of the energy to bypass the simulator.

However, even with this reduced amount of electrical energy, a significant effect on the ignition and burning of the propellant was observed. Instead of a firing interval of about 250 ms, typical of a single module ignited by a conventional primer, the pressure within the simulator, generated by burning propellant, continued to rise immediately following the end of the electrical pulse. This allowed the firing interval to fall to approximately 12 ms.

When the simulator firing was modelled, a good match between the predicted result and the actual firing could only be achieved by increasing the propellant burn rate used in the model. It was found that an increase of 50 % during the plasma pulse followed by a linear reduction to zero at maximum pressure, i.e. a period of about 10 ms, allowed a good fit to be obtained (figure 8).

Further firings of the simulator were planned, but a problem arose dismantling the vessel after the last round. Rather than risking further damaging, a temporary halt was called until after the parts had been modified. The modification work has now been completed and the trials have resumed.

## **Conclusions**

### **Theoretical assessment**

The theoretical computer simulation work undertaken on the existing MCS confirmed two main problems that exist when firing only one or two TCMs. First, some propellant would remain unburnt at the time of shot exit which could lead to debris remaining within the gun. Second, variations in shot start pressure lead to variations in muzzle velocity which in turn leads to inaccuracy.

The use of electrical energy could overcome both of the above problems. Six 6 MJ of electrical energy, input at shot start would result in a much lower mass of propellant remaining at shot exit. The exact amount would be dependent on the shot start pressure, but typical experimental values from gun firings suggest that it is likely that all the propellant would be burnt.

Experimental evidence suggests that it is possible to maintain an enhanced burn rate after the application of a plasma to a propellant. If this effect could be induced in the MCS propellant, then far lower amounts of electrical energy would need to be used and all burnt would easily be achieved before shot exit.

## Experimental assessment

A ballistic simulator was designed and built to validate the theoretical simulation work without the need to go to the expense of actually carrying out gun firings.

To date four firings have been undertaken using the simulator. The first two were to check its operation and to commission the system, the third was a single module firing with conventional ignition and the last, a single module firing with plasma ignition. Modelling of the fourth round showed good agreement with firing data.

The results from the fourth round showed the benefits that a plasma would have on the MCS charge system. The ignition delay, as indicated by the rise in chamber pressure, was reduced from around 250 ms with a conventional igniter to less than 10 ms with a plasma jet. There was some evidence of an increase in burning rate of the propellant. This could lead to a significant reduction in the quantity of electrical energy required to obtain a substantial increase in performance.

The simulator has been modified and is currently being used in further trials.

This work has shown that modelling and simulator work suggests that if ET technology was used in conjunction with the a MCS, important operational advantages could be achieved in terms of logistics, flexibility and to a lesser extent maximum range performance although this has not been described here. Further research is required to confirm these findings and to determine the most effective means of utilising ET technology to enhance the performance of an artillery gun.

## References

1. D. Melnik, L. Perelmutter et al, *The Solid Propellant Electro Thermal Chemical Technology Development at Soreq*. Proceedings of the 1st International Conference on the All Electric Combat Vehicle, Haifa, Israel, May 1995.
2. C Woodley, S.Fuller, *Apparent Enhanced Burn Rates of Solid Propellants Due to Plasmas*. Proceedings of the 16th International Ballistics Symposium and Exhibition, Sept 1996.

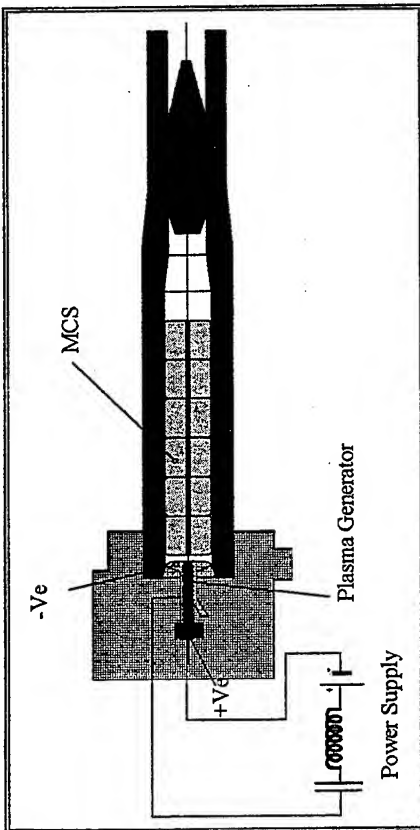


Figure 1. Medium calibre electrothermal gun system.

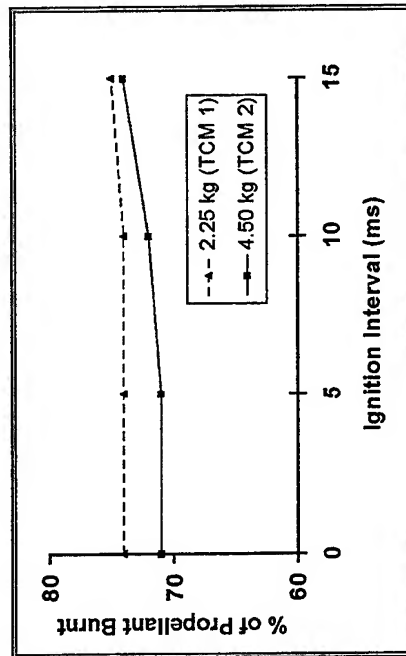


Figure 3. Effect of ignition interval on propellant burnt

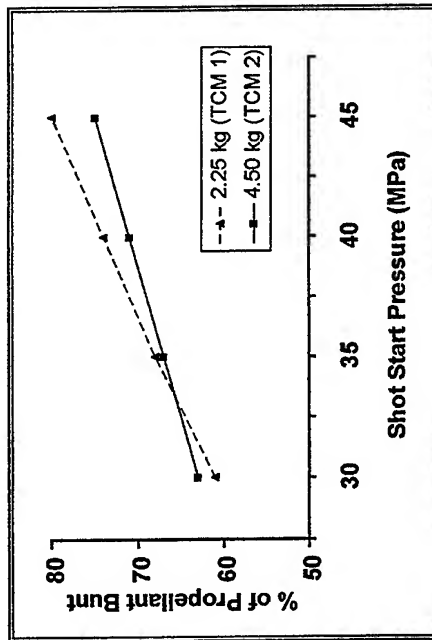


Figure 2. Effect of shot start pressure on propellant burnt

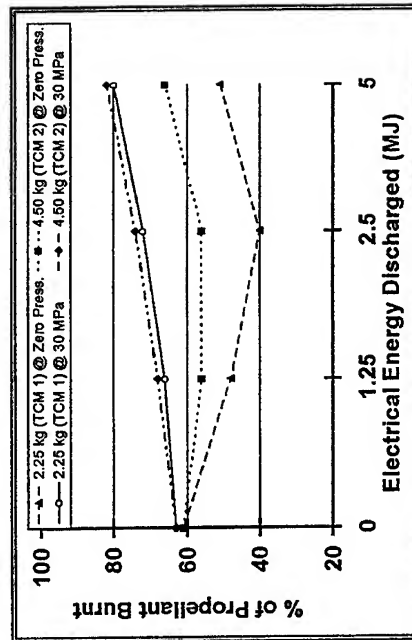


Figure 4. Effect of electrical energy input on percentage of propellant burnt at shot exit.

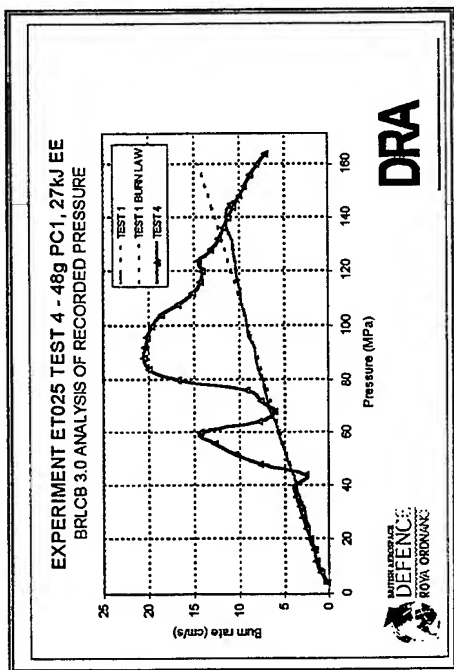


Figure 5. Experiment ET025, test 4.

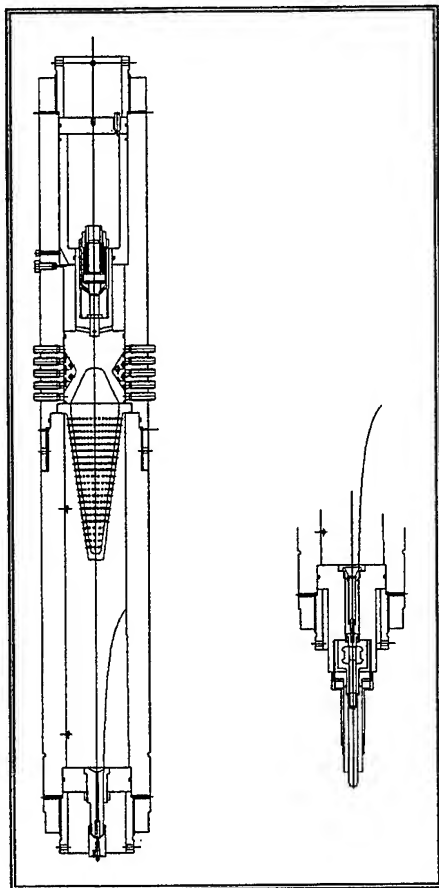


Figure 6. UPCS gun simulator.

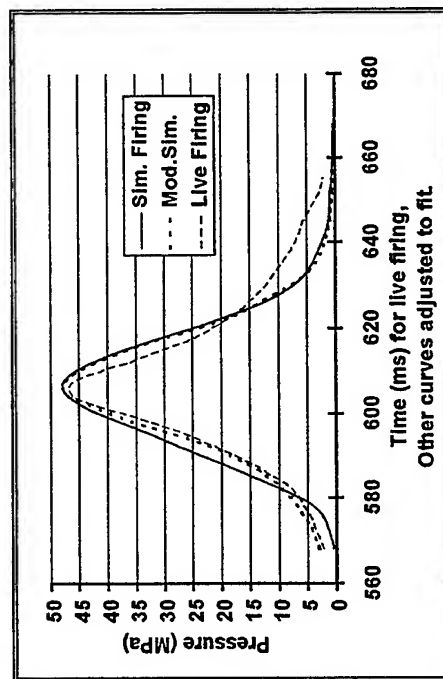


Figure 7. Comparison of simulation of TCC pressure-time curves.

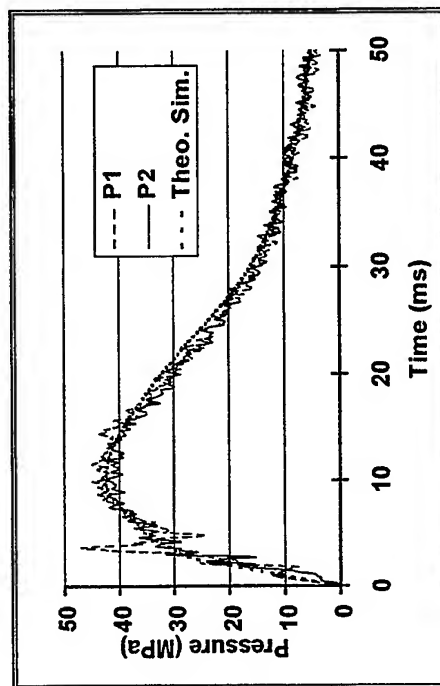


Figure 8. Comparison of simulation firing and theoretical model.

# Experimental Observation of the Rail Resistance Contribution to Muzzle Voltage

Jerald V. Parker

Institute for Advanced Technology, The University of Texas at Austin  
4030-2 W. Braker Lane, Suite 200, Austin, TX 78759-5329

**Summary**—In 1994, Dreizen and Barber [1] presented an analysis of the muzzle voltage developed in a railgun with a solid contact armature. They showed that there is a significant contribution to the measured muzzle voltage arising from the current flow in the rails ahead of the armature. They further argued that this voltage is influenced by velocity skin effect and that it may become the dominant effect on muzzle voltage at high velocity.

The results of that paper, although on solid theoretical foundations, generated some controversy because many previous investigations of armature behavior had obtained good agreement between theory and observation without taking this term into account.

In this paper, we report a novel experimental technique that permits direct observation of the effect of precursor rail current on muzzle voltage. The observed magnitude of the voltage is in agreement with the estimates provided by Dreizen and Barber, including the contribution of velocity skin effect.

## I. INTRODUCTION

In 1994, Dreizen and Barber [1] presented an analysis of the muzzle voltage developed in a railgun with a solid contact armature. In their analysis, they included a voltage source that had not been previously considered in electromagnetic launcher research, namely the voltage generated by the precursor magnetic field ahead of the armature. The physical situation is shown schematically in Fig. 1. The current in the armature, in addition to strengthening the propulsive magnetic field behind the armature, also generates a weaker field that extends several bore heights in front of the armature. The strength of this field varies substantially with the physical geometry of the armature and containment. Typical values range from 50% of the field behind the armature for very compact armatures to less than 5% for long armatures or armatures closely surrounded by shielding conductors.

The importance of this field with regard to muzzle voltage lies in the boundary condition  $B_s = \mu_0 J_s$  that requires a surface current to flow whenever a transient magnetic field is generated parallel to a conducting surface. The surface current in the rails ahead of the armature creates an electric field equal to  $\rho J_s / \delta$  where  $\rho$  is the resistivity of the rail material and  $\delta$  is the depth the current has diffused into the rail. Dreizen and Barber analyze the direction and magnitude of this surface electric field and show that it adds to the measured muzzle voltage. They estimate the magnitude of the voltage using a simplified armature geometry for the field strength and a diffusion depth given by the length scale of the field divided by armature velocity. They conclude that at high velocity this effect may contribute significantly to the measured muzzle voltage.

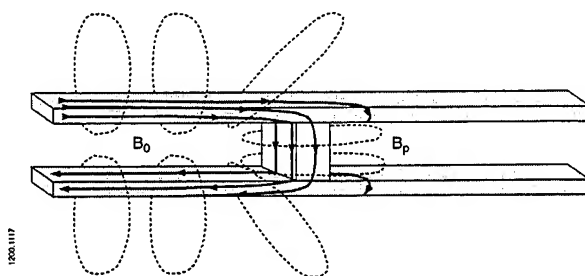


Fig. 1. The armature current produces a magnetic field ahead of the armature. It is accompanied by surface currents that contribute to the muzzle voltage.

Although the physics behind the effect is unquestionably correct, there have been questions concerning its magnitude and importance since a number of investigators have neglected this contribution to muzzle voltage and still obtained reasonable agreement between measurement and theory. To address this issue, it would be desirable to measure the additional voltage explicitly rather than attempting to infer its presence by subtracting calculated voltage drops in the armature and contacts from the measured muzzle voltage.

In Section II, a technique is described by which the precursor voltage contribution can be observed experimentally. The data presented include both the muzzle voltage contribution and a direct measurement of the precursor magnetic field. This provides the foundation for a comparison of the measured voltage to the predictions of the model put forth by Dreizen and Barber.

Section III presents the details of a 1D diffusion calculation of the precursor electric field using the measured magnetic field as a source.

Finally, in Section IV, results are presented for several different experimental conditions and compared to the 1D predictions.

## II. EXPERIMENTS

The experimental configuration used to observe the precursor voltage is shown in Fig. 2. A conventional square bore railgun is modified by machining a shallow recess over the full width of both rails and inserting a thin layer of high resistivity metal. Application of a large preload force during assembly ensures good electrical contact between the high resistivity insert and the underlying copper rail.

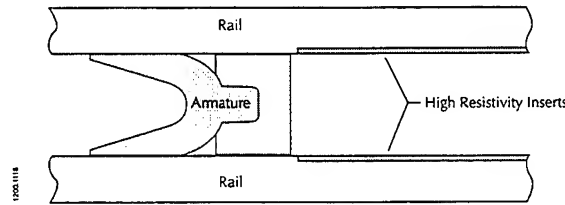


Fig. 2. The presence of precursor currents can be observed by placing a high resistivity insert into the rails.

The effect of the high resistivity inserts on muzzle voltage can be calculated by performing the line integral of electric field from muzzle to armature and back to muzzle as described in Reference [1]:

$$V_m^I = 2 \int_L^{x_i} \rho_I \frac{J_s(x' - x_c)}{\delta_I(x')} d\xi + 2 \int_{x_i}^{x_c} \rho_c \frac{J_s(x' - x_c)}{\delta_c(x')} d\xi + \int_{Rail}^{Rail} E_{arm}, \quad (1)$$

where  $\rho_I$  is the insert resistivity,  $\rho_c$  is the copper resistivity,  $J_s(x' - x_c)$  is the surface current at position  $x'$  generated by the armature at position  $x_c$ ,  $\delta(x')$  is the current penetration depth at position  $x'$  and the insert extends from  $x_i$  to  $L$ . The third term represents the contribution of resistance in the armature itself. Comparing  $V_m^I$  to the muzzle voltage without an insert,  $V_m$ , we see that there is an excess voltage given by,

$$V_m^I - V_m = 2 \int_L^{x_i} \left( \frac{\rho_I}{\delta_I(x')} - \frac{\rho_c}{\delta_c(x')} \right) J_s(x' - x_c) d\xi. \quad (2)$$

This excess voltage is a function of armature position. When  $x_i - x_c \gg$  than the rail separation  $h$ , that is, when the armature is far from the insert, the precursor field is small and the excess voltage vanishes. As

the armature approaches the insert, the excess voltage increases until at  $x_c = x_i$  the excess voltage is nearly equal to the precursor voltage predicted by Reference [1] for a rail of resistivity  $\rho_l$ . Furthermore, if  $J_s$  ( $x' - x_c$ ) is known, then Equation 2 provides the basis for a direct comparison between experiment and theory.

Figure 3 is a photograph of the apparatus used to perform an experiment of this type. The launcher is a 40-mm square bore device with half-hard copper rails. This photo, taken during assembly, shows the "C" type armature made of 7075 aluminum and its Lexan bore rider between the rails on the left. On the right, one sees an insert in each rail made of 2.29-mm thick low carbon, mild steel (U. S. type 1015). The armature is not shown in its actual starting position which is approximately 37 cm from the insert to permit the armature to achieve a significant velocity prior to the interaction.

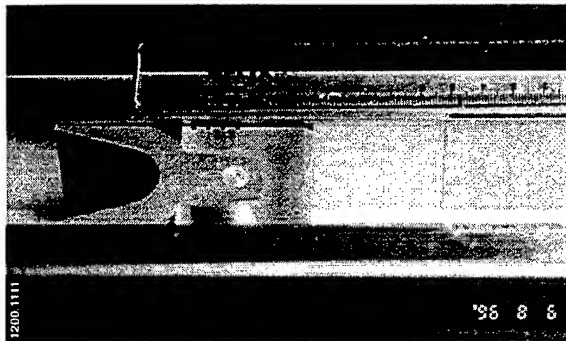


Fig. 3. Photograph of the experimental apparatus during assembly. The inserts can be seen just to the right of the armature.

Figure 4 shows the measured muzzle voltage for this experiment. The armature was accelerated by a nearly constant current of 1.03 MA as shown. The muzzle voltage on the copper rail is approximately 17 volts. In previous experiments without the inserts the muzzle voltage continues at ~17 volts, increasing slowly due to resistive heating out to a distance of 150-180 cm. In this experiment, the muzzle voltage begins to rise at approximately 26 cm and, just before contact with the insert, the voltage has increased by 13 volts.

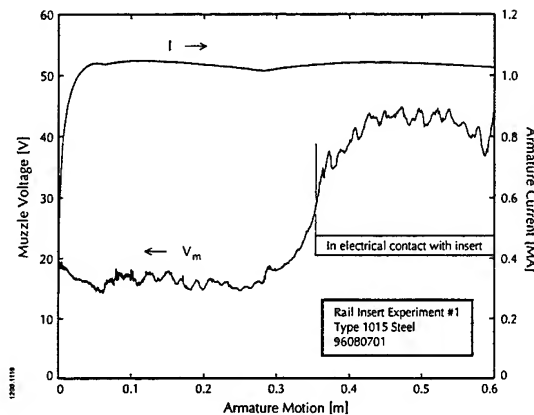


Fig. 4. Experimental measurement of the muzzle voltage with a 1015 steel insert.

Figure 4 is *prima facie* evidence that the precursor magnetic field generates a contribution to the muzzle voltage. During the majority of the time when the voltage is rising, the armature current distribution is unaffected by the presence of the inserts. Only the precursor magnetic field has the physical extent required to explain this measurement. The remainder of this paper is devoted to a quantitative comparison between theory and measurement.



An essential requirement for this comparison is a measurement of the magnetic field in front of the armature. Ideally, one would like to measure the transverse magnetic field at the rail surface on the center line. Practical considerations led to a measurement close to the rail surface and near one edge, as shown in Fig. 5. The sensing coil has 10 turns of #32 AWG wire wound on a 6.4-mm diameter form. The calculated sensitivity of the coil is  $3.46 \times 10^{-4}$  Vs/T. The signal is recorded on a 12 bit digitizer at 1  $\mu$ s/sample and the resulting record is integrated numerically to obtain the magnetic field. A typical result from test #96103101 at a current of 0.82 MA is shown in Fig. 6 where the magnetic field is plotted versus the position of the front edge of the armature contact.

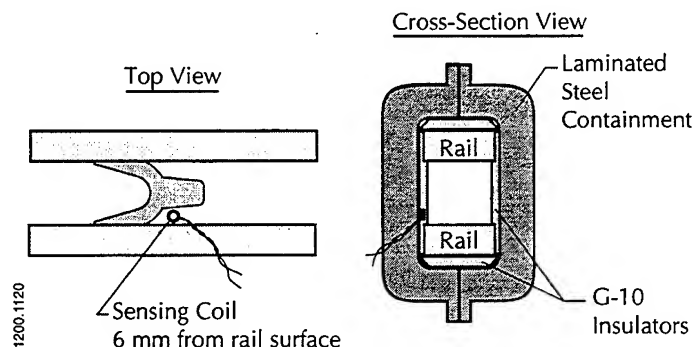


Fig. 5. Scale drawing of the launcher cross-section and rails showing the location of the coil used to measure the precursor magnetic field.

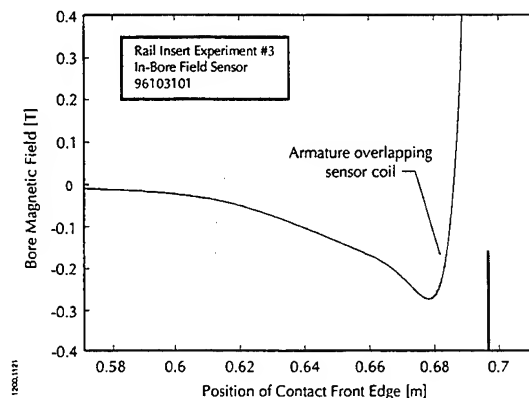


Fig. 6. The measured precursor magnetic field at a current of 830 kA and a velocity of 955 m/s.

The position of the armature as a function of time is determined in two steps. First, the equation of motion is integrated over a region that spans the three standard rail B-dot sensors closest to the insert position. By adjusting  $L'$ ,  $v_0$  and  $x_0$ , one obtains an accurate equation for the position for the magnetic center of the armature. For a solid contact armature, the magnetic center position is quite stable with respect to the armature, however, its absolute position is difficult to establish to better than approximately  $\pm 10$  mm. The bore magnetic field sensor is used to refine the absolute position since it is located much closer to the armature.

In Fig. 6, the physical location of the sensor coil is indicated at 69.7 cm. This is the position where the front edge of the contact is aligned with the center of the sensor coil. However, because the sensor is above the rail surface and the armature is "C" shaped, the armature begins to overlap the sensor coil 2.3 cm before the front of the contact. The region where overlap is occurring is shown by a shaded bar in Fig. 6. Precision position of the armature was set by aligning the beginning of overlap with the peak of the magnetic field. The estimated accuracy of the armature position is  $\pm 3$  mm.

The magnitude of the precursor field is rather small, about 3% of the field immediately behind the armature. Calculations of the precursor field for this armature using the 3D code EMAP3D [2] predict a peak precursor about 50% of the field behind the armature if the effect of the laminated steel containment is neglected. We believe that the laminated containment is responsible for reducing the precursor field in this launcher.

A final note concerning this experiment. In the analysis leading to Equation 2, it is implicitly assumed that the diffusion depth in the insert,  $\delta_I(x')$ , is significantly less than the physical thickness of the insert. If this is not true, then the surface current will diffuse into the underlying copper and the surface electric field will reflect the copper resistivity rather than the insert resistivity. For this reason, no effect would be expected for rails plated with a thin layer of high resistivity material.

### III. COMPARISON WITH THEORY

Equation 2 provides the basis for a comparison of theory with experiment. Unfortunately, the calculation is not so simple as it looks because at any time,  $t$ , the diffusion depth,  $\delta_I(x')$ , is a function of the magnetic field values at all times prior to  $t$ . Thus, performing the integral in Equation 2 requires first solving a diffusion equation at each position  $x'$ . The procedure for doing this and some simplifying assumptions are discussed next.

The physical situation to be modeled is shown in Fig. 7 at time  $t = 0$ . The precursor magnetic field is assumed to extend a distance  $S$  in front of the armature. The armature is located at  $x = -S$  and is moving with velocity  $v_c$ . The length of the inserts  $L \gg S$ .

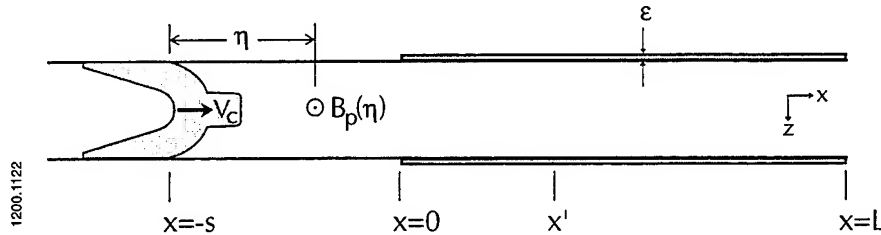


Fig. 7. Geometry of the armature and rail inserts used in the 1D calculation. The armature starts at a distance  $S$  from the inserts where  $S$  is the range of the precursor field.

The calculation required is a solution of the diffusion equation in the  $z$  direction (into the insert) at an arbitrary position  $x'$ . The actual diffusion is a complex 3D problem. We assume here that the analysis can be performed in 1D because the insert is very thin compared to the distance from the source of the field. Thus the local field at the insert surface is uniform over distances comparable to the insert thickness.

The diffusion equation in 1D is:

$$\frac{\rho}{\mu(H)} \frac{\partial^2 H(x', z, t)}{\partial z^2} = \frac{\partial H(x', z, t)}{\partial t}, \quad (3)$$

subject to the boundary conditions, (1)  $H(x', 0, t) = B_p(x' + S - v_c t)/\mu_0$  where  $B_p(\eta)$  is the field a distance  $\eta$  in front of the armature, and (2)  $H(x', \epsilon, t) = 0$ . The second boundary condition assumes, for convenience, that the current does not diffuse to the back surface of the insert before the armature reaches the insert.

Boundary condition (1) introduces another simplification, i.e., that the velocity is constant. In reality the armature is accelerating as it approaches the insert, but the distance is short and the velocity change is not significant. The constant velocity assumption is important because it reduces the problem from finding many diffusion solutions at different  $x'$  to finding a single solution at  $x' = 0$ . This follows from the fact that every location  $x'$  experiences the same magnetic field variation, only delayed in time by  $\Delta t = x'/v_c$ . Thus the general solution can be written:

$$H_s(x', z, t) = H_s\left(0, z, t - \frac{x'}{v_c}\right), \quad (4)$$

where  $0 \leq t - x'/v_c \leq s - x'/v_c$  and  $x' \leq 0$ .

After finding the solution to Equation 3 at  $x' = 0$ , we can complete the calculation of muzzle voltage as follows:

$$j(x', t) = \left. \frac{\partial H_s}{\partial z} \right|_{z=0} = \frac{\partial H\left(0, z, t - \frac{x'}{v_c}\right)}{\partial z} = j\left(0, t - \frac{x'}{v_c}\right) \quad (4a)$$

$$\varepsilon(x', t) = \rho_I j\left(0, t - \frac{x'}{v_c}\right) \quad (4b)$$

$$V_m(t) = 2 \int_0^L \rho_I j\left(0, t - \frac{x'}{v_c}\right) dx' \quad (4c)$$

Changing variables to  $u = t - x'/v_c$ , the integral becomes:

$$V_m(t) = 2v_c \int_0^t \rho_I j(0, u) du, \quad (5)$$

where the restriction on the range of  $u$  has been used to replace the lower limit  $(t - x'/v_c) < 0$  by 0.

#### IV. COMPARISON WITH EXPERIMENT

Equations 3, 4 and 5 provide a 1D solution for the muzzle voltage. They were used to calculate the expected muzzle voltage for an experiment on 4130 alloy steel. The experimental parameters are  $\delta_1 = 23 \times 10^{-8}$  ohm - m,  $v_c = 1130$  m/s. Type 4130 steel is ferromagnetic and this has an effect on current diffusion. Because the applied magnetizing force  $B_p / \mu_0$  is much larger than the magnetizing force required to saturate the steel, an accurate treatment of saturation is not needed. However, it is important to provide the correct saturation magnetic field. The assumed form of the magnetic properties for this calculation was:

$$\mu(H) = \mu_0 + \frac{M_s / H_s}{\sqrt{1 + (H/H_s)^2}}, \quad (6)$$

where  $M_s$  is the saturation magnetization. The property values used were  $M_s = 2$  Tesla,  $H_s = 1590$  A/m.

The value of  $H_s$  chosen corresponds to an initial permeability of only 1000. Higher values produce little effect on the calculated result and tend to make the numerical solution more difficult.

For the numerical solution of the diffusion equation, the insert was divided into 50 cells to provide good resolution of the diffusion process. An explicit algorithm was used for the solution and numerical stability was maintained by reducing the time step to  $10^{-4}$  of the total problem time. The results of this calculation are shown in Fig. 8.

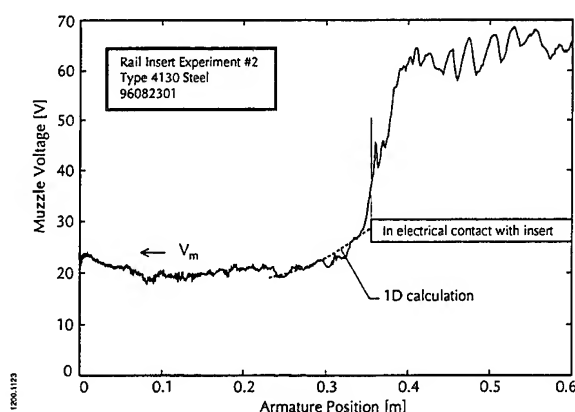


Fig. 8. Comparison of the measured and calculated muzzle voltage for a 4130 steel insert at 1.2 MA and 1070 m/s.

The experimental signal is noisy and it is difficult to establish an average muzzle voltage to which the calculated signal should be added. The calculated curve was positioned approximately in the middle of the experimental curve for ease of comparison. The fit between calculation and experiment is satisfactory in the sense that the duration of the rise and the general amplitude of the voltage are correct. The detailed shape does not agree as well. The most significant discrepancy is the slow rise in the calculated signal just before contact when the experimental voltage is increasing rapidly. The most likely explanation for this is the inadequacy of the experimentally measured precursor magnetic field. Because the probe coil is not at the rail surface, it misses the highest field region just in front of the armature contact. Also, the assumption that the precursor field and current distribution are not influenced by the insert may not be valid when the armature is very near the insert.

Additional experiments have been performed with inserts made of beryllium copper and 304 stainless steel. The results of all the experiments are summarized in Table I, along with the results of 1D simulations. The agreement between theory and experiment is about the same quality as that shown above for 4130 steel. The 4130 steel produces a larger voltage rise than the 304 stainless steel despite the 3 times higher resistivity of 304. Ferromagnetic inhibition of diffusion is the primary reason.

TABLE I.

| MATERIAL   | PROPERTIES                   |          | EXPERIMENT |          |                    | CALCULATION        |
|------------|------------------------------|----------|------------|----------|--------------------|--------------------|
|            | RESISTIVITY                  | MAGNETIC | CURRENT    | VEL      | $\Delta V$ CONTACT | $\Delta V$ CONTACT |
| 4130 STEEL | $23 \times 10^{-8} \Omega m$ | YES      | 1.2 MA     | 1070 M/S | 16.3V              | 8.7V               |
| 1015 STEEL | $11.5 \times 10^{-8}$        | YES      | 1.03       | 910      | 13.0               | 5.5                |
| 1015 STEEL | $11.5 \times 10^{-8}$        | YES      | 0.81       | 950      | 5.0                | 4.6                |
| BeCu       | $8.2 \times 10^{-8}$         | No       | 0.8        | 570      | 2.5                | 1.0                |
| 304 S.S.   | $72 \times 10^{-8}$          | No       | 0.87       | 1290     | 11.2               | 3.0**              |

\*\* Assumption of diffusion depth less than thickness was not valid for this calculation.

The small voltage calculated and measured for BeCu suggests that the precursor field contribution is negligible for conventional high conductivity rails. It must be remembered, however, that the laminated containment of our launcher suppresses the precursor field by a factor of about 16. Extrapolating these results to a launcher without a laminated containment and scaling up to a velocity of 2.5 km/s, the precursor field contribution to muzzle voltage is 16 volts on conventional copper rails. Even higher voltages, increasing as the square root of resistivity (or more with ferromagnetism), are expected for other rail materials.

## V. CONCLUSIONS

The measurements reported above show clearly and incontestably that the muzzle voltage contribution described by Dreizen and Barber exists and can make a significant contribution to the measured voltage. However, the quantitative formula for the additional voltage presented in Reference [1] is only useful for an order of magnitude estimate and is not suitable for interpreting experimental results.

A more accurate correction to an experimental muzzle voltage signal might be based either on a measurement of the precursor magnetic field combined with a simple 1D current diffusion calculation or on a full 3D calculation of the precursor current distribution. By measuring the precursor field we were able to obtain factor of two agreement between measured and calculated voltage. With further refinement this approach may be capable of 50% accuracy but much greater accuracy is unlikely. The fundamental problem with this approach is that a significant fraction of the precursor voltage is developed near the armature-rail contact, a region difficult to access experimentally for magnetic field measurements.

Fully 3D calculations offer the greatest promise for accurate interpretation of muzzle voltage but these calculations are presently at or beyond the capability of 3D electromagnetic codes. To provide an accurate calculation, the 3D code must treat velocity and sliding contact properly, the problem must be meshed finely enough to resolve gradients in the rail close to the armature contact, and all external elements, such as containment structure, that influence the precursor magnetic field must be included. Calculations satisfying the first two of these requirements have been carried out in our laboratory using the code EMAP3D but it has not been feasible yet to include the effect of a laminated stainless steel containment.

## ACKNOWLEDGMENT

This work was supported by the U.S. Army Research Laboratory under contract DAAA21-93-C-0101.

## REFERENCES

- [1] Y. A. Dreizin and J. P. Barber, "On the Origins of Muzzle Voltage," *IEEE Trans. on Magnetics*, Vol. 31, No. 1, pp. 582-586, January 1995.
- [2] K.T. Hsieh, "A Lagrangian Formulation for Mechanically, Thermally Coupled Electromagnetic Diffusive Processes with Moving Conductors," *IEEE Trans. on Magnetics*, Vol. 31, No. 1, pp. 604-609, January 1995.

# Calculation of Plasma Radiation for the Simulation of Plasma Ignition and Combustion in ETC Guns

K. Kappen

Industrieanlagen-Betriebsgesellschaft mbH  
Einsteinstraße 20, D-85521 Ottobrunn, Germany

Prof. Dr.-Ing. U.H. Bauder

Technische Universität München  
Arcisstraße 21, D-80333 München, Germany

- **Abstract** - For the ignition and combustion processes of propellant charges by a plasma in electrothermal-chemical (ETC) guns, the radiation is an important factor. The energy transport by radiation in hot, dense plasmas – as produced in the temperature/density range of ETC guns – is the dominant effect. This transport must be known if the energy balance equation has to be solved for the simulation of interior ballistics. With the assumption of local thermodynamic equilibrium (LTE) this can be done in a diffusion approximation for plasmas with substantial optical depth. For this purpose the frequency dependent absorption coefficients or rather their mean value over all frequencies (Rosseland mean opacity) have to be known. Therefore the IABG has developed the program POCAL which calculates line and continuum absorption/emission coefficients using a model of detailed configuration accounting.

Results of published experiments indicate a strong interaction between the plasma radiation and the surrounding propellant and combustion products. For this reason radiation may be used to optimize the ignition and combustion processes in ETC guns.

Given these facts it is very important for the simulation of the interior ballistic of ETC guns and for the optimization of the ignition/combustion to perform an explicit computation of the radiation transport by solving the complete equation of radiation transport. This solution may then be used in the conservation equations as presented in another contribution of this conference.

## I. Introduction

For the simulation and optimization of electrothermal-chemical accelerators a detailed knowledge of the interior ballistics is required. For this reason, IABG developed the 2D-code IBECA /Gru 95/. One of the basic equations in this code is the energy balance equation. The radiation term in this equation can be neglected at low temperatures as they occur in conventional powder guns. If temperature is rising, the part of energy transport by radiation becomes more and more important. Specifically in the temperature/density range of an ETC gun, it is the dominant effect. As an example Fig. 1 shows a radial profile of energy balance for an Argon plasma at 10 MPa /Sch 96/. It can be seen that the energy by ohmic heating and axial convection is largely dissipated by radiation.

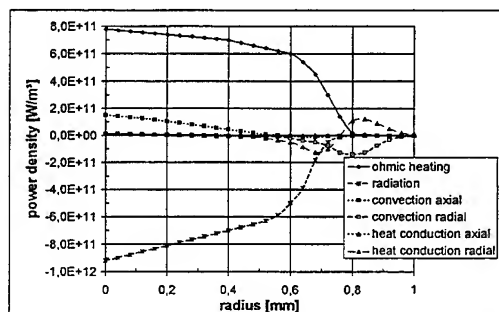


Fig. 1: Radial energy balance of an argon plasma in the middle of the arc,  $P=10$  MPa,  $I=100$  A, distance of electrodes=3 mm

For this reason it was necessary to develop a code for the calculation of radiation effects in

hot, dense plasmas. In the following chapter the theory and some results of calculations with POCAL are given.

Results of published experiments indicate a strong interaction between the plasma and the surrounding powder. For this reason it is possible, that the radiation is not only the dominant effect of energy transport in the hot plasma, but is also responsible for the transmission of energy to the powder leading to ignition. Due to the discussed reasons radiation may be used to optimize the ignition and combustion processes in ETC guns. In order as to examine this theoretically and to guide future planned experiments a detailed solution of the radiation transport equation is necessary. The follow-on activities undertaken to this purpose are shown in section IV.

## II. The atomic model

Many calculations are based on the screened hydrogenic model (SHM). In this model the atomic levels are described by the principal quantum number only /May 48/, /Tsa 87/. A more sophisticated model is the SHML where *l*-splitting is considered, too /Per 87/. The models avoid self-screening to calculate the electronic levels and occupation numbers /Mor 82/. An other approximation is used simultaneously: the average ion model (AIM) /May 48/, /Pom 73/. This model is employed to calculate the occupation numbers of the electronic levels – using the SHM/SHML – of a fictitious average ion, assuming LTE conditions.

If all species and ionisation stages in the plasma are known, the calculation of occupation numbers can be done taking into account all ion species (detailed ion model, DIM) /Dar 91/.

A problem is the numerical convergence of the SHM/SHML at low temperatures. Using an iterative algorithm developed by Mancini and Fontán /Man 85/ for the solution of the non-linear algebraic system of equations, it is still not possible to obtain a selfconsistent solution in all cases. Therefore IABG decided to develop the POCAL code using the method of detailed configuration accounting.

In the model of detailed configuration accounting each atom/ion is considered separately and the interaction with other species and free electrons is treated as a mean perturbation. Calculating the ion abundance with PLASMADAT<sup>1</sup>, the number of ions in any excitation state *i* is given by the Boltzmann - Statistic:

$$N_{ijk} = N_{jk} \frac{g_{ijk}}{Z_{jk}} \exp\left\{-\left[E_{ijk} - \Delta E_{ijk}\right]/T\right\}. \quad (1)$$

$N_{ijk}$  is the number density of specie *k* in ionisation level *j* in excitation state *i*,  $Z_{jk}$  the partition function,  $g_{ijk}$  the corresponding statistical weight and  $E_{ijk}$  the energy of the excited level (taken from tables of /Moo 71/). For low plasma densities the interaction correction term  $\Delta E_{ijk}$  is calculated by the Debye-Hückel theory (DHT), and for high densities, where the DHT is not valid anymore, the correction term is computed by the ion sphere model described by /May 48/, /Mor 82/, and /Pom 73/.

## III. Absorption and emission

In the case of local thermodynamic equilibrium the relation between emission and absorption is given by the Kirchhoff - law:

$$\varepsilon_v = \kappa_v B_v \quad (2)$$

with the Planck function

$$B_v = \frac{2hv^3}{c^2} (e^{hv/kT} - 1)^{-1}. \quad (3)$$

Therefore it is sufficient to calculate either the emission or the absorption if LTE is assumed.

In the interesting temperature/density range of an ETC launcher the following relevant absorption mechanisms in the plasma have to take into account:

|                          |               |                |
|--------------------------|---------------|----------------|
| - photoabsorption        | $\kappa^{bb}$ | } line radiat. |
| - photoionisation        | $\kappa^{bf}$ |                |
| - inverse Bremsstrahlung | $\kappa^{ff}$ |                |

<sup>1</sup> thermochemical code to calculate material functions and equilibrium concentrations in plasmas

- rotational, vibrational and } line radiat.,  
electronic excitation of (bands)  
molecules

The bound-bound transitions are calculated for all subshells in each configuration of the various ion stages explicitly. The spectrum is treated in LS coupling.

The cross section for photoabsorption is given by

$$\sigma_{ij}^{bb}(\nu) = \frac{\pi e^2}{m_0 c} \cdot f_{ij} \cdot b(\nu). \quad (4)$$

$\nu$  is the frequency,  $m_0$  the electron mass,  $e$  the electronic charge and  $c$  the velocity of light.  $b(\nu)$  is the normalized line profile that depends on several broadening mechanisms. The following types of line broadening are taken into account: Natural, Doppler and collision broadening. The collision broadening due to the Stark effect is the dominant mechanism in ETC accelerators. For the calculation of the oscillator strength  $f_{ij}$  a hydrogenic approximation is used. The total line absorption coefficient is then given by

$$\kappa^{bb}(\nu) = \sum_{i=0}^{(i_{max}-1)} \sum_{j=i}^{i_{max}} \sigma_{ij}^{bb}(\nu) \cdot N_{ijk}. \quad (5)$$

$i_{max}$  is the maximum number of bound levels and  $N_{ijk}$  is the number density of species  $k$  in ionisation level  $j$  in excitation state  $i$ . The bound-free cross section for photoionisation from the energy level  $i$  is

$$\sigma_i^{bf}(\nu) = \begin{cases} \frac{64\pi^4 e^{10} m_0 Z_i}{3\sqrt{3} h^6 c \nu^3 n_i^5} g_i^{bf}(\nu) & , \quad h\nu \geq I_i \\ 0 & , \quad h\nu < I_i \end{cases} \quad (6)$$

$h$  is the Planck constant,  $Z_i$  the effective nuclear charge for the  $i$ th level,  $I_i$  the ionisation energy and  $g_i^{bf}$  the Gaunt - factor:

$$g_i^{bf}(\nu) = 1 - 0.1728 \left( \frac{h\nu}{13.6 Z_i^2} \right)^{\frac{1}{3}} \cdot \left[ \frac{2}{n_i^2} \left( \frac{13.6 Z_i^2}{h\nu} \right) - 1 \right] \quad (7)$$

Equation (7) describes the quantum-mechanical correction for the classical result. Defining  $i_{min}$  as the lowest level for which the condition  $h\nu \geq I_i$  is valid, the total absorption coefficient for photoionisation is given by:

$$\kappa^{bf}(\nu) = \sum_{i \geq i_{min}} \sigma_i^{bf}(\nu) N_{ijk} \quad (8)$$

Assuming a Maxwellian velocity distribution for the free electrons, the semiclassical result for the free - free cross section is

$$\sigma^{ff}(\nu) = \frac{4}{3} \left( \frac{2\pi}{3m_0 kT} \right)^{\frac{1}{2}} \frac{Z_0^2 e^6}{h m_0 c \nu^3} N_e. \quad (9)$$

$Z_0$  is the nuclear charge,  $k$  the Boltzmann constant,  $N_e$  the electron density,  $T$  the temperature,  $m_0$  the electron mass,  $h$  the Planck constant,  $c$  the velocity of light and  $\nu$  the frequency.

Again a Gaunt factor  $g^{ff}$  is used to consider the quantum-mechanical correction /Men 35/.

$$g^{ff} = 1 + 0.1728 \cdot \left( \frac{h\nu}{13.6 Z^2} \right)^{\frac{1}{3}} \left( 1 + 2 \frac{kT}{h\nu} \right) \quad (10)$$

The total free-free absorption coefficient then is given by

$$\kappa^{ff}(\nu) = \sigma^{ff}(\nu) \cdot g^{ff}(\nu) \cdot N_i \quad (11)$$

In the present form of POCAL the absorption of radiation by molecules is not taken into account. This is only valid if the temperature is high enough. Fig. 2 shows the number densities of  $CH_2$  plasma at 100 MPa, as it can occur in electrothermal launchers.

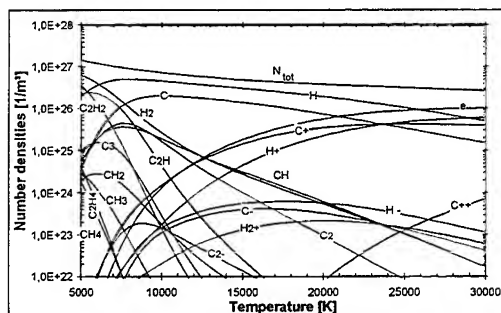


Fig. 2: Number densities of methanol,  $p=100$  MPa, (PLASMADAT)

From Fig. 2 it can be seen, that in the present case it is not justified to neglect the molecule absorption for temperatures lower than ~9000 K. For lower temperatures – e.g. in the colder boundary layer of the plasma – the ratio of atoms/ions expressed in total number densities of the plasma is rapidly decreasing.



As an example:

$$N_{a,i} / N_{\text{tot}} (T = 9000\text{K}) \cong 0,85 ,$$

$$N_{a,i} / N_{\text{tot}} (T = 7000\text{K}) \cong 0,52 .$$

In order to take into account molecule absorption in the simulations, IABG is in cooperation with the Fraunhofer-Institut für Chemische Technologie (ICT). There exists a code to calculate radiation effects of diatomic and triatomic molecules for temperatures up to 3000 K. At present an effort is on the way to extend the ICT code for calculations at higher temperatures and densities and the coupling of the IABG and ICT code.

As an example for calculated absorption coefficients Fig. 3 shows a spectrum for a  $\text{CH}_3\text{OH}$ -plasma. Methanol is a possible working fluid for electrothermal guns.

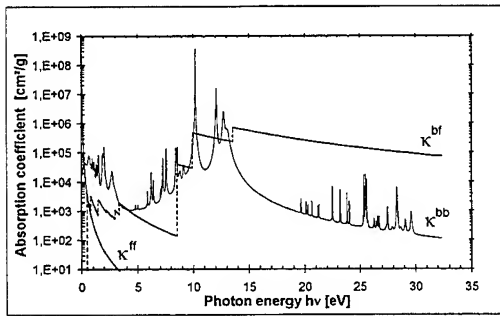


Fig. 3: Absorption spectrum of methanol at  $T=15000\text{ K}$ ,  $p=35\text{ MPa}$

#### IV. Radiative Transfer

In optically thick plasmas, energy transport by radiation can be calculated in a radiation diffusion approximation. For this purpose frequency - averaged absorption coefficients (Rosseland mean opacities) have to be known. They are defined by

$$\frac{1}{\kappa_R} = \frac{15}{4\pi^4} \int_0^\infty u^4 e^{-u} \left[ \kappa^{\text{tot}}(v) (1 - e^{-u})^2 \right]^{-1} du \quad (12)$$

where  $u = hv/kT$  is the normalized photon energy. The total frequency dependent photoabsorption coefficient corrected for stimulated emission can be written as

$$\kappa^{\text{tot}}(v) = (\kappa^{\text{ff}}(v) + \kappa^{\text{bf}}(v) + \kappa^{\text{bs}}(v)) [1 - e^{-u}] + \kappa^{\text{cs}} \quad (13)$$

Fig. 3 and Fig. 4 show calculated Rosseland mean opacities and the mean free paths for  $\text{CH}_2$  and  $\text{CH}_3\text{OH}$ .

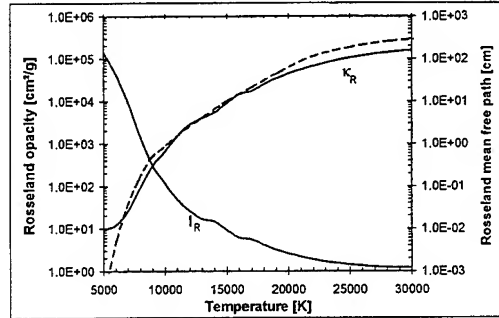


Fig. 4: Rosseland opacity and mean free path for Polyethylene at  $p=400\text{ MPa}$ . The dashed curve are results from Darée.

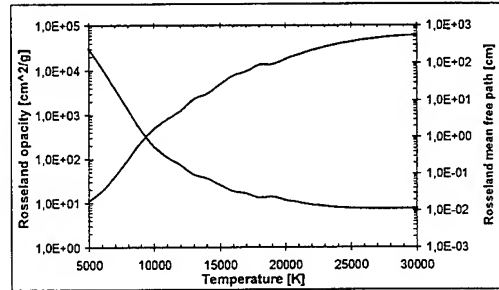


Fig. 5: Rosseland opacity and mean free path for Methanol at  $p=100\text{ MPa}$

These values are in good agreement with other published results; but it has to be remembered that they, just as all known published calculated data, are not correct in the low temperature range where absorption by molecules takes place. Darée /Dar 94/ introduced an empirical limiting factor for this case. It is based on the fact, that the radiative flux should not exceed that of a black body radiator at that temperature.

For the accurate calculation of the radiative transfer a more sophisticated model is required. The basis for quantitative studies of radiative heat/energy transport is the radiative transfer equation (RTE). Assuming again local thermo-dynamic equilibrium (LTE) the RTE has the following form

$$\frac{dI_v(r,s)}{ds} = -(\kappa_v + \sigma_s)I_v(r,s) + \kappa_v B_v(r) + \sigma_s \bar{I}_v(r,s) \quad (14)$$

This equation describes the increase in radiative intensity  $I_\nu(r,s)$  for frequency  $\nu$  at spatial location  $r$  over the path length  $ds$  in the direction of the unit vector  $s$ , as shown in Fig. 6. The terms of the right hand side of equation (14) represent the decrease in intensity due to absorption and out-scattering, the third term being the increase through emission and in-scattering. In the temperature-density range of an ETC gun, the part of scattering in total absorption/ emission can be neglect.

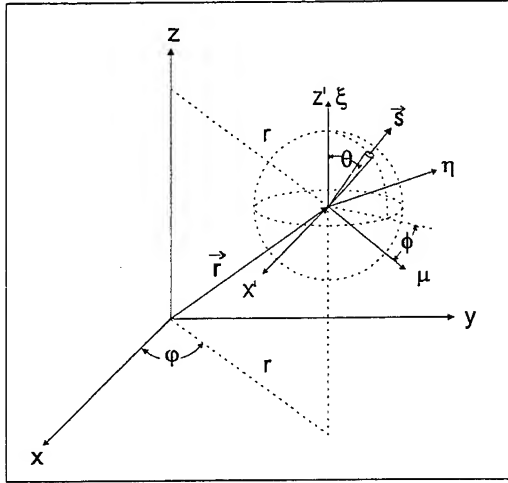


Fig. 6: Cylindrical coordinates for the equation of radiative transfer

In spherical cylinder coordinates (Fig. 6) the radiation intensity  $I_\nu$  depends on position  $r(r, \phi, z)$  and direction  $s(\theta, \phi)$ . If axisymmetry exists, the intensity distribution becomes invariant with  $\phi$  so that the RTE for axisymmetric intensity  $I_\nu(r, z, \theta, \phi)$  yields

$$\left( \mu \frac{\partial}{\partial r} + \xi \frac{\partial}{\partial z} - \frac{\eta}{r} \frac{\partial}{\partial \phi} \right) I_\nu(r, z, \theta, \phi) = \kappa_\nu [B_\nu(r, z) - I_\nu(r, z, \theta, \phi)] \quad (15)$$

where  $\mu$ ,  $\eta$ , and  $\xi$  are direction cosines defined as  $\mu = \sin \theta \cos \phi$ ,  $\eta = \sin \theta \sin \phi$ ,  $\xi = \cos \theta$  /Pom 73/, /Chu 92/.

Many models have been applied to the problem of axisymmetric radiative transfer. They contain a varying number of assumptions. Raithby and Chui /Rai 90/ proposed a finite volume method (FVM) that

uses the same philosophy and grid as the finite volume techniques currently used in fluid flow and convective heat transfer /Pat 80/. In this method the computational domain is subdivided into discrete (finite) volumes, and the direction is subdivided into discrete solid angles. IABG plans to implement the FVM used by Gruber to solve the RTE. For more information about the FVM see /Gru 95/, /Rai 90/ and /Chu 92/.

## V. Conclusion

A simulation model for the calculation of line and continuum radiation of atoms and ions has been developed. If molecule radiation can be neglected and if the plasma is optically thick, the calculated opacities can be used in the Rosseland diffusion approximation. It represents a good approximation of radiative transfer in the arc. By coupling the codes of ICT and IABG a better calculation of the absorption/emission in the colder boundary layer of a plasma is possible. To validate the coupled code and to show its accuracy, experiments will be performed at ICT. Furthermore the diffusion approximation is not applicable in the colder boundary layer where the plasma is not optically thick. For this reason it has to be replaced by the exact solution of the transport equation. Last but not least a detailed solution of the radiation transport equation should be useful to predict ignition/combustion effects of radiation in ETC accelerators and to aid future experiments.

## VI. References

- /Chu 92/ Chui, E.H., Raithby, G.D., Hughes, P.M.J.: *Prediction of radiative transfer in cylindrical enclosures with the finite volume method*, Journal of Thermophysics and Heat Transfer, Vol.6, No.4, 1992
- /Dar 91/ Darée, K.: *Opacities of high pressure arc plasmas*, ISL - CO 214/91, 1991
- /Dar 94/ Darée, K.: *Eindimensionale Modellrechnungen zum elektrothermischen Beschleuniger des ISL*, ISL - R 127/94, 1994
- /Gru 95/ Gruber, K.: *Two-dimensional modelling of electrical arcs for use in electrothermal launchers*, 5<sup>th</sup> EML 1995

- /Man 85/ Mancini, R.C. and Fontán, C.F.: *Ionisation state and bound level populations in hot, dense plasmas*, JQSRT Vol.34, pp.115, 1985
- /May 48/ Mayer, H.: *Methods of opacity calculations* LA-647, Los Alamos 1948
- /Men 35/ Menzel, D.H. and Pekeris, C.H.: *Absorption coefficients and hydrogen line intensities*, Mon. Not. R. astr. Soc., Vol.36, pp.77, 1935
- /Moo 71/ Moore, C.E.: *Atomic energy levels*, NSRDS-NBS 35, Vol.1, 1971
- /Mor 82/ More, R.M.: *Electronic energy-levels in dense plasmas*, Journal of Quantitative Spectroscopy and Radiative Transfer Vol.27, pp.345, 1982
- /Pat 80/ Patankar, S.V.: *Numerical heat transfer and fluid flow*, McGraw-Hill, New York, 1980
- /Per 89/ Perrot, F.: *Fast calculation of electronic structure*, Physica Scripta Vol.39, pp.332, 1989
- /Pom 73/ Pomraning, G.C.: *The equation of radiation hydrodynamics*, Pergamon Press, 1973
- /Rai 90/ Raithby, G.D. and Chui, E.H.: *A finite-volume method for predicting a radiant heat transfer in enclosures with participating media*, Journal of Heat Transfer Vol.112, pp.415, 1990
- /Ric 89/ Rickert, A.: *Berechnung frequenzabhängiger Opazitäten für Hoch-Z Plasma mit l-Aufspaltung*, MPQ 148, 1989
- /Sch 96/ Schmidt, H.P. and Speckhofer, G.: *Experimental and theoretical investigation of high pressure arc, Part I: The cylindrical arc column (Two dimensional modelling)*, IEEE Vol. 24 No 4, pp.1229, 1996

# Rail Accelerator Control Using Spline-Algorithms for Launch Velocity Stabilization

Vladimir A.Alexandrov, Ilya B.Azanov, Mikhail M.Khrustalev, Stanislav S.Obydennikov,  
Natalya I.Pipin, Valery K.Tyutin, Viktor I.Yudas

State Research Institute of Applied Mechanics and Electrodynamics of Moscow State Aviation  
Institute  
4, Volokolamskoye shosse, GSP-47, Moscow, 125810, Russia

## SUMMARY

The work is concerned with solution of the launch velocity stabilization problem in rail accelerators of the macroparticles by means of controlling the acceleration process in real time. The control spline-algorithm has been studied. It is based on the use of several nominal trajectories and of the spline approximation of the algorithm coefficients. According to the results of numerical modeling the proposed algorithm allows the decrease of the spread in launch velocity under the considerable deviations of the accelerator parameters from their nominal values.

## I. INTRODUCTION

The rail accelerators of macroparticles are characterized by considerable spread in launch velocity and by poor repetition of experimental results in the process of simulating the interaction of orbital debris with spacecraft elements. To a great extent this drawback can be eliminated by controlling the acceleration process in real time. The similar approach to solution of the launch velocity stabilization problem was used by the authors for the first time in the work [1].

Due to short duration of the acceleration process the simple control methods and strategies are of interest. In [1] the control method was considered with single correction of the macroparticle velocity by means of by-passing electrodes of the accelerator under the commutator  $K_s$  closing (Fig.1) at some time  $t = t_s$  which leads to a decrease in the armature current  $I_a$  at  $t > t_s$ . At the nominal mode of the accelerator operation without disturbances of the acceleration process the closure time  $t = t_{s,nom}$  is selected so that the launch velocity  $V_e$  would coincide with the required one  $V_r$ . If the acceleration process differs from the nominal one the control system, which realizes the control algorithm, forms the times for by-passing the armature circuit depending on the results of the accelerator parameter measurements.

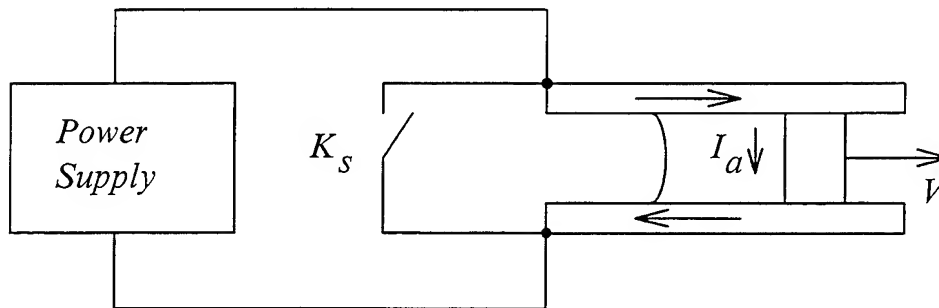


Fig.1 Rail accelerator schematic

In [1] the control algorithm was studied for single nominal trajectory describing the variation of the accelerator state parameters without disturbances. In the present work in order to increase control accuracy the algorithms, which are based on the use of several nominal trajectories and of the spline approximation methods, have been developed.

## II. MATHEMATICAL MODEL

The control algorithm under study allows the use of various mathematical models for the rail accelerator, described by ordinary differential equations. In this work a relatively simple model for the rail accelerator with plasma armature was used. It takes into account the ablation processes, gas-dynamic drag accompanying the plasma armature and macroparticle motion, variable electric resistance of the electrode skin-layers.

The equivalent circuit for the rail accelerator and pulse power supply is shown in Fig.2. As in the work [1] the power supply was modeled as an electric circuit with two sections comprising capacitive and inductive elements. The first branch ( $C_1, L_1, R_1$ ) forms the front part of the pulse under the commutator  $K_1$  switching on. Commutator  $K_2$  and crowbar  $K_3$  are closed simultaneously after reaching the maximum current value in the accelerator at the time  $t = t_f$ . The flat top of the pulse is formed as a result of discharge of inductance  $L_1$  and capacitance  $C_2$ . Commutator  $K_s$  with minimum resistance  $R_s$  and inductance  $L_s$  is switched on at the time  $t = t_s$ , defined by the control system. The rail accelerator itself is modeled as the variable inductance  $L_e$ , the time varying resistance  $R_e$  of the electrode skin-layers and the plasma resistance  $R_p$ . According to [2] the  $R_p$  value was considered constant.

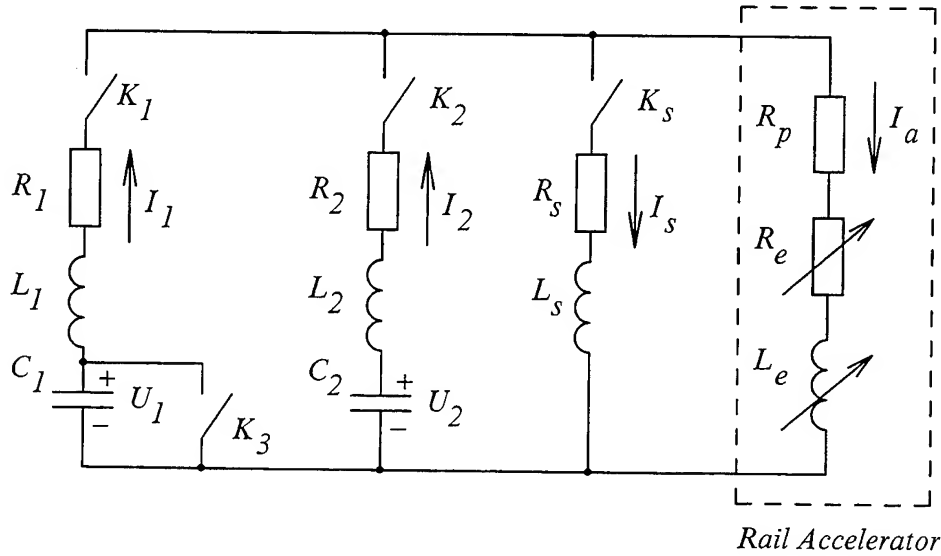


Fig.2 Equivalent circuit for the rail accelerator and power supply.

The macroparticle and plasma motion is described by the equations :

$$\frac{dx}{dt} = V, \quad (1)$$

$$\frac{dV}{dt} = \frac{0.5LI_a^2 - \alpha I_a^2 R_p V - 0.5\lambda m_p V^2 / d - k\rho d^2 V^2}{m_0 + m_p}, \quad (2)$$

$$\frac{dm_p}{dt} = \alpha I_a^2 R_p, \quad (3)$$

where  $\alpha$  is the ablation coefficient,  $\lambda$  is the coefficient of plasma drag,  $m_p$  is the plasma mass,  $m_0$  is the macroparticle mass,  $\rho$  is the density of nonperturbed gaseous medium in front of a

macroparticle,  $k$  is the drag coefficient,  $d$  is the distance between walls of the square cross section channel.

The form of the electric circuit equations, to be included into the mathematical model, depends on the time interval of the operating process. For example, for  $0 \leq t \leq t_f$  ( $t_f$  is the duration of the front of the current pulse) these equations are written as (Fig.2):

$$\frac{dU_1}{dt} = -\frac{I_1}{C_1}, \quad (4)$$

$$\frac{dI_1}{dt} = \frac{U_1 - (R_1 + R_e + R_p + L'V)I_1}{L_1 + L'x}, \quad (5)$$

where  $R_e = \frac{3l}{k_b b t_k} \sqrt{\frac{\mu_0 t}{\sigma}}$  is the resistance of the accelerator electrodes,  $l$  is the electrode length,

$t_k$  is the time of the operating process termination corresponding to reaching the point  $x = l$  by the back part of a macroparticle,  $k_b \approx 2.5$  is the boundary condition coefficient under the calculation of the current skin-layer thickness,  $b$  is the electrode width ( $b \geq d$ ),  $\sigma$  is the average electric conductivity of the electrode material.

For the time interval  $t_f < t \leq t_s$  the electric circuit equations have the form:

$$\frac{dU_2}{dt} = -\frac{I_2}{C_2}, \quad (6)$$

$$\frac{dI_1}{dt} = F, \quad (7)$$

$$\frac{dI_2}{dt} = \frac{L_1}{L_2} \cdot F + \frac{R_1}{L_2} \cdot I_1 - \frac{R_2}{L_2} \cdot I_2 + \frac{U_2}{L_2}, \quad (8)$$

where

$$F = -\frac{[L'xR_1 + L_2(R_1 + R_e + R_p + L'V)]}{L_1L_2 + L'x(L_1 + L_2)} \cdot I_1 - \frac{[(R_e + R_p + L'V)L_2 - L'xR_2]}{L_1L_2 + L'x(L_1 + L_2)} \cdot I_2$$

For the interval  $t > t_s$  the electric circuit equations take additionally into account the parameters  $L_s, R_s$  of the branch with the commutator  $K_s$ . For brevity they are not given here.

### III. CONTROL ALGORITHM

The rail accelerator control algorithms developed in this work are based on comparison of the launch velocity for the nominal trajectory with the predicted launch velocity for the real trajectory. The nominal trajectory reflects the state vector variation in time when there are no disturbances. The real trajectory corresponds to measured parameters in the presence of the acceleration process disturbances and the measurement errors. The control algorithm realizes the selection of time,  $t_s$ , for by-passing the armature circuit. It takes into account the disturbances of the accelerator state parameters and the measurement errors for those parameters which can be recorded during the experiment.

The discrete measurements of the accelerator parameters are effected at the consequent times  $t_0, t_1, \dots, t_N$ , while the control is realized at time  $t_s > t_N$ .

In [1] the method of forming the linear strategy with memory has been proposed. In the case of three measurements this strategy has the form:

$$t_s = t_{s,nom} - (P_0^T \Delta y_0 + P_1^T \Delta y_1 + P_2^T \Delta y_2) / B_e, \quad (9)$$

where  $\Delta y_j = y_j - y_{j,nom}$  ( $j = 0, 1, 2$ ),  $y_j$  and  $y_{j,nom}$  are the vectors, the components of which are the measured and nominal parameters of an accelerator for  $t = t_j$ , correspondingly,  $P_j$  ( $j = 0, 1, 2$ ) are the vectors defined in the work [1],

$$B_e = \frac{\partial \Delta V_e}{\partial \Delta t_s}, \Delta V_e = V_e - V_r, \Delta t_s = t_s - t_{s,nom}.$$

Upper symbol "T" means the transposition.

The components  $P_j^i$  ( $i = 1, 2, \dots, Q$ ), of the vectors,  $P_j$ , can be found from the system of linear equations obtained in [1] from the condition of minimum influence of measurement errors and parameter disturbances on the mean square deviation of the launch velocity from the required value. This system of equations is derived under assumption that ranges of the error and disturbance variations are known.

As the disturbed parameters the initial conditions and those accelerator parameters, the values of which are not accurately known, are considered. For example, the electrode inductance gradient, macroparticle mass, times of macroparticle passing the fixed points of an accelerator, where the positional sensors are located, and other parameters can be related to such parameters.

The calculations have shown that the control algorithm proposed in [1] ensures the acceptable accuracy of the launch velocity stabilization for the rather small ranges of the disturbance variations. In this work the method is proposed for increasing the accuracy of the control algorithm under substantial deviations of some parameters of an accelerator from their nominal values.

Let a vector  $D_j = (D_j^1, D_j^2, \dots, D_j^q)^T$  of such parameters, which can substantially deviate from their nominal values, have been isolated among measured parameters. The number of the components of the vector,  $D_j$ , may be different at the different times  $t = t_j$ ,  $j = 0, 1, \dots, M < N$ . The measured values of the  $D_j^1, D_j^2, \dots, D_j^q$  components of the vector,  $D_j$ , differ from the true ones by the values of measurement errors  $\delta D_j^1, \delta D_j^2, \dots, \delta D_j^q$ .

In this case the following idea can be used. The domain  $\Omega$  of the  $D_j$  parameter vector variation is divided into the sufficiently small non-overlapping subdomains,  $\Omega_k$ , so that the union of these subdomains coincides with  $\Omega$ . For each of these subdomains the own nominal trajectory is selected and the own control strategy of the form (9) is generated. After measuring the  $D_j$  vector it is possible to identify the subdomain,  $\Omega_k$ , to which the measured value of the vector belongs. Then the strategy (9) with a coefficients corresponding to the subdomain  $\Omega_k$  should be applied. Such method would allow the increase of the control accuracy.

Further increasing the control accuracy and decreasing the number of the  $\Omega_k$  domains can be attained in the following way. Let us assume, that the  $\Omega$  domain of variation of the  $D_j$  parameter vector is a parallelepiped:

$$D_{\min}^i \leq D^i < D_{\max}^i, i = \overline{1, q} \quad (10)$$

Then let us take the smaller parallelepipeds

$$D_{\min}^{ik} \leq D^i < D_{\max}^{ik}, k = \overline{1, K}, \quad (11)$$

as a system of the  $\Omega_k$  subdomains, union of which constitutes the  $\Omega$  parallelepiped. These smaller parallelepipeds can be obtained by setting in  $\Omega$  a uniform or nonuniform rectangular grid.

For each grid node a nominal trajectory is formed and the coefficients of the control strategy (9) are computed. Then for each small parallelepiped  $\Omega_k$  of the form (11) the values of coefficients  $P_0^T, P_1^T, P_2^T, B_e$  are known. In this algorithm in contrast to the earlier procedure the coefficients of the strategy (9) are suggested to be found for the measured value of the  $D_j$  parameter vector, if it proves to be in  $\Omega_k$ , with the help of a lined function (linear in each variable

for fixed values of others). This function defined on the  $\Omega_k$  parallelepiped allows the computation of the coefficients,  $P_0^T, P_1^T, P_2^T, B_e$ , by means of interpolation of the coefficient values in the  $\Omega_k$  apexes. It is this difference that ensures the increase of the control algorithm accuracy and the decrease of the number of subdomains.

For example, in case of two parameters  $D_j^1, D_j^2$  ( $D_j = (D_j^1, D_j^2)^T$  is the two dimensional vector) the control strategy coefficients are determined in the following way. The lined function, which approximates the dependence  $B_e(D_j^1, D_j^2)$  on the  $\Omega_k$  rectangle

$$[D_{\min}^{1k}; D_{\max}^{1k}] \times [D_{\min}^{2k}; D_{\max}^{2k}], \quad (12)$$

has the form

$$B_e = \beta_0 + \beta_1 \chi_j^1 + \beta_2 \chi_j^2 + \beta_{12} \chi_j^1 \chi_j^2, \quad (13)$$

where

$$\chi_j^1 = (2D_j^1 - D_{\max}^{1k} - D_{\min}^{1k}) / (D_{\max}^{1k} - D_{\min}^{1k}),$$

$$\chi_j^2 = (2D_j^2 - D_{\max}^{2k} - D_{\min}^{2k}) / (D_{\max}^{2k} - D_{\min}^{2k}),$$

$$\beta_0 = (B_e^{00} + B_e^{01} + B_e^{10} + B_e^{11}) / 2,$$

$$\beta_1 = (-B_e^{00} - B_e^{01} + B_e^{10} + B_e^{11}) / 2,$$

$$\beta_2 = (-B_e^{00} + B_e^{01} - B_e^{10} + B_e^{11}) / 2,$$

$$\beta_{12} = (-B_e^{00} + B_e^{01} + B_e^{10} - B_e^{11}) / 2.$$

Here  $B_e^{00}, B_e^{01}, B_e^{10}, B_e^{11}$  are the values of the  $B_e$  coefficient in apexes of the rectangle (12), calculated according to the procedure of the work [1]. For the entire  $\Omega$  domain the obtained piecewise lined spline, which approximate the dependence  $B_e(D_j^1, D_j^2)$ , will be a continuous function [3].

The approximations for other coefficients of the control strategy (components of the vectors  $P_0, P_1, P_2$ ) are constructed quite analogously. A set of such approximations for all coefficients of the strategy (9) forms the proposed spline-algorithm of the launch velocity stabilization.

It is possible to suggest another version of the spline-algorithm. In this algorithm the values of the time,  $t_s$ , of closing the by-passing circuit, and not coefficients of the strategy (9), are approximated by the piecewise lined spline. Here coefficients, calculated for each node of the  $\Omega_k$  parallelepipeds are used. Such version of the algorithm has its advantages and disadvantages. The advantage is that only one dependence is to be approximated. For example, in case of two parameters  $D_j^1, D_j^2$  this is the dependence  $t_s(D_j^1, D_j^2)$ . The disadvantage is that under functioning of the algorithm in real time the calculation of values,  $t_s$ , in apexes of the  $\Omega_k$  parallelepiped and the interpolation can be performed only after carrying out all measurements at  $t > t_M$ , i.e. directly before closing the by-passing circuit.

In case of the first version of the spline-algorithm, if the totality of the  $D_j^i$  parameters substantially deviating from their nominal values is presented only as the  $D_0$  vector ( $M = 0$ , i.e. the  $D_j$  vector components are measured only at the time  $t = t_0$ ), the calculations of interpolated values of the control strategy coefficients can be realized immediately after measurement of  $D_0$  vector ( $t > t_0$ ). The problem of utility of this or that version of the control algorithm should be resolved in each particular case.



#### IV. NUMERICAL MODELING

The accuracy verification of the proposed control algorithms was made by numerical modeling of the laboratory rail accelerator of 1 m length and 1 cm<sup>2</sup> cross-section. The macroparticle mass and its starting velocity at the accelerator input were accepted to be 1.8 g and 1 km/s, correspondingly. Values of the electrode inductance gradient,  $L'$ , capacitances,  $C_1$ ,  $C_2$ , and initial voltages,  $U_{10}$ ,  $U_{20}$ , in the power supply were the following:  $L' = 3.65 \cdot 10^{-7}$  H/m,  $C_1 = 1.6$  mF,  $C_2 = 62.5$  mF,  $U_{10} = 19.2$  kV,  $U_{20} = 10$  kV. According to the calculations the required launch velocity was 3.3 km/s at a peak current of 406 kA.

It was assumed in the numerical modeling of the control algorithms that a single correction of velocity is made to compensate the disturbances of initial voltages in the power supply,  $\pm \Delta U_{10}$  and  $\pm \Delta U_{20}$ , and the disturbance of inductance gradient,  $\pm \Delta L'$ .

The following maximum values of relative deviations were accepted for the calculations:

$$\Delta \tilde{U}_{10} = \Delta U_{10} / U_{10} = \pm 10\%, \quad \Delta \tilde{U}_{20} = \Delta U_{20} / U_{20} = \pm 10\%, \quad (14)$$

$$\Delta \tilde{L}' = \Delta L' / L' = \pm 15\%. \quad (15)$$

The accuracy of the control algorithms was estimated by calculating the maximum value of the relative spread in the launch velocity,  $\Delta \tilde{V}_e = (V_e - V_r) / V_r$ , of the controlled accelerator for all possible deviations (14)-(15). For comparison, the value,  $\Delta \tilde{V}_e$ , was also determined for the non-controlled accelerator. In it the by-passing circuit is closed at the same time  $t_s = t_{s, nom}$  independently of the deviation values  $\Delta U_{10}$ ,  $\Delta U_{20}$ ,  $\Delta L'$ . It was assumed that measurements of the accelerator parameters were made without errors. The value,  $\Delta \tilde{V}_e$ , was computed for the following cases: 1) only disturbances,  $\Delta U_{10}$ ,  $\Delta U_{20}$ , act, 2) only disturbance,  $\Delta L'$ , acts, 3) disturbances,  $\Delta U_{10}$ ,  $\Delta U_{20}$ ,  $\Delta L'$ , act jointly.

The values of the relative spread in the launch velocity,  $\Delta \tilde{V}_e$ , for the non-controlled accelerator and for the accelerator controlled by the algorithms with single and two nominal trajectories as well as by the spline-algorithm with two nominal trajectories are presented in the Table 1. Here these control algorithms are denoted by Alg1, Alg2 and S-Alg, correspondingly.

TABLE 1

THE SPREAD IN LAUNCH VELOCITY,  $\Delta \tilde{V}_e$ , (IN %) FOR THE NON-CONTROLLED ACCELERATOR AND FOR THE ACCELERATOR CONTROLLED BY VARIOUS ALGORITHMS.

| Algorithm<br>Parameter deviations   | Non-controlled<br>accelerator | Controlled<br>accelerator |      |       |
|---|-------------------------------|---------------------------|------|-------|
|   |                               | Alg1                      | Alg2 | S-Alg |
| $\Delta \tilde{U}_{10} = \Delta \tilde{U}_{20} = \pm 10\%$                                  | 6.28                          | 1.06                      | 0.27 | 0.21  |
| $\Delta \tilde{L}' = \pm 5\%$   | 3.25                          | 0.53                      | 0.14 | 0.11  |
| $\Delta \tilde{L}' = \pm 15\%$  | 9.88                          | 2.15                      | 0.56 | 0.43  |
| $\Delta \tilde{U}_{10} = \Delta \tilde{U}_{20} = \pm 10\%$<br>$\Delta \tilde{L}' = \pm 5\%$ | 9.29                          | 1.54                      | 0.4  | 0.31  |

From the Table 1 it is seen, that in comparison with the algorithm using single nominal trajectory the control algorithm with two nominal trajectories and the spline-algorithm allow the decrease of the spread in launch velocity and the extension of the range of the accelerator parameter deviations from the nominal values.

It should be noted that for the controlled accelerator the power supply has to have the necessary store of energy for ensuring the required launch velocity under the state parameter disturbances resulting in the decrease of  $V_e$ .

#### V. CONCLUSION

The new method of synthesis of the rail accelerator control strategy in real time has been proposed. The principle of the accelerator control is based on varying the armature current under by-passing the armature circuit at some time. This time is selected depending on results of measurements of the acceleration process parameters stored in the control system memory. The new method differs from the one proposed earlier by authors in that it uses several nominal trajectories and the spline approximation of values forming the control strategy. It ensures the decrease of the spread in macroparticle launch velocity under the substantial deviations of the acceleration process parameters. Three modifications of the method have been proposed.

The numerical modeling has demonstrated the essentially higher accuracy of the synthesized control strategies in comparison with the strategy earlier proposed. This improvement has been achieved at the expense of some complication of the control strategy.

#### REFERENCES

- [1] I.B.Azanov, V.A.Alexandrov, S.S.Obydennikov, V.K.Tyutin, M.M.Khrustalev, and V.I.Yudas, "Macroparticle Launch Velocity Control in Rail Accelerators", The 8th Electromagnetic Launch Symposium, Abstracts booklet, April 21-24, 1996, Baltimore, USA, p.21.
- [2] V.E.Ostashev, A.A.Zubkov, E.F.Lebedev, A.V.Ul'yanov, "Formation and Evolution of a Current-Plasma Armature in a Magnetoplasma Accelerator of Macrobodies", High Temperature, vol.32, No.1, pp.16-22, 1994.
- [3] I.B.Azanov, "Quasilined Splines with Semilimited Curvature", MAI, Moscow, 1993, deposited at VINITI on March, 19, 1993, No.656-B93.

# **Preliminary Results of Experimentally Validated Applied Electromagnetic Issues of Railguns**

by

**W.J. Sarjeant**  
University of Buffalo  
P.O. Box 601900  
Buffalo, NY 1426-1900  
USA

**I. Kohlberg**  
Kohlberg Associates  
P.O. Box 23077  
Alexandria, VA 22304  
USA

**C. Le**  
U.S. Army Research Laboratory  
Attn: AMSRL-SE-DE  
Powder Mill Road  
Adelphi, MD 20783-1145  
USA

**R. Zworka**  
Center for Electromechanics  
10100 Burnett Road  
University of Texas at Austin  
Austin, TX 78712  
USA

## **Abstract**

This paper addresses a number of related fundamental applied electromagnetic issues connected with the optimization of overall mission effectiveness of electrically energized gun and tube design. The practical factors that affect the electromagnetic performance of railguns are addressed using a first-order physical railgun model, which with some limitations can be extended to augmented rails. Results of ARL theoretical and experimental studies of this basic physical model of the railgun, from both pulsed power conditioning and electromagnetic field considerations, have shown that several critical issues remain to be better understood pertaining to optimizing performance. These factors include: determination of the surface currents and the acceleration of the armature, establishing the relationship between the currents and the acceleration of the armature, evaluating changes in "inductance" gradient as a result of shielding, characterizing the information that can be obtained from the measurement of muzzle voltage, and assessing the level of current that can flow ahead of the armature. This report concentrates on those factors dominating the muzzle voltage behavior of 1-5 centimeter bore class electrically energized guns, which is shown to be related to all of the a forementioned technology issues.

## **1. INTRODUCTION**

Fully electrically-energized gun and tube propulsion systems (often referred to as "Railguns") can potentially provide the capability of launching projectiles at both high kinetic energy and velocity that exceed capabilities of present chemical launch systems. Because weaponization of these systems will generally involve mobile platforms, and hence finite electrical energy storage, the operational utility of such systems depends strongly on their mission-duration, and in most cases, their per-shot, energy efficiency.

The practical factors that affect the electromagnetic performance of railguns can be addressed using the first-order Railgun model shown in Fig. 1. Analyses for this type of Railgun can be extended to the augmented Railgun with some limitations. The Army Research Laboratory (ARL) has been conducting tests and performing related theoretical analyses on a system such as that shown in Fig. 1 from both pulsed power and electromagnetic environment viewpoints. Results of these studies have shown that several issues remain to be better understood pertaining to maximizing

efficiency, clarifying the role of muzzle voltage in the interpretation of the performance, and quantifying the electromagnetic fields generated by these devices [1]-[8].

All of the above factors relate to the same fundamental scientific issues impacting on overall system performance and cycle-life effectiveness, namely:

- \* What is the current distribution on the Railgun including the currents in-front-of, on the sides, or, and behind the armature?
- \* What is the relationship of these currents to the acceleration of the armature?
- \* How are these currents related to the inductances of the system?
- \* What can be learned from the temporal behavior of the muzzle voltage?

The relative importance of these factors is a function of the type of railgun, and the accompanying losses in the system such as: ohmic heating, contact frictional resistance between the rails and armature, and aerodynamic drag forces. These latter effects are neglected in this initial assessment, described in more detail in [8].

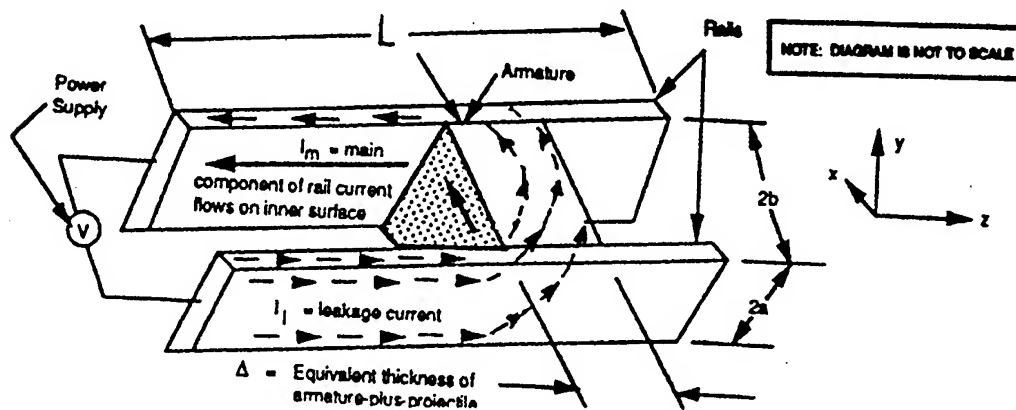


Fig. 1. Basic Railgun Used in ARL Experiments

## 2. ELECTRICAL EFFICIENCY AND ELECTROMAGNETIC EFFICIENCY

The starting point of the theoretical foundation is the armature force equation:

$$m_a \frac{dV_a}{dt} = F_z \quad (1)$$

where  $m$  is the mass of the armature,  $V_a = dZ_a / dt$  is the armature velocity,  $Z_a$  is the armature position, and  $F_z$  is the force in the direction of motion; as noted in Fig. 1,  $z$  is the direction of travel.

Initial investigations of railguns used the following expression for the force:

$$F_z = \frac{1}{2} L'_R I^2 \quad (2)$$

where  $L'_R$  is the rail inductance gradient (inductance per unit length of the rails), and  $I$  is the current through the rails. The derivation of Eq. (2) is not claimed to be obvious; it appears to have

been derived some years ago from energy considerations relevant to a bounded system. Experiments have typically produced results that show that the actual force on armatures is less frequently than that given by Eq. (2), and in some cases by significant amounts (25-50%). As reported in numerous articles, reasons for this disparity were initially attributed to drag forces, friction forces, and other losses in the system. For whatever the reason, it was concluded that a Railgun typically operated with an effective inductance gradient,  $L'_e$ , that was less than the theoretical value  $L'_R$  [1, 8].

In 1994 another explanation was proposed that accounted for the experimental observations [1,2]

$$L'_e \leq L'_R \quad (3)$$

Using a combination of conformal mapping it was shown that the effective inductance gradient could be related to the theoretical results [9-13] by the equation:

$$L'_e = E_o L'_R \quad (4)$$

where  $E_o$  is called the "Electromagnetic Efficiency".  $E_o$  is computed solely from the geometry of the system. It is essentially time independent for the entire length of travel [16]. A modest time dependence occurs at the beginning (breach) and exit (muzzle) of armature travel, where end effects come into play [1, 8].

A general formula for  $E_o$  using the principle of linearity can be derived and related to the electrical efficiency,  $E_e$ , as:

$$E_e = \frac{E_o}{E_o + f} \quad (5)$$

where

$$f = \frac{2 Z_A \dot{V}_A}{V_A^2} \quad (6)$$

The quantity,  $f$ , represents an inherent potential energy loss in the system that occurs when there is a finite acceleration,  $\dot{V}_A > 0$ , at muzzle exit,  $Z_A = L$ . Finite acceleration at muzzle exit also implies that  $I > 0$ , which means that magnetic energy is left over, and hence lost to acceleration of the projectile. This lost energy resides in the leakage field created by the rail-armature structure.

For an optimized design of a Railgun  $E_o$  should be much larger than  $f$ ; in this case we can use the power series approximation:

$$E_e = 1 - (f / E_o) + (f / E_o)^2 + \dots \quad (7)$$

Equation (7) shows that the electrical efficiency increases when the ratio  $f / E_o$  decreases. This is accomplished by using all of the magnetic stored energy in the acceleration process. This simplicity of the expression  $f / E_o$  masks a multitude of electromagnetic interactions that occur through examination of muzzle voltage, an observation made earlier by Barber and Dreizen [3, 4].

We see that  $E_o$  may become an important factor in the overall electrical efficiency of the system under circumstances determined by the system design requirements. Consideration of these factors is quite complex and is the subject of systems-level research and model development, outside of this study.

The resources of muzzle voltage for the railgun of Fig. 1 are quantified and compared with experiment in the next two sections. From this analysis we obtain a preliminary estimate of the importance of some factors that contribute to electrical efficiency.

### 3. MUZZLE VOLTAGE AS A DIAGNOSTIC TOOL

The general model developed in ref. [8] shows that the armature does indeed provide the dominant contribution to the muzzle voltage for the railgun configuration considered in this study. This contribution is much larger than that due to the mutual inductance between the primary and secondary loops [3, 4, 8] and also includes surface impedance losses on the interior wall of the rails ahead of the armature. For the railgun of Fig.1 we do not find significant current ahead of the armature.

The armature voltage,  $V_{ARM}$ , consists of three distinct contributions, two of which are dominant in the early time region, while the remaining one is dominant in the latter phases of armature motion. Hence:

$$V_{ARM} = V_{IND} + V_{RES} + V_{EMF} \quad (8)$$

where  $V_{RES}$  is the voltage due to ohmic losses, and  $V_{EMF}$  is the counter *emf* attributed to the acceleration of the armature, and  $V_{IND}$  is the armature inductance contribution.  $V_{IND}$  is a easiest contribution to evaluate, and is given by:

$$V_{IND} = L_{ARM} \dot{I} \quad (9)$$

where  $L_{ARM}$  is the inductance of the armature. For our system  $L_{ARM} = 1.5$  nH, and the measured input current in kiloamps for the ARL gun is approximated by:

$$I = 189 (\exp(-0.5 t_m) - \exp(-13 t_m)) \quad (10)$$

where  $t_m$  is the time measured in milliseconds. As determined from experiment, the peak value of current,  $I_p$ , is 160 kA, which occurs at  $t_m = 0.26$  ms.

Using the experimental current waveforms of Eq. (10) in Eq. (9) we obtain the resulting predicted peak voltage is 1.5 V. As observed experimentally, this contribution is dominant in the early time region which corresponds to the characteristics of  $\dot{I}$ .

Another voltage contribution to muzzle voltage is attributed to the ohmic losses associated with the surface on the back of the armature. The electric field on the back face of the armature is given by [8]:

$$E_{ARM}(t) = \sqrt{\frac{\mu_o}{\pi \sigma_{ARM}}} \int_0^t \frac{1}{\sqrt{t-\tau}} \dot{H}_{ARM}(\tau) d\tau \quad (11)$$

where  $\sigma_{ARM}$  is the conductivity on the back of the armature and  $\dot{H}_{ARM}(\tau)$  is the time derivative of the magnetic field intensity on the back face of the armature. Since  $H_{ARM}(\tau) = I(\tau)/h$ , the voltage  $V_{RES} = wE_{ARM}$  is given by:

$$V_{RES} = \left(\frac{w}{h}\right) \sqrt{\frac{\mu_o}{\pi \sigma_{ARM}}} \int_0^t \frac{1}{\sqrt{t-\tau}} \dot{I}_{ARM}(\tau) d\tau \quad (12)$$

The solid line on Fig. 2 shows  $V_{RES}(t)$  using  $\sigma_{ARM} = 3.7 \times 10^7$  mhos/m for aluminum at room temperature. This conductivity value may underestimate the voltage due to ohmic losses for several reasons. First, it is noted that the bulk conductivity for aluminum used in the calculation may be too high. The armature used in the experiment is not pure aluminum, and contamination of the surface may reduce the conductivity by the factor of 2 or higher. In addition to the surface ohmic contribution and the contact resistive losses must also be accounted for.

For mathematical convenience, the surface and contact loss terms are combined from now on into an "effective" surface conductivity denoted by  $\sigma_{ARM}^*$ , and use this to compute new  $V_{RES}$  from Eq. (12). The dotted line in Fig. 2 shows the result for  $\sigma_{ARM}^* = 0.5 \times 10^7$  mhos/m. This particular value of  $\sigma_{ARM}^*$  was chosen to provide a good comparison to an empirical result for the armature resistance deduced earlier [15]. Using Eq. (12) with  $\sigma_{ARM} = \sigma_{ARM}^* = 0.5 \times 10^7$  mhos/m, one can deduce an empirical resistance given by:

$$R_{RES} = V_{RES}^*(t) / I(t) \quad (13)$$

where  $V_{RES}^*$  is the time dependent voltage obtained using  $\sigma_{ARM}^*$ .  $R_{RES}(t)$ , compares well ( $\pm 20\%$ ) with earlier experimental investigations [14].

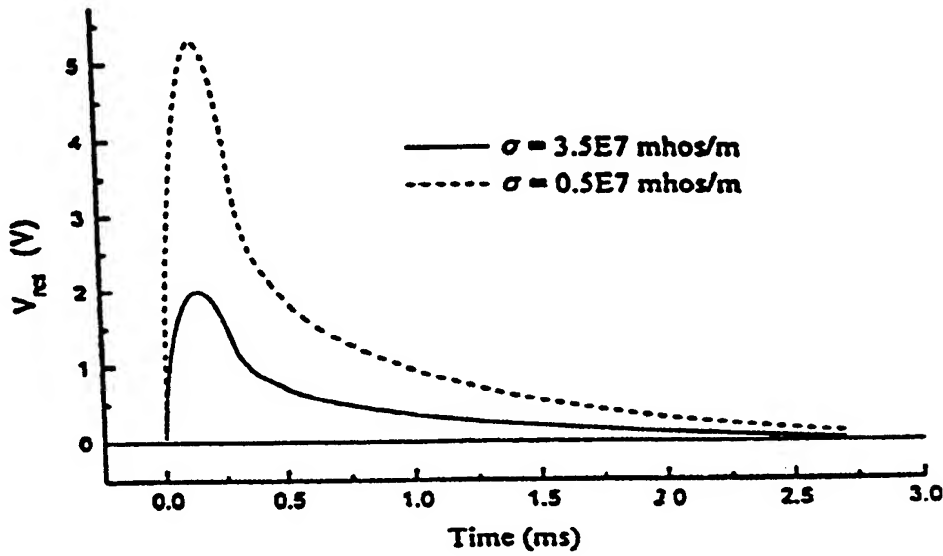


Fig. 2. Bulk and contact armature resistance contribution to armature voltage.

The counter *emf* contribution,  $V_{EMF}$ , is determined from the energy balance responsible for the acceleration of the armature. The force on the armature is given by:

$$F_A = \frac{1}{2} E_o L'_R I^2 \quad (14)$$

where  $L'_R$  is the theoretical inductance gradient of the rails and  $E_o$  is the electromagnetic efficiency factor. The electrical power supplied to the armature,  $V_{EMF} I$ , must equal the mechanical power, which is the force,  $F_A$ , times the velocity, this gives:

$$V_{EMF} = [(1/2) E_o L'_R \dot{Z}_A] I = R_{EMF} I \quad (15)$$

where

$$R_{EMF} = (1/2) E_o L'_R \dot{Z}_A \quad (16)$$

From Eqs. (15) and (16) it is evident that the counter *emf* can be associated with a time dependent resistance that is proportional to the armature's velocity,  $\dot{Z}_A(t)$ . During the latter stages of armature motion the velocity is essentially constant, thus leading to a time independent resistance which is, indeed, the dominant contribution to the muzzle voltage [8].

As observed from Eq. (16),  $R_{EMF}$  is proportional to  $E_o$ , and therefore provides an experimental determination of the electromagnetic efficiency provided that the factors contributing to muzzle voltage can be isolated.



#### 4. COMPARISON WITH EXPERIMENT

In the experiments modeled in this work a basic railgun, 1 meter long, was used. The rails were copper, with the following dimensions: height,  $h = 19$  mm, thickness,  $\Delta = 10$  mm, and rail separation distance,  $w = 15$  mm. The aluminum armature is roughly 25 mm in length. Fig. 3 shows the total muzzle voltage contribution for different components described in the previous section. As noted earlier, there is an uncertainty in the value of the conductivity associated with the back face of the armature. Thus, two curves are presented for muzzle voltage in Fig. 3. One used the room temperature conductivity of pure aluminum,  $\sigma_{ARM} = 3.5 \times 10^7$  mhos/m, and excluded the contact resistance, which results in underestimating the measured value in the early time. The other curve used a conductivity of  $\sigma_{ARM} = 0.5 \times 10^7$  mhos/m to account for both contact and armature resistance, which gives a better comparison to the measured value [8]. In both cases, the wave shape of the predicted muzzle voltage is consistent with measured value. Notice that only the temperature independent conductivity was used to compute the muzzle voltage, which results in some discrepancies in comparison to the measured value.

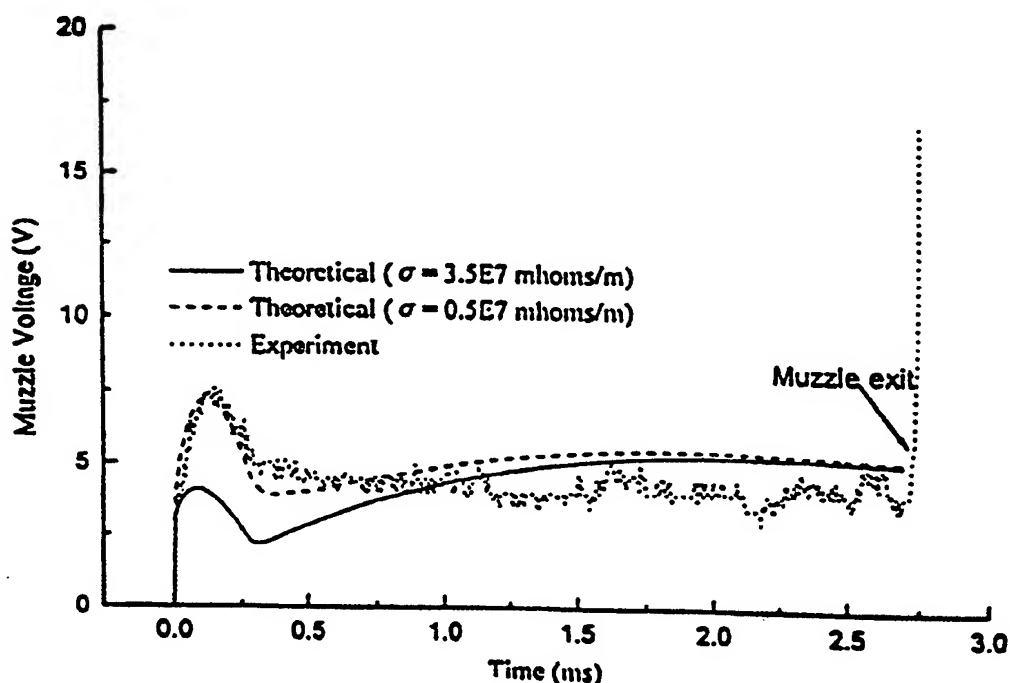


Fig. 3. Muzzle Voltage for Different Armature's Values

#### 5. CONCLUSIONS

The results of the study [8], summarized in this work, have shown several approaches to addressing potential outstanding issues in Electromagnetic gun and tube propulsion. Especially interesting is that of overall efficiency of the system, subject of course to substantial experimental validation at scale. These include:

1. Defining the space-time current distribution on all relevant surfaces
2. Evaluating the current distribution on all the surfaces for a variety of pulse shapes.

3. Determining (from the current) the magnetic field energy surrounding the system., the electromagnetic efficiency, the electrical efficiency, and the muzzle voltage.

## 6. REFERENCES

- [1] I. Kohlberg and W.O. Coburn, "A Solution for the Three Dimensional Rail Gun Current Distribution and Electromagnetic Fields of a Rail Launcher", *IEEE Trans. Magnetics*, Vol. 30, No. 1, January 1995.
- [2] I. Kohlberg, "Prediction of Electromagnetic Fields Generated by Rail Guns", Kohlberg Associates, Inc., Final Report to Army Research Laboratory, Prime Contract: DAAL03-91-C-0034, Subcontract No. 93419 from Battelle, Report ARL-CR-148, September 1995.
- [3] J.P. Barber and Y. Dreizin, "On the Origins of Muzzle Voltage in Railguns", Presented at the 11th Meeting of the Electric Launcher Association, Huntington, WV, September 1993.
- [4] J.P. Barber and Y. Dreizin, "On the Origins of Muzzle Voltage", *IEEE Trans. Magnetics*, Vol. 30, No. 1, January 1995.
- [5] I. Kohlberg and W.O. Coburn, "Theoretical and Experimental Investigations of Electromagnetic Fields Generated by Rail Guns," Proc. of the 12th International Wroclaw Symposium on Electromagnetic Compatibility, Wroclaw, Poland, June 18-July 1, 1994.
- [6] I. Kohlberg, et.al., "Modeling Magnetic Fields Produced by Railguns Using Principles of Conformal Mapping in Combination with Numerical Electromagnetic Techniques," Proc. of the Fifth European Symposium on Electromagnetic Launch Technology, Toulouse, France, 10-14 April, 1995.
- [7] W. Williams, et.al., "Experimental and Theoretical Analysis of Electromagnetic Fields Near a Series Augmented Railgun", Proc. of the Fifth European Symposium on Electromagnetic Launch Technology, Toulouse, France, 10-14 April, 1995.
- [8] I. Kohlberg, C. Le, and W.J. Sarjeant, "Related Theoretical and Experimental Investigations of Muzzle Voltage and Surface Current Issues of Railguns: Initial Assessment," ARL Technical Report, in press.
- [9] Moon and Spencer, Field Theory Handbook, Springer, 1961.
- [10] F. Assadourian and F. Rimai, "Simplified Theory of Microstrip Transmission Systems," Proc. IRE, 40: 1651 (1952).
- [11] ELCUT Finite Element Analysis System, TOR Cooperative Enterprise, St. Petersburg, Russia.
- [12] G.J. Burke and A.J. Poggio, "Numerical Electromagnetics Code (NEC)--Method of Moments," Lawrence Livermore National Laboratory, Report UCID-18834, January 1981.
- [13] C.E. Baum, D.V. Giri, and R.D. Gonzalez, "Electromagnetic Field Distribution of the TEM Mode in a Symmetrical Two-Parallel-Plate Transmission Line", AFWL Sensor and Simulation Note No. 29, April 1976.
- [14] B.L. Mass, J.P. Barger, and D.P. Bauer, "In-Bore Armature Contact Voltage Measurement," *IEEE Trans. Magnetics*, Vol. 25, No. 1, pp. 353-356, January 1989.

# MODEL AND NUMERICAL SIMULATION OF LIGHTWEIGHT PROJECTILES ACCELERATION PROCESS IN ELECTROTHERMAL LAUNCHERS WITH ABLATIVE AND NON-ABLATIVE BARRELS

David Zoler  
School of Physics and Astronomy, Tel-Aviv  
University, Tel-Aviv 69978, Israel.  
E-mail: davidz@halo.tau.ac.il)

## Abstract

Modeling and numerical simulation of lightweight projectile acceleration process in electrothermal launchers with ablative and non-ablative barrels have been carried out. The main goal was to evaluate the possibility to optimize the electrothermal launcher work by suitable changes of "external" process variables as: the input energy or device geometry and, at the same time, to describe the plasma parameters spatial dependence and temporal evolution. In the frame of the proposed model we used the SESAME equations of state, an expression for the plasma resistivity which takes into consideration the electron-neutrals collisions and the friction between the projectile and the barrel. To obtain the numerical results we used a coordinate change which allows to use a fixed mesh in order to describe the processes in a variable physical domain.

## 1 INTRODUCTION

The growing interest for the study and development of electrothermal launchers is mainly due to their potential to accelerate small projectiles to hypervelocities. Due to this capability the electrothermal launcher can be used, for example, as a small caliber gun, to simulate the micro-meteoroid and space debris impacts [1], hopefully as a frozen pellet accelerator [2,3] as well as in plasma manufacturing processes as a powder particle accelerator [4,5]. The electrothermal launcher usually contains two sections. The first one, the discharge capillary, is a thin tube (capillary) in which a high density warm plasma (1-5 eV) is produced by a high power ablative electrical discharge [1-9]. This plasma can be used as a propulsion agent for projectiles acceleration along a barrel (or "accelerating channel" [10]). The barrel, can be non-ablative or, as proposed in [5,8], an ablative one. In the last case it is built from the same material as the discharge section, and represents (see Fig.1) the second section of the electrothermal launcher. Another possibility is to use plasma in order to heat and vaporize a so called "working fluid" [11,12]. In such a case the plasma-working fluid mixture, with a higher density and lower temperature, will be the accelerating agent. In some respect the use of an ablative barrel leads to the same result because, as the plasma flows through the barrel, its density increases as a result of continuous

ablation and the temperature goes down [5,8]. It is expected [1,5,8,13,14] that the geometry of the capillary+barrel system as well as the input energy have a strong effect on the electrothermal launcher performance. In fact, a specific change of one

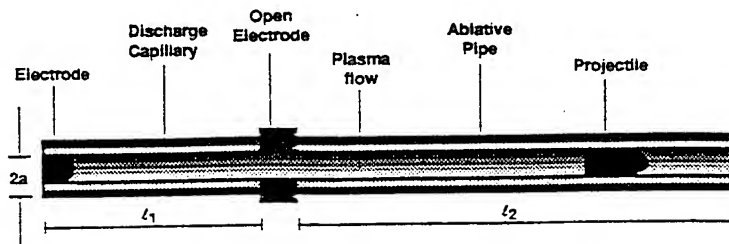


Fig. 1

of these parameters, which we can call "first order external" process variables, leads to changes of the thermodynamic and hydrodynamic characteristics of the plasma which we will call "internal" process variables and, finally, to changes of the "second order external" process variables. In this last category enter (depending on the purpose) parameters, such as the projectile velocity or powder particles temperature and velocity. It is also clear that, in order to optimize the electrothermal launcher yield, we need to know as well as possible the relationship between these variables. Such a knowledge should be helpful for an optimum design of the device for specific purposes. At this point, if we recall that due to the specific features of the electrical ablative discharges, only a limited number of parameters (especially the electrical ones) can be measured with an acceptable degree of precision, the need for consistent models able to describe the above mentioned relationship becomes obvious [8,12,15,16]. In the present work we used a one-dimensional model for the plasma evolution and projectile acceleration in an electrothermal launcher when the discharge section (the ablative capillary) is built from polyethylene and the barrel (the "accelerating channel") can be ablative (also from polyethylene) or non-ablative. In Sec.2 we present the model equations, in Sec.3 the computational results will be analysed and, in Sec.4 the main conclusions will be summarized.

## 2 MODEL EQUATIONS

To describe the plasma evolution and projectile acceleration in an electrothermal launcher we will use the one-dimensional system of equations for the time-dependent plasma flow in an ablative capillary discharge as given in [18]. To save space, we write directly the dimensionless form of the equations we obtained after performing the coordinate transformation [17] which allows the use of a fixed mesh in the numerical

calculations for the description of an expanding physical domain.

$$\frac{\partial \tilde{\rho}}{\partial \tau} = -\frac{1}{\tilde{z}_p} \left( \tilde{\rho} \frac{\partial \tilde{v}}{\partial y} - \tilde{v} \frac{\partial \tilde{\rho}}{\partial y} - \tilde{z}_p y \frac{\partial \tilde{\rho}}{\partial y} \right) \quad (1)$$

$$\frac{\partial \tilde{v}}{\partial \tau} = -\frac{1}{\tilde{z}_p} \left[ \tilde{v} \frac{\partial \tilde{v}}{\partial y} + \frac{1}{\gamma \tilde{\rho}} \left( \frac{\partial \tilde{p}}{\partial \tilde{\rho}} \frac{\partial \tilde{\rho}}{\partial y} + \frac{\partial \tilde{p}}{\partial \tilde{T}} \frac{\partial \tilde{T}}{\partial y} \right) \right] - \tilde{z}_p y \frac{\partial \tilde{v}}{\partial y} + (\alpha_{\eta_1} + L_\rho) \frac{\tilde{v}}{\tilde{\rho}} \quad (2)$$

$$\begin{aligned} \frac{\partial \tilde{T}}{\partial y} = & -\frac{1}{\tilde{z}_p} \left( \tilde{v} \frac{\partial \tilde{T}}{\partial y} - \tilde{z}_p y \frac{\partial \tilde{T}}{\partial y} \right) + \left\{ \frac{g}{\tilde{z}_p} \frac{\tilde{p}}{\tilde{\rho}} \frac{\partial \tilde{v}}{\partial y} - \frac{\partial \tilde{\varepsilon}}{\partial \tilde{\rho}} \left( L_\rho - \frac{\tilde{\rho}}{\tilde{z}_p} \frac{\partial \tilde{v}}{\partial y} \right) - \frac{L_\rho}{\tilde{\rho}} \left( \tilde{\varepsilon} - \frac{1}{2} \gamma g \tilde{v}^2 \right) + \right. \\ & \left. \frac{1}{\tilde{z}_p^2} \left[ \frac{\partial}{\partial y} \left( \alpha_c \frac{\tilde{T}^{5/2}}{Z} \frac{\partial \tilde{T}}{\partial y} + \alpha_r \frac{\tilde{T}^{13/2}}{Z(1+Z)} \frac{1}{\tilde{\rho}^2} \frac{\partial \tilde{T}}{\partial y} \right) + \alpha_{\eta_2} \tilde{v}^2 \right] + \Omega_{II} \frac{\beta}{\tilde{\rho} \tilde{T}^{3/2}} \right\} / \frac{\partial \tilde{\varepsilon}}{\partial \tilde{T}}. \quad (3) \end{aligned}$$

All the steps we took in order to obtain the system of equations (1)-(3) for the main plasma parameters: the density  $\tilde{\rho}$ , the velocity  $\tilde{v}$  and the temperature  $\tilde{T}$  as well as the expressions for the dimensionless coefficients can be found in [18]. Other quantities in (1)-(3) are:  $\tilde{p}$  - the dimensionless plasma pressure,  $\tilde{\varepsilon}$  - the internal energy,  $Z$  - the ionization degree,  $\gamma = 1.4$ ,  $g = 0.4$ ,  $\alpha_{\eta_1}$  and  $\alpha_{\eta_2}$  are dimensionless coefficients connected to plasma viscosity,  $\alpha_c$  is connected to the plasma thermal conductivity and  $\alpha_r$  to the radiative transfer of energy for which we considered that the diffusive approximation [19] is correct.  $\tilde{z}_p$  and  $\dot{\tilde{z}}_p$  are respectively the projectile instantaneous position and velocity.  $L_\rho$  is the dimensionless rate of ablation,  $\tau$  and  $y$  are the dimensionless time and the axial coordinate. To calculate the projectile velocity and position we use Newton's law as given in [15] which includes a frictional force between the projectile and the device walls as proposed in [15,20]. The reference values used to obtain the (1)-(3) form of the problem equations are the following ones:

$$\begin{aligned} t_0 &= 12.25 \mu\text{sec}; & l_0 &= 0.18\text{m}; & v_0 &= 1.47 \cdot 10^{-4} \text{m/sec}; & \rho_0 &= 1.3 \text{kg/m}^3; \\ T_0 &= 4.664 \cdot 10^4 \text{K}; & P_0 &= 209 \text{MPa}; & \varepsilon_0 &= 368 \text{MJ/kg}; & I_0 &= 80 \text{kA}. \end{aligned}$$

As in other previous papers we take the electrical current flowing through the plasma as an input parameter. The main dimensionless coefficients which appear in (1)-(3) have the following expressions:

$$\begin{aligned} \alpha_A &= 2.5/R; & \alpha_{\eta_1} &= 3.63 \cdot 10^{-6} / R; & \alpha_c &= 2.94 \cdot 10^{-6}; \\ \alpha_r &= 3.66 \cdot 10^{-4}; & \alpha_{\eta_2} &= 3.68 \cdot 10^{-4} / R; & \Omega_{II} &= 1.95 \cdot 10^{-2} \tilde{I}^2 / R^4. \end{aligned}$$

with  $R$  the device radius given in *cm* and  $\tilde{I} = I_{max}/I_0 \cdot \sin(0.154 \cdot \tau)$  ( $I_{max}$  being the maximum value of the electrical current flowing through the plasma.  $\alpha_A$  enters in the ablation rate expression [18]).

### 3 RESULTS AND DISCUSSION

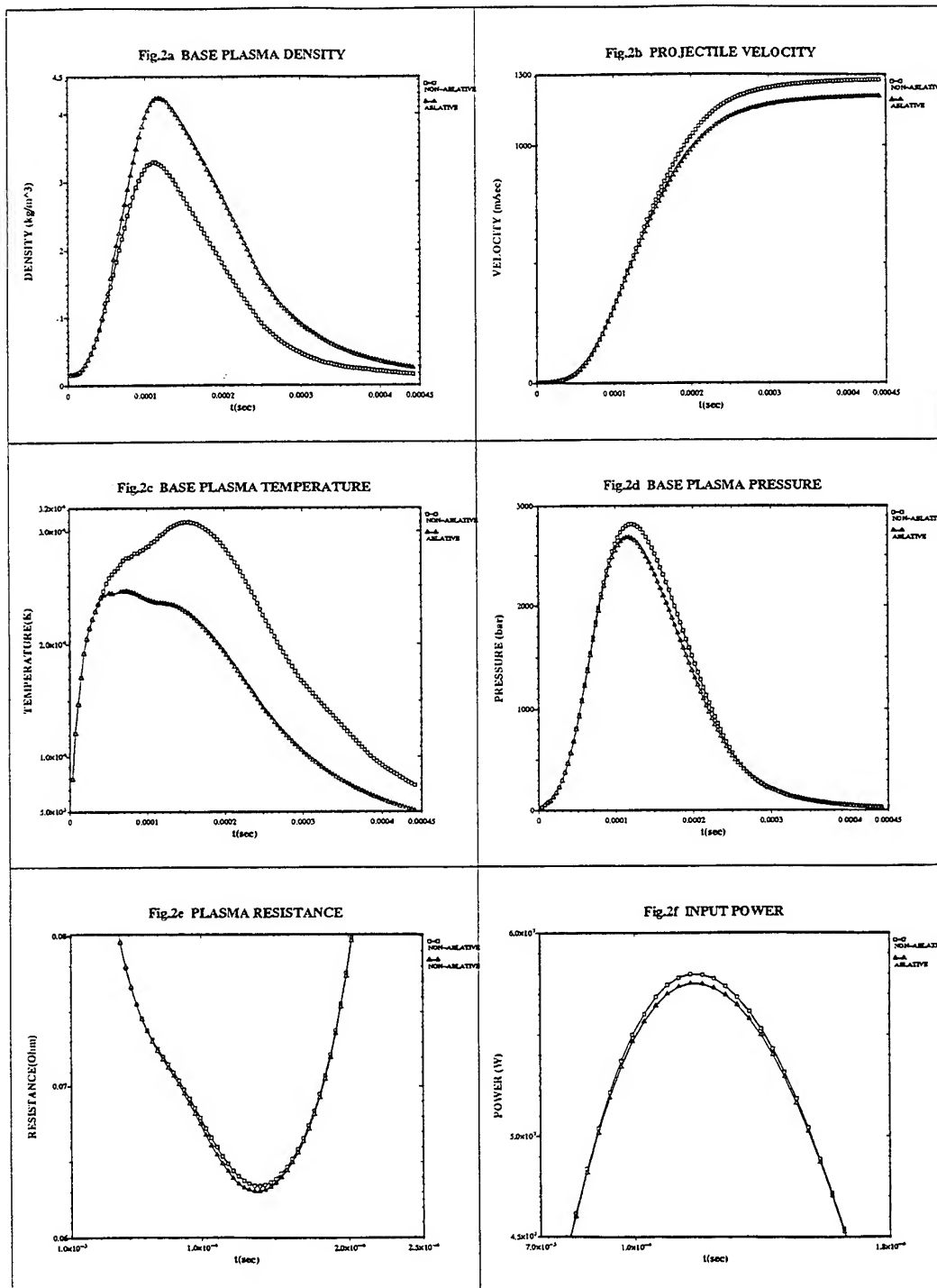
An extensive study concerning the effect of the device geometry and input energy on the plasma electrical, hydrodynamic and thermodynamic characteristics as well as on the projectile acceleration process has been done. Due to space limitations, we present here only a part of the results namely: 1) the effect of the input energy on the plasma parameters and projectile kinetics for a fixed device geometry and 2) we compare the same parameters when different types of barrels (ablative and non-ablative) are used for a fixed geometry and an electrical current.

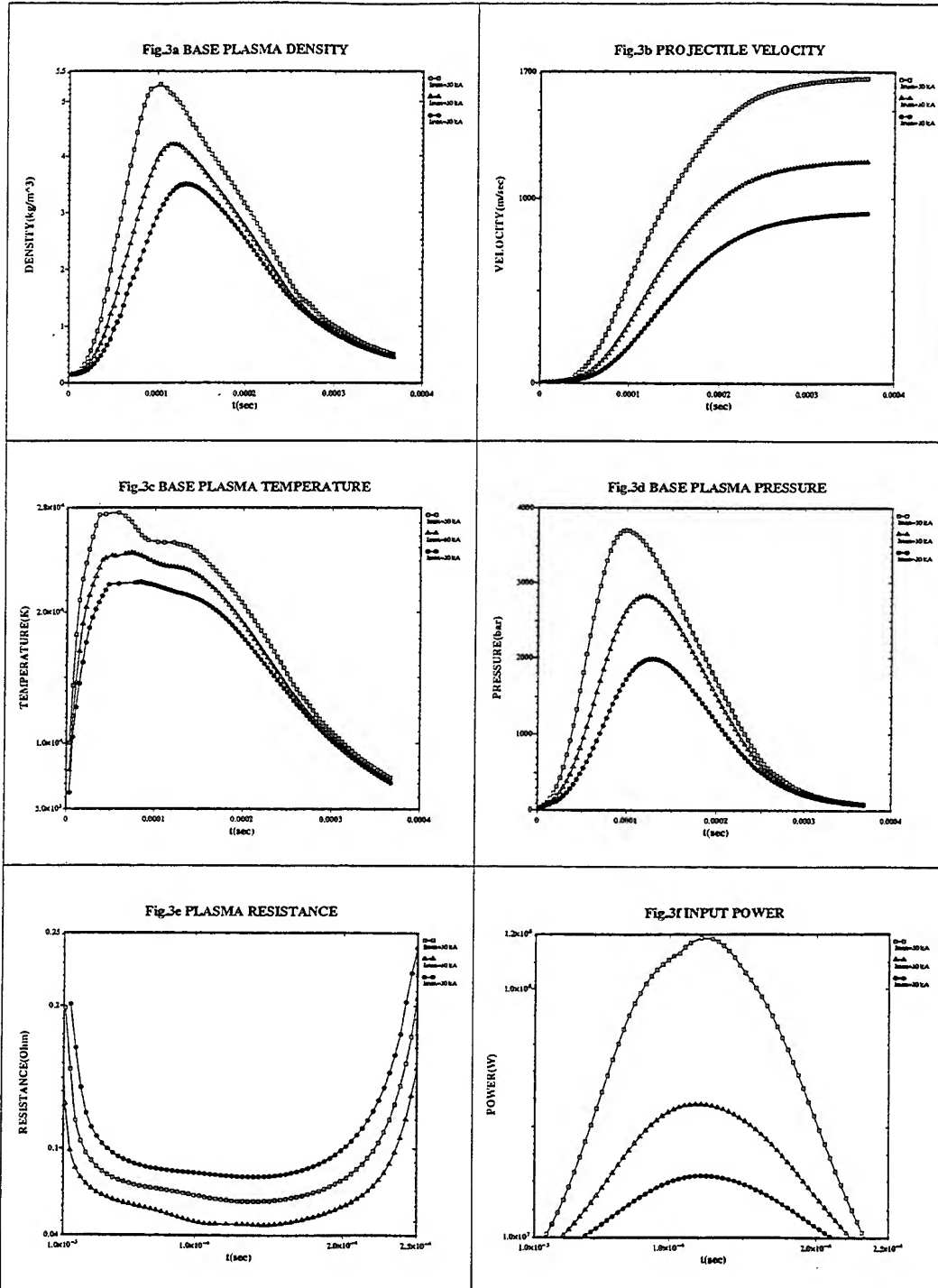
#### 3.1 Problem Presentation

In all the calculations we have done, the discharge section length (Fig.1) was taken  $l_1 = 6.09\text{cm}$ . Also, for the results we will present here, both sections have the same diameter  $D = 6.25\text{mm}$ . We consider sinusoidal electrical pulses, all of them  $250\mu\text{sec}$  long with three different maximum values of the electrical current flowing through the plasma namely,  $I_{max} = 20, 30$  and  $50\text{kA}$ . The projectile mass is  $m = 1\text{g}$ .

#### 3.2 Computational Results Analysis

The results that we will discuss further are presented in Figs.2a- 3f and Table I. In Figs.2a-2f we compare the main plasma electrical, thermodynamic and hydrodynamic characteristics at the projectile base for a non-ablative barrel (squares) and an ablative one (triangles) for a fixed device geometry and an electrical pulse with  $I_{max} = 30\text{ kA}$ . In Figs.3a-3f we plot the temporal behavior of the same parameters for a fixed geometry and three different maximum values of the electrical current flowing through the plasma. In Table I we provide numerical values for a number of parameters, as the projectile velocity at  $t = 250\mu\text{sec}(v_e)$ , the projectile position at the same moment ( $z_e$ ), the projectile velocity at  $t = 370\mu\text{sec}(v_f)$ , the total input energy ( $W_t$ ) and the device efficiency ( $\eta$ ) calculated as the ratio between the projectile maximal kinetic energy and the total input energy. From Figs.2e and 2f we can see that the type of barrel we use (ablative or non-ablative) does not affect significantly the electrical processes inside the first section of the device (the capillary). These results agree well with those reported in [9] concerning the effect of a working fluid on the plasma inside the capillary. Our calculations have shown that the same is true for the plasma density, velocity, temperature and pressure, which reach practically the same values in both considered cases. The value of the pressure at the projectile base (Fig.2d) is somehow larger in the case of a non-ablative barrel (the maximum difference being about  $137\text{bar}$ ). This leads to a larger projectile velocity (by about  $70\text{m/sec}$  at  $t = 370\mu\text{sec}$ ). The main differences appear in the behavior of the plasma density and temperature inside the barrel. From Figs.2a and 2b, in which the time dependence of these parameters at the projectile base is presented, one can see that in the case of an ablative barrel the temperature is significantly lower, while the







density is larger than in the case of a non-ablative barrel. This result agrees with those reported in [5,8] for plasma steady state flow in a capillary-ablative pipe system. The much lower temperatures reached while using ablative barrels is a positive result if one considers the use of this kind of device as a frozen accelerator [2,3] or for plasma manufacturing processes [4,5]. Now, the data presented in Figs.3a-3f show that the rate of input energy value strongly affects all the flow picture in both device sections. For the three studied cases the plasma resistance is practically constant during almost the whole electrical pulse duration, in agreement with some previously reported results [1,9]. As expected the plasma thermodynamic characteristics (Figs.3a-3c,3d) and the projectile velocity (Fig.3b) are strongly dependent on the rate of energy input. The most affected parameters are the plasma density,

Table I

| $I_{max}(kA)$ | $v_e(m/sec)$ | $z_e(m)$ | $v_f(m/sec)$ | $W_t(kJ)$ | $\eta(\%)$ |
|---------------|--------------|----------|--------------|-----------|------------|
| 20            | 836          | 0.15     | 910          | 4.33      | 19.1       |
| 30            | 1119         | 0.20     | 1196         | 7.82      | 18.3       |
| 50            | 1572         | 0.25     | 1664         | 15.54     | 17.8       |

pressure and projectile velocity. From Fig.3b results that most of the projectile velocity increase occurs while there is an energy input. After the impulse ends, the rate of velocity increase is very low. This fact points, for example, to the possibility to predict, using the present model, the optimum length of the acceleration channel required to reach a specific projectile velocity. To the same conclusion lead also the data presented in Table I. The device efficiency  $\eta$  (Table I) is under 20% for all the analyzed cases, and depends slightly on the rate of energy input.

## 4 CONCLUSIONS

The one-dimensional model used in the present study allows us to follow the evolution of physical processes in an electrothermal launcher. It is able to give a detailed picture of the temporal and spatial (not presented here) dependence of all the important plasma and projectile parameters. As a consequence, we have the possibility to study the effect of the type of barrel, energy input or device geometry changes on the above mentioned parameters. In other words, we can obtain useful indications for the device design and optimization, in order to reach a specific goal. The results presented in this work show that the type of barrel, (ablative or non-ablative) practically does not affect the processes inside the capillary, and very slightly affects the projectile acceleration process. Only the plasma temperature and density inside the barrel are effectively influenced. This situation is quite different in what concerns the energy input. A change of the energy input rate leads to changes of all the process parameters in both sections of the device. Some of the results we presented here agree qualitatively with some previously reported data.

## References

- [1] Rott,M., *IEEE Trans. on Magnetics* **29**,1,597-602 (1993)
- [2] Bourham, M.A. et al, *IEEE Trans. on Plasma Science* **17**,386 (1989)
- [3] Kincaid, R.V. and Bourham, M.A., *Fusion Technology***26**,11,236 (1994)
- [4] Shcolnikov E.Ya. et al, *IEEE Trans. on Magnetics***31**,758-762 (1994).
- [5] Zoler,D.,Kaplan,Z. and Ashkenazy,J., *Plasma Sources Sci. Technol.*, **5**,588-601 (1996)
- [6] Zoler,D. and Cuperman, S., *J. Plasma Phys.*,**48**,215-227 (1992).
- [7] Powell,J.D. and Zielinski,A.E., *IEEE Trans. on Magnetics*,**29**,591- 596 (1993).
- [8] Cuperman,S.,Zoler,D. and Ashkenazy,J., *Plasma Sources Sci. Technol.***3**,593-601 (1994).
- [9] Vernon,L., Noiret,P. and Roux,S., *IEEE Trans. on Magnetics*,**31**,1, 452-456 (1995).
- [10] Kadyrov,V. et al, "Calculation of the Limiting Parameters for Oxide Ceramic Particles During HVOF Spraying", *Proceedins of the 7th National Thermal Spray Conference 20-24 June 1994,Boston, Massachusetts.*
- [11] Arensburg,A. and Wald,S., *J.Appl.Phys.*, **75**,5,2145-2154 (1993).
- [12] Hensel,D.,Daree,K. and Silvestre,N., *IEEE Trans. on Magnetics*,**31**, 1,414-418 (1995)
- [13] Benson,D.A. and Kempka,S.N., *IEEE Trans on Magnetics*,**29**,1,544- 549 (1993).
- [14] Zimmermann,K. et al "Experimental and Theoretical Investigation of a 12mm Electrothermal Accelerator", *Proceedings of the 2nd European Symposium on EML Technology (1989).*
- [15] Kincaid,R.V. et al, "Projectile Acceleration and Plasma Flow in the Electrothermal Plasma Gun SIRENS" , *8th EML Symposium on Electromagnetic Launch Technology,Baltimore, Maryland, April 21-24 (1996).*
- [16] Silvestre,N., Hensel,D.and Daree,K., *IEEE Trans. on Magnetics*,**31**, 1,603-607 (1993).
- [17] Sheu,T.W. and Lee,S.M., *Numerical Heat Transfer*,Part A,**27**,395-415 (1995).
- [18] Zoler,D. and Alimi,R., *J.Phys. D:Appl.Phys.***28**,8,1141-1152 (1995).
- [19] Zeldovich,Ya.B. and Raiser,Yu.P., "*Physics of Shock Waves and High Temperature Hydrodynamic Phenomena*" vol.**I**,Academic Press, N.Y. 1963.
- [20] Aigner,S. and Igenberg,E., *IEEE Trans. on Magnetics*,**25**,1,33-39 (1989).

# Method of Analysis of Propelling Gas in Electrothermal Launcher

A.M. Voronov, Th. G.G. H. Weise

TZN Forschungs- und Entwicklungs Zentrum Unterlues,   
Neuesothrieter Str., 20, 29345, Unterlues,   
Federal Republic of Germany

## Summary

A detailed study of the physical processes of pulsed high-pressure, heavy-current arcs is appropriate in view of the technological progress in the application of electrothermal launchers. The results of a Fourier analysis of pressure in the electrothermal launcher are presented. The propelling gas was evolved from an organic substance. The spectral analysis of pressure curves showed the presence of radial acoustic waves in the propelling gas in the discharge chamber. These acoustic waves are revealed in a Fourier spectrum by some frequencies that shift in the measured time. The shift of the frequency is defined as given through the input of electrical energy into the discharge. The sound velocity in the propelling gas was determined according

to the frequency of the radial acoustic waves.

## Introduction

Intensive development and investigation of electrothermal (ET) and electrothermal-chemical (ETC) guns is warranted by the promising results<sup>1</sup> of these guns. By using light gases as the propelling gas projectile velocities in excess of 2300 m/s at efficiency of about 20-25 % have been achieved. Use of pure light gas, e.g., hydrogen, poses technical problems in connection with hydrogen storage. Currently, as a source of light gas some organic substances, e.g., methanol are used. During the firing methanol is evaporated in the gas phase and dissociated into various byproducts, e.g., CO, CO<sub>2</sub>, H<sub>2</sub>O, CH<sub>4</sub>. As a result, a

complex composition of the propelling gas in ET and ETC guns is formed. Usually, a thermodynamic equilibrium calculation for the propelling gas composition is used. It provides the information about an adiabatic coefficient, sound velocity and so on.

The further development and optimization of ETC guns requires detailed understanding of the physical processes in plasma, filling the discharge chamber and the barrel. The present paper describes an experimental method for the propelling gas analysis. The method is based on a Fourier analysis of the pressure waveforms.

### Experimental results

The results of a typical shot of the ET gun are presented. Initially, the discharge chamber is filled with methanol. The input of the electrical energy from a capacitor bank provides evaporation and atomization of the methanol. The discharge chamber of the ET gun has the following specifications:

- $V_o = 6.5 \times 10^{-3} \text{ m}^3$  - volume of the discharge chamber;
- $R = 7 \times 10^{-2} \text{ m}$  - radius of the discharge chamber.

The discharge is initiated by the wire exploding. An ignition wire is placed along the axis of the discharge chamber. The current and voltage waveforms during the shot are shown in figures 1 and 2.

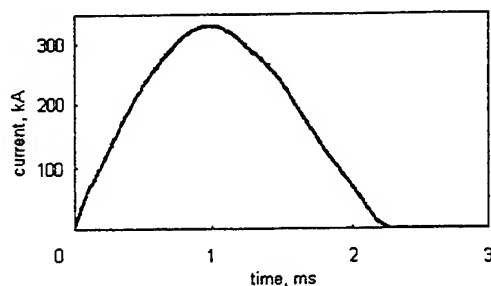


Fig. 1 Current waveform

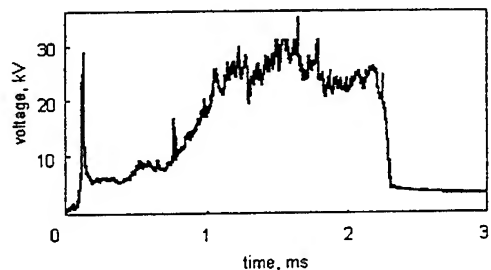


Fig.2 Voltage waveform

The pressure is measured by two Kistler gauges at two points of the chamber (see fig. 3). One is positioned in the end plug and is insulated from the body of the chamber. The second is in the top port of chamber and is directly connected to the chamber.

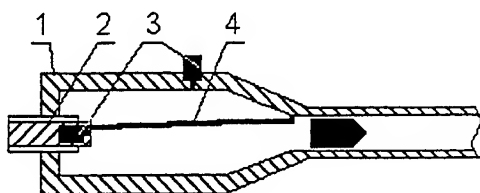


Fig.3 Discharge chamber of ET gun.

1 - body of chamber; 2 - central electrode;  
3 -- pressure gauges; 4 -- initiation wire.

The results of the measurements are shown on figures 4 and 5. The pressure gauge on the wall recorded significantly more oscillations in comparison with the electrode gauge put in the electrode.

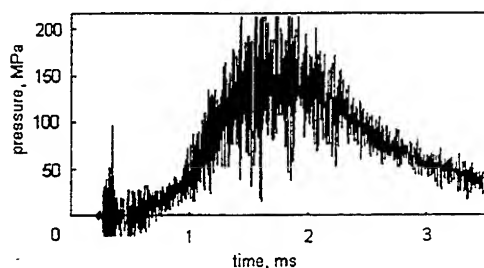


Fig.4 Pressure measured at the wall of the chamber

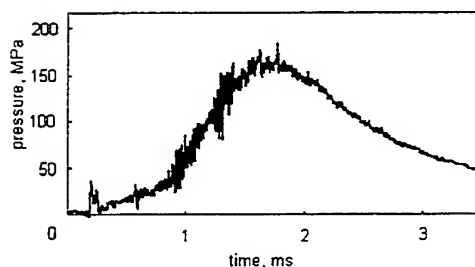


Fig.5 Pressure measured at the electrode.

Fourier spectra of these pressure waveforms in the range of 0 -- 200 kHz are shown in fig. 6 and 7 respectively.

The Fourier spectrum of the pressure measured on the wall shows three maxima: around 20 -- 40 kHz, 90 -- 100 kHz and 160 -- 180 kHz. Two of them are revealed in the Fourier spectrum of pressure measured at the electrode: at 20 -- 40 kHz and 160 -- 180 kHz.

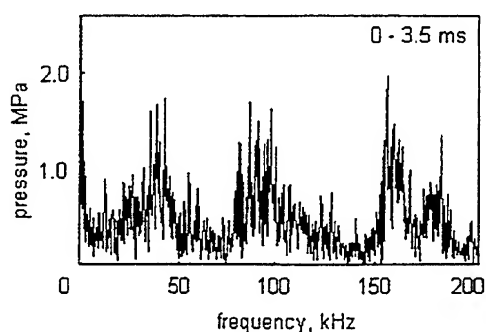


Fig. 6 Fourier spectrum of pressure measured at the wall

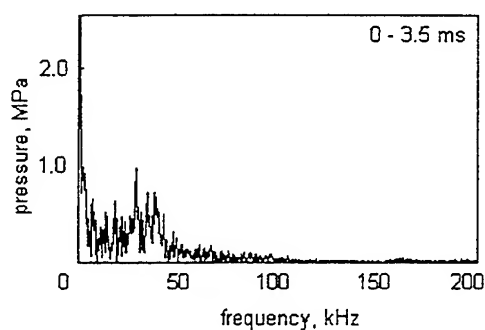


Fig. 7 Fourier spectrum of pressure measured at the electrode

## Discussion

The maximum in the Fourier spectrum at 160 -- 180 kHz is caused by the resonance frequency of a piezoelectric gauge. It corresponds to the data of the gauge manufacturer<sup>2</sup>. The feature between 90 – 100 kHz is revealed only in the pressure measured at the wall of the discharge chamber. Most likely, it is combined with the resonance frequency of a technological cylindrical metal insertion in the discharge chamber. This frequency is not presented on the "electrode" pressure curve because of an acoustic insulation of the electrode from the body of chamber. An electrical insulation of the electrode made of a fiberglass reinforced epoxy resin accounts for an acoustic decoupling.

Both Fourier spectra contain peaks within 20 – 40 kHz. The time resolved Fourier analysis shows the drift of this peak (see figure 8). In accordance with the electrical energy input the peak drifts from 20 up to 40 kHz.

These oscillations are caused by radial acoustic waves in the plasma, filling the discharge chamber. It is confirmed by three aspects:

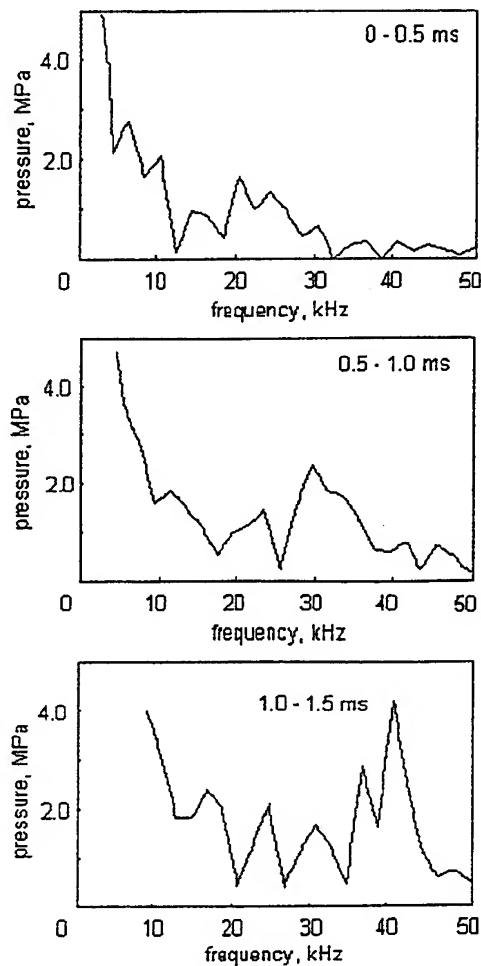


Fig.8 Fourier spectra of pressure for various time intervals.

1. the wire explosion produces the radial acoustic waves<sup>3,4</sup> due to the axial symmetrical position of the wire;
2. the cylindrical symmetry of the discharge chamber causes spreading radial waves;
3. the amplitude of this frequency measured on the wall is significantly

larger than one measured at the electrode.

Based on these oscillations, it is possible to estimate the sound velocity  $U_s$  in the plasma filling the discharge chamber.

$$U_s = R \cdot f \quad \text{Eq. 1}$$

The frequency  $f = 30$  kHz corresponds to a sound velocity  $U_s = 2.1 \times 10^3$  m/s. However, the direct calculation of the plasma temperature  $T$  from the following equation

$$U_s = \sqrt{\frac{\kappa k T}{\mu m_p}} \quad \text{Eq. 2}$$

is not possible since the value of a mean molecular weight of plasma  $\mu$  and an adiabatic coefficient  $\kappa$  are unknown (here:  $k$  – Boltzmann constant,  $m_p$  – mass of proton). The determination of the plasma temperature  $T$  from the equation of state according to the measured pressure value is also incorrect, because the equation of state allows one to find only the mean temperature in the discharge chamber. In fact, the temperature distribution in the chamber

over the radius is strongly inhomogeneous (see fig. 7).

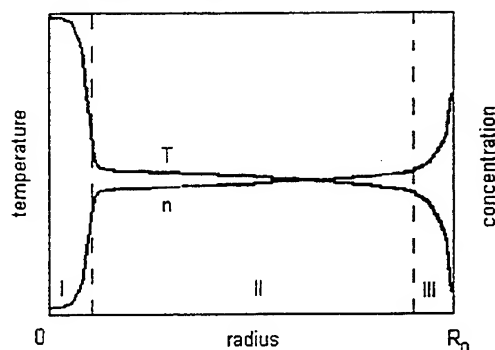


Fig. 9 Qualitative temperature and concentration distribution over the radius.

There are three zones: the first the arc column, the second with relatively high temperature, low density, low mean molecular weight and, respectively, high sound velocity, and the third with low mean temperature, high density, high molecular weight and low sound velocity. This fact can explain such high sound velocity  $U_s = 2.1 \times 10^3$  m/s, calculated from the frequency of radial acoustic waves. The time taken by acoustic oscillations to pass in the chamber is basically defined by the time needed for passing the second zone because the size of that is much bigger than one of the first and the third.

## Conclusions

The complexity of physico-chemical processes in the plasma, technical problems of diagnostics because of extreme plasma parameters make it difficult to investigate ET and ETC guns. Using a new approach in data analysis allows one to get more information about physical mechanisms in the discharge plasma of a ET gun. The Fourier analysis of experimental pressure waveforms provides important plasma specifications, such as the sound velocity that is defined by plasma temperature, mean molecular weight, and an adiabatic coefficient.

## References

---

- <sup>1</sup> T.G.H.H. Weise, P. Noiret. 4th European Symposium on EML Technology, 1993, Paper No 503
- <sup>2</sup> Kistler Instrumente GmbH. Datenblätter. 1994
- <sup>3</sup> A.M. Voronov, et al. 4th European Symposium on EML Technology, 1993, Celle, Paper No 508
- <sup>4</sup> C.R. Spikings, E.Thompson. 4th European Symposium on EML Technology, 1993, Paper No 505



# ETC-TECHNOLOGIES

## CATEGORIES, PHYSICAL PRINCIPLES AND INTERIOR BALLISTIC PERFORMANCES

Th. H.G.G. Weise, H.-K. Haak  
TZN Forschungs- und Entwicklungszentrum Unterlüß GmbH  
Neuensothriether Straße 20  
D-29345 Unterlüß  
Federal Republic of Germany

### Abstract

After having successfully finished the electrothermal gun programme in 1995 ETC-technologies have been investigated at TZN under contract of the German MoD. The goal of the investigations is the demonstration of the technology by introducing an operating 120mm ETC-gun in 1999.

Preliminary studies have been performed in order to identify the potential of ETC-technologies. These studies lead to the classification of ETC-principles with different performance improvements and electrical energy consumptions. Based on these ETC-categories with their different physical principles theoretical and experimental investigations are performed. By theoretical models ETC-relevant combustion laws and form functions are evaluated which have to be realized by new solid propellant designs which are interacting with electrical arcdischarges.

Ignition of modified propellants with high loading densities as well as combustion control by electrothermally supplied energy have to be realized using proper methods of electrical energy input into the charge chamber of the gun. In addition the electrical energy may be used for igniting new chemical processes which lead to a significant decrease of the molecular weight of the propelling gases by the generation of light additives.

The paper gives an overview on the different ETC-categories and their basic physical principles. First predictions on the energy consumption as well as on the expected interior ballistic performance are presented.

### 1 Introduction

The quick progress in the development of armour plating technologies for combat vehicles requires the improvement of the interior ballistic performance of future anti armour gun systems. The already existing gap between required and requested performance is continuously increasing.

The interior ballistic performance of todays accelerating technologies is limited by:

- thermodynamic parameters of propellants
- temperature coefficient of propellants
- combustion behaviour of propellants.

Electrical and electrically supported acceleration technologies promise possible performance upgrades for future tank gun applications.

Until the end of 1995 electrothermal acceleration methods were investigated in Germany. It was the goal to identify new acceleration technologies for barrel weapons to be applied in future defence systems. The investigations have been finished successfully. The acceleration of a 2kg projectile to up to 2.400m/s was demonstrated in a 105mm electrothermal gun which was supplied from a capacitive 30MJ pulsed power supply system. By this result the potential of the

electrothermal technology was shown.

Short and medium term perspectives for the realization of high energy density pulsed power supply technologies to be applied in combat vehicles could not be presented with sufficient risk so far. It was decided to continue the programme with the investigation of ETC-technologies with regard to their reduced electrical energy requirements. First fundamental considerations are given in this paper. The investigations performed within the German ETC-programme at Rheinmetall/TZN have the goal to validate these considerations experimentally.

## 2 Basic Interior Ballistic Principles of ETC-Technologies

In general different measures can be applied for improving the processes in the charge chamber of a gun with the usage of electrical energy. Figure 1 gives an overview on the basic possibilities. The setup of a barrel gun with a KE-projectile is shown schematically. The charge chamber is filled with energetic material i.e. a solid propellant or an alternative propellant from which the propelling gas pressure has to be generated. The input of electrothermally converted energy into the propellant can lead to the realization of the following processes:

- the propellant will be ignited
- the combustion of the propellant will be controlled
- additional chemical processes which are not realizable under normal conditions are ignited
- alternative propellants from which a significantly improved propelling gas can be generated are converted (electrothermal gun).

The basic improvement of electrothermally converted energy in an ETC-setup will be the control of charges with significantly increased energy content. In general this increase can be realized by:

- increase of the loading density by modification of the geometry of a solid propellant
- increase of the explosion heat by using high energetic propellants.

If an alternative inert propellant is used the electrical energy results in its conversion into propelling gas by evaporation processes.

The modification of a solid propellant and its electrothermal combustion control will mainly result in an increase of the muzzle energy of the gun. The magnitude of the muzzle energy increase is directly related to the increase of chemical energy in the charge chamber. Due to the limitation of the thermodynamical parameters of the solid propellant an increase of the muzzle velocity of the gun would result in a decrease of its interior ballistic efficiency. A significant increase of the muzzle velocity requires a modification of the average molecular weight and the specific heat of the propelling gas. Electrothermal guns realize these requirements by the usage of alternative propellants. It seems possible that the propelling gas of ETC-guns can be improved in a similar way by adding Hydrogen atoms or molecules before or during the combustion of the solid propellants.

## 3 Classification of ETC-Technologies

Different combinations of the ETC-mechanism showed in chapter 2 result in a classification of ETC-technologies due to their electrical energy requirements. Figure 2 gives an overview on this classification. The left diagram shows different combinations of ETC-measures plotted versus the electrical energy consumption. The right table gives the interior ballistic influences in general.

ETC-category A uses a conventional charge setup which is ignited by an electrothermal igniter instead of the conventional chemical primer. The electrical energy, 60kJ to 100kJ, is

low. Neither an influence on the muzzle energy nor on the muzzle velocity can be expected. By reducing the jitter of the primary ignition the precision of the gun can be improved.

ETC-category B uses a charge setup with increased loading density. By the electrothermal conversion of energy into this charge the ignition will be realized due to the interior ballistic requirements of the gun. It is expected that pulse duration of the electrothermal energy conversion will be limited to the first phase of the powder combustion. Due to the calibre of the gun (120mm or 140mm) 300kJ up to 600kJ might be sufficient to realize this process. The interior ballistic result will be the increase of muzzle energy due to the increase of the chemical energy in the powder charge.

With ETC-category C the possibility of controlling the temperature coefficient of the powder charge will be opened. This category includes the measures of categories A and B. By the control of the temperature coefficient the gun can be operated with its maximum operating pressure under all temperature conditions. A further increase of the muzzle energy will be the result. The time duration of the electrothermal energy input will be as long as the pressure maximum in the charge chamber is reached. In order to achieve this process the amount of electric energy supplied to the gun is expected to be in between 900kJ and 1.8MJ (due to the calibre of the gun).

ETC-category D gives the most pretentious version with regard to its electrical energy requirements. Including the measures of categories A through C the electrical energy will be supplied during the entire burning phase of the solid propellant. By control of the combustion of the powder the gas pressure curve shall be matched to the maximum operating pressure curve of the gun system which is given by the material properties. In addition to the measures of categories A through C it is the goal to use the electrothermally converted energy for the ignition of chemical reactions between materials of high content of hydrogen, which are added to the solid propellant. The generation of hydrogen during the combustion phase will result in a modification of the thermodynamic and thermochemic parameters of the propelling gases. An increase of the muzzle energy as well as of the muzzle velocity is expected as shown by Knöchel et al. in [1]. The electrical energy requirements are expected to be in between 2.5MJ and 5MJ due to the calibre of the gun.

In order to complete the classification the requirements of an electrothermal gun are shown also in figure 2. It is marked as category E. The electrothermal gun uses an alternative inert propellant, i.e. methanol, which is converted by electrothermally supplied energy via evaporation processes into a propelling gas with very low molecular weight as described in several papers, i.e. Weise et. al. in [2]. Significantly increased muzzle velocities at sufficient gun efficiencies are the results. Due to the inert character of the propellant the energy consumption of the acceleration process has to be converted by the electrical energy entirely. 70MJ until 90MJ per shot have to be supplied into a large calibre gun.

#### **4 Physical Principles and Interior Ballistic Performances**

The ETC-categories are based on different modifications of the charge setups as well as different principles of the electrical energy conversion. In the following the physical principles and its predicted interior ballistic performances are described.

##### **4.1 Electrothermal Ignition of conventional Powder Charges**

Existing large calibre powder guns use chemical primers with ultra fast combustion to ignite the solid propellant in the charge chamber. The ignition of the primer is performed by an electric spark of low energy and power. The jitter of the combustion of the primer leads to a

jitter of the ignition of the main powder charge. A jitter in the time duration between the trigger event and the output of the projectile at the muzzle of the gun is obtained. The compensation of this process by the fire control system is difficult.

Figure 3 shows the basic principle of ETC-category A in which the chemical primer is substituted by an electrothermal igniter. The igniter is connected to an electrical pulsed power supply system PPS with an energy content of up to 100kJ. After triggering the PPS discharges into the igniter in which the discharge energy is electrothermally converted into the powder charge. The diagram in figure 3 shows the expected effect by comparing the breech pressure signals with and without electrothermal ignition versus time schematically. The jitter of the electrothermal energy conversion can be neglected. The precision of the gun is improved.

#### 4.2 Electrothermally controlled Ignition of Solid Propellants with increased Loading Densities

The increase of the muzzle energy of a powder gun requires the increase of the chemical energy of the propellant in the charge chamber. Today's gun systems use solid propellants consisting of powder grains with increased surface. Additional holes are located in the powder grains. Basically it is possible to increase the loading density of the powder charge by renouncing these additional holes. A significant decrease of the burn rate of the powder will be the result and the efficiency of the gun will be decreased. By the input of electrothermally converted energy a compensation of this behaviour is expected. Experiments conducted by Woodley and Fuller [3] show that the burn rate of a solid propellant can be increased by the input of electrothermally converted energy.

The basic principle of this technology and its predicted influence on the pressure generation is shown in figure 4. The charge chamber of the gun is filled with a solid propellant with increased loading density. In addition a system consisting of several electrothermal energy converters is located in the charge chamber. The energy converters are connected to a PPS with an electrical energy content of 300 kJ up to 600 kJ depending on the calibre of the gun (120mm to 140mm). In a conventional 120mm gun the maximum of the breech pressure is reached about 5 ms after ignition. It is the goal of ETC-category B to influence the first phase of the combustion of the high loading density powder charge by the electrical energy until the optimal starting conditions for an independent combustion due to the interior ballistic requirements of the gun are reached. A time duration of 2ms for this process is expected. In the diagram in figure 4 the breech pressure curves of a conventional powder gun and of a gun with ETC-category B are plotted versus time schematically. The electrothermally ignited powder charge with high loading density will result in a more fully breech pressure curve followed by an increase of the muzzle energy of the gun.

#### 4.3 Electrothermally controlled Temperature Compensation of Propellants with increased Loading Densities

By the temperature coefficient of conventional solid propellants the usage of the gun at maximum operating pressure is prevented. Low environmental temperatures result in a lower breech pressure and high environmental temperatures result in a higher breech pressure than operating the gun at  $T=20^{\circ}\text{C}$ . Consequently a conventional powder charge is designed to generate a maximum breech pressure of ca. 550MPa at normal environmental temperature.

It is the goal of ETC-category C to compensate the temperature coefficient. A controlled input of electrothermally converted energy due to the development of pressure in the charge chamber enables the adjustment of the pressure magnitude to the maximum operating pressure.

Pulse shape and electrical power magnitudes are adjusted from the measurement of the pressure development in the gun.

Figure 5 shows the physical principle and the interior ballistic performance schematically. The modifications at the gun are in conformity with ETC-category B but the energy content of the PPS is significantly higher. Energy requirements inbetween 0.9MJ and 1.8MJ are expected due to the calibre. In the diagram the conventional breech pressure, the ETC-advanced breech pressure and the maximum operating pressure shape are plotted versus time. The input of electrical energy will last until the maximum breech pressure is achieved. The electrical energy input is controlled by the pressure development in the charge chamber. The maximum breech pressure obtained from the electrothermal combustion control is equal to the maximum operating pressure independantly from the environmental temperature. An increase of the muzzle energy will be the result.

#### 4.4 Electrothermal controlled Combustion of Propellants with increased Loading Densities and integrated Additives

In the ETC-categories described above the time duration of the electrical energy input is limited until the achievement of the maximum breech bressure. ETC-category D has the goal to influence the powder combustion as long as the powder is burning. This shall result into a flat top pressure shape which is matched to the maximum operating pressure shape of the construction of the gun. Without further measures the thermodynamic parameters of the propelling gas generated from the powder limit an increase of muzzle energy and muzzle velocity to the results of ETC-category C. In addition to the flat top pressure shape further measures have to be performed in order to improve the molecular weight of the propelling gas. It is the goal to include additional materials into the powder. The interaction of these materials with the electrothermally converted energy lead to the generation of hydrogen with masses in the range of up to 20% of the weight of the solid propellant. As shown by Knöchel et al. [1] the hydrogen is expected to decrease the molecular weight, to decrease the temperature and to increase the explosion heat of the propelling gas.

The physical principle and the expected interior ballistic performance is given schematically in figure 6. The charge chamber is filled with a solid propellant of high loading density in which materials with high content of hydrogen are included. These materials can be i.e. Aluminumhydride and water. The design of the electrothermal energy converter enables the continuous interaction of an arcdischarge with the powder during the burning phase. During this interaction the hydrogen is generated.

In the diagram the breech pressure of a conventional charge, the breech pressure of the ETC-advanced charge, the pressure acting on the bottom of the projectile and the shape of the maximum operating pressure of the gun are plotted versus time schematically. Both effects of this ETC-categroy are given. The breech pressure has a flat top shape. The pressure acting on the bottom of the projectile approaches the breech pressure signal. Both an increase of the muzzle energy as well as an increase of the muzzle velocity will be the consequence. The amount of electrical energy to be converted into the gun is expected to be inbetween 2.5MJ and 5MJ due to the calibre of the gun.

#### 4.5 Performance Potential of ETC-Technologies

First predictions on the potential of ETC-technologies in terms of performance increase are obtained from interior ballistic simulations in which optimum conditions are assumed. Table 1 gives an overview on some results obtained from these simulations with a 120mm gun. In

addition the simulated performance values of a conventional 120mm gun and those of a 120mm electrothermal gun are given. It is expected that ETC-technologies have a 50% performance increase potential in which either the muzzle energy or the muzzle velocity or portion of both can be improved.

## 5 Conclusions

The potential of pure electric guns have been demonstrated successfully in several locations so far but the status of the pulsed power supply technology gives a significant risk for an application in the next generation of combat fighting vehicles. ETC-technologies are supposed to provide a wide range of possibilities for a performance increase of anti tank weapons to be realized in mid term future. Several ETC-categories with different performance improvements and different power supply requirements enable an evaluation for the application in current and in currently investigated future tank gun systems.

## References

- [1] H. Knöchel et al. Grundlagen und Technologie einer Leistungssteigerung von Treibmitteln durch Schußgaskonversion, Proceedings International Symposium on internal Ballistics of Barrel Weapons, Mannheim 1995
- [2] Th.H.G.G. Weise et al. Recent Experimental results obtained from 45mm ET-Gun Investigations, Proceedings of the 4th European Symposium on Electromagnetic Launch Technology, Celle 1993
- [3] C.R. Woodley et al. Apparent Enhanced Burn Rates of Solid Propellants due to Plasmas, Proceedings of the 6th European Symposium on Electromagnetic Launch Technology, The Hague 1997

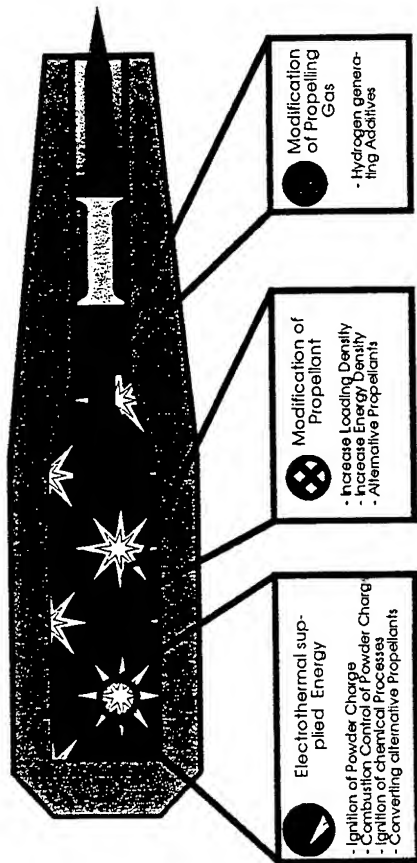


Figure 1: Interior Ballistic Principles of ETC-Technologies

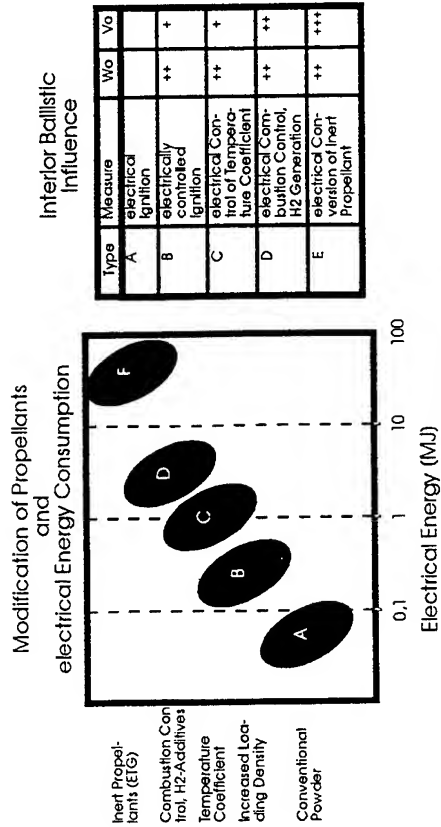


Figure 2: Classification of ETC-Technologies

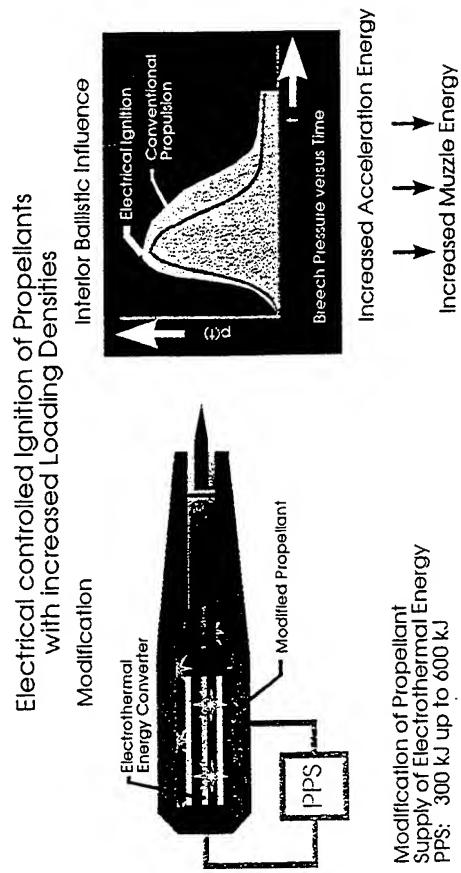


Figure 4: Basic principle of ETC-category B

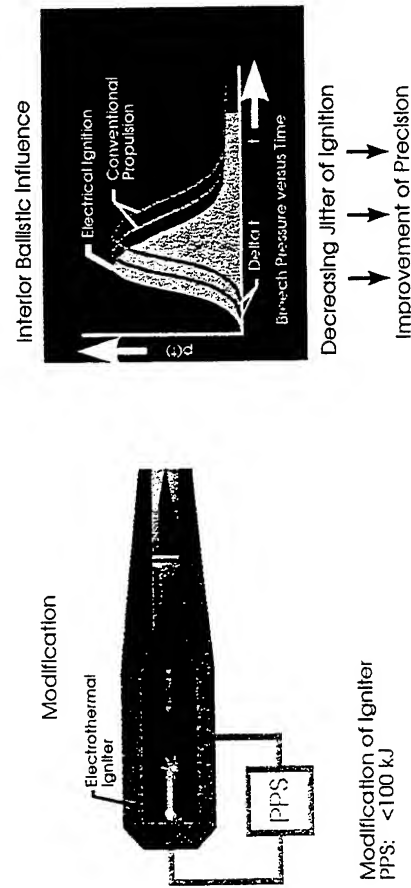


Figure 3: Basic principle of ETC-category A

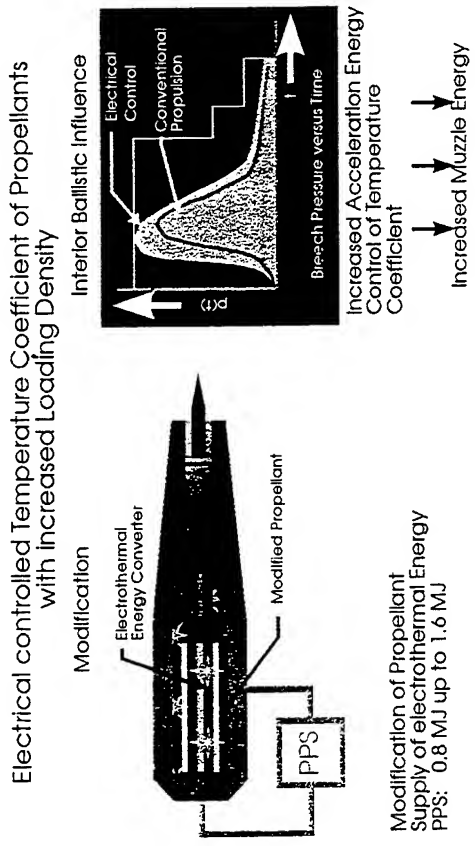


Figure 5: Basic principle of ETC-category C

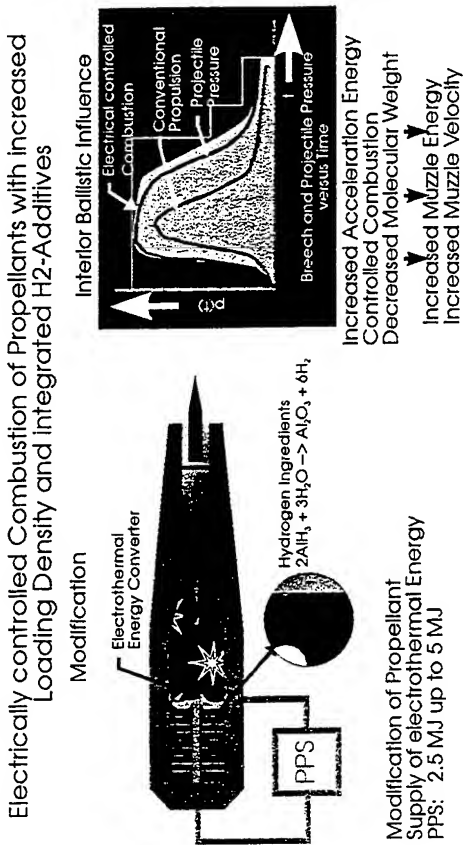


Figure 6: Basic principle of ETC-category D

| Technology        | Launch Mass | v0       | W0      | Improvement |
|-------------------|-------------|----------|---------|-------------|
| Conventional LKE2 | 7.4 kg      | 1750 m/s | 12 MJ   | Reference   |
| ETC Type A        | 7.4 kg      | 1750 m/s | 12 MJ   | 0 %         |
| ETC Type B        | 10 kg       | 1800 m/s | 16.2 MJ | 35 %        |
| ETC Type C        | 10 kg       | 1900 m/s | 18 MJ   | 50 %        |
| ETC Type D        | 10 kg       | 2000 m/s | 20 MJ   | 66 %        |
| ETC Type E        | 7.4 kg      | 2500 m/s | 23 MJ   | 90 %        |

Table 1: Performance Potential of ETC-Technologies for Calibre 120mm



# Electromagnetic Limits to the Performance and Efficiency of Rail Launchers

Trevor E James

JEMSystems, 51 Park Road, Abingdon, Oxon, OX14 1DG, UK  
(Tel: (01235) 524298, Fax: (01235) 520067)

**Summary:** Electromagnetic limits to the performance and efficiency of Rail Launchers are imposed by energy losses in the rail and armature, arcing losses following transition and the final barrel magnetic energy at exit. These are derived analytically including the effect of field diffusion, velocity skin-effect (VSE), predicted transition velocities and arcing phenomena. A range of aluminium alloy armatures with copper rails are considered with kinetic energies up to 20MJ and bore diameters from 40 to 250mm.

The fundamental electromagnetic parameters that influence electrical efficiency are shown to be: mechanical energy/bore volume ( $p_0$ ), effective magnetic flux density ( $B_0$ ) and the total mass/bore area ( $m$ ). To achieve a high electrical efficiency these parameters should be minimised by increasing the bore diameter subject to other design constraints and the bore length should be minimised. The optimum bore diameter would maximise the kinetic energy while limiting the increase in armature mass.

Electrical efficiencies for 10 and 20MJ kinetic energy launchers with minimum diameters are estimated to be about 53 and 62% respectively. An increase in efficiency to 70% is predicted for 20MJ launchers if the arcing transition can be avoided. However it is considered this would be difficult to achieve because of the probable theoretical VSE limit of about 1.5km/s for the transition velocity of typical 90mm aluminium alloy armatures, unless more resistive and lower erosion rate contact region materials are used.

## INTRODUCTION

The performance and efficiency limits of Rail Launchers for a given energy input are ultimately dependent on electromagnetic phenomena which define the energy losses and kinetic energy output. The critical fundamental parameters that influence launcher performance are the RMS magnetic field flux density, the barrel bore volume and the arcing transition velocity [1 to 5]. The efficiency is mainly dependent on the rail energy losses, the arcing losses following transition and the final barrel magnetic energy at exit [6]. Launcher efficiencies are deduced for a range of aluminium alloy armatures with copper rails having a total package mass ( $M$ ) up to 8kg, kinetic energy up to 20MJ, exit velocities from 1.5 to 3.0km/s and bore diameters from 40 to 250mm.

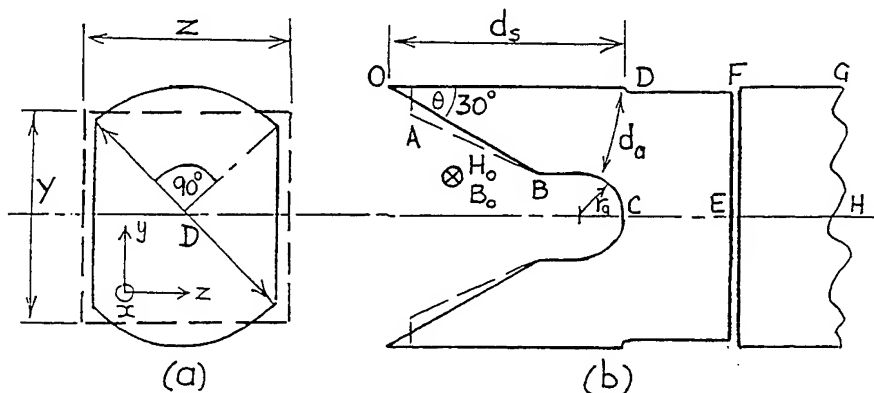


Fig 1 Armature Geometry  
(a) Round bore ( $D$ ) and effective square bore ( $Y, Z$ ) (b) Optimum contact region geometry

# REFERENCE PARAMETERS AND GEOMETRY

The general solution from which the mechanical energy output  $W_o$  and launcher electrical efficiency  $\eta_e$  are derived is based on the armature geometry in Fig 1. The rear angle ( $\theta$ ) of about  $30^\circ$  (or near  $30^\circ$  as shown by the surface AB) is considered to be near optimum in maximising the transition velocity ( $v_t$ ) as proposed in [4] and is similar to experimental 90mm armatures for which the highest transition velocities have been reported [7, 8, 9]. The analysis below is based on a rectangular bore geometry having an effective rail height (Z), rail separation (Y) and barrel length (X) with (x, y, z) co-ordinates as in Fig 1(a). For round bore launchers of diameter (D) an effective square bore is used which has the rail height (Z) and rail separation (Y = Z) equal to the rail/armature contact surface distance ( $\pi D/4$ ) with a  $90^\circ$  subtended angle as in Fig 1(a). The bore volume (XYZ) then closely equals the effective round bore volume  $0.63 (D^2 X)$ .

The total mechanical energy output  $W_o$  is assumed to be 10% greater than the kinetic energy  $W_k$  to allow for mechanical losses (mostly friction). It will be useful to define the fundamental parameters: 'output coefficient'  $p_o$  (equal to the mechanical energy/bore volume); effective magnetic field energy density  $B_o^2/2\mu_o$  (which equals  $p_o$ ); the effective current line density  $H_o$  (equals  $B_o/\mu_o$ ) and the specific mass  $m$  (equal to  $M/YZ$ ) where  $M$  is the total package mass. It then follows, for the RMS current (I), velocity (v), time (t), mean acceleration (a) and inductance gradient  $L' = 0.43\mu H/m$ , that:

$$p_o = \frac{W_o}{XYZ} = \frac{1.1 m v_e^2}{2 X} = 1.1 m a = \frac{B_o^2}{2\mu_o} = \frac{\mu_o H_o^2}{2} \quad (1)$$

$$\frac{B_o^2}{2\mu_o} = \frac{I^2 L'}{2 Y Z} \quad \text{hence} \quad B_o = \frac{\mu_o I}{Z} \left( \frac{Z L'}{Y \mu_o} \right)^{1/2} \quad \text{and} \quad H_o = \frac{I}{Z} \left( \frac{Z L'}{Y \mu_o} \right)^{1/2} \quad (2)$$

$$B_o = \frac{\mu_o I}{Z} \left( \frac{L'}{\mu_o} \right)^{1/2} = \frac{0.59 \mu_o I}{Z} \quad \text{and} \quad H_o = \frac{0.59 I}{Z} \quad \text{for square bore} \quad (3)$$

Then from (1) and (3):

$$\left( \frac{I^2 t}{Z^2} \right) = 5.10^6 (m v) \quad \text{and} \quad (H_o^2 t) = 1.75 \times 10^6 (m v) \quad \text{for square bore} \quad (4)$$

Equations (1) to (4) enable the performance of launchers to be evaluated based only on the fundamental parameters  $p_o$ ,  $B_o$ ,  $m$ , dimensions Y, Z or D and barrel length X. The reference parameters for a 90mm diameter launcher are given in Table I. It follows from (3) and Table I that the required RMS current ( $I = 2.8MA$ ), exit velocity and time would be achieved with the reference current

TABLE I  
EM LAUNCHER REFERENCE PARAMETERS  
90mm BORE DIAMETER (D), 6.8m BARREL LENGTH (X)

|                                  |                              |  |                               |
|----------------------------------|------------------------------|--|-------------------------------|
| Rails                            | Copper                       | Armature                               | Al. Alloy                     |
| Rail Resistivity                 | $3 \times 10^{-8} \Omega m$  | Armature resistivity                   | $7.2 \times 10^{-8} \Omega m$ |
| Total Package Mass (M)           | 4kg                          | Bulk Armature Depth ( $d_a$ )          | 30mm (Fig 1)                  |
| Effective Square Bore (YxZ)      | 71x71mm <sup>2</sup> (Fig 1) | Armature Rear Angle ( $\theta$ )       | $30^\circ$ (Fig 1)            |
| Specific Mass ( $m=M/YZ$ )       | 800kg/m <sup>2</sup>         | Rail/Armature Contact Length           | >60mm (Fig 1)                 |
| Bore Volume (X Y Z)              | 0.034m <sup>3</sup>          |  |                               |
| Mean Acceleration ( $\bar{a}$ )  | $0.375 \times 10^6 m/s^2$    | Peak Current ( $\hat{I}$ )             | 3.6MA (Fig 2)                 |
| Exit Velocity ( $v_e$ )          | 2.24km/s (Fig 2)             | RMS Current (I)                        | 2.8MA (Fig 2)                 |
| Exit Time ( $t_e$ )              | 6.0ms (Fig 2)                | Inductance Gradient ( $L'$ )           | $0.43\mu H/m$                 |
| Exit Mechanical Energy ( $W_o$ ) | 11.0MJ                       | Output Coefficient ( $p_o$ )           | 330MJ/m <sup>3</sup>          |
| Exit Kinetic Energy ( $W_k$ )    | 10.0MJ                       | Effective EM Parameters ( $B_o, H_o$ ) | 29T, 23MA/m                   |

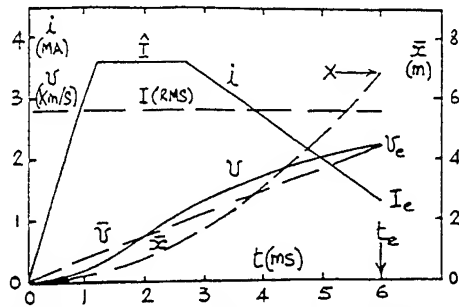


Fig 2 Reference current ( $i$ ), velocity ( $v$ ,  $\bar{v}$ ) and distance ( $\bar{x}$ ) for 90mm bore reference launcher (Table I)

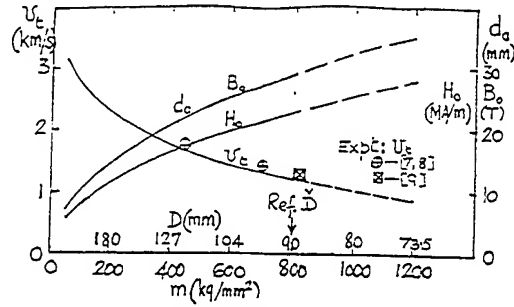


Fig 3 Predicted transition velocity ( $v_t$ ), field parameters ( $B_0$ ,  $H_0$ ), diameter ( $D$ ) for  $M = 4\text{kg}$ ,  $W_0 = 11\text{MJ}$ , specific mass ( $m$ ) and armature depth ( $d_a$ ). Experimental results [7, 8, 9] for 90mm armatures.

waveform in Fig 2.

Variation of the bore dimensions ( $Z$  or  $D$ ) and consequently the specific mass ( $m$ ) are critical factors in launcher design optimisation as they affect  $B_0$  and  $d_a$  as shown in Fig 3. The specific mass ( $m$ ) is also the critical parameter that affects the velocity skin-effect (VSE) limit to the transition velocity ( $v_t$ ) [1 to 5] being related to the action ( $I^2 t$ ) and the action line density ( $H_0^2 t$ ) at the rear of the armature as in (4) and Fig 3. Theoretical predictions of  $v_t$  derived as described in [4] are plotted in Fig 3 and also published experimental values of  $v_t$  for 90mm armatures [7, 8, 9].

It is necessary to limit the maximum values of  $B_0$  and  $p_0$  to prevent structural failure. If the maximum flux density ( $\hat{B}_0$ ) is about 29T the minimum diameters ( $\check{D}$ ) would be about 90 and 125mm respectively for  $W_0$  values of 11 and 22MJ respectively. There is also a limit to  $\check{D}$  due to the requirement of a sufficiently large armature bulk depth ( $d_a$ ) and internal radius ( $r_a$ ) in Fig 1. This would limit  $\check{D}$  for  $W_0$  of 5.5MJ to about 75mm.

## ELECTROMAGNETIC ENERGY LOSSES

### Electromagnetic (EM) Field Configuration

The EM field between the rails about a distance  $> 5Z$  away from the armature is 2-dimensional (2D). A flux-plot showing lines of constant flux ( $\phi$ ) and constant magnetomotive force (MMF) are shown in Fig 4(a) for a square bore launcher assuming the inner flux surface is located close to the rail. This 'field diffusion' model applies because the rail flux skin-depth  $\delta_r < d_r$ , the rail depth. For copper rails  $\delta_r$  is about 14mm for a pulse time of 6ms compared with  $d_r$  of about 35mm for a 90mm diameter launcher. The mean flux density  $\bar{B}_r$  between the rails equals  $(I L'/Y)$  and the RMS flux density ( $B_r$ ) at the inner rail surface, allowing for non-uniformity of the field, is estimated to be 10% higher.  $B_r$  is then  $1.1 (I L'/Y)$  where  $L'$  is based on the flux inside the rail bore surface.

The EM field at the armature surface is 3-dimensional (3D) and very non-uniform. The mean flux density  $\bar{B}$  between the rails increases from  $\bar{B}_r$  to a higher value  $\bar{B}_b$  (about  $1.5 \bar{B}_r$ ) at the rear armature surface as shown in Fig 4(b). A reversed field  $\bar{B}_f$  exists at the front armature surface falling to near zero at a sufficient distance ahead of the armature. The field distribution in Fig 4(b) is a 'diffusion model' estimate for the reference armature in Table I with parallel surfaces ( $d_a$  apart) from which it is deduced that  $B_f/B_0$  will be  $< 0.2$  for typical armatures and electrically conducting launch packages.

The total axial magnetic force is obtained by integrating the axial components of the ( $J \times B$ ) forces over the front and back surfaces of the armature only, since the forces on the armature sides have no significant axial component. The armature geometry has no significant effect on the axial force so that the latter can be evaluated assuming parallel armature surfaces. For the 'field diffusion' model and RMS

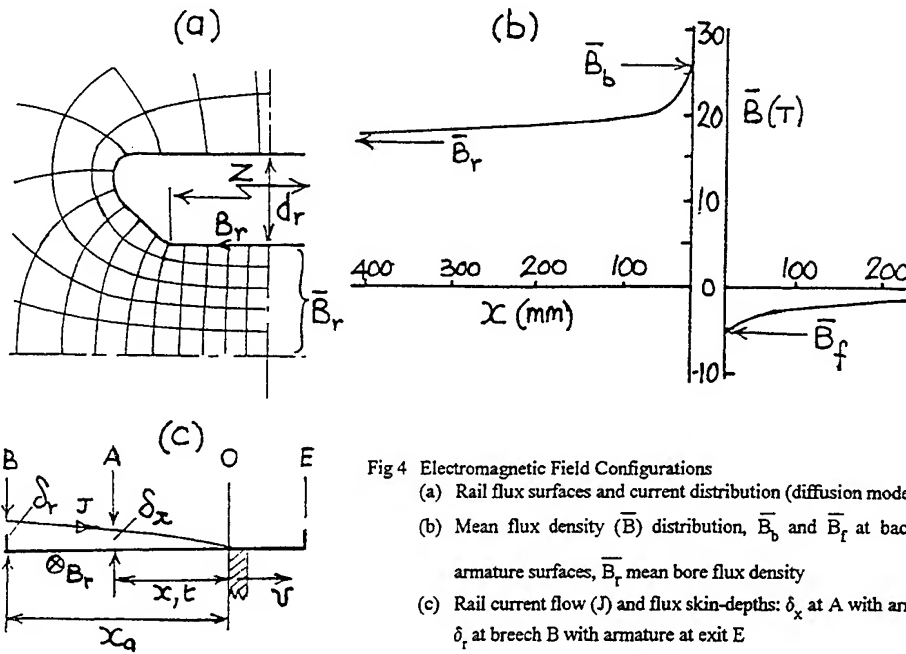


Fig 4 Electromagnetic Field Configurations  
 (a) Rail flux surfaces and current distribution (diffusion model)  
 (b) Mean flux density ( $\bar{B}$ ) distribution,  $\bar{B}_b$  and  $\bar{B}_f$  at back and front armature surfaces,  $\bar{B}_r$  mean bore flux density  
 (c) Rail current flow ( $J$ ) and flux skin-depths:  $\delta_x$  at A with armature at O,  $\delta_t$  at breech B with armature at exit E

forces are  $B_b^2 (YZ)/2 \mu_0$  (accelerating) and  $-B_f^2 (YZ)/2 \mu_0$  (decelerating). The net axial forces are also equal to  $p_o (YZ)$  and  $B_o^2 (YZ)/2 \mu_0$  where  $p_o$  and  $B_o$  are as defined above.

$$\text{Hence: } B_b^2 - B_f^2 = B_o^2 \quad (5)$$

However  $B_f^2$  is typically  $< 0.04 B_b^2$  and therefore it can be assumed that  $B_b = B_o$  with an error of  $< 2\%$ , so that for the reference parameters in Table I  $B_b = B_o = 29\text{T}$  and the current line density ( $H_o$ ) at the rear of the armature is  $23\text{MA/m}$ . This is consistent with the estimated mean value of  $\bar{B}_b = 26\text{T}$  in Fig 4(b) allowing for field non-uniformity. Thus the critical armature EM field parameters can be derived directly from  $B_o$  and  $p_o$  in (1) to (4).

#### Rail Losses ( $W_p$ )

The rail energy losses consist of the dissipated resistive energy and inductive energy stored in the rail, taking account of field diffusion, the velocity skin-effect (VSE) and variation of the EM field at the rail surface (Fig 4(a)). The ratio of resistive to inductive losses is about 70/30 [10]. In Fig 4(c) the armature at O is moving with constant acceleration  $a$  along the rail surface BE at velocity  $v$ , so that the flux skin-depth  $\delta_x$  at A is  $D_r (K_o t)^{1/2}$  where  $K_o$  is  $(\rho_r/\mu_0)$ ,  $\rho_r$  is the rail resistivity and  $D_r = 1.13$  for a constant surface flux density [10]. The surface electric field  $E_x$  with a surface flux density  $B_r$  is  $B_r d\delta_x/dt$ . The rail energy surface flux density ( $w_x$ ) at A is then given by:

$$w_x = \frac{1}{\mu_0} \int_0^t E_x B_r dt = \frac{B_r^2}{2 \mu_0} \int 2 d\delta_x = 2 p_r \delta_x \text{ (joules/m}^2\text{)} \quad (6)$$

where  $p_r = B_r^2/2 \mu_0$  is the surface magnetic field energy density. The RMS flux density is  $B_r$  over the inner rail surface of height ( $Z$ ) and length ( $X$ ), the total rail energy loss behind the armature ( $W_{ro}$ ) for 2 rails is then:

$$W_{ro} = 4 g_r Z \int_0^x p_r \delta_x dx = \frac{32}{15} g_r p_r \delta_r (XZ) \quad (7)$$

$$W_{ro} = 4 g_r Z \int_0^x p_r \delta_x dx = \frac{32}{15} g_r p_r \delta_r (X Z) \quad (7)$$

where  $\delta_r = (K_o t_e)^{1/2}$  the flux skin-depth at the breech B when the armature is leaving the muzzle at E (Fig 4(c)). The variation of flux density B round the rail surface (Fig 4(a)) is accounted for by evaluating the integral  $\int B^2 ds$  round the rail surface (s) and deriving the non-dimensional surface parameter  $g_r$  for the field configuration from:

$$g_r = \frac{1}{B_o^2 Z} \int B^2 ds = 2.3 \text{ from Fig 4(a)} \quad (8)$$

The Rail Losses ( $W_{rf}$ ) in front of the armature have been derived similarly to  $W_{ro}$  above. However due to the low value of  $B_f$  at the front armature surface and the short effective rail length over which the field decays  $W_{rf}$  is only about 1% of  $W_{ro}$ . The total rail energy losses ( $W_r$ ) are therefore almost equal to  $W_{ro}$ .

#### Armature Bulk Losses ( $W_a$ )

The bulk armature losses ( $W_a$ ), excluding the contact surface losses ( $W_c$ ), are derived in a similar manner to the rail losses ( $W_r$ ) in (6) and (7) as:

$$W_a = 2 g_a (p_o \delta_b) Z l_a = 5 g_a p_o \delta_b Z^2 \quad (9)$$

where  $l_a$  is the length of the inner surface of the armature, 2 (OBC) in Fig 1(b), typically about 2.5Z. The armature surface parameter  $g_a$  is derived as in (8) to be 1.85,  $p_o = B_o^2 / 2 \mu_o = 330 \text{MPa}$  for the reference armature (Table I) and  $\delta_b$  is the bulk armature flux skin-depth at exit (about 20mm).

#### Armature Contact Surface Losses ( $W_p$ )

Before transition a liquid metal contact surface probably exists with a very low contact voltage ( $V_c$ ) of < 2V and consequently very low losses. Following transition to arcing the arc voltages  $2 V_p$  increase over a typical arcing time of about 3ms (due to arcing erosion) from about 100V to a mean value of about 400 volts with oscillations of about  $\pm 100$  volts at 5 to 10kHz. These phenomena have been considered in [5] and conclusions regarding arc voltage and energy losses, expressed as a function of the charge Q carried by arcing, are summarised in Fig 5. The arcing resistive losses are  $W_p = 2 \int V_p dQ$  and also possible additional contact surface resistive and inductive energy losses are indicated as  $W_s$ . The latter are based on a model of accelerated arcing current 'sheets' with commutation to re-strike arcs at the rear of the contact surface [5]. There is little quantitative experimental evidence for this arcing

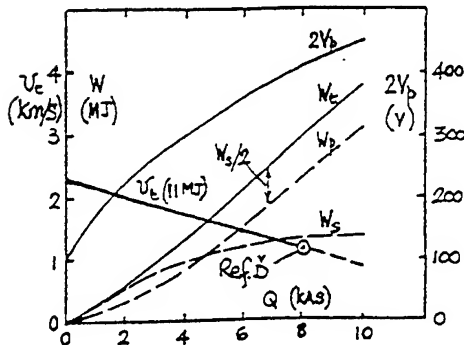


Fig 5 Arcing and surface energy losses ( $W_p$ ) after transition. Charge flow (Q), arc resistance losses ( $W_p$ ), assumed surface energy losses ( $W_s/2$ ).

model at present so that the values of  $W_s$  derived in [5] may be excessive. Therefore for this present study it is assumed that the contact energy losses after transition ( $W_t$ ) are equal to  $(W_p + W_s/2)$  as given in Fig 5. The derivation of  $W_t$  requires the evaluation of  $Q$  and the arcing time after transition from the predicted transition velocities  $v_t$  (Fig 3) taking account of the falling current ( $i$  in Fig 2) during this period. At high values of  $Q$  and  $W_t$  the 'explosive' forces generated by the arc energy in the rail/armature gap [5] may result in critical structural design problems.

#### Final Magnetic Energy ( $W_o$ )

The final magnetic energy in the barrel at exit ( $W_o$ ) is a significant energy loss equal to  $W_o (I_e/I)^2$ . For the reference current waveform in Fig 2  $W_o = 0.21 W_0 = 2.3 \text{ MJ}$  for  $W_0 = 11 \text{ MJ}$ .

### ENERGY OUTPUT AND EFFICIENCY

#### Electrical Efficiency ( $\eta_e$ )

The total electromagnetic losses discussed above are  $W_l = (W_r + W_a + W_t + W_o)$  and have been evaluated for mechanical energy outputs ( $W_o$ ) up to 22 MJ. They are plotted in Fig 6(a) and (c) against bore diameter  $D$  for a fixed barrel length of 6.8m. The corresponding electrical input at the breech  $W_b$  is  $(W_o + W_l)$  and the electrical efficiencies  $\eta_e = W_o/W_b$  are given in Figs 6(b) and (d).

Larger bore diameters ( $D$ ) result in large reductions in losses (Fig 6(a)) due to the lower values of magnetic energy densities  $p_r$  and  $p_o$  in (7) and (9) and the higher values of transition velocities  $v_t$  in Fig 3. Increases in  $\eta_e$  for  $W_o$  of 11 MJ occur from 53% to 65% as  $D$  increases from 90mm to 150mm (Fig 6(b)). The transition arcing energy losses are critical in reducing  $\eta_e$  (Fig 6(b)) for values of  $D < 125 \text{ mm}$  due to the resulting increases in  $W_t$  (Figs 6(a)). If it proves to be possible to prevent transition

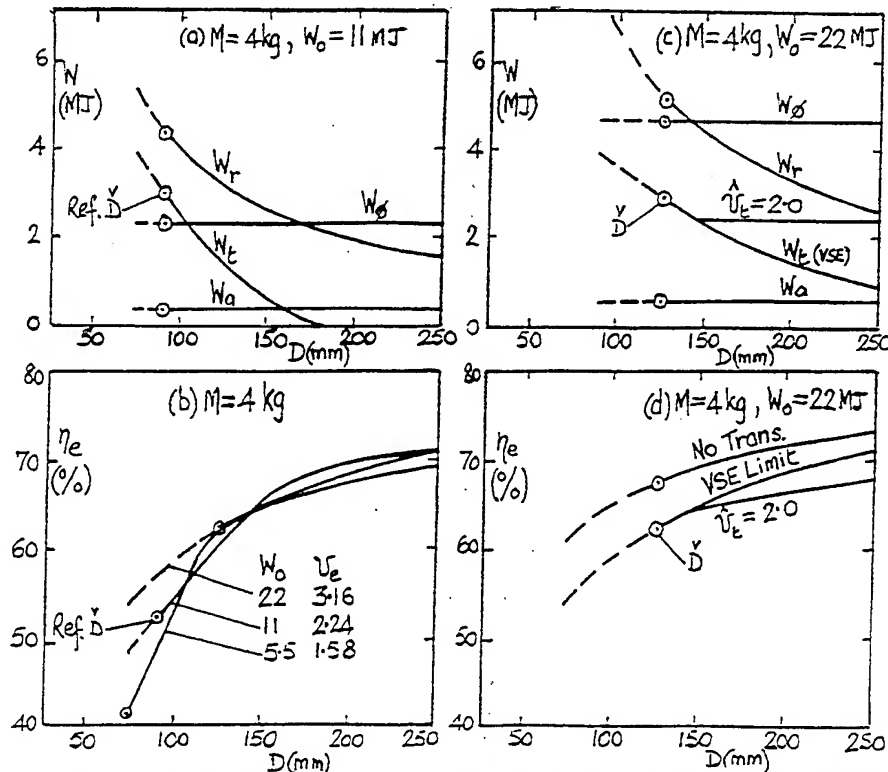


Fig 6 Energy losses ( $W$ ) and electrical efficiency ( $\eta_e$ ) for bore diameter ( $D$ ), mass ( $M$ ), mechanical energy ( $W_0$ ) and exit velocity ( $v_e$ ). Barrel length ( $X$ ) = 6.8m. (a) and (c) Energy Losses ( $W$ ), (b) and (d) Electrical Efficiency ( $\eta_e$ ).

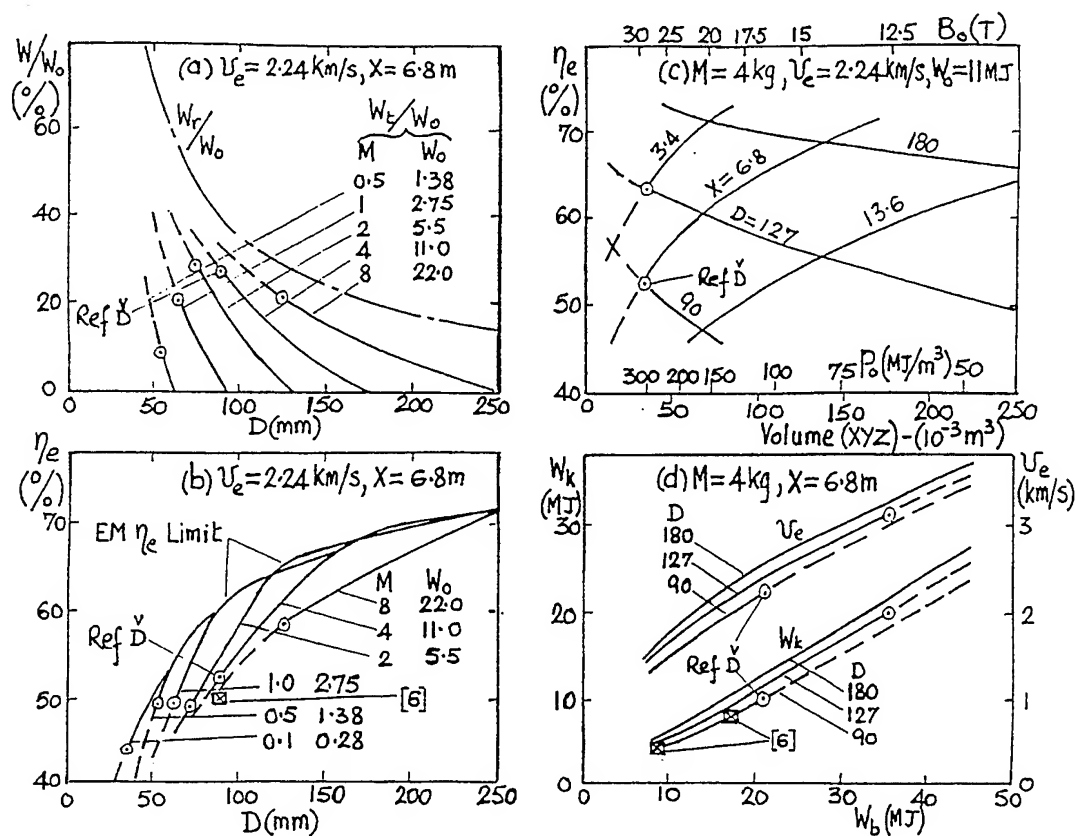


Fig 7 Electrical efficiency ( $\eta_e$ ), mechanical energy ( $W_o$ ), kinetic energy ( $W_k$ ) and breech energy ( $W_b$ ). Output coefficient ( $p_o$ ), effective flux density ( $B_o$ ) and bore volume ( $XYZ$ ). Experimental data [6] for  $D = 90 \text{ mm}$ ,  $W_k = 4$  and  $8 \text{ MJ}$ .

(a) Energy Loss Ratio ( $W_r/W_o$ ) (c) Electric Efficiency ( $\eta_e$ ) and barrel length ( $X$ )

(b) Electric Efficiency ( $\eta_e$ ) (d) Breech energy ( $W_b$ ) and kinetic energy ( $W_k$ )

completely the increase in  $\eta_e$  for  $W_o = 22 \text{ MJ}$  could be about 5% at  $\vec{D}$  (Fig 6(d)). Alternatively there is some experimental evidence [8, 11] that the surface condition known as 'gouging' could limit  $v_t$  to about  $2.0 \text{ km/s}$ , in which case  $\eta_e$  would be reduced at larger  $D$  values (Fig 6(d)), since  $W_t$  would be maintained at about  $2.4 \text{ MJ}$  (Fig 6(c)).

A fundamental electromagnetic 'VSE limit' is predicted to the transition velocity ( $v_t$ ) for  $90 \text{ mm}$  aluminium alloy armature contact regions in the range  $1.2$  to  $1.7 \text{ km/s}$  [2, 4], which is supported by experimental results (Fig 3). The use of more resistive contact region materials has been proposed to achieve  $v_t$  values in the  $2.5$  to  $3.0 \text{ km/s}$  range [2] which could also have much lower arcing erosion rates than aluminium alloy and consequently lower arc voltages and energy losses. However these higher transition velocities have not been demonstrated experimentally.

For a constant exit velocity  $v_e$  the energy ratio  $W_r/W_o$  is independent of  $M$  and  $W_o$  whereas the ratio  $W_t/W_o$  is critically dependent on these parameters as shown in Fig 7(a) for  $v_e = 2.24 \text{ km/s}$  and  $X = 6.8 \text{ m}$ . The corresponding values of  $\eta_e$  are given in Fig 7(b) for  $M$  and  $W_o$  from  $0.1$  to  $8 \text{ kg}$  and  $0.28$  to  $22 \text{ MJ}$  respectively. As the diameter  $D$  is increased and  $W_t/W_o$  decrease all values of  $\eta_e$  tend to the same maximum value indicated as the 'EM  $\eta_e$  limit' in Fig 7(b). This represents the fundamental electromagnetic limit to the maximum efficiency that is achievable when the arcing transition does not occur.

#### *Output Coefficient ( $p_o$ ), Flux Density ( $B_o$ ) and Kinetic Energy ( $W_k$ )*

The effect of varying the bore volume (XYZ) by increasing the bore length from 3.4 to 13.6m (compared with the reference value of 6.8m) is given in Fig 7(c) with the corresponding values of  $p_o$  and  $B_o$  for values of D from 90 to 180mm. Increasing X reduces  $\eta_e$  due to higher rail and arcing transition losses, so that maximising D and minimising X will result in the highest efficiency. The kinetic energies  $W_k$  (assuming 10% mechanical losses) and exit velocities  $v_e$ , derived from Fig 6(b), are given in Fig 7(d) for the breech electrical input  $W_b$ . For the reference case with  $W_k$  of 10MJ  $W_b$  is reduced from 21 to about 18 or 16MJ as D is increased from 90 to 127 or 180mm respectively. The experimental results for  $W_k$  values of 4 and 8MJ [6] in Figs 7(b) and (d) are in reasonable agreement with predicted parameters.

The optimum choice of bore diameter (D) depends on other design constraints, such as the resulting increase in armature mass with larger diameters. However it is probable that the increase in efficiency of about 7% due to an increase in D for a 11MJ launcher from 90 to 127mm (Fig 6(b)) would more than compensate for the possible increase in mass.

### CONCLUSIONS

The most critical energy losses in conventional rail launchers occur in the rails and due to arcing after transition. Electrical efficiencies (mechanical energy/breech electrical input) for typical 10 and 20MJ launchers (copper rails and aluminium alloy armatures) with bore diameters of 90 and 125mm and a total package mass of 4kg are deduced as 53% and 62% respectively. Efficiencies > 70% are predicted for larger bore diameters.

The arcing losses after transition are derived based on predicted VSE limits to transition velocities and experimental results for aluminium alloy armatures. Significant reductions in these losses require transition velocities in the 2.5 to 3.0km/s range which may be possible with more resistive contact regions having lower arcing erosion rates, though this has not been demonstrated experimentally.

The general electromagnetic limits to the performance and efficiency of rail launchers are dependent on the fundamental parameters: mechanical energy/effective bore volume ( $p_o$ ), effective magnetic field flux density ( $B_o$ ) and total mass/effective bore area (m). To achieve high efficiency these parameters need to be minimised by increasing the bore diameter to the limit imposed by other design constraints and the bore length should be minimised.

### ACKNOWLEDGMENT

Helpful discussions with David Haugh of DRA (Fort Halstead) concerning experimental results are gratefully acknowledged.

### REFERENCES

- [1] T E James, IEEE Trans Magn, vol 27 no 1, pp482-7, 1991
- [2] T E James, D C James, IEEE Trans Magn, vol 31 no 1, pp162-7, 1995
- [3] T E James, IEEE Trans Magn, vol 31 no 1, pp622-7, 1995
- [4] T E James, D C James, 8th Symposium on EML Technology, Baltimore, USA, April 1996
- [5] T E James, 8th Symposium on EML Technology, Baltimore, USA, April 1996
- [6] D P Bauer, IEEE Trans Magn, vol 31 no 1, pp263-6, 1995
- [7] D C Haugh, D J Kirkpatrick, A P J Argyle, M D Barrett, 5th European EML Symposium, Toulouse, France, April 1995
- [8] D J Kirkpatrick, D C Haugh, 8th Symposium on EML Technology, Baltimore, USA, April 1996
- [9] J H Price, H D Yun, IEEE Trans Magn, vol 31 no 1, pp219-24, 1995
- [10] H Knoepfel, Pulsed High Magnetic Fields, North Holland Publishing Co, ch 3 and 4 and p77, 1970
- [11] R A Marshall, C Persad, K A Jamison, M J Matyac, IEEE Trans Magn, vol 31 no 1, pp156-61, 1995



# Numerical Simulation of Electrothermal Accelerators

K. Gruber

Industrieanlagenbetriebsgesellschaft mbH, Ottobrunn, Germany

U.H. Bauder

Technische Universität München, Lehrstuhl für Technische Elektrophysik, Germany

## Abstract

In order to evaluate the performance of electrothermal and electrothermal/chemical guns it is necessary to solve the complete set of balance equations of magnetohydrodynamics (continuity equation, momentum balance, energy balance). Therefore the simulation code IBECA yielding the time dependent temperature-, velocity- and pressure distribution within the accelerator barrel including the modeling of the energy supply has been developed at IABG.

Concerning the treatment of small caliber plasma burners (diameters up to 10...15 mm) with currents of several 10 kA it is possible to use a one dimensional version of the simulation code which averages the plasma temperature with respect to radius. The radial temperature profile of this type of arcs is assumed to be flat at the arc center with a steep gradient at the edge which should be especially valid for high pressure arcs. In this case the above mentioned assumption of a radial averaged plasma temperature seems to be justified and the simulation model IBECA produces results which are in good agreement with experimental data. Some examples are shown in this paper.

At larger arc diameters however the assumption of an arc which almost occupies the total volume of the plasma burner is no longer applicable and a two dimensional treatment of the arc becomes necessary. First results are shown in this paper.

In both cases the radiation losses play the dominant role in the energy balance and the proper treatment of radiation decisively influences the simulation results. Therefore a theoretical model describing radiation in plasmas has been developed at IABG. The results of this work are presented in an other contribution to this conference.

## Introduction

For the evaluation of electrothermal accelerators a simulation model has been developed at IABG that solves the coupled set of basic equations of magnetohydrodynamics: continuity equation, radial and axial momentum balance, energy balance and Maxwells equation for the determination of current density and magnetic field.

The model is two dimensional in space and time dependent. The physical processes are described in cylindrical coordinates with an assumed azimuthal symmetry. In this case the balance equations read

$$\frac{\partial}{\partial t}(\rho) + \text{div}(\rho \vec{v}) = 0 \quad \text{Continuity Equation}$$

$$\frac{\partial}{\partial t}(\rho v_r) + \text{div}(\rho \vec{v} v_r) = \text{div}(\eta \text{grad} v_r) - \frac{\partial p}{\partial r} - j_z B_\phi + \frac{\partial}{\partial z} \left( \eta \frac{\partial v_z}{\partial r} \right) - 2\eta \frac{v_r}{r^2} - \frac{\partial}{\partial r} \left[ \frac{2}{3} \eta \left( \frac{1}{r} \frac{\partial(r v_r)}{\partial r} + \frac{\partial v_z}{\partial z} \right) \right]$$

Radial Momentum Balance

$$\frac{\partial}{\partial t}(\rho v_z) + \text{div}(\rho \vec{v} v_z) = \text{div}(\eta \text{grad} v_z) - \frac{\partial p}{\partial z} + j_r B_\phi + \rho g + \frac{1}{r} \frac{\partial}{\partial r} \left[ \eta \left( \frac{\partial v_r}{\partial z} \right) \right] - \frac{\partial}{\partial z} \left[ \frac{2}{3} \eta \left( \frac{1}{r} \frac{\partial(r v_r)}{\partial r} \right) \right]$$

Axial Momentum Balance

$$\frac{\partial}{\partial t}(\rho h) + \text{div}(\rho \vec{v} h) = \text{div} \left( \frac{\kappa}{c_p} \text{grad} h \right) + \frac{\partial p}{\partial t} + \frac{j_r^2 + j_z^2}{\sigma} - u$$

Energy Balance

For the solution of this system of equations the material functions of the propellant gas as well as an appropriate equation of state have to be known. The solution method uses finite volumes, it is described in detail in /1/.

In order to validate the numerical model an accelerator configuration with measured values of current, pressure and plasma resistance has been simulated. The measured values are published in /2/.

### Accelerator Configuration

The investigated accelerator consists of a plasma burner with a diameter of 10 mm and a length of 90 mm. The wall of the plasma burner tube consists of polyethylene which is evaporated by the plasma and thereby supplies the plasma material. The plasma is ignited via an exploding wire. A plasma jet expels into an expansion volume of about 10 ccm, heats up and pressurizes the gas in the expansion volume and thereby drives a 5 g projectile in a 12 mm caliber accelerator barrel with a total length of 1.3 m. A schematic drawing of the accelerator is shown in Fig. 1, a detailed description is given in /2/.

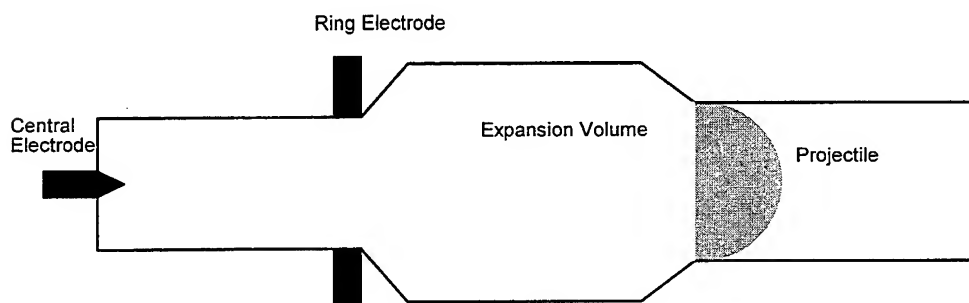


Fig. 1 Plasmaburner with accelerator barrel

The conical transitions from the plasmaburner to the expansion volume and from the expansion volume to the accelerator barrel are not represented in the model. Instead an accelerator barrel with a constant diameter of 12 mm is used. In order as to maintain an expansion volume of 10 ccm the projectile is shifted to the right.

The energy supply used in the experiments and modeled in the simulation code is a RLC-circuit with a stored energy of 100 kJ

### One dimensional modeling

According to a length / diameter ratio of 9 the electric arc in the plasma burner can be treated by the one dimensional version of the simulation code IBECA. (Interior Ballistics of Electrothermal/Chemical Accelerators). Here it is assumed that the arc has a flat temperature profile at the center and a steep temperature gradient at the border. The validity of this assumption is supported by the fact that the arc pressure is in the order of several 10 MPa for the most part of the discharge. The temperature in the model is therefore kept constant along the arc radius and only an axial temperature variation is simulated. Due to this fact the model yields only the mean plasma temperature with respect to radius.

The pressure generation and consequently the innerballistic properties of the accelerator are mainly determined by the radial mass inflow of the ablated wall material.

The mass flow  $\mu_0$  at the wall is given by /3/

$$\mu_0 = \frac{S_R + Q_R}{\Delta h_v}$$

with

$S_R$  = radiant energy flux at  $r=R$

$Q_R$  = conductive energy flux at  $r=R$

$\Delta h_v$  = evaporation enthalpy of polyethylene

The mass flow is mainly influenced by the plasma radiation and the proper treatment of the radiation losses therefore strongly influences the simulation results, especially the pressure and the projectile velocity. As in other publications /3/, we assume that the arc column radiates like a black body with a plasma temperature  $T_{Pl}$

$$S_{Pl} = \sigma_{SB} T_{Pl}^4$$

A fraction  $(1-A_V)$  of the plasma radiation is absorbed in the intermediate region between plasma and surrounding gas, a fraction  $(1-A_{V0})$  is absorbed in the cold gas and a part  $A_{C0}$  of the remaining radiation is absorbed by the wall material.

The radial mass flow at the wall caused by radiation can thus be described by

$$\mu_0 = \frac{A_{C0}(1-A_{V0})(1-A_V)\sigma_{SB}T_{Pl}^4}{\Delta h_v}$$

In /3/ sophisticated calculations concerning radiation trapping in the intermediate sheath between plasma and cold gas and radiation trapping in the cold gas in a polyethylene atmosphere have been carried out, and in our contribution the values of  $A_{C0}$ ,  $A_{V0}$  and  $A_V$  published in /3/ have been used in the appropriate temperature and pressure ranges.

## Results

The total acceleration cycle including energy supply, pressure generation and projectile movement has been simulated with the one dimensional version of the IBECA code under the above mentioned assumptions concerning radiative losses.

In the following figures histories of current, pressure and temperature in the plasma burner and plasma resistance with respect to time are shown:

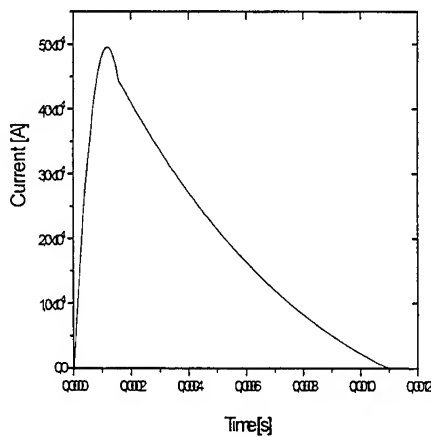


Fig. 2: Current in Plasmaburner

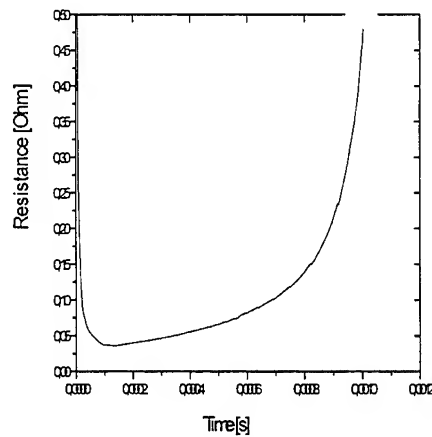


Fig. 3: Plasma Resistance

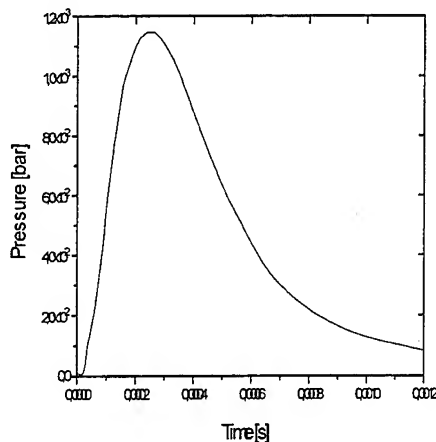


Fig. 4 Pressure in Plasmaburner

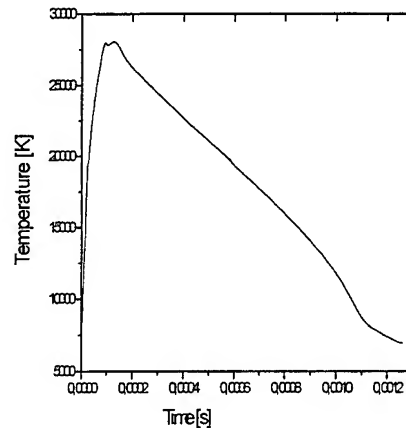


Fig. 5: Mean Plasma Temperature

The simulated values of current, pressure, plasma resistance and arc voltage are in good agreement with the measured ones published in /2/. Maximum deviations are less than 10 %. Since the temperature was not measured in /2/ a comparison is not possible but comparative simulations between ISL, DRA and IABG currently performed show good agreement as well.

### Two dimensional modeling

Although the model yields good results in the case of large length to diameter ratios the basic assumptions made above do not longer hold if the diameter of the discharge chamber is comparable to the length of the arc discharge. Here the diameter of the arc is not necessarily constant along the length of the discharge and the isothermal two zone model for ablation stabilized arcs is not applicable. Therefore in the case of large caliber accelerators a two dimensional model is highly desirable. This should allow for variable arc diameters and radial temperature profiles which not necessarily have to be flat at the center and steep at the border. In order as to demonstrate the applicability of the two dimensional version of the IBECA code and to prove the assumptions concerning the temperature profile of an arc burning in a narrow tube postulated above, the following Fig. 6 shows the two dimensional temperature profiles at an early moment of the above simulated acceleration process.

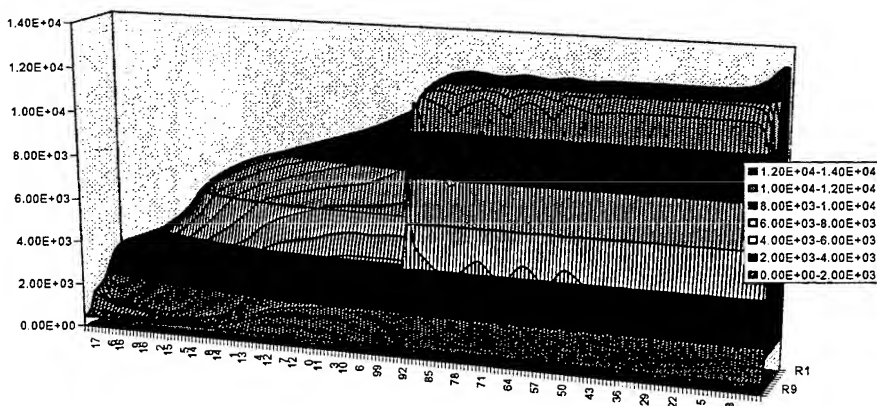


Fig. 6 Two Dimensional Temperature Distribution in the Accelerator Barrel

From Fig. 6 it can be seen that the temperature distribution in the plasmaburner is indeed very flat with steep gradients at the edge. The plasma jet from the burner into the expansion volume is also visible.

### Conclusions

Although one dimensional models are good tools for predicting the processes in plasmas burning in narrow tubes, they fail as the arc diameter approaches to values equal to the length of the discharge because the basic assumptions concerning the temperature profile are not longer valid in this case. Therefore there is still a need for two dimensional models. Also the assumptions concerning radiation losses do not longer hold in arcs with considerable diameters and further work has to be done in the domain of plasma radiation

### Literature

- /1/ S.V. Patankar, Numerical Heat Transfer and Fluid Flow, MacGraw-Hill, New York 1980
- /2/ K. Zimmermann, J. Raupp, D. Mura, C. Steinbach, Parametrische Untersuchungen an einem elektrothermischen Beschleuniger vom Kaliber 12 mm, Technischer Bericht RT 514/92, ISL 1992
- /3/ K. Darée, D. Hensel, N. Silvestre, Eindimensionale Modellrechnungen zum elektrothermischen Beschleuniger des ISL, Technischer Bericht R 127/94, ISL 1994

# A GENERALIZED GOODNESS FACTOR CRITERION APPLIED TO ADVANCED ROTATING ELECTRICAL MACHINES FOR HYPERVELOCITY ACCELERATORS?

M. D. Driga

Professor, The University of Texas at Austin  
Electrical and Computer Engineering Department  
Austin, Texas 78712

## SUMMARY

The rotating, pulsed, electrical generators represent the most compact and promising solution as power supplies for hypervelocity macroparticle accelerators. Due to the extremely high power, high energy ratings and the controlled transient nature of such devices, the normal quality indicators for steady-state electrical machines (equivalent circuits and electrodynamic similitude criteria) become inappropriate for an accurate characterization of their operation and for performance prediction.

Starting from the two-axis theory of electrical machines expressed by Park's equations, and using the Kron's tensorial formulations for transient and "pulsed" conversion, a "goodness factor" generalization is considered from steady-state to pulsed, electrical machines and, further, to systems of machines. The optimality of the comparative interplay of the magnetic circuits with the electrical circuits in the condition of rapidly pulsed conversion, as well as a scale factor obtained from thermal considerations from steady-state to short-time duty are taken into account.

A new "generalized goodness factor" must contain, also, an interconnection clause which allows consideration of the rotating power supply, together with its hypervelocity accelerator, as a global indicator.

## INTRODUCTION

Within the last two decades, the subject of electromagnetic launchers (EML) so well treated by A.L.O. Fauchon-Villepleé in his book, "Canons Electriques" (1920) [1], came again, intensely, to life, together with the topic of their power supplies [2, 3, 4].

In 1995, in the Introductory Address to the last (the 5th) European Symposium on Electromagnetic Launch Technology held in Toulouse (France), Dr. F. Jamet, the President of the European Launch Society, noticed "the missing of papers devoted to the reduction of sizes and weights of high power storage components...new technologies in electrical power supplies." [5]

For an objective reader of the public domain technical literature on the subject, it seems obvious that the rotating, pulsed electrical generators of heteropolar topology represent the most promising direction toward a solution for power supplies for hypervelocity macroparticle accelerators, due to their potential compactness.

This paper tries not to introduce new concepts, but to stand back and explore the means to assess theoretically the relative merits of the mentioned rotating pulsed electrical machines. For instance, how the known "Goodness Factor" criterion (introduced by Laithwaite [6], but known and implied by many classical books on electrical machine design [7, 8, 9]), performs the task of a yardstick for advanced power supplies for hypervelocity EML.

The methodology starts from the two-axis theory of electrical machines of Blondel and Park [10] and uses Kron's tensorial formulation [11] as applied to transient and pulsed

electromechanical power conversion. It treats the optimality of the comparative interplay of the magnetic circuits with electrical circuits in conditions of rapidly pulsed conversion. An interconnection clause is necessary in order to allow the treatment of the power supply together with the EM launcher in a system approach as a global indicator.

#### INTRINSIC CHARACTERISTICS OF THE ROTATING PULSED POWER SUPPLIES (RPPS) FOR ELECTROMAGNETIC LAUNCHERS (EML)

The peculiar nature, "the strangeness", of the RPPS for EML is due not only to constraints related to their very high energy and very high power ratings under conditions of extreme transient characteristics (they operate under load for few milliseconds only), but also to strong differences with respect to other electromechanical power converters.

1) One, casually disregarded, but carrying important theoretical implications is that such machines belong not to the customary constant voltage systems, but to a totally new world of constant current systems in which the supplied current is always the same and the voltage is variable, according to the power required by the load. Pestarini [12] has described in detail such a world mainly for d.c. machines, calling them Metadynes, and patenting numerous applications - the majority in complex drive systems.

Laithwaite alluded to it [6] and, as Pestarini did years before him, commented about how unprepared the common electrical machine designer is to adapt himself to a system of reference diametrically opposite to the usual practice and requirements.

2) The second intrinsic characteristic of the RPPS is the so-called "compensation." The compensation is actually a misnomer for a complex phenomenon used by the electrical machine designer to adapt the characteristics of the power supply to those needed by the electromagnetic launcher. The term is borrowed from the theory of operation of d. c. machines in which the armature current flows in series through a separate winding (compensation winding) embedded in the pole-pieces of the machine stator, canceling in large part the magnetic field of armature reaction. The success of the operation is assured by the constant (and opposite) relative position in space of the two magnetic fields - armature reaction and compensation - maintained by the brush and commutator system.

In the first approximation, the notion of armature reaction compensation can be generalized to a synchronous generator by using a conductive uniform shield - placed on the excitation poles and opposing the armature. During the machine discharge into the low impedance load (such as the electromagnetic launcher), image currents in the shield produce a magnetic field opposite to the armature reaction field, canceling a large part of it and achieving an important reduction of the internal impedance of the power supply, thus increasing the efficiency of the power transfer. A refinement of the method involves an anisotropic shield, permitting compensation while reducing losses by providing magnetic decoupling during the self-excitation process.

Armature reaction compensation applied to pulsed synchronous generators by means of a conductive shield (continuous or partially distributed) is always imperfect due to the phase shift of the induced currents and their resultant magnetic field and the transient field penetration. Such apparent imperfections are actually used by electrical machine designers in order to achieve the goal of variability of the internal electromagnetic fields structure of the RPPS in order to adapt itself to the continuous changing power requirements of the EML and launch package in every instant of acceleration [3]; for example, to the condition of a constant acceleration impressed on the projectile requiring, generally, a constant current power supply under a variable, continuously increasing voltage, which drops sharply at the end of launching.

### VARIABILITY OF INTERNAL STRUCTURE OF RPPS FOR EMLS

Phasorial formalism in the Blondel's two reaction theory of synchronous machines, as well as in Doherty and Nickle's, and in Park's transformation [10, 11] shows that the general theory of electrical machinery was conceived for steady-state analysis. Even Kron's [11] generalized theory and its "Application of Tensors to the Analysis of Rotating Machines" is still, in large part, devoted to the same type of treatment. However, the generalized electrical machine theory and the notion of primitive machine offers the best analytical tools for the treatment and evaluation of quality factors (goodness) of the RPPS for EMLS.

Fig. 1 shows the diagram of a synchronous machine as a primitive machine with fictitious axis coils, using the two-axis (direct,  $D$ , and quadrature  $Q$ ) theory [10]. When compared to the normal, primitive machine, fig. 1 takes into account the compensation winding as a nonuniformly-distributed shield. It can characterize in this way a wide spectrum of "compensation" windings, from continuous shields to very selective and asymmetrical windings, obtained through modification of the parameters of the  $m$  winding in the direct axis and the  $n$  windings in the quadrature axis, correspondingly.

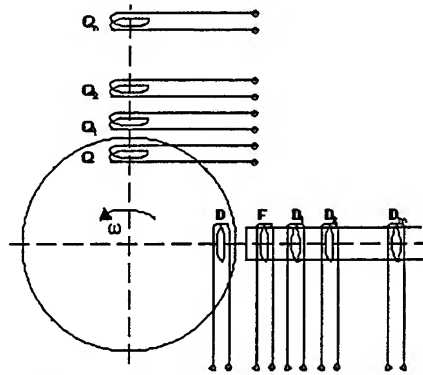


Figure 1. Generalized "primitive" synchronous machine with several (nonuniform) compensation windings.

Since the pulsed power supply has a highly transient behavior, the equations are written using operational calculus formalism, replacing the phasor formalism used for steady state. The equations for the system of coils are written in function of their self and mutual inductances and, for armature coils including the rotation voltage term, leading in the case of fig. 1 to a set of  $(m + 2)$  equations containing  $(m + 2)$  currents, as well as the excitation (field) voltage  $v_f$  and the magnetic flux linkage in the direct axis  $\psi_d$ . The relation between the Laplace transforms of flux, current, and voltage is:

$$\bar{\psi}_d = \frac{X_d(p)}{\omega_0} \bar{i}_d + \frac{G(p)}{\omega_0} \bar{v}_f \quad (1)$$

where  $\omega_0$  allows for the proper dimensionality in (1) above, and:

$$X_d(p) = \frac{a_{(m+1)}p^{m+1} + a_m p^m + \dots + a_1 p + a_0}{b_{(m+1)}p^{m+1} + b_m p^m + \dots + b_1 p + b_0} \text{ is the direct-axis operational impedance.}$$

$G(p)$  has the same denominator as  $X_d(p)$ , but a numerator of  $m$  order only. For the quadrature axis, the elimination of currents from a set of  $(n + 1)$  equations gives, similarly:



$$\overline{\psi}_q = \frac{X_q(p)}{\omega_0} \overline{i}_q \quad (2)$$

where  $X_q(p)$  is the quadrature axis operational impedance being the quotient of two polynomials of order  $n$  while  $\overline{\psi}_q$  is the Laplace transform of the magnetic flux in the quadrature axis.

Equations (1) and (2) apply to the transient regimes. During the steady state operating condition when all the variables in the two-axis reference frame are constant,  $p = 0$  and as an example, the direct axis operational impedance  $X_d(p)$  degenerates into the direct axis synchronous reactance  $X_d$ .

Despite idealizations and linearizations, the operational impedances,  $X_d(p)$  and  $X_q(p)$ , characterize and define very efficiently a large spectrum of different transient behaviors of RPPS for EMLs. In a preliminary design characterization, the direct axis operational impedance  $X_d(p)$  is often used in the form of an operational admittance  $Y_d(p)$  expanded into partial fractions. As an example, in the well-known short-circuit characterization of synchronous generators:

$$Y_d(p) = \frac{1}{X_d(p)} = \frac{(1 + T_{d'0}p)(1 + T_{d''0}p)}{(1 + T_{d'}p)(1 + T_{d''}p)} Y_d \quad (3)$$

where  $T_{d'0}$ ,  $T_{d''0}$ ,  $T_{d'}$ , and  $T_{d''}$  are the principal time constants of the synchronous machine. After expanding into partial fractions and using the canonical notations, we obtain the classical:

$$Y_d(p) = \frac{1}{X_{d'}} + \left( \frac{1}{X_{d'}} - \frac{1}{X_d} \right) \frac{T_{d'}p}{1 + T_{d'}p} + \left( \frac{1}{X_{d''}} - \frac{1}{X_{d'}} \right) \frac{T_{d''}p}{1 + T_{d''}p} \quad (3')$$

The last partial fraction represents the compensation winding as one of the three branches in parallel in the equivalent, modified, direct axis equivalent circuit. A similar modified quadrature axis equivalent admittance is used for design evaluation. It is interesting to see the operational admittance transformed for sinusoidal changes of frequency  $\omega$  in which replacing  $p$  by  $j\omega$ , we obtain the operational admittance frequency locus in fig. 2 (direct axis).

An alternative approach is the use of Kron's re-establishment of transient dynamical equations from the equivalent circuits and the introduction, by using Kron's method of reference frames, of an interconnection clause [11]. In the first approach (fig. 3), if the transient equations of the machine (pulsed generator) or of a group of machines (pulsed generator and electromagnetic launcher) are required, they can be obtained from the equivalent circuit containing the variable frequency feature. The transient system is found by replacing  $f$  by the  $p/j$  operator, where  $j$  is the imaginary unit. The transformation for the reference frames is described in [11]. The interconnection clause is used not only to study the power supply (compensated synchronous generator) together with the electromagnetic launcher, but also to include the process of self-excitation as the interconnection of separate equivalent circuits.

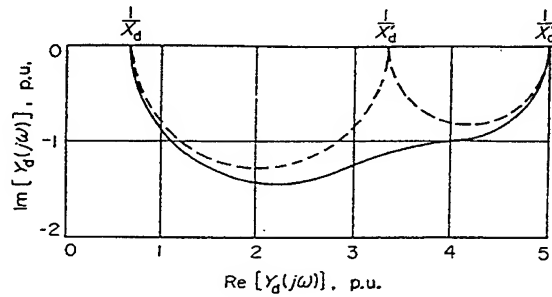


Figure 2. Operational admittance frequency loci on direct (d).

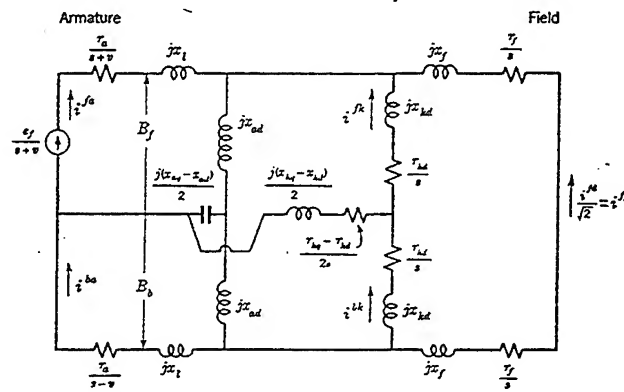


Figure 3. Generalized transient equivalent circuit (Kron).

#### QUALITY INDICATORS AND ELECTRODYNAMICS SIMILITUDE CRITERIA FOR CLASSICAL ELECTRICAL MACHINES

The theory of electrical machine design [7, 8, 9] called in [13] "an esoteric preoccupation of the few" uses a complex methodology to arrive to an optimal design. Such methodology can be formally checked and verified at each logical step, the procedures, being almost canonical, matured for more than a century and reaching asymptotically a level which has remained almost flat for the last forty years. Several quality indicators, similitude criteria, and scaling laws will be reminded to the reader.

##### A. Mean Shear Stress (MSS) and Mean Apparent Shear Stress (MASS).

The design of electrical machines starts from the average tangential force referred to the peripheric area of the armature: Mean Shear Stress,  $\tau$  [7]:

$$\tau = \frac{1}{\pi^2} \cdot \frac{P_i}{n} \cdot \frac{1}{D^2 l_i} = \frac{2M}{\pi D^2 l_i} \left[ \frac{J}{m^3} \right] \quad (4)$$

where:  $P_i$  = interior power of the machine (w),  $n$  = rotational speed (rps),  $D$  = armature diameter (m),  $l_i$  = ideal armature length (m) and  $\frac{P_i}{2\pi n}$  represents the torque,  $M(N \cdot m)$ ; The surface density of the tangential force is a measure of the instantaneous electromagnetic utilization of the machine. From [7] and [8]; the MSS -  $\tau$  can be expressed as:

$$\tau = \xi_E \xi \bar{A} \bar{B} \cos(E, I) \quad (5)$$

where  $\bar{A}$  = the average current sheet (A/m),  $\bar{B}$  = the average magnetic flux density in the air gap, per pole (T),  $\xi_E$ ,  $\xi$  = distribution winding coefficients, and  $\cos(E, I)$  = interior power factor. The a. c. synchronous generators are designed for their apparent interior (volt ampere) power ( $S_i$ ) and not for their active (watt) power ( $P_i$ ).

$S_i = \frac{P_i}{\cos(E, I)}$ . The apparent surface density of the tangential force (or the Mean Apparent Shear Stress - MASS), resulting from the use of  $S_i$  instead of  $P_i$ , is denoted by  $\tau_s$ :

$$\tau_s = \frac{\tau}{\cos(E, I)} = \xi_E \xi \bar{A} \bar{B} \left( \frac{J}{m^3} \right). \quad (5')$$

The values of  $\tau_s$  in function of electromagnetic loading are dependent on the number of phases of the machine: for a single phase machine  $\tau_s = 0.390AB$ ; for a triphase machine,  $\tau_s = 0.675AB$ .

#### B. Electrodynamics Similitude and Scaling Relations

The apparent interior power:  $S_i = mEI$  (VA) is the product of number of phases  $m$ , phase current  $I$  (A) and phase electromotive force  $E$  (V).  $E = \pi\sqrt{2}\Phi f w k_w$  (V) where:  $\Phi$  is the fundamental of main magnetic flux (Wb),  $f = pn$  = frequency (rps), and  $k_w$  = winding factor. The flux  $\Phi$  can be expressed as:

$$\Phi = B_\delta \frac{2}{\pi} \tau_p l_i \quad (6)$$

where:  $B_\delta$  = flux density in the air gap (T),  $\tau_p$  - polar pitch (m), and  $l_i$  = ideal length (m). If the phase current  $I$  is expressed in terms of the sheet of current density  $A$  (A/m):

$$A = \frac{2mIw}{\pi D} \quad (7)$$

Substituting (5), (6), and (7) in (5'), the fundamental formula relating the apparent power, geometrical dimension and the rotational velocity  $n$  (rps) is obtained:

$$S_i = \frac{\pi k_w}{2\sqrt{2}} (2p\Phi)(\pi DA) \quad n = \frac{\pi^2 k_w}{\sqrt{2}} D^2 l_i \quad n \quad AB_\delta = (2p)\sqrt{2}f k_w (\tau_p)^2 l_i B_\delta A. \quad (8)a, b, c$$

For classical machines, the expressions 8 (a, b, c) are usually translated in the simple form of a "machine constant" as the power per unit speed obtained from the armature unit volume. A more elaborate analysis shows that the power increases faster than the cube of the linear dimensions of the electric machine, let the current density  $J$  be expressed as:

$$J = \frac{At_1}{H_{cu} b_{cu}} = \frac{A}{h_c \beta k_{cu}} \left( \frac{A}{m^2} \right) \quad (9)$$

where  $h_c$  is the height of the slot and  $\beta = \frac{b_c}{t_1}$ , the ratio between the slot width to the slot pitch, and the copper filling coefficient of the slot:

$$k_{cu} = h_{cu} b_{cu} / h_c b_c.$$

The average flux density along the tooth is obtained from:

$$B\zeta k_{Fe} = B_\delta \quad (10)$$

where  $\zeta = \frac{b}{t_1}$  is the ratio between the average width of the tooth to the slot pitch and  $k_{Fe}$  is the ratio between the net length of the active ferromagnetic iron to the total length of the armature. Then, 8(a, b, c) can be transformed as:

$$S_i = \frac{\pi^2 k_w}{\sqrt{2}} \beta k_{cu} \zeta k_{Fe} D^2 l_i n h_c J B = (2p) f \sqrt{2} k_w \frac{\tau^4}{\lambda} k_{cu} \beta_1 J B \quad (\text{where } \delta = \tau/l_i), \quad (11)a, b$$

leading to the conclusion that in electrical machines, with similar geometry the apparent power increases proportionally to the linear dimensions to the forth:

$$S_i = kL^4 \text{ or } L = \frac{1}{k'} \sqrt[4]{S_i} \text{ or } L = \frac{1}{k'} (S_i)^{\frac{1}{4}}. \text{ The weight of machine } G \text{ is: } G = k_2 L^3 = k_2' (S_i)^{\frac{3}{4}}$$

#### ACTIVE CONDUCTOR ELECTROMAGNETIC POWER CONVERSION DENSITIES

In spite of the appearance of describing the local power density, the density obtained in the last two paragraphs of the previous chapter is an average one since its definition involves the rated apparent power of the entire machine.

The local power density in the condition of lossless electromechanical power conversion per unit volume of active conductor of the generator, is:

$$-(\vec{J} \times \vec{B}) \cdot \vec{u} = (\vec{u} \times \vec{B}) \cdot \vec{J}$$

which, multiplied by the elementary volume,  $dv$  is the truly local definition of instantaneous conversion. The "active conductor" is the seat of the power conversion and by the principle of equality of action and reaction, is equally felt in both the stator and rotor of the electromechanical converter.

The flux density  $\vec{B}$  in expression (12) is the vectorial sum of the impressed excitation field  $\vec{B}_{imp}$  and the induced field by the armature reaction,  $\vec{B}_{a,ind}$  (invoking the Lenz rule) such that:

$$[-\vec{J} \times (\vec{B}_{imp} - \vec{B}_{a,ind})] \cdot \vec{u} = [\vec{u} \times (\vec{B}_{imp} - \vec{B}_{a,ind})] \cdot \vec{J}.$$

A "compulsator" exploits the manner in which the two  $\vec{B}$  vectors add (or rather subtract) in different moments of discharge. Controlling the compensation, by eliminating partially the direct axis shield and allowing the armature reaction in the initial moment of discharge to almost completely demagnetize the armature field  $B_{imp} - B_{a,ind} \approx 0$ ; and gradually, after that, to reach a high degree of compensation in the latest moments of launching, the machine will apply a voltage linearly increasing from zero to maximum, the ideal one for EMLs.

For large RPPS, this solution leads to a more compact system than the one proposed in [14] by Driga in which, in a polyphase compensated generator, the output wave shape, and magnitude are solid-state controlled, thus decoupling the velocity of the generator and output wave control. The same relation applies to the launcher in which the back *emf* is locally described as the motional field  $(\vec{u}_a \times \vec{B}_a)$ , increasing

linearly with the projectile velocity  $\bar{u}_a$  and, for a constant current (and constant acceleration), increasing ideally from zero to the exit velocity.

#### THE "GOODNESS FACTOR" CRITERION: IS IT TOO SIMPLISTIC?

The criterion of "Goodness" of an electrical machine was introduced by Laithwaite in [6] as a means of comparing the relative performance (from the design point of view) of different electrical machines. It had to be an objective measure of the ability of the electrical machine to convert power electromechanically - a property which is more general than, for example, the efficiency which can be increased at the expense of other indicators of vital importance to the machine operation.

Since the electromechanical power conversion is determined by the coupling of the electric and magnetic circuits, Laithwaite defined it as the proportionality:

$$G \approx \frac{1}{\text{Resistance}} \times \frac{1}{\text{Reluctance}} \times \text{frequency} \text{ or } G \approx \left( \frac{A_e}{\rho l_e} \right) \times \left( \frac{\mu_0 A_m}{l_m} \right) \times f. \quad (12')$$

This is a simplistic approach to quality of a design and is based on the ability of an electric circuit to produce current ( $I$ ) for a given electromotive force ( $E$ ), namely  $\left( \frac{I}{E} \right)$  combined with the ability of a magnetic circuit to produce flux for a given magnetomotive force  $I'$ , namely  $\left( \frac{\Phi}{I'} \right)$ . The product  $\left( \frac{I}{E} \right) \times \left( \frac{\Phi}{I'} \right)$  is made dimensionless by multiplying it with the frequency. It is an imperfect approach to "goodness," but leads to interesting inferences. For instance: In the example considered by Laithwaite [6], the length of the magnetic circuit is equal to the thickness of the gap. What happens to the "goodness factor" in the case of air core machines considered, almost exclusively as RPPS for EMLs and made entirely of "gap?"

According to the chapters paragraph, the generalization of the "goodness factor" for pulsed, transient machines requires the replacement of the simple reluctance and resistance by corresponding very complex operational impedances in a dimensionless form, containing (as suggested by Kron) a connection clause. Such clause permits adding to the same expression the contribution of the launcher and the self-excitation stages, considered as intermediate interconnected machines. In such generalized "goodness factor," the frequency is replaced by the square root of the ratio between the machine discharge time  $t_d$  and the thermal time constant of the power supply  $\tau_i$

namely  $\sqrt{\frac{t_d}{\tau_i}}$ . This factor takes into account the scaling of the machine from steady-state to short pulse discharge. Then the "generalized goodness" is

$$GG \approx \frac{\bar{Y}_1(p) \cdot \bar{Y}_2(p) \dots \bar{Y}_k(p)}{\omega_{01} \cdot \omega_{02} \dots \omega_{0k}} \sqrt{\frac{t_d}{\tau_i}} \quad (12)$$

where the factors  $\omega_{01} \dots \omega_{0k}$  at the denominator make dimensionless the product of the partial operational admittances at the numerator.

In a subsequent paper, such generalized goodness will be constructed, evaluated, and compared for pulsed machines already built - such as the "Cannon Caliber Compulsator" and compared to more traditional quality factors.

### AIR CORE VERSUS IRON CORE

RPPS as reported in the literature are in majority air core synchronous machines. The listed advantages are a) the absence of ferromagnetic materials, allowing a high magnetic flux density in the air gap, well above the saturation limits: (2.4 Tesla for the Task C Compulsator and 2 Tesla for the "Cannon Caliber Compulsator," as reported in the public domain literature) and b) the use of new, high-performance, composite materials.

1. There are serious drawbacks for both such departures from the classical ferromagnetic machines. The first is related to the air core structure. In order to obtain flux density  $B = 2.4$  Tesla, a magnetic field intensity  $H = 1.91 \cdot 10^6 \text{ A/m}$  is needed, compared with two orders of magnitude less  $\sim 18,000 \text{ A/m}$  for Permendur for the same flux density or  $\sim 9,000 \text{ A/m}$  in order to obtain 1.8 Tesla using high-permeability silicon steel. Is the increase in  $B$  worth the extremely high price paid in the magnetomotive force necessary for excitation, even in self-excitation conditions?
2. The second, but with more far-reaching effects, is the magnetic field distribution around the excitation coil for the air core magnetic circuit when compared to iron core systems. It refers to the leakage flux, the magnetic flux linked with the conductors of the field winding only, without linking the armature winding. The median line (fig. 4) of the stator ( $S$ ) must be at a distance sufficient to accommodate the composite wrap needed to contain the heavy excitation winding on the rotor, spinning at very high velocities, the air gap itself, and the insulation and confinement wrap of the stator. To such distances, we must add half the thickness of the rotor and stator windings, respectively. Assigning relative numbers, we find that the magnetic flux crossing the second median line ( $S$ ) is almost half of the total produced flux compared to more than 90% in ferromagnetic machines.
3. As an extension of paragraph above which considers the flux magnitude, the flux density angle is unfavorable in the air core machines [7]. In all the electrical machines, the magnetic flux must cross the conducting medium in order to induce the electromotive forces leading to currents and electromechanical conversion.

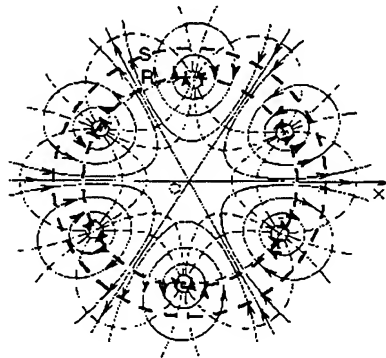


Figure 4. Referring to the leakage factor of an air core, multipole excitation system.

For a higher efficiency, the crossing must be done at an angle of  $90^\circ$  between the flux and the conducting medium - which is idealized as a thin current sheet, but which usually consists of separate strips of copper embedded in slots, cut in the structure of the armature, as close to the air gap as possible.

For ferromagnetic structures, even at high saturations (see fig. 5), the  $B$  crosses the conductor at almost  $90^\circ$  - even at very high saturation level and low angle of

incidence. The maximum value for the product  $(J \times B) \cdot \vec{u}$  is obtained for all the iron core design, without requiring any effort.

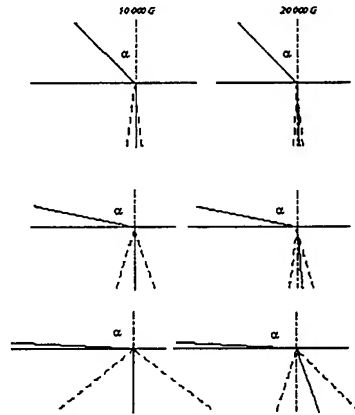


Figure 5. Refraction of B-field of 1 and 2 Tesla lines for different angles of incidence. (Dotted lines show the contribution of armature mmf of  $A = \pm 32,000 A/m$ ..

### CONCLUSION

The introduction of a generalized "goodness factor" for RPPS for EMLs is possible through the use of interconnected operational admittances, not only for the power supply, but for accelerator and self-excitation system, as well. Such a "goodness factor" is actually a complex transient function describing the comparative interplay of several magnetic and electric circuits in the condition of rapid conversion. Additionally, several other quality indicators and similitude criteria from the classical electrical machine theory must be taken into account.

### REFERENCES

- [1] A.L.O. Fauchon-Villeplée, Canons Electriques, (book), Berger-Levrault, 1920.
- [2] W. F. Weldon, M. D. Driga, and H. H. Woodson, "Compensated Pulsed Alternator," U. S. Patent 4,200,831, April 29, 1980.
- [3] M. D. Driga, et al., "Design of Compensated Pulsed Alternators with Current Waveform Flexibility," Proceedings of the 7th IEEE Pulsed Power Conference, Washington, D. C., June 28 - July 1, 1987.
- [4] M. D. Driga, et al, "Advanced Compulsator Designs," IEEE Transactions on Magnetics, Vol MAG 25, pp. 142-146, January, 1989.
- [5] F. Jamet, "Introductory Address," Proceedings of the 5th European Symposium on EML Technology, Toulouse, France, April 10-13, 1995, page 1.
- [6] Eric R. Laithwaite, Induction Machines for Special Purposes, Chemical Publishing Co., 1966.
- [7] R. Richter, Elektrische Maschinen, Band 1, 2, Birkhauser Verlag, Basel, 1967.
- [8] E. Levi, M. Panzer. Electromechanical Power Conversion. Dover Publications, Inc., New York, 1974.
- [9] J. Chatelain, Machines Electriques, Vol 1, 2, Dunod, Paris, 1993.
- [10] B. Adkins, R. G. Harley. "The General Theory of Alternating Current Machines." Chapman and Hall, 1986.
- [11] G. Kron, Application of Tensors to the Analysis of Rotating Electrical Machinery, General Electric Review, 1942.
- [12] J. M. Pestarini, Metadyne Statics (1952), MIT Press and John Wiley and Sons, Inc.
- [13] H. C. J. de Jong, A. C. Motor Design: Rotating Magnetic Fields in a Changing Environment, Hemisphere Publishing Corporation, 1989.
- [14] M. D. Driga, "Metadynes as Pulsed Power Electrical Machines for Use in Advanced Robotics." The 10th IEEE Pulsed Power Conference Proceedings, pp. 1005-1012.

**PRELIMINARY FINDINGS ON MAGNETIC SHIELDING  
EFFECTIVENESS  
FOR  
ELECTROMAGNETIC (EM) RAILGUN APPLICATIONS**

*Calvin Le, and Alexander Zielinski  
US Army Research Laboratory  
Attn: AMSRL-SE-DE  
2800 Powder Mill Road  
Adelphi, MD 20783-1197  
USA*

**ABSTRACT**

There is a need for the development of a lightweight electromagnetic shield that can be easily installed and maintained for use in electromagnetic (EM) railgun applications. This type of gun generates electromagnetic fields whose dominant energy spectrum frequency component lies between tens of hertz (Hz) and a few kilohertz (kHz). For low-frequency magnetic shielding, thick magnetic materials are typically used, which drastically increases the system weight. A lightweight multilayered material such as TI-Shield, manufactured by Texas Instruments, Inc., has been developed to provide low-frequency magnetic shielding. Subscale magnetic shielding tests were conducted on a 15-mm squared-bore railgun to evaluate its performance.

**1. Background**

Electromagnetic (EM) launcher systems are emerging systems that are of increasing importance to the armed forces. Included in this category are the EM railguns, EM induction plate launcher, electrothermal gun (ET), and electrothermal-chemical gun (ETC). The EM environments generated by these devices and their associated pulse power system have not been experienced before in fielded military applications. These fields may not only be a concern for the traditional electromagnetic interference (EMI) and electromagnetic compatibility (EMC) effects, but they may also affect biological systems.

Although all of the above EM launcher systems are in the prototype stages, the electromagnetic environment (EME) associated with these systems should be addressed. It is much more economical to identify and correct potential concerns during the design phase than at the deployment phase. The EMI and EMC issues can be defined from theoretical predictions and experimental observations of laboratory models. With only a few exceptions, the results will scale to actual system dimensions. Over the last decade, there has been steadily increasing attention, at both national and international levels, on the potential adverse effects of EM fields in the extremely low frequency (ELF) range on biological systems. It is interesting to note that papers presented on this issue by leading figures at international conferences and workshops in recent years could not provide conclusive evidence of any adverse biological effects resulting from exposure to ELF fields.



## 2. Introduction

The essential features of a simple EM railgun are illustrated in Fig. 1. A robust pulsed power source provides a burst of energy lasting several milliseconds that accelerates the armature/projectile down the length of the launcher; the armature/projectile eventually leaves the railgun with a velocity in the kilometers per second range. Intense EM fields are generated due to railgun current, which is typically on the order of hundreds kiloamperes (kA). Experimental measurements were conducted to obtain the EM environment [1]. An analytical solution also has been developed to predict the transient magnetic field given the railgun parameters [2,3]. To reduce this magnetic field environment without seriously degrading the performance of the railgun, magnetic shielding material is needed to enclose the EM environment. Different thickness of TI-Shield materials are used for this task. TI-Shield is a lightweight, composite, multilayered, shielding material consisting of copper-permalloy 49-copper. These layers which are bonded by a cladding process, are available in sheets ranging in thickness from 0.25 mm-0.63 mm. A near-field planar magnetic field insertion loss measurement on the test samples was conducted to quickly evaluate the performance of the material before it was applied on the railgun. Magnetic shielding effectiveness (MSE) tests were conducted on a 15-mm squared-bore railgun to evaluate the TI-Shield performance during the shorted rail tests and live-fire tests.

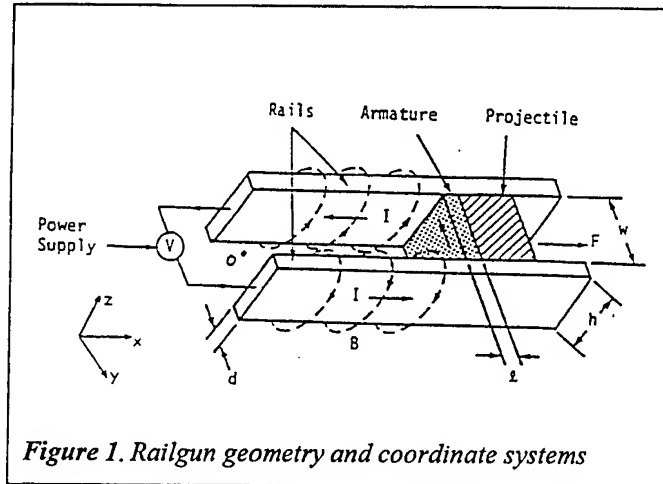


Figure 1. Railgun geometry and coordinate systems

TI-Shield is a lightweight, composite, multilayered, shielding material consisting of copper-permalloy 49-copper. These layers which are bonded by a cladding process, are available in sheets ranging in thickness from 0.25 mm-0.63 mm. A near-field planar magnetic field insertion loss measurement on the test samples was conducted to quickly evaluate the performance of the material before it was applied on the railgun. Magnetic shielding effectiveness (MSE) tests were conducted on a 15-mm squared-bore railgun to evaluate the TI-Shield performance during the shorted rail tests and live-fire tests.

## 3. Experimental Description

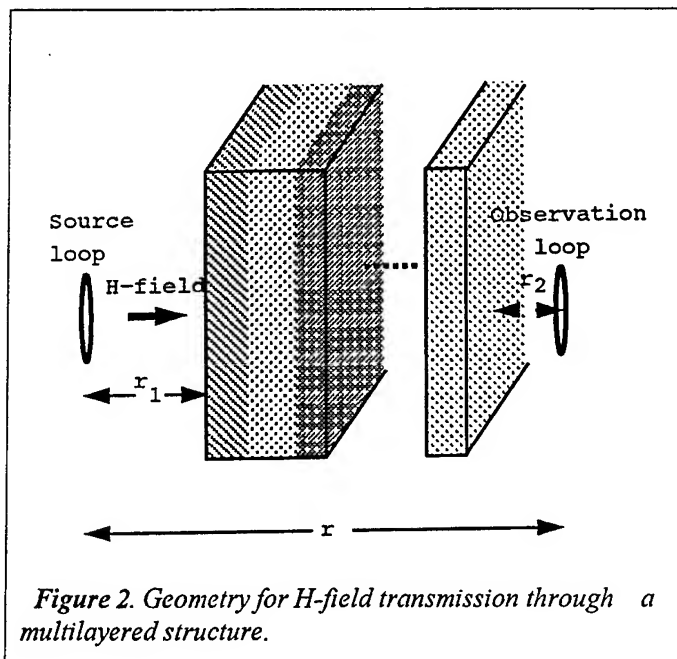
### A. Simple Railgun

In our experiments the rails are copper, with the following dimensions: height,  $h = 19$  mm; thickness,  $d = 10$  mm; width,  $w = 15$  mm; and length,  $l = 1$  m. The bore insulators are fabricated from a fiberglass and epoxy laminate (G-11), and with the rails form a bore having a cross-section of 15 mm x 15 mm. The containment structure for the bore components consists of two clamped housings. Each housing is composed of alternating 2-mm-thick stainless steel plates and glass/epoxy lamination. The armature is fabricated from 6061-T6 aluminum and has a mass of 7 grams. The gun can also be used with a "shorting block." This "shorting block," which is bolted between the rails roughly 5 cm from the railgun muzzle, acts like stationary armature.

The gun is supported by a wooden platform 1 m above the ground plane. The coordinate system used for the EM field measurements is centered between the rails and has its origin at the breech, as indicated by  $O$  in Fig. 1 (a). The railgun plane of symmetry is the  $xz$ -plane, whereas the plane containing the rails is the  $xy$ -plane. The test point location is defined by its  $(x,y,z)$  coordinates, in centimeters (cm). Testing took place at the EM Facility, Aberdeen Proving Ground, MD. The facility consists of a 1.6-MJ capacitor based pulse power supply (PPS) with over 200 m of free-flight range [4]. The PPS comprises eight banks, each with the flexibility to be charged to different initial voltages, as well as to be triggered independently in time. The railgun is connected to the PPS output plates via four high-power coaxial cables.

### B. Planar MSE Setup

Near-field insertion loss was obtained on 31 cm by 31 cm samples. The H-field attenuation was measured for several samples of TI-Shield. Data were also taken on a pure copper panel for comparison. The near-field technique uses the rapidly decaying fields in the near zone of an antenna to isolate the measurement. The EM fields produced by an electrically small antenna fall as  $1/r^3$  if  $r$  is kept much less than the wavelength of interest. This behavior provides isolation from the leakage field while using a relatively small test sample and no Faraday enclosure. The test setup consisted of two small transmitting and receiving multiple-turn loop antennas that are placed 5 cm apart, as shown in Fig 2. The resulting path length ratio between the leakage field and those directly penetrating the material is approximately 6 to 1 [5]. Thus, the measurement dynamic range of the near-field test configuration is at least 47 dB.



### C. Cylindrical MSE Setup

A cylindrical plastic tube was used to electrically isolate the TI-Shield material from the railgun. The TI-Shield was wrapped around the 15 cm diameter by 1 m long tube. Multiple-turn loop antennas, to sense the time rate of change in magnetic induction field ( $dB/dt$  or  $B\cdot$ ), were placed above the center of the gun (50, 0, z),

and near the gun muzzle (90, 0, z) during the shorted rail test to compare the magnetic shielding effect of the TI-Shield along the rail.

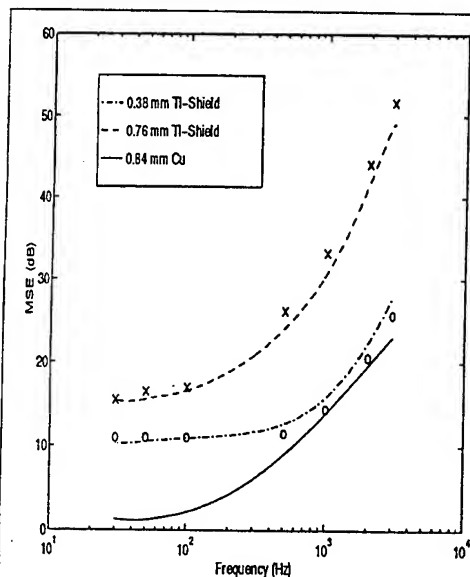
#### 4. Experimental Results

##### A. Planar MSE

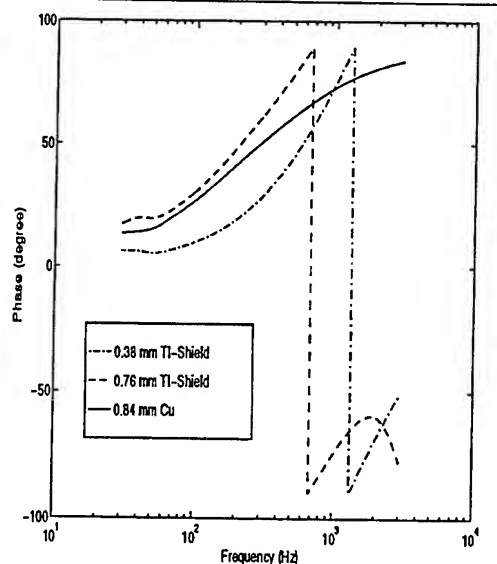
TI-Shield which is under investigation for its EM shielding properties, is constructed of copper/permalloy 49/copper with the total thickness of copper and permalloy being 40% and 60% of the TI-Shield thickness, respectively. We define the magnetic field shielding effectiveness,

$$MSE = -20 \log \left| \frac{H_b}{H_a} \right|,$$

as the ratio of the field before,  $H_b$ , and after,  $H_a$ , shielding is applied at antennas



**Figure 3.** Magnetic shielding effectiveness at  $r = 5\text{cm}$ . Calculated values indicated with markers.



**Figure 4.** Phase angle differences of the magnetic fields with and without shield at  $r = 5\text{cm}$ .

separation distance. It is important to note that the MSE level is strongly dependent on the antennas locations. Figure 3 shows the theoretical results [6] and experimental data for the MSE of one layer of 0.38-mm TI-Shield and two layers of 0.38-mm of TI-Shield, respectively. The theoretical results are based on the transmission line theory. Figure 3 includes the MSE of 0.84 mm thick copper sheet for comparison. Although the MSE of TI-Shield material has performed well, the phase angle of the ratio ( $H_b / H_a$ ) is not constant for the whole frequency spectrum, as shown in Fig. 4.

## B. Cylindrical MSE

A combination of 0.2 mm, 0.38 mm, and 0.63 mm of TI-Shield is used to determine the best configuration for magnetic shielding. Two conditions were studied: shorted rails and live-fire.

In the shorted rail experiment, we applied a double-exponential pulse current to a stationary armature located 5 cm from the muzzle. The rail current has a rise-time of 0.38 ms

and a peak amplitude of 260 kA. This generated an EM environment that was quasi-static and directly related to the rail current distribution. Magnetic field data were obtained before and after the application of TI-Shield at several locations, as shown in Fig. 5. As expected, the magnetic field environment decays roughly as the square of the distance. Selected magnetic field environments with and without different TI-Shield thickness are displayed in Fig. 6, and 7. Note that the reduction in magnetic

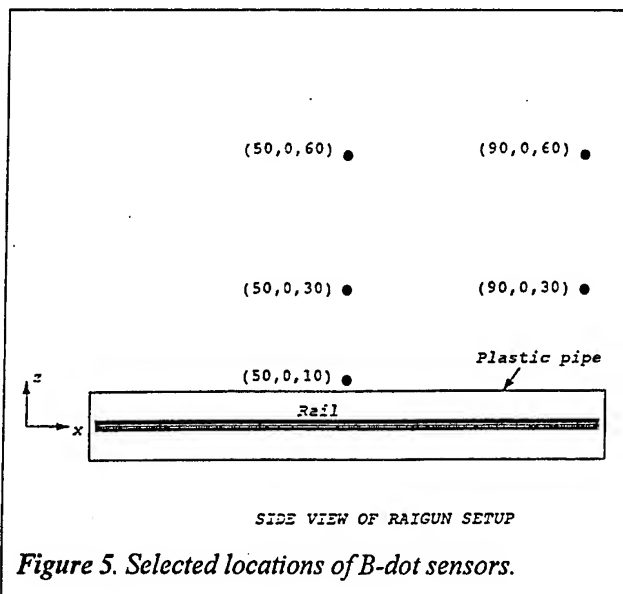


Figure 5. Selected locations of B-dot sensors.

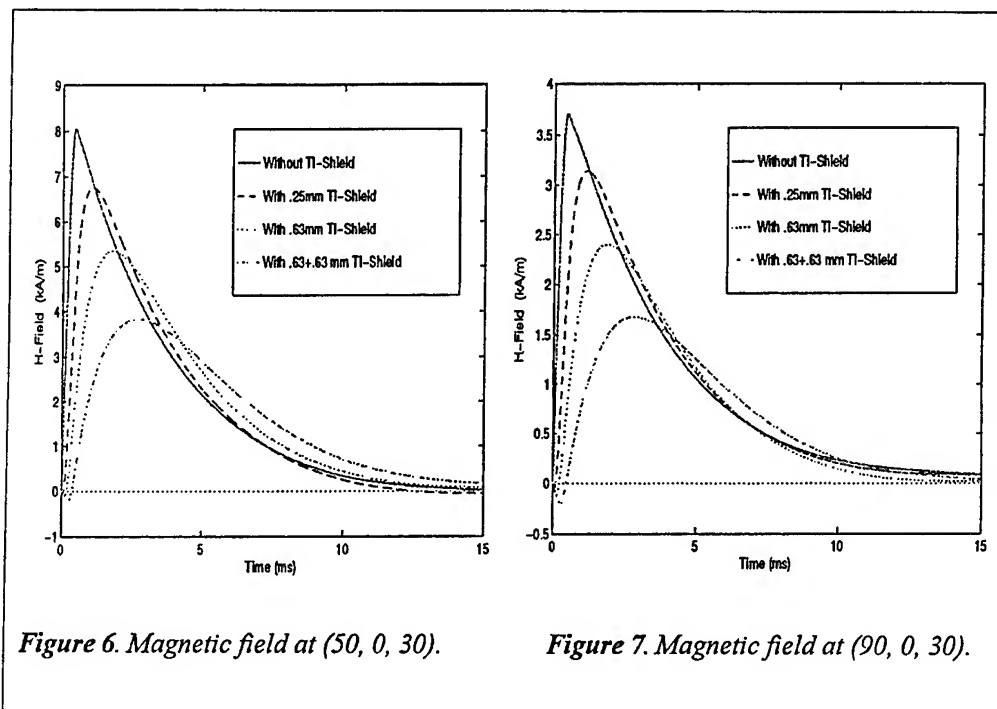
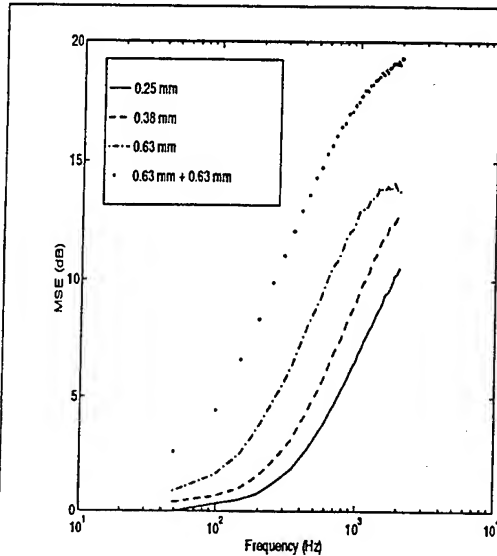


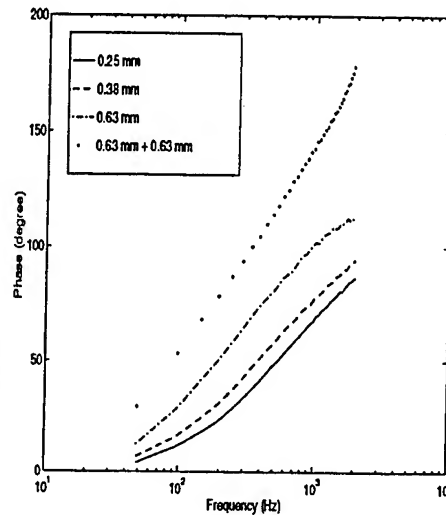
Figure 6. Magnetic field at (50, 0, 30).

Figure 7. Magnetic field at (90, 0, 30).

field near the muzzle is on the same order of magnitude as the measurements made near the center of the gun. In the early time, the magnetic field with TI-Shield shielding was larger than expected. This may be due to the saturation effects of the permalloy within the TI-Shield. Furthermore, TI-Shield enhances the magnetic field environment at the later time. This phenomenon is due to a long diffusion time in the shield associated with a slow incident waveform. As illustrated in Fig. 8 and 9,



*Figure 8. Magnetic shielding effectiveness of figure 6 for  $r = 30$  cm.*

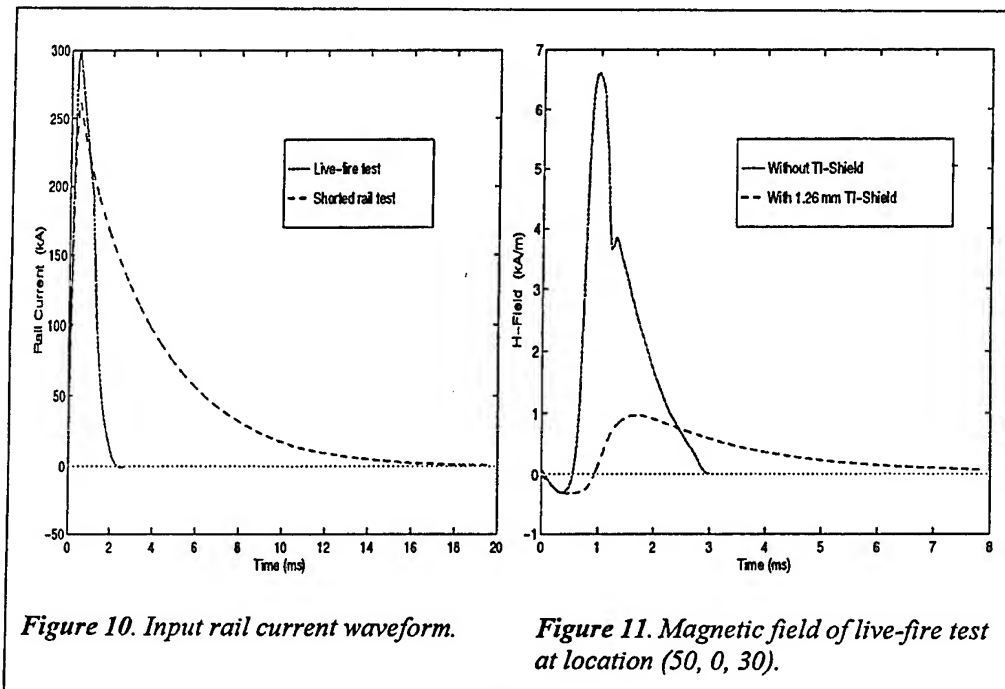


*Figure 9. Phase angle differences of figure 6 for  $r = 30$  cm.*

although the MSE of Fig. 6 has shown positive reduction across the frequency spectrum, there were also changes in the phase of the magnetic field before and after the shield was applied. Hence, care must be taken when one evaluates the performance of the shield in the frequency domain for transient pulse application. Test data have also shown that the MSE of the TI-Shield is determined by the total thickness of the material rather than the order of multiple layers for frequencies below 2 kHz. For example, the magnetic field environments with 0.63 mm + 0.63 mm TI-Shield is almost identical with the magnetic field environments of 0.25 mm + 0.38 mm + 0.25 mm + 0.38 mm layers of TI-Shield.

During the live-fire test, the EM environment is more complex and includes nonlinear effects such as muzzle arcing and velocity skin effect. The time duration of a 300-kA peak rail current is much shorter than the aforementioned shorted rail tests, as shown in figure 10. The armature exits the railgun at 1.1 ms with the velocity of

1670 m/s. Thereafter, the slope of the rail current changes due to the high impedance arc at the muzzle. With and without TI-Shield, the exit velocity of the armature, as determined by the in-bore dB/dt sensors, indicates no degradation of the launcher performance. Certainly, more accurate measurements of exit velocity are needed to



fully assess the quality of the impact of the shield material on the system. Figure 11 shows the comparison of the measured magnetic field with and without 1.26-mm-thick TI-Shield. Unlike the shorted rail test, the magnetic field environment due to the live-fire test is highly dependent on the armature location. It is also interesting to note that with the shorter incident magnetic field pulsewidth, due to the shorter input current waveform, better shielding performance is observed for the live-fire test in comparison with the shorted rail test.

## 5. Conclusion

Preliminary test data have shown that, for the live-fire test, TI-Shield provides excellent low frequency magnetic shielding without the weight penalty. One concern for the application of the TI-Shield onto the railgun is the degradation of gun performance. The shielding material has the tendency to reduce the inductance of the launcher, which will lower the gun performance. However, based on the preliminary live-fire test data, use of the TI-Shield material resulted in no measurable effect on the gun performance. Another concern is the saturation value of the TI-Shield material along with its realistic permeability values after bending, forming, and welding. Hence, additional test data are needed to provide more information on the relationship of the shield versus the gun performance, and the saturation issues associated with the TI-Shield or other shielding materials.

### *Acknowledgements*

The authors would like to thank Mr. Ken Paxton for his significant contributions in setting up the test site. We also thank Dr. Ira Kohlberg and Dr. Jerry Parker for many helpful discussions.

### *References*

1. W. Coburn, C. Le, D. DeTroye, W. William, and G. Blair, "Electromagnetic field measurements near a railgun," *IEEE Trans. on Magn.*, Vol. 31, No. 1, pp 698-703, January 1995.
2. I. Kohlberg, and W. Coburn, "A solution for the three dimensional railgun current distribution and electromagnetic fields of a rail launcher," *IEEE Trans. on Magn.*, Vol. 31, No. 1, pp 628-633, January 1995.
3. I. Kohlberg, and C. Le, "Modelling magnetic fields produced by railguns using principles of conformal mapping in combination with numerical electromagnetic techniques," *5th European Symposium on EML Technology*, Toulouse (France), May 1995.
4. A. Zielinski, "Preliminary assessment of recoil in a 15 mm solid armature railgun," *Proceedings of the 11th Electromagnetic Launcher Association Meeting*, Huntington, West Virginia, September 1993.
5. J. Latess, C. Le, and J. Jaucian, "Investigations on the use of near-field measurements to determine the effective conductivity of composite materials," Army Research Laboratory, ARL-TR-707, July 1995.
6. C. Le, "Electromagnetic characteristics of multilayered materials," Army Research Laboratory, ARL-TR-636, February 1995.

# Electromagnetic Launch Technology: A Review of the U.S. National Program

Harry D. Fair

Institute for Advanced Technology, The University of Texas at Austin  
4030-2 W. Braker Lane, Suite 200, Austin, Texas 78759-5329

**Summary** — The U.S. efforts in electric launch are largely focused on specific fundamental physics and engineering challenges in pulsed power, power conditioning, armatures, launch packages, electromagnetic and electrothermochemical launchers and the introduction of new or novel materials and diagnostics to resolve these challenges and integration of these elements into practical electric launch systems. Major significant technical achievements have occurred in all of the critical technical areas. The successful integration of these technologies provides a new paradigm in the design of mobile combat vehicles and enables a new generation of revolutionary all-electric ground combat vehicles.

Details of the U.S. research in electromagnetic and electrothermal chemical (ETC) launch technology have been published biennially as a special January edition of the *IEEE Transaction on Magnetics* [1]. This publication represents selected scientific contributions which have been presented at the biennial Symposia on Electromagnetic Launch Technology (EML) and were accepted by the *IEEE* for publication. The intent is to ensure a high quality of research and provide an archival record of the development of this science and technology.

A summary of the major U.S. research results and achievements since the 7th EML Symposium (April 1994) was presented at the 8th EML Symposium which was held in Baltimore, Maryland, in April 1996 and is available in the January 1997 *IEEE Transactions on Magnetics* [2]. The purpose of this current presentation is to briefly review the highlights of that presentation and provide an update of major scientific achievements in the U.S. in electric launch science and technology.

During the past decade, the research and technology efforts on electric guns in the U.S. were primarily focused on demonstrating the ability of electric launchers to accelerate large (at least several kilograms) projectiles to velocities higher than can be achieved by conventional chemical propellant-driven guns. These efforts were extremely successful, and there are two large facilities in the U.S. which have each demonstrated the ability to accelerate projectiles to an energy on the order of 9 MJ achieving velocities between 2 and 4 km/sec [3]. Both of these facilities employ large laboratory power supplies and both have successfully demonstrated the basic feasibility of railguns to operate in this hypervelocity regime.

Upon successful demonstration of the acceleration of large masses to hypervelocity, the U.S. research efforts then turned to the acceleration of projectile configurations which have practical utility, primarily for military applications. Interest in accelerating complex guided projectiles to extremely long ranges led to the design and successful experimental testing [4] of components such as accelerometers, miniature valves and related control mechanisms, sensors, and hypersonic aeroshells. Concurrently, integrated projectiles for air defense and anti-armor applications were envisioned. Launch packages integrating heavy metal penetrators, armatures and discarding sabots were demonstrated with base push and mid-riding sabots employing plasma or solid armatures, as shown in Fig. 1 [5].

Power source development for these electric launchers has focused primarily on high energy density capacitors, homopolar generators and more recently, pulsed alternators [6]. Since much of the military interest is in employing electric launchers on some form of mobile tactical vehicle, considerable effort has been directed toward compact high energy, high power sources compatible with repetitive operation, which are capable of meeting the electrical requirements in addition to severe weight and volume constraints. The most successful demonstration of such a power source is the pulsed compensated alternator developed by The University of Texas at Austin Center for Electromechanics (UT-CEM) [7]. This device



is an air core, 4-pole rotating armature, self-excited pulsed alternator. At the full design speed of 12,000 rpm, the composite rotor stores 40 MJ and is capable of delivering 2.5 GW of electric power into its matching 2.21-m long series-augmented railgun. Figure 2 shows the cannon caliber electromagnetic gun (CCEMG) pulsed alternator in the UT-CEM laboratory.

Although there are no presentations from the United States at this Symposium on ETC launchers, a substantial U.S. effort has led to considerable progress in the last several years. The contributions by Oberle et al. [8] have demonstrated significant improvement in understanding the plasma ignition/combustion process.

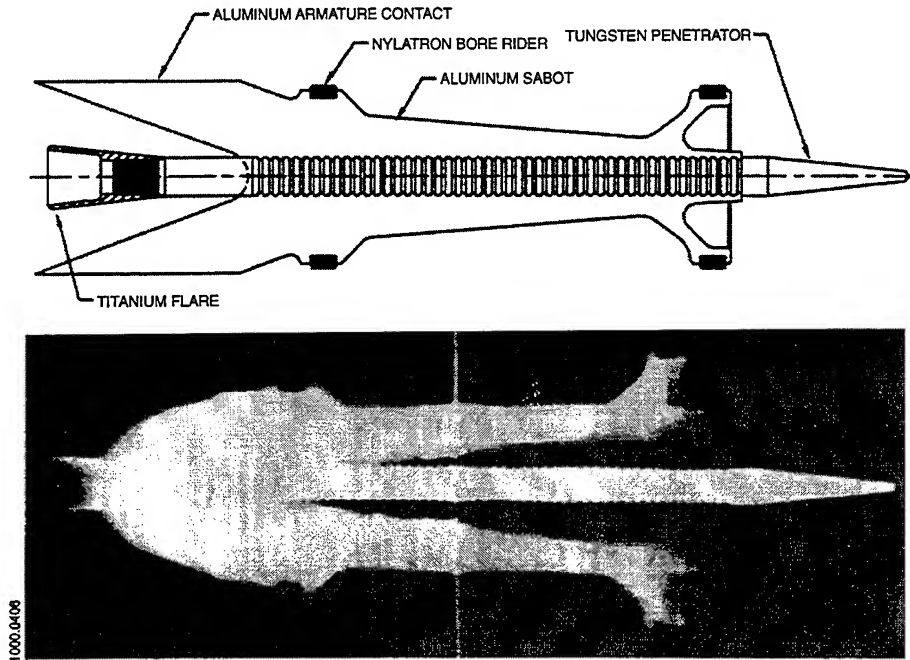


Fig. 1. The long rod with its integrated two-petal aluminum sabot/armature demonstrated mid-riding drive from EM railguns. The muzzle X-ray shows the long rod after a successful launch from the Green Farm 90-mm railgun [5].



Fig. 2. CCEMG pulsed alternator at UT-CEM [7]. Photograph courtesy of UT-CEM.

Recent attention has also been given to the integration of electric launcher components into practical launch systems for a variety of applications. Hypervelocity electric launch of miniature guided interceptors has been investigated as a cost-effective bottom-tier element of the overall U.S. Theater Missile Defense (TMD) architecture. A field experiment [9] performed at Eglin Air Force Base, Florida, led by the Ballistic Missile Defense Organization demonstrated the hypervelocity launch of the D-2 miniature guided interceptor from a 105-mm solid propellant ETC launcher with guidance and control from a novel interferometric radar fire control system (see Fig. 3).

Electric launchers are also being investigated for the direct fire ground combat mission. Dr. Scott Fish et al. [10] are addressing the integration of electric components for an all-electric vehicle in which the electric power is generated at one or more central locations and then distributed to a variety of electric vehicle loads (as shown in Fig. 4). The Army Research Laboratory has assessed the feasibility of mounting an ETC launcher on the M-1 Abrams tank to enhance the lethality without increasing weapon caliber [11].

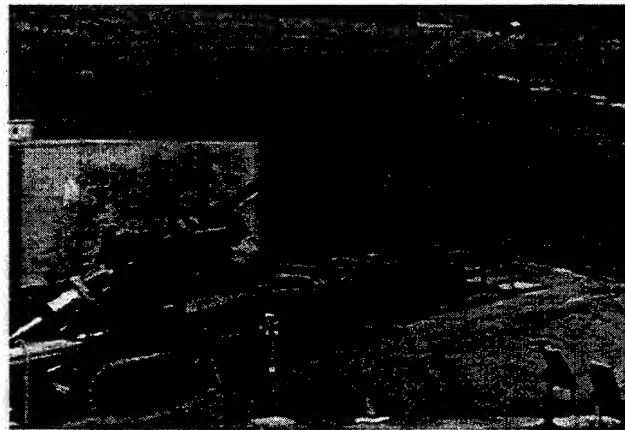


Fig. 3. Photograph of a 105-mm solid propellant ETC hypervelocity launcher mounted on a M-110. Photograph courtesy of Jere Brown, Sverdrup Technology, Inc.

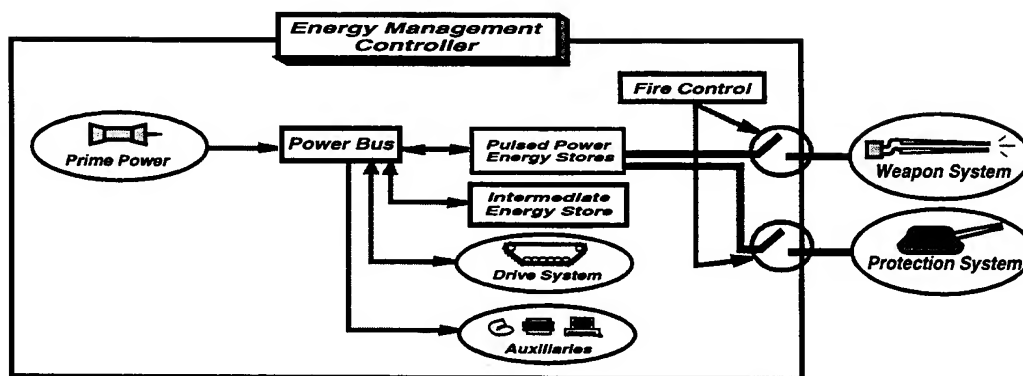


Fig. 4. Simulation architecture [10].

The U.S. presentations at this Symposium represent a broad spectrum of our current research activities. In addition to our efforts to develop advanced pulsed alternators as power supplies, we are evaluating all forms of energy storage as pulsed power sources for electric launchers. Dr. Ian McNab [12] reviews the physical principles of magnetohydrodynamic (MHD) power generation, provides an overview of the cur-

rent state of the art and explores possible application of MHD to provide power for electric launchers. Although MHD power generation is appealing in its elegance since there are no moving parts, attempts to date to use it either for continuous power generation in commercial electric utility power generating plants or for short electric pulse generation for military applications have not proven to be very attractive. The relatively low conductivity of the plasma, low overall system efficiency and requirement for a high magnetic field and accordingly, substantial mass of a magnet system, all serve to limit this interesting technology as a practical power source. The basic MHD generator geometry is shown in Fig. 5.

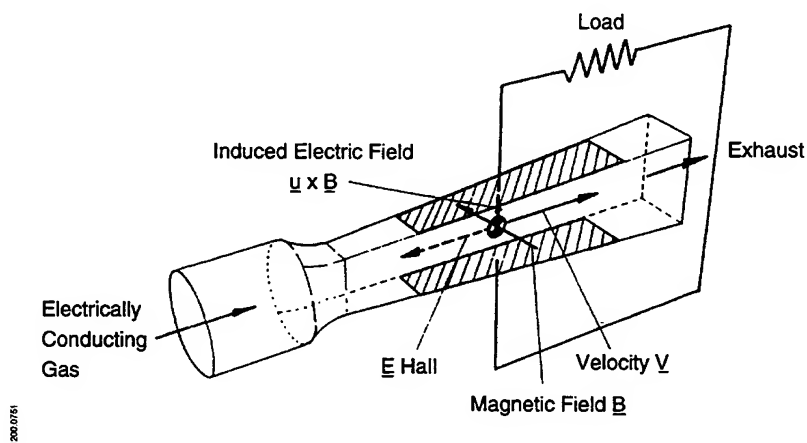


Fig. 5. Basic MHD generator geometry [12].

The initial appeal of pulsed alternators as power sources for railguns was the possibility that their output current pulse could be matched to the railgun pulse length without the need for switches. However, for multiphase, multi-pole rotors turning at higher and higher rotational speeds, pulse forming by the use of switch modules is required. A contribution by Singh et al. [13] reviews EML switch requirements for pulsed alternators, the current state of the art for a number of quite different switch technologies, and the current approach being pursued in the U.S. Unfortunately, the electric gun requirements of interest to the military require switch capabilities which exceed the performance of a single switch, and the multiple switch modules under consideration have a large number of active elements taking up larger amounts of space than is desirable. Mercury ignitrons have been used in most of our laboratory power supplies, but these are not suitable for practical, mobile applications. Triggered vacuum switches are capable of handling high peak currents and the transfer of large numbers of coulombs. But, immediately after the switch has conducted a high current, the high frequency pulsed alternator application requires that a voltage be applied across the switch in the reverse direction — known as the reverse blocking voltage. The triggered vacuum switches have moderate reverse blocking capabilities.

Solid state switches such as Silicon Controlled Rectifiers (SCR) have better blocking voltage capabilities but the need to connect these devices in modules to handle the high currents results in large numbers of elements and auxiliaries. Replacing silicon by silicon carbide is an active area of research since silicon carbide has high breakdown voltage, operating temperature and thermal conductivity. The major hurdle is the production of large, reliable defect-free wafers of this material. In general, for the applications of interest, solid state switch modules and triggered vacuum switches are the most appealing candidates.

The Institute for Advanced Technology (IAT) is extensively investigating the materials and geometries of railguns and armatures to understand the physics of the high current, hypervelocity sliding contact interface in solid armature railguns and to understand phenomena which might limit rail life. Professor Leslie Woods and Dr. Andrew Yeoh present their analysis [14] of aluminum deposits on rails resulting from the ohmically heated liquid layer formed between the rails and solid armature.

Dr. Chadee Persad et al. [15] report on their continuing detailed post-shot analyses of rail surfaces after single shot experiments. They evaluated rails of copper-chromium alloy, unalloyed copper and molybdenum, all tested following single railgun shots with aluminum armatures. They conclude that a liquid metal layer forms between the rail and armature at an early stage of the launch and they investigate the different areal coverages of the resolidified liquid metal. This leads them to believe that the early movement of the armature is aided by the presence of a lubricant — in this case the molten aluminum from the armature. They further conclude that shearing of the softening armature surface at the armature-rail interface permits the initial armature motion. Unfortunately, none of the three materials investigated as candidate rails were recommended as good practical materials. Figure 6 shows the monolithic aluminum armature configuration.

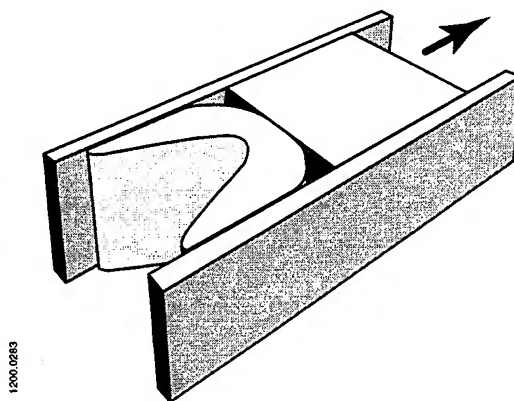


Fig. 6. Monolithic aluminum armature configuration [15].

Rail damage in the form of large teardrop-shaped craters can severely limit the useful life of railguns. Mr. Francis Stefani and Dr. Jerald Parker have made significant advances in understanding this phenomenon by concluding that gouging occurs when interactions between slider and rail create stresses that exceed the strength of the *harder* material [16]. In a series of careful experiments and analyses, they demonstrate a relationship between shock pressure at the gouging threshold velocity and room temperature hardness which permits them to predict the gouging threshold velocities for any combination of materials from the materials shock characteristics and hardness. Figure 7 shows gouges in the form of tear-shaped craters along the velocity vector.

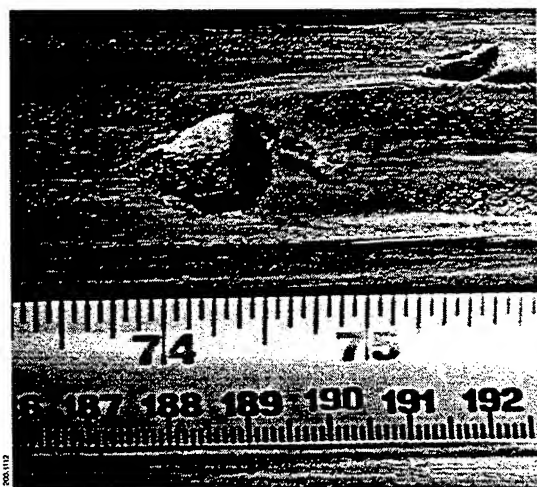


Fig. 7. Typical hypervelocity gouges produced by aluminum sliding on copper [16].

At the 1994 EML Symposium, Dreizin and Barber [17] predicted that there is a significant contribution to the measured muzzle voltage arising from the precursor magnetic field ahead of the armature. This has been a controversial issue since some investigators have shown agreement between experiment and theory ignoring this contribution to the muzzle voltage. Dr. Jerald Parker reports the results of a novel experimental technique and elegant analysis to provide a direct measurement of the precursor magnetic field and the precursor voltage and the effect of the associated rail current on the muzzle voltage [18]. Dr. Parker's observed magnitude of the voltage is in good agreement with the predictions of Dreizin and Barber. The experimental configuration used to observe the precursor voltage is shown in Fig. 8(a). A scale drawing of the launcher cross section and rails showing the location of the coil used to measure the precursor magnetic field is shown in Fig. 8(b).

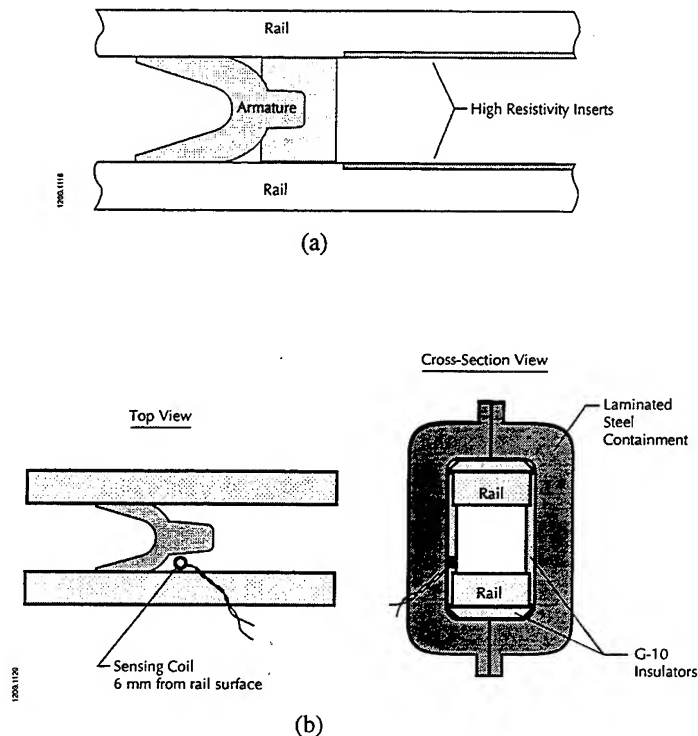


Fig. 8. (a) The presence of precursor currents can be observed by placing a high resistivity insert into the rails; (b) Scale drawing of the launcher cross section and rails showing the location of the coil used to measure the precursor magnetic field [18].

Dr. Richard Marshall continues to make innovative contributions [19] to railgun technology by introducing laminated rails and the "pseudo-liquid" armature. As a consequence of his research on armature-rail contact forces, he developed a device using flexible rails made of thin laminations of copper instead of the thick monolithic rails normally used (see Fig. 9). Based on his observations of rail current distribution in this device, he applied the same logic to a railgun in which the rails were composed of copper laminations with only physical contact between them. This novel approach permits the evaluation of numerous materials as candidate rail materials.

In a separate paper [20], Dr. Marshall evaluates the relative merits of railgun bore geometry for different applications. Specifically, he considers round and square bore configurations. The Cannon Caliber EML railgun is not treated in this analysis, but it is an augmented rectangular bore railgun.

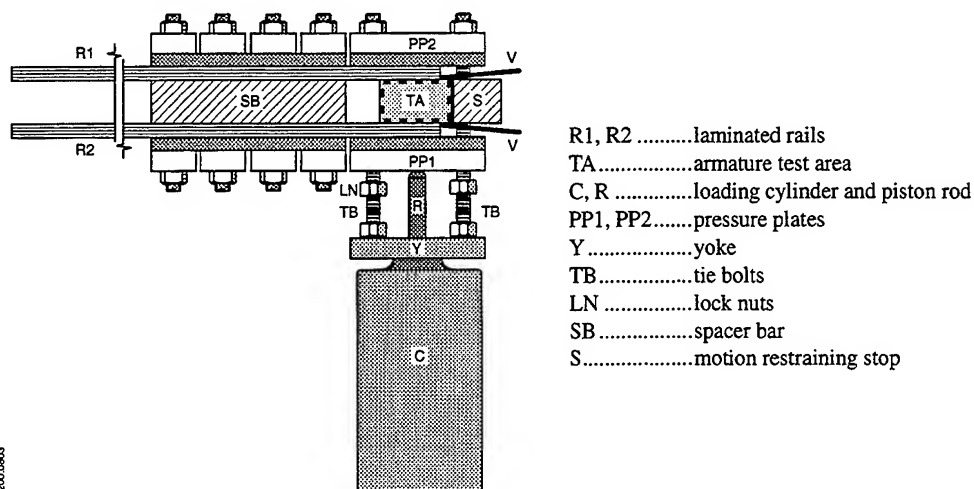


Fig. 9. Apparatus using flexible rails made of thin laminations of copper which are simply clamped together—they are not soldered or welded together in any way [19].

The integration of railgun, power source and related technical components is of growing interest. Dr. Scott Fish et al. [21] have developed simulations to assess the overall performance and component performance in an all-electric ground combat vehicle. This simulation enables them to evaluate excursions of the use of components beyond their design envelope. This capability enables system designers to determine performance degradation of individual electrical components and provides insight into design requirements for the system and critical components.

All of this current research is integrated into a joint US/UK program to develop the critical science and technologies for electric launch systems.

#### Acknowledgment

I wish to thank all of the participants in the U.S. electric launch program for providing illustrations, photographs, and descriptions of their work. I also want to thank IAT's Publications and Graphics personnel for their assistance in the preparation of this manuscript.

This work was supported by the U.S. Army Research Laboratory (ARL) under contract DAAA21-93-C-0101.

#### References

- [1] See for example, *IEEE Trans. on Magn.*, vol. MAG-18, no. 1, January 1982 through vol. 33, no. 1, January 1997.
- [2] H.D. Fair, "Electromagnetic Launch: A Review of the U.S. National Program," *IEEE Trans. on Magn.*, vol. 33, pp. 11-16, 1997.
- [3] R.J. Hays and R.C. Zowarka, "Experimental Results from CEM-UT's Single Shot 9-MJ Railgun," *IEEE Trans. on Magn.*, vol. 27, pp. 33-38, 1991. And also, I.R. McNab, F. Levine, and M. Aponte, "Experiments under the Green Farm Electric Gun Facility," *Trans. on Magn.*, vol. 31, pp. 338-344, 1995.
- [4] T.C. Aden, et al., "Summary of the Hypervelocity Weapon System Field Experiment," *IEEE Trans. on Magn.*, vol. 33, pp. 636-641, 1997.
- [5] D.J. Elder, "The First Generation in the Development and Testing of Full-Scale, Electric Gun-Launched, Hypervelocity Projectiles," *IEEE Trans. on Magn.*, vol. 33, pp. 53-62, 1997.

- [6] I.R. McNab, "Pulsed Power for Electric Guns," *IEEE Trans. on Magn.*, vol. 33, pp. 453-460, 1997.
- [7] J.R. Kitzmiller, et al., "Laboratory Testing of the Pulse Power System for the Cannon Caliber Electromagnetic Gun System (CCEMG)," *IEEE Trans. on Magn.*, vol. 33, pp. 443-448, 1997.
- [8] See for example, G.L. Katulka, et al., "Pulsed-Power and High Energy Plasma Simulations for Application to Electrothermal-Chemical Guns," *IEEE Trans. on Magn.*, vol. 33, pp. 299-304, 1997 and W.F. Oberle and G. P. Wrenn, "An Analysis of Ballistic Parameters/Mechanisms Affecting Efficiency in Electrothermal-Chemical Guns," *IEEE Trans. on Magn.*, vol. 33, pp. 310-315, 1997.
- [9] T.C. Aden, et al., "Summary of the Hypervelocity Weapon System Field Experiment," *IEEE Trans. on Magn.*, vol. 33, pp. 636-641, 1997.
- [10] S. Fish and E. Redding, "Prime Power and Pulsed Energy Storage for EM Gun Equipped Tank Combat Missions," *IEEE Trans. on Magn.*, vol. 33, pp. 642-646, 1997.
- [11] T. Podlesak, et al., "On the Feasibility of Mounting an Electrothermal Chemical Gun System on a Combat Vehicle," *IEEE Trans. on Magn.*, vol. 33, pp. 651-656, 1997.
- [12] I.R. McNab, "Magnetohydrodynamic (MHD) Generators," to be presented at the 6th European Symposium on Electromagnetic Launch Technology, The Hague, The Netherlands, 25-28 May, 1997.
- [13] H. Singh, et al., "High Action Switching for Next Generation Multi-Megajoule Power Conditioning System," to be presented at the 6th European Symposium on Electromagnetic Launch Technology, The Hague, The Netherlands, 25-28 May, 1997.
- [14] L.C. Woods and A. Yeoh, "Investigation of Transverse Striations on Aluminum Rails," to be presented at the 6th European Symposium on Electromagnetic Launch Technology, The Hague, The Netherlands, 25-28 May, 1997.
- [15] C. Persad, et al., "Investigation of the Performance of Rail Conductor Materials," to be presented at the 6th European Symposium on Electromagnetic Launch Technology, The Hague, The Netherlands, 25-28 May, 1997.
- [16] F. Stefani and J.V. Parker, "Experiments to Measure Gouging Threshold Velocity for Various Metals against Copper," to be presented at the 6th European Symposium on Electromagnetic Launch Technology, The Hague, The Netherlands, 25-28 May, 1997.
- [17] Y.A. Dreizin and J.P. Barber, "On the Origins of Muzzle Voltage," *IEEE Trans. on Magn.*, vol. 31, pp. 582-586, 1995.
- [18] J.V. Parker, "Experimental Observation of the Rail Resistance Contribution to Muzzle Voltage," to be presented at the 6th European Symposium on Electromagnetic Launch Technology, The Hague, The Netherlands, 25-28 May, 1997.
- [19] R.A. Marshall, "Advanced Low Cost Rails and Armatures for Rail Launchers," to be presented at the 6th European Symposium on Electromagnetic Launch Technology, The Hague, The Netherlands, 25-28 May, 1997.
- [20] R.A. Marshall, "Factors Influencing Choice of Bore Geometry for Rail Launchers," to be presented at the 6th European Symposium on Electromagnetic Launch Technology, The Hague, The Netherlands, 25-28 May, 1997.
- [21] S. Fish, et al., "Weapon Charging Effects on Land Vehicle Mobility with Shared Prime Power," to be presented at the 6th European Symposium on Electromagnetic Launch Technology, The Hague, The Netherlands, 25-28 May, 1997.

## Potentiality of Electric Guns in the Field of Land Armaments

Frantz CAILLAU

Giat Industries

Division des Systèmes d'Armes et de Munitions  
7, route de Guerry - F-18023 Bourges Cedex - France

Thierry VAILLANT

Délégation Générale pour l'Armement

Etablissement Technique de Bourges - Centre Technique  
Carrefour Zéro Nord - BP 712 - F-18015 Bourges Cedex - France

### Abstract

This paper presents the principal results obtained regarding the potentiality of the electric guns in the field of land armaments. Anti-tank and air-defence missions have been evaluated.

This study confirms the advantages of the electric guns for anti-tank applications where the evolution of protection requires a higher velocity than the conventional guns to be attained.

For air-defence applications, the type of mission is very sensitive, but the velocity must be over 2000 m/s.

In the long term, the electromagnetic guns and, in particular the rail gun system, seem to be the best candidates but now the principal limit is the pulsed power density. In the term, ETC technology with a low electric energy level is a good compromise between pulse power capability and ballistics performances. The development of the electric gun technology will be possible only if we developed pulsed power technology with very high energy and power densities.

### Introduction

The performance of the defence systems increases with the evolution of the technology. In the field of land armaments we know very well the competition, for example for tanks, between the evolution of armour performance and penetrator perforation. In this context it is necessary to analyse the potentiality of electric propulsion concepts against the new targets (tanks, helicopters, hypervelocity missiles, and so on). It is necessary to examine the benefits in terms of ballistics performance but also the implications on systems of the use of electric gun propulsion. For example, it will be necessary to examine mobility constraints, logistics aspects and to identify necessary technological improvements.

In this paper, we consider anti-tank applications and air-defence systems for land armament. For each type of target we describe the level of protection or vulnerability and we define the ballistics performance of each type of electric gun.

In the second part, we analyse the design of mobile systems including electric gun technology and power supply.

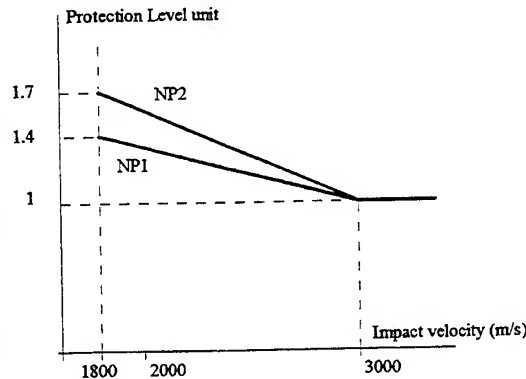


## Type of targets and performance requirements

### Anti-tank applications

Concerning the requirements of terminal ballistics performance, we have assumed some technological evolutions of armour in the future. In the long term it will also be necessary to consider active armour. For these types of protection the impact velocity will be very high. The higher the velocity the lower the damage to the penetrator.

The curves beside show the evolution of armour brought to equivalent homogeneous armour at two horizons. Curve NP1 represents the performances of a reactive armour for medium term development. The curve NP2 represents performances hypothesis for a new type of reactive armour (long term evolution). For the NP2 curve, a velocity increase of 67 % allows the equivalent thickness to be decreased by 70 %.



### Air defence applications

In air defence it is necessary to consider various targets such as cruise missiles, aircrafts, helicopters, drones and tactical ballistic missiles. The targets are defined by their vulnerability (necessary impact energy and surface) and by their scenarios.

|                |                         | Catastrophic mission      | Neutralization |
|----------------|-------------------------|---------------------------|----------------|
| Cruise missile | uniform straight flight | ignition of military head | impact         |
| Aircrafts      | manoeuvrable            | cockpit surface           | impact         |
| Helicopter     | pop-up                  | cockpit surface           | impact         |
| Drone          | go down flight          | ignition of military head | impact         |
| TBM            | go down flight          | ignition of military head | impact         |

For these targets, the interest of electric gun is to lower the flight time, for example for the helicoptere the apparition time is around 5 and 10 secondes so at 5000 m the mean projectile velocity must be upper than 1000 m/s.

For the aircraft and helicopter we have sized the projectiles to obtain residual energy after penetrating into the cockpit.

## Sizing of weapon and ammunition system

### Technology used

#### *Gun technologies considered*

Among the different electric guns technologies (railgun, coilgun, electrothermal and electrothermal chemical gun) we have only considered the technologies that seem to have a good potentiality (development of technology in the "reasonable" future).

For the electromagnetic guns, we have carried out sizing only for the rail gun system. This technology is more mature and the performance estimation is performed more accurately than for the coil gun.

The electrothermal concept (without chemical energy) requires too much energy to be integrated in the future in a vehicle.

So, we have privileged railgun and ETC gun and this for anti-tank and air defence applications. For rail guns we have retained the Distributed Energy Stored concept with a solid armature. For ETC guns, we have sizing the gun for the US CAP gun concept.

#### *Pulse power considered*

Different kinds of technologies have been explored and for each we have assumed an energy value and power density for medium and long term.

The following chart sums up the different values :

|                                    | Energy density (MJ/m <sup>3</sup> ) |                   | Power density (MW/m <sup>3</sup> ) |           |
|------------------------------------|-------------------------------------|-------------------|------------------------------------|-----------|
|                                    | Mid term                            | Long term         | Mid term                           | Long term |
| Capacitor PFN (incl. coil, switch) | 8                                   | 16                | > 10000                            |           |
| Superconductive PFN                | 30                                  | 180<br>(nitrogen) | 10000                              | 90000     |
| Compulsator (included rotor)*      | around 23* (165)                    |                   |                                    |           |
| Converter (AC/DC and transformer)  | 8                                   | 8                 | 9                                  | 9         |
| Magneto dynamic storage            | 600                                 | 1200              | 20                                 | 30        |

The energy and power density for the compulsator is a function of the shot characteristics (discharge time, energy delivered)<sup>1</sup>.

#### *Munition technologies considered*

For anti-tank applications we have considered the penetrator whose advantages are a higher velocity resulting from the electric acceleration.

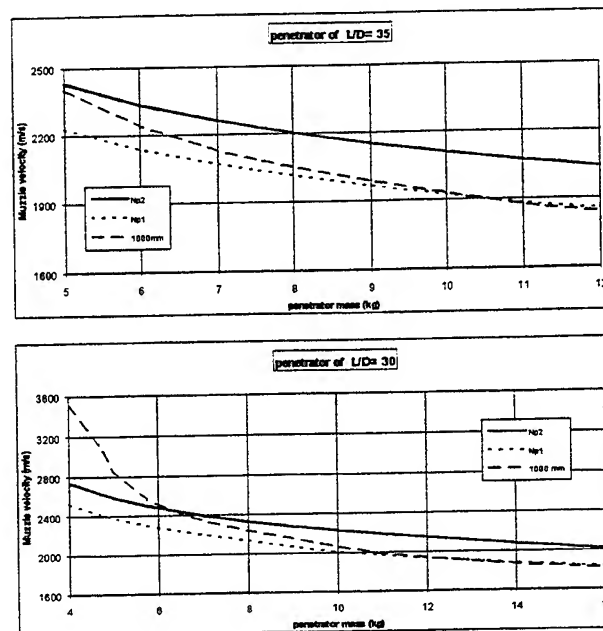
<sup>1</sup> Electric Gun Propulsion and power Conditioning - Report of the propulsion and power conditioning - Panel of the electric gun system - David C. Hardisson.

For air-defence we have looked at different sorts of projectiles such as small penetrators (darts), cargo projectiles, unguided or guided flight warhead. The munitions are detailed in the following parts.

### Anti-tank gun and ammunition sizing

The first studies have shown that the penetration is improved if we increase the penetrator length and if we decrease the barrel radius. The limits are fixed by the mechanical constraints and by the conditions of use (loading system, ..). For our study we fixed the minimal diameter at 22.5 mm and the maximal length at 790 mm. We computed the muzzle velocity necessary to defeat the different hypothesis of armours.

The curves beside show the initial velocity in relation to  $L/D$ .



These curves show that the  $L/D=35$  penetrator allows initial velocity to be decrease by a coefficient of over 20% in comparison with the  $L/D=30$ .

From these results we have sized the electric gun and the pulse power supply necessary to defeat the target. We have chosen the couple ( $V_0$  ;  $M_p$ ) to minimize the energy stored in the pulse power.

For the rail gun and ETC and for the NP2 armour we have the following sizing ; the sizing has been computed by interior ballistics code :

|                             | RAIL GUN | ETC                              |
|-----------------------------|----------|----------------------------------|
| Muzzle velocity (m/s)       | 2400     | 2150                             |
| Penetrator mass (kg)        | 5.5      | 9                                |
| Sabot mass (kg)             | 5.8      | 5.4                              |
| Kinetic energy (MJ)         | 16.7     | 33                               |
| Calibre (mm)                | 115      | 140                              |
| Ballistics lenght (m)       | 6        | 7                                |
| Electric energy stored (MJ) | 64       | around 40 MJ for CAP gun concept |

The rail gun calibre is sized to maintain the maximal current (5 MA), the limit is fixed at 60 kA/mm. Le sabot is sized to dissipate the Joule energy without reaching the melting point and to support the mechanical constraints.

For this level of performance, the ETC concept has some disadvantages in relation to the rail gun system because, for this velocity range, ETC efficiency is very low (around 25%) in comparison with rail gun efficiency. These efficiency decrease with the velocity and for initial velocity upper than 2000 m/s, the amount of electric energy increased considerably. The electric energy diminution is not sufficient to allow an easy integration. In our case, the ratio between electric energy and chemical energy was 50 %. The mechanical constraints induced on the structure are higher (impulse, recoil force) than for rail guns.

*In fact, the ETC concept will be a good solution for intermediate level of performance under 2000 m/s). The level of electric may be reduce by using high chemical energy density and in this case, the ETC could be used as a retrofit for conventional artillery in the near future.*

#### Integration aspects

After having sized the weapon system we studied the integration of rail gun system in a chassis. For rail gun system with a long term and superconductive power supply we have the mass and volume of power supply.

|                              | effi.<br>(%) | Es<br>MJ   | Dm kJ/kg<br>Dv MJ/m3 | Pmax MW<br>Pmoy MW | Dm kW/kg<br>Dv MW/m3 | Mass<br>kg | Volume<br>m3 |
|------------------------------|--------------|------------|----------------------|--------------------|----------------------|------------|--------------|
| <b>Supra<br/>&amp; gun</b>   | 50%          | 127        | 100<br>180           |                    | 50000<br>90000       | 1 300      | 0,70         |
| <b>Converter<br/>(AC/DC)</b> | 80%          | /          | /                    | 12,72<br>6,36      | 8<br>9               | 1 600      | 1,40         |
| <b>MDS</b>                   | 97%          | 954<br>477 | 300<br>600           | 15,90<br>7,95      | 10<br>20             | 3 200      | 1,60         |
| <b>Alternator</b>            | 90%          | /          | /                    | 0,82               | 20<br>25             | 40         | 0,03         |

The MDS storage is sized to store enough energy for one shot sequence, that is to say 6 shots in one minute (two shots every 20 secondes).

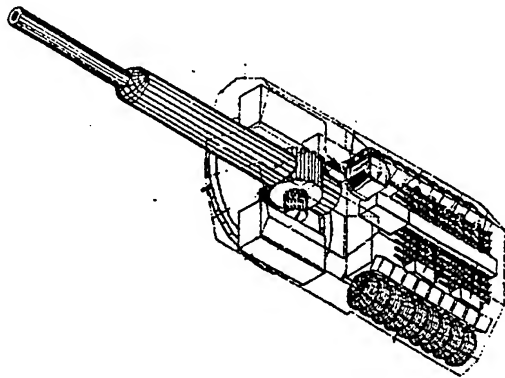
This system is integrated on a tracked vehicle with 7 road wheels and with two crewmen.

Concerning the integration aspects, we have integrated the pulse power in the turret and the energy storage (MDS) in the chassis. This choice is motivated by the size of the slip ring between the turret and the chassis and to minimize the length of cables between the pulse power and the gun. The sizing of (swing join) for high voltage (10 kV) is incompatible with integration. So, all the power system converters and the PFN are located in the turret.

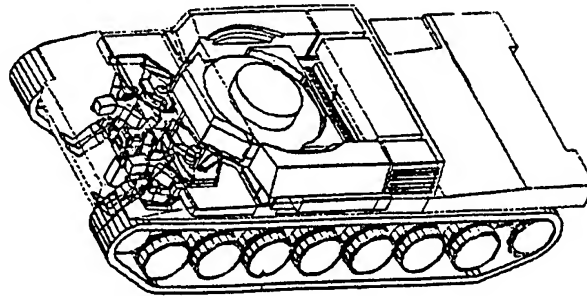
Rail gun vulnerability is lower than that of conventional power guns because we do not have a storage of the energetic materials in tanks but it is necessary to develop a safety system to prevent general short circuiting in the superconductive storage modules. The muzzle flash will be decreased by closing a switch at the end of the gun. But during firing, the electromagnetic signature is high ( $8 \cdot 10^{-2}$  Tesla at one meter of the tube). A risk of detection is possible.

This total mass is too heavy in comparison with present tanks and the height is greater than for conventional battle tanks. The following scheme show the important mass and

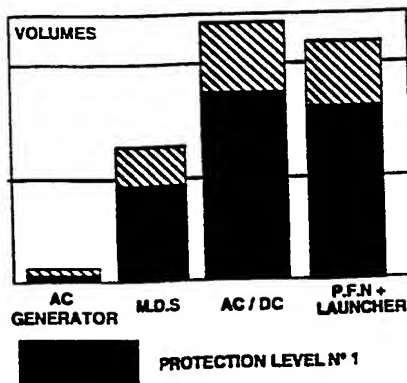
volume for converter (AC/DC) and PFN. So as to decrease the mass and volume and to maintain the mobility performance it is necessary to increase the power supply density and, by way of an example, to use electrical transmission instead of mechanical transmission.



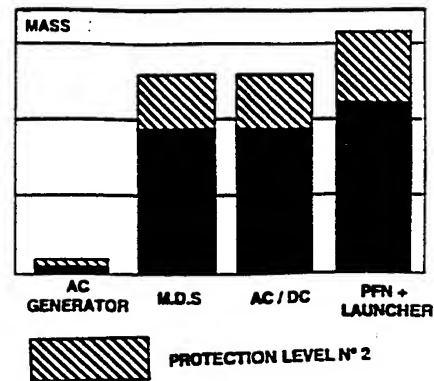
View of turret



View of chassis



Volumes of components



Mass of components

### Air-defence gun and ammunition dimensionning<sup>2</sup>

For sizing air-defence systems we used the same methodology than for anti-tank systems. We considered different types of munitions and fire systems. A parametric study shows that the hard kill mission is very restricting for the range investigated (between 4000 to 8000 m) and the need for electric energy prevents a development in the medium term. In this paper we present the principal sizing for neutralization missions. The main concepts investigated and ballistics sizing are as follows.

<sup>2</sup> Study in cooperation with Thomson CSF Airsys - France

|  | Muzzle velocity (m/s) | Mass of projectile (g) | Number of projectiles | Kinetic energy * (kJ) |
|--|-----------------------|------------------------|-----------------------|-----------------------|
| Darts and optronic fire system (1)           | 3000                  | 10                     | 50 **                 | 50*45                 |
| Splinter and radar fire systems (2)          | 2000                  | 4500                   | 1                     | 9000                  |
| Cargo of darts with optronic fire system (3) | 2500                  | 2000                   | 1                     | 6250                  |
| Guided penetrator in shell (4)               | 2500                  | 3*0.4                  | 1                     | 5000                  |
| Splinter and guided fire system (5)          | 2000                  | 7.5                    | 1                     | 15000                 |

\* The kinetic energy is for one mission.

\*\* Burst of 50 darts in one second

The initial velocity is a function, for each type of projectile, of exterior ballistics and terminal ballistics characteristics.

In performance terms, all the concepts are limited for ballistic missiles and for manoeuvring aircrafts, the guided concepts and the cargo concepts seem to give the best results for all targets. The guided concepts are expensive and technologically complex in comparison with ballistics concepts.

We have sized the electric technology for each concept. Only the concepts where the velocity is of 2000 m/s are compatible with ETC technology, for the others we have privileged the rail gun.

|   | Technology | Estored (MJ)/ per shot | Volume* (m3) | Mass* (kg) |
|---|------------|------------------------|--------------|------------|
| Darts and optronic fire system (1)        | Rail       | 19                     | 6            | 11000      |
| Warhead and radar fire system (2)         | ETC        | 9                      | 3            | 6200       |
| darts cargo with optronic fire system (3) | Rail       | 23                     | 7            | 13000      |
| Guided penetrator in shell (4)            | Rail       | 20                     | 6            | 11000      |
| Warhead and guided fire system (5)        | ETC        | 15                     | 5            | 9000       |

\* : Volume and mass are given for capacitor technology in the medium term.

The Darts concept (1) needs low energy but it is necessary to perform 50 discharges in one second. The complexity of pulsed power systems prevents use of this concept for electric guns. It would be better to use a monoshot concept.

In the medium term, with our energy density hypothesis, only the projectile with unguided warhead launched by ETC (2) will allow integration mid-term on a light mobile platform (30 tonnes), but in the long term the electromagnetic system is the best candidate.

This air-defence study has shown the necessity of using hypervelocity projectiles. But the "hard kill" mission needs a large evolution of pulsed power supply to consider it being used in the field of land armaments. The monoshot concept associated with the electric gun technology offers more potentiality than burst concepts.

## Conclusion

The use of electric gun technology could improve the performance of weapon systems in the field of land armaments. In the long term, electromagnetic guns seem to be the best trade off. Rail gun technology is more mature than coil gun technology. But before using rail gun technology some problems must be resolved.

In the medium term, the ETC technology (with improvement of chemical energy) is a solution for velocity lower than 2000 m/s because it needs a low electric energy but the performances are limited by principle (expansion of gas).

The increase of the pulsed power density is the first priority ; without improvement of these performances technology, it appears that mobile contact between rail and projectile is the major problem. Future work on rail gun must concentrate on this subject.

The limit of the performance of pulsed power in the medium term obliges the ETC technology to be studied in detail so as evaluate the performance and to position this technology between conventional powder guns and rail guns for anti-tank applications.

## References

- [1] : Power conditioning requirements for Electric Guns  
F. Jamet, P. Lehmann, V. Wegner - ISL - AECV Conference 14 -17 May 1995
- [2] : Applicabilité des lanceurs électromagnétiques à rails à diverses missions militaires  
P. Lehmann - ISL - EMA - PL 9311 - Novembre 1993
- [3] : Lanceurs électriques et projectiles hypervéloces : analyse technico-opérationnelle synthétique"  
F. Jamet, P. Lehmann, V. Wegner - ISL - EMA - FJ 9312 - Décembre 1993
- [4] : Simulation numériques de probabilité d'atteinte de cibles aériennes diverses"  
B. BAUER - ISL - R 106/94
- [5] : Electric Gun Propulsion and power Conditionning - Report of the propulsion and power conditioning - Panel of the electric gun system -  
David C. Hardisson.
- [6] : Technical tradeoffs for downsizing ETC power systems  
W. J. Sarjeant, B.D. Goodell, S.L. Langlie; K.C. Pan - IEEE Transactions on magnetics Vol29 - January 1993
- [7] : Electromagnetic weapon system integration into combat vehicles  
B.D. Goodell, J.S. Perry, M.V. Arkinson, E.B. Goldman, J.T. DeWitt, T. Mohler, J. Kitzmiller - IEEE Transactions on magnetics Vol31 January 1995
- [8] : Tactical applications for electromagnetic launchers  
J.J. Scanlon, J.H. Batteh, G. Chryssomaliss - IEEE Transactions on magnetics Vol31 January 1995
- [9] : Electric drive and high energy storage systems for tracked and wheeled combat vehicles - The future electric weapon platform.  
M. Heeg, P. Ehrhart, G. Heidelberg, G. Reiner - MM - AECV Conference 14 -17 May 1995

# Weapon Charging Effects on Land Vehicle Mobility with Shared Prime Power

Dr. Scott Fish, Troy Savoie, and Bill Barth  
Institute for Advanced Technology, The University of Texas at Austin  
4030-2 W. Braker Lane, Suite 200, Austin, Texas 78759-5329

**Summary**—Allocation of weight and volume for independent power supplies driving weapons and mobility systems will be a difficult process for future electric land combat vehicle designers. A more feasible approach is to utilize some form of shared prime power and capitalize on the operational use of the vehicle and some form of energy storage to maximize the utility of available prime power while maintaining desired performance from all subsystems. Since it is impossible to predict all possible operational scenarios, it would be helpful to determine what penalties are incurred under the rare conditions that firing beyond the design envelope imposes on the drive system of the vehicle. We will assume that the vehicle power system is series hybrid electric, consisting of a prime power internal combustion engine driving an electrical generator which provides power to both the drive system and weapon system. The drive system is assumed to be single speed, capitalizing on the advantages of electrical machines for their broad power vs. shaft speed capabilities. Proper design of such a power system includes an energy storage device such as a flywheel or battery which can be used to augment or independently power some of the loads during brief periods of high performance. For instance, several shots could be fired from an electric weapon with little or no degradation in mobility provided that the weapon energy was derived from the energy storage device while the prime mover effectively drove the wheels/tracks. However, if the vehicle commander operates the vehicle beyond the design conditions (energy storage capacity) of the power system, one would like to understand what performance degradation can be expected. The impact on performance will be illustrated with both steady state and dynamic analysis and shows that performance degradation can be significant if the balance in prime power and energy storage too heavily emphasizes the energy store.

## I. BACKGROUND

In addressing the operation of the vehicle outside its design envelope, the primary assumption is that sufficient energy has been extracted from available energy storage systems that they can no longer be used to augment the power produced by internal combustion engine sources. The reader is cautioned that this paper does not deal with how the energy store has become so depleted since a variety of operational sequences could cause it, some of which are given below:

- firing more high energy shots than energy store is designed for
- operating for extended periods in silent mobility mode (no engine running)
- operating for extended periods in hypermobility mode (with drive motors) consuming more power than prime mover can produce for high acceleration or hill climbing

In this study, we are concerned with how the vehicle mobility is affected by diversion of prime power to the weapon system under these extreme conditions. We will focus our attention on reduction of maximum speed of the vehicle since this is a simple measure of the performance capability of the vehicle. If the vehicle commander desired to operate the vehicle at or below this resulting speed, he/she could do so at will.

One should also note that in today's vehicles with the only major load for the prime mover being the mobility system, the drive system is sized to take the full power capability of this prime mover. As will be shown later, a properly sized prime mover for a vehicle with mobility and weapon loads may result in a prime power level greater than the mobility system is capable of using for extended periods of time. This could provide high acceleration capability for brief periods but would not draw large power under steady operations. The additional power not being used for mobility could be used to top off the energy storage device and effectively drive the weapon loads, or could be turned off.



## II. STEADY STATE ANALYSIS

In the first phase of this study we examine the steady state maximum speed for the vehicle as power is diverted from the drive system to a weapon system or other load. Several assumptions must be made to confine the parameter space to regions of interest, and these will be explained after deriving the appropriate relationships.

Since we are interested in the case where the energy store has been depleted, we will neglect it in the steady state analysis. This means that the power that is available to drive the vehicle is determined by the prime mover alone. Figure 1 shows the rough architecture assumed with simple efficiencies indicated for each path of energy flow.

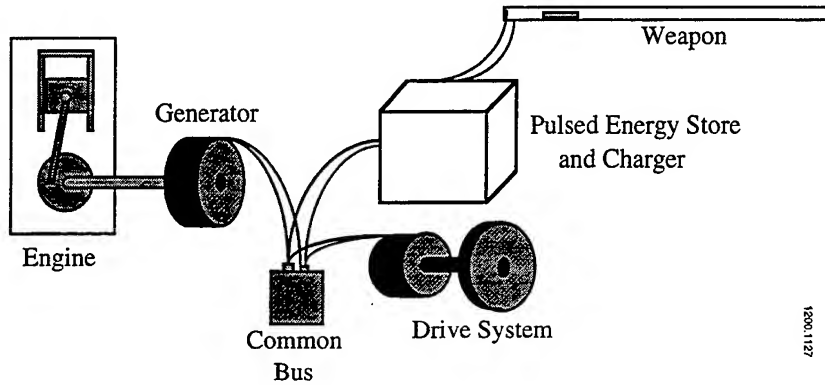


Fig. 1. Power architecture.

The sum of the forces acting on the vehicle can be written as follows [1]:

$$F_{thrust} = F_{gravity} + F_{windage} + F_{rolling} + ma \quad (1)$$

where:  $m$  = vehicle mass

(we will neglect the rotational inertia effects of the drivetrain here)

$a$  = vehicle acceleration

$$F_{rolling} = m \cdot RR$$

RR is rolling resistance (we will neglect the velocity dependent contribution to RR)

$$F_{gravity} = m \cdot g \cdot \sin(\theta)$$

$g$  is gravitational acceleration,  $\theta$  is grade slope

$$F_{windage} = C_d \cdot A_{frontal} \cdot V^2$$

$V$  is vehicle velocity

For steady speed calculations,  $a = 0$ , we can rewrite (1) as:

$$F_{thrust} = m(RR + g \sin(\theta)) + C_d \cdot A_{frontal} \cdot V^2 \quad (2)$$

This thrust force can also be derived from the power generated at the ground through the drive system:

$$F_{thrust} = \frac{P_{effective} \cdot \eta_{drive}}{V} \quad (3)$$

Substitution of (3) into (2) gives a cubic equation in  $V$ :

$$0 = -P_{\text{effective}} * \eta_{\text{drive}} + m(RR + g \sin(\theta))V + C_d A_{\text{frontal}} V^3 \quad (4)$$

The positive real root of this equation is the one of interest, and we solve for it numerically using a polynomial root solver in the commercial program Matlab [2].

A range of vehicle masses are investigated from 5,000 to 40,000 kg, and the rolling resistance is linearly varied with vehicle mass from between 0.219 N/kg (50 lb/ton) for the 5000 kg vehicle to 0.657 N/kg (150 lb/ton) for the 40,000 kg vehicle. All of the vehicles are assumed to have a wind drag coefficient of 0.5 and their frontal area is assumed to linearly vary from 3 to 6 m<sup>2</sup> over the 5,000 to 40,000 kg mass range.

If we assume that the power-to-weight ratio for the vehicles are similar and set it to 0.0147 kW/kg (20 hp/ton) we can plot the speed of the vehicle as a function of vehicle mass, weapon charger power/effective prime power, and grade of terrain as shown in Fig. 2.

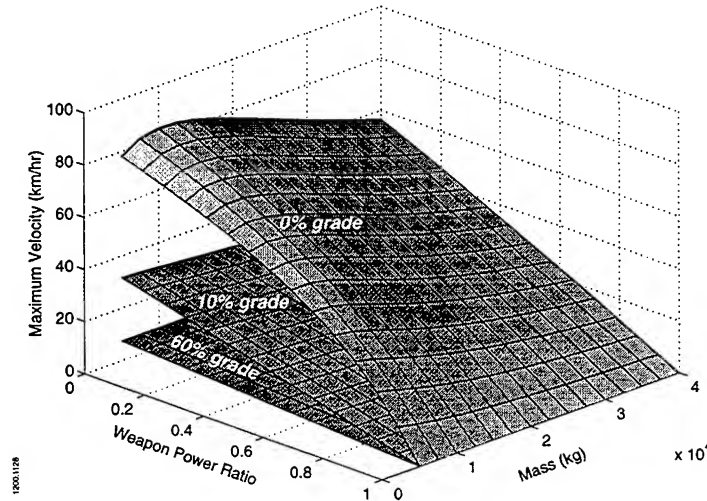


Fig. 2. Vehicle velocity as a function of mass, grade, and weapon charging power diversion.

This plot can be further simplified by nondimensionalizing with respect to the velocity of the vehicle with no drive power being diverted to the weapon system, as shown in Fig. 3. Here we confine our view to solutions at grades of 0 and 30%. Note that with modest increases in grade, and mass, the curves collapse onto a straight line. This is because the grade effect adds with the rolling resistance in the first power of velocity in the power Equation (4), and this term is dominant over the  $V^3$  term from aerodynamics. The greater curvature of the light vehicles at low grades reflects the influence of the cubic term in Equation (4).

### III. SIMULATION ANALYSIS

In order to account for the transient speed effect associated with the inertia of the vehicle (which can be significant in the heavier armor applications) we combined the power supply assumptions made above for a hybrid electric power train, with a dynamic model of the vehicle which included its inertia [3]. This model also included the derivation of weapon power based on the influence of a firing sequence on the

pulsed energy storage system. In this way, one could observe the decrease in velocity and measure the direct effect of diversion of mobility power in terms of a sustained firing rate for the weapon.

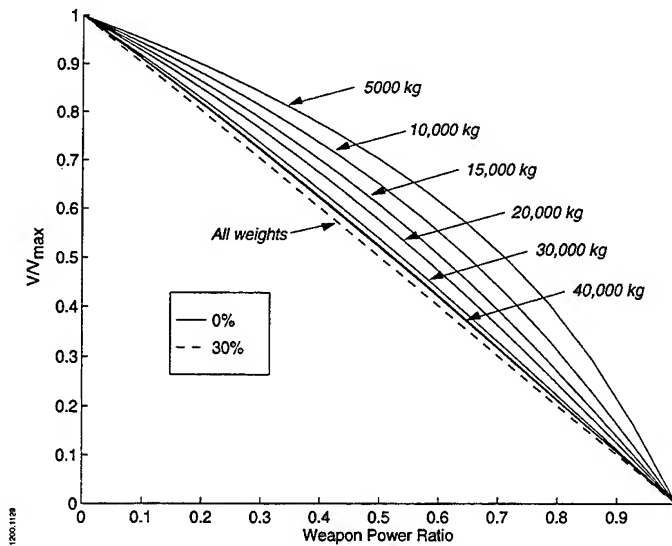


Fig. 3. Fractional velocity vs. mass, grade and weapon charging power diversion.

An example of this is shown in Figs. 4a and b where the grade has been set to zero. This case shows the 40-ton vehicle accelerating to full speed and then firing eight shots. Each shot drains 20 MJ from a pulsed power supply which initially contains 60 MJ of available weapon energy. Note that for a pulsed power/launcher efficiency of 50%, this represents the equivalent of a 10-MJ muzzle energy. After the third shot, the pulsed energy store is depleted of usable energy (we assume that below 60% energy, the speed of the pulsed power supply is insufficient to provide adequate voltage to fire these full energy shots) and subsequent shots can only be made at a firing rate defined by the available charger power. If the effective prime power is completely consumed at the maximum non-shooting velocity, then we can easily examine the tradeoff in vehicle velocity vs. firing rate for this vehicle and shot energy. The three time histories correspond to diversions of 25, 50 and 75% of the vehicle drive power to the weapon system. As predicted in the steady state analysis, the speed is reduced in direct proportion to the lost drive power. The sustained firing rate increases from 2.3 minutes per round to 45 seconds per round as the weapon power is increased from 25% to 75% of available power, and the vehicle is returned to full speed sooner. The dynamic analysis graphically shows the tradeoffs involved if one can afford to slow significantly, to achieve the higher firing rate and returning to high speed over a shorter period of time. The overall ability to cover distance however is invariant among the three cases. The commander's choice in selecting a recharge strategy therefore depends on his/her mobility plans (i.e., how fast the vehicle needs to travel), and how terrain can be used if a speed reduction is required.

Examination of the same firing and mobility scenario for the 5-ton vehicle is shown in Figs. 5a and b. In this case we have scaled the energy per shot down by a factor of eight following the scaled reduction in prime and mobility power. Although a very similar energy storage history results, the mobility penalties are reduced due to the reduced level of rolling resistance. Note that in this case, a 50% reduction in mobility power only results in an approximately 30% reduction in maximum speed.

For the assumed power-to-weight ratios, the time constant of the vehicle dynamics was found by comparison of the speed response to step changes in the throttle to a first order exponential response. The time constant,  $\tau$ , in the exponential was found to be approximately fifteen seconds regardless of the vehicle mass when the two curves were matched at the  $2\tau$  response time.

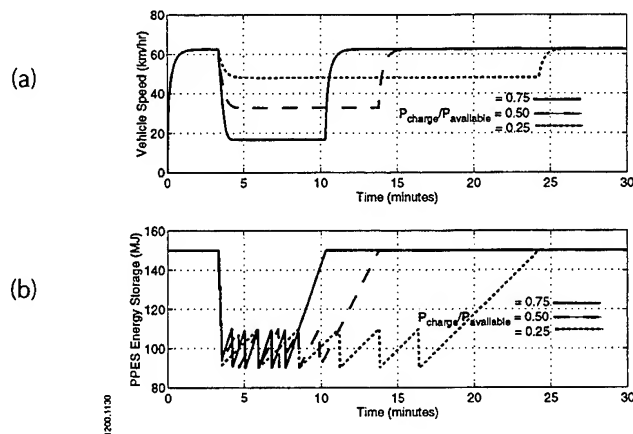


Fig. 4. (a) and (b) Vehicle and pulsed energy store performance for heavy (40,000 kg) conditions (20-MJ stored/shot, 8 shot burst with 3 shots stored).

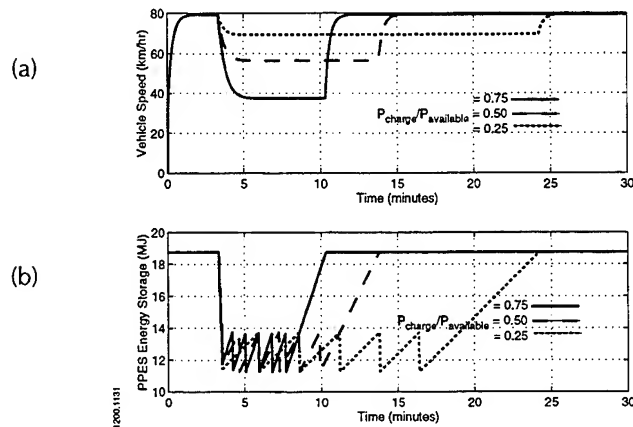


Fig. 5. (a) and (b) Vehicle and pulsed energy store performance for light (5,000 kg) conditions (2.5-MJ stored/shot, 8 shot burst with 3 shots stored).

If firing operations often accompany high speed or high agility maneuvers, the prime mover should be sized with some margin to allow substantial weapon charging without heavy impact on mobility. As an example, the prime mover could be sized for 50% extra capacity for the weapon. This could allow adequate weapon recharge rate even when full mobility power is being used. Under normal operating conditions however, when full mobility power is not in use, substantially more prime power could be utilized by the weapon charger, thus extending the effective performance envelope for the whole vehicle. Although the behavior can be deduced from Figs. 4 and 5, an example simulation of this characteristic is shown in Fig. 6. We select the light vehicle displayed in Fig. 5, and apply a 50% margin to the prime mover for weapon charging while moving at maximum speed. The firing scenario is altered to consist of two quick shots followed by a single shot in the first engagement, then four quick shots in a second engagement. Again the energy store is sized for three shots. Note that the last shot of the second engagement utilizes 50% of the mobility power with only a temporary reduction of approximately 25% in vehicle speed.

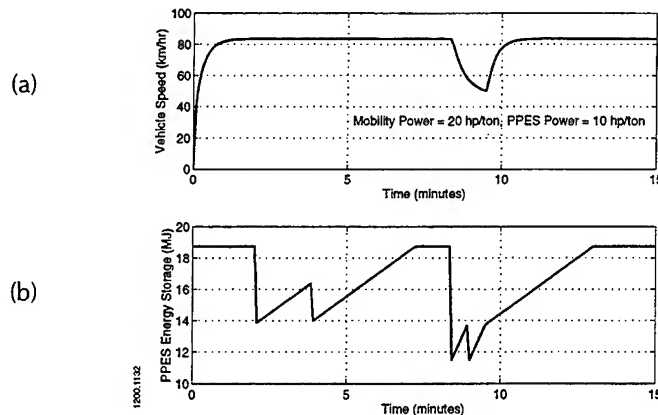


Fig. 6. Vehicle and pulsed energy store performance for light (5,000 kg) conditions (2.5-MJ stored/shot, 3 shot engagement followed by a 4 shot engagement with 3 shots stored).

#### IV. CONCLUSIONS

As one would suspect, the increasing dependence on energy storage to buffer loads and share the prime power provide big benefits in reducing prime power requirements provided that the duty cycle for both mobility and firing can be bounded over a high percentage of the time. However, this form of optimization can lead to poor performance when the energy store is depleted of usable power as we have shown. In no way does the vehicle become incapable of fighting once outside of its design envelope, but rather it may fight in a much degraded mode. This should not be a surprise to system designers, and is a direct consequence of power supply minimization for a given mission sequence. Relaxation of this optimization may result in heavier designs (more prime power or energy storage) with larger envelopes of operation and more gently degraded performance associated with ever more autonomous power supplies for the weapon and drive system. In general, the restraint on increasing prime power can be both the weight of the engine, and the weight of the fuel required for extended operations. Higher efficiency engines, or the temporary use of a very high power auxiliary engine, may prove beneficial in cases where engagement times are long but infrequent.

Careful consideration for worst case mission sequences will be required for design of the power system for future combat vehicles with electric weapons. Mission planning, as with any new combat system, will play a critical role in the effectiveness of these systems.

#### ACKNOWLEDGMENT

This work was supported by the U.S. Army Research Laboratory under contract DAAA21-93-C-0101.

#### REFERENCES

- [1] Ogorkiewicz, R.M., *Technology of Tanks*, Jane's Information Group, London, 1991, pp. 237-232.
- [2] *Matlab User's Guide*, Mathworks Inc., Natick, MA, USA, pp. 2-47.
- [3] Fish, S., E. Redding, and T. Savoie, "Prime Power and Pulsed Energy Storage for EM Gun Equipped Tank Combat Missions," *IEEE Transactions on Magnetics*, Vol. 33, No. 1, pp. 642-646.

# **Magnetodynamic Storage as a Main Storage in a Diesel-electric Main Battle Tank**

G. Reiner\*, P. Ehrhart, M. Heeg, A. M. Jean-Jacques and W. Weck  
Magnet-Motor GmbH, Petersbrunner Str. 2, D-82319 Starnberg, Germany

**Abstract** — The performance and integration of a Magnetodynamic Storage (MDS) as a main energy storage in an electric combat vehicle is described and discussed.

For an example the following system features have been chosen: Base vehicle: Diesel-electric propelled 60 t battle tank; power of the Diesel engine: 1100 kW; main weapon: ETC with 6 MJ electrical energy per shot (preassuming a pulse storage with a corresponding capacity).

Based on Magnet-Motor GmbH's (MM) to the year 2000 extrapolated MDS data and compared with the data of the MDS-technology, available in the laboratory today (80 MJ/t, 2.5 MW/t) an MDS is defined, which is suitable for mobile operation with 60 MJ stored energy and 3 MW peak power. Its suitability for the vehicle's drive and weapon is shown and discussed. One main advantage of an onboard-MDS is a significantly increased vehicle mobility.

Exemplary scenarios are investigated and analysed by evaluating the energy and power balances of the MDS and the complete electrical system of the vehicle.

## **I. Introduction**

Contemporary concepts envision battle tanks of the future that will be equipped with electric drive as well as weapon and protection systems that will either partially or totally be supplied with electric power.

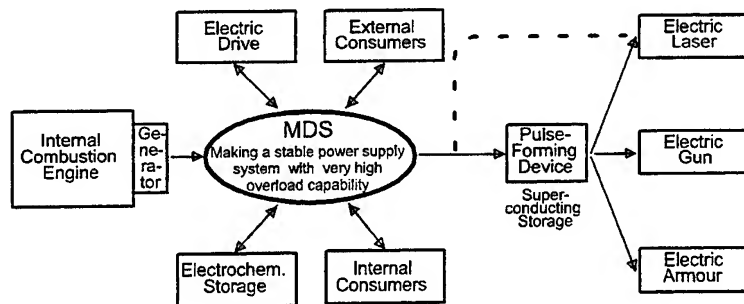
The electric energy in the vehicle will be generated either from fossil or chemical fuels, for example via a diesel-generator system. The performance of this primary power source will mainly depend on the averaged power requirements of the drive system, which would be approx. 1 MW to 1.5 MW for a 60 ton class battle tank.

Electric weapons, such as the electrothermal cannon (ET) or electrothermal-chemical cannon (ETC), a laser weapon, a high power microwave weapon or active armour systems can not be supplied directly from the primary source of energy. They will require an ultrahigh-power storage system specifically designed for the respective weapon. This storage system will deliver power pulses to the particular weapon in the range of up to 10 GW for micro- or milliseconds. But no technology is presently available [1,2] to design an ultrahigh-power storage system that can be installed in a tank and that can provide not only the necessary pulse power for one discharge but can also store sufficient energy for successive discharges. So the energy required for fire bursts or successive discharges will have to be supplied from other sources.

To be able to achieve this, reloading capacities for the pulse storage system in the range between 1 MW and 10 MW will be necessary, depending on the tactical demands placed on the weapon (firing cadence). This will clearly exceed the rated capacities of the internal combustion engine of 1 MW.

To meet these energy and power requirements, Magnet-Motor GmbH (MM) has developed the MDS. The present experimental type of a Magnetodynamic Storage system

possesses an energy density of 80 MJ/t and can store sufficient energy not only for a sequence of discharges but with its power density rated at 2.5 MW/t it is also able to recharge the pulse generating device so that the weapon can be fired in rapid sequence. This paper will describe an example of a storage system that will be available around the year 2000, and which will possess an energy density of 150 MJ/t and power densities exceeding 5 MW/t.



*Fig. 1: Basic concept of a vehicle equipped with diesel generator, electric drive and electric weapons supported by a MDS*

Figure 1 displays the basic concept of such a vehicle. The figure also shows that the MDS, as a central storage system that possesses both high energy and high power densities, can supply all the consumers in the vehicle, that is, not only the weapons systems but also the electric drive and secondary internal and external consumers. It can also supplant or support the primary power supplier for a period of 50 seconds to minutes.

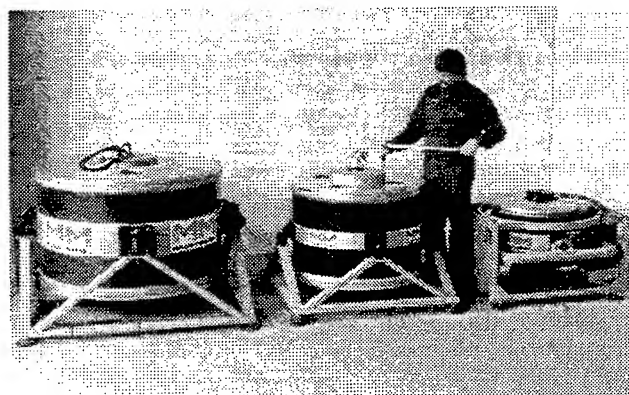
These capacities result in redundancies and considerably expanded system properties and tactical opportunities, such as high acceleration and mobility, sudden attack from cover, reconnaissance from cover with primary power source turned off with full battle readiness, crossing rivers or stealth operations.

## II. Magnetodynamic Storage (MDS)

The MDS system has been described in detail in various publications [1,2,3]. The following sections will therefore serve as an overview only:

The Magnetodynamic Storage system is a flywheel storage unit with a vertical rotation axis. The rotor is a hollow cylinder and is made primarily of carbon fibre composite. To make the system very compact, the motor/generator (M/G) unit is integrated inside the hollow cylindrical rotor.

The system stores energy when the M/G unit works as a motor and increases the speed



*Fig. 2: Magnetodynamic Storage Units*

*l: Test stand unit for demonstration of 80 MJ / 5 MW (1994)*

*m: Test stand unit for demonstration of 80 MJ / 2.5 MW (1996)*

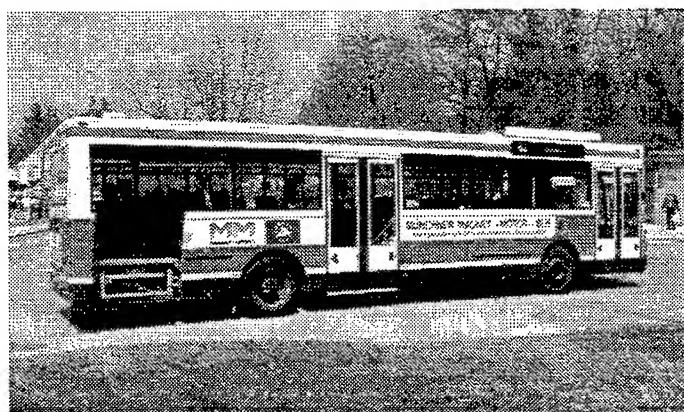
*r: Small series version for application in public buses (Fig. 3)*

of the rotor. The system delivers energy when the M/G unit is switched to generator mode, thus reducing the rotor speed.

For use in vehicles, the MDS is mounted in a housing suspended on cardan-type joints (Fig. 2, right hand side). The purpose of this is to reduce the forces acting between the rotating MDS masses and the vehicle that is moving in the terrain, thereby tipping the MDS rotor axle.

Magnet-Motor GmbH is systematically continuing the development of energy and power densities and the general system properties of MDS systems for use in military vehicles according to a research and development plan of the German MOD. The current prototype for laboratory research is the MDS L2, shown in Fig. 2 (center) among other models of MDS systems.

Other MDS types have been successfully been implemented as energy storage systems in urban service buses since 1988. Figure 3 shows an example of a diesel-electric bus in



*Fig. 3: Magnetodynamic Storage MDS K (Fig. 2, right hand side) Since 8 years operated in diesel-electric or overhead cable supplied local public buses*

service in Munich [4]. The MDS model installed in this bus is shown on the right hand side of Fig. 2.

In order to specify the aims of further MDS development Tab. 1 gives an overview over characteristic data of the laboratory type MDS L2 and a future component MDS L3.

|                 |      | Existing laboratory type<br>MDS L2 | Discussed example<br>MDS L3 |
|-----------------|------|------------------------------------|-----------------------------|
| Stored energy   | MJ   | 80                                 | 60                          |
| Maximum power   | MW   | 2.5                                | 3                           |
| Mass            | kg   | 1000                               | 400                         |
| Diameter        | m    | 0.9                                | 0.7                         |
| Height          | m    | 0.85                               | 0.65                        |
| Specific energy | MJ/t | 80                                 | 150                         |
| Specific power  | MW/t | 2.5                                | 7.5                         |

*Tab. 1: Main data of existing (MDS L2) and in 3 years as a laboratory test model (MDS L3) available MDS-hardware*

The specific data of the MDS L3 are 150 MJ/t and >5 MW/t. It will be available as a laboratory test model in approx. 3 years and as a prototype for use in a vehicle in approx. 5 years. The MDS L3 described in Tab. 1 is considered to be the main storage system for a 60 ton tank and the following sections will describe the resulting system.



### III. Definition of specifications for an electric 60 ton tank

To display the system properties resulting from the use of an MDS system in a tank, the definition of the MDS is now followed by the definition of a vehicle. The selected vehicle and its properties as well as the performance of the MDS and the electrical consumers are not to be taken to be suggestions for design and configuration but rather as an

|                               |       |      |
|-------------------------------|-------|------|
| Gross weight                  | 60    | tons |
| Diesel engine power           | 1,100 | kW   |
| Generator power               | 1,100 | kW   |
| Tractive force                | 60    | t    |
| Maximum speed                 | 70    | km/h |
| Maximum climb rate            | 60    | %    |
| ETC; energy required from MDS | 6     | MJ   |
| Fire repetition rate ETC      | 4     | sec  |

*Tab. 2: Data of a tracked vehicle, considered as an example to demonstrate system features, if a MDS is implemented*

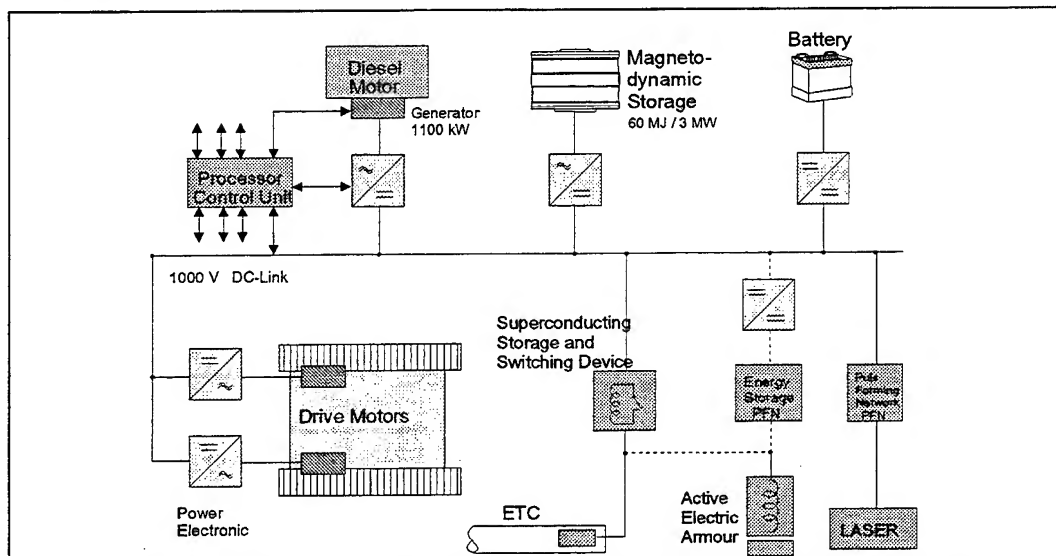
example to be used to demonstrate the features of such a system.

The vehicle and its components are assumed to have the specifications listed in Tab. 2.

The electric power circuit of the vehicle is shown in the block diagram of Figure 4.

Magnet-Motor GmbH uses a computer simulation program for this type of vehicle. The program simulates the energy flow between all components of the vehicle.

Results of the computer simulations for this vehicle will constitute the basis for the following two chapters.



*Fig. 4: Bloc diagram of the electric power circuit of a diesel-electric tank, equipped with a MDS*

### IV. System advantages of an electric MBT having a MDS as a main storage

When evaluating the utility of an MDS system in an electric main battle tank (MBT), it is necessary to evaluate how this storage system can contribute to increase the tactical performance of the system. The tactical system performance is determined by several

criteria, three of which are relevant for our considerations and will be discussed in the following sections. The relevant criteria are

- Mobility
- Survivability
- Firepower

Additional criteria relevant to the system performance, such as logistics will not be considered here.

Generally speaking, the flexibility of the energy supply on board the vehicle increases considerably when using an MDS system, since the MDS can either replace or supplant the primary energy source during a period ranging from approx. several dozen seconds to several minutes. This means that if the maximum power of the MDS is 3 MW and that of the diesel-generator unit is 1 MW, the vehicle will have 4 MW available for a short period of time. This maximum power can serve to supply the vehicle's weapons and active defence systems. Since the combined corner power of the drive motors is approx. 6 MW, because they are designed to deliver high torque values, the available system power can also be used to supply the drive motors, which results in a significant increase in mobility.

The following activities are possible with a vehicle which is equipped with a 60 MJ / 3 MW MDS:

- *A sufficient supply of energy to the pulse storage units for electric weaponry and active protection systems.*

The electrothermal-chemical gun (ETC) is assumed to require 6 MJ of energy per discharge, which would mean that the energy stored in the MDS would last for 10 shots in this simplified scenario. Going further in detail, one has to take into account that the power that can be delivered by the MDS reduces, while the MDS is discharged. To be able to deliver for example 1.5 MW, the MDS must still have a reserve of 20 % of its rated energy capacity. But this seems to be no serious restriction, because there is no need to fire the gun 10 times in succession, so that there is ample opportunity to recharge the MDS with the diesel-generator unit.

- *A significant increase in acceleration at all speed ranges.*

As mentioned above, the MDS and the diesel engine can deliver 4 MW for short periods of time. Even with the diesel turned off, the vehicle would have considerably better acceleration values with the 3 MW maximum power from the MDS than a diesel-electrical and especially a conventional diesel-mechanical vehicle. With 3 MW total power, acceleration from 0 to 70 km/h is possible in 6 - 8 s in all kinds of (flat) terrain.

- *Considerably increased manoeuvrability especially in heavy terrain.*

The MDS can provide the system with maximum power for special manoeuvres, to match a sudden threat or to overcome specific conditions of terrain.

- *Ambush action from cover, with diesel engine turned off.*

- *Rapid startup of the diesel engine to maximum speed.*

Approximately 1 MJ is necessary to start up the diesel and push it to maximum speed. An MDS unit with its enormous power can rapidly accelerate the diesel, extensively improving the survivability of the vehicle.

- *Surveillance from safe position with diesel engine turned off and full combat readiness.*

The IR and noise signatures are reduced drastically by turning off the diesel engine. The MDS guarantees not only absolute readiness of the ETC but also unlimited availability of power to the drives.

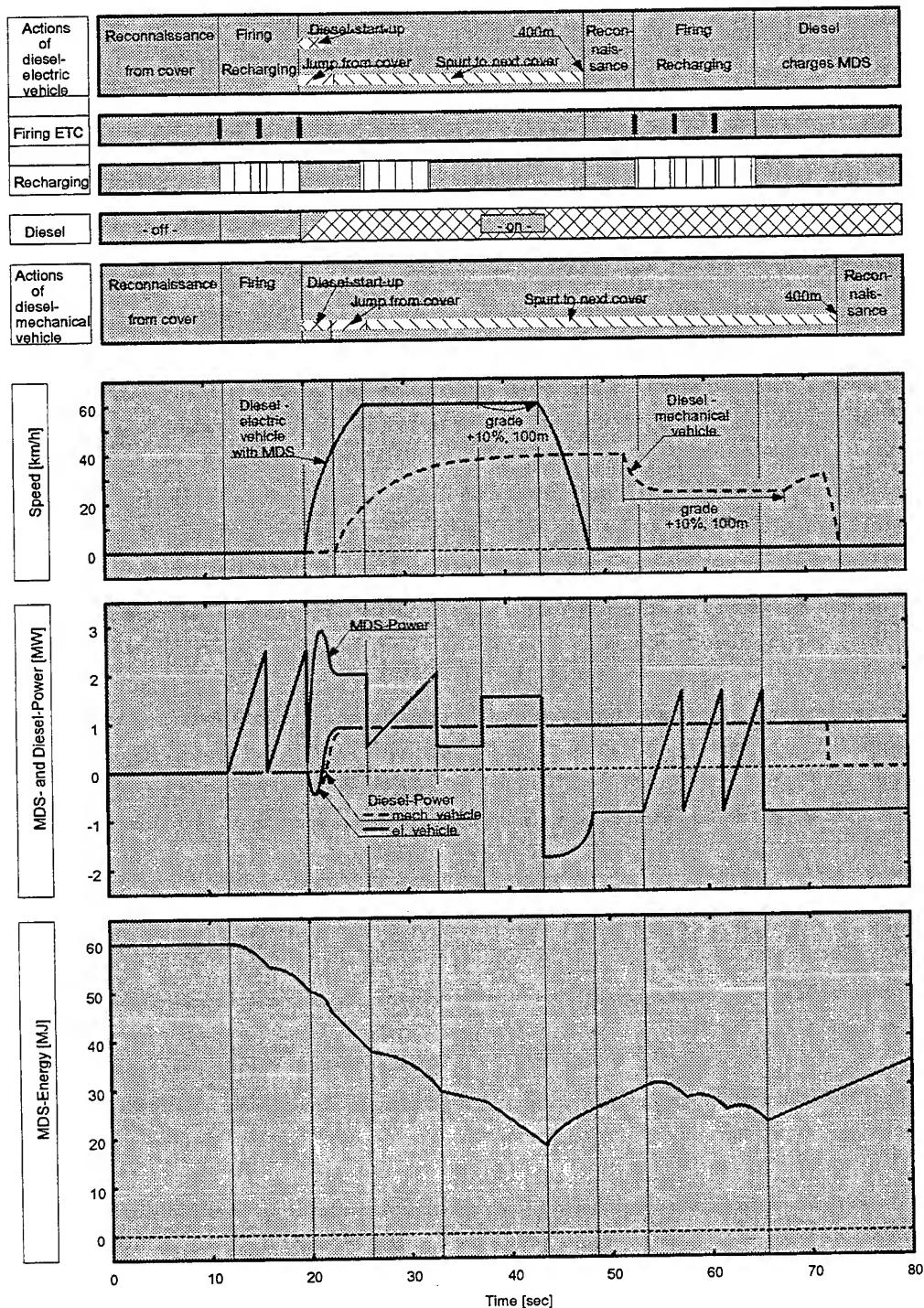
- *A reduction of fuel consumption and an increase in the operating range result from the option to recover the brake energy and to perform an expanded peak levelling while travelling.*
  - *Stealth movement option over a distance exceeding 1 km.*
  - *River crossing option with power from the storage unit.*
- This possibility offers a decisive reduction in time and logistics as compared to a river crossing with a diesel-powered vehicle, because there is no need to funnel in air nor funnel out the exhaust fumes.
- *Sufficient power for future internal and/or external secondary consumers in turned-off mode of the diesel engine, especially if these consumers require high power.*
  - *Redundant system if the diesel engine or the generator should fail.*

With the MDS unit a limp home capability is guaranteed with several possibilities of proceeding. With a fully charged MDS the vehicle is able to bridge a distance of over 1 km (to find cover, for example), depending on the situation or terrain conditions. For longer distances, it would be possible to connect the crippled vehicle via cable to another electric vehicle, which would supply sufficient mid-range power to limp home. The MDS would then make it possible to overcome any terrain.

## **V. Example of a scenario with successive driving and firing actions**

To illustrate and demonstrate the possibilities, the following chapter and Figure 5 will describe a series of actions that can be carried out with the vehicle and MDS example. The individual actions are as follows:

- Reconnaissance from cover position with diesel engine turned off, fully charged MDS and fully charged ETC pulse storage unit.
- Three discharges with the ETC, recharge from the MDS at 6 MJ/4 s.
- Jump from cover with 1 MW power output from the MDS for 4 seconds.
- At the same time rapid start-up of the diesel engine via the generator within approx. 2 sec, with a total of 1 MJ of energy output from the MDS
- Spurt to next possibility of cover, overcoming a distance of 400 m, with 1.2 MW power output from the MDS, for a period of 20 sec, and 1 MW power output from the diesel-generator. After the vehicle reaches 60 km/h, part of the power coming from the MDS is used to recharge the pulse storage unit of the ETC (6 MJ) for the remaining seconds, the dash takes.
- Regenerative braking recovers approx. 4 MJ, which is used to recharge the MDS.
- The vehicle waits under the new cover and can use the full power of the diesel engine to recharge the MDS unit.
- After a short orientation period under cover, the vehicle's crew can immediately resume fire with the electric weapons.



**Fig.5:** Description of a series of actions that can be carried out with the MDS-equipped electric tank example, and comparison with the drive and acceleration capability of a diesel-mechanical vehicle. The upper four parts of the graphic give the assumed actions of the MDS-equipped electric tank. The fifth part of this graphic gives the respective action of a diesel-mechanical tank, based on its lower system performance. The sixth and seventh part show the speed and the power rate of the power supply components of the electrical (—) and diesel-mechanical (---) vehicle. The bottom illustration shows the energy contents of the MDS during the actions.

The actions and their succession as well as a comparison with a diesel-mechanical vehicle are shown in Figure 5. The upper illustrations of the figure show the actions and the operating states of the respective components. The illustration underneath shows the vehicle movement profiles. Below that, the figure displays the MDS and diesel power behaviour. Power output from the components is represented with a plus symbol and power input to the components with a minus symbol. The bottom illustration shows the energy administration of the MDS, based on a fully charged 60 MJ MDS unit.

## VI. Conclusions and outlook

The discussion of the possibilities resulting for the vehicle used as an example show that a vehicle equipped with such a 60 MJ / 3 MW-MDS unit would offer considerable increases in the quantitative system performance and it would open up new opportunities. A weapon with a power requirement of several MJ per discharge requires a storage unit that will recharge the pulse system for a succession of discharges because the primary power unit (the diesel engine) cannot deliver the necessary power. Even if the primary power unit were able to deliver sufficient power, it could do so only with a long delay, considering that action should also start from silent surveillance mode. The MDS unit would be a substantial advantage also to supply the power for secondary weapons and active protection of the vehicle.

There are drastic advantages in the mobility of the vehicle, because on the one hand, the combined power of the diesel engine-generator unit and the MDS unit can be added up to 4 MW and on the other hand, the MDS unit alone can provide a maximum of 3 MW for silent operation.

Other advantages related to redundancy of systems or fuel savings as well as for example the possibility of crossing rivers enhance the application spectrum of an MDS unit in a MBT.

## References

- [1] M. HEEG, G. HEIDELBERG, P. EHRHART, G. REINER, W. WECK: **Electric Drive and High Energy Storage Systems for Tracked and Wheeled Combat Vehicles - The Future Electric Weapon Platform**. 1<sup>st</sup> Int. Conf. on AECV, Haifa, Israel, May 1995
- [2] M. HEEG, G. HEIDELBERG, P. EHRHART, G. REINER, W. WECK: **Power Supply System for Electromagnetic Launch Applications - Results of Component Tests**. Proc. 5<sup>th</sup> Europ. Symp. EML Techn., Toulouse, France, April 1995
- [3] P. EHRHART, M. HEEG, G. HEIDELBERG, G. REINER, W. WECK: **The Magnet-Motor Energy Supply System for EML together with a new Coil-Accelerator Concept**. Proc. 6<sup>th</sup> Symp. EML Techn., Austin, TX, 1992
- [4] G. HEIDELBERG, G. REINER: **The Magnetodynamic Storage Unit - Test Results of an Electrical Flywheel Storage System in a Public Transport Bus with a Diesel-Electrical Drive**. IECEC Proceedings, Denver, Colorado, 1988

## LIST OF PARTICIPANTS

---

ANDERSSON, Mr. G.  
FOA, Defence Research Establishment  
Sweden  
**Bad Hotel**

ANDREASSON, Mr. H.  
FOA, Defence Research Establishment  
Sweden  
**Ibis Hotel**

ANDREU, Mr. H.  
DGA  
France

ANISIMOV, Dr. G.  
Lavrentyev Institute of Hydrodynamics  
Russia  
**Atlanta Zee Hotel**

BARTELS, Drs. P.J.  
Ministry of Defence, Directorate-General  
of Material  
The Netherlands

BAUDER, Prof. dr. H.  
Technical University Munich  
Germany  
**Atlanta Zee Hotel**

BERG, Mr. H.C.  
FMV  
Sweden  
**Kurhaus Hotel**

BOGDANOV, Dr. A.V.  
State Committee for Science and Technology  
of the Russian Federation  
Russia  
**Atlanta Zee Hotel**

BRAMOULLÉ, Mr. M.  
Thomson CSF  
France  
**Bad Hotel**

CAILLAU, Mr. F.  
Giat Industries  
France  
**Atlanta Zee Hotel**

CANNAVÓ, ICA C.  
DGA  
France  
**Carlton Beach Hotel**

CHEMERYS, Dr. T.  
Institute of Electrodynamics Ukrainian National  
Academy of Sciences  
Ukraine  
**Carlton Beach Hotel**

CHRYSSOMALLIS, Dr. G.  
Science Applications International Corporation  
(SAIC)  
USA  
**Kurhaus Hotel**

CHUNG, Mr. K.J.  
Seoul National University  
Rep. of Korea

CONDUROVICI, Maj. eng. M.  
Ministry of National Defence  
Roumania  
**Atlanta Zee Hotel**

CRITCHLEY, Dr. R.  
DERA  
UK  
*Mrs. D. Critchley*  
**Atlanta Zee Hotel**

DAKIN, Dr. R.  
Science Applications International Corporation  
USA

DARÉE, Dr. K.  
French German Research Institute of  
Saint-Louis (ISL)  
France  
**Atlanta Zee Hotel**

DRIGA, Prof. dr. M.D.  
University of Texas at Austin  
USA  
**Kurhaus Hotel**

EDWARDS, Mr. C.D.G.  
DERA  
UK

EKELUND, Mr. T.  
Bofors AB, Weapon Systems  
Sweden  
**Kurhaus Hotel**

FAIR, Dr. D.  
University of Texas at Austin  
USA  
**Kurhaus Hotel**

## LIST OF PARTICIPANTS

---

FISH, Dr. S.  
University of Texas at Austin  
USA  
**Kurhaus Hotel**

FORD, LT S.  
United States Navy, The Chief of Naval  
Operations' Strategic Studies Group  
USA  
**Kurhaus Hotel**

FRANÇOIS, Dr. C.F.  
Giat Industries  
France  
**Kurhaus Hotel**

FULLER, Mr. S.R.  
DERA  
UK  
**Bad Hotel**

GALANIN, Prof. M.P.  
Keldysh Institute of Applied Mathematics  
The Russian Academy of Science  
Russia

GILMAN, Mr. M.  
PRIMEX Physics International  
USA  
**Carlton Beach Hotel**

GORA, Mr. Th.  
US Army ARDEC  
USA  
**Atlanta Zee Hotel**

GUSTAVSSON, Mr. L.  
Bofors AB, Weapon Systems  
Sweden  
**Kurhaus Hotel**

HA, Dr. H.C.  
Korea Heavy Industries &  
Construction Co., Ltd.  
Rep. of Korea

HAINSWORTH, Dr. G.M.G.  
DERA  
UK

HAUGH, Mr. D.C.  
Defence Research Agency  
United Kingdom  
**Kurhaus Hotel**

HEEG, Mr. R.  
Magnet-Motor GmbH  
Germany

HENSEL, Dr. D.  
French German Research Institute of  
Saint-Louis (ISL)  
France  
**Atlanta Zee Hotel**

JAMES, Mr. T.E.  
JEM Systems  
United Kingdom  
**Carlton Beach Hotel**

JAMET, Dr. F.J.  
French German Research Institute of  
Saint-Louis (ISL)  
France  
**Kurhaus Hotel**

JOHANSSON, Mr. S.  
Bofors AB, Weapon Systems  
Sweden  
**Kurhaus Hotel**

JOHNSON, Mr. L.  
US Army Research Laboratory  
USA  
**Carlton Beach Hotel**

JONES, Mr. D.G.  
DERA  
UK

JORDAN, Mr. Y.  
Giat Industries  
France  
**Atlanta Zee Hotel**

KAPLAN, Dr. Z.  
Soreq N.R.C.  
Israel

KARTHAUS, Mr. W.  
TNO Prins Maurits Laboratory  
The Netherlands  
*Mrs N. Karthaus*

KIM, Mr. J.S.  
Agency for Defense Development  
Rep. of Korea

## LIST OF PARTICIPANTS

---

KLEBING, Mr. J.  
Wegmann & Co. GmbH  
Germany  
**Carlton Beach Hotel**

KOLKERT, Dr. W.J.  
TNO Prins Maurits Laboratory  
The Netherlands  
*Mrs E. van Puffelen*

KOOPS, Mr. M.  
TNO Prins Maurits Laboratory  
The Netherlands

KRUSE, Dr. H.  
TZN Unterlüß GmbH  
Germany  
**Ibis Hotel**

LADD, Mr. D.  
US Army ARDEC  
USA  
**Bad Hotel**

LEBEAU, Mr. F.  
US Army  
USA  
**Ibis Hotel**

LEHMANN, Dr. P.  
French German Research Institute of  
Saint-Louis (ISL)  
France  
**Kurhaus Hotel**

LEVINE, Mr. F.  
Maxwell Technologies, Inc./ Federal Division  
USA  
**Carlton Beach Hotel**

LEWIS, Mr. D.R.  
HQS Defense Special Weapons Agency  
(D.S.W.A.)  
USA  
**Carlton Beach Hotel**

MA, Mr. K.H.  
Korea Heavy Industries &  
Construction Co., Ltd.  
Rep. of Korea

MACDOUGALL, Mr. F.  
Maxwell Technologies  
USA  
**Ibis Hotel**

MAGUDER, Mr. L.  
Defense Special Weapons Agency (D.S.W.A.)  
USA  
**Carlton Beach Hotel**

MALY, Dr. V.I.  
Lavrentyev Institute of Hydrodynamics  
Russia  
**Atlanta Zee Hotel** -

MARSHALL, Dr. R.  
University of Texas at Austin  
USA  
**Kurhaus Hotel**

McNAB, Dr. R.  
University of Texas at Austin  
USA  
**Kurhaus Hotel**

MILLS, Mr. R.J.  
DERA  
UK  
**Bad Hotel**

MORGAN, Dr. E.  
US Army Materiel Command  
Germany  
*Mrs I. Morgan*  
**Atlanta Zee Hotel**

MÜLLER, Mr. C.  
French German Research Institute of  
Saint-Louis (ISL)  
France  
*Mrs A.M. Müller*  
**Atlanta Zee Hotel**

MÜLLER, Mr. A.  
Magnet-Motor GmbH  
Germany  
**Bad Hotel**

MURPHY, Mr. D.  
Lockheed Martin Vought Systems  
USA  
*Mrs L. Murphy*

PAEK, Mr. K.H.  
Seoul National University  
Rep. of Korea  
**Bad Hotel**



## LIST OF PARTICIPANTS

---

PARKER, Dr. J.  
University of Texas at Austin  
USA  
**Kurhaus Hotel**

PERSAD, Dr. C.  
University of Texas at Austin  
USA  
**Kurhaus Hotel**

PETER, Dr. H.  
French German Research Institute of  
Saint-Louis (ISL)  
France  
**Atlanta Zee Hotel**

REINER, Dr. G.S.K.  
Magnet-Motor GbmH  
Germany  
**Bad Hotel**

REITS, Drs. B.J.  
Hollandse Signaalapparaten B.V.  
The Netherlands

ROEMHILD, Mr. W.  
Industrieanlagen-Betriebsgesellschaft mbH  
Germany  
**Atlanta Zee Hotel**

RUTGERS, Prof. dr. R.  
Kema Nederland B.V.  
The Netherlands

SARJEANT, Prof. W.J.  
High Power Electronics Institute  
USA  
**Kurhaus Hotel**

SCHMIDT, Dr. M.  
Army Research Laboratory  
USA  
**Atlanta Zee Hotel**

SCHMITT, Ms. A.G.  
French German Research Institute of  
Saint-Louis (ISL)  
France  
**Atlanta Zee Hotel**

SCHOOLDERMAN, Dr. A.J.  
TNO Prins Maurits Laboratory  
The Netherlands

SCHOT, Prof. J.A.  
The Netherlands

SCOTT, Mr. D.J.  
DERA  
UK

SHCOLNIKOV, Mr. E.Ya.  
Moscow Engineering Physics Institute  
Russia  
**Atlanta Zee Hotel**

SHVETSOV, Dr. A.  
Lavrentyev Institute of Hydrodynamics  
Russia  
**Atlanta Zee Hotel**

SONG, Mr. S.H.  
Korea Heavy Industries &  
Construction Co., Ltd.  
Rep. of Korea

SPAHN, Dr. E.  
French German Research Institute of  
Saint-Louis (ISL)  
France  
**Atlanta Zee Hotel**

TYUTIN, Dr. V.K.  
State Research Institute of Applied Mechanics  
and Electrodynamics of  
Moscow State Aviation Institute  
Russia  
**Atlanta Zee Hotel**

VAN DER PLOEG, Mr. B.  
MOD NL Navy  
The Netherlands

VAN DIJK, Ir. E.  
Delft University of Technology  
The Netherlands

VAN DONGEN, Mr. A.A.F.  
RDM Technology b.v.  
The Netherlands

VAN GELDER, Ir. P.  
TNO Prins Maurits Laboratory  
The Netherlands

VAN HOEK, Drs. E.A.  
Ministry of Defence  
The Netherlands

VANCE, Mr. K.  
Royal Ordnance Plc.  
UK

## LIST OF PARTICIPANTS

---

WALES, Mr. K.

DERA

UK

WEGNER, Dr. V.

French German Research Institute of  
Saint-Louis (ISL)

France

**Atlanta Zee Hotel**

WEIR, Mr. W.F.

Ministry of Defence

UK

WEISE, Dr. H.G.G.

TZN Forschungs- und Entwicklungszentrum

Unterlüß GmbH

Germany

**Bad Hotel**

WEY, Mr. J.

French German Research Institute of  
Saint-Louis (ISL)

France

**Atlanta Zee Hotel**

WISKEN, Dr. H.

TZN Forschungs- und Entwicklungszentrum

Unterlüß GmbH

Germany

**Bad Hotel**

WITALIS, Dr. A.

National Defence Research Establishment  
Sweden

**Bad Hotel**

WOLFE, Mr. T.

Maxwell Technologies, Inc./Federal Division

USA

**Carlton Beach Hotel**

WOODLEY, Mr. C.

DERA

UK

**Bad Hotel**

WOODS, Prof. L.C.

University of Texas at Austin

UK

ZABAR, Prof. Z.

Polytechnic University

USA

*Ms L. Zabar*

**Atlanta Zee Hotel**

ZIELINSKI, Mr. A.E.Z.

US Army Research Laboratory (ARL),

AMSRL-WT-PB

USA

*Ms K.A.H. Hoover*

**Bad Hotel**

ZOLER, Dr. I.

Tel-Aviv University

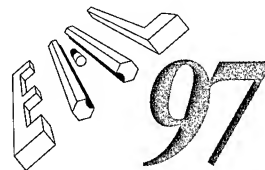
Israel

*Mrs C.H. Zoler*

**Bad Hotel**

# 6th European Symposium on Electromagnetic Launch Technology

The Hague, 25 - 28 May, 1997



# 6th European Symposium on Electromagnetic Launch Technology

The Hague, 25 - 28 May, 1997

